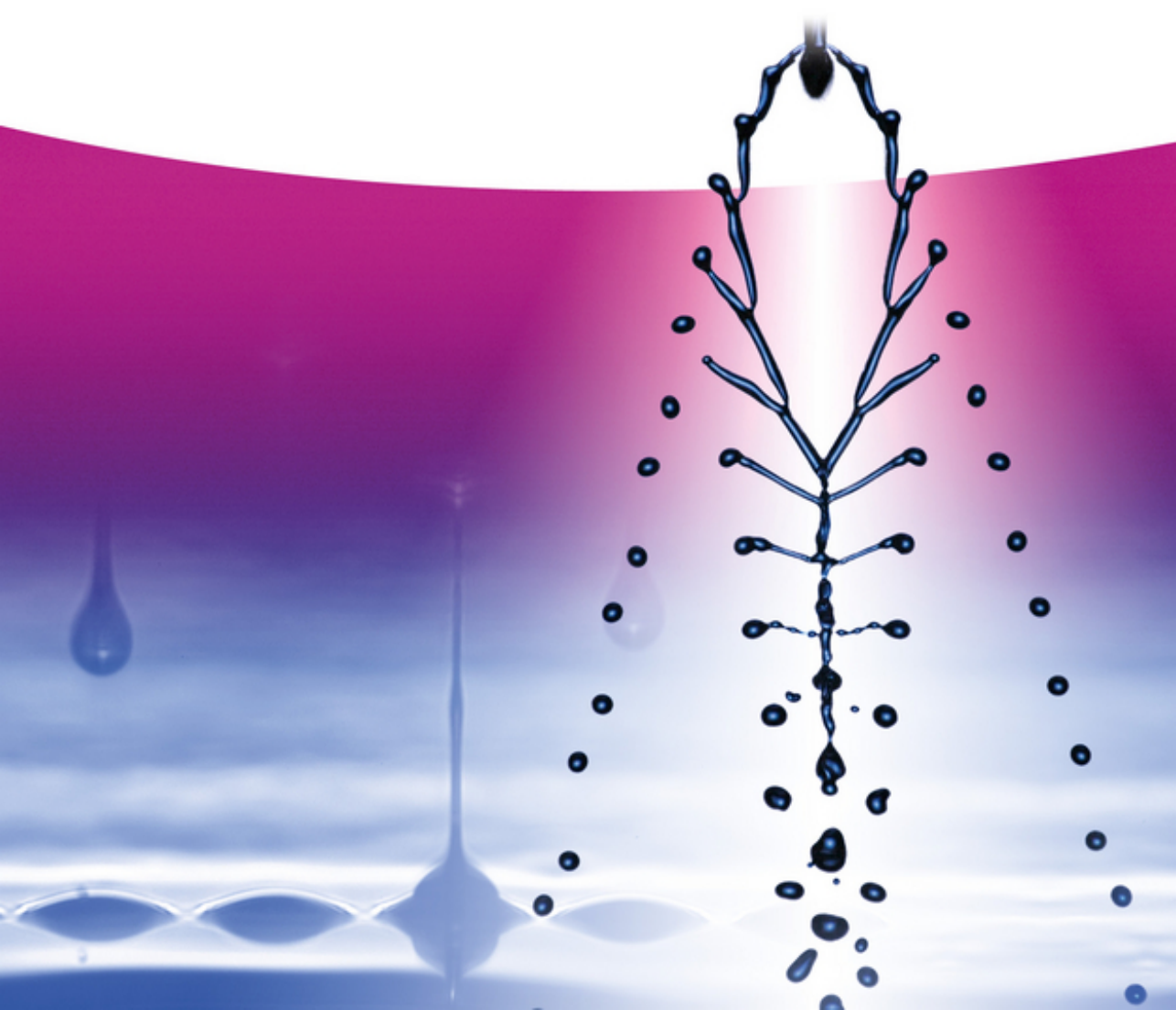


Edited by Stephen D. Hoath

# Fundamentals of Inkjet Printing

The Science of Inkjet and Droplets





*Edited by*  
*Stephen D. Hoath*

**Fundamentals of Inkjet Printing**





*Edited by*  
*Stephen D. Hoath*

# **Fundamentals of Inkjet Printing**

The Science of Inkjet and Droplets

**WILEY-VCH**  
Verlag GmbH & Co. KGaA

## Editor

*Dr. Stephen D. Hoath*  
University of Cambridge  
Department of Engineering  
Institute for Manufacturing  
17 Charles Babbage Road  
Cambridge CB3 0FS  
United Kingdom

Cover image: © by Stephen D. Hoath

All books published by **Wiley-VCH** are carefully produced. Nevertheless, authors, editors, and publisher do not warrant the information contained in these books, including this book, to be free of errors. Readers are advised to keep in mind that statements, data, illustrations, procedural details or other items may inadvertently be inaccurate.

Library of Congress Card No.: applied for

### British Library Cataloguing-in-Publication Data

A catalogue record for this book is available from the British Library.

### Bibliographic information published by the Deutsche Nationalbibliothek

The Deutsche Nationalbibliothek lists this publication in the Deutsche Nationalbibliografie; detailed bibliographic data are available on the Internet at <<http://dnb.d-nb.de>>.

© 2016 Wiley-VCH Verlag GmbH & Co. KGaA, Boschstr. 12, 69469 Weinheim, Germany

All rights reserved (including those of translation into other languages). No part of this book may be reproduced in any form – by photoprinting, microfilm, or any other means – nor transmitted or translated into a machine language without written permission from the publishers. Registered names, trademarks, etc. used in this book, even when not specifically marked as such, are not to be considered unprotected by law.

Print ISBN: 978-3-527-33785-9

ePDF ISBN: 978-3-527-68473-1

ePub ISBN: 978-3-527-68483-0

Mobi ISBN: 978-3-527-68474-8

oBook ISBN: 978-3-527-68472-4

Cover Design Formgeber, Mannheim, Germany

Typesetting SPi Global, Chennai, India

Printing and Binding

Printed on acid-free paper

## Contents

**List of Contributors** *XV*

**Preface** *XXI*

- 1**      **Introductory Remarks** *1*  
*Ian M. Hutchings, Graham D. Martin, and Stephen D. Hoath*
- 1.1      Introduction *1*
- 1.2      Drop Formation: Continuous Inkjet and Drop-on-Demand *2*
- 1.3      Surface Tension and Viscosity *6*
- 1.4      Dimensionless Groups in Inkjet Printing *8*
- 1.5      Length and Time Scales in Inkjet Printing *9*
- 1.6      The Structure of This Book *11*
- 1.7      Symbols Used *11*  
References *12*
  
- 2**      **Fluid Mechanics for Inkjet Printing** *13*  
*Edward P. Furlani*
- 2.1      Introduction *13*
- 2.2      Fluid Mechanics *13*
- 2.3      Dimensions and Units *14*
- 2.4      Fluid Properties *15*
- 2.4.1    Density *15*
- 2.4.2    Viscosity *16*
- 2.4.2.1    Newtonian Fluids *17*
- 2.4.2.2    Non-Newtonian Fluids *17*
- 2.4.3    Surface Tension *18*
- 2.5      Force, Pressure, Velocity *19*
- 2.6      Fluid Dynamics *20*
- 2.6.1    Equations of Fluid Dynamics *20*
- 2.6.1.1    Conservation of Mass *21*
- 2.6.1.2    Conservation of Momentum *21*
- 2.6.1.3    Conservation of Energy *22*
- 2.6.2    Solving the Equations of Fluid Dynamics *24*
- 2.7      Computational Fluid Dynamics *25*

2.7.1	Preprocessor	26
2.7.2	Solver	28
2.7.3	Postprocessor	28
2.8	Inkjet Systems	29
2.8.1	Inkjet Modeling Challenges	31
2.8.1.1	Free-Surface Analysis	32
2.8.1.2	Fluid–Structure Interaction	35
2.8.1.3	Phase Change Analysis	35
2.8.1.4	Ink–Media Interaction	35
2.8.1.5	Non-Newtonian Fluids	35
2.8.2	Inkjet Processes	36
2.8.2.1	DOD Droplet Generation	36
2.8.2.2	CIJ Droplet Generation	43
2.8.2.3	Crosstalk	45
2.8.2.4	Aerodynamic Effects	47
2.8.2.5	Ink–Media Interactions	48
	Summary	52
	Acknowledgments	53
	References	53
<b>3</b>	<b>Inkjet Printheads</b>	<b>57</b>
	<i>Naoki Morita, Amol A. Khalate, Arend M. van Buul, and Herman Wijshoff</i>	
3.1	Thermal versus Piezoelectric Inkjet Printing	57
3.2	Thermal Inkjet	58
3.2.1	Boiling Mechanism	58
3.2.1.1	Theoretical Model	58
3.2.1.2	Observation of Boiling Bubble Behavior	59
3.2.2	Printhead Structure	63
3.2.3	Jetting Characteristics of TIJs	64
3.2.3.1	Input Power Characteristics and Heat Control of TIJs	64
3.2.3.2	Frequency Response and Crosstalk Control	65
3.2.4	Problems Associated with Pressure and Heat Generated in TIJs	66
3.2.4.1	Cavitation Damage on the Heater Surface	66
3.2.4.2	Ink Residue Scorching (Kogation) on the Heater Surface	67
3.2.5	Evaporation of Water in Aqueous Ink	69
3.2.5.1	Approaches to Compensate for Condensed Ink through Evaporation	69
3.2.5.2	Measurement of Physical Properties of Flying Droplets	70
3.3	Future Prospects for Inkjets	72
3.3.1	Printing Speed Limit Estimated by Drop Behavior	72
3.3.2	Control of Bleeding Caused by High-Speed Drying	72
3.4	Continuous Inkjet (CIJ)	74
3.5	Examples and Problems (TIJ)	76
3.5.1	Example	76
3.5.2	Problem	76

3.6	Piezo Inkjet Printhead	78
3.6.1	Introduction	78
3.6.2	Working Principle	79
3.6.3	Ink Channel Behavior	82
3.6.3.1	Residual Oscillations	82
3.6.4	Control of Inkjet Printhead	84
3.6.4.1	Constrained Actuation Pulse Design	84
3.6.4.2	Complex Actuation Pulse Design: Feedforward Control Approach	86
3.6.5	Industrial Applications	88
	References	89
<b>4</b>	<b>Drop Formation in Inkjet Printing</b>	<b>93</b>
	<i>Theo Driessen and Roger Jeurissen</i>	
4.1	Introduction	93
4.1.1	Continuous Inkjet Printing	93
4.1.2	Drop-on-Demand Inkjet Printing	94
4.2	Drop Formation in Continuous Inkjet Printing	95
4.2.1	Rayleigh–Plateau Instability	96
4.2.2	Satellite Formation	99
4.2.3	Final Droplet Velocity	99
4.2.3.1	Capillary Deceleration	99
4.2.3.2	Acceleration due to Advection	101
4.3	Analysis of Droplet Formation in Drop-on-Demand Inkjet Printing	102
4.3.1	The Scenario of the Analyzed Droplet Formation	102
4.3.1.1	Head Droplet Formation	103
4.3.1.2	Tail Formation	105
4.3.1.3	Pinch-Off and Tail Breakup	108
4.4	Worked Examples	111
4.4.1	Tail Formation for the Purely Inertial Case	111
4.4.2	Dispersion Relation of the Rayleigh–Plateau Instability	112
	Acknowledgment	114
	References	114
<b>5</b>	<b>Polymers in Inkjet Printing</b>	<b>117</b>
	<i>Joseph S.R. Wheeler and Stephen G. Yeates</i>	
5.1	Introduction	117
5.2	Polymer Definition	117
5.3	Source- and Architecture-Based Polymer Classification	118
5.4	Molecular Weight and Size	118
5.5	Polymer Solutions	122
5.6	Effect of Structure and Physical Form on Inkjet Formulation Properties	124
5.7	Zimm Interpretation for Polymers in High Shear Environments	125

5.8	Printability of Polymer-Containing Inkjet Fluids	126
5.9	Simulation of the Inkjet Printing of High-Molecular-Weight Polymers	129
5.10	Molecular Weight Stability of Polymers during DOD Inkjet Printing	130
5.11	Molecular Weight Stability of Polymers during CIJ Printing	132
5.12	Molecular Weight Stability of Associating Polymers During DOD Inkjet Printing	134
5.13	Case Studies of Polymers in Inkjet Formulation	135
5.13.1	Role of Polymer Architecture	135
5.13.2	Inkjet Printing of PEDOT:PSS	136
5.13.3	Inkjet Printing of Polymer–Graphene and CNT Composites	136
	References	137
<b>6</b>	<b>Colloid Particles in Ink Formulations</b>	<b>141</b>
	<i>Mohmed A. Mulla, Huai Nyin Yow, Huagui Zhang, Olivier J. Cayre, and Simon Biggs</i>	
6.1	Introduction	141
6.1.1	Colloids	141
6.1.2	Inkjet (Complex) Fluids	141
6.2	Dyes versus Pigment Inks	142
6.3	Stability of Colloids	143
6.3.1	DLVO Theory	144
6.3.2	van der Waals Attractive Force	144
6.3.3	Electrostatic Repulsive Force	145
6.3.4	Stabilization of Colloidal Systems	146
6.4	Particle–Polymer Interactions	149
6.4.1	Steric Stabilization	149
6.4.2	Bridging Flocculation	150
6.4.3	Depletion Flocculation	151
6.5	Effect of Other Ink Components on Colloidal Interactions	152
6.5.1	Surfactants	152
6.5.2	Viscosity Modifiers	153
6.5.3	Humectants	153
6.5.4	Glycol Ethers	154
6.5.5	Storage – Buffers and Biocides	154
6.5.6	Other Additives	155
6.6	Characterization of Colloidal Dispersions	155
6.6.1	Dynamic Light Scattering (DLS)	155
6.6.2	Electrophoretic Mobility (Zeta Potential)	156
6.6.3	Rheology	157
6.6.4	Bulk Colloidal Dispersion	157
6.6.5	Jetting	159
6.7	Sedimentation/Settling	160
6.7.1	Sedimentation Characterization Techniques	162

6.8	Conclusions/Outlook	165
	References	166
<b>7</b>	<b>Jetting Simulations</b>	<b>169</b>
	<i>Neil F. Morrison, Claire McIlroy, and Oliver G. Harlen</i>	
7.1	Introduction	169
7.2	Key Considerations for Modelling	172
7.3	One-Dimensional Modelling	177
7.3.1	The Long-Wavelength Approximation	177
7.3.2	A Simple CIJ Model	178
7.3.3	Error Analysis for Simple Jetting	180
7.3.4	Validation of the Model by Rayleigh's Theory	180
7.3.5	Exploring the Parameter Space	183
7.3.6	A Numerical Experiment	184
7.4	Axisymmetric Modelling	185
7.4.1	Continuous Inkjet	186
7.4.2	Drop-on-Demand	189
7.5	Three-Dimensional Simulation	194
	References	196
<b>8</b>	<b>Drops on Substrates</b>	<b>199</b>
	<i>Sungjune Jung, Hyung Ju Hwang, and Seok Hyun Hong</i>	
8.1	Introduction	199
8.2	Experimental Observation of Newtonian Drop Impact on Wettable Surface	201
8.2.1	Effect of Initial Speed on Drop Impact and Spreading	202
8.2.2	Effect of Surface Wettability on Drop Impact and Spreading	206
8.2.3	Effect of Fluid Properties on Drop Impact and Spreading	208
8.3	Dimensional Analysis: The Buckingham Pi Theorem	209
8.4	Drop Impact Dynamics: The Maximum Spreading Diameter	211
8.4.1	Viscous Dissipation Dominates Surface Tension	213
8.4.2	The Flattened-Pancake Model	214
8.4.3	The Kinetic Energy Transfers Completely into Surface Energy	215
8.4.3.1	Evaporation: A Scaling Exponent of the Radius	216
	References	218
<b>9</b>	<b>Coalescence and Line Formation</b>	<b>219</b>
	<i>Wen-Kai Hsiao and Eleanor S. Betton</i>	
9.1	Implication of Drop Coalescence on Printed Image Formation	219
9.2	Implication of Drop Coalescence on Functional and 3D Printing	220
9.3	Coalescence of Inkjet-Printed Drops	222
9.3.1	Coalescence of a Pair of Liquid Drops on Surface	222
9.3.2	Coalescence with Drop Impact	226
9.3.3	Coalescence of a Pair of Inkjet-Printed Drops	229

9.3.3.1	Experimental Setup	230
9.3.3.2	Necking Stage Dynamics	230
9.3.3.3	Discussion	234
9.3.3.4	Summary	234
9.4	2D Features and Line Printing	235
9.4.1	Model of Drop–Bead Coalescence	236
9.4.2	Experiment and Observations	237
9.4.2.1	Effect of Drop Spacing	238
9.4.2.2	Effect of Drop Deposition Interval	242
9.4.3	Stability Regimes and Discussion	244
9.4.4	Summary	246
9.5	Summary and Concluding Remarks	247
9.6	Working Questions	248
	References	249
<b>10</b>	<b>Droplets Drying on Surfaces</b>	<b>251</b>
	<i>Emma Talbot, Colin Bain, Raf De Dier, Wouter Sempels, and Jan Vermant</i>	
10.1	Overview	251
10.2	Evaporation of Single Solvents	252
10.3	Evaporation of Mixed Solvents	259
10.3.1	Marangoni Flows	260
10.3.1.1	Thermal Marangoni Flows	260
10.3.1.2	Solutal Marangoni Flows	262
10.4	Particle Transport in Drying Droplets	263
10.4.1	The “Coffee Ring Effect”	263
10.4.1.1	Disadvantages to the Ring-Shaped Pattern	265
10.4.1.2	Exploiting the Coffee Ring Effect	266
10.4.1.3	Avoiding the Coffee Ring Effect	267
10.4.2	Particle Migration	268
10.5	Drying of Complex Fluids	268
10.5.1	Contact Line Motion	269
10.5.2	Particle Character	269
10.5.3	Segregation of Solids	272
10.5.4	Local Environment	273
10.5.5	Substrate Patterning	273
10.5.6	Destabilization of Colloids during Drying	274
10.6	Problems	274
	References	275
<b>11</b>	<b>Simulation of Drops on Surfaces</b>	<b>281</b>
	<i>Mark C T Wilson and Krzysztof J Kubiak</i>	
11.1	Introduction	281
11.2	Continuum-Based Modeling of Drop Dynamics	282
11.2.1	Finite Element Analysis	282
11.2.2	Finite Element Boundary Conditions for Free Surfaces	283



11.2.3	The Moving Contact-Line Problem	284
11.2.3.1	The Contact Angle as a Boundary Condition	285
11.2.3.2	An Interface Formation Model	285
11.2.4	The Volume of Fluid Method	286
11.3	Challenging Contact Angle Phenomena	288
11.3.1	Apparent Contact Angles	288
11.3.2	Contact Angle Hysteresis	289
11.3.3	Dynamic Contact Angles	291
11.3.4	Dynamic Contact Angles in Numerical Simulations	292
11.3.5	Resting Time Effect	293
11.4	Diffuse-Interface Models	294
11.5	Lattice Boltzmann Simulations of Drop Dynamics	296
11.5.1	Background and Advantages of the Method	296
11.5.2	Multiphase Flow and Wetting	299
11.5.3	Capturing Contact Angle Hysteresis	301
11.5.4	Rough Surfaces	305
11.5.5	Chemically Inhomogeneous Surfaces	306
11.6	Conclusion and Outlook	307
	Acknowledgment	309
	References	309
<b>12</b>	<b>Visualization and Measurement</b>	<b>313</b>
	<i>Kye Si Kwon, Lisong Yang, Graham D. Martin, Rafael Castrejón-García, Alfonso A. Castrejón-Pita, and J. Rafael Castrejón-Pita</i>	
12.1	Introduction	313
12.2	Basic Imaging of Droplets and Jets	314
12.3	Strobe Illumination	317
12.4	Holographic Methods	320
12.5	Confocal Microscopy	325
12.6	Image Analysis	330
12.6.1	Binary Image Analysis Method	330
12.6.1.1	Edge Detection Method (Droplet Volume Calculation Using LabVIEW)	331
12.6.1.2	Edge Detection Method (Threshold Detection Using MATLAB)	335
	References	336
<b>13</b>	<b>Inkjet Fluid Characterization</b>	<b>339</b>
	<i>Malcolm R. Mackley, Damien C. Vadillo, and Tri R. Tuladhar</i>	
13.1	Introduction	339
13.2	The Influence of Ink Properties on Printhead and Jetting	340
13.3	The Rheology of Inkjet Fluids	341
13.3.1	Base Viscosity	342
13.3.2	Viscoelasticity (LVE)	344
13.4	The Measurement of Linear Viscoelasticity for Inkjet Fluids	347

13.5	The Measurement of Extensional Behavior for Inkjet Fluids	351
13.6	Linking Inkjet Rheology to Printhead Performance	356
13.7	Conclusions	361
	Acknowledgments	362
	References	362
<b>14</b>	<b>Surface Characterization</b>	<b>365</b>
	<i>Ronan Daly</i>	
14.1	Introduction	365
14.1.1	Understanding Surface Characterization Requirements	366
14.2	Process Map to Define Characterization Needs	367
14.2.1	Prejetting Surface Quality	367
14.2.1.1	Example 1: Graphical Printing	367
14.2.1.2	Example 2: Printed Electronics	370
14.2.1.3	Summary	373
14.2.2	Drop Impact Behavior	373
14.2.2.1	Example 1: 3D Printing	374
14.2.2.2	Example 2: Reactive Inkjet Printing and High-Throughput Screening	375
14.2.2.3	Summary	376
14.2.3	Delivery of Function	376
14.2.3.1	Example 1: Graphical Printing	377
14.2.3.2	Example 2: Advanced Functional Materials	378
14.2.4	The Final Functionalized Surface	379
14.2.5	Long-Term Behavior	380
14.2.5.1	Example 1: Paper	380
14.2.5.2	Example 2: Protein Printing	380
14.2.5.3	Example 3: Cured Ink Adhesion	381
14.3	Surface Characterization Techniques	381
14.3.1	Chemical Analysis of Surfaces	381
14.3.1.1	Surface Tension and Wettability Studies	381
14.3.1.2	Liquid Drops on Solid Surfaces	382
14.3.1.3	Example of Contact Angle Measurement	385
14.3.1.4	Liquid Drops on Liquid Surfaces	385
14.3.1.5	Role of Surface Chemistry on Imbibition	386
14.3.2	Mechanical Testing of Surfaces	387
14.3.2.1	Atomic Force Microscopy (AFM)	388
14.3.2.2	Nanoindentation	388
14.3.3	Electrical Analysis of Surfaces	389
14.3.4	Optical Analysis	390
14.3.5	Biological Analysis	393
14.4	Conclusion	394
14.5	Questions to Consider	394
	References	395

<b>15</b>	<b>Applications in Inkjet Printing</b>	<b>397</b>
	<i>Patrick J. Smith and Jonathan Stringer</i>	
15.1	Introduction	397
15.2	Graphics	398
15.3	Inkjet Printing for Three-Dimensional Applications	399
15.4	Inorganic Materials	404
15.4.1	Metallic Inks for Contacts and Interconnects	404
15.4.2	Ceramic Inks	405
15.4.3	Quantum Dots	406
15.5	Organic Materials	407
15.6	Biological Materials	410
15.6.1	Biomacromolecules for Analysis and Sensing	411
15.6.2	Tissue Engineering	412
	References	414
<b>16</b>	<b>Inkjet Technology: What Next?</b>	<b>419</b>
	<i>Graham D. Martin and Mike Willis</i>	
16.1	Achievements So Far	419
16.2	The Inkjet Print-Head as a Delivery Device	420
16.3	Limitations of Inkjet Technology	421
16.3.1	Jetting Fluid Constraints	421
16.3.2	Control of Drop Volume	421
16.3.3	Variations in Drop Volume	422
16.3.4	Jet Directionality and Drop Placement Errors	423
16.3.5	Aerodynamic Effects	424
16.3.6	Impact and Surface Wetting Effects	424
16.4	Today's Dominant Technologies and Limitations	424
16.4.1	Thermal Drop-on-Demand Inkjet	425
16.4.2	Piezoelectric Drop-on-Demand Inkjet	427
16.5	Other Current Technologies	428
16.5.1	Continuous Inkjet	428
16.5.2	Electrostatic Drop-on-Demand	429
16.5.3	Acoustic Drop Ejection	429
16.6	Emerging Technologies and Techniques	431
16.6.1	Stream	431
16.6.2	Print-Head Manufacturing Techniques	431
16.6.3	Flextensional	434
16.6.4	Tonejet	435
16.6.5	Ink Recirculation	435
16.6.6	Indirect Inkjet Printing	436
16.6.7	Wide Format Printing	438
16.6.8	Failure Detection	438
16.7	Future Trends for Print-Head Manufacturing	439
16.8	Future Requirements and Directions	440
16.8.1	Customization of Print-Heads for Nongraphics Applications	440

16.8.2	Reduce Sensitivity of Jetting to Ink Characteristics	440
16.8.3	Higher Viscosities	441
16.8.4	Higher Stability and Reliability	441
16.8.5	Drop Volume Requirements	442
16.8.6	Lower Costs	442
16.9	Summary of Status of Inkjet Technology	443
	References	444

	<b>Index</b>	<b>445</b>
--	--------------	------------

## List of Contributors

**Colin D. Bain**

Durham University  
Department of Chemistry  
Lower Mountjoy South Road  
Durham DH1 3LE  
UK

**Eleanor S. Betton**

Domino Printing Sciences Ltd.  
Trafalgar Way  
Bar Hill  
Cambridge CB23 8TU  
UK

**Simon Biggs**

University of Queensland  
School of Chemical Engineering  
Faculty of Engineering  
Architecture and Information  
Technology  
Brisbane  
Queensland 4072  
Australia

**Arend M. van Buul**

Océ Technologies  
B.V., Research and Development  
Van der Grintenstraat 1  
5914 HD Venlo  
The Netherlands

**Rafael Castrejón-García**

Instituto Nacional de Astrofísica  
Óptica y Electrónica  
1 Luis Enrique Erro  
Tonantzintla  
Puebla 72840  
Mexico

**Alfonso A. Castrejón-Pita**

University of Oxford  
Department of Engineering  
Sciences  
Parks Road  
Oxford OX1 3PJ  
UK

***J. Rafael Castrejón-Pita***

University of Cambridge  
Department of Engineering  
Institute for Manufacturing  
17 Charles Babbage Road  
Cambridge CB3 0FS  
UK

*and*

Queen Mary University of  
London  
School of Engineering and  
Material Science  
Mile End Road  
London E1 4NS  
UK

***Olivier J. Cayre***

University of Leeds  
School of Chemical and Process  
Engineering  
Institute of Particle Science and  
Process Engineering  
School of Process,  
Environmental and Materials  
Engineering  
Engineering Building  
Leeds LS2 9JT  
UK

***Ronan Daly***

University of Cambridge  
Department of Engineering  
Institute for Manufacturing  
17 Charles Babbage Road  
Cambridge CB3 0FS  
UK

***Raf De Dier***

Katholieke Universiteit Leuven  
Department of Chemical  
Engineering  
Willem de Croylaan 46 B-3001  
Heverlee (Leuven)  
Belgium

***Theo Driessen***

ASML Research  
De Run 6501, 5504 DR  
Le Sage ten Broeklaan 1  
5615CP Veldhoven  
The Netherlands

***Edward P. Furlani***

University of Buffalo  
Department of Chemical and  
Biological Engineering  
Department of Electrical  
Engineering  
Buffalo  
NY 14260-4200  
USA

***Oliver G. Harlen***

University of Leeds  
School of Mathematics  
Woodhouse Lane  
Leeds LS2 9JT  
UK

***Stephen D. Hoath***

University of Cambridge  
Department of Engineering  
Institute for Manufacturing  
17 Charles Babbage Road  
Cambridge CB3 0FS  
UK

**Seok Hyun Hong**

Pohang University of Science and  
Technology  
Department of Mathematics  
77 Cheongam-Ro  
Nam-gu  
Pohang-si 37673  
Gyeongsangbuk 790-784  
South Korea

**Wen-Kai Hsiao**

Research Center Pharmaceutical  
Engineering (RCPE) GmbH  
A-8010 Graz  
Inffeldgasse 13  
Austria

**Ian M. Hutchings**

University of Cambridge  
Department of Engineering  
Institute for Manufacturing  
17 Charles Babbage Road  
Cambridge CB3 0FS  
UK

**Hyung Ju Hwang**

Pohang University of Science and  
Technology  
Department of Mathematics  
77 Cheongam-Ro  
Nam-gu  
Pohang-si 37673  
Gyeongsangbuk 790-784  
South Korea

**Roger Jeurissen**

ACFD Consultancy  
St Camillusstraat 26  
6045 ES  
Roermond  
The Netherlands

*and*

Eindhoven University of  
Technology  
Department of Applied Physics  
P.O. Box 513  
5600 MB Eindhoven  
The Netherlands

**Sungjune Jung**

Pohang University of Science and  
Technology  
Department of Creative IT  
Engineering  
77 Cheongam-Ro  
Nam-gu  
Pohang-si 37673  
Gyeongsangbuk-do  
South Korea

**Amol A. Khalate**

Océ Technologies  
B.V., Research and Development  
Van der Grintenstraat 1  
5914 HD Venlo  
The Netherlands

***Krzysztof J Kubiak***

University of Huddersfield  
School of Computing and  
Engineering  
Queensgate  
Huddersfield HD1 3DH  
UK

***Kye Si Kwon***

Soonchunhyang University  
Department of Mechanical  
Engineering  
646, Eupriae-ri,  
Shinchang-myeon, Asan-si  
Chungcheongnam-do  
336-745  
South Korea

***Malcolm R. Mackley***

University of Cambridge  
Department of Chemical  
Engineering and Biotechnology  
Pembroke Street  
Cambridge CB2 3RA  
UK

***Graham D. Martin***

University of Cambridge  
Department of Engineering  
Institute for Manufacturing  
17 Charles Babbage Road  
Cambridge CB3 0FS  
UK

***Claire McIlroy***

University of Leeds  
School of Mathematics  
Woodhouse Lane  
Leeds LS2 9JT  
UK

*and*

University of Georgetown  
Department of Physics  
506 Reiss Science Building  
37th & O St NW  
Washington DC  
20057  
United States

***Naoki Morita***

Fuji Xerox Co., Ltd,  
Marking Technology Lab.  
2274, Hongo  
Ebina  
Kanagawa 243-0494  
Japan

***Neil F. Morrison***

University of Leeds  
School of Mathematics  
Woodhouse Lane Leeds LS2 9JT  
UK



**Mohmed A. Mulla**

University of Leeds  
School of Chemical and Process  
Engineering  
Leeds LS2 9JT  
UK

**Wouter Sempels**

Katholieke Universiteit Leuven  
Department of Chemistry  
Celestijnenlaan 200F  
Box 2404  
Leuven B-3001  
Belgium

**Patrick J. Smith**

University of Sheffield  
Department of Mechanical  
Engineering  
Laboratory of Applied Inkjet  
Printing  
64 Garden Street  
Sheffield S1 4BJ  
UK

**Jonathan Stringer**

University of Sheffield  
Department of Mechanical  
Engineering  
Laboratory of Applied Inkjet  
Printing  
64 Garden Street  
Sheffield S1 4BJ  
UK

**Emma L. Talbot**

Durham University  
Department of Chemistry  
Lower Mountjoy  
South Road  
Durham DH1 3LE  
UK

*and*

University of Cambridge  
Biological and Soft Systems  
Cavendish Laboratory  
J J Thomson Avenue  
Cambridge CB3 0HE  
UK

**Tri R. Tuladhar**

Trijet Ltd,  
59 Eland Way  
Cambridge CB1 9XQ  
UK

**Damien C. Vadillo**

Akzo Nobel Research  
Development and Innovation  
Stonegate Lane  
Felling  
Gateshead NE10 0JY  
UK

***Jan Vermant***

ETH Zurich  
Department of Materials  
Vladimir-Prelog-Weg 1-5/10  
8093 Zurich  
Switzerland

***Joseph S.R. Wheeler***

The University of Manchester  
School of Chemistry  
Oxford Road  
Manchester M13 9PL  
UK

***Herman Wijshoff***

B.V., Research and Development  
Van der Grintenstraat 1  
5914 HD Venlo  
The Netherlands

***Mark C.T. Wilson***

Institute of Thermofluids  
University of Leeds  
School of Mechanical  
Engineering  
Leeds LS2 9JT  
UK

***Mike Willis***

Pivotal Resources Ltd,  
11 Glebe Way  
Histon  
Cambridge CB24 9HJ  
UK

***Lisong Yang***

Durham University  
Department of Chemistry  
Lower Mountjoy  
South Road  
Durham DH1 3LE  
UK

***Stephen G. Yeates***

The University of Manchester  
School of Chemistry  
Oxford Road  
Manchester M13 9PL  
UK

***Huai Nyin Yow***

Briggs of Burton PLC  
Briggs House  
Derby Street  
Burton-on-Trent DE14 2LH  
UK

***Huagui Zhang***

University of Leeds  
School of Chemical and Process  
Engineering  
Leeds LS2 9JT  
UK

## Preface

What is this *Fundamentals of inkjet printing* book actually for? Who would want to use it? When? To help answer these questions, first consider some basic statements about the core subject itself.

Inkjet printing, from a pragmatic viewpoint, can result in distributions of materials across substrate areas that are ultimately useful for communication purposes or in digital manufacturing processes. A major feature of inkjet printing is that it transfers materials as liquid drops, without requiring any mechanical contact between the print head producing the drops and the substrate receiving them. Such a decoupling allows machines comprising hundreds of inkjet print heads with multiple jets each delivering perhaps 1 kg of material per year in the form of drops with diameters typically less than a human hair's breadth. The engineering design and construction, and software control, necessary for machines to reliably, repeatedly, and rapidly deliver drop patterns, are all subjects in their own right, as are the systems to handle and process the substrates with and without the deposited ink drops.

The Science of Inkjet and Droplets is concerned far more with how fluids can be formed into jets and drops, which travel to and impact the substrate and then spread (or interact) and dry (or cure), than with the engineering and science needed to manufacture inkjet print heads and printing machines. An early title suggested for this book, *How to fix an inkjet printer* was, however saleable, firmly rejected by the Editor on behalf of the contributors. The point of this new volume is to help explain quantitatively why fluids might behave the way they do under jetting, free flight, impact, spreading, coalescing, and drying conditions, by using scientific knowledge as gleaned from recent theoretical, numerical, and experimental research work. Such knowledge is never complete; many of the chapters' (co)authors are currently probing some of its boundaries in order to extend the core subject to develop new print head designs or applications, characterization methods, or improved numerical tools.

So, this textbook is unlikely to directly help someone "fix" their inkjet printer, but is intended for students and early-stage research workers in academia or industry who would like a deeper more quantitative understanding of inkjet printing than might be found in more general introductions, such as "Inkjet technology for digital fabrication," [1] yet different again from those written for

specific industrial markets, such as “Inkjet-based micro-manufacturing” [2] or the more specific if related tomes that deal primarily with continuous streams of drops and sprays, such as “Dynamics of droplets” [3].

Materials that can be found at a suitable level in any of these books or in the cited academic papers will not be repeated in the textbook: its contents are focused on simple quantitative explanations, and are meant to represent the ordered sequence through which the fluid is jetted and deposited, with chapters explaining theoretical tools now increasingly applied to understand the processes involved and the final chapters to the methods of visualization and measurement, the characterization of fluids and surfaces, some applications, and updated discussion of future directions for inkjet printing.

I am very grateful to the coauthors and Wiley-VCH Editors who have contributed to this volume, which I hope will help extend the fundamental understanding of inkjet research and also provide a useful reference resource for those working or entering this field for many years to come. My work on this volume was supported by I4T, a UK Engineering & Physical Sciences Research Council project “Innovation in Industrial Inkjet Technology,” under grant number EP/H018913/1, and a consortium of companies. My (co)authors, whether academic or industrial, also thank their employers for their vision and support during chapter drafting; any mistakes are of course the Editor’s responsibility. Last, but by no means least, thank you to my wife and family for all their interest and support throughout my work.

Cambridge  
May 2015

*Stephen D. Hoath*

## References

1. Ian M. Hutchings and Graham D. Martin (eds) (2012) *Inkjet Technology for Digital Fabrication*, John Wiley and Sons Ltd, Chichester, UK.
2. Jan G. Korvink, Patrick J. Smith, and Dong Yuan Shin (eds) (2012) *Inkjet-based micro-manufacturing*, Wiley-VCH verlag, Weinheim.
3. Arnold Frohn and Norbert Roth (eds) (2000) *Dynamics of droplets*, Springer-Verlag, Berlin Heidelberg.

# 1

## Introductory Remarks

*Ian M. Hutchings, Graham D. Martin, and Stephen D. Hoath*

### 1.1

#### Introduction

From newspapers to food packaging, from magazines to junk mail and roadside advertising, we live in a world of printed materials. The process of printing involves the reproduction of a pattern on a substrate, usually in order to represent text or images or, in many cases, both. Conventional printing methods, including, for example, lithography, flexography, gravure, and screen printing, have evolved over several centuries and can now achieve remarkable levels of quality at very low cost. All these processes share a common feature: the pattern to be printed is embodied in a physical form such as on a roll, plate, or screen and transferred from this template during the act of printing through direct or indirect contact with the substrate. The pattern of ink that forms the printed text or image on the substrate thus originates in a pattern that is defined before the printing machine starts to run. Changes to the printed product can be achieved only by changing the master pattern, which involves making physical changes to the template within the printing machine.

Inkjet printing, in contrast, employs a fundamentally different principle. Rather than the printed pattern being created by transfer of ink from a pre-existing master pattern, it is progressively built up directly on to the substrate by the deposition of a large number of individual, tiny drops of ink. Each small droplet, typically 10–100  $\mu\text{m}$  in diameter, is created and deposited under digital control, so that each pattern printed in a sequence by the same machine can just as readily be different from all the others as it can be the same.

Today's printing industry represents a major area of economic activity, currently accounting for some US \$900 billion per annum globally and likely to exceed US \$1000 billion by 2020. Over the past 20 years, a small but increasing fraction of this activity has been based on inkjet technology, and this proportion is forecast to grow significantly. There are several reasons for this. Because the patterns to be printed by inkjet are defined digitally and thus represented by digital data files and never as physical master templates, they can very easily be changed, and the setup costs and times for inkjet printing are, therefore, low. As a digital printing

process, inkjet is thus ideally suited for short print runs for which profit margins can be high, and as the process has increased in reliability and robustness, the run lengths at which inkjet competes with more conventional processes in terms of cost have also increased. High resolution and image quality, once the sole preserve of conventional printing, can be more readily attained by inkjet methods. Inkjet printing is very well established for printing variable information such as use-by dates and batch codes on to products in a manufacturing environment, and as inkjet print quality increases, more opportunities become available for printing bespoke, personalized products. Table 1.1 summarizes the very wide range of applications in which printing is used and shows how inkjet technology is progressively encroaching into major areas. Already ubiquitous in the small office and home environment, inkjet printing is likely to take an increasingly important share of the commercial printing market soon and to become more widely used for decorative products, packaging, general industrial applications, and textile printing as well [1].

The principles of inkjet printing were first developed commercially during the 1970s and 1980s and first applied practically to marking products with dates and codes and addressing mail. As indicated in Figure 1.1, the technology used for these purposes, which demand high operating speeds but can tolerate quite low resolution in the printed text, is now fully mature. These printers, which use “continuous inkjet” (CIJ) technology, are widely used as standard equipment in factories worldwide. The next development, from the 1990s onward, involved “drop-on-demand” (DOD) printing, which is capable of achieving much higher resolution than these early coders and achieving digital reproduction of text and images at low cost in the domestic and small office environment. More recently, applications of inkjet printing in the commercial world, and for other uses listed in Table 1.1, have been developing rapidly, and these applications also predominantly use the DOD technology. The principles by which small drops of ink are formed and manipulated, in both CIJ and DOD modes, are described in the next section.

## 1.2

### Drop Formation: Continuous Inkjet and Drop-on-Demand

In both the CIJ and DOD methods, the liquid ink flows through a small hole (usually called a *nozzle*). The essential difference between the two methods lies in the nature of the flow through the nozzle. In CIJ, as the name implies, the flow is continuous, while in DOD, it is impulsive.

A CIJ system produces a continuous stream of drops, from which those to be printed on to the substrate are selected as required, whereas in DOD printing, the ink is emitted through the nozzle to form a short jet, which then condenses into a drop, only when that drop is needed.

A continuous stream of liquid emerging from a nozzle is inherently unstable and will eventually break up into a stream of droplets under the influence of surface tension forces, as shown, for example, in Figure 1.2a. This process was first studied

**Table 1.1** Range of applications for which printing is currently used, showing market penetration of inkjet-based processes.

	Small office and home	Commercial print	Decorative products	Packaging	General industrial	Textiles
Already widely used	Home printers, local office printers/copiers	Billing and ticketing, graphic displays, point-of-purchase	Signage, banners, stickers, ceramic tiles		Coding and marking	T-shirts
Starting to be used	Books, brochures, flyers, newspapers, magazines	Wallpaper		Labels: self-adhesive, shrink, and so on	Displays, dashboards, plastic cards, 3D printing	“Designer” fabrics, ties, scarves
Medium-term target		Flooring, décor (e.g., melamine)		Corrugated board, cartons, cans, glass bottles	Printed circuit boards, electronic devices	Soft furnishings, other clothing
Not a current target		Banknotes, security printing		Flexible packaging, molded tubs, bottles	Toys, other durables	Carpets, rugs

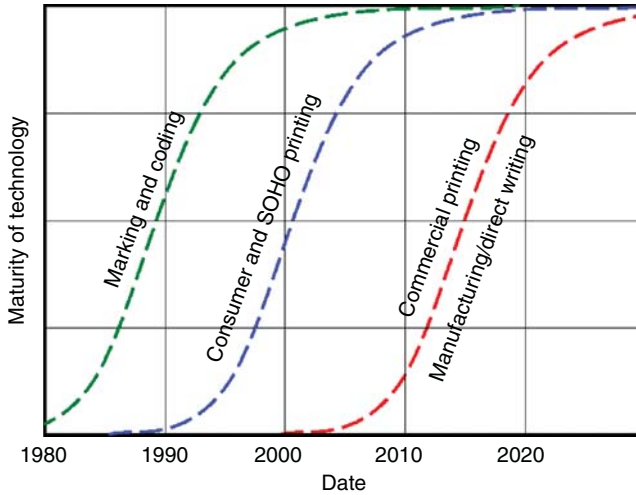


**Figure 1.1** The applications of inkjet technology have developed in three waves: initially for marking and coding, followed by desktop printing of text and graphics

in the home and small office environment, and currently, increasing use in commercial printing and manufacturing [2].

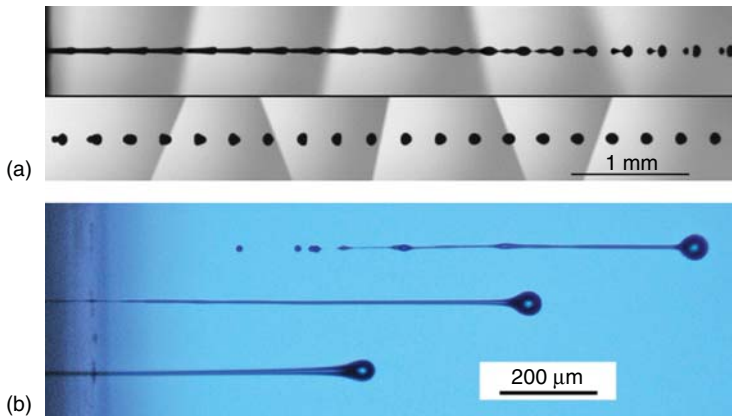


**Figure 1.2** Images of liquid jets, moving from left to right, showing (a) breakup of a continuous jet to form drops (the lower image is a continuation of the upper image)

and (b) jet and drop formation in drop-on-demand mode from three nozzles situated toward the left of the frame. (from Martin and Hutchings [3].)

as long ago as 1833 by Savart [4] and analyzed quantitatively by Rayleigh in 1879, who showed that the wavelength of the most rapidly growing disturbance in the jet (and, thus, the distance between the centers of the resulting drops) was about 4.5 times the diameter of jet (see also Chapter 7). This phenomenon, often called *Rayleigh breakup*, was first employed as the basis for a CIJ printer (for recording oscillograph traces) by Sweet at Stanford University in the early 1960s. Sweet's



design introduced the key concepts of stimulating jet breakup by modulating it at an appropriate frequency and using electrostatic forces to deflect the drops [5]. In the stream shown in Figure 1.2a, the breakup was stimulated by vibration applied to the fluid upstream of the nozzle, but an unstimulated jet will also break up in a similar way, although after traveling a longer distance.

In modern CIJ printing, the drops to be printed on to the substrate are usually steered electrostatically. As each drop detaches from the end of the continuous stream, an electric charge is induced on it so that, when it subsequently passes through a fixed electric field, it is deflected by the correct amount to land at the right place on the substrate. Drops that carry no charge, in contrast, are arranged to land in a gutter from which the surplus ink can be recovered and recycled back to the nozzle. In this way, a stream of drops from a single nozzle, in combination with a moving substrate, can be used to print a swathe of text or image. CIJ is also used in multi-nozzle configurations, with each jet addressing one pixel position across the printed swathe. The printed pattern is created by switching drops from individual jets either into a gutter or on to a substrate by deflection in an electric field, as described above, or by other means.

Figure 1.2b shows images of jets ejected from three nozzles in DOD mode and traveling to the right. The main droplet, which forms the head of the jet, is followed by a long ligament of liquid, which eventually detaches from the nozzle (at the left-hand edge of the picture) and is pulled toward the head of the jet, while, at the same time, becoming thinner and, in this case, forming a series of “satellite” drops. The final form of the jet may be a single spherical drop (the ideal case) or, quite commonly, a main drop followed by one or more, smaller, “satellite” drops. In DOD printing, the drops are not “steered”; many nozzles (from hundreds to thousands) are arranged in an array in each printhead, and the position at which each drop lands on the substrate is controlled by the relative motion between the drop and the substrate and by the timing of the drop ejection, as well as by the selection of the appropriate nozzle from the array.

Most current DOD printers use one of two different methods to generate the pressure pulse needed to eject an ink drop. Many printheads use the deformation of a piezoelectric ceramic element for this purpose, while in other types (thermal inkjet, sometimes called *bubble jet*), the pressure pulse which ejects the drop is generated from the expansion of a small bubble of vapor produced by the action of a small electric heating element on the liquid. There are advantages and disadvantages of both types of actuation. Piezoelectric printheads can handle a wider range of liquids than thermal printheads (which are restricted to inks which satisfactorily vaporize), while the latter can be simpler and cheaper to fabricate. Piezoelectric DOD printheads were first devised in the 1970s, with thermal DOD being developed a little later [3, 5].

The drop diameters used in inkjet printing, typically from 10 to 100  $\mu\text{m}$ , correspond to drop volumes from 0.5 to 500 pl. Drop speeds, at the point where the drops strike the substrate, are typically 5–8  $\text{m s}^{-1}$  for DOD printing and 10–30  $\text{m s}^{-1}$  for CIJ.

## 1.3

**Surface Tension and Viscosity**

Two physical properties dominate the behavior of the liquid jets and drops involved in inkjet printing: *surface tension* and *viscosity*. We shall remind ourselves briefly of their definitions, following the discussion by Martin and Hutchings [3].

The surface tension of a liquid reflects the fact that atoms or molecules at a free surface have a higher energy than those in the bulk. There is a cost in terms of energy in creating new surface area. For a free droplet of liquid, the shape with the lowest surface area, and therefore the lowest surface energy, is a sphere, and in the absence of other influences such as electrostatic, gravitational, or aerodynamic forces, that is the shape a free drop will adopt. If the liquid is in contact with a solid surface, for example after it has been printed on to a substrate, then we need to consider not only the energy of its free surface (which is usually in contact with air or solvent vapor) but also the energy of the interface between the liquid and the solid substrate. In that case (and where, as in inkjet printing, the effect of gravity is negligible), the equilibrium shape of the drop becomes a spherical cap, as discussed in Chapters 8 and 9.

The surface tension in a liquid causes a force to act in the plane of the free surface perpendicularly to a free edge in that surface, which can be measured directly by various experimental arrangements. The force is proportional to the length of the edge, and the surface tension  $\gamma$  can therefore be defined as the force per unit length. Since by moving the edge in the direction of the force we will increase the area of the surface and also do work on the system against the surface tension, we can also treat the force per unit length as a *surface energy*: the work done in creating unit area of new surface. The two are equivalent, as are the SI units of  $\text{N m}^{-1}$  and  $\text{J m}^{-2}$ . Most liquids of practical interest for inkjet printing have surface tensions,  $\gamma$ , of the order of tens of  $\text{mN m}^{-1}$  (or  $\text{mJ m}^{-2}$ ). For pure water at  $20^\circ\text{C}$ ,  $\gamma = 72.5 \text{ mN m}^{-1}$ , while for many organic liquids (which have smaller intermolecular energies than water),  $\gamma$  lies in the range from 20 to  $40 \text{ mN m}^{-1}$ .

The tendency of a liquid to form the shape with the lowest total energy, which in the case of a free drop causes it to become a sphere, is responsible for the breakup of the stream in CIJ printing and for the formation of the main drop and any satellite drops in DOD printing.

The forces that resist the contraction of a liquid jet through the action of surface tension have two origins: the inertia of the liquid and its viscosity. Inertial forces are those associated with a change in a body's momentum: in the case of a moving liquid, they are proportional to its density and the rate of change of velocity. Viscous forces arise from the interactions between molecules of the liquid and act between regions of liquid moving relative to each other. A simple example, which forms the basis for the definition of viscosity, is given by a shear flow as shown in Figure 1.3a.

A region of liquid is defined by two parallel surfaces a distance  $d$  apart. The lower surface is stationary, and the upper surface moves relative to it at a constant

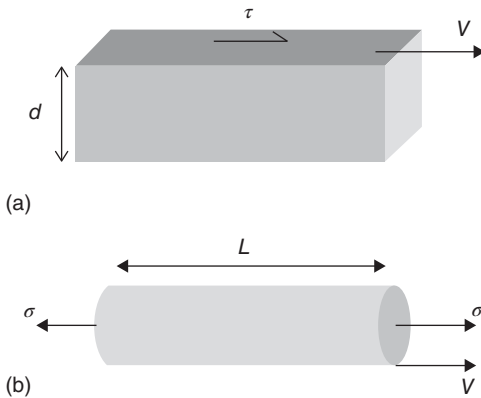


**Figure 1.3** Geometry used to define: (a) shear flow and (b) extensional flow [3].

velocity  $v$ . We assume that this generates a linear gradient of velocity through the liquid, normal to the upper and lower surfaces. The shear strain rate  $\dot{\gamma}$  is given by:

$$\dot{\gamma} = V/d$$

and for many liquids, the shear stress  $\tau$  acting on the upper and lower surfaces is proportional to  $\dot{\gamma}$ :

$$\tau = \eta\dot{\gamma}$$

The constant  $\eta$  is the *dynamic viscosity* of the liquid, and if  $\eta$  is independent of  $\dot{\gamma}$ , then this behavior is termed *linear* or *Newtonian*. The simple term “viscosity,” without further qualification, usually means the dynamic viscosity as defined for a shear flow. The SI unit for dynamic viscosity is the pascal second (Pa s). The older (c.g.s.) unit of viscosity, the poise (symbol P), or more commonly centipoise (cP), is still in widespread use and conversion is straightforward: 1 mPa s = 1 cP. Water has a viscosity of almost exactly 1 mPa s at 20 °C, while fluids used in inkjet printing typically have viscosities in the range from  $\sim 2$  to  $\sim 50$  mPa s. The viscosity of most liquids falls rapidly with increasing temperature, and this is often exploited in inkjet printing: by varying the temperature of the printhead, it is possible to optimize the viscosity of the ink for drop generation.

The shear flow shown in Figure 1.3a represents a particular pattern of liquid flow, but it does not represent well the flow that occurs in the formation or collapse of a jet. We may also need to consider the extensional or elongational flow, which is shown in idealized form in Figure 1.3b. If a cylindrical column of liquid of length  $L$  is stretched along its axis at a velocity  $V$ , the uniaxial strain rate  $\dot{\epsilon}$  is given by:

$$\dot{\epsilon} = V/L$$

and the axial stress  $\sigma$  is linearly proportional to the strain rate:

$$\sigma = \eta_T \dot{\epsilon}$$

The constant of proportionality  $\eta_T$  is called the *extensional viscosity*, and for a Newtonian liquid,  $\eta_T$  is three times the shear viscosity  $\eta$ . The ratio  $\eta_T/\eta$  is called the *Trouton ratio* and can be significantly greater than 3 for non-Newtonian liquids that are viscoelastic. Viscoelastic liquids exhibit a time-dependent elastic response as well as viscosity due, for example, to the presence of polymer molecules in solution. Organic solvents are usually Newtonian, as is water, but practical inkjet inks often exhibit some degree of viscoelasticity (also see Chapters 5, 6, and 13).

#### 1.4

##### Dimensionless Groups in Inkjet Printing

Surface tension, inertia, and viscosity play key roles in the formation and behavior of liquid jets and drops. Two dimensionless numbers can be used to characterize the relative importance of these: the Reynolds and Weber numbers. The Reynolds number  $Re$  represents the ratio between inertial and viscous forces in a moving fluid and is defined by Eq. (1.1):

$$Re = \frac{\rho V d}{\eta} \quad (1.1)$$

where  $\rho$  is the density of the fluid,  $V$  is its velocity,  $\eta$  is its viscosity, and  $d$  is a characteristic length: typically, the diameter of the jet, nozzle, or drop.

The Weber number  $We$  depends on the ratio between inertia and surface tension:

$$We = \frac{\rho V^2 d}{\gamma} \quad (1.2)$$

where  $\gamma$  is the surface tension. For a spherical drop traveling at velocity  $V$ , the ratio between its kinetic energy and the energy of its free surface is  $We/6$ .

The influence of velocity in these two dimensionless groups can be removed by forming a further group, the Ohnesorge number  $Oh$  defined by:

$$Oh = \frac{\sqrt{We}}{Re} = \frac{\eta}{\sqrt{\gamma \rho d}} \quad (1.3)$$

The value of the Ohnesorge number, which reflects only the physical properties of the liquid and the size scale of the jet or drop, but is independent of the driving conditions (which control the velocity), turns out to be closely related to the behavior of a jet emerging from a nozzle and, thus, to the conditions in DOD printing. If the Ohnesorge number is too high ( $Oh > \sim 1$ ), then viscous forces will prevent the separation of a drop, while if it is too low ( $Oh < \sim 0.1$ ), the jet will form a large number of satellite droplets. Satisfactory performance of a fluid in DOD inkjet printing thus requires an appropriate combination of physical properties, which will also depend on the droplet size and velocity (through the value of the Reynolds or Weber number) as shown in Figure 1.4 [6]. Some authors use the symbol  $Z$  for the inverse of the Ohnesorge number ( $Z = 1/Oh$ ). The range over which

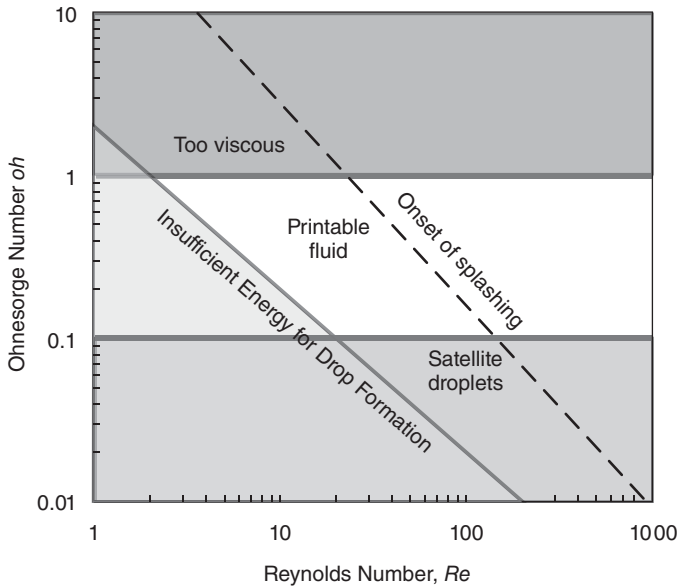


**Figure 1.4** Schematic diagram showing the operating regime for stable operation of drop-on-demand inkjet printing, in terms of the Ohnesorge and Reynolds numbers.

(Reproduced with permission from McKinley and Renardy [6]. Copyright (2011) American Institute of Physics.)

liquids can be printed is often quoted as  $10 > Z > 1$  (e.g., [7]), although other work has suggested that  $14 < Z < 4$  may be more appropriate [8].

These ranges of Ohnesorge number provide some bounds to the “printability” of the liquid, but other factors must also be considered: the jet must possess enough kinetic energy to be ejected from the nozzle (leading to the solid diagonal line in Figure 1.4 corresponding to  $Re = 2/Oh$ ), and it is also desirable to avoid splashing of the drop on impact with the substrate (which leads to the broken diagonal line for which  $OhRe^{5/4} = 50$ ) [9].

## 1.5 Length and Time Scales in Inkjet Printing

It is useful to review the wide range of length and time scales involved in inkjet printing, because these pose challenges for the scientific study and optimization of the various processes involved. Figure 1.5 shows that the length scales concerned extend from nanometers to meters.

At the smallest length scales, atomic and molecular diameters provide a fundamental limit to any treatment of fluids as homogeneous continua, while inks often contain colloidal pigments and other small particles 10–100 nm in diameter. The liquid drops, jets, and ligaments formed from the printhead range in dimensions

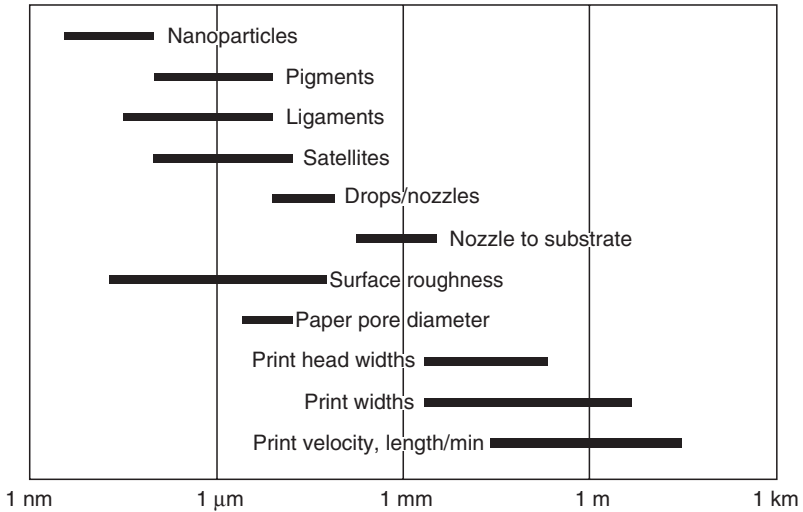


Figure 1.5 Length scales involved in inkjet printing.

from far below 1 μm (for thinning ligaments) to tens of micrometers (for main drop diameters) and hundreds of micrometers (for ligament lengths). The main drops are usually of size similar to the diameters of the nozzles (10–100 μm), while the standoff distance over which the drop travels from the printhead to the substrate may range from less than 1 mm (for typical DOD systems) to several tens of mm (for CIJ printing). Shorter standoff distances will generally give more precise drop placement but demand greater accuracy of substrate movement

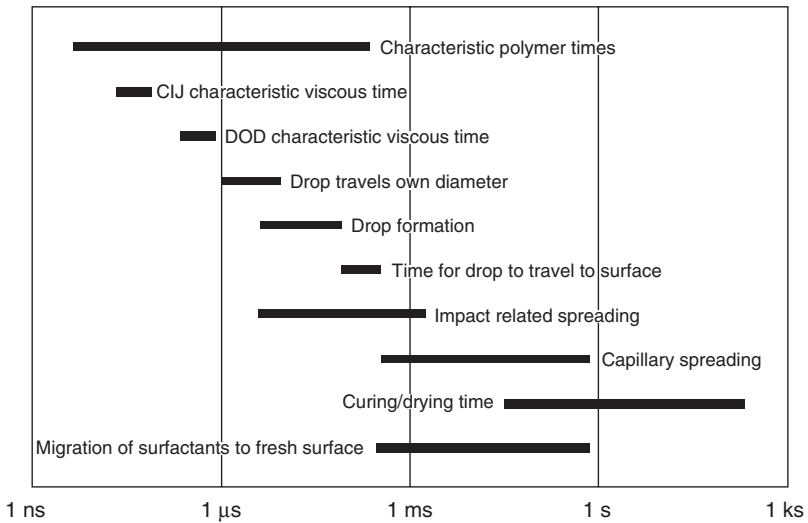


Figure 1.6 Time scales involved in inkjet printing.

and a smoother, flatter surface. The substrates for many applications have surface roughness below 100 nm (0.1  $\mu\text{m}$ ), but porous media such as paper have significant inhomogeneity due their inherent fibrous structure, producing pores on the surface through which liquid and pigment particles can penetrate. Lower limits to printed line widths, for example, for printed electronics, are about 10  $\mu\text{m}$ ; the width of the printed substrate may in contrast extend to several meters, for advertising banners and vehicle wraps.

The time scales shown in Figure 1.6 exhibit a similarly wide range. Some characteristic times are intrinsic to the fluid and independent of the diameter and speed of the jet or drop, while others are independent of the fluid but linked via length and speed. Impact of the drop on to a substrate is fundamental to inkjet printing; capillary spreading and the curing/drying timescale provide the basis for controlling the extent of the deposit on the substrate. As surfactants and other additives may be required for the functionality of the inkjet applications, it is important to understand that they are generally slow-acting for jetting but not for the deposition.

## 1.6

### The Structure of This Book

This textbook is structured with chapters discussing the behavior of liquid as it is jetted from within an inkjet printhead through the air and then impacts on to and spreads on a substrate to form a deposit. Fluid mechanics relevant to inkjet printing and the principles underlying the jetting action of printheads are introduced. The nature of complex fluids is shown to have significant influence on fluid behavior under inkjet printing conditions. Numerical simulations explore the jetting, free flying, and spreading behavior of such liquids, with serious discussion about validation of the correspondence between computed and observed behavior in each phase. Experimental techniques for visualization and measurement of jets and droplets and the characterization of fluids and surfaces are described. Some inkjet applications and a forward look to the near future of inkjet technology complete the story told by “The Science of Inkjet and Droplets.” Needless to say, the scientific story continues to unfold with new discoveries and insights gained through research and applications. There are undoubtedly some omissions from the story and some particular topics which are only mentioned in passing, although this textbook aims to remain a standard reference.

## 1.7

### Symbols Used

In view of the breadth of science covered by the many contributors, and in the references cited, variable symbols are defined within each chapter quite independently, to reflect their usage in the particular scientific fields, so that the user

can recognize them in context. This also means that some of the key parameter definitions are repeated in slightly different forms across the textbook.

## References

1. Castrejón-Pita, J.R., Baxter, W.R.S., Morgan, J., Temple, S., Martin, G.D., and Hutchings, I.M. (2013) Future, opportunities and challenges of inkjet technologies. *Atomization and Sprays*, **23**, 571–595.
2. Hutchings, I.M. and Martin, G.D. (2013) in *Inkjet Technology for Digital Fabrication* (eds I.M. Hutchings and G.D. Martin), Wiley-Blackwell, pp. 1–20.
3. Martin, G.D. and Hutchings, I.M. (2013) in *Inkjet Technology for Digital Fabrication* (eds I.M. Hutchings and G.D. Martin), Wiley-Blackwell, pp. 21–44.
4. Eggers, J. (2006) in *Non-smooth Mechanics and Analysis*, Chapter 1 (eds P. Alarnt, O. Maïsonneuve, and R.T. Rockafellar), Springer, pp. 163–172.
5. Le, H.P. (1998) Progress and trends in ink-jet printing technology. *J. Imaging Sci. Technol.*, **42**, 49–62.
6. McKinley, G.R. and Renardy, M. (2011) Wolfgang von Ohnesorge. *Phys. Fluids*, **23**, 127101.
7. Reis, N. and Derby, B. (2000) Ink jet deposition of ceramic suspensions: modelling and experiments of droplet formation. *Mater. Res. Soc. Symp. Proc.*, **625**, 117–122.
8. Jang, D., Kim, D., and Moon, J. (2009) Influence of fluid properties on ink-jet printability. *Langmuir*, **25**, 2629–2635.
9. Derby, B. (2010) Inkjet printing of functional and structural materials: fluid property requirements, feature stability and resolution. *Annu. Rev. Mater. Res.*, **40**, 395–414.



## 2

# Fluid Mechanics for Inkjet Printing

*Edward P. Furlani*

### 2.1

#### Introduction

In this chapter, we provide an overview of the principles of fluid mechanics with applications in the field of inkjet technology. The presentation is intended to be a survey of key topics. More detailed and in depth discussions of this material are provided in subsequent chapters. The topics covered include the basic properties of the fluids, underlying principles and equations that govern fluids in motion, computational methods for modeling fluid behavior, a brief overview of inkjet technology, and challenges in modeling inkjet systems.

### 2.2

#### Fluid Mechanics

Fluid mechanics is a branch of physics that involves the study of fluids at rest or in motion [1–4]. Broadly speaking, a fluid is a material that deforms continuously when subjected to a shear (tangential) stress as shown in Figure 2.1. Unlike solids where neighboring atoms are strongly bound and essentially rigid, fluid molecules are free to move past one another. Consequently, they lack the ability to resist deformation and accordingly flow as long as a shear stress is applied. Solids also deform under shear but quickly obtain an equilibrium configuration when internal elastic forces balance the applied force. The rate at which a fluid flows under shear depends on both the magnitude of the applied force and the viscosity, a fluid property that measures resistance to shear deformation or flow. Because of their ability to flow, fluids do not have a fixed shape but rather assume the shape of their container. Liquids and gases are both fluids albeit with significant differences in properties. These two types of fluids together with solids and plasmas constitute four phases of matter. In liquids, the molecules are densely packed. Consequently, liquids have relatively high densities and viscosities, the latter being due to attractive intermolecular forces.

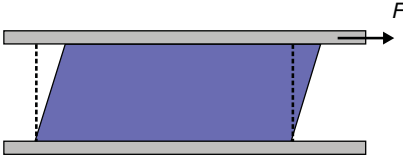


**Figure 2.1** Fluid subjected to a shearing force (original shape indicated by dotted lines).

Liquids are essentially incompressible, that is, their volume remains relatively constant, substantially independent of pressure and temperature. In contrast, gas molecules are spaced far apart relative to a liquid. Consequently, gasses have relatively low densities and viscosities and can be highly compressed. An interface (surface) forms between a liquid and gas when they are in contact. This surface exhibits membrane-like behavior due to an interfacial surface tension caused by an imbalance of molecular forces at the interface. Specifically, there are strong attractive forces from within the liquid due to the closely spaced liquid molecules and comparatively weak (essentially negligible) forces from the gas molecules outside the liquid. Surface tension plays a critical role in the formation of liquid jets and droplets, which form the basis for inkjet printing technology. Fluids have many additional properties that collectively describe their kinematic, transport, and thermodynamic behavior. A thorough understanding of these properties combined with the ability to predict fluid behavior is needed for the development and design of inkjet systems.

### 2.3

#### Dimensions and Units

When analyzing phenomena involving fluids, it is important to use consistent dimensions and units. There are four primary (independent) dimensions, mass ( $M$ ), length ( $L$ ), time ( $t$ ), and temperature ( $T$ ), from which all other secondary (dependent) dimensions can be obtained. The dimensions of a variable are denoted by including its symbol within brackets, for example, the dimensions of force  $F$  are denoted as  $[F]$ , that is,

$$[F] = [\text{mass} \cdot \text{acceleration}] = \left[ M \cdot \frac{L}{t^2} \right] = \left[ \frac{ML}{t^2} \right] \quad (2.1)$$

Many different units can be used to measure a dimension. In fluid mechanics, three different systems are commonly used; the International System (SI), the British Gravitational (BG) System (Imperial System), and the English Engineering System, often referred to as *English units* [2]. The dimensions (mass, force, length, time, and temperature) in the SI system are as follows:

International System (kg, N, m, s, K)

where kg = kilogram, N = newton, m = meter, s = second, K = kelvin. The SI units are the most widely accepted and are used throughout this chapter unless stated otherwise. Some key physical quantities along with their SI units are listed in Table 2.1.

**Table 2.1** Physical properties with SI units.

Physical quantity	Unit (symbol)	Relations
Mass	kilogram (kg)	
Length	meter (m)	
Time	second (s)	
Force	newton (N)	$1 \text{ N} = 1 \text{ kg} \cdot \text{m} \cdot \text{s}^{-2}$
Pressure	pascal (Pa)	$1 \text{ Pa} = 1 \text{ N} \cdot \text{m}^{-2} = 1 \text{ kg} \cdot \text{m}^{-1} \cdot \text{s}^{-2}$
Energy	joule (J)	$1 \text{ J} = 1 \text{ N} \cdot \text{m} = 1 \text{ kg} \cdot \text{m}^2 \cdot \text{s}^{-2}$
Power	watt (W)	$1 \text{ W} = 1 \text{ J} \cdot \text{s}^{-1} = 1 \text{ N} \cdot \text{m} \cdot \text{s}^{-1} = 1 \text{ kg} \cdot \text{m}^2 \cdot \text{s}^{-3}$

As noted, the SI unit of temperature is the kelvin, which is known as an *absolute temperature scale* as 0 K is absolute zero, that is, there is no lower temperature. There is also the relative temperature scale in degrees Celsius where

$$^{\circ}\text{C} = \text{K} - 273.15 \quad (2.2)$$

In the Engineering System, the absolute temperature unit is Rankine ( $^{\circ}\text{R}$ ) and the relative temperature unit is the degree Fahrenheit ( $^{\circ}\text{F}$ ). They are related to the SI units as follows:

$$^{\circ}\text{R} = 1.8(\text{K}) = ^{\circ}\text{F} + 459.67 \quad (2.3)$$

where  $^{\circ}\text{F} = 1.8(^{\circ}\text{C}) + 32$ .

## 2.4

### Fluid Properties

Fluids have many different properties that collectively describe kinematic, transport, and thermodynamic behavior. Many of these properties depend on both the nature of the constituent fluid molecules and the operating conditions imposed on the fluid. In this section, we briefly review three key properties: density, viscosity, and surface tension.

#### 2.4.1

##### Density

The density  $\rho$  of a fluid is defined as its mass per unit volume. In the SI system,  $\rho$  has the units of kilogram per cubic meter. Density depends on the mass of the constituent molecules and number of molecules per unit volume [1–3]. The latter can depend on factors such as temperature and pressure that affect intermolecular spacing. For example, as the temperature increases, fluid molecules become more energetic and separated, which results in a fewer number of molecules per unit volume and consequently a lower density. The density of a liquid depends mainly on its molecular content and to a lesser extent on temperature. This is different

for a gas. For an ideal gas,  $pV = nRT$ , where  $p$  is the absolute pressure,  $V$  is the volume of the gas,  $n$  is the number of moles,  $R$  is the gas constant, and  $T$  is the absolute temperature. The density of the gas is given  $\rho = M_w p / RT$ , where  $M_w$  is the molecular weight. Thus, the density of an ideal gas is strongly dependent on the molecular weight, pressure, and temperature.

The specific gravity  $s$  of a fluid is the ratio of its density  $\rho$  to the density  $\rho_{sc}$  of a reference fluid at some standard condition. For liquids,  $\rho_{sc}$  is usually considered as the density of water at 4 °C, which equals 1000 kg m<sup>-3</sup> (1 g ml<sup>-1</sup>). For gases,  $\rho_{sc}$  is sometimes considered as the density of air at 60 °F and 14.7 psi (1 bar) and, other times, at 0 °C and one atmosphere absolute. As there is no unique standard for gases, care must be taken when reviewing the literature.

#### 2.4.2

##### Viscosity

Viscosity is the fluid property that defines its resistance to shear deformation or flow [3]. The resistance is caused by a cohesive intermolecular force that gives rise to friction between adjacent layers of fluids that are in relative motion as they slide past one another. The viscosity depends on the attractive force between molecules and the momentum interchange between molecules in adjacent layers of fluid as they move relative to one another. Viscosity depends on temperature, but the effect is different for liquids and gases. In a liquid, molecular cohesion dominates the viscosity. As the temperature increases, the molecules in a liquid become more energetic and separated. Thus, the cohesive force decreases, and so does viscosity. In a gas, the viscosity is dominated by the molecular interchange between adjacent layers that are in relative motion. As the temperature increases, there is an increase in frequency of intermolecular collisions and intermolecular forces. Thus, the viscosity of a gas increases with temperature.

The viscosity of a liquid can be determined using the system shown in Figure 2.2. This consists of two closely spaced parallel plates with fluid between them. Both plates have an area  $A$ , and the upper plate moves laterally to the right with a velocity  $U$  due to an applied force  $F$ , while the lower plate is stationary. Fluid molecules adhere to the walls of the plates, and therefore, the fluid velocity  $u$  matches the wall

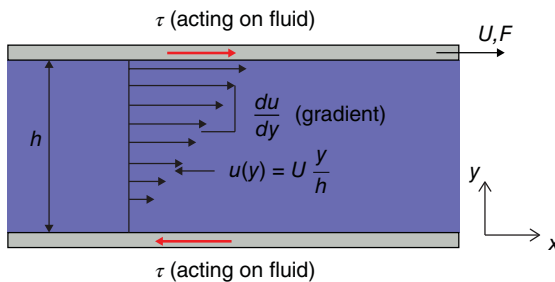


**Figure 2.2** Illustration of a viscosity measurement showing a cross section of a thin layer of fluid subjected to a shear stress between two plates that are in relative linear motion.

velocity at each interface. This is called a *no-slip boundary condition*. Thus,  $u = U$  at the upper boundary and  $u = 0$  at the lower boundary. The velocity varies with distance  $u(y)$  between the plates. If the plates are closely spaced and the velocity  $U$  is low and there is no net fluid flow between the plates, then the velocity profile in the gap will be linear.

#### 2.4.2.1 Newtonian Fluids

Experiments have shown that for a large number of fluids, the applied shear stress  $\tau = F/A$  is proportional to the velocity gradient

$$\tau = \mu \frac{du}{dy} \quad (2.4)$$

where the constant of proportionality  $\mu$  is called the *coefficient of viscosity*, also known as the *absolute viscosity*, *dynamic viscosity*, or *simply the viscosity* [2]. The kinematic viscosity is the ratio of the dynamic viscosity  $\mu$  to the density  $\rho$  and is usually denoted by the  $\nu = \mu/\rho$ . Equation (2.4) is called *Newton's law of viscosity*. The ratio  $U/h$  is called the *rate of shear deformation* or *shear velocity*, and the gradient  $du/dy$  is called the *local shear velocity* or *strain rate*, which has the unit of per second and is often denoted as  $\dot{\gamma}$ . Fluids that obey Newton's law of viscosity, that is, for which  $\mu$  is a constant independent of the shear velocity, are known as *Newtonian fluids*.

#### 2.4.2.2 Non-Newtonian Fluids

Fluids for which  $\mu$  varies with the shear velocity are known as non-Newtonian fluids [5]. Three general classes of non-Newtonian liquids can be distinguished: time-independent, time-dependent, and viscoelastic fluids. In time-independent fluids, the rate of shear at a point is determined only by the value of the shear stress at that point at that instant. These are referred to as *purely viscous*, *inelastic*, or *generalized Newtonian fluids*. In time-dependent fluids, the relation between the shear stress and the shear rate depends on the duration of shearing and the kinematic history of the fluids. Viscoelastic fluids exhibit characteristics of both ideal fluids and elastic solids and show partial elastic recovery after deformation. The following is a brief list of different non-Newtonian fluid categories (Figure 2.3):

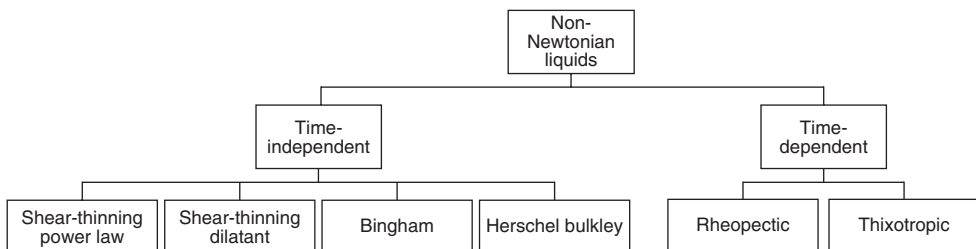


Figure 2.3 Non-Newtonian liquids.

- *Plastic*: A shear stress must reach a minimum threshold before flow commences.
- *Bingham Plastic*: Similarly to plastic, a minimum shear stress must be achieved.
- *Pseudoplastic*: No minimum shear stress is necessary and the viscosity decreases with the rate of shear.
- *Dilatant Substances*: Viscosity increases with the rate of shear, for example, quicksand.
- *Thixotropic Substances*: Viscosity decreases with the length of time the shear force is applied.
- *Rheopectic Substances*: Viscosity increases with the length of time the shear force is applied.
- *Viscoelastic Materials*: Similar to Newtonian fluids, but their behavior is similar to that of plastic when a sudden large change in shear is applied.

### 2.4.3

#### Surface Tension

As previously noted, molecules in a liquid exhibit cohesion, that is, an attractive intermolecular force. At the interface (surface) between a liquid and a gas (or between two immiscible (not mixable) liquids), there is an asymmetric attractive force on the molecules that gives rise to a tension at the surface, that is, a surface tension as shown in Figure 2.4. The surface tensions of liquids cover a wide range of values, and most decrease slightly with increasing temperature [4]. The molecules of a liquid exhibit adhesion as well as cohesion. The adhesive force, attractive force between unlike molecules, enables a liquid to adhere to another body. When a liquid is placed on a substrate, the shape it takes depends on the relative strengths of these forces. If the adhesive force dominates, the liquid will be pulled onto (wet) the substrate. If the cohesive force dominates, the liquid will tend to “bead up” on the surface.

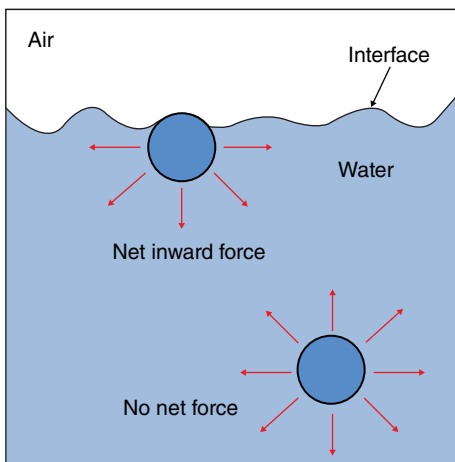


Figure 2.4 Illustration of how intermolecular forces give rise to surface tension.

Capillarity is the property of exerting forces on fluids by fine tubes or porous media. When the cohesive force within a liquid dominates the adhesive force to a wall, the surface of the liquid will form a concave down shape in order to reduce contact with the wall. However, when the adhesive force dominates, the liquid has a stronger attraction to the wall than its interior and its surface will adopt a concave upward shape. The curved liquid surface that forms is called a *meniscus*.

## 2.5

### Force, Pressure, Velocity

Forces, in one form or another, drive the motion of fluids. Two different types of force are encountered in fluid mechanics: surface forces, which are proportional to area, and body forces, which are proportional to volume. Surface forces are usually expressed in terms of stress  $\sigma$  (i.e., force per unit area). The major surface forces constitute pressure  $p$ , which always acts normal to a surface, and viscous shear stresses  $\sigma_{ij}$ , which develop within a fluid when its molecules are in relative motion with respect to one another. Pressure is a normal stress that equals  $F_n/A$ , where  $F_n$  is the force acting normal to a surface with an area  $A$ . Pressure is referred to as *tensile* or *compressive*, depending on whether it tends to stretch or compress a fluid, respectively. Standard atmospheric pressure is 1 atm, that is, 1 atm = 101 325 Pa and is equivalent to 760 mm Hg (torr) or 29.92 in Hg or 14.696 psi. The amount by which a pressure exceeds the ambient atmosphere pressure is called the *gauge pressure*. Many pressure gauges report the gauge pressure, not the absolute pressure, which equals the gauge pressure plus the atmospheric pressure.

A flowing fluid is described by a velocity field  $\vec{v}$ , that is, a vector-valued function of space and time that typically varies in both magnitude and direction from point to point within the fluid:

$$\vec{v}(x, y, z, t) = u(x, y, z, t)\hat{x} + v(x, y, z, t)\hat{y} + w(x, y, z, t)\hat{z} \quad (2.5)$$

The fluid velocity field  $\vec{v}$  for practical applications is often very complicated and typically needs to be predicted using numerical analysis. The volumetric flow rate  $Q$  through an area  $A$  with a unit normal  $\hat{n}$  is

$$Q = \int \vec{v} \cdot \hat{n} dA \quad (2.6)$$

If  $U_{\text{ave}}$  is the average velocity normal to a planar area  $A$ , then  $Q = U_{\text{ave}} \cdot A$  ( $\text{m}^3 \text{s}^{-1}$ ). The corresponding mass flow rate is

$$\dot{m} = \rho U_{\text{ave}} A \text{ (kg s}^{-1}\text{)} \quad (2.7)$$

where  $\rho$  is the fluid density. The momentum flow rate  $\dot{M}$  is obtained by multiplying  $\dot{m}$  by the fluid velocity, that is,  $\dot{M} = \rho U_{\text{ave}}^2 A$ . These expressions are useful for estimating mass and momentum transport for relatively simple applications. A more rigorous analysis is discussed in the next section.

## 2.6

## Fluid Dynamics

The underlying physics and corresponding equations that govern fluids in motion can be understood by analyzing the fluid at either the molecular or the continuum level. The molecular description is needed when the dimensions of a system are comparable to, or smaller than, the mean free path of the fluid molecules. For liquids, this length scale is on the order of nanometers. In most conventional fluidic applications such as inkjet printing, the length scales are several orders of magnitude greater than this. For such applications, we can ignore the discrete molecular nature of a liquid and adopt instead a continuum approximation wherein properties such as density, pressure, and velocity are well-defined within infinitely small volumes and vary continuously from point to point. The continuum equations that govern fluid flow can be derived from the fundamental conservation laws for mass, linear momentum, and energy combined with constitutive relations between stress and strain within the fluid [6–8]. While the conservation laws broadly apply to all fluids, the constitutive relations are fluid-dependent.

## 2.6.1

## Equations of Fluid Dynamics

In this section, we introduce the equations that govern fluid flow. These can be derived using a Lagrangian or Eulerian approach. In the Lagrangian approach, the fluid is treated as a large number of finite sized fluid particles (see Figure 2.5a). The

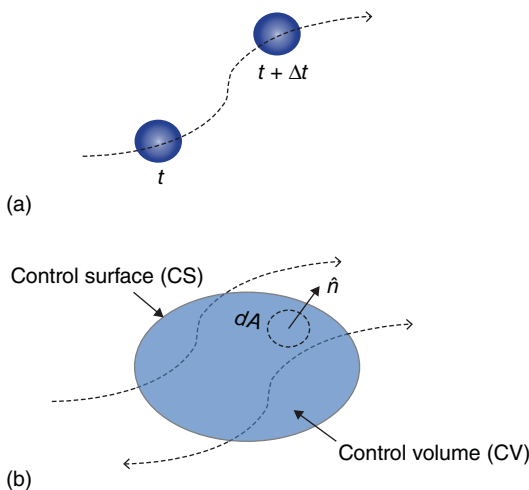


**Figure 2.5** Analysis of fluid flow: (a) Lagrangian approach showing the movement of an individual fluid particle and (b) Eulerian approach showing flow through a control volume.



particles have mass, momentum, and internal energy and are governed by physical laws. However, it is problematic to track the behavior of the large number of individual particles that are needed to represent fluid flow in the continuum limit. Thus, the Lagrangian approach is seldom used to analyze fluid flow. Instead, an Eulerian approach is adopted wherein a control volume (CV) is defined and the flow properties, e.g. pressure and velocity, are described as fields within the CV. A CV and fluid streamlines are shown in Figure 2.5b. The streamlines are instantaneously tangent to the velocity vector of the flow. The equations that govern the flow dynamics can be derived by applying the conservation of mass, momentum, and energy to fluid flowing through the CV. Consider a closed, stationary, and nondeformable CV with a control surface (CS) as shown in Figure 2.5b. We assume that the CV is fixed in space and that fluid moves through it. The conservation laws of mass, momentum, and energy are applied to the fluid within the CV. In doing so, we obtain equations for the conservation laws in integral form and then transform these to the more commonly used differential form [6, 7, 9].

### 2.6.1.1 Conservation of Mass

The rate of change of mass in a CV equals the net inflow of mass through its surface. This can be expressed in integral form as follows:

$$\underbrace{\frac{d}{dt} \int_{CV} \rho dV}_{\text{rate of change of mass in CV}} = \underbrace{- \int_{CS} \rho \vec{v} \cdot \hat{n} dA}_{\text{net in flow of mass through CS}} \quad (2.8)$$

where  $\vec{v}$  is the fluid velocity field and  $\hat{n}$  is the unit normal on CS (Figure 2.5). This integral equation can be transformed into differential form using the Divergence theorem,

$$\frac{\partial \rho}{\partial t} + \nabla \cdot (\rho \vec{v}) = 0 \quad (\text{conservation of mass}) \quad (2.9)$$

This can be expanded as follows:

$$\frac{\partial \rho}{\partial t} + (\vec{v} \cdot \nabla) \rho + \rho \nabla \cdot (\vec{v}) = 0 \quad (2.10)$$

If the fluid is incompressible, that is, if

$$\frac{\partial \rho}{\partial t} + (\vec{v} \cdot \nabla) \rho = 0 \quad (\text{incompressible fluid}) \quad (2.11)$$

Then, we find that the continuity equation reduces to

$$\nabla \cdot (\vec{v}) = 0 \quad (\text{incompressible fluid}) \quad (2.12)$$

The assumption of incompressibility as expressed in Eq. (2.12) enables simplification of the momentum and energy equations as we show in the following sections.

### 2.6.1.2 Conservation of Momentum

The conservation of momentum follows from Newton's second law of motion. The sum of the forces on a mass of fluid within a CV equals the rate of change of its

momentum. The integral equation that embodies this principle is

$$\underbrace{\sum_{\text{sum of forces}} \vec{F}} = \underbrace{\frac{d}{dt} \int_{CV} \rho \vec{v} dV}_{=\text{rate of change of momentum}} = \underbrace{\int_{CS} \overleftrightarrow{S} \cdot \hat{n} dA}_{=\text{surface forces}} + \underbrace{\int_{CV} \vec{f} dV}_{+\text{body forces}} \quad (2.13)$$

where  $\rho \vec{v}$  is the momentum of the fluid per unit volume,  $\vec{f}$  represents external body forces (e.g., gravitational) that act on the CV. In the last term,  $\overleftrightarrow{S}$  is a (second rank) tensor that accounts for surface forces. It consists of an isotropic pressure component  $p \overleftrightarrow{I}$  and a component  $\overleftrightarrow{\tau}$  due to viscous stress,

$$\overleftrightarrow{S} = -p \overleftrightarrow{I} + \overleftrightarrow{\tau} \quad (2.14)$$

In this expression  $\overleftrightarrow{I}$  is the unit tensor and  $\overleftrightarrow{\tau}$  is the viscous stress tensor, which depends on the fluid, for example, its functional form is different for Newtonian and non-Newtonian fluids. For example, for a Newtonian fluid,

$$\overleftrightarrow{\tau} = \mu(\nabla \vec{v} + \nabla \vec{v}^T) + \zeta(\nabla \cdot \vec{v}) \overleftrightarrow{I} \quad (2.15)$$

where  $\mu$  and  $\zeta$  are the first (absolute) and second (bulk) coefficients of viscosity, respectively. We substitute Eq. (2.15) into Eq. (2.13) and transform the resulting integral equation into an equivalent differential equation using the Divergence Theorem, which yields

$$\rho \left( \frac{\partial \vec{v}}{\partial t} + \vec{v} \cdot \nabla \vec{v} \right) = -\nabla p + \nabla \cdot \overleftrightarrow{\tau} + \vec{f} \quad (\text{Navier-Stokes equation}) \quad (2.16)$$

This is the Navier–Stokes equation for a compressible Newtonian fluid. If the fluid is incompressible, we can apply Eq. (2.12) and obtain the following simplified equation:

$$\rho \left( \frac{\partial \vec{v}}{\partial t} + \vec{v} \cdot \nabla \vec{v} \right) = -\nabla p + \mu \nabla^2 \vec{v} + \vec{f} \quad (2.17)$$

The first term in Eq. (2.17) is the temporal acceleration of the fluid while the second term, which is nonlinear, is a convective acceleration. The terms of the right-hand side (RHS) of the equation account for the effects of pressure, viscosity, and body forces, respectively.

### 2.6.1.3 Conservation of Energy

The conservation of energy follows from the first law of thermodynamics. We analyze this by equating the change in energy  $E$  of a mass of fluid in an arbitrary (stationary) CV to the difference of the thermal energy  $Q$  added to the fluid minus the work  $W$  done by the fluid, that is,  $dE = dQ - dW$ . The time rate of change of energy  $\dot{E}$  (the dot indicates the time derivative) can be expressed in integral form by summing the change in internal energy  $e$  per unit mass within the CV and the flux of  $e$  through CS [6],

$$\dot{E} = \frac{d}{dt} \int_{CV} \rho e dV + \int_{CS} \rho e (\vec{v} \cdot \hat{n}) dA \quad (2.18)$$

where,

$$e = \tilde{u} + \frac{1}{2}|\vec{v}|^2 + gz \quad (2.19)$$

The variable  $\tilde{u}$  is the internal molecular energy,  $\frac{1}{2}|\vec{v}|^2$  is the kinetic energy, and  $gz$  is the gravitational potential energy, all on a per unit mass basis. The energy balance for the CV can be written as

$$\frac{d}{dt} \int_{CV} \rho e dV + \int_{CS} \rho e (\vec{v} \cdot \hat{n}) dA = \dot{Q} - \dot{W} \quad (2.20)$$

where  $\dot{Q}$  is due to heat transfer through the CS and  $\dot{W}$  represents different forms of work done by the fluid.  $\dot{Q}$  can have contributions from conduction, radiation, and convection heat transfer.

Here, we simplify the analysis and consider thermal conduction only. It follows from Fourier's law of thermal conduction that  $\dot{Q} = \int_{CS} k(\nabla T \cdot \hat{n}) dA$  over CS, where  $k$  and  $T$  are the thermal conductivity and temperature of the fluid, respectively. Similarly,  $\dot{W}$  can include contributions from a number effects, for example, mechanical manipulation, pressure-driven and viscous drag, among others,

$$\dot{W} = \dot{W}_{\text{mech}} + \dot{W}_p + \dot{W}_{\text{viscous}} + \dots \quad (2.21)$$

$\dot{W}_{\text{mech}}$  is the rate of work done by the fluid via mechanical means (e.g., an impeller) inside the CV,  $\dot{W}_p = \int_{CS} p(\vec{v} \cdot \hat{n}) dA$  is due to pressure  $p$ , and  $\dot{W}_{\text{viscous}} = - \int_{CS} (\vec{v} \cdot \overleftrightarrow{\tau}) \cdot \hat{n} dA$  is due to the effects of viscous stress. Note that these two terms only involve surface integrals because any actions between fluid elements within the CV are self-canceling (i.e., equal and opposite forces). We substitute these expressions into Eq. (2.20) and obtain an integral equation for the conservation of energy,

$$\begin{aligned} \frac{d}{dt} \int_{CV} \rho e dV = & - \int_{CS} \rho e (\vec{v} \cdot \hat{n}) dA + \int_{CS} k(\nabla T \cdot \hat{n}) dA - \int_{CS} p(\vec{v} \cdot \hat{n}) dA \\ & + \int_{CS} (\vec{v} \cdot \overleftrightarrow{\tau}) \cdot \hat{n} dA + \int_{CV} \rho(\vec{f} \cdot \vec{v}) dV \end{aligned} \quad (2.22)$$

The third and fourth terms on the RHS correspond to the rate of work done by pressure  $p$  and viscous stress ( $\overleftrightarrow{\tau}$ ), respectively. The last term on the RHS represents the work done by the net body force  $\vec{f}$  on the fluid. If we assume  $\vec{f} = 0$  and apply the Divergence theorem to the surface integrals in Eq. (2.22), we obtain a volume integral over CV

$$\int \left( \frac{\partial}{\partial t} (\rho e) + \nabla \cdot (\rho e \vec{v}) - \nabla \cdot (k \nabla T) + \nabla \cdot (p \vec{v}) - \nabla \cdot (\vec{v} \cdot \overleftrightarrow{\tau}) \right) dV = 0 \quad (2.23)$$

Since the CV is arbitrary, the integrand in Eq. (2.23) must be zero,

$$\frac{\partial}{\partial t} (\rho e) + \nabla \cdot (\rho e \vec{v}) - \nabla \cdot (k \nabla T) + \nabla \cdot (p \vec{v}) - \nabla \cdot (\vec{v} \cdot \overleftrightarrow{\tau}) = 0 \quad (2.24)$$

This equation can be rewritten as

$$\rho \left[ \frac{\partial e}{\partial t} + \nabla \cdot (e\vec{v}) \right] - \nabla \cdot (k\nabla T) + \nabla \cdot (p\vec{v}) - \nabla \cdot (\vec{v} \cdot \vec{\tau}) = 0 \quad (2.25)$$

It should be noted that we combined Eq. (2.9) with Eq. (2.24) to obtain Eq. (2.25).

Next, we introduce the viscous dissipation function  $\Phi = \vec{\tau} \cdot (\nabla \cdot \vec{v})$  and use this to simplify Eq. (2.25),

$$\rho \frac{De}{Dt} + p(\nabla \cdot \vec{v}) = \nabla \cdot (k\nabla T) - \vec{v} \cdot \nabla p + \vec{v}(\nabla \cdot \vec{\tau}) + \Phi \quad (2.26)$$

where  $\frac{D}{Dt} = \frac{\partial}{\partial t} + \vec{v} \cdot \nabla$  is the convective derivative. From Eq. (2.19), we have

$$\rho \frac{De}{Dt} = \rho \left( \frac{D\tilde{u}}{Dt} + \vec{v} \cdot \frac{D\vec{v}}{Dt} + \frac{D(gz)}{Dt} \right) \quad (2.27)$$

The second term on the RHS of Eq. (2.27) can be written as  $\rho\vec{v} \cdot \frac{D\vec{v}}{Dt} = \vec{v} \cdot (\rho\vec{g} - \nabla p + \nabla \cdot \vec{\tau})$  (see Eq. (4.32) in [6]). We equate Eqs. (2.26) and (2.27), and after some manipulation, we obtain a differential equation for the conservation of energy for a compressible fluid,

$$\rho \frac{D\tilde{u}}{Dt} + p(\nabla \cdot \vec{v}) = \nabla \cdot (k\nabla T) + \Phi \quad (\text{conservation of energy}) \quad (2.28)$$

This equation can be rewritten to account for heat transfer. To this end, note that the internal molecular energy  $\tilde{u}$  is related to temperature, that is,  $\left( \frac{d\tilde{u}}{dT} \right)_V = C_V$ , where  $C_V$  is the specific heat of the fluid at constant volume. Thus, we can eliminate  $\tilde{u}$  from Eq. (2.28) and obtain an equation for heat transfer in a compressible fluid,

$$\rho C_V \left( \frac{\partial T}{\partial t} + \vec{v} \cdot \nabla T \right) + p(\nabla \cdot \vec{v}) = \nabla \cdot (k\nabla T) + \Phi \quad (\text{heat transfer}) \quad (2.29)$$

where  $T$  is the fluid temperature in  $K$ . If the fluid is incompressible, Eq. (2.29) reduces to

$$\rho C_V \left( \frac{\partial T}{\partial t} + \vec{v} \cdot \nabla T \right) = \nabla \cdot (k\nabla T) + \Phi \quad (\text{incompressible fluid}) \quad (2.30)$$

It should be noted that the viscous loss term  $\Phi$  is often ignored in heat transfer analysis as it is often negligible as compared to thermal conduction.

## 2.6.2

### Solving the Equations of Fluid Dynamics

The equations that govern fluid flow are based on the fundamental conservation laws of mass, momentum, and energy. The conservation laws along with the corresponding differential equations are as follows:

*Conservation of mass:*

$$\frac{\partial \rho}{\partial t} + \nabla \cdot (\rho\vec{v}) = 0 \quad (2.31)$$

Conservation of momentum (Navier–Stokes):

$$\rho \left( \frac{\partial \vec{v}}{\partial t} + \vec{v} \cdot \nabla \vec{v} \right) = -\nabla p + \mu \nabla^2 \vec{v} + \vec{f} \quad (2.32)$$

Conservation of energy:

$$\rho \frac{D\tilde{u}}{Dt} = \nabla \cdot (k \nabla T) + \Phi \quad (2.33)$$

The viscous dissipation function  $\Phi$  is defined and depends on  $\vec{v}$ . It should be noted that Eq. (2.32) only applies for Newtonian above fluids and that this equation and Eq. (2.33) are only valid for an incompressible fluid (see Eq. 2.12), for which

$$\nabla \cdot \vec{v} = 0 \quad (2.34)$$

The conservation Eqs. (2.31)–(2.33) collectively represent five equations (one for mass, three for momentum, and one for energy). However, these equations contain seven unknown variables: pressure  $p$ , density  $\rho$ , internal molecular energy  $\tilde{u}$ , temperature  $T$ , and three velocity components  $v_i$ . Thus, there are more unknowns than independent equations and two additional independent equations are needed to provide a complete (closed) system of equations that can be solved. These are provided by state relations for the thermodynamic properties, for example,  $\rho = \rho(p, T)$  and  $\tilde{u} = \tilde{u}(p, T)$ . For example, as noted, the internal molecular energy  $\tilde{u}$  is related to temperature, and we can eliminate  $\tilde{u}$  from Eq. (2.33), and obtain the equation for heat transfer Eq. (2.29), thereby reducing the number of unknowns from seven to six.

Finally, in order to solve these equations, we need initial values for the unknown variables  $p, \rho, \tilde{u}, T$ , and  $v_i$ , that is, an initial spatial distribution of the form  $p = p(x, y, z)$ , and so on. Appropriate boundary conditions (BCs) must also be specified. It is important to note that these equations are usually too difficult to solve analytically for practical applications. Instead, a numerical solution is often required, as described in the following section.

## 2.7

### Computational Fluid Dynamics

The equations that govern fluid flow cannot be solved analytically for most practical applications. Instead, they are usually solved using some form of numerical technique. Computational fluid dynamics (CFD) is the science of predicting the behavior of fluid flow and related transport phenomena by solving the underlying governing equations using numerical methods [6, 9–12]. The development of CFD solution methods is a complex undertaking that requires multidisciplinary expertise in fields that include fluid mechanics, multiphase and phase change phenomena and numerical methods, and so on. These specialized skills fall outside the expertise of many scientists and engineers that work with fluids. Fortunately, commercial CFD programs have been developed that can be used by practitioners to analyze a broad range of fluidic applications. Some popular commercial CFD programs include PHOENICS, FLUENT, FLOW3D, STAR-CD and

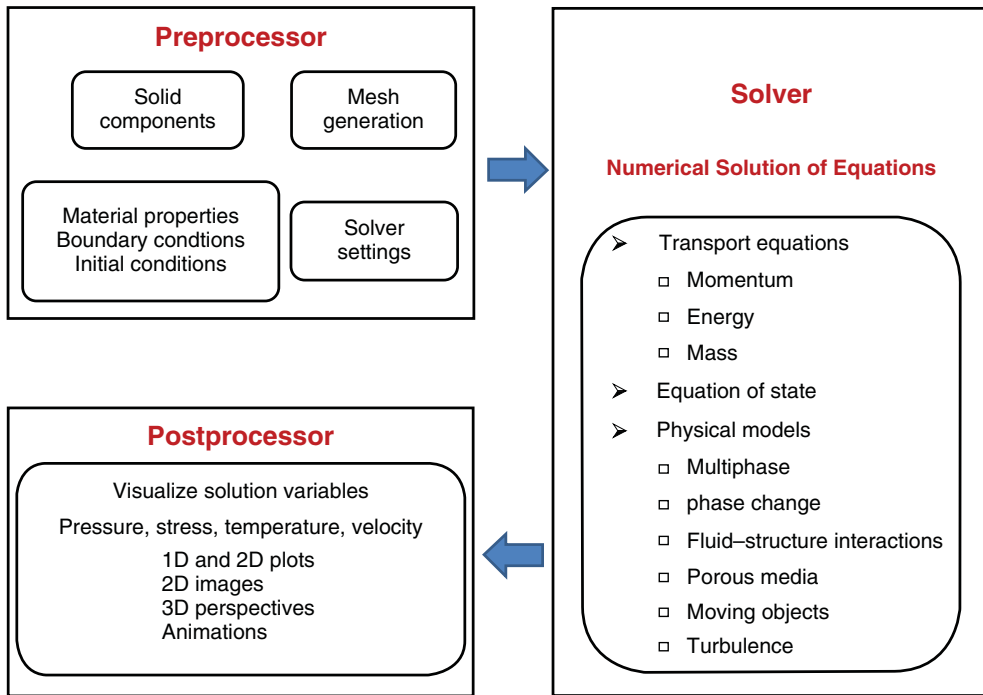


Figure 2.6 Illustration of workflow in CFD analysis.

CFX, FLOWTHERM, and SMARTFIRE, among others. The availability of such programs combined with a dramatic increase in computational power at reduced cost has had a transformative impact in the development of fluidic applications. CFD simulations play an increasingly important role in the development of new fluidic-based technology by enabling both fundamental understanding and the rational design of processes and devices in advance of fabrication. The use of CFD can greatly expedite the development of a new technology.

Many commercial CFD programs employ a user-friendly graphic user interface (GUI) to facilitate the setup, solution, and analysis of an application. A schematic of the work flow for CFD analysis is shown in Figure 2.6. Most CFD programs implement this workflow using three distinct subprograms: a preprocessor, a solver, and a postprocessor. The functionality of these subprograms is described in the following sections.

### 2.7.1

#### Preprocessor

The preprocessor is a GUI-driven subprogram that is used to set up and initialize an application. This usually involves specifying the (a) computational domain, that is, the size and shape of the solution region; (b) system geometry, dimensions, and properties of all materials and fluids; (c) initial conditions (ICs), initial values of the

dependent variables (e.g., pressure, velocity, temperature) throughout the computational domain; and (d) BCs, for example, the values of the dependent variables at the boundary of the computational domain. The BCs most often used in CFD analysis are the no-slip velocity condition in which the fluid velocity at a boundary equals the velocity of the boundary itself, an axisymmetric BC that reflects cylindrical symmetry of the system, inlet and outlet (pressure, velocity, temperature) BCs, periodic BCs that are used to study a unit cell of a periodic structure, and various symmetry BCs that exploit symmetry of the system to reduce the computational domain and complexity of the analysis.

A computational grid (mesh) is also defined in the preprocessing stage of analysis. The mesh divides the computational domain into smaller, nonoverlapping subdomains. Figure 2.7 shows the preprocessing steps for a CFD model of a piston-driven droplet ejector. The device geometry is shown in Figure 2.7a along with the computational domain and mesh in Figure 2.7b. The mesh provides a geometric framework for the discretization of the equations of motion, that is, transformation of partial differential equations (PDEs) into matrix equations that are solved to obtain discrete values of the dependent variables (e.g., pressure, velocity, temperature) in the grid elements. In general, a finer discretization produces a more accurate solution. The grid can be Cartesian or polar, orthogonal or nonorthogonal. In regular Cartesian grids, the cell length in each direction is constant. In orthogonal grids, the grid lines in the different directions are normal

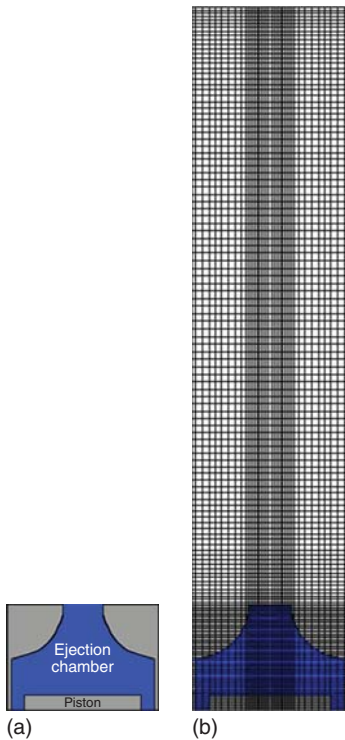


**Figure 2.7** Preprocessing of CFD model of a piston-driven droplet ejector: (a) device geometry and (b) computational domain and mesh.

to one another, and in curvilinear grids, the grid lines can be arbitrary curves in space. Three types of grids are commonly used: structured, unstructured, and hybrid grids where some portions of computational domain are structured and others are unstructured.

In a structured grid, all nodes have the same number of neighboring elements. A structured grid is useful for relatively simple domains. For more complex domains, an unstructured grid is advised. However, an unstructured grid has certain disadvantages, that is, it is more difficult to store system variables because the data structure is irregular. A hybrid block structure grid represents a compromise between a structured and an unstructured grid. In this case, the domain is divided into several blocks, and structured grids are used in different blocks. Optimal grids are often nonuniform wherein a finer mesh is used in regions where there is a large variation in the variables and a coarse mesh is used in regions where there is relatively little change in the variables.

### 2.7.2

#### **Solver**

Once the preprocessing phase of analysis is complete, the solver subprogram is invoked. This subprogram solves the governing equations for the dependent variables (e.g., pressure, velocity, temperature) using numerical methods. In this approach, the underlying differential equations are transformed to a system of algebraic equations that are typically solved either directly or via an iterative process. Most programs enable the user to control the solution by selecting an appropriate numerical technique and parameters that govern the numerical analysis such as the maximum time step and convergence tolerance. The most common numerical methods used in commercial CFD programs are the finite volume method (FVM) (~80%) and the finite element method (FEM) (~15%). Additional solution techniques include the finite difference method, spectral methods, boundary element method, and lattice Boltzmann analysis, among others. The details of these methods are beyond the scope of this chapter but can be found in the literature [10, 11].

### 2.7.3

#### **Postprocessor**

Once the problem has been solved, the postprocessor subprogram is used to examine and visualize the solution variables. Figure 2.8a,b shows the postprocessing of a CFD model of a piston-driven droplet ejector. Images of a) the fluid ejection and b) droplet formation are shown together with a color bar showing the vertical fluid velocity. Most postprocessors enable the user to display all or select portions of the device geometry from various desired viewpoints. The view of the system can be manipulated, that is, translated, rotated, and magnified. Similarly, the grid can be displayed separately or overlaid on the geometry if desired. Solved variables such as pressure, velocity, and temperature can be plotted within specified volumes, on surfaces and along designated lines. Vector



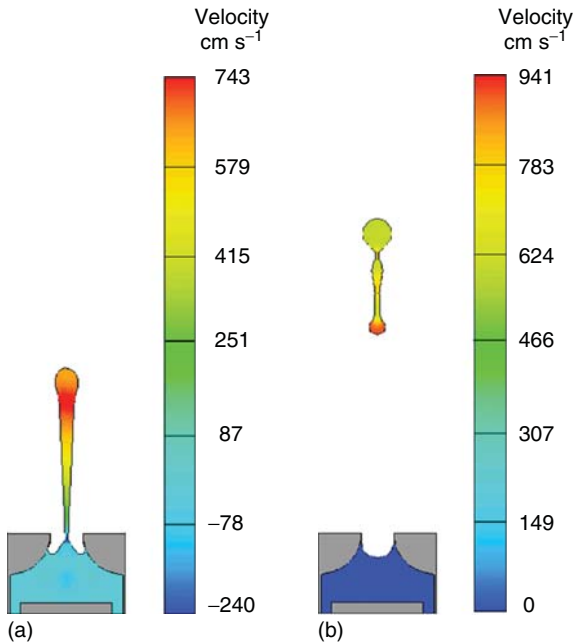


**Figure 2.8** Postprocessing of a piston-driven droplet ejector CFD model: (a) ejection of fluid and (b) droplet formation.

fields such as velocity can be visualized using 2D and 3D plots that show a prescribed number of vectors per unit volume or area and with a length that is scaled according to the magnitude of the vector. 2D and 3D surface plots as well as line and shaded contour plots of solved variables can also be displayed. Most postprocessors enable animation of the solution to visualize dynamic behavior.

## 2.8

### Inkjet Systems

In this section, we briefly discuss the key components and processes of inkjet systems and the application of computational modeling for the rational design of these systems. More detailed discussions of these topics are presented in the following chapters. An inkjet system basically consists of three fundamental components: inks, a print engine (printhead), and an imaging medium (e.g., paper) [13–15]. Inks produce color by selectively absorbing and scattering light. Inks can be broadly categorized into three groups based on their colorant, that is, organic dyes, polymeric dyes, and pigments. Organic dyes consist of organic dye molecules, polymeric dyes consist of dye polymers, and pigmented inks contain a dispersion of inorganic pigment particles. The printhead operates under digital control and projects droplets of ink, typically 10–100  $\mu\text{m}$  in diameter depending on the technology, onto the imaging medium to form an image. Modern inkjet systems utilize microfabricated printheads that contain hundreds to thousands

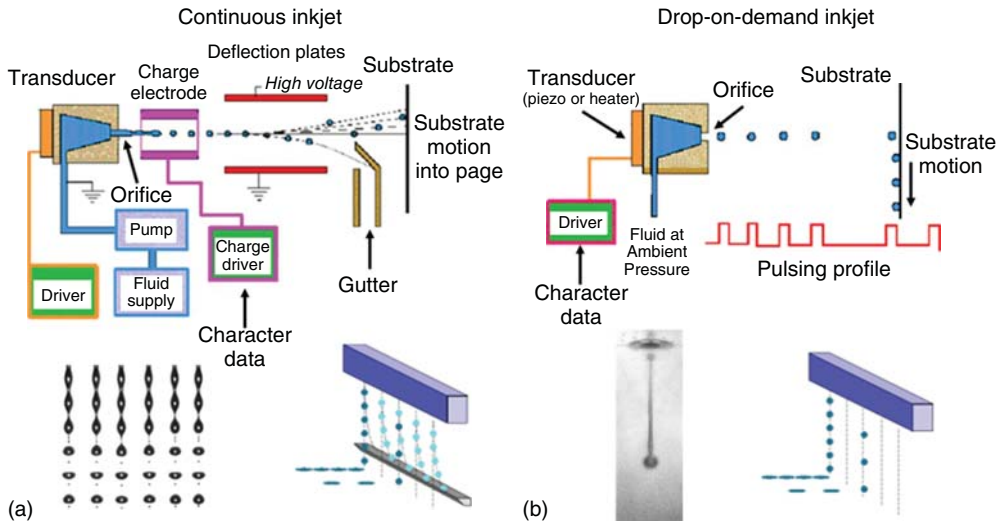


**Figure 2.9** Inkjet printing methods: (a) continuous inkjet and (b) drop-on-demand inkjet.

of integrated micronozzles. A printhead can produce millions of droplets of ink per second with remarkable uniformity in both volume and velocity. The droplets are projected onto the imaging medium with precision placement to render high-quality images. While traditional printing has been the dominant impetus for the advancement of inkjet systems, this technology is rapidly evolving toward applications in emerging fields such as the printing of functional materials, deposition of biomaterials, production of pharmaceuticals, and 3D rapid prototyping [15–18] (see Chapter 15).

Inkjet systems broadly fall into two categories, continuous inkjet (CIJ) and drop-on-demand (DOD) inkjet as shown in Figure 2.9 [13, 14, 18, 19]. In CIJ, continuous jets of ink are produced at each nozzle by applying pressure in a common ink reservoir. The jets are inherently unstable (Rayleigh instability) and can be modulated using a periodic stimulus to break up into a stream of uniformly spaced droplets. When the jets are properly modulated, the droplets will have a well-defined volume and velocity ( $10\text{--}20\text{ m s}^{-1}$ ) and will form at a consistent distance downstream from the nozzle [18–21]. The most common method for modulating the jets is mechanical vibration, usually provided by a piezoelectric transducer as shown in Figure 2.9a. A relatively new CIJ technology that is based on periodic thermal modulation of the fluid at the nozzle is described in the following. [22]. A CIJ printhead can produce hundreds of thousands of droplets per second from each nozzle; however, only select droplets are allowed to reach the imaging medium to form the image. The unused droplets are deflected in flight and recycled to the ink reservoir that feeds the printhead. In electrostatic-based CIJ, the nozzle is held at a potential and a small charge is imparted to each drop as it forms. Individual droplets in the stream are steered (deflected) using voltage-driven deflection plates as shown in Figure 2.9a.

In DOD systems, droplets are produced as needed (on demand) to form an image [13–15, 18, 19]. The droplets are generated by applying a raised pressure pulse within an ejection chamber that feeds a nozzle as shown in Figure 2.9b. The time-dependent pressure profile is tuned to eject a droplet with a desired volume and velocity, usually 15–55  $\mu\text{m}$  in diameter and between 3 and 15  $\text{m s}^{-1}$ , respectively [23]. DOD printheads are categorized according to the mechanism used for droplet ejection. The vast majority of commercial DOD printers utilize either piezoelectric or thermal-based droplet generation. Piezo DOD printheads use a voltage-induced deformation of a piezoelectric transducer to produce the pressure pulse needed to eject a droplet [13–15, 19, 24]. In thermal inkjet (TIJ) printers (also referred to as *bubble jet*), a resistive heating element is used to superheat the ink within the ejection chamber to generate a homogenous vapor bubble that expands rapidly and provides the pressure needed to eject a droplet [25].

The development of an inkjet system is a complex undertaking that requires an interdisciplinary team of scientists and engineers to address a broad range of technical issues. The commercialization process involves numerous diverse yet coupled efforts. These include the preparation of custom inks, printhead design and fabrication, development of mechanisms for controlling the deposition of droplets onto a moving imaging medium with extreme placement precision, and the optimization of ink media interactions, that is, the spreading, absorption, and coalescence of droplets to achieve a desired image quality. Computational modeling is increasingly used throughout the development effort to advance fundamental understanding of these processes, determine proof-of-concept in advance of fabrication, design and optimize system components, and generally guide the experimental effort. Multiscale and multidisciplinary modeling is required to analyze coupled phenomena that span multiple length and time scales, and multiple disciplines, for example, fluid dynamics, heat transfer, colloidal science, structural analysis, aerodynamics, and microfabrication technology. CFD is the method of choice for much of this analysis, and various commercially available CFD programs are capable of the kind of multiphysics analysis that is needed for inkjet development. However, despite the recent advances in computational capability, many challenges exist in modeling inkjet systems, both processes and components. Some of these challenges are unique to the type of inkjet printing (e.g., modeling fluid–structure interactions in piezo DOD), while others are common to all inkjet systems, for example, modeling drop formation and ink–media interactions. CIJ and DOD inkjet printers and processes are described in detail throughout this book. In this section, we briefly discuss the challenges of using CFD modeling for the development of inkjet systems.

### 2.8.1

#### Inkjet Modeling Challenges

Applications of CFD have proliferated in recent years due to rapid progress in the underlying numerical methodology and the dramatic increase in computational power at reduced cost. However, despite these advances, many challenges remain

in applying CFD modeling to inkjet systems. A major reason for this is the complexity of inkjet technology, especially the multiscale and multiphysics nature of the underlying processes. As an example, consider a printhead, the central component of an inkjet printer. A modern printhead can contain hundreds to thousands of integrated micronozzles, each capable of producing tens to hundreds of thousands of droplets per second depending on the mode of operation. The length scales involved in printhead analysis range from microns for the nozzles to millimeters or centimeters for the entire printhead. Similarly, the timescales that govern droplet generation, formation, and transport can range from submicrosecond to hundreds of microseconds. Moreover, the droplet generation process can involve coupled phenomena that span multiple disciplines, for example, fluid and structural dynamics, multiphase analysis, and heat transfer, among others. Currently, it is not feasible to model the operation of a printhead using CFD exclusively, much less model an entire inkjet system. Instead, a combination of modeling techniques is used, which can range from multiphysics CFD simulations for microscale analysis to analytical or lumped-element modeling for meso- to macroscale (e.g., system-level) analysis. These are usually applied in a hierarchical fashion wherein the results obtained from small-scale models are used as input for larger scale models.

Many of the challenges in applying CFD to inkjet systems fall within broader categories of challenges that are encountered in a wide range of applications. Some of the more relevant modeling challenges can be classified as follows:

- *Free-Surface Analysis (FSA)* – droplet generation, dynamics of ink–air interface.
- *Fluid–Structure Interaction (FSI)* – piezo DOD fluid–structural dynamics.
- *Phase Change Analysis (PCA)* – TIJ bubble generation.
- *Ink–Media Interaction (IMI)* – image formation on a porous medium.
- *Non-Newtonian Fluids* – printing functional materials.

All of these topics are active areas of research in the field of CFD. We describe these in general terms and then refine the discussion to the modeling of specific inkjet processes in the following section.

### 2.8.1.1 Free-Surface Analysis

The term free surface is often used to describe the interface between a liquid and any gas. Technically a free surface defines an interface between a liquid and a second medium that cannot support an applied pressure gradient or shear stress. Thus, the interface is unconstrained by the medium. This is the case for liquid–gas interfaces because of the large difference in densities between the two phases of matter (e.g., 1000 to 1 for water and air). The inertia of the gas is negligible, and the liquid moves independent of it, that is, the liquid–gas interface is unconstrained by the gas. The concept of a free surface is fundamental in inkjet systems as it describes the interface between ink and air, for example, the surfaces of jets, droplets, and ink menisci. FSA falls within the broader category of multiphase analysis, which applies to systems that contain materials in different states of

matter (e.g., ink and air) or materials in the same state but with different chemical properties (e.g., oil droplets in water). The ability to numerically track the evolution of a free surface is critical for predicting droplet generation for all inkjet systems. However, free-surface flows are difficult to model because the interface changes in time, which presents many complications, for example, the dynamic determination and application of interface BCs [26, 27]. Several techniques have been developed to track interfaces. Some of the more popular techniques are as follows:

- Volume of Fluid (VOF)
- Level Set
- Lagrangian Grid Methods
- Surface Height Method
- Marker-and-Cell (MAC) Method.

Many interface tracking techniques can be classified as either Eulerian or Lagrangian. In the Eulerian approach, the fluid moves through a fixed mesh, whereas in the Lagrangian approach, the mesh moves with the fluid. The VOF method is among the most popular Eulerian-based interface tracking techniques. VOF is based on the concept of a fluid volume fraction that advects (moves) with the flow [28]. The fluid volume fraction is calculated in each computational cell during each time step and ranges from 0 for an empty cell to 1 for a full cell as shown in Figure 2.10. The partially filled cells indicate the location of the fluid surface, but they do not define its shape. The shape (curvature) of the free surface needs to be reconstructed throughout the computational domain using the local values of the volume fraction.

Figure 2.11 shows a VOF-based CFD simulation of a free-standing oscillating droplet moving through a fixed Eulerian grid in the absence of gravity. The droplet is initially in the shape of an oblate spheroid and oscillates until it obtains a spherical shape, that is, the lowest surface energy. The oscillation is damped by viscous drag. One problem in using the VOF method is that interface reconstruction can be problematic and can lead to errors in the surface curvature, which in turn produces errors in the predicted fluid pressure and velocity. These numerical errors can propagate and produce numerical instabilities in a simulation.

1	1	1	0.68	0
1	1	1	0.42	0
1	1	0.92	0.09	0
1	0.85	0.35	0	0
0.31	0.09	0	0	0
0	0	0	0	0

**Figure 2.10** VOF method: 2D mesh with filled, partially filled, and empty cells.

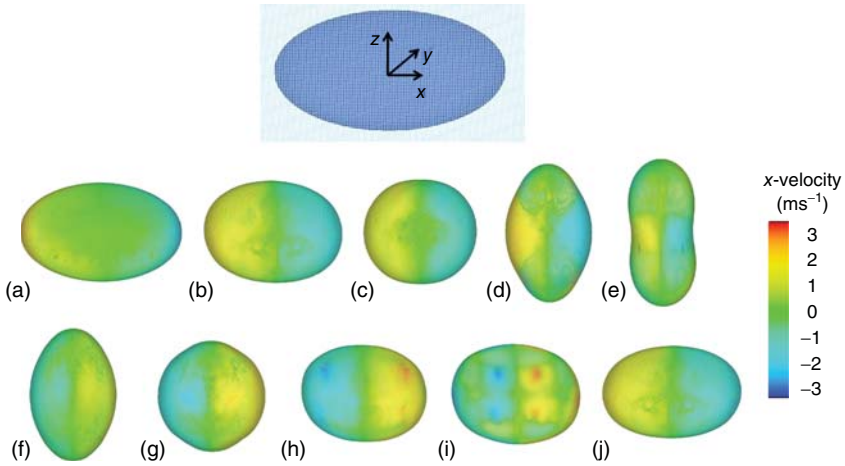


**Figure 2.11** A VOF-based CFD simulation of an oscillating droplet (colored by  $x$ -velocity). The top figure shows the droplet in its initial oblate spheroidal shape within a fixed

uniform (Eulerian) computational mesh: Panels (a–j) show a time-ordered sequence of simulation images that show the droplet evolving into a spherical shape.

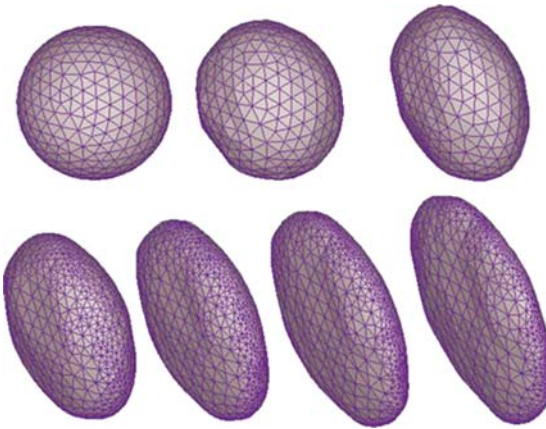


**Figure 2.12** Lagrangian grid tracking of an oscillating droplet showing mesh deformation.

In the Lagrangian approach the computational grid moves with the fluid. Since the grid and fluid move together, the grid automatically tracks the free surface. An example of Lagrangian interface tracking of a free-standing droplet is shown in Figure 2.12. The main problem with this approach is that it cannot track surfaces that break apart or intersect without regridding. Such mesh manipulation is complicated and problems of mesh distortion can lead to numerical instability.

A major difficulty in applying CFD interface tracking methods to inkjet systems is the fact that critical processes such as droplet pinch-off and the formation of

satellite droplets involve the breakup and merging of small fluid volumes that can take place over submicrosecond time frames. While commercial CFD programs can predict drop volume and velocity that is consistent with experimental observations, a rigorous prediction of critical small-scale fluid behavior is problematic and remains to be validated.

#### 2.8.1.2 Fluid–Structure Interaction

A FSI occurs whenever a structure displaces fluid [29]. The structure may be partially or fully immersed in the fluid or simply in contact with it. As the structure moves, it alters flow within the fluid, and this, in turn, produces a pressure load on the fluid–structure interface. A rigorous analysis of FSI involves a coupled solution of the fluid and structural dynamic equations. FSI modeling is especially critical for the design of DOD systems such as piezoelectric or electrostatic DOD that utilize the motion of a transducer to generate pressure within an ejection chamber to effect droplet ejection and refill. A major challenge in modeling FSI is the difficulty in tracking the fluid–structure interface, especially when the structural displacements are incremental, for example, during each time step of a numerical simulation [29]. An error in tracking the interface results in a corresponding error in the pressure and velocity within the fluid, which impacts the prediction of device performance.

#### 2.8.1.3 Phase Change Analysis

PCA involves predicting the conversion of a material from one state of matter to another and tracking the interface between the two phases when they coexist [30, 31]. PCA is very challenging because it needs to account for the phase diagram of a material, the dynamics of a change in phase, the interface between the phases as they evolve, and the mass and energy transfer at the interface. PCA is especially relevant to TIJ where it is used to study superheat-induced homogeneous bubble nucleation and expansion, which causes the ejection of a droplet [25, 32].

#### 2.8.1.4 Ink–Media Interaction

An IMI occurs whenever ink interacts with a substrate. In inkjet systems, IMI is particularly relevant to image quality, which depends on the impact, coalescence, absorption, and drying of ink droplets, usually on a porous media [33]. Parameters that impact IMI include surface tension (capillary forces), viscous drag, porosity and permeability of paper, and advancing and receding contact angles between the ink and the paper. Challenges encountered in IMI simulations involve the prediction of ink flow into and through a permeable medium, that is, tracking the fluid interface within the medium.

#### 2.8.1.5 Non-Newtonian Fluids

Most inks used in commercial inkjet printers are essentially Newtonian fluids, that is, their viscosity is independent of the strain rate as discussed [5]. The numerical implementation of Newtonian viscosity in CFD analysis is well-established. Hence, commercial CFD programs are routinely used to model Newtonian fluids



for a broad range of applications. However, many emerging nontraditional inkjet applications utilize non-Newtonian fluids, which have complex rheological properties [17]. Examples of such applications include the printing of polymeric-based functional materials for a variety of applications and the deposition of biological media for tissue engineering. A major challenge in using CFD to model non-Newtonian fluids is the numerical implementation of the complex rheology [5]. Currently, only a limited number of non-Newtonian constitutive relations have been implemented in commercial CFD programs. An example of such an expression that takes into account both temperature and strain rate dependence is

$$\mu = \mu_{\infty} + \frac{\mu_0 E_T(T) - \mu_{\infty}}{\lambda_{00} + (\lambda_0 + (\lambda E_T(T) e_{ij} e_{ij})^2)^{(1-n)/2}} + \frac{\lambda_2}{\sqrt{2} e_{ij} e_{ij}} \quad (2.35)$$

where

$$e_{ij} = \frac{1}{2} \left( \frac{\partial u_i}{\partial x_j} + \frac{\partial u_j}{\partial x_i} \right) \quad (2.36)$$

and

$$E_T(T) = \exp \left( a \left( \frac{T^*}{T - b} - c \right) \right) \quad (2.37)$$

In this expression,  $T$  is temperature (K),  $\mu_0$  and  $\mu_{\infty}$  are the molecular and infinite shear viscosities, respectively. The other parameters are described in the vendor documentation ([www.flow3d.com](http://www.flow3d.com)). Finally, it should be noted that, while specialized CFD programs that model a variety of non-Newtonian fluids have been reported in the literature, these typically have a limited scope of application and are not well suited for analyzing and designing commercial inkjet printing systems.

## 2.8.2

### Inkjet Processes

In this section, we discuss the challenges of modeling specific inkjet processes. These processes along with the required CFD modeling functionality (in parenthesis) are as follows:

- DOD Droplet Generation
  - Piezoelectric DOD (FSI, FSA)
  - Thermal DOD (PCA, FSA)
  - Droplet Formation (FSA)
- CIJ Droplet Generation (FSA)
- Image Formation (IMI)
- Crosstalk (Multiscale Effects)
- Functional Printing (Non-Newtonian Fluids)

#### 2.8.2.1 DOD Droplet Generation

As previously noted, a modern DOD printhead can contain hundreds to thousands of integrated micronozzles that can be individually activated to produce



droplets as needed. Each nozzle is fed by an ejection chamber, and various methods are used to create a raised pressure pulse within the chamber to eject a droplet [13–15, 19, 23, 24, 34–36]. The pressure pulse is tuned to produce droplets with well-defined volume and velocity. Piezo DOD and TIJ are by far the most popular inkjet printers, although electrostatic and acoustic DOD printers have also been developed. In DOD systems, the droplet generation cycle can be considered as three distinct phases: (i) drop ejection, wherein a raised pressure pulse is generated within the ejection chamber to eject a mass of ink through the nozzle; (ii) drop formation, where the ejected column of ink deforms and pinches off to form a droplet [24, 34, 35]; and (iii) refill, where ink flows from a reservoir into the ejection chamber to fill it for the next droplet ejection. The complete droplet generation cycle can be simulated using CFD analysis. FSA is a common modeling challenge for each phase of the cycle. Other modeling challenges are specific to the ejection mechanism. We discuss the modeling of piezo DOD and TIJ separately in the following subsections.

**2.8.2.1.1 Piezoelectric DOD** In piezo DOD, a voltage-driven piezoelectric transducer is used to mechanically deform the walls of the ejection chamber to eject a droplet [13–15, 19, 24]. Each nozzle is driven by a separate transducer, and when a voltage is applied, it produces an electric field across a layer of piezoelectric material that causes the transducer to deform. The deformation causes the volume of the ejection chamber to contract or expand depending on the polarity of the applied voltage. This controls the pressure within the chamber, that is, higher pressure when the chamber contracts and lower pressure when it expands. A custom voltage waveform is applied to provide a desired time-dependent pressure within the chamber to optimize both droplet ejection and refill of the chamber [35–39]. The simulation of piezo DOD involves both FSI, that is, the coupled motion of the transducer and the fluid, and FSA to track the surface of the ink throughout the ejection cycle. Specifically, FSA is needed to track the motion of the ink meniscus in the nozzle during the initial stages of ejection, the surface of the ejected mass of ink as it evolves into a droplet, and the meniscus of the ink in the ejection chamber during refill.

A major challenge in simulating piezoelectric DOD involves the accurate prediction of FSI, that is, two-way coupling between the transducer as it deforms and the resulting change in the flow field within the ink. As the transducer deforms, it displaces ink, and the flowing ink provides a pressure load on the transducer that impacts its deformation. A rigorous analysis of this process requires the simultaneous and self-consistent calculation of both the ink and structural dynamics. However, the majority of piezo DOD models do not take into account fully coupled FSI. Instead, the ejection process is often simplified, either by assuming a limited one-way coupling wherein the transducer deformation ejects ink but the back reaction of the ink on the transducer is ignored or by ignoring mechanical actuation altogether and replacing it with a time-dependent pressure condition in the ejection chamber. In the latter approach, the imposed pressure eliminates the need for FSI analysis altogether. Specifically, given an imposed time-dependent

pressure, a CFD/FSA is performed to predict the mass of ejected ink, droplet formation, and capillary refill of the ejection chamber. These models provide an understanding of the ejection process and predict droplet velocity and volume are usually consistent with experimental observations [36–39]. However, more rigorous CFD/FSI models are desired for ejector design and optimization.

Rigorous FSI analysis poses a major challenge in modeling piezo DOD. It is difficult to track the fluid–structure interface and associated fluid flow and pressure during ejection and refill, especially because of the incremental structural displacements that occur during each time step of the simulation. Various numerical methods have been developed to address this challenge. In one such approach, a VOF CFD analysis is used to predict the unsteady fluid flow and associated pressure at the fluid–structure interface, while a different numerical technique, finite element analysis (FEA), is used to calculate the structural deformation. As the interface deforms, it defines a new boundary for the CFD calculation, which gives rise to a new pressure loading. The details of this complex coupled modeling approach are beyond the scope of this chapter. However, it should be noted that fully coupled FSI analysis is currently an active area of CFD research.

**2.8.2.1.2 TIJ DOD** A TIJ printhead can also contain hundreds to thousands of integrated micronozzles, each with its own ejection chamber. A thin-film resistive heater is integrated into a wall of the ejection chamber. When a droplet is desired, the heater is activated using a short (microsecond)-duration voltage pulse. The voltage is of sufficient magnitude to raise the temperature of a thin layer of ink in contact with the wall (above the heater) to its superheat temperature, approximately 300 °C for water under atmospheric pressure [25]. Once the superheat temperature is reached, the ink evaporates explosively and forms a homogeneous vapor bubble, with a high initial pressure (>100 bar) [25]. Given this pressure, the bubble expands rapidly within the ink chamber and ejects ink through the nozzle with enough momentum to form a droplet with a desired volume and velocity [32, 40–43] (see Chapter 3). The bubble subsequently collapses and the chamber refills with ink from a reservoir due to capillary pressure provided by surface tension.

A rigorous analysis of TIJ droplet ejection is complicated. It includes the prediction of voltage-driven excitation of a resistive heater, heat transfer from the heater to the ink, phase change from superheated ink to vapor, vapor bubble dynamics, drop ejection, refill of the ejection chamber, and the formation (pinch-off) of the ejected droplet [25, 32]. Various models have been developed to simulate this process by both academic and industrial research groups [25, 32, 42–45]. However, most of these have limitations and do not take into account all of the aforementioned effects. In some models, the analysis is simplified by imposing a time-dependent pressure BC that mimics the pressure exerted by the bubble as it expands [25]. Given an imposed pressure, a CFD/FSA is used to predict the mass of ink ejected through the nozzle and subsequent droplet formation. A few CFD programs can simulate the complete TIJ DOD cycle and have been used for the development of commercial printers. One such program is FLOW3D ([www.flow3d.com](http://www.flow3d.com)). This program predicts the heater-induced nucleation of the

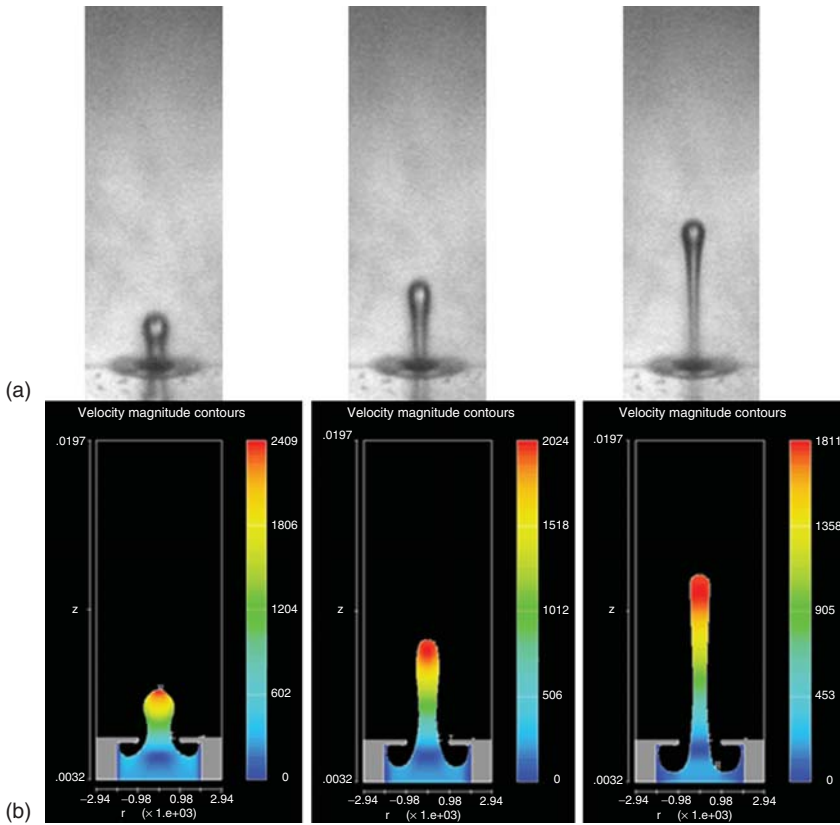


**Figure 2.13** TIJ droplet ejector with heater embedded in the nozzle plate. (a) Stroboscopic images of drop generation from a single nozzle. (b) CFD simulation showing bubble growth and droplet generation. (Notice that the maximum velocity scale reduces from left to right.)

bubble at the superheat temperature and tracks the bubble interface throughout the ejection cycle. The pressure and temperature within the bubble are computed using the ideal gas law, and evaporation and condensation at its interface are predicted using a saturation curve based on the Clapeyron equation. The complete ejection cycle including ink ejection, drop formation, and refill are predicted within one simulation, usually within several hours on a modern workstation, depending on the complexity of the ejector. An example of this analysis is shown in Figure 2.13. This figure shows a comparison between experimentally imaged droplet ejection from a prototype TIJ ejector developed in the Eastman Kodak Research Labs and a corresponding CFD simulation. The ejection chamber is essentially axisymmetric and a ring-like heater is embedded in the nozzle, concentric with the orifice, and in proximity to the nozzle–fluid interface. When the heater reaches a sufficient temperature, a homogeneous bubble forms on the bottom surface of the nozzle plate and rapidly expands downward into the ejection chamber, thereby ejecting a mass of fluid out the nozzle. The top panel in

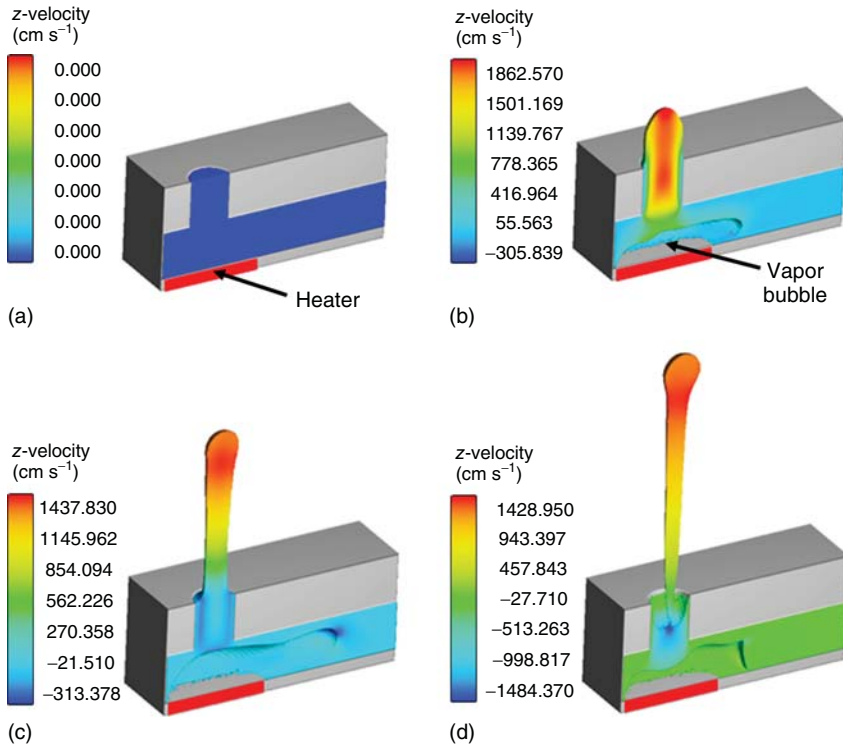


**Figure 2.14** Cutaway cross-sectional view of a 3D CFD simulation of TIJ droplet ejection. The heater (red) is embedded in the bottom of the ejection chamber and the color bar shows the fluid velocity magnitude for: (a) ejector before heating; (b) onset of bubble

growth and fluid flow through the nozzle; (c) expanding bubble with continued flow through the nozzle; and (d) collapsing bubble with onset of droplet formation in ejected fluid.

Figure 2.13 shows stroboscopic images of drop generation from a single nozzle. The bottom panel shows the corresponding CFD simulation. The images from the simulation are matched time-wise with the corresponding experimental images. The measured and predicted droplet volume and velocity were in reasonable agreement with this analysis.

The TIJ droplet formation processes are further illustrated in the VOF-based CFD simulation shown in Figure 2.14. This figure shows a cutaway cross-sectional view of the ejection process. The heater (shown in red) is embedded in a wall of the ejection chamber beneath the nozzle. Once the ink is heated to the superheat temperature, a homogeneous vapor bubble forms and rapidly expands into the ejection chamber, which ejects a mass of ink through the nozzle as shown in Figure 2.14b. The ejected ink forms a liquid column with a leading edge that becomes rounded (hemispherical) in order to achieve a lower surface energy as shown in Figure 2.14b. The rate of expansion of the bubble decreases as the bubble grows, which results in decrease in the flow rate of the ejected ink. Thus, there

is a difference in velocity between the faster moving leading edge of the ejected column of ink and its slower moving trailing portion. This causes the column to stretch taking on the appearance of a rounded hemisphere with a trailing tapered (conical) tail as shown in Figure 2.14c,d.

The tail necks down at the nozzle as the flow continues to decrease. In some cases, some of the ejected ink is drawn back into the nozzle due to a negative pressure created within the ink chamber. A second necking point often appears just behind the rounded head of the column, which necks down and produces a bulbous head. The tail of the ink column eventually pinches off near the nozzle, thereby creating a tapered conical filament with a bulbous head as shown in Figure 2.14d.

After pinch-off, the volume of the free-standing filament remains constant, but it continues to extend due to the differences in velocity between its head and tail. The rate of extension decreases as the kinetic energy of the fluid is transferred to surface energy as the surface of the filament grows. The filament extension eventually stops and then reverses with the tail recoiling toward the head as the surface contracts to reduce surface energy. During the contraction, a second neck often appears behind the bulbous head, which pinches off. When this occurs, two parts are formed, a primary secondary droplet and a smaller secondary detached liquid filament, which can contract into one or more smaller droplets (satellite droplets) or break into even smaller filaments. In some cases, satellite droplets are formed and then recombine with the primary droplet to form a larger droplet. When this occurs, the excess surface energy is transformed into oscillatory kinetic energy of the droplet, which dampens out over time due to viscosity.

CFD analysis can be used to predict DOD drop formation. However, a major challenge in this analysis is the accurate prediction of the free surface of the ejected fluid as the droplet forms. FSA is especially problematic during pinch-off and when small ink filaments detach and merge, which occurs over submicron length and submicrosecond timescales. DOD droplet generation represents a multiscale problem because the computational domain must be large enough (hundreds of microns) to model the 3D ejector geometry, while the computational mesh (sub-micron) and time-stepping must be fine enough to accurately predict the details of fluid behavior of pinch-off and breakup, oscillation, and merging of small ink filaments and satellite droplets. Errors in predicting the curvature of the free surface during these processes result in corresponding errors in the pressure and velocity in the fluid element. While various groups have obtained reasonable estimate of DOD droplet volume and velocity using CFD, validated predictions of the fine details of droplet formation are often lacking (see Section 7 in Ref. [18] and also [25, 32, 41–45]). An understanding of the small-scale effects in droplet formation is needed in order to optimize the DOD process to achieve superior image quality. For example, if satellite droplets are produced, they can randomly deposit on the imaging medium and significantly degrade the image quality. Currently, only specialized numerical codes can predict the fine details of drop formation [46]. However, these programs typically apply to a restricted class of ejector geometries (e.g., axisymmetric), or they impose time-dependent pressure BCs in lieu of an

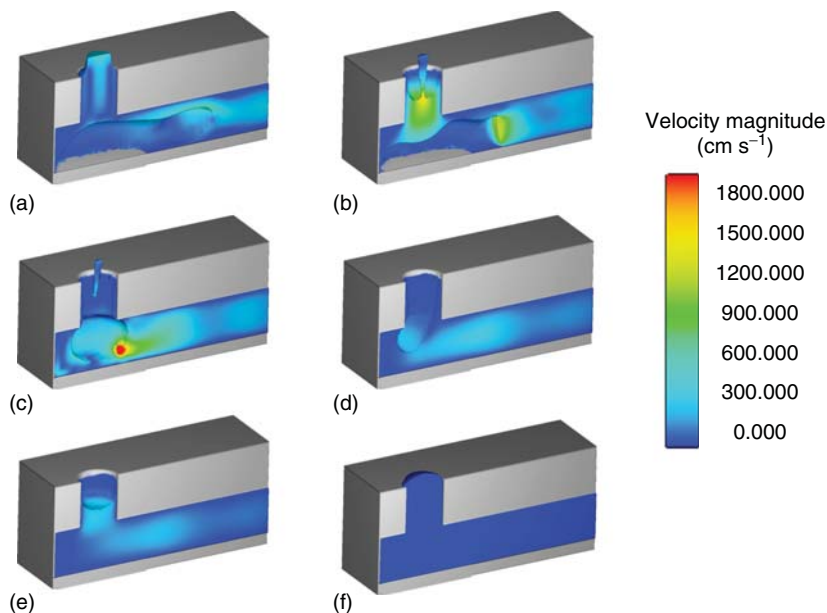


**Figure 2.15** Cutaway cross-sectional view of a 3D CFD simulation showing the refill of a TIJ ejection chamber: (a–f) show a sequence of simulation images of the ejector chamber at various stages of refill. The fluid is colored according to the magnitude of its velocity.

analysis of piezo DOD FSI or TIJ bubble generation. More comprehensive CFD modeling capability is desired for the development of a commercial inkjet system where 3D ejector geometries need to be designed and optimized using parametric design of experiment (DOE) analysis.

**2.8.2.1.3 Refill** After a droplet is ejected, the ejection chamber refills with ink to enable the next droplet ejection. At the onset of refill, the chamber is only partially filled and the ink within it forms a meniscus that provides a capillary force that pulls fluid into the chamber from a reservoir. The refill process is driven by surface tension and resisted by viscous drag. Time is required for the ink to refill the chamber and reach a proper state of equilibrium to enable the generation of the next droplet.

Figure 2.15 shows a cutaway cross-sectional view of a 3D CFD simulation showing the refill of a TIJ ejection chamber. The throughput of the printhead (nozzle firing frequency) can be limited by the refill time. The surface tension must be high enough and the viscosity low enough to enable refill within a reasonable time, for example, tens of microseconds. Many commercial CFD programs can accurately simulate capillary refill of an isolated ejection chamber.

However, a major difficulty in refill analysis is the ability to model coupled fluidic effects due to the simultaneous or staggered ejection and refill of multiple neighboring ejectors. Specifically, when a droplet is ejected from a given nozzle, it creates a pressure wave that can cause undesired pressure perturbations



in neighboring ejectors because they are fluidically connected, that is, they are fed by a common reservoir. These effects are important because they can cause variations in the volume and velocity of droplets ejected from the perturbed nozzles, which can degrade the image quality. A rigorous analysis of these coupled effects requires a computational model that encompasses multiple nozzles and ejection cycles. However, such simulations would require prohibitively long run times. This type of large-scale numerical analysis is not well suited for the optimization of a commercial printhead, which can require substantial parametric DOE analysis. Instead, a hierarchical multiscale modeling approach can be taken wherein the analysis of a small-scale model, for example, single nozzle ejection and refill, is used as input for a larger scale model, for example, as time-dependent pressure source for an acoustic analysis of an extended portion of the printhead.

### 2.8.2.2 CIJ Droplet Generation

In a CIJ printhead, ink from a common pressurized reservoir flows through a manifold of micronozzles to form an array of continuous microjets as shown in Figure 2.9a. These jets are energetically unstable, and in the absence of an external force, the jets break into drops of varying size and velocity at random times and locations from the printhead [18–21, 47]. In an inkjet system, the breakup of the jets is synchronized using a periodic stimulus, and under ideal conditions, all of the drops form at the same distance from the printhead and with the same volume and velocity, typically  $10\text{--}20\text{ m s}^{-1}$  [13, 18–23, 35, 48]. A CIJ printhead can produce continuous streams of droplets at rates up to several hundred thousand droplets per second from each nozzle. However, not all of the droplets are used for printing. Indeed, if all the droplets were printed, the image would consist of parallel straight lines. In order to print an image, only certain droplets are printed, the others are recycled to the printhead reservoir. CIJ systems can be classified according to the methods used for droplet generation and selection. Most commercial CIJ systems use a vibrating piezoelectric transducer to stimulate drop generation and electrostatic deflection of charged droplets for drop deflection as shown in Figure 2.9a [13, 14, 18, 19, 48]. In such systems, droplets are charged by an electrode and then deflected downstream by high-voltage electrode plates. Either the print drops or the nonprint drops can be deflected. In the former case, the droplets are deflected onto the imaging medium (paper), while in the latter case, the deflected droplets are recycled. Recently, a fundamentally different method of CIJ printing has been developed by the Eastman Kodak Company. This is known as *Stream Technology* and has been commercialized in Kodak's Prosper Imprinting Systems. In Stream CIJ, a pressurized reservoir feeds a microfabricated printhead manifold that can contain hundreds to thousands of nozzles ( $\sim 10\text{--}20\text{ }\mu\text{m}$  in diameter). Each nozzle produces a continuous microjet of ink. The jets are inherently unstable and individually modulated using a thermal pulse at the nozzle that induces the formation of uniform droplets downstream with well-defined volumes and velocities as shown in Figure 2.16.

The Stream Technology leverages advances in complementary metal-oxide-semiconductor (CMOS)/Micro-Electro-Mechanical Systems (MEMS)

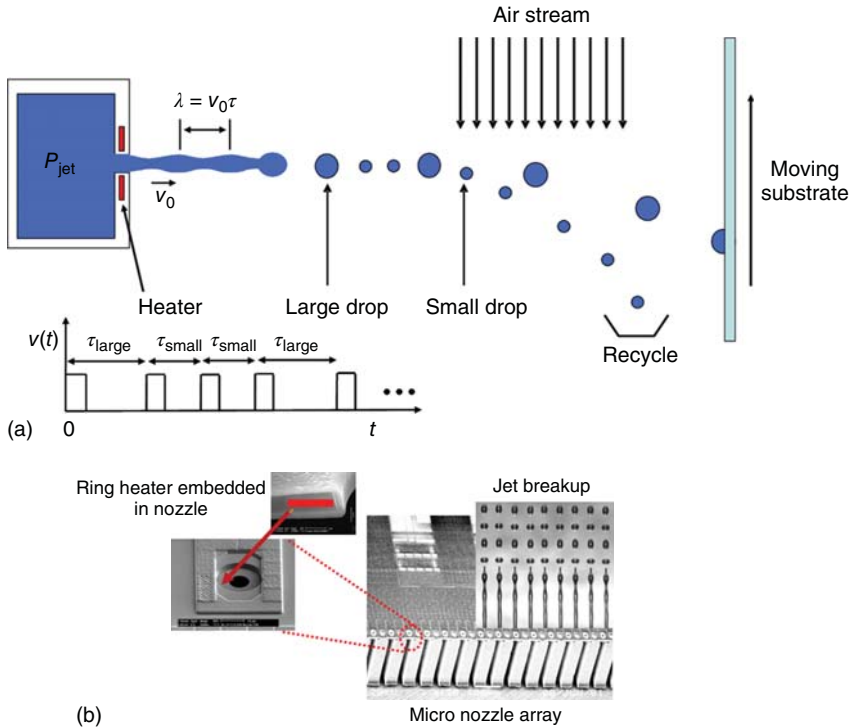


**Figure 2.16** Stream CIJ: (a) illustration of droplet generation showing a cutaway cross-sectional view of a micronozzle with an integrated ring-like (red) heater surrounding the orifice and a voltage pulse used to provide thermal modulation of the

microjet to produce different sized droplets downstream from the nozzle. Air flow size selection for large drop printing is also shown. (b) Microfabricated prototype print-head with magnified view of an orifice with an embedded (red) heater.

technology that enable the integration of ring-like micro heater elements into each nozzle. To modulate a jet, a periodic voltage pulse is applied to the heater, and the thermal energy it generates diffuses into the jet at the nozzle and is advected downstream, largely confined to the surface of the jet [22, 46, 49–51]. The temperature of the ink and hence its temperature-dependent properties, surface tension, viscosity, and density, are modulated at the orifice. The dominant cause of jet instability and drop formation is the modulation of surface tension  $\sigma$ , which has a temperature dependence given by  $\sigma(T) = \sigma_0 + \beta(T - T_0)$ , where  $\beta$  is a constant and  $\sigma(T)$  and  $\sigma_0$  are the surface tension at temperatures  $T$  and  $T_0$ , respectively. The pulsed heating modulates  $\sigma$  at a wavelength  $\lambda = v_0 \tau$ , where  $v_0$  is the jet velocity and  $\tau$  is the period of the heat pulse as shown in Figure 2.16. The downstream advection of thermal energy produces a spatial gradient of surface tension along the jet. This induces a shear stress at the free surface that is balanced by inertial forces in the ink, which induce a Marangoni flow from regions of lower to higher surface tension (from warmer regions toward cooler regions). This



causes a deformation of the free surface (slight necking in the warmer regions and ballooning in the cooler regions) that ultimately leads to instability and drop formation [18, 22, 46, 49–51]. The drop volume can be adjusted on demand by varying the voltage pulse width  $\tau$ , that is,  $V_{\text{drop}} = \pi r_0^2 v_o \tau$ . Thus, longer pulses produce larger drops, shorter pulses produce smaller drops, and different sized drops can be produced from each orifice as desired. For printing applications, two different sized drops are usually produced from each nozzle. In one mode of operation, the larger drops are projected onto a substrate to form an image while the smaller sized drops are deflected using airflow and recycled as shown in Figure 2.16. The use of airflow to deflect the droplets eliminates the need for complex and cumbersome electrostatic charging and deflection mechanisms.

The Stream CIJ process has been modeled using CFD analysis [22, 46, 49–51]. Specifically, drop generation for a prototype printhead has been studied by taking into account the printhead materials, nozzle chamber geometry, ink properties, and the characteristics of the applied voltage pulse. The CFD simulation tracks the formation of droplets during and after pinch-off. The results of a typical simulation are shown in Figure 2.17. The predicted drop formation is compared with corresponding strobe image of the jet during pinch-off. Note that the CFD analysis is able to accurately predict the details of pinch-off and drop formation. A CFD simulation of this process typically requires several hours to complete on a workstation.

### 2.8.2.3 Crosstalk

Crosstalk in an inkjet system occurs whenever the intentional activation of drop ejection in one or more nozzles unintentionally impacts drop ejection in others. It is a common and significant problem in both CIJ and DOD systems. Crosstalk needs to be controlled because it can cause undesired variations in drop velocity and volume that can lead to perceivable artifacts in the printed image. There are many forms of crosstalk, structural, hydroacoustic, thermal, electrical, and coupled combinations thereof (see Chapter 5 in [52]). Structural crosstalk can occur because the nozzles are mechanically connected to one another, that is, they are integrated into the printhead structure. Thus, a mechanical actuation or disturbance at a given nozzle can be felt by neighboring nozzles. Moreover, resonant vibration modes may be excited under certain circumstances that propagate within the printhead and alter drop ejection across several nozzles [53, 54]. Similarly, hydroacoustic crosstalk can occur for nozzles that share a common reservoir. When a pressure pulse is imposed at a given nozzle to eject a droplet, it can cause undesired pressure perturbations at neighboring nozzles. Acoustic resonances may be excited, which produce sustained and long-range pressure perturbations across the printhead [55]. Thermal crosstalk can occur due to the diffusion of thermal energy. In TIJ systems, the thermal energy from an activated nozzle can diffuse into neighboring nozzles through the printhead structure [56]. This can cause an undesired increase in the temperature of the ink that alters its viscosity and surface tension, which impact droplet ejection and refill. Finally, electrical crosstalk can occur when groups of nozzles are driven by a common electrical source/controller. Parasitic electrical coupling in the feed circuitry for densely

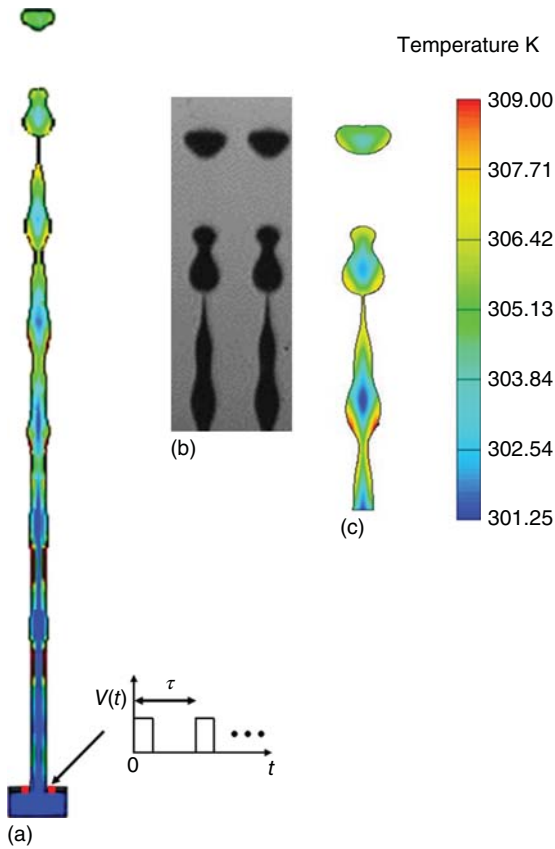


**Figure 2.17** CFD simulation of stream CIJ drop formation and comparison with experimental images: (a) CFD analysis of a micro-jet showing periodic thermal modulation of the jet at the orifice and downstream drop

formation; (b) corresponding stroboscopic images of drop formation; and (c) magnified view of simulated pinch-off and drop formation including the temperature distribution within the jet.

packed nozzles can cause undesired variations in the activation signals of nozzles. In piezo DOD systems, the electric field that is generated to activate a transducer for drop ejection at a given nozzle can couple to neighboring transducers, causing undesired perturbations to drop ejection.

Predicting crosstalk is very challenging because of the multiscale nature of the problem and the relatively small amplitudes of the undesired perturbations. As noted, crosstalk can be generated by individual nozzles and its impact can be felt for sustained periods of time across relatively large portions of the printhead. Moreover, it can depend on coupled phenomena, which require multiphysics analysis, for example, coupled FSIs wherein structural vibrations induce pressure variations. A rigorous analysis of these effects requires a fully coupled multiphysics computational model that spans a sufficient portion of the printhead to account

for long-range effects but with a fine enough spatial and temporal discretization to accurately predict the local generation of the crosstalk, for example, at the individual nozzle level. However, there is several orders of magnitude difference in the length- and timescales for these effects, for example, nozzles are on the order of microns, whereas the printhead is on the order of millimeters. Thus, it is not computationally feasible to rigorously model many aspects of crosstalk by taking into account both short- and long-range effects. Instead, a hierarchical analysis can be performed wherein the output of a small-scale model is used as an input to a larger scale device-level model. For example, a small-scale model could be used to predict the amplitude of generated pressure pulses at individual nozzles, and these could be used as point sources in a large-scale acoustic model of the printhead.

#### 2.8.2.4 Aerodynamic Effects

Inkjet printers project streams of closely spaced droplets onto a medium in order to produce high-resolution images with high throughput. The droplets, which are tens of microns in diameter, travel millimeters from the printhead to the imaging medium through air at speeds of several meters per second, usually  $3\text{--}15\text{ m s}^{-1}$  for DOD and  $10\text{--}20\text{ m s}^{-1}$  for CIJ [19, 23]. The droplets experience a viscous drag force due to their relative motion with respect to the surrounding air, and their motion in turn causes the air to circulate. Thus, there is coupled droplet–air motion that gives rise to many complex and interesting effects. For example, aerodynamic drafting can occur wherein trailing colinear droplets experience reduced drag due to aerodynamic shielding by the leading droplets. There is also air-mediated crosstalk between droplets from neighboring nozzles wherein circulating airflow induced by a stream of droplets from one nozzle alters the velocity and trajectory of the droplets from an adjacent nozzle and vice versa [57]. Airflow near the moving imaging media can also affect droplet placement [58]. Such aerodynamic effects are undesired because they can cause variations in the velocities and trajectories of the droplets that can lead to perceivable artifacts in a printed image. Aerodynamic effects can be modeled using a variety of approaches. The simplest approach is to consider one-way coupling wherein the droplets are treated as isolated solid spheres and their trajectories are predicted using Newtonian dynamics with a simple Stokes' drag term used to account for air resistance. However, while this level of analysis provides some insight into the motion of the droplets, it is inadequate for the design of a commercial printing system. A fully coupled aerodynamic analysis can be performed using CFD analysis. To simplify this, the droplets are treated as solid spheres. The moving surface of each droplet defines a dynamic BC for the surrounding airflow. Flow-induced forces are computed on the droplets, and their motion is self-consistently calculated with the pressure and velocity distribution of the air during each time step. An example of this analysis is shown in Figure 2.18. Here, CFD is used to predict the aerodynamic interaction of 4 streams of  $30\text{ }\mu\text{m}$  drops that are initially moving at  $10\text{ m s}^{-1}$ . The droplets are initially equally spaced, but downstream from the printhead the spacing between the leading and trailing droplets is reduced due to aerodynamic drag.

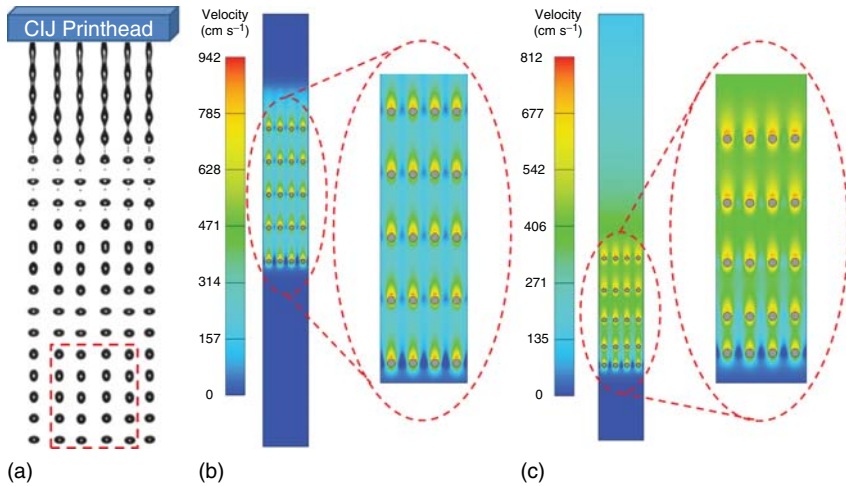


**Figure 2.18** CFD simulation showing aerodynamic interactions of streams of droplets: (a) illustration of CIJ printhead generating; (b) 3D CFD analysis of an initial configuration of equally spaced droplets moving at  $10 \text{ m s}^{-1}$  showing the velocity field

of the surrounding air; and (c) CFD simulation showing downstream grouping of droplets and velocity field of the air with reduced spacing between leading and trailing droplets due to aerodynamic drag.

#### 2.8.2.5 Ink–Media Interactions

Ink–media interactions play a critical role in the formation of an image in inkjet printing. Droplets are projected onto an imaging medium (typically some form of paper) at speeds of several meters per second. The droplets spread upon impact, coalesce, absorb, and eventually dry to render the image [33]. Paper is a complex material that consists of a random network of fibers as seen in Figure 2.19 [59, 60]. The fibers are usually much longer than the thickness of the paper, and therefore,

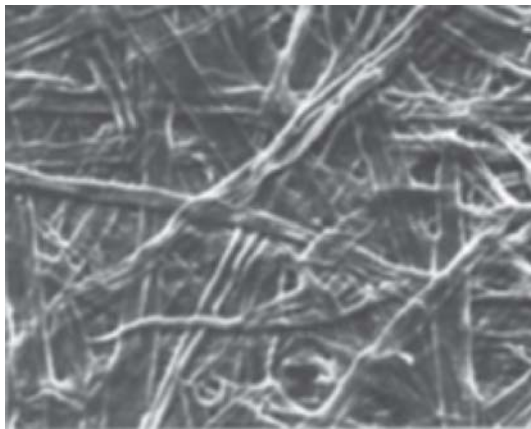


**Figure 2.19** Micrograph of the surface of paper. (Adapted with permission from Ref. [59].)

the fiber network is essentially 2D in the plane of the paper. There are usually 5–20 layers of fibers, and these define a complex porous medium with a 3D network of pores into which the ink is absorbed.

The porosity  $\phi$  is defined as the ratio of pore volume to total volume  $V$  of the paper

$$\phi = \frac{V - V_{\text{fib}}}{V} \quad (2.38)$$

where  $V_{\text{fib}}$  is the volume occupied by the fibers. The porosity has a significant impact of the penetration of ink into the paper, which in turn impacts image quality. Fluid flow into a porous medium can be estimated using flow equations where the frictional flow resistance of the porous structure is described by Darcy-type interaction terms

$$u = -k \frac{\Delta p}{\mu h} \quad (2.39)$$

where  $u$  is the fluid velocity,  $\Delta p$  is the fluid pressure difference across a thickness  $h$  of the material,  $\mu$  is the dynamic viscosity of the fluid, and  $k$  is the permeability coefficient of the material.

The absorption of ink and its constituents is governed by the capillary forces, thermodynamic interaction between the ink and the paper, and chemical diffusion gradients. The capillary pressure is described by Young's equation,

$$p_c = \frac{4\sigma \cos(\theta)}{d} \quad (2.40)$$

where  $\sigma$  is the surface tension,  $d$  is the diameter of the capillary, and  $\theta$  is the contact angle between the liquid and the capillary wall. The time dependence of ink penetration into a porous medium can be estimated using the Washburn expression [61],

$$z^2(t) = \frac{r\sigma \cos(\theta)}{2\mu} t \quad (2.41)$$

where  $z$  is the penetration depth of the ink and  $\mu$  is the fluid viscosity. From this equation, we find that the depth of penetration is proportional to square root of the capillary radius  $r$ , but inversely proportional to the square root of the viscosity of the ink.

While the previous analysis is useful for first-order estimates of ink absorption, more rigorous models are needed to optimize ink–media interactions to achieve superior image quality. Some key factors that affect these interactions are the velocity of the incident drop, its surface tension and viscosity, and the porosity and permeability of the imaging medium, among others. CFD analysis can be used to simulate ink–media interactions, and various approaches can be considered to study the governing phenomena at different length and time scales [62–66]. In one such approach, the medium is treated as a continuum with effective bulk properties, notably porosity and permeability. We will refer to this as the porous media model. In another approach, a small-scale model is used wherein a microscopic region of the medium is represented by its constituent materials,

for example, microfibers. Since the structure of the media is specified, there is no need to estimate bulk values of porosity and permeability. A CFD analysis can be performed to understand fundamental interactions of a relatively small number of droplets with the media. We discuss these two approaches in the following subsections.

**2.8.2.5.1 Porous Media Model** Various CFD programs have porous media modeling capability that can be used to predict ink–media interactions. In this approach, the fluid dynamic equations are adapted to account for flow inside the medium.

For example, in the FLOW3D program ([www.flow3d.com](http://www.flow3d.com)), the Navier–Stokes equation is modified to account for a distributed flow resistance within the medium (Figure 2.20), that is,

$$\frac{\delta \vec{v}}{\delta t} + \frac{1}{V_f} \left\{ \vec{A}_f \times \vec{v} \cdot \nabla \vec{v} \right\} = -\frac{1}{\rho} \nabla p + \frac{1}{\rho V_f} \nabla \cdot (\vec{A}_f \cdot \vec{v}) + \vec{G} - K \vec{v} \quad (2.42)$$

where  $u$  and  $p$  are the velocity and pressure in the fluid,  $V_f$  is the volume fraction (porosity) of a computational cell, and  $\vec{A}_f$  is the diagonal tensor for the area fractions of a cell.  $\vec{G}K$  is a drag coefficient that accounts for the flow resistance in

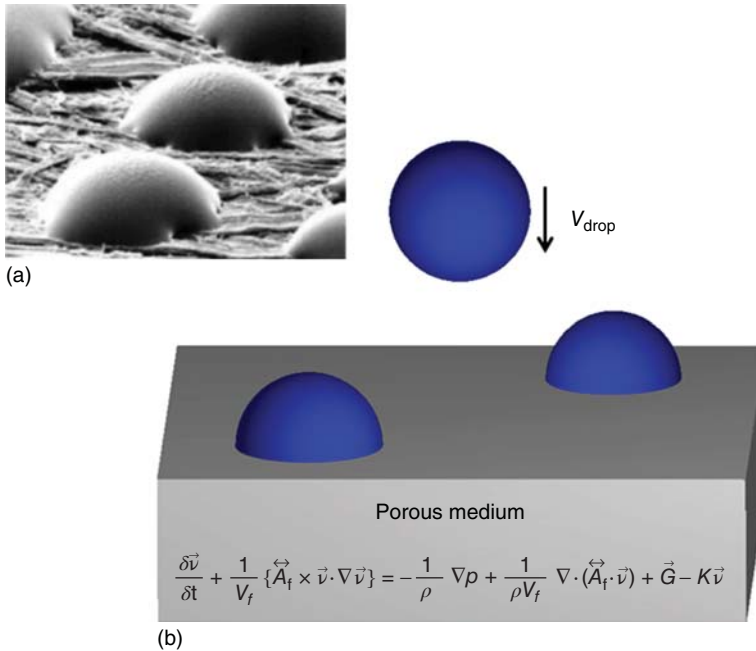


**Figure 2.20** Ink–media interaction: (a) a SEM photograph of ink droplets on the surface of a bond paper and (b) illustration of a CFD model used to predict ink absorption in a porous medium.

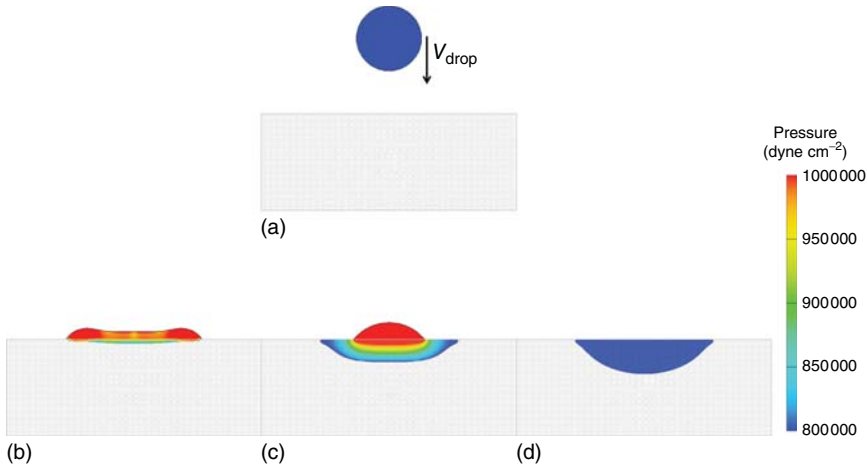


**Figure 2.21** CFD analysis of ink impacting and absorbing into a porous medium: (a) droplet with a velocity  $V_{\text{drop}}$  incident on the medium; (b) impact and initial spreading; (c) partial absorption into medium; and (d) complete absorption.

the medium, that is,

$$K = \frac{\mu V_f}{\rho \kappa} \quad (2.43)$$

where  $\kappa$  is the permeability of the media. An illustration of this analysis is shown in Figure 2.21. As shown in this figure, a  $30\ \mu\text{m}$  drop of water is incident on a porous media at a velocity of  $10\ \text{m s}^{-1}$ . Upon impact, the droplet initially spreads and then absorbs into the medium. Figure 2.21b–d show the pressure distribution after impact and during absorption.

**2.8.2.5.2 Microscale Ink–Medium Model** Ink–media interactions can also be studied using microscale analysis wherein a microscopic region of the medium is represented by its constituent microelements. An example of such a model is shown in Figure 2.22. Here, a random network of microfibers has been created, which mimics the 3D fiber network that exists in paper as shown in Figure 2.19. Once the geometry and properties (e.g., contact angle) of the constituent elements have been specified, a CFD analysis can be performed to study the details of the ink–medium interactions.

Figure 2.22 shows a sequence of images from a CFD simulation of a  $50\ \mu\text{m}$  droplet of water impacting a medium at a velocity of  $10\ \text{m s}^{-1}$ . The drop spreads upon impact and then absorbs into the medium. A key difference between this approach and the porous media model is that the porosity and permeability are determined by the relative orientations and properties of the constituent elements, rather than being defined in terms of bulk effective properties. Small-scale models can be used to study ink–media interactions for random or ordered assemblies of arbitrary microelements, each with its own properties (e.g., contact angle). In



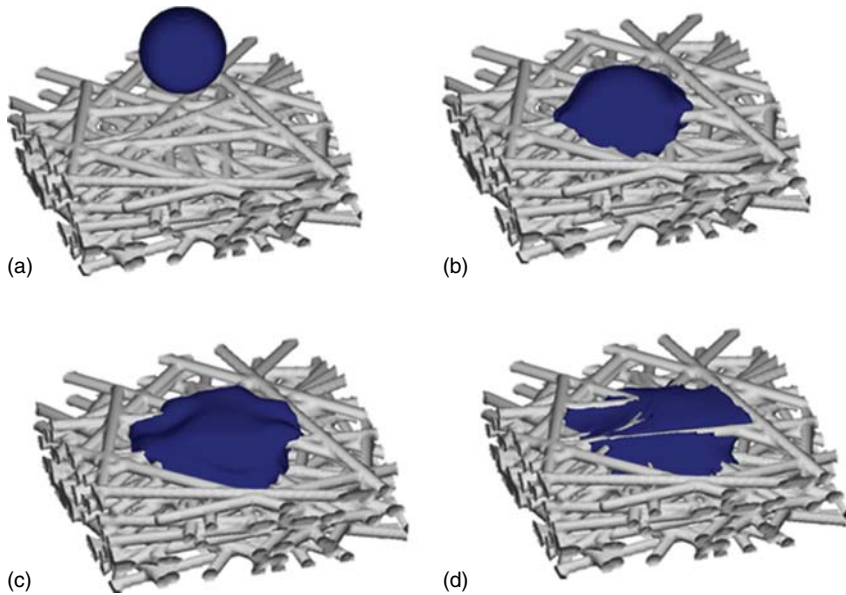


**Figure 2.22** Small-scale CFD model of droplet absorption in a porous medium consisting of a random network of microfibers: (a) droplet incident on the medium; (b) droplet spreading upon impact; (c) partial absorption into the medium; and (d) more complete absorption into the medium.

principle, one can extract effective bulk material properties from this analysis. However, it is computationally costly to use a small-scale model to study long-range ink–media interactions such as the coalescence, absorption, and drying of large areas of ink or the formation of an extended image on a medium.

### Summary

Inkjet printing is the most successful commercial application of microfluidics to date. While the market for traditional printing has matured, there is a proliferation of emerging applications that range from the high-throughput fabrication of functional materials and devices, to the patterned deposition of biological media, to spray cooling of electronic microchips. These new applications of inkjet deposition hold potential for transformative advances across a broad range of technologies, both in terms of fundamental understanding and the development of commercial products. However, as discussed, the development of inkjet-based technology is a complex undertaking, usually involving substantial costly and time-consuming trial-and-error experimental work. Computational modeling can greatly accelerate the development effort and reduce both the cycle time and associated cost by establishing proof-of-concept prior to fabrication and enabling the rational design of inks, receiving media, and printing components.



CFD is the method of choice for modeling inkjet applications. A key area of CFD research for many emerging applications will be the implementation of the complex rheological properties of functional inks into numerical CFD solvers. In this chapter, we have discussed the use and challenges of using CFD to model various inkjet processes. The rapid enhancement of CFD methods combined with the availability of computational capability at reduced cost will no doubt greatly facilitate the development of future inkjet technologies.

### Acknowledgments

The author would like to thank Christopher Delametter for many insightful technical discussions and for providing CFD simulation materials for TIJ drop ejection. The author is also grateful for the contributions of Dr. Dennis Perchak, who provided technical information and CFD simulation materials for small-scale ink–medium analysis. Special thanks are due to Ioannis Karampelas for his invaluable help with the preparation of the manuscript and for careful review of its content. The author is also thankful for the help of Xiaozheng Xue for his input on the equations of fluid dynamics and for careful reading of the manuscript.

### References

- Munson, B.R., Young, D.F., and Okiishi, T.H. (1990) *Fundamentals of Fluid Mechanics*, John Wiley & Sons, Inc., New York.
- Crowe, C.T., Elger, D.F., and Roberson, J.A. (2005) *Engineering Fluid Mechanics*, vol. 9, John Wiley & Sons, Inc., Hoboken, NJ.
- White, F.M. and Corfield, I. (1991) *Viscous Fluid Flow*, vol. 3, McGraw-Hill, New York.
- Blevins, R.D. (1984) *Applied Fluid Dynamics Handbook*, Van Nostrand Reinhold Co., New York.
- Astarita, G. and Marrucci, G. (1974) *Principles of Non-Newtonian Fluid Mechanics*, vol. 28, McGraw-Hill, New York.
- White, F. (2011) *Fluid Mechanics*, 7th edn, McGraw-Hill, New York.
- Batchelor, G.K. (2000) *An Introduction to Fluid Dynamics*, Cambridge University Press, Cambridge.
- Pozrikidis, C. (2011) *Introduction to Theoretical and Computational Fluid Dynamics*, Oxford University Press, Oxford.
- Blazek, J. (2015) *Computational Fluid Dynamics: Principles and Applications*, 3rd edn, Butterworth-Heinemann, Oxford.
- Chung, T.J. (2010) *Computational Fluid Dynamics*, Cambridge University Press, Cambridge.
- Ferziger, J.H. and Perić, M. (2002) *Computational Methods for Fluid Dynamics*, vol. 3, Springer, Berlin.
- Peyret, R. (1996) *Handbook of Computational Fluid Mechanics*, Academic Press, London.
- Hutchings, I.M. and Martin, G.D. (2012) *Inkjet Technology for Digital Fabrication*, John Wiley & Sons, Ltd.
- Le, H.P. (1998) Progress and trends in ink-jet printing technology. *J. Imaging Sci. Technol.*, 42 (1), 49–62.
- Doring, M. (1982) Ink-jet printing. *Philips Tech. Rev.*, 40, 192–198.
- Singh, M., Haverinen, H.M., Dhagat, P., and Jabbour, G.E. (2010) Inkjet printing process and its applications. *Adv. Mater.*, 22, 673.
- Derby, B. (2010) Inkjet printing of functional and structural materials: fluid

- property requirements, feature stability, and resolution. *Annu. Rev. Mater. Res.*, **40**, 395–414.
18. Basaran, O.A., Gao, H., and Bhat, P.P. (2013) Nonstandard inkjets. *Annu. Rev. Fluid Mech.*, **45**, 85–113.
  19. Martin, G.D., Hoath, S.D., and Hutchings, I.M. (2008) Inkjet printing the physics of manipulating liquid jets and drops. *J. Phys. Conf. Ser.*, **105**, 012001.
  20. Rayleigh, L. (1879) On the instability of jets. *Proc. London Math. Soc.*, **10**, 4–13.
  21. Eggers, J. (1997) Non-linear dynamics and breakup of free-surface flows. *Rev. Mod. Phys.*, **69** (3), 865.
  22. Furlani, E.P., Price, B.G., Hawkins, G., and Lopez, A.G. (2006) Thermally induced Marangoni instability of liquid micro-jets with application to continuous inkjet printing. Proceedings of NSTI-Nanotechnology Conference, Vol. 2, pp. 534–537.
  23. Castrejon-Pita, J.R., Baxter, W.R.S., Morgan, J., Temple, S., Martin, G.D., and Hutchings, I.M. (2013) Future, opportunities and challenges of inkjet technologies. *Atomization Sprays*, **23** (6), 571.
  24. Wijshoff, H. (2010) The dynamics of the piezo inkjet print-head operation. *Phys. Rep.*, **491**, 77–177.
  25. Asai, A. (1992) Three-dimensional calculation of bubble growth and drop ejection in a bubble jet printer. *ASME J. Fluids Eng.*, **114**, 638–641.
  26. Hervouet, J.M. (2007) *Hydrodynamics of Free Surface Flows: Modelling with the Finite Element Method*, John Wiley & Sons, Ltd, Chichester.
  27. Yeung, R.W. (1982) Numerical methods in free-surface flows. *Annu. Rev. Fluid Mech.*, **14**, 395.
  28. Hirt, C.W. and Nichols, B.D. (1981) Volume of fluid (VOF) method for the dynamics of free boundaries. *J. Comput. Phys.*, **39** (1), 201–225.
  29. Bazilevs, Y., Takizawa, K., and Tezduyar, T.E. (2012) *Computational Fluid-Structure Interaction: Methods and Applications*, John Wiley & Sons, Ltd, Chichester.
  30. Carey, V.P. (2007) *Liquid Vapor Phase Change Phenomena: An Introduction to the Thermophysics of Vaporization and Condensation Processes in Heat Transfer Equipment*, 2nd edn, Taylor & Francis, London.
  31. Kandlikar, S.G. (1999) *Handbook of Phase Change: Boiling and Condensation*, CRC Press, Boca Raton, FL., US.
  32. Lindemann, T., Sassano, D., Bellone, A., Zengerle, R., Koltay, P., and Olvetti, I. (2004) Three-dimensional CFD-simulation of a thermal bubble jet print-head. Proceedings of the NSTI Nanotechnology Conference, pp. 227–230.
  33. Yang, L. (2003) Ink-paper interaction: a study in ink-jet color reproduction. Doctoral dissertation. Linköping University, Linköping, Sweden.
  34. Dong, H. (2006) Drop-on-demand inkjet drop formation and deposition. Doctoral dissertation. Georgia Institute of Technology.
  35. Basaran, O.A. (2002) Small-scale free surface flows with breakup: drop formation and emerging applications. *AIChE J.*, **48** (9), 1842–1848.
  36. Wu, H.C., Hwang, W.S., and Lin, H.J. (2004) Development of a three-dimensional simulation system for micro-inkjet and its experimental verification. *Mater. Sci. Eng.*, **373** (1), 268–278.
  37. Shield, T.W., Bogy, D.B., and Talke, F.E. (1987) Drop formation by DOD ink-jet nozzles: a comparison of experiment and numerical simulation. *IBM J. Res. Dev.*, **31** (1), 96–110.
  38. Chen, P.H., Peng, H.Y., Liu, H.Y., Chang, S.L., Wu, T.I., and Cheng, C.H. (1999) Pressure response and droplet ejection of a piezoelectric inkjet print-head. *Int. J. Mech. Sci.*, **41** (2), 235–248.
  39. Min, S. (2008) Analysis and computational modelling of drop formation for piezo-actuated DOD micro-dispenser. Doctoral dissertation.
  40. Asai, A. (1991) Bubble dynamics in boiling under high heat flux pulse heating. *J. Heat Transfer*, **113** (4), 973–979.
  41. Asai, A., Hara, T., and Endo, I. (1987) One-dimensional model of bubble growth and liquid flow in bubble jet printers. *Jpn. J. Appl. Phys.*, **26** (10R), 1794.

42. Chen, P.H., Chen, W.C., and Chang, S.H. (1997) Bubble growth and ink ejection process of a thermal ink jet print-head. *Int. J. Mech. Sci.*, **39** (6), 683–695.
43. Tseng, F.G., Kim, J.Y., and Ho, C.M. (2002) A high-resolution high-frequency monolithic top-shooting micro-injector free of satellite drops-part I: concept, design, and model. *J. Microelectromech. Syst.*, **11** (5), 427–436.
44. Dong, H., Carr, W.W., and Morris, J.F. (2006) Visualization of drop-on-demand inkjet: drop formation and deposition. *Rev. Sci. Instrum.*, **77**, 85–101.
45. Xu, Q. and Basaran, O.A. (2007) Computational analysis of drop-on-demand drop formation. *Phys. Fluids*, **19**, 102–111.
46. Furlani, E.P. and Ng, K.C. (2007) Numerical analysis of nonlinear deformation and breakup of slender microjets with application to continuous inkjet printing. Proceedings of the NSTI Nanotechnology Conference, May 2007. Vol. **3**, pp. 444–446.
47. Eggers, J. (1995) Theory of drop formation. *Phys. Fluids*, **7**, 941.
48. Heinzl, J. and Hertz, C.H. (1985) Ink-jet printing. *Adv. Electron. Electron Phys.*, **65**, 91–171.
49. Furlani, E.P. (2005) Temporal instability of viscous liquid micro-jets with spatially varying surface tension. *J. Phys. A: Math. Gen.*, **38**, 263–276.
50. Furlani, E.P. (2005) Thermal modulation and instability of Newtonian liquid micro-jets. Proceedings of the Nanotechnology Conference, Vol. **1**, pp. 668–671.
51. Furlani, E.P. and Hanchak, M.S. (2011) Nonlinear analysis of the deformation and breakup of viscous microjets using the method of lines. *Int. J. Numer. Methods Fluids*, **65** (5), 563–577.
52. Brand, O., Fedder, G.K., Hierold, C., and Tabata, O. (2012) In *Inkjet-based micromanufacturing* (eds J.G. Korvink, P.J. Smith, and D.Y. Shin), Chapter 5, pp. 73–84, Wiley-VCH Verlag & Co. KGaA, Boschstr. 12, 69469 Weinheim, Germany.
53. McDonald, M. and Zhou, Y. (1999) *NIP and Digital Fabrication Conference Proceedings*, 1999(1), Society for Imaging Science and Technology, pp. 40–43.
54. Seitz, H. (2003) *NIP and Digital Fabrication Conference Proceedings* 2003(1), Society for Imaging Science and Technology, pp. 343–347.
55. Dijkstra, J.F. (1998) Hydro-acoustics of piezoelectrically driven ink-jet print heads. *Flow Turbul. Combust.*, **61** (1-4), 211–237.
56. Lee, Y.S., Kim, M.S., Shin, S.J., Shin, S., Kuk, K., and Sohn, D.K. (2004) Lumped modeling of crosstalk behavior of thermal inkjet print heads, in *ASME 2004 International Mechanical Engineering Congress and Exposition*, American Society of Mechanical Engineers.
57. Ikegawa, M., Ishii, E., Harada, N., and Takagishi, T. (2014) *NIP & Digital Fabrication Conference Proceedings*, 2014(1), Society for Imaging Science and Technology, pp. 176–180.
58. Hsiao, W.K., Hoath, S.D., Martin, G.D., and Hutchings, I.M. (2012) *NIP & Digital Fabrication Conference Proceedings*, 2012(2), Society for Imaging Science and Technology, pp. 412–415.
59. Nilsson, L. and Stenstrom, S. (1997) A study of the permeability of pulp and paper. *Int. J. Multiphase Flow*, **23**, 131–153.
60. Niskanen, K., Kajanto, I., and Pakarinen, P. (1998) *Paper Physics*, Chapter 1, Fapet Oy, Helsinki.
61. De Gennes, P., Brochard-Wyart, F., and Quere, D. (2004) *Capillarity and Wetting Phenomena*, Springer Publications, New York.
62. Rioux, R.W. (2003) The rate of fluid absorption in porous media. MSc dissertation. The University of Maine.
63. Daniel, R.C. and Berg, J.C. (2006) Spreading on and penetration into thin, permeable print media: application to ink-jet printing. *Adv. Colloid Interface Sci.*, **123**, 439–469.
64. Alam, P., Toivakka, M., Backfolk, K., and Sirvio, P. (2007) Impact spreading and absorption of Newtonian droplets on topographically irregular porous materials. *Chem. Eng. Sci.*, **62**, 3142–3158.

65. Yang, L., Kruse, B., and Pauler, N. (2001) Modelling ink penetration for ink-jet printing. Proceedings of IS&T's NIP17 Conference, September 2001, Fort Lauderdale, FL.
66. Reis, N.C., Griffiths, R.F., and Santos, J.M. (2004) Numerical simulation of the impact of liquid droplets on porous surfaces. *J. Comput. Phys.*, **198**, 747–770.

## 3

# Inkjet Printheads

*Naoki Morita, Amol A. Khalate, Arend M. van Buul, and Herman Wijshoff*

### 3.1

#### Thermal versus Piezoelectric Inkjet Printing

At the end of the twentieth century, humans experienced a paradigm shift due to the computer and Internet revolution. Inkjet printers grew in popularity with computers. Today, there is an inkjet printer alongside a computer in many households. Approximately three quarters of all inkjet printers are thermal inkjet (TIJ) printers, making TIJs commercially superior to their rival, piezoelectric inkjets (PIJs) (Figure 3.2 in Ref. [1]). Canon Inc. (Canon) and Hewlett–Packard Development Company L.P. (HP) are the founders of TIJ printers and are prospering from their commercial success. It has been said that in the late 1970s, both companies independently conceived the idea of TIJ printers – from syringes and soldering iron for Canon and from coffee percolators for HP. Then, in the mid-1980s, both companies were able to commercialize TIJ printers. Subsequently, reflecting their business domains, these companies succeeded in meeting the demands of the photography, small-office/home-office, and wide-format markets. Inkjet printers are also found in the publishing market as high-speed continuous feed printers, such as the HP InkJet Web Press, which realizes a printing speed of  $244 \text{ m min}^{-1}$  with a paper width of 42 in. [2].

Starting around the year 2000, the use of inkjet technology in micromanufacturing became frequently studied, and the applications of inkjets expanded from printing to manufacturing [1]. By replacing the ink with a liquid material suited for a specific purpose, and jetting and depositing the liquid, new possible uses of inkjets have been discovered, such as the fabrication of electrical circuits and liquid crystals. In these applications, the kind of liquid used to substitute the ink is important. However, TIJs are seldom developed for manufacture because they necessarily heat the ink. Accordingly, PIJs dominate the domain of micromanufacturing.

In recent years, three-dimensional (3D) printing has attracted attention because it has the ability to easily fabricate unique, complex 3D objects at low cost, such as stereographs (figures) of human beings. In particular, the “Multi Jet Fusion” technology for industrial use announced by HP in October 2014 has received a

great deal of interest from the 3D printing market. This technology ensures the strength of 3D objects and printing (manufacturing) speed, while allowing a high level of freedom in shape formation as well as precise coloring. Multi Jet Fusion uses TIJ instead of PIJ technology, and there are expectations that it may greatly contribute to the success of inkjet-based manufacturing.

## 3.2

### Thermal Inkjet

#### 3.2.1

##### Boiling Mechanism

The boiling temperature of water is 100 °C at 1 atm. However, if rapid heating occurs, the boiling temperature of water rises to nearly 300 °C. Bubbles that are generated when water boils at this temperature are the driving force for ink jetting in TIJs. Here, rapid boiling is defined as that which occurs when the rate of heating is faster than  $10^7 \text{ K s}^{-1}$ , or in other words, when the time taken for the temperature of water at 0 °C to rise to 100 °C is less than 10  $\mu\text{s}$ .

Allen *et al.* [3] from HP were the first researchers to describe TIJ bubbles in 1985 and suggested that “generation of thermal ink-jet vapor bubbles does not lie within the regime of conventional boiling.” In 1991, Asai from Canon was the first to clearly describe the mechanism of coalescent bubble formation from the incipience of boiling for TIJs; the following is an excerpt from this paper [4].

##### 3.2.1.1 Theoretical Model

**3.2.1.1.1 Nucleation Probability** In boiling under extremely high heat flux pulse heating, however, the dominant bubble generation mechanism is spontaneous nucleation due to thermal motion of liquid molecules [5]. This is because the liquid temperature rises so rapidly that vapor or gas nuclei, which may be trapped on the heating surface, do not grow large before the spontaneous nucleation occurs.

**3.2.1.1.2 Bubble Growth in the Early Stage** When heat flux is so large, the surface is instantly covered by many small nuclei, and they combine into a thin vapor film before they grow large. The bubble growth process may be idealized by the growth of a very thin vapor film.

$$\sigma_1/d_h \ll P_v - P_{\text{amb}} \quad (3.1)$$

where  $\sigma_1$  is the surface tension of the liquid,  $d_h$  is heater length,  $P_v$  is the initial pressure of the bubble, and  $P_{\text{amb}}$  is ambient pressure. By assuming that the pressure in the vapor film is uniform and neglecting the discontinuity of pressure at the liquid–vapor interface, the bubble volume  $V_v$  satisfies the following equation:

$$\frac{d^2 V_v(t)}{dt^2} = \frac{P_v(t) - P_{\text{amb}}}{I_1} \quad (3.2)$$

where  $I_1$  is the inertance [6] of the liquid region; the value of  $I_1$  strongly depends on the shape of the liquid region. If the heater is a square of sides  $d_h$  located on a flat wall and the liquid is filled in a semi-infinite region defined by the wall and infinite open boundary, the inertance of the semi-infinite region is  $I_1 \approx 0.43\rho_l/d_h$ .

**3.2.1.1.3 Bubble Growth in the Later Stage** When the heat pulse duration is so short and the superheated liquid layer is so thin, the temperature and the pressure of the bubble rapidly decrease before the vapor film grows large. In such a highly subcooled condition, the liquid is given an initial supply of kinetic energy by the pressure impulse, and thereafter, the bubble growth and collapse process are dynamically controlled by the pressure difference and the liquid inertia [7].

By assuming that  $P_v \gg P_{amb}$ , the pressure impulse  $P_{imp} = \int_0^t (P_v(t) - P_{amb})dt$  and the work  $W$  done by the bubble to liquid are given by:

$$W = \frac{P_{imp}^2}{2I_1} \quad (3.3)$$

By further assuming that the bubble pressure decreases rapidly to the value  $P_{sat}(T_{amb})$  and that the liquid motion stops when the bubble volume  $V_v$  attains the maximum value,  $V_{max}$ :

$$V_{max} = \frac{W}{P_{amb} - P_{sat}(T_{amb})} \quad (3.4)$$

Defining the equivalent bubble radius  $R_v(t)$  by the radius of a hemisphere of volume  $V_v(t)$ , the maximum equivalent bubble radius  $R_{max}$  is:

$$R_{max} = \left( \frac{3V_{max}}{2\pi} \right)^{1/3} \quad (3.5)$$

The bubble behavior after it reaches its maximum volume can be treated as a cavitation bubble [8]:

$$R_v(t) \frac{d^2 R_v}{dt^2} + \frac{3}{2} \left( \frac{dR_v(t)}{dt} \right)^2 = - \frac{P_{amb} - P_{sat}(T_{amb})}{I_1} \quad (3.6)$$

The time  $t_{col}$  required by the bubble to collapse is given by:

$$t_{col} = 0.915 R_{max} \left( \frac{\rho_l}{P_{amb} - P_{sat}(T_{amb})} \right)^{1/2} \quad (3.7)$$

### 3.2.1.2 Observation of Boiling Bubble Behavior

In this experiment, to observe the behavior of boiling bubbles, a thin-film heater with dimensions of  $100 \times 250 \mu\text{m}$  and made of platinum was used [9]. Platinum is inert to various liquids and can also be used as a thermometer. Figure 3.1a shows the temperature of the heating surface and boiling configurations according to the elapsed time ( $t$ ) after boiling incipience upon applying a heating pulse power of  $Q = 15 \text{ W}$  for a heating time of  $\tau = 2.5 \mu\text{s}$  to the heater. A sequence of

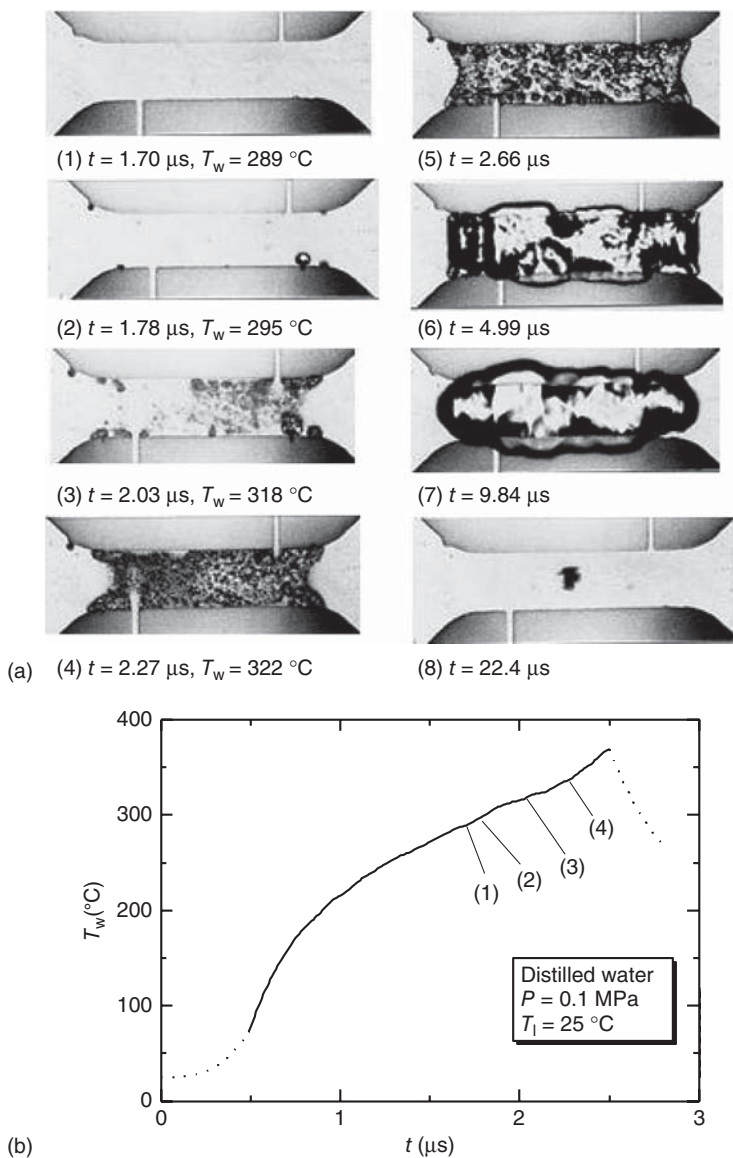


**Figure 3.1** Boiling configuration and corresponding wall temperature of a platinum film heater ( $Q = 15 \text{ W}$ ,  $\tau = 2.5 \mu\text{s}$ ) over time: (a) photographs of bubble progres-

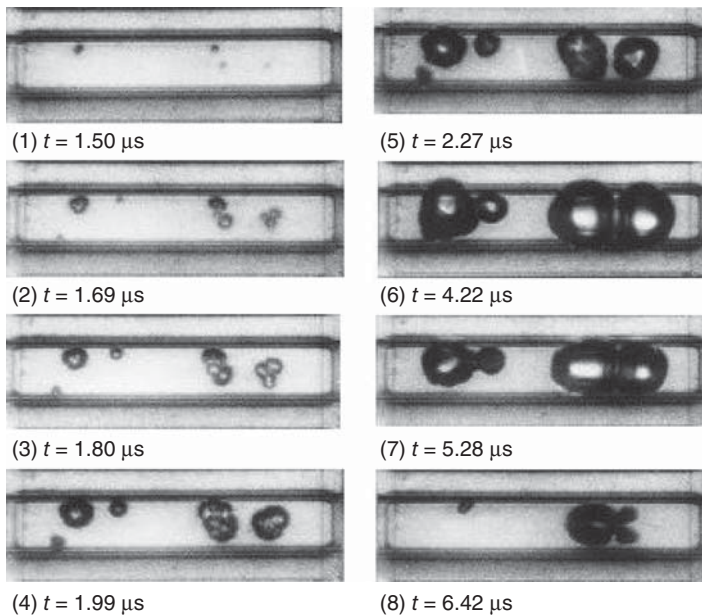
sion from generation to collapse on the heater surface and (b) heater temperature changes induced by pulse heating (heating rate =  $1.6 \times 10^8 \text{ K s}^{-1}$ ).



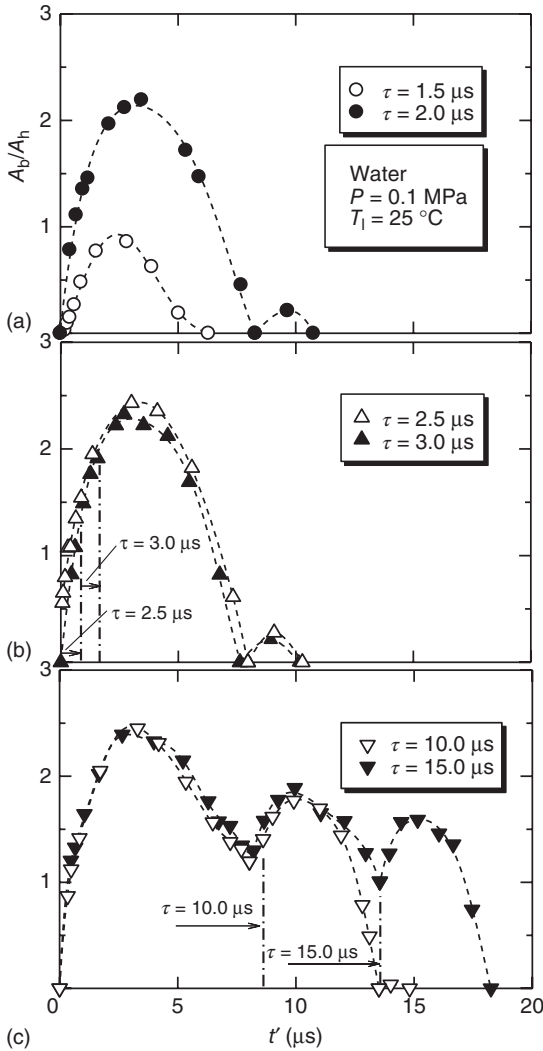
events occurs as follows from a state where there are: (1) no changes on the heater surface; (2) bubbles are generated; then, (3) a large number of small bubbles are generated simultaneously over the whole heater surface within a short period of time; (4), (5) the bubbles coalesce; and start to grow (6), (7); after becoming a single bubble and reaching its maximum size (8), the bubble starts to shrink and then collapses in the center of the heater. This boiling mechanism is based on spontaneous nucleation. Here, the temperature of the heater surface when the bubbles are generated ( $T_w$ ) is  $295^\circ\text{C}$ , as shown in Figure 3.1b, which is lower than the theoretical value of the temperature of homogeneous nucleation ( $312.5^\circ\text{C}$ ) suggested by Skripov [5]. This discrepancy is the same as observed in the previous research [10]. The average heating rate at boiling incipience is approximately  $1.6 \times 10^8 \text{ K s}^{-1}$ .

Figure 3.2 shows the observed boiling configurations for  $\tau = 1.5 \mu\text{s}$  and  $Q = 4 \text{ W}$  using a heater installed onto a TIJ printer that was launched by Fuji Xerox Co., Ltd (Fuji Xerox) in 1997 [11]. Normally, this heater prints at a heating period of  $\tau = 2.5 \mu\text{s}$ , so the energy that is applied to the liquid layer is insufficient to induce boiling for the configuration shown in Figure 3.1. As a result, the location where boiling is generated is limited to the pit, cavity, and wherever the nuclei and heterogeneous sites form bubbles that grow and collapse without coalescing. This boiling mechanism is based on the pre-existing nuclei.

The change in bubble volume with elapsed time ( $t'$ ) after boiling incipience upon changing the heating period from 1.5 to  $15 \mu\text{s}$  using the heater shown in Figure 3.2 is presented in Figure 3.3. As heating period increases, the volume of



**Figure 3.2** Boiling configuration on a TIJ heater ( $Q = 4.0 \text{ W}$ ,  $\tau = 1.5 \mu\text{s}$ ).



**Figure 3.3** Change of bubble volume over time for several pulse widths using a TIJ heater ( $Q=4.0 \text{ W}$ ).

the bubbles increases; after  $2.5 \mu\text{s}$ , there are no longer many changes; that is, the bubbles are saturated and do not grow. Here, the generation of bubbles after  $8 \mu\text{s}$  (see Figure 3.3b) is referred to as the rebound phenomenon, where bubbles regrow because of the bubbles that had collapsed colliding against the heater surface and rebounding. In addition, when the heating time exceeds the collapsing time of bubbles, as in Figure 3.3c, after the liquid comes in contact with the heating surface, bubbles are regenerated and grow.

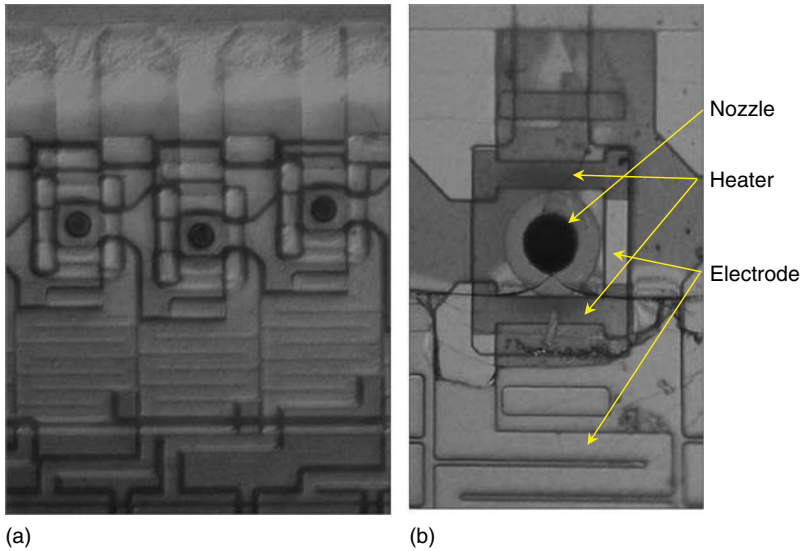


**Figure 3.4** Structure of a back-shooter-type BenQ printhead: (a) front surface of the nozzle and (b) rear surface of the nozzle.

### 3.2.2

#### Printhead Structure

When the aforementioned microheater is covered with a nozzle plate, it becomes a TIJ printhead that jets ink from the nozzle. Many such structures have been realized (Table 3.1 in Ref. [1]). The most common printhead structure is the “roof shooter” adopted by Canon and HP, where the nozzle is installed in the direction of growth of bubbles (Figure 3.3 in Ref. [1]). In this structure, the heater and nozzle are fundamentally separate components; the heater and driving transistor are fabricated on a silicon (Si) substrate during processing of the integrated circuit. Subsequently, a liquid chamber that surrounds the heater is fabricated from, for example, a resin such as polyimide. Finally, a nozzle is constructed as an open port to release bubble pressure.

The “back shooter” type of printhead commercialized by BenQ Corporation (BenQ) is unique in that the heater and nozzle are an integrated structure (Table 3.1 in Ref. [1]). Figure 3.4 shows the printhead of a BenQ printer purchased in Taiwan. Figure 3.4a depicts the nozzle surface where wiring is observed on the back side of the nozzle composed of transparent resin or glass. In this printhead, the electrical current flows through the heater to surround the nozzle by passing through the wiring from the driving transistor on the bottom until it reaches the common electrode at the top. The nozzles are not aligned to allow position adjustment to change the timing of jetting. Figure 3.4b shows the rear side of the nozzle of the BenQ printhead. The two wires that surround the nozzle are presumed to be the heater because as there is discoloration above and below them, whereas the wiring on the side of the nozzle is not considered to be the heater.

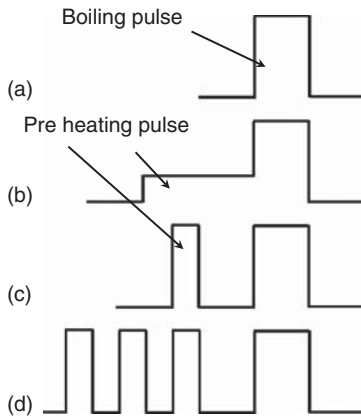


**Figure 3.5** Heating pulse configuration used in TIJs: (a) single pulse; (b) pulse with connected preheating pulse; (c) pulse with isolated preheating pulse; and (d) pulse with multiple preheating pulses.

The area of the actuator element of a TIJ is approximately 100th of that of a PIJ. This is because, while piezoelectric oscillations are of submicron level, the height of air bubbles reaches more than  $10\ \mu\text{m}$  [4, 12]. As a result, in TIJs, a density equivalent to 1600 dots per inch (dpi) per scan is realized by making the distance between the closest nozzles  $31.8\ \mu\text{m}$  and forming an array of nozzles with two rows [13].

### 3.2.3

#### Jetting Characteristics of TIJs

##### 3.2.3.1 Input Power Characteristics and Heat Control of TIJs

The momentum of the bubbles in an inkjet printer is directly reflected in its ink jetting characteristics. Ink is pushed through the nozzle by an impulse that is generated by boiling bubbles. The ink then turns into droplets, flies toward the paper (Figure 3.9 in Ref. [1]), and forms images on the paper surface. With regard to the dependence of jetting characteristics on pulse power (Figure 3.5 in Ref. [1]), when pulse power is low, as shown in Figure 3.2, jetting force becomes weak and unstable. As pulse power increases, jetting force becomes saturated and stable based on the boiling behavior shown in Figure 3.1.

For TIJs, as bubbles are generated from a “superheated liquid layer,” the size of the bubbles depends on the temperature of the liquid before boiling incipience. This characteristic is indicated by temperature dependence of the printhead of the TIJ (Figure 3.7 in Ref. [1]). This characteristic gives rise to a problem where, after starting printing at room temperature, heat accumulates in the printhead because of repeated heating, resulting in the print density becoming too high near the end of printing.

Conversely, when the printhead temperature is held constant, it is possible to increase the amount of ink that is jetted by preheating the liquid layer [12]. Figure 3.5 shows an example of a pulse waveform that carries out preheating.

A boiling experiment was conducted using the pulse shown in Figure 3.5b and a commercially available HP51604 with dimensions of  $100 \times 110\ \mu\text{m}$ , which is shown in Figure 3.6a. As compared with the bubble volume formed by a normal

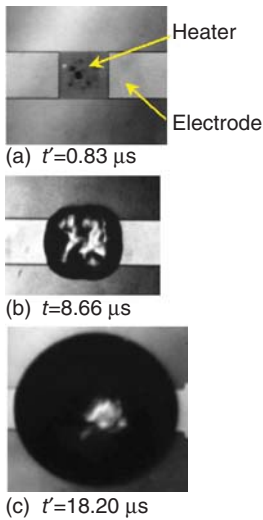


**Figure 3.6** Photographs of boiling on an HP51604 heater: (a) boiling incipience; (b) bubble formed by a standard single pulse; and (c) bubble formed by a preheating pulse.

single pulse (see Figure 3.6b), preheating lead to a bubble volume that was 12 times larger, as indicated in Figure 3.6c [14]. As a measure for heat storage using this characteristic, a mechanism using preheating that controls the size of the bubble, or the drop volume, is installed in TIJ printers [15] (see Question 3.5.1).

The fundamental means of resolving heat storage issues for TIJs is to efficiently heat the ink up until boiling incipience and to discharge the heat promptly after boiling. Because the layer structure of the heater contributes greatly to heat storage properties, investigations of heat simulation are being carried out (Figure 3.8 in Ref. [1]).

### 3.2.3.2 Frequency Response and Crosstalk Control

The speed of printers can be raised by increasing the jetting frequency or, in other words, by refilling the flow channel with ink, promptly after the ink is jetted. In TIJs, refilling is controlled by capillary action based on the surface tension inside the nozzle. In comparison, because PIJs use piezoelectric oscillations, fluid velocity can be controlled, so compulsory refilling is possible, which is advantageous to increase the speed of a printer.

In TIJs, the distance between adjacent heaters is approximately several tens of micrometers, and as a result, crosstalk occurs between the jets. Crosstalk is composed of an acoustic effect where pressure oscillation from boiling travels in the ink and interferes with the adjacent jets, as well as a fluidic effect where each nozzle competes against others to draw the ink in the flow channel using capillary force. Figure 3.7 shows the situation when jetting begins at the same time from Jet 5 to 8, and starts  $5 \mu\text{s}$  later from Jet 1 to 4 simultaneously. A shortage of ink supply occurs at Jet 4 because of the previous jetting from Jet 5 to 8. Jet elongation occurs (Figure 3.6 in Ref. [1]), and then the system returns to a relaxation state from Jet 4 to 1. This is an example of fluid crosstalk, resulting in jetting becoming unstable, particularly at Jet 4, which causes streaks in prints.

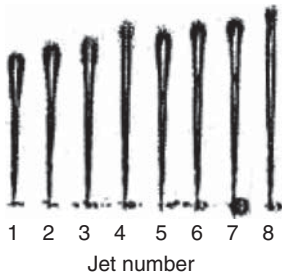


**Figure 3.7** Ink jetting conditions with induced crosstalk (Jets 5–8 fired simultaneously, and then Jets 1–4 simultaneously fired 5  $\mu$ s later).

As countermeasures to the problem of crosstalk, the first would be to lower the jetting frequency, but this is unfavorable because it lowers the speed of the printer. Thus, solutions such as intentionally increasing the distance between heaters, narrowing the ink flow channel that supplies ink to the heater, or installing obstacles in the flow channel to achieve acoustic and fluid resistance, as well as interlacing the jetting (heating) start time, have been examined. As compared to PIJs, TIJs require a high electrical current, and because time-sharing drive is necessary for the heater, interlacing is also intrinsically required. A method to compensate for the timing interlace is to use a nozzle array as that shown in Figure 3.4.

As described, to refill ink faster using capillary force, the resistance of the fluid channel needs to be lowered. However, because this contradicts the problem of crosstalk, it is necessary to carefully optimize the resistance of the fluid channel while also considering the surface tension and viscosity of the ink (Figure 3.9 in Ref. [1]).

### 3.2.4

#### Problems Associated with Pressure and Heat Generated in TIJs

##### 3.2.4.1 Cavitation Damage on the Heater Surface

While it can be said that the heater in a TIJ is a highly efficient actuator, problems arise when the pressure that is generated from this microsized area is too large. Pressure is generated twice with the generation and collapse of bubbles on the heater surface [16] and reaches several MPa (Figure 3.4 in Ref. [1]). In particular, the cavitation during bubbles collapse is concentrated in the center of the heater, and thus, the heater suffers mechanical damage. If printing continues, that is, if cavitation repeatedly damages the heater surface, then the heater will eventually break [17]. Manufacturing technology has progressed and the operating life of TIJs has become longer; the lifetime is said to be  $\sim 10^8$  cycles. However, PIJs have a lifetime of  $\sim 10^9$  to  $10^{10}$  cycles, which is considered the lifetime of a piezoelectric device, meaning that there is room to further improve the operating life of TIJs.

A simple method to avoid heater breakage caused by cavitation damage is to make the heater protection layer of tantalum (Ta) (Figure 3.8 in Ref. [1]) thicker, which increases operating life. However, because this approach increases the heat capacity of the heater, it is not favorable from the perspective of efficiency (see Problem 3.5.2). Numerous investigations of the composition and materials

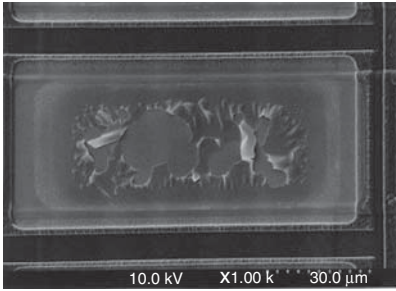


**Figure 3.8** Ink residue scorched onto the heater of the TIJ in Figure 3.2 ( $Q=4.0$  W, 27 000 pulses).

for the protection layer have been conducted; in particular, research using tantalum silicon oxide (TaSiO) is noteworthy [18]. The surface layer ( $\sim 10$  nm thick) of the rigid TaSiO heater is thermally oxidized to form an electrically insulating layer on its surface and simultaneously works as a protective layer to prevent cavitation. Accordingly, it is not necessary to newly laminate protection and insulation layers, and as a result, it is possible to maintain a small heat capacity. Cavitation may also be avoided by using an “air communication” design where bubbles that have grown interact with the atmosphere at the nozzle and pressure is released. However, although this air communication method has been proposed for TIJs that contain a regular heater [19], it may not be used in actual printers.

In the unique structure developed by Memjet (Table 1 in Ref. [1]) where a heater is suspended in ink as a bridge [13], prevention of cavitation damage is maximized. However, in this structure, after bubbles are generated and coalesce along the heater from the center toward both ends and then shrink in the same manner along the heater, the bubbles collapse by colliding with each other in the ink rather than on the heater surface. As a result, there is no problem with regard to cavitation (Kia Silverbrook, personal talk).

#### 3.2.4.2 Ink Residue Scorching (Kogation) on the Heater Surface

It is thought that the heater in a TIJ exceeds  $300^{\circ}\text{C}$  and can easily reach around  $400^{\circ}\text{C}$  [20], and as a result, residue generated by pyrolysis of ink deposits is scorched on the heater surface. This is one of the intrinsic problems of TIJs [21]. Figure 3.8 shows ink residue depositing so as to avoid the cavitation point, which is the center of the heater, upon subjecting the heater shown in Figure 3.2 to 27 000 pulses. This is the initial stage of scorching, and as the pulse number increases, the residue adheres firmly to the heater surface (Figure 3.10 in Ref. [1]). This residue degrades print quality, because it prevents boiling and ultimately stops the jetting [22] (Figure 3.11 in Ref. [1]). As a countermeasure, ink components were investigated, and chemical adjustments were made to prevent scorching. Canon stated that they performed trials of 3000 kinds of ink materials.

Morita *et al.* [23, 24] have resolved this scorching problem by using boiling to remove residue from the heater, rather than adjusting the ink. Figure 3.9a shows the phenomenon of residue detaching off at a given pulse height upon applying



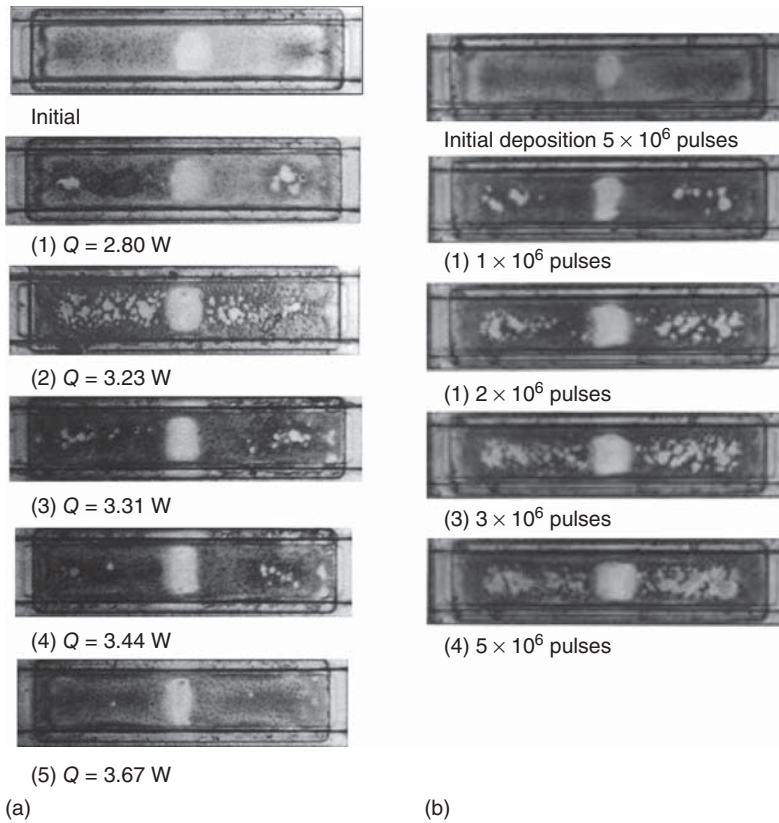


**Figure 3.9** Removal of ink residue scorched on a heater surface: (a) detachment of residue from a heater surface after pulse heating 2 million times at a low heating

pulse power and (b) progression of residue detachment on heater surface per million heating pulses at  $Q = 3.2$  W.

different heating pulses to the heater surface after causing scorching by using a heating power of  $Q = 4.0$  W and applying 5 million pulses. Residue detaches from the center of the heater because of cavitation when bubbles collapse, and although this occurs with any pulse, detachment of the residue from the whole heater surface can be observed near  $Q = 3.23$  W as shown in Figure 3.9a. Figure 3.9b shows a phenomenon where, after generating residue using the same method as shown in Figure 3.9a, the residue is detached by the application of pulses or, in other words, the heater surface is recovered to its original state. When the pulse power is low, boiling begins at heterogeneous sites such as the pit or cavity, and the pressure that is generated at this time is reasonably high. Because scorching residue itself becomes heterogeneous sites, it is considered that residue is detached by the pressure generated during boiling only when boiling is based on the pre-existing nuclei.



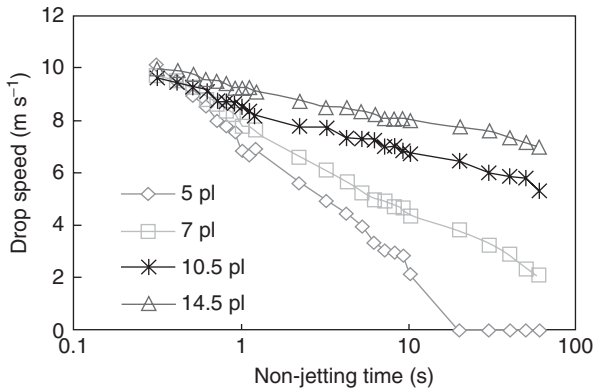


**Figure 3.10** Jetting speed degradation by water evaporation from the nozzle for different droplet volumes.

### 3.2.5

#### Evaporation of Water in Aqueous Ink

##### 3.2.5.1 Approaches to Compensate for Condensed Ink through Evaporation

When using aqueous ink in drop-on-demand (DoD) printers, evaporation of water from the ink is an issue that is common to both TIJs and PIJs, and various approaches to mitigate this have been developed [25]. Figure 3.10 shows the degradation of drop speed with elapsed time caused by the rate of water evaporation from the nozzle for different droplet volumes, which indicates that the drop velocity decreases with the elapsed time after the last jetting. Even for a “non-jetting” or “latency” period of 1 s, the influence of evaporation becomes greater as the drop speed becomes slower and eventually results in clogging. For this reason, “dummy” or “dehydration” jet technology is adopted in DoD inkjet printers to intentionally discharge ink that has become highly viscous because of evaporation in the nozzle, which prevents clogging by refreshing the nozzle.

In the case of scan-type heads, the printhead returns to the home position and jets ink in the gutter between sheets of paper or even during printing; however, because this is a waste of ink, it is naturally not preferable. If using a continuous sheet of paper with a page-width head, dummy jetting on the paper surface is inevitable, and it can affect the image quality. To solve this problem, for PIJs, it is possible to use a “shaking” or “tickle” wave that temporarily lowers ink viscosity by agitating the nozzle by applying a slight oscillation so that the ink in the nozzle does not jet using a piezoelectric actuator.

In contrast, for TIJs, because considerable energy is generated by boiling, it is not easy to shake the ink weakly so that it does not jet, even in the area of pre-existing nuclei.

This shaking technology acts in a narrow area from the oscillating plate to the nozzle, so the effect is only temporary. As a further improvement, a circulatory

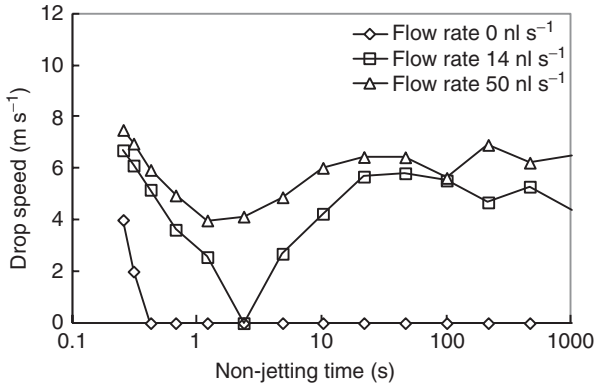


**Figure 3.11** Effect of ink circulation on jetting in relation to water evaporation from the nozzle.

flow channel was installed so that viscous ink could flow back to outside the nozzle area [26]. Using this flow channel in PIJs, it is possible to maintain a jetting state for 1000 s or longer without dummy jetting; accordingly, PIJs are advantageous over TIJs with regard to water evaporation. Figure 3.11 shows the experimental results obtained upon conducting circulation without shaking; when the flow rate is 0, jetting stops in less than 1 s, but using a flow rate of  $50 \text{ nl s}^{-1}$ , it is possible to maintain jetting. When the flow rate is  $14 \text{ nl s}^{-1}$ , jetting stops once after a few seconds, but then recovers; jetting restarts after a long non-jetting time. This is caused by formation of an equilibrium in the difference between the evaporation speed from the nozzle and ink diffusion speed in the nozzle [27].

### 3.2.5.2 Measurement of Physical Properties of Flying Droplets

One way to better understand evaporation from a micronozzle is to measure the physical properties of flying droplets. This is achieved by vibrating droplets while they are flying and observing their oscillation period and damping [28]. The vibration of ink droplets is expressed by the following formulae based on surface tension and viscosity [29].

$$\alpha_2 = \pi \sqrt{\frac{\rho a^3}{2\sigma}}, \quad \beta_2 = 5 \frac{\eta}{\rho a^2} \quad (3.8)$$

where  $\alpha_2$  is the vibration period,  $\beta_2$  is a damping coefficient (second mode),  $a$  is the droplet radius,  $\rho$  is the density,  $\sigma$  is the surface tension, and  $\eta$  is the viscosity. The main drop may vibrate because of collision with satellites [30], which continue to be generated. Figure 3.12a shows that the satellites gradually come near the main drop, collide and coalesce with it, and then the drop vibrates.

Figure 3.12b shows the surface tension in relation to the non-jetting time ( $t_{\text{nj}}$ ) that was obtained by jetting deionized water containing surfactant and measuring the vibration cycle. Here, the decrease in surface tension in this experiment is 0.3 s

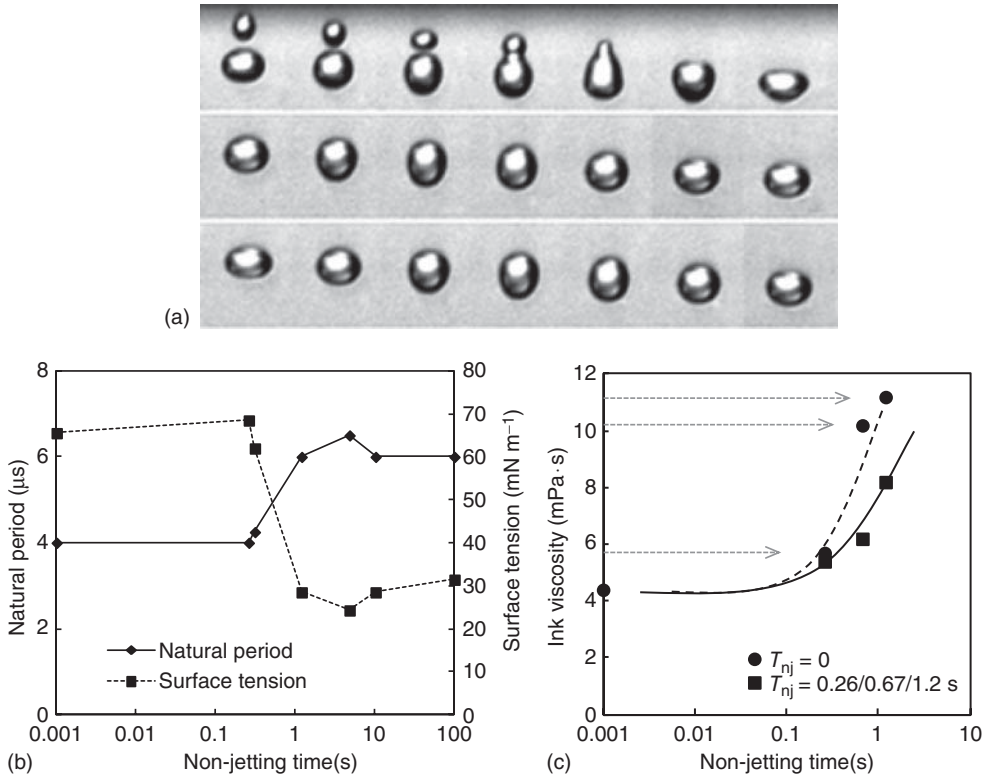


**Figure 3.12** Properties of evaporated ink measured by vibration of flying droplets: (a) observed vibration caused by satellite collision with the main droplet (water + 0.2% surfactant, time delay =  $1 \mu\text{s}$ ); (b) estimated surface tension measured by droplet

vibration (water + 0.2% surfactant); and (c) changes in ink viscosity over time for a droplet velocity of  $7.0 \text{ m s}^{-1}$ . (solid line  $Q = Q_1, Q_2, Q_3$  at each  $t_{\text{nj}}$ , dotted line  $Q = Q_1, Q_2, Q_3$  at  $t_{\text{nj}} = 0$ ).

later than that of water, which is thought to be the time required for the surfactant to coordinate to the liquid surface.

Similarly, Figure 3.12c shows the viscosity measured from the damping of vibration in relation to the non-jetting time. For each non-jetting time, an input power ( $Q_1, Q_2, Q_3$ ) where the drop velocity becomes  $7 \text{ m s}^{-1}$  was applied, and the viscosity was measured from each vibration. Next, the same input power as when the non-jetting time was 0 was applied and estimated to be the viscosity where the drop velocity becomes  $7 \text{ m s}^{-1}$ . The viscosity of the ink droplet increased exponentially in a short period of time, and the viscosity of each non-jetting droplet, which was averaged in a droplet, was shown to be lower. Accordingly, it is thought that a capping layer may exist at the nozzle surface that disturbs jetting [31].

### 3.3

#### Future Prospects for Inkjets

##### 3.3.1

##### Printing Speed Limit Estimated by Drop Behavior

Inkjets are a direct printing tool where drops fly through the air, and furthermore, because the paper or printhead moves at high speed, droplets are subject to airflow pressure [32]. In modern high-speed inkjets [2], for example, Fuji Xerox's Inkjet Continuous Feed Printer (CF Printer), a speed of  $200 \text{ m min}^{-1}$  ( $3.33 \text{ m s}^{-1}$ ) is realized. The speed limit of a printer is defined by the performance and cost of the controller that processes the image. However, the speed limit of ink jetting is also of interest. Accordingly, a high-speed printing experiment was conducted using the aforementioned printer and an experimental bench [33].

Figure 3.13a shows the displacement of a 5-pl droplet (droplet of interest) in relation to an 8-pl droplet as a comparison base with increasing printing speed. A displacement of approximately  $20 \mu\text{m}$  is observed up to a speed of  $200 \text{ m min}^{-1}$  with a continuous feed printer. Then, displacement increases nearly in proportion to the paper speed up to  $820 \text{ m min}^{-1}$  using this experimental bench. It was shown that nonlinear problems such as droplets not reaching the paper surface because of airflow do not disturb in this speed range. An analysis was conducted using a simulation model for the displacement of droplets. The changes in droplet velocity were measured and then compared with calculated values. After confirming that the values mostly matched, they were applied to the conditions indicated in Figure 3.13a, represented by the dashed line, confirming that these results are reasonable.

Figure 3.13b shows the effects of displacement factors on a 2-pl droplet. Rather than the airflow that arises because of paper feeding (Couette flow), the different speeds that droplets move at are a dominant factor affecting their displacement. This indicates that, for example, in relation to a paper speed of  $200 \text{ m min}^{-1}$ ,  $800 \text{ m min}^{-1}$  is fourfold, so to achieve an allowable image quality, it is necessary to decrease the unevenness of the speed of all drops to  $1/4$  of that at  $200 \text{ m min}^{-1}$ .

##### 3.3.2

##### Control of Bleeding Caused by High-Speed Drying

For aqueous inkjets, "bleeding" or "feathering" on plain paper has been an eternal issue. Although it is possible to reduce bleeding using inks with slow penetration ignoring the offset issue, and treating with a precoating fluid before ink jetting [34], it has been the goal of aqueous inkjet researchers for many years to eliminate bleeding regardless of paper type. Until this bleeding issue is eliminated, inkjets cannot win against their rival, electrophotography.

In high-speed inkjets [2], after ink reaches the paper, the wet surface moves at the rate of the paper feed, so the ink needs to start drying within approximately 1 s

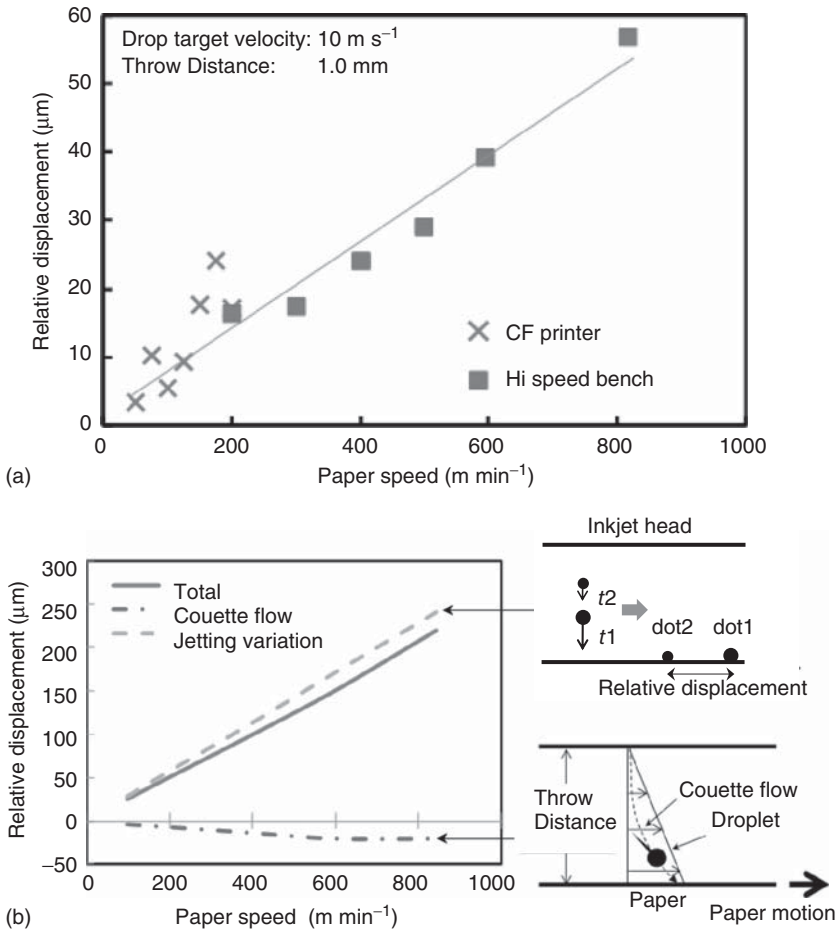


**Figure 3.13** Speed limit of inkjet printing considering the kinetics of the jetting droplet: (a) dependence of dot displacement on paper speed and (b) influences of airflow and droplet speed unevenness on dot displacement.

to meet machine structural restrictions. However, because the penetration of ink during high-speed printing ends within approximately 0.1 s, bleeding still occurs. Thus, high-speed drying using an experimental setup where a laser was installed near the printhead was examined [35].

Figure 3.14a shows that the time from when printing ends until drying starts is 20 ms, and the laser exposure time is 20 ms. As compared with the case where there was no laser exposure, when there was laser exposure of  $2.5 \times 10^4 \text{ J m}^{-2}$ , fine lines that were illegible became recognizable. In other words, laser exposure controlled bleeding. Figure 3.14b shows that the optical density could be increased by changing the laser exposure energy. This increase in density indicates that ink

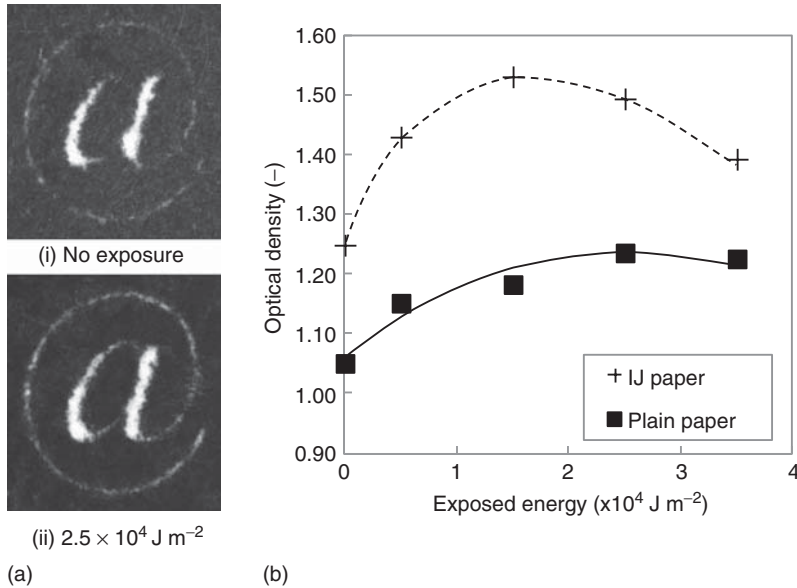


**Figure 3.14** High-speed drying using laser exposure (interval between printing and drying: 20 ms, exposure time: 20 ms): (a) effect of laser exposure on image quality and (b) dependence of laser energy on image density for different types of paper.

penetration was controlled, and ink pigments remained on the paper surface. The behavior of papers depended on their difference in penetration speed. Although there are many issues in equipping printers with drying lasers in terms of cost, safety, and photosensitivity of inks, realization of this feature may be possible.

### 3.4

#### Continuous Inkjet (CIJ)

Continuous inkjet (CIJ) technology uses a pressurized stream jetted from the nozzle to generate droplets in accordance with a timing signal or frequency and then selects the necessary droplets to form dots on the paper. The history of CIJs is longer than that of DoDs, and it is common to date CIJs back to Rayleigh [36] and Weber [37]. Because ink is jetted by pressure, clogging does not occur easily in CIJs. CIJs are also characterized by a long drop throw distance ( $>10 \text{ mm}$ ). Research and development of CIJs was actively conducted in the 1960s and 1970s for the purpose of their practical application. Early CIJ products include AB Dick's Videojet 9600 (jetting frequency = 66 kHz) released in 1969 and IBM 6640 (jetting frequency = 117 kHz) released by IBM in 1976. There was also competition from various companies such as Siemens, Mead, Hitachi, Sharp, and Nippon Telegraph and Telephone (NTT) Corporation. In

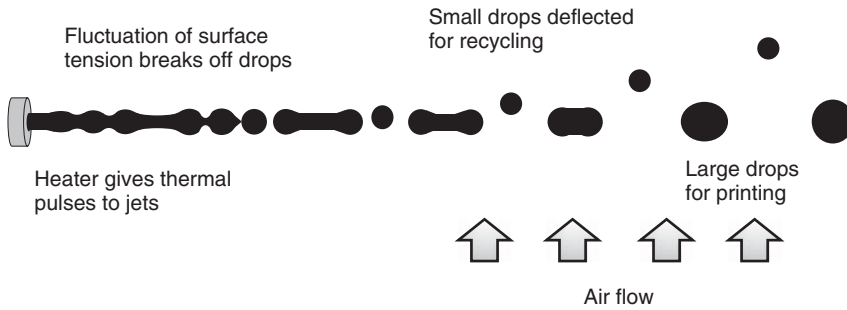


**Figure 3.15** Schematic diagram showing the principles of the thermal CIJ Kodak Prosper.

1989, Iris Graphics 3407 (jetting frequency = 1 MHz) was widely recognized in the market as a high-definition color proofer and set a precedent for wide format. This technology was transferred to Scitex and Kodak and was commercialized as Prosper (jetting frequency = 360 kHz). CIJ printers are still used industrially because their long drop throw distance makes them suitable for applications such as printing on cardboard and curved surfaces such as that of eggs.

Ultrasonic vibrations [38] induced by piezoelectric devices are the most common method of drop generation in CIJs. Other techniques for drop generation include an electrostatic method [39] and heat, as used in Prosper [40]. Figure 3.15 illustrates the printing method of Prosper, where the nozzle is the heater [41], and droplets are generated by changing the surface tension based on heat fluctuation of several degrees [42]. While it is not possible to escape from echo caused by ultrasonic waves, because heat is not reflected, this parameter may be modulated. In addition, the operation signal is supplied at the nozzle, so there are benefits such as being free from air bubbles that exist in the printhead and from mechanical resonance.

In the past technology, a method where droplets are charged using charging electrodes and then controlled using electrical fields formed by deflection electrodes has been used for drop selection. In Prosper, however, a selection signal is supplied simultaneously when droplets are generated in each nozzle, so charge electrodes are not necessary. With regard to deflection, by applying airflow (air current) in a direction that intersects the jet, large droplets fly straight ahead and print while small droplets are deflected toward the gutter by the airflow and collected. Charge and deflection require complex electrical equipment, and in addition, positional displacement occurs because of slight charge noise and there is the problem of electrical leakage in the deflection field. In contrast, Prosper's drop selection using airflow is an extremely simple and safe system.

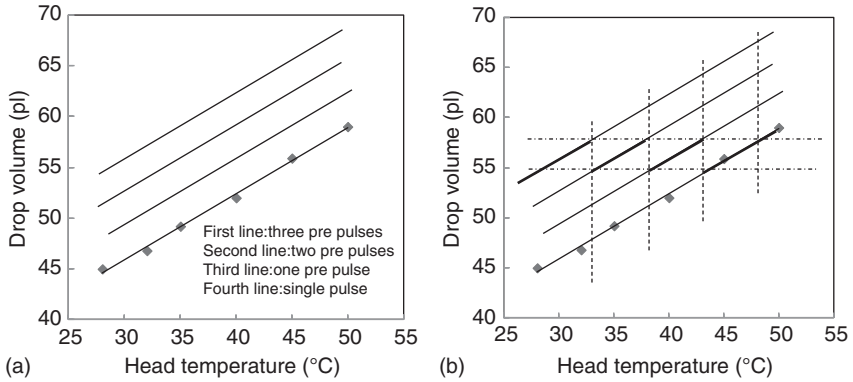


**Figure 3.16** Temperature dependence of drop volume on preheating pulse: (a) question and (b) answer.

### 3.5

#### Examples and Problems (TIJ)

##### 3.5.1

##### Example

Currently, under single-pulse driving, ink volume (printing density) varies from 45 to 58 pl ( $\pm 12\%$ ) with environmental temperature changes (Figure 3.7 in Ref. [1]). Figure 3.16a illustrates the head temperature characteristics when the preheating pulse and multiple preheating pulses shown in Figure 3.5c,d, respectively, are used based on a single pulse. As the number of preheating pulses increases, the drop volume increases at each temperature, and the temperature dependence is parallel to each other. Design the printhead conditions to stabilize ink volume using preheating pulse control. The printhead has a thermometer.

Change the number of preheating pulses by detecting the temperature of the head in intervals of  $5^\circ\text{C}$ . This is achieved by conducting a drive of three preheating pulses up to  $33^\circ\text{C}$ , followed by a drive of two preheating pulses up to  $38^\circ\text{C}$ , one up to  $43^\circ\text{C}$  and zero up to  $48^\circ\text{C}$ , and then the volume variation becomes 55–58 pl ( $\pm 3\%$ ), as indicated by the thick lines in Figure 3.16b.

##### 3.5.2

##### Problem

Calculate the heat flux into the ink and thermal efficiency for bubble generation, where efficiency is heat flux for boiling divided by total input, at the platinum heater shown in Figure 3.17 using the following table of specifications.



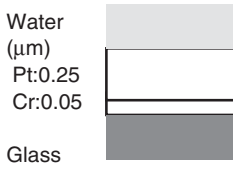


Figure 3.17 Layers of materials around a platinum heater.

	$\rho$ (kg m <sup>-3</sup> )	$C_p$ (kJ kg <sup>-1</sup> ·K <sup>-1</sup> )	$\lambda$ (W m <sup>-1</sup> ·K <sup>-1</sup> )	$\kappa$ (mm <sup>2</sup> s <sup>-1</sup> )	$\delta$ (μm)
Water	1 000	4.2	0.61	0.1466	—
Glass	—	—	1.38	0.85	—
Cr	7 190	0.446	—	—	0.05
Pt	21 700	0.133	—	—	0.2

**Answer**

Heat flux at the glass below the heater ( $q_s$ ) and water above ( $q_l$ ) is [43]:

$$q_s : q_l = \frac{\lambda_s}{\sqrt{\kappa_s}} : \frac{\lambda_l}{\sqrt{\kappa_l}}$$

where  $\lambda$  is the thermal conductivity and  $\kappa$  is the thermal diffusivity.

---


$$q_s : q_l = 1.38 / (0.85)^{1/2} : 0.61 / (0.1466)^{1/2} = 1.497 : 1.593$$


---


$$\text{heat capacity} = C_p \times \rho \times \delta \times dT/dt$$


---

where  $C_p$  is the specific heat,  $\rho$  is the density,  $\delta$  is the thickness,  $T$  is the temperature, and  $t$  is the time. In this heater,

$$\frac{dT}{dt} = \frac{295 - 25}{1.78 \times 10^{-6}}$$

because the boiling temperature is 295 °C, and incipience time is 1.78 μs. Therefore, the heat capacity of Pt is  $0.133 \times 21700 \times 0.2 \times dT/dt = 0.876$  and that for Cr is  $0.446 \times 7190 \times 0.05 \times dT/dt = 0.243$ . Overall, Pt + Cr:  $(C_p \rho \delta)(dT/dt) = 1.119 \times 10^8 \text{ W m}^{-2}$ .

Total input heat flux  $q = 15.0 / (100 \times 250 \times 10^{-12}) = 6.0 \times 10^8 \text{ W m}^{-2}$ , because  $Q = 15 \text{ W}$ , and the heater dimensions are  $100 \times 250 \text{ μm}$ .

Total input minus  $(6.0 - 1.119)$  heat capacity is  $6.0 - 1.119 = 4.881 \times 10^8 \text{ W m}^{-2}$ , so the heat flux into the ink is

$$4.881 \times 10^8 \times \frac{1.593}{1.497 + 1.593} = 2.52 \times 10^8 \text{ W m}^{-2}$$

Efficiency =  $2.52 / 6.0 \times 100 = 42\%$

### 3.6

#### Piezo Inkjet Printhead

##### 3.6.1

###### Introduction

The first pioneering work in the development of piezo inkjet printhead was performed in the late 1940s by C.W. Hansell of the Radio Corporation of America (RCA), who invented the first Drop-on-Demand (DoD) device. By means of a piezoelectric disc, coaxially arranged with an ink-filled conical nozzle, pressure waves could be generated, which caused a spray of ink drops. However, this invention, intended for use as a writing mechanism in a pioneering RCA facsimile concept, was never developed into a commercial product.

Generally, the basis of Piezo Inkjet (PIJ) printers is attributed to three patents in the 1970s [44]. Common denominator of these three patents is, as in the first pioneering patent of 1950, the use of a piezoelectric unit to convert an electrical driving voltage into a mechanical deformation of an ink chamber, which generates the pressure required for the drop formation from a nozzle.

The first is that of Zoltan of the Clevite company in 1972 (US Patent 3 683 212), proposing a squeeze mode of operation. In this mode, a hollow tube of piezoelectric material is used, either surrounding a glass nozzle or with a piezoceramic tube cast in plastic to enclose the ink channel. The radial polarized tube is provided with electrodes on its inner and outer surfaces. When a voltage is applied to the piezoelectric material, the ink chamber is squeezed and a drop is forced out of a nozzle.

The first PIJ printer to reach the market was in 1977, the Siemens PT-80, which used the squeeze mode. The PT-80 printed 270 characters per second at a resolution of 120 dpi with a printhead comprising 12 nozzles, firing drops at a maximum repetition frequency of 2.5 kHz. The PT-88 was introduced a few years later, and this was the first sub \$1000 inkjet printer. The development of a 32-nozzle follow-up printhead failed due to problems with nozzle-to-nozzle uniformity.

The second patent of Stemme of the Chalmers University in 1973 (US Patent 3 747 120) utilizes the bend mode of piezoelectric operation. In this mode, the bending of a wall of the ink chamber is used to eject a drop. Therefore, the wall is made of a diaphragm with a piezoceramic bonded onto it. The bend mode is also referred to as bimorph or unimorph mode.

The third patent of Kyser and Sears of the Silonics company in 1976 (US Patent 3 946 398) also used the bend mode operation. Both bend-mode patents were filed in the same year. The minor difference between the two is that Stemme used a flat disc of piezoelectric material to deform a rear wall of an ink chamber and Kyser and Sears used a rectangular plate to deform the roof of an ink chamber. Silonics was the second company to introduce a piezoelectric DoD printer, namely the Quietype, in 1978, which used the bend mode of the Kyser patent. The printhead, which required 150 V driving amplitude, fired drops with a maximum repetition

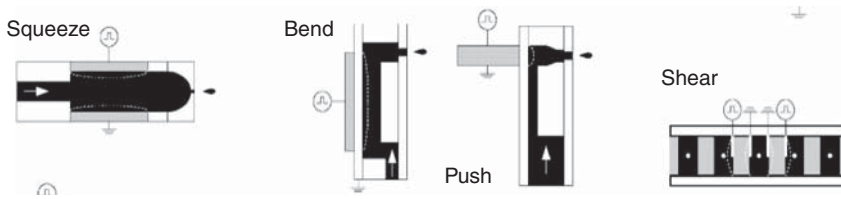


**Figure 3.18** Classification of piezo inkjet (PIJ) printhead technologies by the deformation mode used to generate the drops [44].

rate of 3 kHz. The electrical field is applied in the polarization direction of the piezo material. The deformation was perpendicular to the poling direction, not in the poling direction. Since the piezoceramic is bonded onto a passive membrane, the actuator will bend. Obviously, the main discriminator between the PIJ patents is the dominating deformation mode of the piezoelectric material, together with the geometry of the ink channels.

The 1984 patent of Stuart Howkins (US Patent 4 459 601) of the Exxon company describes the push-mode version. With the push mode, also referred to as bump mode, a piezoelectric element pushes against an ink chamber wall to deform the ink chamber. The electrical field is applied in the poling direction, and the deformation is in the same direction or perpendicular to the poling direction. Finally, the patent of Fischbeck (US Patent 4 584 590) proposed the shear mode. In the shear mode, the strong shear deformation component in piezoelectric materials is used to deform an ink chamber wall. The electric field is perpendicular to the polarization direction of the piezoceramic.

These modes complete the now commonly accepted categorization of the piezo inkjet printhead configurations: the squeeze, push, bend, and shear mode. In Figure 3.18, a special version of the shear-mode inkjet is shown, using the shared-wall principle, where the piezoceramic is also the channel plate.

### 3.6.2

#### Working Principle

Figure 3.19 represents the simplified geometry of the inkjet device, following [45], with a long ink channel with a nozzle on the right side and a large reservoir on the left side. Only the part of the pressure wave that fires a drop is drawn below this.

An electric voltage on a piezo element enlarges the channel and a negative pressure is generated. After reflection at the reservoir, this becomes a positive-pressure wave. The positive-pressure wave is amplified by the second slope of the driving waveform to obtain a large positive-pressure peak at the nozzle, which fires a drop.

A piezo actuator element drives each channel. To fire a droplet, an electric voltage is applied, and the channel cross section will be deformed by the inverse piezoelectric effect. This results in pressure waves inside the channel. The

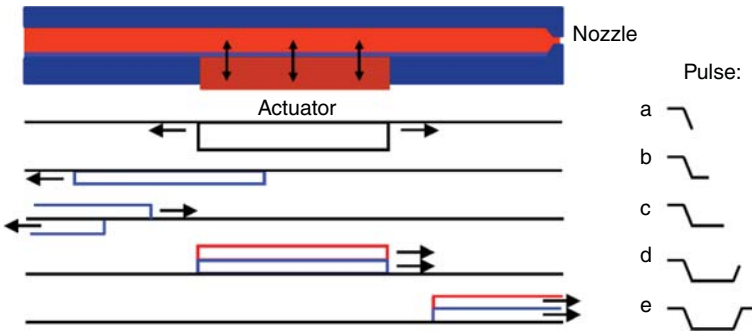


Figure 3.19 Schematic drawing of the actuation principle.

pressure waves propagate in the channel direction and will be reflected when the characteristic acoustic impedance  $Z$  of the channel changes. The acoustic impedance of the channel depends on the size of the channel cross section  $A$ , the density of the ink  $\rho$ , and the speed of sound  $c$  as:

$$Z = \frac{\rho c}{A} \quad (3.9)$$

The speed of sound is influenced by the compliance of the channel cross section. The reflection  $R$  and transmission  $T$  coefficients at the interface between domain 1 and 2 are

$$R = \frac{Z_2 - Z_1}{Z_1 + Z_2}, \quad T = \frac{2Z_2}{Z_1 + Z_2} \quad (3.10)$$

When the compliance does not change, the following relationship holds:

$$R = \frac{A_1 - A_2}{A_1 + A_2}, \quad T = \frac{2A_1}{A_1 + A_2} \quad (3.11)$$

At the large reservoir ( $A_2 \gg A_1$ ), the transmission coefficient is zero and the reflection coefficient equals  $-1$ . This means that the pressure wave will be completely reflected and the amplitude of the wave will change.

The charging of the piezo element (a in Figure 3.19) enlarges the channel cross section, and the resulting negative pressure wave will be reflected at the reservoir on the left (b). The large reservoir acts as an open end, and the acoustic wave returns as a positive-pressure wave (c). The discharging of the piezo element reduces the channel cross section to its original size. This will amplify the positive-pressure wave when tuned to the travel time of this acoustic wave (d). The channel structure and driving pulse are designed to obtain a large incoming positive pressure peak at the nozzle (e), which drives the ink through the nozzle. Acceleration of the ink movement in the small cross section of the nozzle (conservation of mass and incompressibility) results in drop formation.

Microelectromechanical Systems (MEMS)-based printheads with very small geometries are used. The inlet becomes a narrow section, which results in a

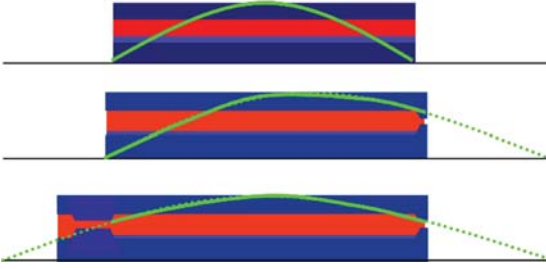


**Figure 3.20** General drawing of pressure amplitude of the base resonance mode with open and partially closed ends.

more closed reflection. This changes the acoustic properties completely. Both the nozzle and inlet sides act as a partially closed boundary, which truncates the standing wave on both sides, resulting in a kind of  $\lambda/6$  resonator, where  $\lambda$  is the wavelength of the fundamental frequency, see Figure 3.20.

With small geometries, the delay time of traveling waves plays no role, and the Helmholtz resonance is a simple way to simulate the acoustic properties. For this mode, the inlet channel must have a minimum impedance. Then, the relatively large volume of the actuation channel can act as a spring, with the ink in the inlet and nozzle as a vibrating mass, for example, a Helmholtz resonator. Helmholtz resonators are very effective in generating a high acoustic pressure.

From the equation of motion, without an external load, we obtain the resonance frequency of this system:

$$F_{\text{res}} = \frac{1}{2\pi} \sqrt{\frac{k}{m} - \frac{c}{2m}} \quad (3.12)$$

The mass  $m$  is equal to  $\rho AL$  with  $A_n$  or  $A_r$  as the cross section and  $L_n$  or  $L_r$  as the length of the nozzle or restriction. The spring constant  $k$  can be derived from the bulk modulus of a liquid, the pressure acting on the cross section of the nozzle or restriction, the change in volume  $V_c$  of the pressure channel, chamber, or cavity proportional to the cross section of the nozzle or restriction, and the linear displacement:

$$m = \rho AL, \quad k = \frac{\rho c^2 A^2}{V} \quad (3.13)$$

Neglecting the damping, and adding the mass of the nozzle and the restriction, the formula for the Helmholtz frequency becomes:

$$F_H = \frac{c}{2\pi} \sqrt{\frac{1}{V_c} \left( \frac{A_n}{L_n} + \frac{A_r}{L_r} \right)} \quad (3.14)$$

With the compliance  $C$  and the acoustic inductance or inductance  $M$  defined as:

$$C = \frac{V}{\rho c^2}, \quad M = \frac{\rho L}{A} \quad (3.15)$$

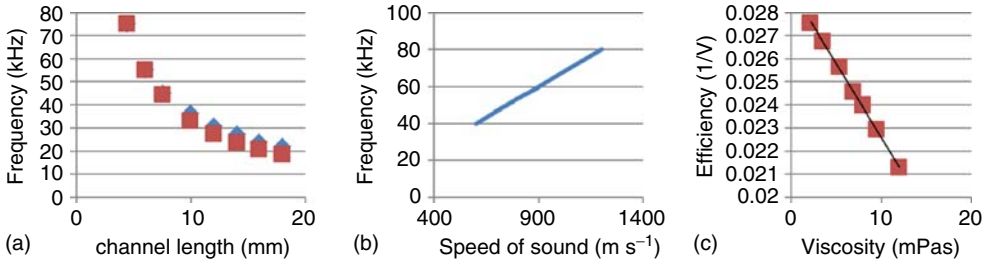


**Figure 3.21** (a) Resonance frequency versus printhead channel length; (b) frequency of the resonance versus speed of sound of the ink; and (c) efficiency ( $1/V$ ) as function of viscosity.

the Helmholtz frequency becomes:

$$F_H = \frac{1}{2\pi} \sqrt{\frac{1}{C_c} \left( \frac{1}{M_n} + \frac{1}{M_r} \right)} = \frac{1}{2\pi} \sqrt{\frac{1}{C_c} \left( \frac{M_n + M_r}{M_n M_r} \right)} \quad (3.16)$$

### 3.6.3

#### Ink Channel Behavior

In the previous section, we have seen the working principle of a piezo ink channel. In this section, we discuss the ink channel behavior of a commercial printhead with respect to the change in channel properties (channel length, speed of sound, ink viscosity).

The narrow channel of a bump-mode printhead is acoustically open on the ink reservoir side and almost closed on the nozzle side. Therefore, it behaves in a first approximation as a  $\lambda/4$  resonator. The resonant frequency of the channel is inversely proportional to the channel length, since the time taken by the waves to travel increases linearly with the length of the channel, as shown in Figure 3.21a [44].

The properties of the ink also determine the performance of the printhead. The productivity is directly related to the maximum DoD frequency at which the printhead can be operated. This frequency is linearly proportional to the speed of sound in the ink, as shown in Figure 3.21b. The amount of energy needed to eject a drop with a certain speed and volume (i.e., the efficiency) decreases linearly with the increase in the viscosity of the ink (see Figure 3.21c).

##### 3.6.3.1 Residual Oscillations

The performance of a PIJ printhead is limited by two operational issues. The first issue is the residual oscillations. After a drop has been ejected from the nozzle, the pressure waves responsible still run through the printhead channel. These oscillations are called residual oscillations. The time required to damp the residual oscillations depends on the geometry and material properties of the channel and the viscosity of the ink. The residual oscillations can be measured using the piezo self-sensing mechanism [46, 47]. The second operational issue is crosstalk. The drop properties through an ink channel are affected when its neighboring

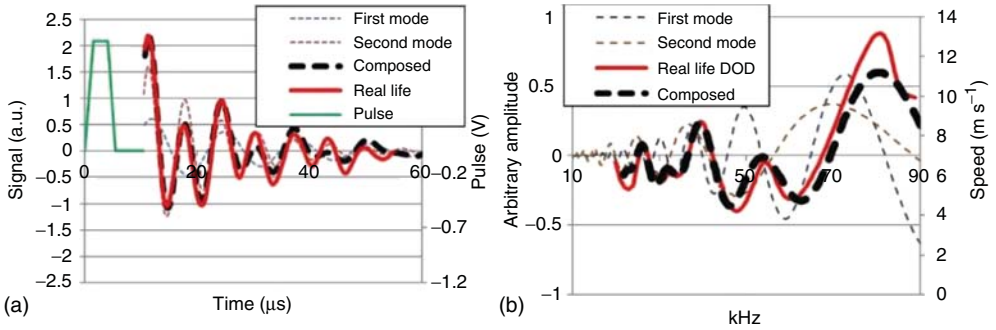


**Figure 3.22** Residual oscillations in a channel. (a) The green line represents the pulse applied to the piezo. The red solid line is the measured residual oscillation. This line is resembled by the black dashed line, which is the sum of the first (dashed blue line)

and second resonance mode (dashed red line). (b) Plotting the same data on the inversed time axis ( $1/t$ ) (black dotted line) closely resembles the measured DoD versus frequency characteristics (red line).

channels are actuated simultaneously. The drop velocity variation caused by the crosstalk is less significant than the variation caused by the residual oscillation. For details on the crosstalk, see [44, 48].

For the considered printhead, the measured residual pressure oscillation is shown (Figure 3.22a, red line). It can be seen that the residual oscillations take more than  $60\ \mu\text{s}$  to damp completely. The frequency response of this signal indicates that two dominant resonances are present at 80 and 160 kHz, respectively. Figure 3.22a also shows the individual time responses of the two resonant modes. The combined response of the two resonant modes is shown by a dashed black line in Figure 3.22. Note that the combined reconstructed response (i.e., dashed black line) is very close to the measured response (i.e., red solid line).

When a jetting pulse is applied before the residual oscillations (generated by the previous drop) are damped completely, the drop properties of the jetted drop will be different from the previous drop. Consequently, the total pressure in the channel and, thus, the droplet speed and volume depend also on the time between the two jetting pulses. This behavior of an ink channel is characterized by a DoD curve (i.e., a plot of the drop speed or volume as a function of the jetting frequency). In Figure 3.22b, we have shown the DoD curve for the considered printhead by the red solid line. In Figure 3.22b, the responses shown in Figure 3.22a are plotted against the inverted time axis  $1/t$ . Note that the combined response approximately matches with the experimentally obtained DoD curve. This simple approach allows approximate predictions of the DoD curve from a single residual oscillation measurement.

For this considered printhead, the drop speed varies from  $4$  to  $11\ \text{m s}^{-1}$  when the maximum DoD frequency is equal to 90 kHz. Even when the DoD frequency is reduced to 70 kHz, the droplet speed variation is  $4\ \text{m s}^{-1}$ . Note that this large speed

variation is the result of undamped residual oscillations when a single trapezoidal pulse is used for jetting droplets. Therefore, in order to improve the drop consistency and to increase the maximum DoD frequency, the actuation pulse should be properly tuned. In the next section, we present different approaches to design actuation pulses, which can damp the residual oscillations and improve the drop consistency.

#### 3.6.4

##### Control of Inkjet Printhead

In the previous section, we have discussed the dynamics of an ink channel. It is seen that the performance of the inkjet printhead is limited by the residual oscillations. Note that the jetting pulses are designed to provide an ink drop of a specified volume and velocity under the assumption that the ink channel is in steady state. Hence, the drop quality will not be consistent if we use this pulse for jetting before damping of the residual oscillations (caused by the previous drop). In the previous section, it is seen that a consequence of the residual oscillations in the ink channel is that the DoD curve is not flat. In this section, we present methods to damp the residual oscillations in order to flatten the DoD curve. We first discuss a simple approach to design a constrained pulse based on the basic understanding of an ink channel and, subsequently, present a systematic approach to design complex waveforms.

##### 3.6.4.1 Constrained Actuation Pulse Design

In Section 3.6.2, it is seen that, commonly, the piezo actuation consists of one positive trapezoidal pulse, which can deliver a droplet of specific properties: we call this pulse the jetting pulse. Often, parameters of this jetting pulse are chosen based on exhaustive experimental or numerical simulations studies [45, 49, 50]. As discussed earlier, this jetting pulse generates undesirable residual oscillations. Therefore, the piezo actuation should consist of an additional pulse after the jetting pulse to damp the residual oscillations. In the literature, we find two categories of actuation pulses to damp the residual oscillations, namely unipolar and bipolar actuation pulse. The unipolar pulse [46, 51] consists of the jetting pulse for the droplet and an additional trapezoidal pulse of the same polarity as the jetting pulse to damp the residual oscillations. We refer the additional pulse as the quenching pulse due to its objective to quench the residual oscillations. The bipolar pulse [52–55] consists of the jetting pulse for the ink droplet, and the residual oscillations are damped by an additional trapezoidal pulse of polarity opposite to that of the jetting pulse. From the driving electronics point of view, the unipolar pulse is beneficial as the required driving voltage range is smaller due to the same polarity of the quenching and jetting pulses. On the contrary, the bipolar actuation pulse allows damping of the residual oscillations earlier as compared to the unipolar pulse and, thus, can improve the maximum jetting frequency.



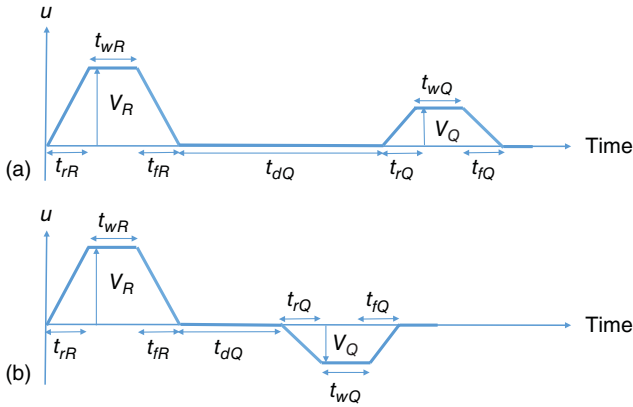


Figure 3.23 Parameterization of unipolar (a) and bipolar pulse (b).

In Figure 3.23, we have shown the parameterization of a unipolar and a bipolar pulse with a pulse parameter vector  $\theta = [t_{rR} \ t_{wR} \ t_{fR} \ V_R \ t_{dQ} \ t_{rQ} \ t_{wQ} \ t_{fQ} \ V_Q]$ . As discussed earlier, often, the pulse parameters  $\theta$  are tuned by exhaustive experiments when users do not have information about printhead acoustics. However, with a proper use of physical insight, it is possible to obtain the actuation pulses with very few experiments. The crucial information for the design of the quenching pulse is the fundamental mode frequency of the inkjet printhead.

It is possible to measure the fundamental period  $T_f$  ( $T_f = 1/F_1$ , where  $F_1$  is the frequency of the fundamental resonance mode) of an ink channel by measuring the channel pressure with piezo self-sensing [46, 47, 55,] or by observing the meniscus position displacement [53, 54]. It is also possible to measure the period of the ink channel by conducting a series of experiments where the droplet velocity is measured as a function of the dwell time of the jetting pulse. The droplet velocity will be maximum when the pulse duration of the jetting pulse ( $t_{rR} + t_{wR} + t_{fR}$ ) is approximately equal to  $T_f/2$ .

Once the fundamental period is known, computation of the time parameters of the actuation pulse can be simplified. For the ink used in document printing, the rise time and the fall time has negligible influence on the droplet properties, although very short rise/fall time may introduce satellite drops. For ink viscosity in the range of 3–15 mPa·s, we found that the rise/fall time equal to  $T_f/8$  is a fairly good choice. The timing parameters of the actuation pulses shown in Figure 3.23 can be parameterized as a function of  $T_f$  as follows:

$$t_{rR} = t_{fR} = t_{rQ} = t_{fQ} = \frac{T_f}{8} \quad (3.17)$$

$$t_{wR} = t_{wQ} = \frac{T_f}{2} - (t_r + t_f) \quad (3.18)$$

$$t_{dQ} = \frac{T_f}{2} \quad \text{for bipolar pulse,} \quad t_{dQ} = T_f \quad \text{for unipolar pulse} \quad (3.19)$$

Note that the jetting pulse amplitude  $V_R$  has to be chosen to deliver droplets of the required velocity. The amplitude of the quenching pulse  $V_Q$  depends on the damping of the ink channel. It is possible to achieve damping of the ink channel based on the measured ink channel pressure or the meniscus displacement. If the user can measure neither the channel pressure nor the meniscus displacement, then  $V_Q$  has to be tuned iteratively. The optimal choice of  $V_Q$  will lead to a flatter DoD curve, which corresponds to proper damping of the residual oscillations. Note that one can think of optimizing the actuation pulse by iteratively updating a pulse based on experimental response of the ink channel to the applied pulse. However, this may require a large number of experiments. With the method described, one can achieve fairly good actuation pulse designs with very few experiments.

#### 3.6.4.2 Complex Actuation Pulse Design: Feedforward Control Approach

In the previous section, we have discussed design of constrained actuation pulse using few experiments and physical insight. Such an approach is useful when the user does not have the knowledge about the inkjet geometry. However, if we use a model of inkjet channel, it is possible to design actuation pulses in a systematic way using a system control approach. The design of complex pulses to control the ink channel is nontrivial even when we use the model of the ink channel. In this section, we present a simple approach to design unconstrained actuation pulses using feedforward control approach.

Note that the meniscus velocity  $y(k)$  greatly determines the droplet properties [44, 54]. Let  $H(q)$  be a model that describes the ink channel dynamics from the piezo input  $u(k)$  to the output meniscus velocity  $y(k)$ , where  $k$  is the discrete time sample and  $q$  is the forward shift operator. In order to improve the drop consistency, we have to ensure that the meniscus velocity behavior is similar for every drop. If we identify a positive trapezoidal pulse that delivers a droplet of desired properties, then we can design a desired reference meniscus velocity trajectory  $y_{\text{ref}}(k)$ . See [54] for the detailed procedure to design  $y_{\text{ref}}(k)$ . By designing the input  $u(k)$ , which allows the meniscus velocity to closely follow  $y_{\text{ref}}(k)$ , we can then jet a droplet with the required properties and damp the residual oscillation in the ink channel quickly.

The optimal unconstrained input is defined as the one minimizing the tracking error  $e(k) = y_{\text{ref}}(k) - y(k)$ . In other words, the optimal input has to minimize the objective function, which is defined as the sum of squared errors:

$$\sum_{k=0}^N (e(k))^2 = \sum_{k=0}^N (y_{\text{ref}}(k) - y(k))^2 = \sum_{k=0}^N (y_{\text{ref}}(k) - H(q)u(k))^2 \quad (3.20)$$

where  $N = T/T_s$ ,  $T_s$  is the sampling time, and  $T$  is the final time.

Remark: It is possible to design the constrained pulse discussed in the previous section using the model-based approach. For this purpose, one has parameterize  $u(k)$  in the given equation using the parameterization shown in Figure 3.23. Note that the objective function will become a nonlinear

function of the actuation pulse parameter  $\theta$ . For details on nonlinear optimization problem to obtain the constrained actuation pulse, readers are referred to [54].

Our objective in this section is to compute an unconstrained pulse with a simple and computationally efficient approach. Therefore, we parameterize the actuation pulse as the pulse response of a Finite Impulse Response filter (FIR) ( $q, \beta$ ):

$$u(k, \beta) = F(q, \beta)\delta(k) \quad (3.21)$$

where  $F(q, \beta) = \beta_0 + \beta_1 q^{-1} + \dots + \beta_{n_\beta} q^{-n_\beta}$ ,  $\delta(k)$  is the unit pulse and  $\beta = (\beta_0, \dots, \beta_{n_\beta})$  is a vector containing the coefficients of the FIR filter.

When the dimension of  $\beta$  is chosen to be equal to the desired length of the actuation pulse, this parameterization allows generation of actuation pulses with arbitrary shape. For an arbitrary vector  $\beta$ , the response of the ink channel  $H(q)$  to the input  $u(k, \beta)$  is given by:

$$y(k, \beta) = H(q)F(q, \beta)\delta(k) = F(q, \beta)H(q)\delta(k) \quad (3.22)$$

$$= F(q, \beta)h(k) \quad (3.23)$$

where  $h(k)$  is the pulse response of the known ink channel dynamics  $H(q)$ .

The optimal control  $u(k, \beta_{\text{opt}})$  is then that which minimizes the difference between the desired meniscus velocity trajectory  $y_{\text{ref}}(k)$  and the achieved meniscus velocity  $y(k, \beta)$ . Therefore, the optimal parameter vector  $\beta_{\text{opt}}$  is the solution to the following optimization problem:

$$\arg \min_{\beta} \sum_{k=0}^N (y_{\text{ref}}(k) - F(q, \beta)h(k))^2 \quad (3.24)$$

Note that the aforementioned optimization problem leading to the unconstrained actuation pulse is a least-squares problem. It is recommended to solve this optimization problem using truncated Singular Value Decomposition (SVD) when the problem (3.24) is numerically ill-conditioned [56].

Remarks: In [47], it is shown that the linear model from the piezo input to the meniscus velocity will be different when an inkjet channel is jetting at different DoD frequencies. A method is proposed to design a robust constrained actuation pulse, which damps the residual oscillations for a set of linear models of the ink channel rather than only for the nominal model. In [57], a method is proposed for designing an unconstrained actuation pulse when the ink channel model is subjected to parametric uncertainty due to jetting at different DoD frequencies. Note that the drive electronics of inkjet printheads may not always allow the use of complex pulses. In this scenario, the user can perform linear fitting to the optimal unconstrained pulse in order to obtain a suboptimal implementable pulse.

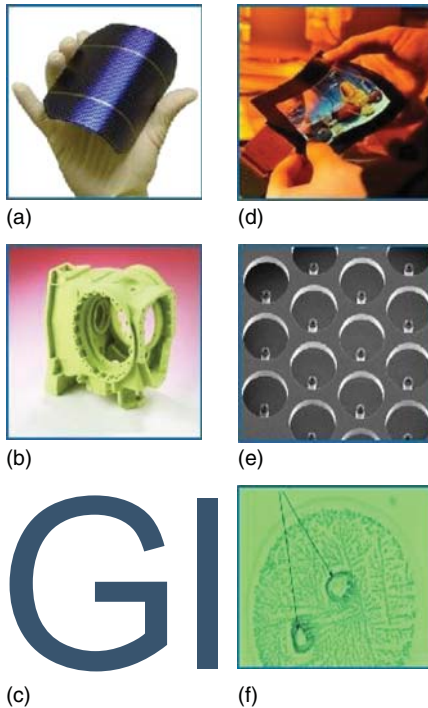


**Figure 3.24** Overview of application of inkjet technology for micro-manufacturing. (a) Electronics – flexible circuits, RFID, PCBs, solar cells; (b) displays – flat panel displays, PLED, LCDs, flexible displays; (c) mechanical – rapid prototyping, metal coating, 3D

models; (d) optics – micro optical lenses, optical waveguides; (e) chemical – materials development, substrate development, adhesives; and (f) life sciences – DNA printing, artificial skin, food science, patient specific drugs, and so on.

### 3.6.5

#### Industrial Applications

A fundamental strength of the PIJ technology is its ability to deposit a wide variety of materials on various substrates in well-defined patterns. Recently, many other applications than printing onto paper emerged [58]. In the display market, inkjet technology is used to manufacture Flat Panel Displays (FPDs), Liquid Crystal Displays (LCDs), color filters as part of LCDs, Polymer Light-Emitting Diodes (PLEDs), flexible displays and sensor tapes, and optical fibers. The accompanying performance criteria are among the major driving forces behind much research and development efforts. Within the chemical market, the inkjet technology is mainly used as a tool for research purposes. The unique capacity of the technology for dispensing small doses of liquids makes it very useful for this market. Applications include material and substrate development as well as coating purposes. In the electronic market, inkjet printheads are used to create functional electrical tracks using conductive fluids on both rigid and flexible substrates. One of the

first applications of inkjet technology within this field was that for the production of Printed Circuit Boards (PCBs). Other applications include the fabrication of electric components such as transistors and circuits such as Radio Frequency Identification (RFID) tags, wearable electronics, solar cells fuel cells, and batteries. Challenges for the inkjet technology within this field include the spreading of the ink and the required guarantees of continuity of the jetted lines and interconnections. Achieving a high productivity requires novel printing concepts.

Three-dimensional mechanical printing exploits inkjet technology as a tool for rapid prototyping, small volume production, production of small sensors, and components for data storage. The jetting of multimaterial structure is another unique feature, and many applications in manufacturing, engineering, science, and education are possible. Jetting of UV-curable optical polymers is a key technology for the cost-effective production of microlenses. These tiny lenses are used in devices ranging from fiber optic collimators to medical systems. The ability of inkjet technology to precisely jet spheres in variable, but consistent, drop sizes provides opportunities for the cost reduction of the existing optical components and innovative new designs.

The life science market is rapidly expanding with new requirements for precise dispensing of DNA and protein substances. The high costs of these fluids make inkjet technology with its precision placement and tight flow control an excellent dispensing tool, but printing without damaging the material is quite a challenge. Applications include the use for DNA research, various medical purposes such as dosing of drugs with, for example, inhalers, biosensors, and food science. A quite futuristic application is the use of inkjet printing for the fabrication of living tissue. An overview of piezo inkjet applications is shown in Figure 3.24.

All names of companies and products that appear in this chapter are trademarks or registered trademarks of the respective companies.

## References

1. Morita, N. (2012) in *Inkjet-Based Micro-manufacturing* (eds J. Korvink, P. Smith, and D.-Y. Shin), Wiley-VCH Verlag GmbH, pp. 41–56.
2. Schlözer, R., Hamilton, J., and Cox, B. (2011) The High-speed Continuous-feed Color Inkjet Opportunity, Global Insights from Leading Customers, Infotrends.
3. Allen, R.R., Meyer, J.D., and Knight, W.R. (1985) Thermodynamics and hydrodynamics of thermal ink jets. *Hewlett-Packard J.*, **36** (5), 21–27.
4. Asai, A. (1991) Bubble dynamics in boiling under high heat flux pulse heating. *Trans. ASME, J. Heat Transfer*, **113**, 973–979.
5. Skripov, V.P. (1974) *Metastable Liquids*, John Wiley & Sons, Inc., p. 101.
6. Olson, H.F. (1957) *Acoustical Engineering*, D. Van Nostrand Company, Inc..
7. Bankoff, S.G. (1966) Diffusion-controlled bubble growth. *Adv. Chem. Eng.*, **6**, 1–60.
8. Rayleigh, J.W. (1917) On the pressure developed in a liquid during the collapse of a spherical cavity. *Philos. Mag.*, **6**, 94–98.
9. Iida, Y., Okuyama, K., and Sakurai, K. (1993) Peculiar bubble generation on a film heater submerged in ethyl alcohol and imposed a high heating rate over

- 10<sup>7</sup> K/s. *Int. J. Heat Mass Transfer*, **36** (10), 2699–2701.
10. Iida, Y., Okuyama, K., and Sakurai, K. (1994) Boiling nucleation on a very small film heater subjected to extremely rapid heating. *Int. J. Heat Mass Transfer*, **37** (17), 2771–2780.
  11. Okuyama, K., Tsukahara, S., Morita, N., and Iida, Y. (2004) Transient behavior of boiling bubbles generated on the small heater of a thermal ink jet print-head. *Exp. Therm Fluid Sci.*, **28**, 825–834.
  12. Okuyama, K., Nakamura, J., Mori, S., and Iida, Y. (2006) *Pre-Heating Effect on the Expansion of Boiling Bubble on a Small Film Heater High Pulse Powered*, International Heat Transfer Conference, vol. **13**, Begel House Inc., p. 55.
  13. Silverbrook, K. (2007) Memjet, a 1600 dpi pagewidth inkjet technology which features cost competitiveness with scanning inkjet in home, office, and wide format applications. 30th Global Ink Jet Printing Conference, Prague, Czech, March 21, 2007.
  14. Okuyama, K., Ichikawa, M., Ichiishi, K., and Mori, S. (2008) Ejection of water droplets from a small nozzle by rapid boiling under two-stage high-pulse heating. 19th International Symposium on Transport Phenomena.
  15. Otuka, N., Hirabayashi, H., Yano, K., and Takahashi, K. (1996) Temperature control of inkjet recording head using heat energy. US Patent 5,559,535.
  16. Meyer, J. (1986) Bubble growth and nucleation properties in thermal inkjet printing technology. SID 86 Digest, pp. 101–104.
  17. Chang, L.S., Moore, J.O., and Eldridge, J.M. (1993) Overcoat failure mechanisms in thermal ink jet devices. The 9th International Congress on Advances in Non-Impact Printing Technologies, Japan Hardcopy '93, pp. 241–244.
  18. Mitani, M. (2003) A new thin film heater for thermal ink jet print heads. *J. Imaging Sci. Technol.*, **47** (3), 243–249.
  19. Nakajima, K., Takenouchi, M., Inui, T., Takizawa, Y., Miyagawa, M., Yaegashi, H., Shirota, K., Ohkuma, N., and Asai, A. (2000) Recording method and apparatus for controlling ejection bubble formation. US Patent 6,155,673.
  20. Morita, N., Hiratsuka, M., Hamazaki, T., Usami, H., Kondoh, Y., Fukunaga, H., Ikeda, H., Inoue, N., and Yamada, S. (2008) Pulse and temperature control of thermal ink jet print-heads without a heater passivation layer. *J. Imaging Sci. Technol.*, **52** (2), 20503-1–20503-5.
  21. Chang, L.S. (1989) Effects of kogation on the operation and lifetime of bubble jet thin-film devices. *Electrophotography*, **28** (1), 2–9.
  22. Kobayashi, M., Onishi, K., Hiratsuka, M., and Morita, N. (1998) Removal of kogation on TIJ heater. Pan-Pacific Imaging Conference/Japan Hardcopy, pp. 326–329.
  23. Morita, N., Onishi, K., Hiratsuka, M., Kobayashi, M., and Tamura, H. (1998) Long-stable jetting on thermal ink jet printers. NIP & Digital Fabrication Conference, pp. 19–22.
  24. Okuyama, K., Morita, N., Maeda, A., and Iida, Y. (2001) Removal of residue on small heaters used in TIJ printers by rapid boiling. *Therm. Sci. Eng.*, **9** (6), 1–7.
  25. Torpey, P. (1990) Evaporation of a two-component ink from the nozzles of a thermal inkjet print-head. Proceedings of NIP6, pp. 453–458.
  26. Hirakata, S., Okuda, M., Nakamura, H., Ishiyama, T., Seto, S., and Morita, N. (2008) Improvement of jetting reliability against ink viscosity increase by installation of an ink circulation path. Pan-Pacific Imaging Conference, pp. 200–203.
  27. Hirakata, S., Ishiyama, T., and Morita, N. (2014) Printing stabilization resulting from the ink circulation path installed inside the print head and the jetting phenomenon during nozzle drying. *J. Imaging Sci. Technol.*, **58** (5), 050503-1–050503-7.
  28. Yamada, T. and Sakai, K. (2012) Observation of collision and oscillation of micro-droplets with extremely large shear deformation. *Phys. Fluids*, **24** (2), 022103-1–022103-9.
  29. Strutt (Lord Rayleigh), J.W. (1879) On the capillary phenomena of jets. *Proc. R. Soc. London*, **29**, 71–79.

30. Dong, H., Carr, W.W., and Morris, J.F. (2006) An experimental study of drop-on-demand drop formation. *Phys. Fluids*, **18**, 072102-1–072102-16.
31. Morita, N., Hirakata, S., and Hamazaki, T. (2010) Study on vibration behavior of jetted ink droplets and nozzle clogging. *J. Imaging Soc. Jpn.*, **49** (1), 14–19.
32. Hsiao, W.-K., Hoath, S., Martin, G., and Hutchings, I. (2012) Aerodynamic effects in ink-jet printing on a moving web. NIP & Digital Fabrication Conference, pp. 412–415.
33. Morita, N., Ono, Y., Isozaki, J., and Hirakata, S. (2015) Inkjet for Industrial Continuous Web Printer and Study on Speed Enhancement. *J. Jpn. Soc. Colour Mater.* **88** (9), 300–305.
34. Doi, T. and Hashimoto, K. (2008) Novel aqueous ink jet technology realizing high image quality and high print speed. *J. Imaging Sci. Technol.*, **52** (6), 1–6.
35. Sakamoto, A., Numata, M., Ogasawara, Y., Hatanaka, M., Motosugi, Y., and Morita, N. (2015) Laser Exposure of Dry Aqueous Ink for Continuous-Feed High-Speed Inkjet Printing. *J. Imaging Sci. Technol.*, **59** (2) 020501-1-020501-7.
36. Rayleigh, J.W. (1878) On the instability of jets. *Proc. London Math. Soc.*, **10**, 4–13.
37. Weber, C. (1931) Zum zerfall eines flüssigkeitsstrahles. *Z. Angew. Math. Mech.*, **11**, 136–159.
38. Sweet, R. (1963) Fluid droplet recorder. US Patent 3,596,275.
39. Crowley, J.M. (1983) Electrohydrodynamic droplet generators. *J. Electrostat.*, **14**, 121–134.
40. Drake, D., Hawkins, W., Markham, R., and LaDonna, R. (1986) Print-head for an ink jet printer. US Patent 4,638,328.
41. Vaeth, K.M. (2007) Continuous inkjet drop generators fabricated from plastic substrates. *J. Microelectromech. Syst.*, **16** (5), 1080–1086.
42. Furlani, E.P., Delametter, C.N., Chwalek, J.M., and Trauernicht, D. (2001) Surface tension induced instability of viscous liquid jets. Technical Proceedings of the Fourth International Conference on Modeling and Simulation of Microsystems, pp. 186–189.
43. Carslaw, H.S. and Jaeger, J.C. (1959) *Conduction of Heat in Solids*, 2nd edn, Oxford University Press, London, p. 62.
44. Wijshoff, H. (2010) The dynamics of the piezo inkjet printhead operation. *Phys. Rep.*, **491**, 77–177.
45. Bogy, D. and Talke, F. (1984) Experimental and theoretical study of wave propagation phenomena in drop-on-demand ink jet devices. *IBM J. Res. Dev.*, **28** (3), 314–321.
46. Kwon, K. and Kim, W. (2007) A waveform design method for high-speed inkjet printing based on self-sensing measurement. *Sens. Actuators, A*, **140** (1), 75–83.
47. Khalate, A., Bombois, X., Scorletti, G., Babuška, R., Koekebakker, S., and de Zeeuw, W. (2012) A waveform design method for a piezo inkjet printhead based on robust feedforward control. *IEEE J. Microelectromech. Syst.*, **21** (6), 1365–1374.
48. Khalate, A., Bombois, X., Ye, S., Babuška, R., and Koekebakker, S. (2012) Minimization of cross-talk in a piezo inkjet printhead based on system identification and feedforward control. *J. Micromech. Microeng.*, **22** (11), 115035.
49. Jo, B., Lee, A., Ahn, K., and Lee, S. (2009) Evaluation of jet performance in drop-on-demand (dod) inkjet printing. *Korean J. Chem. Eng.*, **26** (2), 339–348.
50. Gan, H., Shan, X., Eriksson, T., Lok, B., and Lam, Y. (2009) Reduction of droplet volume by controlling actuating waveforms in inkjet printing for micro-pattern formation. *J. Micromech. Microeng.*, **19** (5), 055010.
51. MicroFab Technologies Inc. (1999) Drive Waveform Effects on Ink-Jet Device Performance. Technical Report 99-03. MicroFab Technologies Inc.
52. Chung, J., Ko, S., Grigoropoulos, C., Bieri, N., Dockendorf, C., and Poulidakos, D. (2005) Damage-free low temperature pulsed laser printing of gold nanoinks on polymers. *J. Heat Transfer*, **127** (7), 724–732.
53. Kwon, K. (2009) Waveform design methods for piezo inkjet dispensers based on measured meniscus motion. *J. Microelectromech. Syst.*, **18** (5), 1118–1125.



54. Khalate, A., Bombois, X., Babuška, R., Wijshoff, H., and Waarsing, R. (2011) Performance improvement of a drop-on-demand inkjet printhead using an optimization-based feedforward control method. *Control Eng. Pract.*, **19** (8), 771–781.
55. Groot Wassink, M. (2007) Inkjet printhead performance enhancement by feedforward input design based on two-port modeling. PhD thesis. Delft University of Technology, Delft.
56. Golub, G. and van Loan, C. (1989) *Matrix Computations*, 2nd edn, John Hopkins University Press, Baltimore, MD.
57. Khalate, A., Bayon, B., Bombois, X., Scorletti, G., and Babuška, R. (2011) Drop-on-demand inkjet printhead performance improvement using robust feedforward control. IEEE Conference on Decision and Control and European Control Conference, Orlando, FL, pp. 4183–4188.
58. Korvink, J., Smith, P., Shin, D., Brand, O., Fedder, G., Hierold, C., and Tabata, O. (eds) (2012) *Inkjet-Based Micromanufacturing*, vol. **9**, Wiley-VCH Verlag GmbH.



## 4 Drop Formation in Inkjet Printing

*Theo Driessen and Roger Jeurissen*

### 4.1

#### Introduction

Droplets are deposited in a controlled way by inkjet printing. Research and development is being carried out to increase the speed and accuracy of this droplet deposition. For printing accuracy, every droplet should travel at the right velocity. The size of each droplet is controlled with a similar precision. In this chapter, we elaborate on the physics that determines the size and speed of the flying droplets generated in inkjet printing.

Inkjet printing is applied in a broad range of applications. Consequently, there are many different operating modes for inkjet printing. The two main methods are Drop-on-Demand (DOD) inkjet printing and Continuous Jet (CJ) inkjet printing. The high precision involved in inkjet printing demands that the jets are axisymmetric. Therefore, this chapter aims at understanding the drop formation from axisymmetric fluid jets.

#### 4.1.1

##### Continuous Inkjet Printing

The simplest way of generating droplets of controlled size and velocity is with continuous inkjet printing, as shown in Figure 4.1. A pressure pump causes a continuous jet of ink from the nozzle. The eventual droplet size is controlled with a piezoelectric actuator. After leaving the nozzle, the droplets are selected to be printed or to be recycled. The unnecessary droplets are charged by an electrode close to the nozzle and directed toward a recycling gutter by an electric field. Continuous inkjet printing is mainly used for coding in the packaging industry, due to its high speed and reliability.

At low jet velocity, it is easy to make such a strong velocity perturbation that the jet breaks up into droplets purely by the velocity fluctuation at the nozzle. When the jet velocity is increased, the relative fluctuation caused by the piezo decreases, and the jet breakup occurs not at the nozzle but further downstream. When there is a stable cylindrical fluid jet, the Rayleigh – Plateau instability starts to play a role

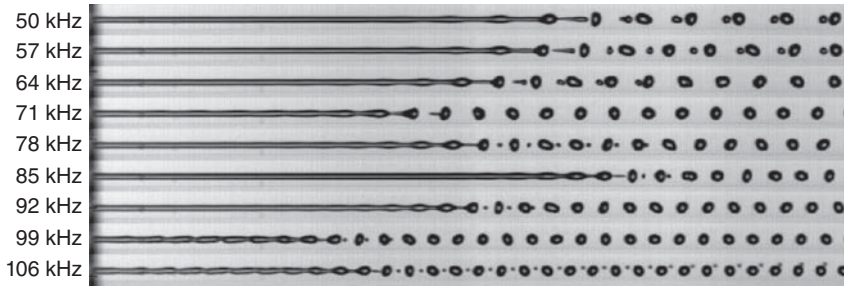


**Figure 4.1** Here, we show the same continuous ink jet process, with nine different perturbation frequencies. The nozzle diameter is  $30\ \mu\text{m}$ , the jet is water, emitted at  $11.8\ \text{m s}^{-1}$ . The actuation voltage was the same for each frequency. In continuous inkjet, the liquid jet is perturbed by a sinusoidal velocity disturbance that

grows exponentially with distance from the nozzle. The jet breaks up into a stream of larger droplets, the main droplets. Satellite droplets can be formed, but the satellite droplets often merge soon with a neighboring main droplet. Image courtesy of Koen Winkels, ASML.

in the jet breakup. Rayleigh–Plateau unstable modes can be used to control the droplet stream. On the other hand, Rayleigh–Plateau unstable modes induced by noise, such as system vibrations, may cause the droplet stream to become unstable.

#### 4.1.2

##### Drop-on-Demand Inkjet Printing

Since its invention in the second half of the twentieth century, DOD inkjet printing has been applied mainly for graphics printing. Recently, it has also been used in additive manufacturing, textile printing, home decorations, and many more applications. This broad variation of applications demands a broad range of inks and printheads. The droplet can vary between  $200\ \text{fl}$  for high-detail functional printing and  $200\ \text{nl}$  for high-speed decorative patterning applications. The drop size and velocity can be varied by using different nozzle sizes but also by using different driving strategies.

In Figure 4.2, the drop formation cycles for two different actuation amplitudes are shown. At a low amplitude, the ligament pinches off at the nozzle. The tail droplet that forms due to the capillary contraction of the ligament has sufficient velocity to catch up with the slow head droplet. When the amplitude is high, the head droplet has such a high velocity that the tail droplet cannot reach the head droplet before the tail breaks up into the Rayleigh–Plateau instability. For some applications, such as the printing of random patterns on ceramic floor tiles, the presence of these satellite droplets is not an issue. For functional printing, where, for example, conductive wires are printed, the satellite droplets are unacceptable. Printing accuracy and productivity increase with drop velocity, but the generation of satellite droplets also increases with drop velocity. It is a challenge in DOD inkjet

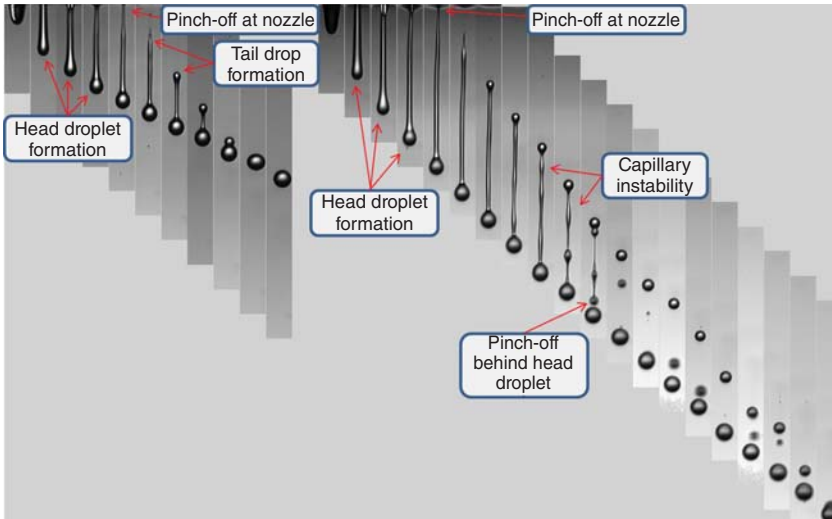


**Figure 4.2** Here, we show two sequences of photographs taken from a drop-on-demand drop formation cycle. The droplets are recorded by single flash stroboscopy. In the left sequence, the actuation signal has a low amplitude, resulting in a slow droplet. The tail remains stable until the tail droplet is merged with the head droplet due to capillary contraction of the ligament. In the

sequence on the right, the actuation signal amplitude is 25% higher. The droplet is so fast that the tail droplet cannot merge with the head droplet before the tail has broken up. Eventually, the tail droplet merges with the head droplet. This figure demonstrates the challenge of producing satellite-free droplets at a high velocity. Image courtesy of Marc van den Berg, Océ Technologies B.V.

printing research to find nozzle geometries and actuation signals that result in fast drops without satellite droplets.

## 4.2

### Drop Formation in Continuous Inkjet Printing

In continuous inkjet printing, droplets are generated at a fixed frequency. The frequency at which the droplets are generated is determined by the perturbation signal delivered by a piezoelectric actuator. To allow high-frequency droplet generation, a high-speed continuous jet is needed. Therefore, the jet velocity in continuous inkjet printing is generally very high: droplets travel with velocities of up to  $50 \text{ m s}^{-1}$ . At these high fluid velocities, the velocity fluctuation amplitude is much lower than the fluid velocity. This implies that the breakup of the jet will not occur at the nozzle exit but much further away from the nozzle. The fluctuations that eventually lead to breakup use the capillary instability of a cylindrical fluid jet, the Rayleigh–Plateau instability. In this section, we analyze the Rayleigh–Plateau instability and show a method by which one can use the Rayleigh–Plateau instability for control of the droplet size and spacing. The droplet velocity is not

necessarily the same velocity as the average velocity over the cross-sectional area of the nozzle. Therefore, we also treat the capillary and inertial effects that determine the final droplet velocity at the end of this section.

#### 4.2.1

##### Rayleigh–Plateau Instability

A perturbed circular cylindrical liquid jet will break up into droplets by the Rayleigh–Plateau instability. The initial perturbation can be random noise such as thermal fluctuations, but it can also be a more coherent perturbation originating from an actuator. The only requirement for a perturbation to be unstable is that the perturbation should have a wavelength that is longer than the circumference of the jet. The surface area and, thus, the surface energy of the fluid jet decrease when the amplitude of an unstable perturbation increases. This surface energy is converted into kinetic energy, and eventually, it is dissipated.

The growth rate of the Rayleigh–Plateau instability depends on the ratio of its wavelength over the jet circumference. If the perturbation wavelength is equal to the jet circumference, the growth rate of the perturbation is zero since the surface area of the jet does not change by an increase in the perturbation amplitude. At the low-frequency end of the spectrum of growing modes, where the wavelength is much greater than the circumference, the growth rate also tends to zero. Between these two extremes are different growth rates for different wave numbers. These growth rates are quantified by the dispersion relation of the Rayleigh–Plateau instability, which is the growth rate as a function of the wavelength. Perturbations with wavelengths smaller than the circumference of the jet are traveling capillary waves. The behavior of these capillary waves is also determined in the same analysis.

The evolution of axisymmetric liquid jets can be derived from the equations of motion. A good explanation can be found in Ref. [1]. For most applications, the solution of the Rayleigh–Plateau instability in the slender-jet approximation suffices. In this axisymmetric approximation of the Navier–Stokes equations, the radial momentum is neglected, and it is assumed that the axial velocity is constant over a cross section of the jet.

In terms of the partial differential operators with respect to time ( $\partial_t$ ) and axial distance ( $\partial_x$ ), respectively,

$$\partial_t \pi R^2 + \partial_x \pi R^2 u = 0 \quad (4.1)$$

$$\partial_t \pi R^2 u + \partial_x \pi R^2 u^2 = \partial_x (\tau_\mu + \tau_\sigma) \quad (4.2)$$

where  $R = R(x, t)$  and  $u = u(x, t)$  are single-valued functions of the axial coordinate and time that describe the jet radius and the axial fluid velocity. The terms  $\tau_\mu$  and  $\tau_\sigma$  are the viscous tension and capillary tension, respectively. In the slender-jet approximation, the viscous tension originates from the extensional viscosity ( $3\mu$ ) as

$$\tau_\mu = 3\mu\pi R^2 \partial_x u \quad (4.3)$$

The capillary tension is the sum of the Laplace pressure integrated over the cross section of jet and the axial component of the force due to surface tension directly integrated over the circumference of the jet. The Laplace pressure is proportional to the mean curvature of the interface

$$P_{\text{Lap}} = \sigma \left( \frac{1}{R(1 + (\partial_x R)^2)^{1/2}} - \frac{\partial_{xx} R}{(1 + (\partial_x R)^2)^{3/2}} \right) \quad (4.4)$$

We add the direct effect of surface tension to obtain the capillary tension

$$\tau_\sigma = \frac{2\pi R\sigma}{(1 + (\partial_x R)^2)^{1/2}} - \pi R^2 P_{\text{Lap}} \quad (4.5)$$

We have now obtained a complete set of governing equations in the slender-jet approximation. We will use this set of equations extensively. The numerical simulation results in this chapter were obtained through a simulation based on these equations [2]. Our first use is in the stability analysis of a perturbed cylindrical liquid jet.

The stability of a cylindrical liquid jet is determined by a linear stability analysis. The governing equations are linearized with respect to the perturbation amplitude, and a complete set of eigenmodes of this linear system of equations is derived. While the stability analysis can be performed exactly, we use the slender-jet approximation since it is sufficiently accurate for most engineering applications and the result is simpler. The corresponding eigenvalues are derived along with the eigenmodes. Since any perturbation can be decomposed into a linear combination of eigenmodes, the eigenmodes, along with the corresponding eigenvalues, give a complete description of the small-amplitude behavior of perturbations of a cylindrical jet.

In the eigenvalue decomposition, we make an ansatz for the perturbation in the radius and the velocity for each individual mode. We try separation of variables, where the perturbation is the product of a part that is constant in space and a part that is constant in time.

$$R(x, t) = R_0 + R_a \exp i(\omega t + kx) \quad (4.6)$$

$$u(x, t) = u_a \exp i(\omega t + kx) \quad (4.7)$$

Here,  $R_0$  is the radius of the jet,  $R_a$  and  $u_a$  are the perturbation amplitudes on the radius and on the velocity, respectively, at  $t = 0$ ,  $k = 2\pi/\lambda$  is the perturbation wave number, and  $i\omega$  is the growth rate of the perturbation. The eigenvalues are  $\omega$ , and the relation between  $\omega$  and  $k$  is called the *dispersion relation* because it also describes the propagation of capillary waves along the jet. In order to obtain a physically relevant solution, we impose the condition that the solution is real. Since the equations are linear, two solutions can be added to obtain another solution. By adding two solutions that are complex conjugates, we necessarily obtain a real-valued solution. When we substitute the ansatz into the mass conservation

law (Eq. 4.1), and neglect the higher order terms in the perturbation amplitude, we obtain a relation between the amplitudes.

$$u_a = \frac{2(i\omega_{\pm})}{ikR_0} R_a \quad (4.8)$$

Since  $i\omega_{\pm}$  is real for growing or decaying modes, the velocity perturbation and the radius perturbation are  $90^\circ$  out of phase.

The dispersion relation is obtained by substituting the ansatz for the radius and the velocity, Eqs. (4.6) and (4.7), into the slender-jet approximation. After the substitution, the system of two equations and two unknowns is solved analytically [3–5].

$$i\omega_{\pm} = \pm \frac{1}{t_{\text{cap}}} \sqrt{\frac{1}{2} \left( (kR_0)^2 - (kR_0)^4 \right) + \frac{9}{4} (kR_0)^4 Oh^2 - \frac{3}{2} (kR_0)^2 Oh} \quad (4.9)$$

$$Oh = \frac{\mu}{\sqrt{\rho R_0} \sigma} \quad (4.10)$$

is the Ohnesorge number, which is the ratio of viscosity to surface tension, and

$$t_{\text{cap}} = \sqrt{\frac{\rho R_0^3}{\sigma}} \quad (4.11)$$

is the capillary timescale. The dispersion relation for the Rayleigh–Plateau instability gives the growth rate of the perturbation as a function of the perturbation wave number. The viscous dispersion relation for the Rayleigh–Plateau instability tells us that the wave numbers  $0 < k < 1/R_0$  have a positive growth rate and that there is one mode with the highest growth rate. As viscosity increases, the growth rates decreases. Furthermore, the wave number of the fastest growing mode decreases with increasing Ohnesorge number. An infinite liquid cylinder with a random radial or velocity perturbation will break up due to perturbations with a wavelength close to the fastest growing mode. However, any growing mode can be imposed with such a large initial amplitude that it dominates over the background noise.

Thus far, we have only considered the breakup of an infinitely long liquid cylinder. In the case of continuous inkjet, a perturbation that is periodic in time is imposed at the nozzle, and the amplitude increases exponentially in space, so that the wave number has a nonzero imaginary part [6]. The derivation is just as valid in this case, although the assumption of small perturbations is no longer valid close to the breakup length and beyond. Usually, the Weber number is large so that the imaginary part of the wave number is small with respect to the real part, and it is neglected.

The dispersion relation has a positive and a negative root for  $kR_0 < 1$ . This means that both a growing mode and a decreasing mode are possible. The velocity perturbation of the decreasing mode is directed toward the thinnest point of the jet, while the velocity perturbation of the growing mode is directed toward the thickest point. At the thinnest point of the jet, the axial velocity is zero for both

the growing and decaying modes. The relation between velocity and radial perturbations plays a key role in understanding what happens when we impose a specific perturbation. For example, a jet with only a sinusoidal velocity perturbation, and no perturbation in the radius, is a superposition of the growing and decreasing modes, where the radial perturbations cancel each other [7]. The result is that, initially, the perturbation of the radius appears to grow at a constant rate. When the decaying mode becomes negligibly small, the growth becomes exponential. Forgetting the decaying mode has left many people puzzled and led many others to believe that they discovered new physics, while it was in the standard Rayleigh–Plateau instability analysis all along [7].

#### 4.2.2

##### Satellite Formation

When the radius perturbation becomes of the order of the jet radius, nonlinear interactions cause the formation of satellite droplets. Satellite droplets are formed between the main droplets, which are the local maxima of the initial sinusoidal perturbations. The satellite droplets are usually smaller than the main drops, but for very long wavelengths, the volume contained in the satellite droplets may be larger than the main drop volume [8]. The nonlinear interactions that cause the formation of the satellite droplets become relevant when the perturbation has grown to the order of the jet radius. In Figure 4.3, the breakup of a liquid jet with a Rayleigh–Plateau instability is shown, including the time-dependent spectrum of the perturbation. Just before the pinch-off, the amplitude of the first harmonic of the linear growing mode becomes visible. In a practical continuous jet, the behavior of the satellite drop can be controlled by adding higher harmonics to the perturbation signal or by drastically increasing the perturbation amplitude at the nozzle.

#### 4.2.3

##### Final Droplet Velocity

The velocity of the droplets is not necessarily the same as the average velocity of the ink that leaves the nozzle. While capillary tension is slowing the droplets down, the imbalance between the advection of mass and advection of momentum may cause the droplet velocity to be higher than the average jet velocity. For printing accuracy, the droplet velocity is more important than the nozzle velocity.

##### 4.2.3.1 Capillary Deceleration

Capillary tension pulls the jet toward the nozzle; hence, it decreases the droplet velocity. The capillary tension is constant along a circular cylindrical fluid jet. From Eqs. (4.4) and (4.5),  $\tau_\sigma = \pi\sigma R_{\text{jet}}$ . Imagine a cylindrical jet connected to the nozzle and ending somewhere after the nozzle. At the end of the jet, the capillary tension changes from nonzero in the jet to zero outside. This difference in capillary tension causes the fluid jet to contract toward the nozzle. This contraction comprises

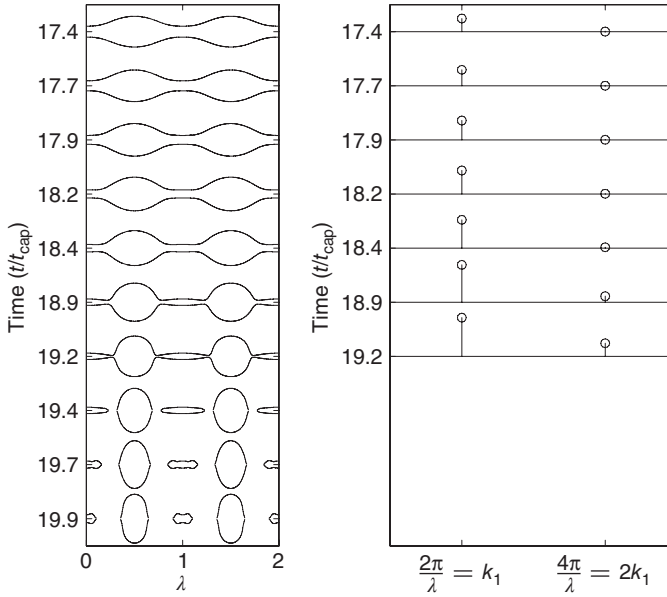


**Figure 4.3** The evolution of the Rayleigh–Plateau instability on an infinite liquid cylinder. In the left-hand graph, we show the time evolution of the jet radius in space. In the right-hand graph, the corresponding spectrum is shown. Just before

the amplitude of the base perturbation  $k_1$  would become equal to the jet radius, nonlinear interactions cause a higher harmonic to grow to a significant amplitude. This higher harmonic causes the formation of the satellite droplets.

gathering fluid at the jet ending with a negative velocity relative to the rest of the infinite fluid jet. When droplets of the same size form at a fixed frequency, such as in the case of continuous inkjet printing, each droplet undergoes the same amount of deceleration. In 1966, Schneider *et al.* derived the capillary deceleration of the fluid during droplet formation [9] by balancing the mass and momentum flux before and after jet breakup. When a fluid jet breaks up into droplets, the momentum flux of the jet is equal to the momentum flux of the resulting droplet stream:

$$\left( \rho \pi (R_{\text{jet}})^2 u_{\text{jet}} \right) u_{\text{jet}} - \pi \sigma R_{\text{jet}} = \left( \rho \pi (R_{\text{jet}})^2 u_{\text{jet}} \right) u_{\text{drop}} \quad (4.12)$$

where  $\rho \pi (R_{\text{jet}})^2 u_{\text{jet}}$  is the mass flux, which is conserved. This equation can be rewritten to find the value of  $u_{\text{drop}}$  from

$$u_{\text{drop}} = u_{\text{jet}} \left( 1 - \frac{1}{We} \right) \quad (4.13)$$

where

$$We = \frac{\rho R_{\text{jet}} u_{\text{jet}}^2}{\sigma} \quad (4.14)$$



is the Weber number of the jet. The Weber number is the ratio of the inertial terms and capillary terms. At increasing Weber number, the drop velocity converges to the jet velocity. The capillary deceleration is independent of the droplet size and, thus, of the driving frequency.

#### 4.2.3.2 Acceleration due to Advection

The droplet velocity is greater than what it would be if the ink were ejected at a constant flow rate and with velocity that is constant across the nozzle. This is due to the variation of the ejection velocity over space and time. The variation of the velocity increases the advection of momentum from the nozzle to the liquid jet, because the momentum flux is proportional to the square of the velocity. Often, the ink flows through the nozzle with a Poiseuille profile, so that there is a variation of the velocity across the nozzle. In continuous inkjet, the flow rate is perturbed with a periodic fluctuation to induce breakup, so that there is a variation of the velocity in time. We will calculate the effect of these velocity variations on the droplet velocity using separation of variables. First, we show the effect of a nonuniform velocity over the cross-sectional area of the nozzle, and then, we show the effect of a nonuniform velocity over time.

Here, we make a comparison of the average velocity over the cross-sectional area before and after the relaxation of the Poiseuille profile into a uniform flow profile. This comparison is performed by means of the mass and momentum flux through the nozzle. The velocity of the fluid can be found by dividing the momentum flux with the mass flux. The mass flux and momentum flux in the nozzle plane are given by the following integrals:

$$\rho \int_0^{2\pi} \int_0^{R_{\text{nozz}}} u_{\text{max}} \left( 1 - \left( \frac{r}{R_{\text{nozz}}} \right)^2 \right) r dr d\theta = \frac{1}{2} \rho u_{\text{max}} \pi R_{\text{nozz}}^2 \quad (4.15)$$

$$\rho \int_0^{2\pi} \int_0^{R_{\text{nozz}}} u_{\text{max}}^2 \left( 1 - \left( \frac{r}{R_{\text{nozz}}} \right)^2 \right)^2 r dr d\theta = \frac{1}{3} \rho u_{\text{max}}^2 \pi R_{\text{nozz}}^2 \quad (4.16)$$

The average velocity of the jet is obtained by dividing the momentum flux by the mass flux, giving  $u_{\text{jet}} = (2/3) u_{\text{max}}$ . When we take the spatial average of the velocity in the nozzle, we find the average velocity  $u_{\text{avg}} = (1/2) u_{\text{max}}$ . Therefore, the average jet velocity is 4/3 times higher than the average velocity over the nozzle area. The cross-sectional area of the jet decreases with the same ratio due to the conservation of mass.

The relative acceleration due to a periodic fluctuation of the velocity in the nozzle is derived in the same way, but now with a uniform flow profile in the nozzle with a temporal velocity fluctuation. The mass and momentum flows during one oscillation period are given by:

$$\rho \pi R_{\text{nozz}}^2 \int_0^T (u_{\text{nozz}} + u_a \sin(2\pi ft)) dt = \rho \pi R_{\text{nozz}}^2 u_{\text{nozz}} T \quad (4.17)$$

$$\rho \pi R_{\text{nozz}}^2 \int_0^T (u_{\text{nozz}} + u_a \sin(2\pi ft))^2 dt = \rho \pi R_{\text{nozz}}^2 T (u_{\text{nozz}}^2 + 1/2 u_a^2) \quad (4.18)$$

where  $T$  is the oscillation period and  $f$  is the oscillation frequency. This effect of acceleration depending on the actuation amplitude  $u_a$  is described by Dressler [10].

The increased droplet velocity will lead to a placement error on the substrate, since the droplets are otherwise all expected to travel at the same velocity.

### 4.3

#### Analysis of Droplet Formation in Drop-on-Demand Inkjet Printing

In this section, we show how droplet formation in DOD inkjet printing can be analyzed by treating one case in depth. While the case that we discuss here is typical and our analysis of it may be sufficient for your application, different droplet formation scenarios are possible. In your application, the order of the events might be different, some phenomena might not occur before the droplet hits the paper, or the droplet might collide with a droplet that was jetted previously. If the droplet formation that we want to analyze differs from the one that we describe next, we will have to modify the analysis accordingly. We expect that the discussion and analysis in this chapter provide sufficient guidance to do so.

#### 4.3.1

##### The Scenario of the Analyzed Droplet Formation

We consider the formation of a single droplet. The first bit of ink that flows out of the nozzle is soon joined by faster moving ink that left the nozzle a little bit later. This results in a droplet of ink that moves away from the nozzle. As long as the ink that leaves the nozzle moves faster than the droplet, that ink joins the droplet, thereby enlarging and accelerating the droplet. Eventually, the velocity of the ink in the nozzle decreases below the velocity of the droplet, and the droplet no longer grows. The ink that is jetted from the nozzle, but is too slow to overtake the droplet, forms a ligament, which we call the tail. For a while, this tail connects the droplet with the nozzle until the radius of the tail decreases to zero somewhere. If the tail radius tends to zero at several locations along the tail almost simultaneously (within one capillary time), we call it tail breakup. If the radius tends to zero near the nozzle or near the head droplet, we call it pinch-off.

Let us assume that the tail first pinches off at the nozzle, before it pinches off at the head droplet and before it breaks up, as shown in Figure 4.2. The rear end of the tail contracts and forms a droplet, the tail droplet, which advances into the tail. If the head droplet velocity is low enough, the tail droplet merges with the head droplet, sweeping up the entire tail in the process. All the jetted ink becomes a single spherical droplet. For most applications, this is the most desirable result of the droplet formation. Unfortunately, this requires a low droplet velocity, which is not always acceptable. At higher droplet velocities, the tail breaks up before the tail droplet has reached the head droplet. After the tail has broken up, the head droplet is followed by a few droplets that were formed at tail breakup, which we

call fragment droplets (but which are often called *satellite droplets*). Some of these fragment droplets are faster than the head droplet, so that they will merge with the head droplet. In some cases, the tail droplet is faster than the head droplet, even after it has absorbed all the fragment droplets, so that all the jetted ink eventually merges into a single droplet. If the tail droplet is slower than the head droplet, the droplet formation results in droplets of multiple sizes. Worse, due to the tail breakup, the exact droplet size distribution depends on noise sources that we cannot control. This is usually not a desired outcome. Therefore, an objective of our analysis is to determine whether the tail droplet will merge with the head droplet.

We break this scenario down into three phenomena:

- Head droplet formation
- Tail formation
- Tail breakup and pinch-off.

This distinction is useful because these phases require different methods of analysis.

#### 4.3.1.1 Head Droplet Formation

The size and velocity of the head droplet are established early in the drop formation process. By integrating the mass and momentum flux into the droplet over time, an accurate estimate of the volume and velocity of the head droplet is obtained. This is a procedure similar to the one proposed by Dijkstra [11], but instead of tracking the kinetic energy in the droplet, we use the momentum. The mass flux is  $\rho A_n u_n$ , where  $\rho$  is the density of the ink and  $u_n$  is the velocity with which the ink is ejected from the nozzle exit area  $A_n$ . The momentum flux consists of the advection of momentum into the droplet  $\rho A_n u_n^2$  and the viscous and capillary tensions. In the next paragraphs, we explain how to estimate the advection of momentum, the viscous tension, and the capillary tension.

The volume of the droplet  $V_{\text{drop}}$  is obtained by integrating the flow rate through the nozzle  $A_n u_n$  over time, starting at the moment  $t_0$  when the meniscus emerges from the nozzle, until the time  $t_e$  when the velocity at which the ink is jetted from the nozzle decreases below the velocity of the droplet. Until that time, the droplet grows because the ink that will join the droplet is being ejected from the nozzle.

$$V_{\text{drop}} = \int_{t_0}^{t_e} A_n u_n dt \quad (4.19)$$

When the meniscus is retracted or the velocity in the nozzle is directed inward, the velocity in the nozzle is taken to be equal to zero.

The momentum transfer due to viscous friction is calculated in the slender-jet approximation. The viscous component of the tension depends only on the stretching rate and the cross-sectional area.

$$\tau_\mu = 3\mu A \partial_x u \quad (4.20)$$

The continuity equation links the stretching rate and the change in cross-sectional area.

$$\frac{D}{Dt}A = -A\partial_x u = -\frac{\tau_\mu}{3\mu} \quad (4.21)$$

The total amount of momentum that is transferred from the droplet through viscous tension, denoted as  $p_\mu$ , is obtained by combining these equations and integrating with respect to time, at a position that moves with the liquid.

$$A(t_2) - A(t_1) = \int_{t_1}^{t_2} \frac{D}{Dt}A dt = \int_{t_1}^{t_2} -\frac{\tau_\mu}{3\mu} dt = -\frac{p(t_2) - p(t_1)}{3\mu} \quad (4.22)$$

Thus, the momentum that is transferred by viscosity as the cross-sectional area decreases from  $A_n$  to zero equals  $p_\mu = -3\mu A_n$ , where the minus sign indicates that the droplet is slowed down, pulled back to the nozzle by this much, in the process of pinching off.

The next step is to determine how much momentum is transferred by surface tension when the ink of the head droplet is ejected. The capillary tension is proportional to the radius of the jet, and it starts as soon as the meniscus protrudes from the nozzle, before the ejection of the bit of the tail where pinch-off will occur. While the ink is ejected, the jet of ink has a radius equal to the nozzle radius, so that the capillary force is  $\pi R_n \sigma$  in that period of time. Thus, the momentum change in the head droplet due to capillary tension is

$$p_c = (t_e - t_0) \pi R_n \sigma \quad (4.23)$$

during the ejection of the ink. By taking advection, viscosity, and surface tension into account, we now obtain an approximation  $u_{\text{drop}}$  of the droplet velocity.

$$u_{\text{drop}} = \frac{1}{\rho V_{\text{drop}}} \left( \int_{t_0}^{t_e} \rho A_n u_n^2 dt - 3\mu A_n - (t_e - t_0) \pi R_n \sigma \right) \quad (4.24)$$

The droplet velocity is given by the value of  $u_{a,\mu,\sigma}$  at the moment when the velocity with which the ink is ejected from the nozzle  $u_n$  becomes lower than this droplet velocity.

This expression implies that if  $\rho R_n u_n^2 < \sigma_n$  at all times, that is,  $We < 1$ , the droplet velocity is negative. The jet velocity at which the droplet velocity passes through zero is known as the *jetting threshold*, which is called the *dripping threshold* in the cases where gravity is relevant. Counterintuitively, a droplet can form in front of the nozzle, which has acquired a velocity toward the nozzle by the time it pinches off [12]. This occurs close to the jetting threshold. If the jet velocity is much lower, no droplet will form.

In this derivation, the velocity profile with which the ink emerges from the nozzle was assumed to be flat, consistent with the slender-jet approximation. The analysis can be modified to take into account different flow profiles by changing the advection. For instance, with a parabolic velocity profile, the advection of momentum is 4/3 times as large as it is with a flat velocity profile with the same flow rate. This modification is also required to obtain correct boundary conditions

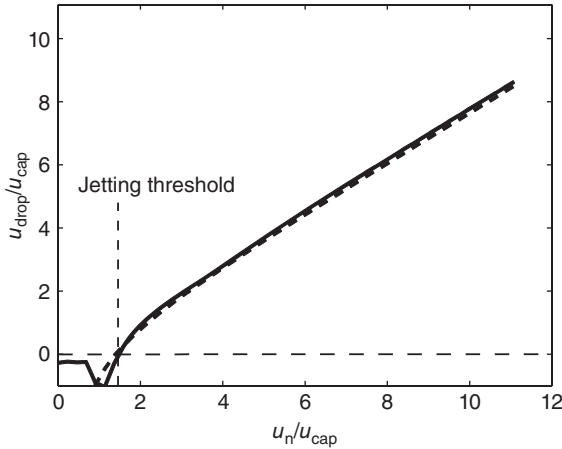


**Figure 4.4** The droplet velocity is plotted versus the maximum ejection velocity. The velocities are scaled with the capillary velocity, so that the square root of the Weber number with which the liquid is ejected is on the horizontal axis. The droplet velocity increases with the velocity in the nozzle.

The dashed line is the analytical prediction. The solid line is the droplet velocity obtained from a numerical simulation using the slender-jet approximation. For Weber numbers below the jetting threshold, no droplet is formed.

for a slender-jet model from a given velocity field at the nozzle exit; determine the advection and flow rate and feed that into the droplet formation calculation.

With the procedure outlined, the droplet velocity and mass can be calculated. The resulting droplet velocity is shown in Figure 4.4, together with the droplet velocity calculated by a slender-jet simulation for reference. The results from the analytical calculation agree with the numerical simulation. The droplet velocity becomes positive when the velocity in the nozzle is slightly greater than the capillary velocity. This is the jetting threshold. If we want to calculate the droplet velocity, this analytical calculation may be sufficient. To obtain more detailed information about the droplet formation, we must calculate how the tail forms, calculate the velocity of the tail droplet, and calculate when the tail will break up.

#### 4.3.1.2 Tail Formation

The shape of a DOD inkjet droplet, including the evolution of the tail, can be understood by neglecting the viscosity and surface tension. The resulting governing equation for the momentum is (inviscid) Burgers' equation

$$\partial_t u + u \partial_x u = 0 \quad (4.25)$$

In this equation,  $t$  is the time,  $x$  is the axial position, and  $u$  is the velocity. This equation is well known as a model equation in gas dynamics, and it can be solved exactly. The standard analysis uses the method of characteristics. For

Burgers' equation, the characteristics are straight lines in space–time along which the velocity is constant. The slope of a characteristic of Burgers' equation is equal to the velocity at that characteristic. Where characteristics intersect, a singularity arises. In gas dynamics, such a singularity is known as a *shock*. In shallow water flows, it is called a *jump*. In road traffic flows, it is called a *traffic jam*. In droplet formation, it is called a *droplet*. Simultaneous conservation of mass and momentum dictates the velocity evolution of the droplet. This extra information, which is not contained in the simplified governing equation, allows us to resolve the singularity.

As an example, the characteristics for a DOD droplet formation are shown in Figure 4.5. These characteristics were obtained by simulating the droplet formation with a slender-jet model and plotting velocity contours that are equidistant in time at the nozzle. In this simulation, the nozzle radius is  $15\ \mu\text{m}$ , the surface tension is  $0.03\ \text{N m}^{-1}$ , and the density is  $1000\ \text{kg m}^{-3}$ . The liquid is ejected with a flat velocity profile  $u_n(t)$  that is a function of time.

$$u_n(t) = u_a \sin(2\pi f_a(t - t_0)) \quad (4.26)$$

Here,  $u_a = 15\ \text{m s}^{-1}$  is the maximum velocity,  $f_a = 20\ \text{kHz}$  is the frequency, and  $t_0 = 5\ \mu\text{s}$  is the time offset, which represents the time taken by the meniscus to emerge from the nozzle. Since viscous tension and capillary tension are nearly constant along the tail, the net force on a part of the tail is negligible, so that

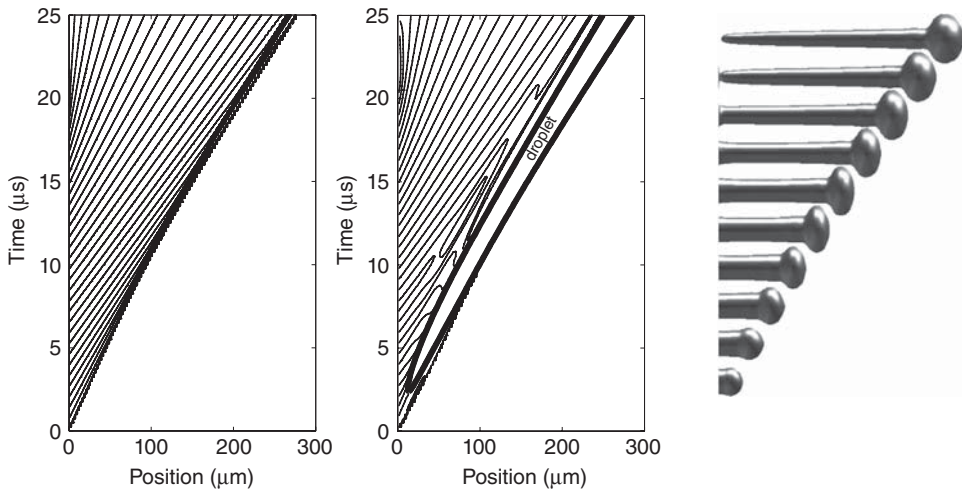


**Figure 4.5** The characteristics for a DOD inkjet droplet are shown here. Where characteristics meet, a singularity arises. In droplet formation, such a singularity is called a *droplet*. The characteristics for Burgers' equation are shown on the left. The characteristics plot in the middle was calculated from a slender-jet simulation with

viscosity and surface tension, so the characteristics are not straight lines near the head droplet, where capillary waves on the tail distort the velocity distribution. The thick line indicates where the head droplet is. The corresponding droplet shapes are shown on the right.

the velocity contours are almost straight lines, and they are a good approximation of the characteristics. Near the head droplet and near the nozzle, where the characteristics are curved, viscosity and surface tension are not constant. The head droplet causes capillary waves on the tail. These capillary waves are the main difference between the characteristics plots in Figure 4.5. At the time of pinch-off, at  $t = 20 \mu\text{s}$ , the characteristics near the nozzle are also curved. Thus, the pinch-off and the details of the flow near the head droplet depend on viscosity and/or surface tension. Inertia is dominant in most of the tail until the tail breaks up.

To determine the deceleration of the head droplet during the formation of the tail, we integrate the capillary tension over time. The capillary tension in the tail is a function of surface tension and the radius of the tail. The radius  $R$  is obtained from the cross-sectional area. Since the net force on most of the tail is negligible, we need to consider only the inertia so that the cross-sectional area can be obtained from Burgers' equation and the continuity equation, as shown in the worked examples. Along a characteristic at  $x = x_0 + ut$ , the radius is inversely proportional to the square root of time.

$$\frac{R}{R_n} = \sqrt{\frac{A}{A_n}} = \sqrt{1 - \frac{x_0}{t_a u}} \sqrt{\frac{1}{1 + \frac{t}{t_a}}} \quad (4.27)$$

The time  $t_a$  is the time at which this characteristic crosses nearby characteristics. The momentum transfer  $\Delta p$  between times  $t_1$  and  $t_2$  is obtained by integrating the resulting capillary tension.

$$\begin{aligned} \Delta p &= \int_{t_1}^{t_2} \sigma \pi R dt = \sigma \pi R_n \sqrt{1 - \frac{x_0}{t_a u}} \int_{t_1}^{t_2} \sqrt{\frac{1}{1 + t/t_a}} dt \\ &= \sigma \pi R_n \sqrt{1 - \frac{x_0}{t_a u}} \left( \sqrt{1 + \frac{t_2}{t_a}} - \sqrt{1 + \frac{t_1}{t_a}} \right) \end{aligned} \quad (4.28)$$

This formula for the capillary tension is what we needed from the analysis of the tail formation.

Now that we know the tension in the tail as a function of time, we can calculate how much the head droplet decelerates during the formation of the tail. To do so, we must determine the integration constants, the time when the tail starts to form, and the time when the tail pinches off from the head droplet. We can also use this formula to calculate the velocity of the tail droplet, to determine whether it will reach the head droplet or not. To calculate the tail droplet velocity, we must determine the time of pinch-off at the nozzle and the time when the tail breaks up. In any case, we must determine the integration boundaries. This requirement makes evaluating the effect of capillary tension much more difficult than the effect of viscous tension. Viscous tension transfers a finite amount of momentum until pinch-off, even if that takes an infinite amount of time. Capillary tension is qualitatively different. If pinch-off and tail breakup would not occur at all, the head droplet is pulled right back to the nozzle, regardless of how fast it was jetted.

In reality, both pinch-off and tail breakup can occur. Usually, they occur so quickly that the effect on the head droplet velocity of capillary tension during tail formation is negligible. This was already apparent from Figure 4.4, which shows that a good approximation of the head droplet velocity is obtained when this effect is neglected. To calculate whether the tail droplet will reach the head droplet, we must determine the time of pinch-off at the nozzle, the time of pinch-off at the head droplet, and the tail breakup time.

#### 4.3.1.3 Pinch-Off and Tail Breakup

To predict whether the tail droplet will merge with the head droplet into a single droplet, we calculate the tail droplet velocity. The tail droplet velocity depends on the tail pinch-off time and on the tail breakup time.

Determination of the pinch-off time of a DOD droplet is an unsolved problem. As far as we know, no research on this topic has been published yet. The research is complicated by the fact that pinch-off can be caused by many different effects. We will describe the effects that cause pinch-off in the droplet formations that we have shown.

In the slender-jet simulation shown in Figure 4.5, the pinch-off time coincides with the zero crossing of the ejection velocity. This is an artifact of the numerical simulation. In the slender-jet approximation with neglected radial momentum, the stretching rate tends to infinity at the nozzle when the ejection velocity decreases through zero. An infinite stretching rate implies an instantaneous pinch-off. Therefore, this pinch-off is imposed through the boundary condition and the approximations in the mathematical model. In reality, radial inertia would limit the stretching rate, so that pinch-off will occur later, caused by a different effect.

In the experiment shown in Figure 4.2, the pinch-off occurs after the ejection velocity has passed through zero, after the meniscus has retracted into the nozzle, after the meniscus has come out of the nozzle, and after the meniscus has retracted again. When the meniscus advanced, it absorbed a part of the tail. When it retracted, the meniscus drew out a very thin thread of liquid, which is called the *secondary tail* [13]. Since the secondary tail is much thinner than the primary tail, it breaks up much earlier. In a sense, there is no clean pinch-off here. The residual motion of the meniscus has made a part of the tail much thinner, so that the tail breakup occurs in two stages; if this breakup is observed with a microscope with which the secondary tail cannot be resolved, it appears to be a clean single pinch-off, but much earlier than it should be if it was induced by the thinning of the tail. The time of this pinch-off is determined by the acoustics of the printhead.

After the tail has pinched off at the meniscus, the imbalance in the capillary tension at the end of the tail causes the formation of the tail droplet. The capillary tension pulls the tail droplet toward the head droplet. At the same time, the tail droplet mass increases as it sweeps up the ink in the tail, which slows down the droplet. The combined effect is that the velocity of the tail droplet relative to the ink in the tail is independent of both viscosity and the size of the tail droplet. To



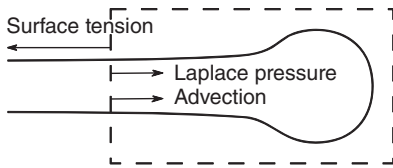


**Figure 4.6** The velocity of a tail droplet is obtained by balancing advection, Laplace pressure, and surface tension in a reference frame that moves with the droplet.

calculate this velocity, consider this problem in a frame of reference in which the tail droplet is stationary. We now determine the forces on a control volume that encloses the tail droplet and the part of the tail that is disturbed by the tail droplet, so that the part of the tail outside the control volume is cylindrical, as shown in Figure 4.6.

The forces on the control volume are advection  $+\rho\pi R^2 u^2$ , Laplace pressure  $+\sigma\pi R$ , and the direct effect of surface tension  $-\sigma 2\pi R$ , which should sum up to zero if the velocity is constant.

$$\rho\pi R^2 u^2 + \sigma\pi R - \sigma 2\pi R = 0 \Rightarrow u = \sqrt{\frac{\sigma}{\rho R}} \tag{4.29}$$

Since this is the velocity of the tail droplet with respect to the ink in the tail that it is sweeping up, the tail droplet accelerates as it reaches the faster moving ink. Also, the tail radius decreases, which requires a higher tail droplet velocity. Using the tail radius that we obtained earlier, we find that the velocity of the tail droplet with respect to the ink in the tail scales with  $\sqrt[4]{(t - t_a)}$ . This shows that, to determine the final tail droplet velocity, we must determine the tail breakup time.

The breakup of liquid filaments has been investigated extensively [5, 14, 15]. There are two distinct breakup mechanisms that are relevant for inkjet printing. The first mechanism is the Rayleigh–Plateau instability. The second breakup mechanism is end pinching. Besides breakup due to the Rayleigh–Plateau instability or end pinching, there is the possibility that the tail droplet will reach the head droplet before pinch-off can occur. These various scenarios are illustrated in Figure 4.7.

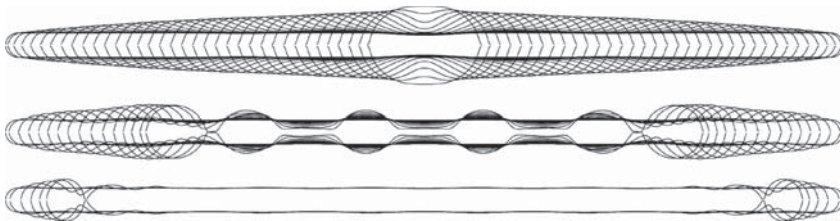


**Figure 4.7** Before coalescing into a single droplet, a freely floating filament can remain intact, break up due to end pinching, or break up due to the Rayleigh–Plateau

instability. Both types of breakup delay the coalescence. Reproduced with permission from Driessen *et al.* [15]. Copyright 2013, AIP Publishing LLC.

Let us first consider end pinching. If viscosity is negligible, the capillary waves that are emitted by the tail droplet do not damp out. The waves with a phase velocity equal to the tail drop velocity will grow until the amplitude of the fluctuation in the radius is as large as the undisturbed radius. At that time, the radius of the tail is zero near the nozzle, which implies pinch-off. This occurs after about five capillary times [16].

$$t_{\text{end pinch}} \sim 5t_{\sigma} = 5\sqrt{\frac{\rho R^3}{\sigma}} \quad (4.30)$$

After the first end-pinching event, a new tail droplet forms, and the process repeats, breaking up the tail from the end inward. Breakup due to the Rayleigh–Plateau instability is greatly complicated by the stretching of the tail, which tends to inhibit breakup [5]. However, the stretching rate decreases, while the growth rate of the unstable modes increases due to the decreasing tail radius. Eventually, the stretching can be neglected. The crossover occurs approximately when the stretching rate (see Eq. 4.39) equals the growth rate.

$$\frac{1}{t_{\text{crossover}}} \sim \sqrt{\frac{\sigma}{\rho R^3}} = \sqrt{\frac{\sigma \left(1 + \frac{t_{\text{crossover}}}{t_a}\right)^{3/2}}{\rho R_n \left(1 - \frac{x_0}{t_a u}\right)^{3/2}}} \quad (4.31)$$

Let us assume that the breakup itself takes four times the capillary time, based on the instantaneous tail radius at the crossover time. By construction, the capillary time equals the crossover time at that instant. This yields the following order of magnitude estimate.

$$t_{\text{crossover}} \sim \sqrt{\frac{\rho R_n^3}{\sigma}} \left(\frac{t_a}{t_{\text{crossover}}}\right)^{3/4} \Rightarrow t_{\text{break}} \sim 5t_{\text{crossover}} = 5t_{\sigma}^{4/7} t_a^{3/7} \quad (4.32)$$

To use this result, we must estimate the time  $t_a$ , for which we cannot use the stretching rate in the slender-jet approximation, because it diverges. A better estimate is obtained from the ratio of the acceleration to the nozzle radius, since radial inertia is dominant near the zero crossing of the ejection velocity.

$$t_a \sim \sqrt{\frac{R_n}{\frac{d}{dt}u_n}} \quad (4.33)$$

For the experiment shown in Figure 4.2, the capillary timescale is about  $t_{\sigma} = 7 \mu\text{s}$ , while the timescale of the stretching is about  $t_a = 3 \mu\text{s}$ , which yields a breakup time of about  $t_{\text{break}} = 25 \mu\text{s}$ , which agrees well with the observation. Note that the important part of this analysis was not to obtain how many capillary times it takes for the Rayleigh–Plateau instability to set in and cause breakup. The important part is to determine the radius at which this instability sets in, because this determines the growth rate and the size of the fragment droplets.

## 4.4

## Worked Examples

## 4.4.1

## Tail Formation for the Purely Inertial Case

**Task:** Calculate the evolution of the thickness of the tail.

**Hints:** Start by writing an expression for the rate at which the tail is stretched locally. Use this expression in the momentum equation, where viscosity and surface tension have been neglected. Rewrite this evolution equation as an ordinary differential equation by collecting the terms into a convective derivative for the stretching rate, and use this to obtain the cross-sectional area of the tail as a function of time.

**Solution:** The first step is to determine the stretching rate, which is a function of space and time.

$$y(x, t) = \partial_x u \quad (4.34)$$

To determine the stretching rate, take the spatial derivative of Burgers' equation, rearrange, and insert the definition of the stretching rate. We thus obtain the following equation.

$$\partial_t y + u \partial_x y = -y^2 \quad (4.35)$$

We now collect the left-hand side into a single convective derivative.

$$\frac{Dy}{Dt} = -y^2 \quad (4.36)$$

This shows that along a characteristic at  $x = x_0 + ut$ , the stretching rate satisfies an ordinary differential equation. We solve this differential equation to obtain the stretching rate.

$$y(x_0 + ut, t) = \frac{1}{t + t_a} \quad (4.37)$$

The integration constants  $t_a$  and  $x_0$  are specified by the boundary condition at the nozzle, where the velocity is equal to the ejection velocity. The point  $(x_0, t_a)$  in space–time is the point at which this characteristic crosses the nearby characteristics. If, at some point in time, the liquid filament has a constant cross-sectional area and a constant stretching rate,  $x_0$  and  $t_a$  are constant along the filament. In other words, the point  $(x_0, t_a)$  in space–time is the point from which the characteristics originate. It is the big bang of this liquid filament in the sense that all the liquid appears to have exploded at this point. In reality, this point lies within the printhead, the liquid was jetted after  $t_a$ , and nothing dramatic happened. For the sake of brevity, an expression for these quantities is not determined here.

The stretching rate is related to the evolution of the cross-sectional area  $A = A(x, t)$  of the tail through the continuity equation.

$$0 = \partial_t A + \partial_x Au = \frac{D}{Dt} A + Ay \Rightarrow A(x_0 + ut, t) = \frac{A_0}{1 + \frac{t}{t_a}} \quad (4.38)$$

The integration constant  $A_0$  can be determined in the case where the ink emerges from the nozzle as a jet with the same cross-sectional area as the nozzle.

$$(x = 0 \Rightarrow A = A_n) \Rightarrow A_0 = A_n \left( 1 - \frac{x_0}{t_a u} \right) \quad (4.39)$$

Here,  $A_n$  is the cross-sectional area of the nozzle. We now know the thickness of the tail as a function of space and time, which is the starting point for the calculation of the tail breakup time. We also need it to calculate how much the head droplet is decelerated by capillary tension during the formation of the tail, but this can usually be neglected.

#### 4.4.2

##### Dispersion Relation of the Rayleigh–Plateau Instability

**Task:** In the main text, we show the dispersion relation for the Rayleigh–Plateau instability. Show the evolution of an infinite cylindrical water ligament. The ligament is initially at rest. The radius has a sinusoidal perturbation with a wavelength of  $\lambda = 2\pi k^{-1}$ , which is larger than the circumference.

**Hints:** Note that the initial velocity is zero, so you will need both roots of the dispersion relation!

**Solution:** The starting point is the ansatz that was used in the analysis of the Rayleigh–Plateau instability. The quantity  $\tilde{R} = R - R_0$  is the sum of the disturbance in the radius due to  $m$  linearly independent modes. To satisfy all the conditions in this problem, we will need four modes in total. We write  $\tau_m = i\omega_m$ , which is a real number for unstable modes, to simplify the notation.

$$\tilde{R}(x, t) = \sum_{m=1}^4 R_m \exp(ik_m x + \tau_m t) \quad (4.40)$$

The velocity  $u$  is decomposed similarly, but the undisturbed velocity is zero.

$$u(x, t) = \sum_{m=1}^4 u_m \exp(ik_m x + \tau_m t) \quad (4.41)$$

The initial disturbance in the velocity is zero.

$$u(x, 0) = 0 \quad (4.42)$$

The initial radius is imposed.

$$\tilde{R}(x, 0) = R_a \cos(kx) \quad (4.43)$$

There are four different modes whose real part satisfies the last requirement. Since we impose both the initial velocity and the initial radius, which implies that the velocity and the radius are real-valued, there are four equations that must be satisfied. This completely determines the four amplitudes.

We select two growing modes as the first two modes. This implies that  $k_1 = k = -k_2$  and  $\tau_1 = \tau_2 = \tau_+ = i\omega_+(k)$ . The sum is an exponentially growing cosine.

$$R_1 \exp(ik_1 x + \tau_1 t) + R_1 \exp(ik_2 x + \tau_2 t) = R_+ \exp(\tau_+ t) \cos(kx) \quad (4.44)$$

This implies that the other two modes are the other complex conjugate pair, which sum to an exponentially decaying cosine.

$$R_3 \exp(ik_3 x + \tau_3 t) + R_4 \exp(ik_4 x + \tau_4 t) = R_- \exp(\tau_- t) \cos(kx) \quad (4.45)$$

To satisfy the initial condition,  $R_+ + R_- = R_a$ . We now proceed with the velocity field. We use the relation between the amplitudes from the stability analysis, Eq. (4.8).

$$u = \frac{2\omega}{R_0 k} R \quad (4.46)$$

This value for the (complex) velocity amplitude is used in the ansatz for the velocity, and the modes are added to obtain the velocity field. First, we obtain the full, real-valued growing mode:

$$\begin{aligned} u_+(x, t) &= \frac{2\tau_+}{iR_0 k} R_+ \exp(ikx + \tau_+ t) - \frac{2\tau_+}{iR_0 k} R_+ \exp(-ikx + \tau_+ t) \\ &= \frac{4\tau_+}{R_0 k} R_+ \sin(kx) \exp(\tau_+ t) \end{aligned} \quad (4.47)$$

The full, real-valued decaying mode is obtained in the same way.

$$\begin{aligned} u_-(x, t) &= \frac{2\tau_-}{iR_0 k} R_- \exp(ikx + \tau_- t) - \frac{2\tau_-}{iR_0 k} R_- \exp(-ikx + \tau_- t) \\ &= \frac{4\tau_-}{R_0 k} R_- \sin(kx) \exp(\tau_- t) \end{aligned} \quad (4.48)$$

At  $t = t_0$ , the velocity is as follows:

$$u(x, 0) = (\tau_+ R_+ + \tau_- R_-) \frac{4\omega}{R_0 k} \sin(kx) \quad (4.49)$$

Note that  $\tau_+ > 0$  and  $\tau_- < 0$ , so that the velocity field of the decaying mode is in the direction opposite to the direction of the velocity field of the growing mode.

If  $\tau_- R_- + \tau_+ R_+ = 0$ , the sum of the velocity fields of the growing mode and decaying mode is zero at  $t = 0$ , as imposed by the initial condition. If viscosity is neglected,  $\tau_- = -\tau_+$  so that  $R_- = R_+ = 1/2 R_a$ , and we can combine both modes into one hyperbolic sine.

$$u(x, t) = -\frac{2\tau_+}{R_0 k} R_a \sin(kx) \sinh(\tau_+ t) \quad (4.50)$$

Similarly, the exponentials in the radius disturbance can be collected in a hyperbolic cosine.

$$\tilde{R}(x, t) = R_a \cos(kx) \cosh(\tau_+ t) \quad (4.51)$$

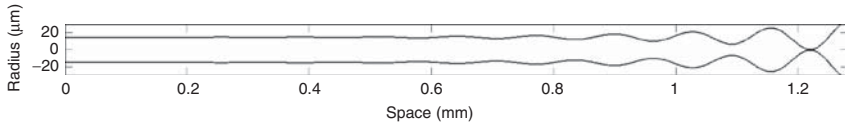


**Figure 4.8** The evolution of the Rayleigh–Plateau instability in the continuous inkjet case, as mentioned in the Section 4.4.2.

This reveals the behavior of a liquid filament that might at first seem puzzling: the radius perturbation does not grow at first. It does not increase appreciably until the decaying mode has become small. A similar effect occurs at a jet from a nozzle with an imposed velocity fluctuation. In that case, the wave numbers of the four modes have both a real part and an imaginary part. They constitute two real-valued functions: one grows exponentially in time and in the jetting direction, while the other decays in time and in the jetting direction. Close to the nozzle, the total radius disturbance appears to grow at a constant rate with distance from the nozzle instead of exponentially, because the decaying mode is still significant [7]. The exponential growth only becomes apparent when the decaying mode has become negligible (Figure 4.8).

### Acknowledgment

We are thankful to Marc van den Berg, Koen Winkels, and Lionel Hirschberg for providing us with experimental and theoretical inputs.

### References

1. Bush, J. (2010) Interfacial phenomena. *MIT OpenCourseWare*, p. 18.357.
2. Driessen, T. and Jeurissen, R. (2011) A regularised one-dimensional drop formation and coalescence model using a total variation diminishing (tvd) scheme on a single Eulerian grid. *Int. J. Comput. Fluid Dyn.*, **25**, 333–343.
3. Rayleigh, J.W.S. (1892) On the instability of a cylinder of viscous liquid under capillary force. *Philos. Mag.*, **34**, 145.
4. Weber, C. (1931) Zum Zerfall eines Flüssigkeitsstrahles. *Z. Angew. Math. Mech.*, **11** (2), 136–154.
5. Eggers, J. and Villermaux, E. (2008) Physics of liquid jets. *Rep. Prog. Phys.*, **71** (3), 036601.
6. Keller, J.B., Rubinow, S.I., and Tu, Y.O. (1973) Spatial instability of a jet. *Phys. Fluids*, **16** (12), 2052–2055.
7. Garcia, F.J. and Gonzalez, H. (2008) Normal-mode linear analysis and initial conditions of capillary jets. *J. Fluid Mech.*, **602**, 81–117.
8. Lafrance, P. (1975) Nonlinear breakup of a laminar liquid jet. *Phys. Fluids*, **18** (4), 428–432.
9. Schneider, J.M., Lindblad, N.R., Hendricks, C.D., and Crowley, J.M. (1969) Erratum: stability of an electrified liquid jet. *J. Appl. Phys.*, **40**, 2680; Schneider, J.M., Lindblad, N.R., Hendricks, C.D., and Crowley, J.M. (1966) Stability of an electrified liquid jet. *J. Appl. Phys.*, **38** (6), 2599–2605.
10. Dressler, J.L. (1998) High-order azimuthal instabilities on a cylindrical liquid jet driven by temporal and

- spatial perturbations. *Phys. Fluids (1994-present)*, **10** (9), 2212–2227.
11. Dijkstra, J.F. (1984) Hydrodynamics of small tubular pumps. *J. Fluid Mech.*, **139** (2), 173–191.
  12. Zengerle, R., Tanguy, L., Liang, D., and Koltay, P. (2012), Droplet Break-Up with Negative Momentum Fluid Dynamics Videos. arXiv:1210.4078 [physics.flu-dyn].
  13. Wijshoff, H. (2010) The dynamics of the piezo inkjet printhead operation. *Phys. Rep.*, **491** (45), 77–177.
  14. Castrejón-Pita, A.A., Castrejón-Pita, J.R., and Hutchings, I.M. (2012) Breakup of liquid filaments. *Phys. Rev. Lett.*, **108**, 074506.
  15. Driessen, T., Jeurissen, R., Wijshoff, H., Toschi, F., and Lohse, D. (2013) Stability of viscous long liquid filaments. *Phys. Fluids*, **25**, 062109.
  16. Notz, P.K. and Basaran, O.A. (2004) Dynamics and breakup of a contracting liquid filament. *J. Fluid Mech.*, **512**, 223–256.





## 5 Polymers in Inkjet Printing

*Joseph S.R. Wheeler and Stephen G. Yeates*

### 5.1

#### Introduction

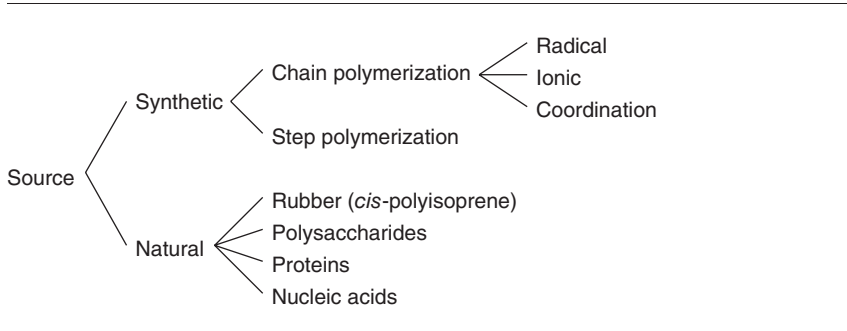
Polymers fulfill many different roles both in formulation and end-use application of inkjet fluids, with the use of polymeric additives in both aqueous and solvent-based ink formulations widely reported in both CIJ and DOD systems [1]. Examples include: use of low concentrations of high-molecular-weight water-soluble polymers as drag-reducing agents [2] and also to control droplet generation [3], low-molar-mass water soluble/dispersible polymers [4] or branched polymers to improve image permanence on substrate [5], pigment dispersants [6] and stabilizers, and as the functional materials, ranging from, for examples, organic semiconductors polymers in electronics applications [7] to biological polymers [8].

However, the formulation of polymer-based fluids presents a number of challenges. Foremost among these is the fact that polymer solutions can show significant non-Newtonian behavior when exposed to the shear rates experienced in inkjet printing, which impacts directly upon both drop ejection and drop formation behaviors and potential degradation of the polymer during the inkjet printing process [9, 10]. In this chapter, we consider the design rules for the formulation and application of polymers in inkjet printing, with particular focus on polymers in solution.

### 5.2

#### Polymer Definition

Polymers are long-chain molecules formed of small repeating units (monomers). They are ubiquitous in modern life, both in industrial and consumer goods. Indeed, it is extremely unlikely that any clothes, technology, buildings near the reader, or even the book one is holding does not contain a significant polymer content. Polymers can be divided into two broad classes: thermoplastics and thermosets. Thermosets are cross-linked, do not melt, and cannot be solution-processed or recycled. Thermoplastics are polymers that are not cross-linked, can usually be dissolved in a solvent, and in most instances will melt and flow [11].

**Table 5.1** Source-based polymer classification.

### 5.3

#### Source- and Architecture-Based Polymer Classification

The properties of polymer solutions are determined by both the molecular weight of the polymeric solute and the interactions between the polymer and the solvent [12]. Both the limiting molecular weight and solution properties are determined by the nature of the monomer and the synthetic method used to produce the polymer [13]. Polymers can be split into two groups, synthetic and natural, with synthetic polymers further characterized by either chain growth or step growth [14] (Table 5.1).

Chain growth is a polymerization technique where unsaturated monomer molecules add onto the active site of a growing polymer chain one at a time. Growth of the polymer occurs only at one (or possibly more) end [15]. Addition of each monomer unit regenerates the active site, which is radical, anionic [16], or cationic [17]. Step-growth polymerization refers to a type of polymerization mechanism in which bifunctional or multifunctional monomers react to form first dimers, then trimers, longer oligomers, and eventually long-chain polymers [18]. Coordination polymerization such as Atom Transfer Radical Polymerisation (ATRP) can be used to produce low-polydispersity polymers and polymers of interesting molecular architecture [19].

Polymers are not limited to a linear configuration. By utilizing different synthetic methodologies, it is possible to generate widely varying polymer architecture, which can be used to control the application properties. Several examples of different polymer architectures are listed in Table 5.2.

### 5.4

#### Molecular Weight and Size

One of the most fundamental questions that need to be answered about any polymer sample concerns the sizes of the molecules of which it is composed, since all of

Table 5.2 Architecture-based polymer classification.

<p>Block copolymer [20]</p>	<p>Statistical linear copolymer [21]</p>
<p>Graft [22]</p>	<p>Hyperbranched/star [23, 24]</p>

the properties of polymers relevant to inkjet performance are critically dependent on the molar mass of the polymer. Molar mass,  $M$ , is commonly expressed in units of  $\text{g mol}^{-1}$  or daltons ( $1 \text{ Da} = 1 \text{ g mol}^{-1}$ ), but it should be borne in mind that if SI units are used in the calculations, then it is appropriate to express  $M$  in  $\text{kg mol}^{-1}$  or kDa. Also widely encountered is the dimensionless quantity “relative molecular mass,” which is the numerical value of  $M$  when expressed in  $\text{g mol}^{-1}$ . The term “molecular weight” is traditionally used in polymer science for “relative molecular mass,” but some workers treat “molecular weight” as synonymous with “molar mass.” When using molar masses from experimental data in any calculation, it is important that appropriate units are used.

For a small molecule,  $M$  is easily calculable from the chemical formula, but for a polymer, the situation is more complex apart from some naturally occurring polymers, which have a defined molecular weight value, that is, they are monodisperse. Virtually all samples of synthetic polymers, and of many natural polymers such as polysaccharides, comprise a very large number of species differing in  $M$ , that is, they are polydisperse. This is due to the inherently random polymerization process in which monomers add on to the growing chains with varying molecular weights. Therefore, it is necessary to consider how the amount of polymer with mass  $M_i$  varies with  $\sum_i M_i$ , that is, the distribution of molar mass. Strictly speaking, polymer molar mass distributions are discontinuous, but for a high polymer, the number of species becomes very large, so distributions can be represented as continuous curves, Figure 5.1.

In the continuous number-fraction distribution,  $n(M)$  versus  $M$ , the area of a slice under the curve,  $n(M)dM$ , is the number fraction with molar mass in the range from  $M$  to  $M + dM$ . Similarly, for the continuous weight-fraction distribution,  $w(M)$  versus  $M$ , the area of a slice under the curve,  $w(M)dM$ , is the weight fraction with molar mass in the range from  $M$  to  $M + dM$ . The case shown is an example of the “most probable” distribution, which is predicted by theory for radical-chain polymerization or linear condensation polymerization in certain situations. Many of the techniques available for the determination of molar mass provide a single value, which, for a polydisperse polymer sample, must therefore

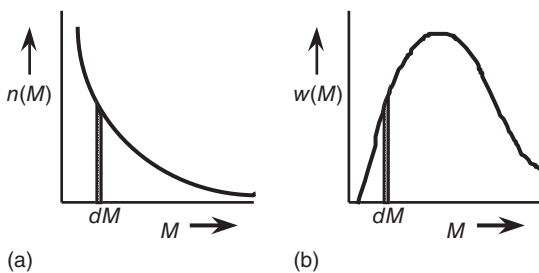
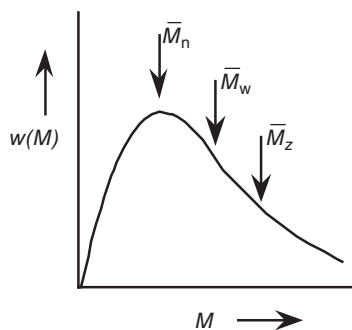


**Figure 5.1** Illustration of (a) a number-fraction distribution and (b) the equivalent weight fraction distribution.



Polydisperse polymers:  $\bar{M}_n < \bar{M}_w < \bar{M}_z$   
 Uniform polymers:  $\bar{M}_n = \bar{M}_w = \bar{M}_z$   
 Most probable distribution:  $\bar{M}_n : \bar{M}_w : \bar{M}_z = 1:2:3$   
 The ratio  $\bar{M}_w / \bar{M}_n$  is a measure of the width of the number distribution  
 The ratio  $\bar{M}_z / \bar{M}_w$  is a measure of the width of the weight distribution

**Figure 5.2** Representative molecular weight distribution showing the most probable distribution with the different molecular weight averages shown.

be an average value. Important averages are:

$$\text{number average } (\bar{M}_n) \quad \bar{M}_n = \frac{\sum_i n_i M_i}{\sum_i n_i} \quad (5.1)$$

$$\text{weight average } (\bar{M}_w) \quad \bar{M}_w = \frac{\sum_i W_i M_i}{\sum_i W_i} = \frac{\sum_i n_i M_i^2}{\sum_i n_i M_i} \quad (5.2)$$

$$\text{z-average } (\bar{M}_z) \quad \bar{M}_z = \frac{\sum_i W_i M_i^2}{\sum_i W_i M_i} = \frac{\sum_i n_i M_i^3}{\sum_i n_i M_i^2} \quad (5.3)$$

and the relative positions of these on the molecular weight distribution are shown in Figure 5.2.

The techniques used to determine molecular weight can give different types of average depending on the physical basis of the experiment. Many of the techniques available for the determination of molar mass provide a single value, which, for a polymer that is polydisperse in molar mass, must be an average value. Some techniques for the determination of molar masses of polymers may be regarded as primary methods, in that they can be used to determine an absolute value for an average molar mass without calibration against samples of known molecular weight. Secondary methods of molecular weight determination require calibration against standards of known molecular weight.

Methods to determine the molecular weight based on colligative properties of polymer solutions (such as membrane osmometry or end-group analysis) give  $\bar{M}_n$ , as these techniques are based on counting the number of polymer chains irrespective of the size [25]. If the measurement system is more responsive to polymer molecules of greater size, then a higher molecular weight average is determined. An example of this is the determination of  $\bar{M}_n$  by static light scattering. A larger polymer molecule will scatter incident radiation to a greater extent than a smaller chain, provided the polymer molecules are of the same size order of magnitude

to the wavelength of the incident radiation [25]. These primary methods require experimentally taxing measurements in dilute polymer solutions (which show ideal solution behavior [12]) and have generally been replaced by chromatographic measurements.

The most common method used to determine molecular weight is gel permeation chromatography (GPC), whereby a dilute polymer solution is eluted through a column packed with porous beads of varying sizes [26]. As the polymer solution passes through the column, the low mass fractions of the polymer molecular weight distribution will be impeded by the packing material, whereas the larger polymers will not fit in the smaller void volumes and will pass through the column at a faster rate. At the end of the column, a concentration-dependent detector will measure the polymer fractions eluting off the column. This produces a chromatogram of elution volume versus time [26]. The molecular weight distribution can be determined from the chromatogram by calibrating the system against a set of standards of very well defined molecular weights, generally polystyrene or poly(methyl methacrylate). This gives relative molecular weights, and workers using different polymer systems to the calibrants must be mindful that their polymers may well adopt different conformations in solutions (swollen/collapsed coil) and the true molecular weight may be very different from the relative molecular weight determined by the GPC experiment [27]. More sophisticated GPC techniques involve the use of multiple detectors. Triple detection GPC involves the use of refractive index, light scattering, and viscometry detectors. This technique has several advantages over a simple calibrated system with a single detector. It can give an absolute molecular weight value and can also be used to characterize polymer architecture such as branching [28].

## 5.5

### Polymer Solutions

A polymer solution, that is, polymer dissolved in a solvent, can be described in terms of three solvent regimes. In a poor solvent, a polymer will occupy a tight, contracted coil conformation because polymer–polymer interactions are energetically favorable as compared to polymer–solvent interactions. In a good solvent, the polymer–solvent interactions are favorable and the polymer adopts an expanded self-avoiding walk conformation [29]. In a solvent at a specific temperature and pressure (theta ( $\theta$ ) conditions), the polymer occupies its ideal random walk/ideal chain orientation. When this condition is met, it is possible to measure the physical properties of the polymer without the influence of solvent effects [30].

When considering polymer solutions in the context of inkjet printing, it is important to know the fundamental nature of the polymer–solvent interaction, and this information can be extracted from the determination of the intrinsic viscosity,  $[\eta]$ . The intrinsic viscosity is the volume occupied in solution by a unit mass of polymer in a specific solvent, commonly expressed in polymer sciences using

the unit  $\text{g dl}^{-1}$ . Depending on the nature of the interactions between the polymer and the solvent, the intrinsic viscosity can vary widely for a specific polymer in different solvent systems. The relationship between the intrinsic viscosity and the molecular weight is expressed by the phenomenological Mark–Houwink–Sakurada, Eq. (5.4):

$$[\eta] = KM^a \quad (5.4)$$

where  $M$  is the molecular weight and  $K$  and  $a$  are the empirical constants, which are tabulated for the most linear polymers in common solvent systems or determined experimentally.  $K$  and  $a$  are dependent upon the specific polymer–solvent system while  $a$  gives additional information on polymer architecture. For  $a = 0.5$ , the polymer is either in its  $\theta$  state or highly branched, 0.6 for a branched system, 0.6–0.8 for a coil conformation in a good solvent, and 2 for an absolute rigid-rod-type polymer [31]. It is common to see  $\alpha$  used interchangeably with  $a$ , but strictly speaking,  $a$  is the correct notation for the exponent.

Polymer solutions can be described by three different regimes dilute, semidilute, and concentrated, as described by de Gennes [32], as shown qualitatively in Figure 5.3. In the dilute solution regime, there are no frictional interactions between polymer chains and there are large concentration fluctuations in a cross section of the solution. As noted previously, it is in the extremely dilute regime that ideal solution behavior is shown by polymer solutions. In the semidilute regime, there are frictional interactions between polymers in solutions and an associated increase in the rate of change of viscosity with change in concentration. The concentration fluctuations across a segment of solution are not as large as in a dilute solution. The extent of chain overlap is such that the solution is still a discernible mixture of separate polymer chains and solvent. Hence, this regime is referred to as *semidilute*; by volume, the polymer concentration is low but the polymer physical properties are dominated by polymer chain effects. This point at which chains interact in solution is defined as the overlap concentration,  $c^*$ . The third regime is that of a concentrated polymer solution. Again, there is associated increase in the rate of change of viscosity with change in concentration. The polymer chains are fully overlapping and the solution on a molecular level is a continuum of polymer

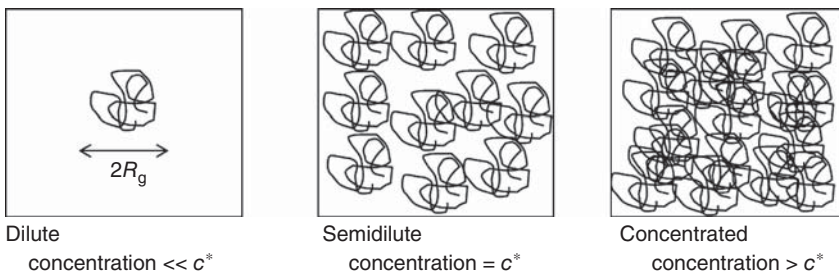


**Figure 5.3** A schematic representation of the three regimes of polymer solutions in relation to the overlap concentration,  $c^*$ .

molecules with very small concentration fluctuations across the solution [33]. The movement of polymer molecules through this extremely viscous medium has been likened to that of a snake or reptile slithering through a tube composed of other polymers and is referred to as *reptation*. This theory postulated by de Gennes based on the Edwards tube model explains the dynamics of concentrated polymer solutions and polymer melts but is out of scope of this chapter [34, 35]. Concentrated solutions are generally too viscous for inkjet printing purposes.

The overlap concentration is related to intrinsic viscosity, while there is some dependency of polymer architecture, for a good solvent  $c^* \sim 1/[\eta]$  as defined by Flory. From this, we can further define the reduced concentration (a unitless measure for chain overlap) as  $c/c^* = c[\eta]$ , with the reduced concentration that polymers interact in an intermolecular manner defined [36] as 1. The advantage of describing polymer solutions in terms of reduced concentrations rather than mass/moles per unit volume is that polymer solutions of differing molecular weights and polymers composed of different monomers or in different solvent systems can be directly compared. It will be described later in this chapter how known polymer formulation rules for inkjet printing fluids are expressed in terms of reduced concentration.

## 5.6

### Effect of Structure and Physical Form on Inkjet Formulation Properties

Before considering the effect of the different physical polymer solution parameters, viscosity, surface tension, temperature, and density, on drop formation, we first consider qualitatively how polymer concentration in inkjet formulations affects drop formation. These effects are most apparent when we consider the ligament that connects the main drop to the printhead just after pinch-off. Drop formation in DOD systems can be categorized according to four different regimes from high to low concentration of polymer in the formulation. These regimes are described in Figure 5.4 with accompanying example images of drop formation in these regimes [3].

Although this behavior is ubiquitous for polymer solutions in inkjet printing, the exact concentration ranges for each regime for a given polymer–solvent combination is determined by the polymer molecular weight, solvent quality, and polymer architecture. These different drop formation regimes can be explained by an increase in viscoelasticity in the printed drops. This results in an elastic-type response of the fluid at higher concentrations and retraction of the ligament into the main drop. When the elasticity reaches a critical value, the drops cannot detach and the printheads are blocked [3].

CIJ drop formation is via the Rayleigh instability mediated by modulation by piezo active drive rods in the CIJ printheads [37] (Chapter 3). It can also be affected by viscoelastic effects associated with polymer solutions, as shown in Figure 5.5 for polymethylmethacrylate (PMMA) in methyl ethyl ketone (MEK). In CIJ printing, discrete drops must be formed before they reach the charging electrode. If the



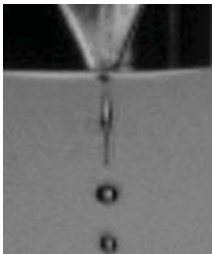
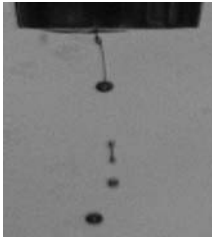
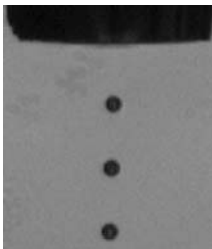

Regime	Characteristic behavior	Typical picture
1	The first regime occurs at either very low concentrations and/or molecular weight, where a long tail is formed that simultaneously disintegrates along its axis to form several satellite droplets. This regime can often be highly chaotic and irreproducible in nature. Characteristic of the dilute polymer regime	
2	The second regime occurs upon increasing concentration or molecular weight when only a few satellites appear at the tail end	
3	Raising concentration or molecular weight further yields a single droplet without a tail. Characteristic behavior of dilute to semi dilute solutions. The ideal printing range	
4	At high concentration or molecular weight, the polymer solution becomes highly viscoelastic and the droplet does not detach and returns into the nozzle. Characteristic of the concentrated regime	

Figure 5.4 Details of four different regimes observed in inkjet drop generation behavior.

polymer concentration is too high, the formation of individual drops is prevented by the formation of a beads-on-a-string morphology.

## 5.7

### Zimm Interpretation for Polymers in High Shear Environments

When we consider polymer solution behavior at very high shear rates or at high extension rates, such as during the inkjet printing process, the polymer is not necessarily in its thermodynamically stable, Gaussian coil chain configuration and may undergo a transition to a rigid-rod-type configuration. This coil-stretch process can be quantified by considering the critical Weissenberg number ( $Wi$ ).  $Wi$  is the product of the relaxation time of a process and the applied stress:

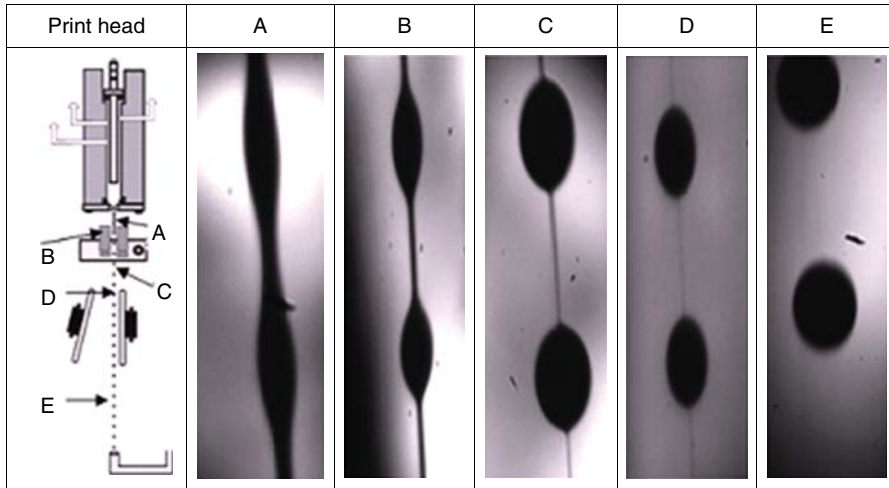


**Figure 5.5** The drop formation of a solution of high-molecular-weight PMMA in MEK in a CIJ printer. A commercial formulation would form individual drops at point B.

$Wi = \lambda \dot{\gamma}_{\text{crit}}$ . In this case, we consider the relaxation time of a polymer from a chain extended state ( $\lambda$ ) to its thermodynamically stable, Gaussian coil conformation and the shear rate ( $\dot{\gamma}_{\text{crit}}$ ). As most polymers have a distribution of molecular weights, and therefore a range of relaxation times, when the value of  $Wi$  in a printhead reaches 0.5, the highest molecular weight chains in formulation are in their coil–stretch conformation [10].

The Zimm relaxation time ( $\lambda_Z$ ) is chosen as it is the longest relaxation time for a fluid and is used in the analysis of inkjet systems.  $\lambda_Z$  is described by Eq. (5.5):

$$\lambda_Z = \frac{\eta_s \cdot [\eta] \cdot M_W}{RT} \quad (5.5)$$

where  $[\eta]$  is the intrinsic viscosity,  $\eta_s$  is the solvent viscosity,  $M_W$  is the weight average molecular weight,  $R$  is the Gas constant, and  $T$  is the absolute temperature. This type of analysis is widely used to explain polymer behavior and indeed degradation in high shear environments such as exposure to elongational flow and ultrasound [38–40]. When a polymer undergoes its coil–stretch transition due to the application of high shear or elongational flow, the shear stress is then placed on the polymer backbone and there is also an entropic driving force for the polymer to return to a thermodynamically stable coil configuration. This can result in the polymer undergoing irreversible molecular weight degradation.

## 5.8

### Printability of Polymer-Containing Inkjet Fluids

Printability of inkjet fluids can be predicted to a first approximation by considering the Weber number ( $We$ ) and the Reynolds number ( $Re$ ). The Weber number is

important in the early stage of drop generation/ejection where the interplay of forward inertia and surface tension is important and the Reynolds number in the middle to latter stages (while the drop is in flight) where the interplay with the viscoelasticity of the ligament is critical.

$$We = \frac{\rho v^2 L}{\sigma} \quad (5.6)$$

$$Re = \frac{\rho v L}{\eta} \equiv \frac{v L}{\nu} \quad \text{as} \quad \nu = \frac{\eta}{\rho} \quad (5.7)$$

where  $\rho$  is the density,  $\sigma$  is the surface tension,  $v$  is the drop velocity,  $\eta$  is the dynamic viscosity,  $\nu$  is the kinematic viscosity, and  $L$  is a characteristic length (often drop length). Fromm carried out a simulation work that predicted inkjet drop behavior and drop morphology for solutions with  $Re/We > 2$ , but did not explicitly state printability conditions or printing ranges [41]. This work was expanded by Reis and Derby, using the Ohnesorge number ( $Oh$ ) to predict drop behavior in flight and give a range of values of  $Oh$  for which inkjet printing is possible [42, 43]. Use of  $Oh$  has the advantage that the drop velocity dependence is removed.

$$Oh = \frac{\sqrt{We}}{Re} = \frac{\eta}{\sqrt{\rho \sigma L}} \quad (5.8)$$

It was found through fluid dynamics simulations and printing studies of fluids with different physical properties that, within the range  $0.1 < Oh < 1$ , DOD printing is possible. When  $Oh > 1$ , viscous dissipation within the liquid prevents drop formation, and if  $Oh < 0.1$ , the balance between surface tension and viscosity results in the liquid breaking into a series of satellite drops rather than a single drop as desired. In some publications, the inverse of the Ohnesorge number ( $Z$ ) is used to describe printability ranges. In practice, systems in which  $Oh$  is much less than 0.1 are printable so long as the satellites merge with the main droplet.

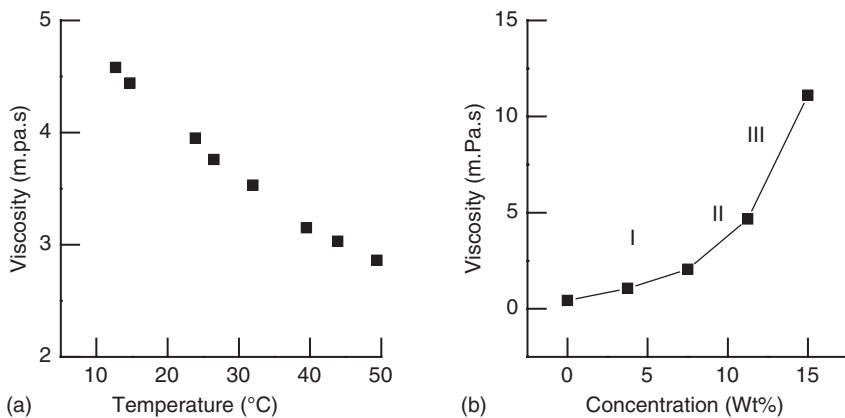
The majority constituent of the ink is the solvent, and the density of the ink will not be largely affected by polymeric or other additives. The generally recognized surface tension range for inkjet formulation is 20–50 mNm<sup>-1</sup>. This is in the general range for the surface tension of organic solvents commonly used for ink jet formulations (xylene, toluene, ethanol, diethylphthalate (DEP), MEK) with the most linear polymers not being surface-active to a great extent. Aqueous inkjet fluids are controlled to be within the surface tension limits by the addition of small amounts of cosolvent and/or surfactants. The characteristic length ( $L$ ) will be determined by nozzle geometry rather than any physical effects due to polymer concentration. Therefore, three out of four ( $L$ ,  $\rho$ , and  $\sigma$ ) of the constituents of the Ohnesorge number are largely insensitive to the presence of polymers in solution. However, even vanishingly small quantities of polymer solutions can significantly change the viscosity of an ink formulation. It can be shown that a high-viscosity solution will not fulfill the printability conditions imposed by the Ohnesorge number. This will result in unprintable solutions, nozzle blockages, or problems with print quality. Furthermore, polymer solutions in high shear environments such

as an inkjet head can also display non-Newtonian behavior resulting in differing transient viscosity value when compared to their zero shear viscosity [44].

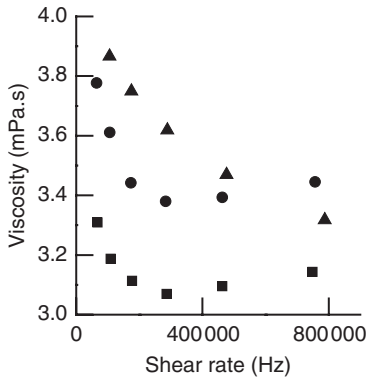
Polymer solution viscosity varies with solution temperature with an Arrhenius-type profile shown in Figure 5.6a for Polymethyl methacrylate (PMMA) ( $M_w = 90$  kDa) in MEK. The viscosity–temperature profile is important for both DOD and CIJ systems. Many DOD systems will have a heating element in the printhead to ensure that the solution viscosity is at its optimum for print performance. Indeed, some polymer-based inks have an optimum printing performance range at extremely small viscosity ranges, which is a major formulation and printhead design challenge to ensure good-quality print. Analysis of variation in viscosity is vital for CIJ systems that run in an industrial setting with inherent variations in temperature. These printers contain an inline viscometer with a preprogrammed viscosity-temperature curve, as shown in Figure 5.6a. If the ink becomes too viscous, additional solvent (makeup) is automatically added from the solvent reservoir; if it is too thin, the ink is run through the print-head until the viscosity regains its predefined viscosity-temperature characteristics.

Figure 5.6b shows the viscosity-concentration range for the same PMMA ( $M_w = 90$  kDa) shown in the viscosity-temperature graph (a). It can be seen that the three regimes of polymer solutions discussed in the main text are represented on the graph. Drop-on-demand printing is limited to regime I with CIJ printing formulations often falling in the semidilute concentration range.

The previous discussions about polymer solution viscosity pertain specifically to polymers in low shear environments less than about  $100\text{ s}^{-1}$ . However, the inkjet printing process imposes shear rates of the order of magnitude of  $10^5\text{--}10^6\text{ s}^{-1}$ . Although the rheology of inks during inkjet printing will be fully explored in Chapter 13, the perturbation and subsequent relaxation of the polymer conformation in high shear flows can affect the viscosity of a polymer solution and thus the printability. Investigation of the high shear rheology of low viscosity fluids is typically beyond the range of conventional mechanical



**Figure 5.6** (a) The viscosity-temperature curve for a solution of 10 Wt% PMMA with  $M_w$  of 90 kDa in MEK. (b) Viscosity-concentration profiles for PMMA with  $M_w$  of 90 kDa in MEK.



**Figure 5.7** The shear-dependent viscosity of solutions of PMMA with  $M_w$  of 90 kDa (▲), 310 kDa (●), and 468 kDa (■), respectively.

rheometers. However, recent advances using microelectromechanical systems (MEMSs) allow the shear ranges found in inkjet printing to be investigated in a controlled laboratory environment [44].

It is found that, when high-molecular-weight linear PMMA 310 and 468 kDa are exposed to shear rates up to  $2 \times 10^5 \text{ s}^{-1}$ , the viscosity of the polymer solution drops. This shear thinning behavior is very common in polymer solutions and is the result of polymer chains disentangling, slightly distorting, and lining up along the flow field. At shear rates greater than  $2 \times 10^5 \text{ s}^{-1}$ , shear thickening behavior is observed as the polymer chains undergo the coil–stretch transition resulting in a larger hydrodynamic size of polymers in solution. This increases association between the polymer chains in a “log-jam” effect and the viscosity of the solution increases [44] (Figure 5.7).

## 5.9

### Simulation of the Inkjet Printing of High-Molecular-Weight Polymers

Due to the high viscosities and non-Newtonian behavior of high-molecular-weight polymer solutions, it is found that there is an inverse relationship between the maximum printable concentrations of polymer solution and the molecular weight [10]. This relationship is shown in Figure 5.8.

The Zimm-type model for polymers in solution can be used to explain the concentration limits observed in the printing of high-molecular-weight polymers. Studies by Hoath *et al.* [45] and McIlroy *et al.* [46] used a finitely extensible nonlinear elastic model (FENE) to investigate the conformation of polymers during the jetting process. These methods can be used both to explain the concentration limits of the printing of polymer solutions and to provide insight into the degradation of polymers during the inkjet printing process.

It can be seen in Figure 5.8 that the maximum printable concentrations of polymer solutions can be split into three distinct regimes. These reflect the different polymer behavior that is encountered in high shear systems across a range of molecular weights. In regime I (molecular weight range  $< 300 \text{ kDa}$ ), the polymers

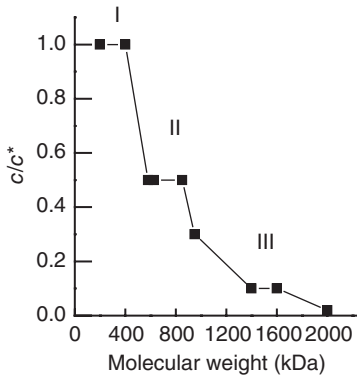


**Figure 5.8** The maximum printable reduced concentrations for polystyrene of varying molecular weights in a Dimatix DMP system.

are jetted in their thermodynamically stable coil conformation, making the limiting factor the low shear viscosity of the formulation. The transition from regime I to regime II (molecular weight range 300–800 kDa) is when the critical Weissenberg number for the jetting of the polymeric ink is about 0.5. This occurs when 50% of the polymers are in their chain extended state, as opposed to a thermodynamically stable coil conformation. As mentioned previously, a rigid-rod-type polymer will occupy a larger volume in solution as compared to a coil conformation. This will increase the probability of either associations between adjacent chains or a “log-jam” type effect. Thus, the limiting factor in the polymer printability shifts from its low shear behavior to its high shear viscoelastic properties in regime II [45, 46].

During the transition between printing regime II and III (molecular weight range 800–2000 kDa), the limiting factor is the extensibility of the polymer chain. At these high molecular weights, all polymers will be in their rigid rod orientation. The result is an even greater log-jam effect further limiting the maximum possible concentration of polymers as compared to a mixture of Gaussian coils and rigid-rod-type polymers in regime II. An important result from the simulation shows exactly when polymer degradation occurs during the printing process. McIlroy *et al.* [46] provide a rigorous argument that the coil–stretch transition does not occur during the flight of the drop or the contraction of the ligament into the main drop after pinch-off. The drop decelerates very rapidly after ejection from the nozzle, the critical shear rate rapidly drops to below  $\dot{\gamma}_{\text{crit}}$ , and the polymer returns rapidly to its stable coil configuration. This shows that the polymer is in a high stress environment only when it is in the printhead undergoing a compressional elongation flow.

## 5.10

### Molecular Weight Stability of Polymers during DOD Inkjet Printing

It is well documented that above  $\dot{\gamma}_{\text{crit}}$ , there is a further critical shear rate  $\dot{\gamma}_{\text{deg}}$ , which will cause the polymer to snap given a critical residence time in this high

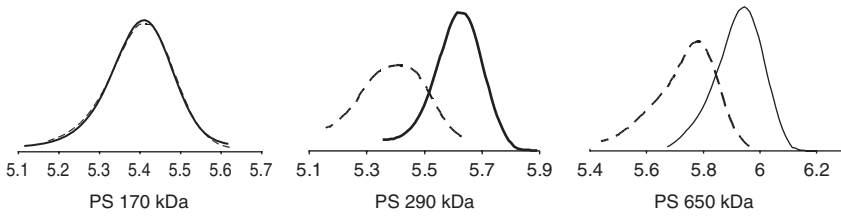


**Figure 5.9** The change in molecular weight distribution (or not) for samples of polystyrene  $M_w = 170, 290,$  and  $650$  kDa.

shear environment. As polymer molecular weight increases,  $\dot{\gamma}_{\text{crit}}$  and  $\dot{\gamma}_{\text{deg}}$  converge. At a critical molecular weight (about  $5 \times 10^6$  kDa), it is not possible for a polymer to undergo its coil–stretch transition without undergoing chain scission. In elongational flow experiments, exposure of polymer to high elongational flow rates is shown to degrade monodisperse polymers centrosymmetrically and polydisperse samples randomly. These elongational flow results are strikingly similar to that observed in DOD printing of high-molecular-weight polymers [10, 38, 39].

Before publication by Al-Alamry *et al.* [10], the assumption was that high-molecular-weight polymers were unaffected by the inkjet printing process. However, it was found that in a molecular weight range of about 200–1000 kDa, polymers are susceptible to molecular weight degradation below a concentration limit of  $c/c^*$  of 0.15. The observed molecular weight degradation is dependent on the nature of the polymer molecular weight distribution and the printhead geometry. Examples of molecular weight distributions of various high-molecular-weight polymers before and after jetting by DOD methods are shown in Figure 5.9.

Polymers below 200 kDa, which incidentally can be printed above their overlap concentration, show no molecular weight degradation when printed by DOD methods. Monodisperse polymers (with polydispersity index (PDI)  $< 1.3$ ) of molecular weight between 200 and 1000 kDa after inkjet printing using a Dimatix DMP printer (average drop speed  $6\text{--}10\text{ ms}^{-1}$ , nozzle diameter  $23\text{ }\mu\text{m}$ , shear rate about 400 kHz) show centrosymmetrical degradation, that is, the chain snaps in the middleweight. This we interpret as a Zimm-type model with the polymer undergoing its coil–stretch transition during the printing process as the ink is fired out of the printhead, with the elongational forces then focused on the center of the polymer chain after the polymer undergoes its coil–stretch transition resulting in the controlled snapping of the polymer at the center. It must be noted that polymers of molecular weight greater than 1000 kDa are stable with respect to the inkjet printing process. To degrade under elongational flow, the polymer must be exposed to the critical elongation flow for a critical residence time, and these larger molecules do not spend enough time in the flow field to undergo the coil–stretch transition and therefore do not degrade. This is not too helpful for the formulation of degradation-resistant high-molecular-weight polymeric inks as the maximum printable concentrations of polymers with molecular weight greater than 1000 kDa are vanishingly small.

When more polydisperse systems of both PMMA and Polystyrene (PS) were printed, the observed degradation was random. This suggests that in polydisperse systems, the degradation is not the result of elongational effects. The polymers relaxing back to their stable coil conformation (which occurs in a large range of times for polydisperse systems due to the differing molecular weights of the constituent macromolecules) would result in randomly overlapping polymer chains in solution with potentially strained chain orientations, which result in the observed random degradation.

A further similarity to well-documented polymer degradation in elongational flow is that the monodisperse systems are less susceptible to degradation in high shear environments. When monodisperse PS is printed using a system with less constricted printhead geometry (MicroFab: average drop speed  $1-4 \text{ ms}^{-1}$ , nozzle diameter  $50 \text{ }\mu\text{m}$ , shear rate about  $150\,000 \text{ s}^{-1}$ ), there is no change in molecular weight distribution. However, polydisperse systems are still susceptible to flow-induced degradation using the MicroFab system. Irrespective of polydispersity, two passes of the solutions through a DOD head will result in a polymer being degraded to a stable molecular weight distribution with respect to DOD printing.

A critical residence time in a flow field with a shear rate above  $\dot{\gamma}_{\text{crit}}$  is required for polymer degradation to occur. This demonstrates that polymer degradation occurs inside the printhead and furthermore is not a simple function of high shear. The printhead design plays a major role in the stability of polymeric inks. The Dimatix DMP head features a sudden contraction, whereas the MicroFab has a cone-shaped ink chamber tapering gradually in diameter up to the printhead. This shows that a compressional elongational flow in the printhead is required to degrade the polymers rather than just a high shear rate. Experimental data obtained from printing high-molecular-weight polymers using CIJ systems also support this hypothesis [47].

### 5.11

#### Molecular Weight Stability of Polymers during CIJ Printing

As stated previously in this book, DOD systems only produce printing drops when they are required to be deposited on the substrate. These polymers are only exposed to the high shear environments in the printhead once. In contrast, CIJ imposes multiples high shear environments: the printhead, pumps, and filters that constitute the ink management system. The ink formulation must be resilient to not just a single pass through a single high shear environment as in DOD but thousands of passes across a timescale of hundreds of hours.

Molecular weight degradation was first reported by Wheeler *et al.* in 2014. This manifests as an increase in solid content of the polymer ink over a timescale of hundreds of hours (thousands of complete statistical passes of the ink through the head). As the ink viscosity is most affected by the highest molecular weight chains in the molecular weight distribution, it shows that there is polymer degradation occurring in CIJ systems preferentially degrading the highest molecular weight chains, Figure 5.10. Furthermore, as there is a steady increase in solid contents,



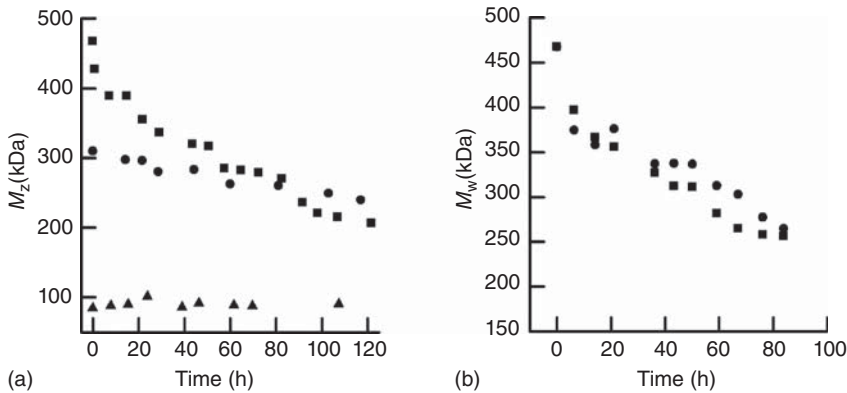


**Figure 5.10** (a) The development in molecular weight of three PMMA formulations of  $M_w$  468 kDa (■), 310 kDa (●), and 90 kDa (▲) in MEK with CIJ printing time. (b) The development of molecular weight with

the time of formulation of a PMMA of  $M_w$  468 kDa in a production CIJ printer (■) and modified CIJ system with the printhead removed (●).

there is a different degradation mechanism in operation in the CIJ systems when compared to the two-pass total degradation observed in DOD systems [10, 47].

The observed molecular weight degradation of three PMMA formulations is shown in Figure 5.10a. The most rapid drop in molecular weight is observed for the highest molecular weight PMMA in the first 15 h of printing time, further demonstrating the preferential degradation of the highest molecular weight chains. Degradation is also observed for the medium-molecular-weight PMMA, after about 100 h printing time, the molecular weights of both formulations converge. The degraded polymer solutes of the ink show an increase in PDI with time showing a random degradation mechanism, that is, they are being sequentially depolymerized at various points along the chain length in many steps rather than the single specific centrosymmetric degradation process shown in the DOD printing of monodisperse polymers. It can also be seen that there is a molecular weight limit below which degradation is not observed in CIJ systems; a formulation of PMMA of molecular weight of 90 kDa was unaffected by the CIJ printing process. This is analogous to DOD printing and other high shear systems such as elongational flow or exposure to ultrasound; below a critical molecular weight, polymers are not degraded, which further strengthens the argument for a Zimm-type model to be applicable to both CIJ and DOD systems. It must be noted that all three of these formulations are well above the overlap concentration, whereas degradation is suppressed at higher concentrations in DOD printing systems. The design of CIJ systems includes many more high shear environments than a DOD printhead, and (nonintuitively) it is found that the main cause of polymer degradation in CIJ systems is not the jetting process (which shows an equivalent shear rate to DOD heads but has printhead configurations with larger nozzle geometry and fast drop velocity) but passing through the pumps in the CIJ ink system, Figure 5.10b. This adds further experimental

evidence to the simulation results that show that a high shear rate is not sufficient to cause polymer degradation in inkjet printing but an elongational flow coupled with a constriction is required to degrade polymers during printing [47].

## 5.12

### Molecular Weight Stability of Associating Polymers During DOD Inkjet Printing

Molecular weight stability studies have been further extended to galactomannan heterogeneous polysaccharides, Figure 5.11. These polymers comprise a mannose backbone with galactose side groups (more specifically, a 1,4-linked beta-D-mannopyranose backbone with branch points from their 6-positions linked to alpha-D-galactose, i.e., 1,6-linked alpha-D-galactopyranose). In this section, we consider the printing behavior of *Dimorphandra gardneriana* Tul polysaccharide (DM), and the results can be considered as representative of the inkjet behavior of polysaccharides, as similar results have been obtained for other related polymers [48].

There are many reports regarding the rheology of galactomannan and due to their complete coil–stretch polymer transition in the dilute to semidilute regimes due to the low barrier to free rotation around the ether linkage. As a consequence of their configuration in solution and the many sites along the polymer backbone allowing for the formation of hydrogen bonding interactions between polymer chains, they form viscous solutions or gels. Consequently, printing is restricted to formulations with  $c/c^* \leq 0.25$  as higher concentrations are not printable [48].

When jetted through a MicroFab printhead at very dilute concentrations,  $c/c^* < 0.1$ , molecular weight degradation is observed for DM. A dramatic single-pass decrease in the molecular weight distribution is observed in Figure 5.11. The calculated ratio of  $M_w$  before printing to  $M_w$  after printing is about 30, and that of  $M_n$  before printing to  $M_n$  after printing is  $>100$ . Aqueous GPC of associating polymer chains is not as accurate as the measurements carried out in organic solvents of nonassociating polymers due to the potential for the formation of large aggregates and the difficulty in differentiating these aggregates from single large polymer chains. These results should, therefore, be considered indicative rather than absolute, although it is clear there is a massive change in molecular weight of the system. These observations are not consistent with either centrosymmetric bond scission in the case of monodisperse polymer or random scission due to entanglement observed in the printing of polydisperse polymers. It is unlikely that this is a consequence in the difference in bond dissociation energies of C–C main chain in PS and PMMA,  $\Delta H^\circ \approx 330 \text{ kJ mol}^{-1}$  against C–O–C in galactomannan polysaccharides  $\Delta H^\circ \approx 340 \text{ kJ mol}^{-1}$ , which are of the same order of magnitude. However, a typical O–H ··· H hydrogen bond is of the order of  $21 \text{ kJ mol}^{-1}$ , and we believe that the significant decrease in molecular weight is a consequence of disaggregation through the breaking of H-bonds with a possible contribution due to the main-chain C–O–C bond rupture [48].

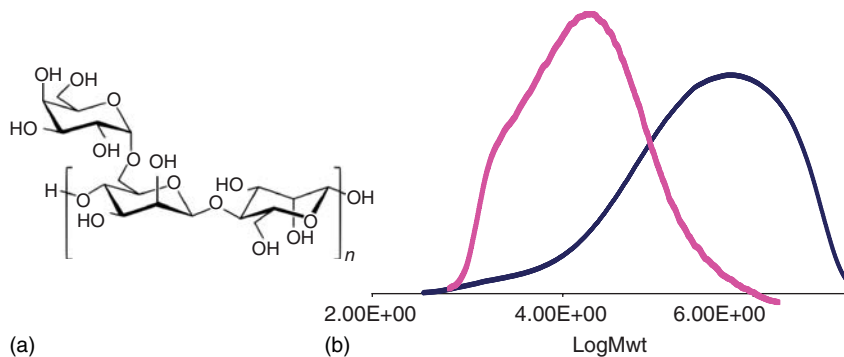


**Figure 5.11** (a) a segment of galactomanan showing mannose backbone ( $[\cdot\cdot]_n$ ) with a branching galactose unit. (b) before (undegraded MWt) and after single-pass

jetting (degraded MWt) for DM polysaccharide at  $c/c^* = 0.25$  at 50 V using a MicroFab printhead at 25 °C.

## 5.13

### Case Studies of Polymers in Inkjet Formulation

In this section, we present representative state case studies of the use of polymers in inkjet formulations. We present data for the inkjet printing of branched systems, conductive polymers, and polymer graphene composites. These will highlight the interplay between innovative polymer chemistry, polymer physics, and additive manufacture by inkjet printing.

#### 5.13.1

##### Role of Polymer Architecture

The polymeric inks that have been referred to, thus far, in this chapter are solutions of linear polymers. These systems face formulation challenges both to prevent polymer degradation and increase the maximum printable weight fraction possible. Obviously, it would be preferable to increase the maximum printable concentration of polymers in ink formulations as this would cut down on printing time as more materials can be deposited in one printing pass, and if a functional material is being deposited, maintaining the molecular weight (and, therefore, the physical properties) is vital.

De Gans *et al.* [49] first investigated the inkjet printing of star polymers and consideration of the relaxation behavior under high shear. Ligament formation was shown to be affected by the polymer architecture with the relaxation rate of the coil–stretch transition being that of the individual arm length and not the overall polymer chain. The arms will have significantly shorter relaxation times, so chain extensional effects are less prevalent than in the linear polymer of equivalent overall molecular weight, and a greater concentration of star polymer could be printable as a consequence.

## 5.13.2

**Inkjet Printing of PEDOT:PSS**

During the past decade, there was a search for low-cost solar cell devices as an alternative to expensive and inflexible inorganic photovoltaics; a further challenge is the rapid manufacture of large-area electronics. Inkjet printing of organic conducting polymers is a growing area of research, which aims to address these issues. In this case study, we focus on poly(3,4-ethylenedioxythiophene) polystyrene sulfonate (PEDOT:PSS). The advantages of this polymer are: good conductivity, high processability, low redox potential, and high transparency. It has been widely investigated in a range of flexible electronic applications [7, 50].

Hoath *et al.* have shown that the print quality of PEDOT:PSS solutions is very high due to the lack of satellite drops formed at high applied voltages [51]. As described previously, non-Newtonian behavior often results in inkjet fluids in the shear ranges found in a DOD head; PEDOT:PSS solutions when investigated using high shear rheological techniques show pronounced shear thinning. However, the interesting behavior that imbues PEDOT:PSS with such excellent printability is the very fast recovery of viscosity and elasticity after printing; this prevents ligament rupture and the formation of satellite drops, which negatively affect print quality. As the formation of satellite drops is prevented by the high shear rheology of the polymer solution, it is possible to use PEDOT:PSS solutions in high-resolution inkjet applications and demonstrate how knowledge of the fundamental rheology of inkjet inks can be used to improve print quality [51].

The drying behavior of PEDOT:PSS after surface deposition is critical in achieving maximum conductivity. This requires an even coating of functional material and low surface roughness. This is accomplished in PEDOT:PSS formulations by the use of two different solvents with differing surface tensions. The Marangoni effect results in an even drying of the printed drops forming a continuous smooth film, which is vital for high electronic performance. A full investigation and description of drop drying in inkjet printing are given in Chapter 10. The interplay between surfactant, polymer, and solvent is important for the formulation and is an excellent example of the formulation challenges to produce an ink with good printing performance while still fulfilling its end-use application. To form a conductive film of PEDOT:PSS, it is necessary for the polymer chains to swell and aggregate. This can be mediated by solvent choice and surfactant concentration. However, too high a concentration of surfactant increases the risk of conductive network dissipation, which can impair the electronic properties of the printed film, and too high a degree of solvent swelling can result in diminution of polymer loading in the ink formulation [7, 50, 52].

## 5.13.3

**Inkjet Printing of Polymer–Graphene and CNT Composites**

Graphene and carbon-based 3D materials such as carbon nanotubes (CNTs) are a current hot research topic of promising potential in a wide range of

application areas [53, 54]. However, their solution processability and solubility remain low, as does the number of nonspecialized methods of purification. Nevertheless, graphene electronics such as sensors have been fabricated using inkjet printing methods, often with polymers playing major roles in the formulations such as dispersants but also showing interesting graphene–polymer interactions resulting in synergistic properties, which improve the electronic properties of the printed composites [55, 56].

Thin-film electrodes were fabricated using dispersions of graphene and polyaniline in water. The formulation of these inks requires a long sonication step, which must be approached with caution in polymer solutions as polymers above a critical molecular weight are susceptible to degradation under sonication. Due to host–guest interactions between the polymer and graphene, the conductance of the composite material increases from  $10^{-9}$  to  $3.67 \text{ S cm}^{-1}$ . A further example of the utilization of host–guest interactions of graphene and conducting polymers was the fabrication, by inkjet methods, of ammonia sensors from graphene dispersed in PEDOT:PSS solutions:  $\pi$ – $\pi$  interactions between graphene and PEDOT:PSS produced sensors displaying sensitivity down to 25 ppm of ammonia [55, 56].

## References

- Magdassi, S. (2010) *The Chemistry of Inkjet Inks*, Chapter 1, World Scientific Publishing, New York, pp. 6–15.
- Smith, R.E. and Tiederman, W.G. (1991) The mechanism of polymer thread drag reduction. *Rheol. Acta*, **30**, 103–113.
- Xu, D., Sanchez-Romaguera, V., Barbosa, S., Travis, W., de Wit, J., Swan, P., and Yeates, S.G. (2007) Inkjet printing of polymer solutions and the role of chain entanglement. *J. Mater. Chem.*, **17**, 4903–4907.
- Xue, C.H., Shi, M.M., Chen, H.Z., Wu, G., and Wang, M. (2006) Preparation and application of nanoscale microemulsion as binder for fabric inkjet printing. *Colloids Surf., A*, **287**, 147–152.
- Żołek-Tryznowska, Z. and Izdebska, J. (2013) Flexographic printing ink modified with hyperbranched polymers: Boltorn<sup>TM</sup> P500 and Boltorn<sup>TM</sup> P1000. *Dyes Pigm.*, **96**, 602–608.
- Merrington, J., Hodge, P., and Yeates, S.G. (2006) A high-throughput method for determining the stability of pigment dispersions. *Macromol. Rapid Commun.*, **27**, 835.
- Eoma, S.H., Senthilarasu, S., Uthirakumar, P., Yoon, S.C., Lim, J., Lee, C., Lim, H.S., Lee, J., and Lee, S. (2009) Polymer solar cells based on inkjet-printed PEDOT:PSS layer. *Org. Electron.*, **10**, 536–542.
- Saunders, R.E., Gough, J.E., and Derby, B. (2008) Delivery of human fibroblast cells by piezoelectric drop-on-demand inkjet printing. *Biomaterials*, **29**, 193–203.
- Clasen, C., Phillips, P.M., Palangetic, L., and Vermant, J. (2012) Dispensing of rheologically complex fluids: the map of misery. *AIChE J.*, **58** (10), 3242–3255.
- Al-Alamry, K., Nixon, K., Hind, R., Odel, J.A., and Yeates, S.G. (2011) Flow induced polymer degradation during ink-jet printing. *Macromol. Rapid Commun.*, **32** (3), 316–320.
- Stevens, M.P. (1999) *Polymer Chemistry An Introduction*, Oxford University Press, p. 10.
- Flory, P.J. (1971) *Principles of Polymer Chemistry*, Cornell University Press, Ithaca, NY, pp. 495–505.
- Cowie, M.G. (1991) *Polymers: Chemistry and Physics of Modern Materials*, 2nd

- edn, Blackie Academic and Professional, London, pp. 5–8.
14. Gedde, U.W. (1995) *Polymer Physics*, Chapman & Hall, London, pp. 10–25.
  15. Ohno, K., Tsujii, Y., Miyamoto, T., and Fukuda, T. (1998) Synthesis of a well-defined glycopolymer by nitroxide-controlled free radical polymerization. *Macromolecules*, **31**, 1064–1069.
  16. Crivello, J.V., Falk, B., and Zonca, M.R. (2004) Photoinduced cationic ring-opening frontal polymerizations of oxetanes and oxiranes. *J. Polym. Sci., Part A: Polym. Chem.*, **42**, 1630–1646.
  17. Hadjichristidis, N., Pitsikalis, M., Pispas, S., and Iatrou, H. (2001) Polymers with complex architecture by living anionic polymerization. *Chem. Rev.*, **101**, 3747–3792.
  18. Pang, K., Kotek, R., and Tonelli, A. (2006) Review of conventional and novel polymerization processes for polyesters. *Prog. Polym. Sci.*, **31**, 1009–1037.
  19. Braunecker, W.A. and Matyjaszewski, K. (2007) Controlled/living radical polymerization: features, developments, and perspectives. *Prog. Polym. Sci.*, **32**, 93–146.
  20. Smith, A.E., Xu, X., and McCormick, C.L. (2010) Stimuli-responsive amphiphilic (co)polymers via RAFT polymerization. *Prog. Polym. Sci.*, **35**, 45–93.
  21. Lee, I. and Bates, F.S. (2013) Synthesis, structure, and properties of alternating and random poly(styrene-*b*-butadiene) multiblock copolymers. *Macromolecules*, **46**, 4529–4539.
  22. Kato, K., Uchida, E., Kang, E., Uyama, Y., and Ikada, Y. (2003) Polymer surface with graft chains. *Prog. Polym. Sci.*, **28**, 209–259.
  23. Isaure, E., Cormack, P.A.G., and Sherrington, D.C. (2004) Synthesis of branched poly(methyl methacrylate)s: effect of the branching comonomer structure. *Macromolecules*, **37**, 2096–2210.
  24. Xue, L., Agarwal, U.S., Zhang, M., Staal, B.B.P., Muller, A.H.E., Bailly, C.M.E., and Lemstra, P.J. (2005) Synthesis and direct topology visualization of high-molecular-weight star PMMA. *Macromolecules*, **38**, 2093–2100.
  25. Flory, P.J. (1971) *Principles of Polymer Chemistry*, Cornell University Press, Ithaca, NY, pp. 273–283.
  26. Trathnigg, B. (1995) Determination of MWD and chemical composition of polymers by chromatographic techniques. *Prog. Polym. Sci.*, **20**, 615–650.
  27. Kostanski, L.K., Keller, D.M., and Hamielec, A.E. (2004) Size-exclusion chromatography—a review of calibration methodologies. *J. Biochem. Biophys. Methods*, **58**, 159–186.
  28. Castignolles, P., Graf, R., Parkinson, M., Wilhelm, M., and Gaborieau, M. (2009) Detection and quantification of branching in polyacrylates by size-exclusion chromatography (SEC) and melt-state <sup>13</sup>C NMR spectroscopy. *Polymer*, **50**, 2373–2383.
  29. Rubenstein, M. and Colby, R.H. (2008) *Polymer Physics*, Oxford University Press, Oxford, pp. 173–183.
  30. Flory, P.J. (1971) *Principles of Polymer Chemistry*, Cornell University Press, Ithaca, NY, p. 425.
  31. Rubenstein, M. and Colby, R.H. (2008) *Polymer Physics*, Oxford University Press, Oxford, p. 34.
  32. Daoud, M., Cotton, J.P., Farnoux, B., Jannink, G., Sarma, G., Benoit, H., Duplessix, R., Picot, C., and de Gennes, P.G. (1975) Solutions of flexible polymers. Neutron experiments and interpretation. *Macromolecules*, **8** (6), 804–818.
  33. Doi, M. and Edwards, S.F. (1994) *The Theory of Polymer Dynamics*, Clarendon Press, Oxford, pp. 141–143.
  34. Rubenstein, M. and Colby, R.H. (2008) *Polymer Physics*, Oxford University Press, Oxford, p. 265.
  35. De Gennes, P.G. (1971) Reptation of a polymer Chain in the presence of fixed obstacles. *J. Chem. Phys.*, **55** (2), 572–579.
  36. Burke, J. (1984) *Solubility Parameters: Theory and Application*, AIC Book Paper Group Annual, vol. 3, p. 13, Oakland Museum, California.
  37. Castrejon-Pita, J.R., Morrison, N.F., Harlen, O.G., Martin, G.D., and Hutchings, I.M. (2011) Experiments and Lagrangian simulations on the formation of droplets in continuous mode.

- Phys. Rev. E: Stat. Nonlinear Soft Matter Phys.*, **83**, 016301.
38. Keller, A. and Odell, J.A. (1985) The extensibility of macromolecules in solution; a new focus for macromolecular science. *Colloid. Polym. Sci.*, **263**, 181–201.
  39. Muller, A.J., Odell, J.A., and Carrington, S. (1992) Degradation of Semidilute polymers in elongational flow. *Polymer*, **33**, 12.
  40. Suslick, K.S. and Price, G.J. (1999) Application of ultrasound to materials chemistry. *Annu. Rev. Mater. Sci.*, **29**, 295–326.
  41. Fromm, J.E. (1984) Numerical calculation of the fluid dynamics of drop-on-demand jets. *IBM J. Res. Dev.*, **28**, 322–333.
  42. Derby, B. and Reis, N. (2003) Inkjet printing of highly loaded particulate suspensions. *MRS Bull.*, **28**, 815–820.
  43. Reis, N., Ainsley, C., and Derby, B. (2005) Ink-jet delivery of particle suspensions by piezoelectric droplet ejectors. *J. Appl. Phys.*, **97**, 094903.
  44. Wheeler, J.S.R. (2015) Polymer degradation in inkjet printing. PhD thesis. University of Manchester.
  45. Hoath, S.D., Harlen, O.G., and Hutchings, I.M. (2012) Jetting behaviour of polymer solutions in drop-on-demand inkjet printing. *J. Rheol.*, **56**, 1109–1129.
  46. McLroy, C., Harlen, O.G., and Morrison, N.F. (2013) Modelling the jetting of dilute polymer solutions in drop-on-demand inkjet printing. *J. Non-Newtonian Fluid Mech.*, **201**, 17–28.
  47. Wheeler, J.S.R., Reynolds, S.W., Lancaster, S., Sanchez-Romanguera, V., and Yeates, S.G. (2014) Polymer degradation during continuous inkjet printing. *Polym. Degrad. Stab.*, **105**, 116–121.
  48. Wheeler, J., A-Alamry, K., Reynolds, S.W., Lancaster, S., Ricardo, N.M.P.S., and Yeates, S.G. (2014) Molecular weight degradation of synthetic and natural polymers during inkjet print. 2014 International Conference on Digital Printing Technologies, Vol. 4, pp. 335–338.
  49. De Gans, B.J., Xue, L.J., Agarwal, U.S., and Schubert, U.S. (2005) Ink-jet printing of linear and star polymer. *Macromol. Rapid Commun.*, **26** (4), 310–314.
  50. Correia, V., Caparros, C., Casellas, C., Francesch, L., Rocha, J.G., and Lanceros-Mendez, S. (2013) Development of inkjet printed strain sensors. *Smart Mater. Struct.*, **22**, 105028.
  51. Hoath, S.D., Jung, S., Hsiao, W.K., and Hutchings, I.M. (2012) How PEDOT:PSS solutions produce satellite-free inkjets. *Org. Electron.*, **13**, 3259–3262.
  52. Xiong, Z. and Liu, C. (2012) Optimization of inkjet printed PEDOT:PSS thin films through annealing processes. *Org. Electron.*, **13**, 1532–1540.
  53. Secor, E.B., Prabhumirashi, P.L., Puntambekar, K., Geier, M.L., and Hersam, M.C. (2013) Inkjet printing of high conductivity, flexible graphene patterns. *J. Phys. Chem. Lett.*, **4**, 1347–1351.
  54. Hu, B., Li, D., Manandharm, P., Fan, Q., Kasilingam, D., and Calvert, P. (2012) CNT/conducting polymer composite conductors impart high flexibility to textile electroluminescent devices. *J. Mater. Chem.*, **22**, 1598–1605.
  55. Xu, Y., Hennig, I., Freyberg, D., Strudwick, A.J., Schwab, M.G., Weitz, T., and Cha, K.C. (2014) Inkjet-printed energy storage device using graphene/polyaniline inks. *J. Power Sources*, **248**, 483–488.
  56. Seekaew, Y., Lokavee, S., Phokharatkul, D., Wisitsoraat, A., Kerdcharoen, T., and Wongchoosuk, C. (2014) Low-cost and flexible printed graphene–PEDOT:PSS gas sensor for ammonia detection. *Org. Electron.*, **15**, 2971–2981.





## 6 Colloid Particles in Ink Formulations

*Mohmed A. Mulla, Huai Nyin Yow, Huagui Zhang, Olivier J. Cayre, and Simon Biggs*

### 6.1

#### Introduction

The colors and brightness of ink deposits are a result of the presence of either molecular dyes or solid pigment particles in the ink formulations. This chapter presents the characteristics of both types of inks and subsequently focuses on pigment-based inks. For such inks, it is paramount to understand the behavior of the particles in suspension and the influence of the other components, of the formulation, on the stability of these particles. This relies on the knowledge of colloidal forces, which this chapter introduces along with the potential influence of the addition of polymers and other ink components. It also briefly describes the important characteristics of these systems.

#### 6.1.1

##### Colloids

No formal description exists for a colloid that fully covers all examples of such systems. However, it is generally accepted that a colloidal dispersion consists of one or more finely divided phases within another phase; for the finely divided phase(s), one or more of the key dimensions are less than 1  $\mu\text{m}$  in size.

Examples of colloids in inkjet inks include pigments polymer dispersions, and emulsions. In order to fully appreciate these systems, the general colloidal properties must be well understood.

#### 6.1.2

##### Inkjet (Complex) Fluids

Inkjet technology was developed in the 1970s and has been in commercial use since the 1980s [1]. Over the past 3–4 decades, continuous developments in the area have led to not only more complex ink formulations but also new nozzle geometries and new printing methods. The printing characteristics of an ink can therefore vary with the printhead type. For example, an ink that has good printing characteristics with a continuous inkjet printhead will most likely

behave differently in a drop-on-demand (DOD) printhead. Consequently, before developing any ink, the printhead technology to be utilized should be carefully considered, as this will dictate the appropriate characteristics required of the ink, such as viscosity and surface tension, among others. The substrate to be printed upon and its wetting characteristics for the ink must also be considered when choosing the ink, such that it will achieve the desired spatial deposition between individual deposited droplets.

Once the required characteristics are known, an ink can be designed by utilizing the appropriate components. These components can be broadly separated into two categories based on their roles within the system. The first group includes surfactants, solvents, and humectants, which are suitably chosen to provide an ink that preserves its properties over its lifecycle (including manufacture, storage, and printing). The second group consists of components used to effect the final deposit and as such can include dyes, pigments, polymers, and so on. The role of most of these components is introduced in Section 6.3. The following section, however, helps in differentiating the ink formulations based on the molecular dyes and those using solid pigments.

## 6.2

### Dyes versus Pigment Inks

Originally inks used for graphic printing were dye-based inks; which although have good print quality, typically have poor image durability [2]. In addition, water fastness, lightfastness, and weather fastness were very quickly highlighted as the weaknesses for these inks. Water fastness refers to the tendency for inks to run when wetted (unless printed on specially coated substrates). All prints, regardless of how they are produced, are susceptible to fading due to light (lightfastness) after a given period of time. Sunlight or UV light exposure is particularly responsible for this effect. Good weather fastness or good weatherability refers to prints that retain integrity against the elements.

Pigments, used in paints, plastics, and coatings, are known to be superior in this respect while producing a good quality final product [3]. The characteristics of pigments and the challenges associated with the dye-based inks led to developments of pigment inks. However, both types of inks offer some advantages and drawbacks as summarized in Table 6.1.

Dye-based inks are typically easier to formulate; there tends to be less of an issue corresponding to precipitation of solubilized dyes rather than aggregation of pigment particles. Through synthetic variations, the brightness and shades of dye-based inks can be very finely tuned to achieve good color variation. In addition, clogging of the nozzle is a rare occurrence. Dyed ink deposits generally have very good rub resistance with a glossy finish. However, they generally have poor water- and lightfastness and thus are typically not considered durable.

Pigmented inks are prepared by dispersing pigments between ~50 and 100 nm in the ink medium to produce a stable suspension [4]. Though, similarly to all colloidal systems, these inks are not thermodynamically stable, and need to be

**Table 6.1** A comparison of some properties of dye-based and pigment-based inks.

Property	Dyes	Pigments
Soluble in ink medium	✓	✗
Dispersed in ink medium	✗	✓
Chemically stable	✗	✓
Low clogging	✓	✗
Rub resistant (dry)	✓	✗
Color strength	✗	✓
Water fastness	✗	✓
Lightfastness	✗	✓
Restricted shades	✗	✓

kinetically stabilized against aggregation and sedimentation. Surfactants or polymer derivatives are often used to prevent particle aggregation through modification of the pigment surface. Despite creating stable suspensions, pigment based inks can still clog printing nozzles, particularly at high pigment concentrations. This is particularly true for current microjets, that can be as small as 10  $\mu\text{m}$  in diameter. Clogging due to high pigment concentrations or from the presence of large particles can cause irreversible damage to these jets. High pigment loading could be required in formulations using lightfast pigments, or for specific applications. Beyond the potential clogging issues, an increase in the solid content can also affect the viscosity of the dispersion. For adequate printhead filling and droplet ejection, a relatively low viscosity is required ( $\sim 1 - 20 \text{ mPa}\cdot\text{s}$ ).

All the aforementioned factors make ink formulation more challenging when using pigments, and as a result, a few influential characteristics of pigment inks typically need to be very well controlled, such as viscosity, particle stability, and surface tension. However, since pigments are insoluble in the application media, the water-fastness of pigment inks is generally superior to dye-based inks. Additionally, the brightness and color density of the final deposit can be manipulated by varying the pigment concentration. These factors all lead to a superior image quality [5–7].

In the following sections, we describe the general behavior of colloidal particles and, on this basis, provide an understanding of the stability of pigment-based inks. We discuss the influence other ink components can have on the pigment properties in suspension, particularly in the case of polymer additives. When introducing each of the typical components of ink formulations, we also briefly describe their roles in the formulation.

### 6.3

#### Stability of Colloids

In order to best understand the influence of different ink components on the pigment dispersion and its resulting characteristics in the printing process, it is

important to understand the general concepts of colloid dispersion stability (i.e., the pigments).

### 6.3.1

#### DLVO Theory

The Derjaguin, Landau, Verwey, and Overbeek (DLVO) theory, first developed in the 1940s, is the classical model of charged colloidal particle stability [8, 9]. It describes the interactions between particles in suspension through the balance of opposing forces acting on them. This model can be used to provide insight into whether a colloidal dispersion should be stable and over what time period we may expect to see significant aggregation.

As colloidal particles are generally small, they undergo Brownian motion, and a large number of particle collisions therefore occur over time. As two particles approach one another (at a distance between the particle surfaces defined as  $h$ ), according to DLVO formalism, they experience two opposing interactions: an attractive interaction due to van der Waals (vdW) forces acting between particles and an electrostatic repulsive interaction resulting from the buildup of a volume of counterions and co-ions near the charged surface of the particles (see Figure 6.1).

The combination of these forces determines whether the system is stable against aggregation of the particles coming into “contact.” In the following sections, we describe the origins of each force and the resulting net force acting on the particles.

### 6.3.2

#### van der Waals Attractive Force

Short-range vdW attractive forces are due to electric dipole fluctuations between neighboring particles and are a sum of all single interactions acting on the components of the particle cores. This attractive interaction is typically effective up to a separation distance,  $h$ , of  $0.1 \mu\text{m}$ . At larger distances, the attractive force decays rapidly due to retardation effects.

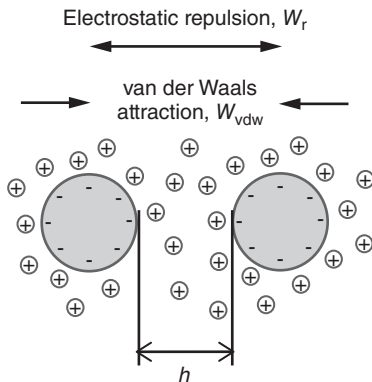


**Figure 6.1** Schematic of DLVO interactions experienced by two approaching colloidal particles.

The summation of all the interactions assumes pairwise additivity and is expressed for a net vdW interaction energy,  $W_{\text{vdW}}$ , for two spherical particles of radii,  $r_1$  and  $r_2$ , with smooth surfaces:

$$W_{\text{vdW}} = -\frac{A}{6} \left[ \frac{2r_1r_2}{a^2 - (r_1 + r_2)^2} + \frac{2r_1r_2}{a^2 - (r_1 - r_2)^2} + \ln \left( \frac{a^2 - (r_1 + r_2)^2}{a^2 - (r_1 - r_2)^2} \right) \right] \quad (6.1)$$

where  $a$  is the center-to-center distance between spherical particles,  $r_1$  and  $r_2$  are the radii of the two particles, and  $A$  is the Hamaker constant, which is material-dependent but typically within a range of  $10^{-21}$  and  $10^{-19}$  J.

Note that, as a result of the aforementioned definitions, the following relationship applies;

$$a = r_1 + h + r_2 \quad (6.2)$$

When the separation distance between particles is significantly smaller than the particle radius (i.e.,  $h \ll r_1$  or  $r_2$ ), Eq. (6.1) can be simplified to:

$$W_{\text{vdW}} = -\frac{Ar_1r_2}{6h(r_1 + r_2)} \quad (6.3)$$

For two equally sized spherical particles of radius,  $r$  this becomes:

$$W_{\text{vdW}} = -\frac{Ar}{12h} \quad (6.4)$$

### 6.3.3

#### Electrostatic Repulsive Force

When a particle is dispersed in an aqueous phase (such as aqueous mixtures of ethylene glycol – a typical ink-jet ink solvent), the particle may acquire a surface charge, which stems from dissociation of surface groups or adsorption of charged molecules/ions. The surface charge attracts counterions and co-ions from the surrounding bulk phase to restore the electroneutrality of the system within a specific volume around the particle surface. This is referred to as the *electrical double layer* and is schematically represented in Figure 6.2. The electrical double layer consists of two regions; (i) counter-ions closest to the particle surface are strongly bound to the surface. This is known as the *Stern layer* and corresponds to a volume of liquid that moves with the particle. (ii) A volume of loosely associated ions form the diffuse layer, which is constantly replenished as the particles undergo Brownian motion.

When two particles approach one another, the electric double layers of the respective particles will overlap. As the local concentration of ions in the overlap volume increases, the variation in concentration with the bulk phase induces a difference in osmotic pressure, which can force the particles apart. Provided the force induced by the electric double layers overlap is sufficiently high, this process will maintain particle stability against aggregation in the suspension. The strength of the repulsive interaction is dependent on the distance between the particles and the thickness of the electric double layer. This thickness is known as the *Debye screening length*,  $K^{-1}$ , which is defined in Eq. (6.5).

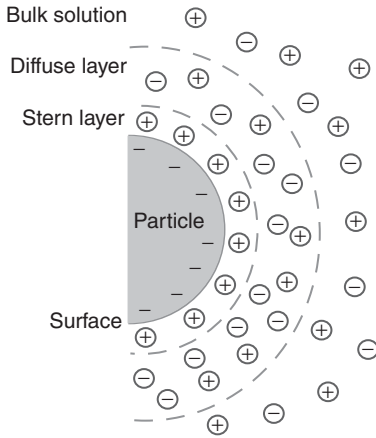


**Figure 6.2** Schematic of electrical double layer of a charged particle.

$$K^{-1} = \left( \frac{F \sum N_i z_i^2}{k_B T \epsilon_0 \epsilon_r} \right)^{1/2} \quad (6.5)$$

where  $F$  is the Faraday constant;  $N_i$  and  $z_i$  are the number density and valence of counterions of type  $i$ , respectively;  $k_B$  is the Boltzmann constant;  $T$  is the absolute temperature;  $\epsilon_0$  is the permittivity of vacuum; and  $\epsilon_r$  is the dielectric constant of medium.

Aside from the characteristics of the bulk phase in which the colloidal particles are suspended,  $K^{-1} = \kappa$  is highly dependent on the type and concentration of electrolytes present in the bulk phase. Indeed, as the concentration of electrolyte in the system increases, the ionic species are said to “screen” the surface charges of the particles, effectively decreasing the electric double layer thickness and allowing for particles to approach shorter distances before the layers overlap. As represented in Figure 6.3, this may allow for vdW attractive interactions to be strong enough at this distance to overcome the repulsive forces and bring the particles into contact to form aggregates.

The long-range electrostatic repulsion interaction energy,  $W_r$ , for two equally sized particles of radius  $r$  is represented by:

$$W_r = \left( \frac{64\pi k_B T r N_i \gamma^2}{\kappa^2} \right) e^{-\kappa h} \quad (6.6)$$

with

$$\gamma = \tanh \frac{ze\Psi}{4k_B T} \quad (6.7)$$

where  $e$  is the charge of an electron and  $\Psi$  is the particle surface potential.

#### 6.3.4

#### Stabilization of Colloidal Systems

Combining vdW and electrostatic repulsion interaction energies, the net interaction energy,  $W_T$ , between two equally sized particles dispersed in a liquid is thus

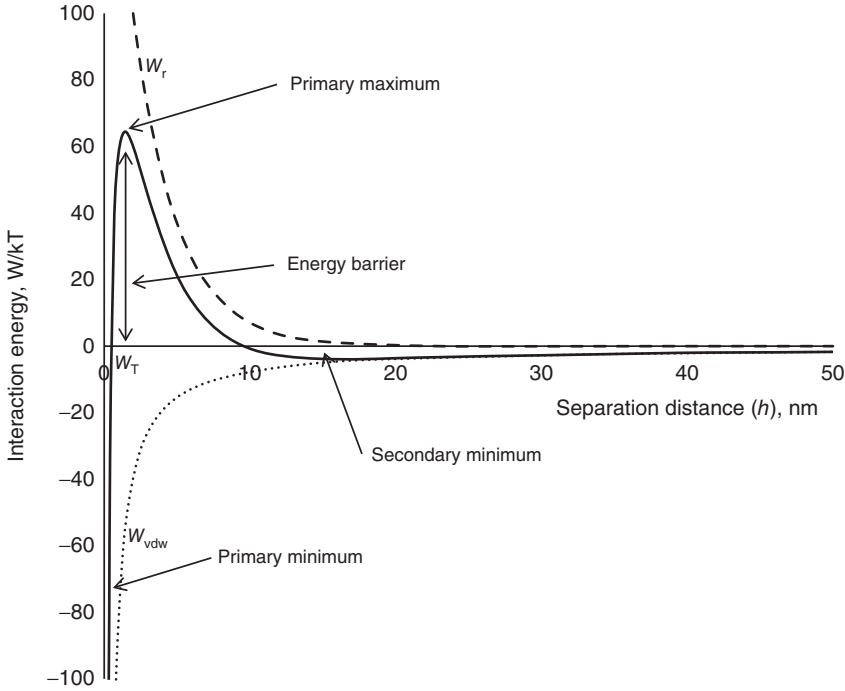


**Figure 6.3** Interaction potential for approaching spherical 150 nm silica particles with a surface potential of 40 mV in the presence of 10 mM electrolyte (according to DLVO theory).

defined by the DLVO theory as:

$$W_T = W_{vdw} + W_r = -\frac{Ar}{12h} + \left( \frac{64\pi k_B Tr N_i \gamma^2}{\kappa^2} \right) e^{-\kappa h} \quad (6.8)$$

This can be represented as a net interaction energy curve (see Figure 6.3). Conventionally, the attractive interactions are negative (dotted line), while the repulsive interactions are positive (dashed line).

The representation of a typical net interaction between two approaching colloidal particles in suspension (Figure 6.3 – read from right to left as the interparticle distance diminishes) indicates that at large interparticle distances, the particles remain stable. As the separation between particles reduces, both repulsive and attractive interactions gain intensity but with different rates so that as the particles approach each other, the net interaction goes through a small (secondary) minimum, a (primary) maximum and a deep (primary) minimum when the particles are close to contacting each other. If two colliding particles have sufficient kinetic energy to overcome the energy barrier, the particles will fall into the primary minimum region and form an irreversible aggregate. The height of this energy barrier determines how stable a colloidal dispersion is. For a stable dispersion over an extended period of time, the primary maximum must be at least  $10k_B T$ . In most

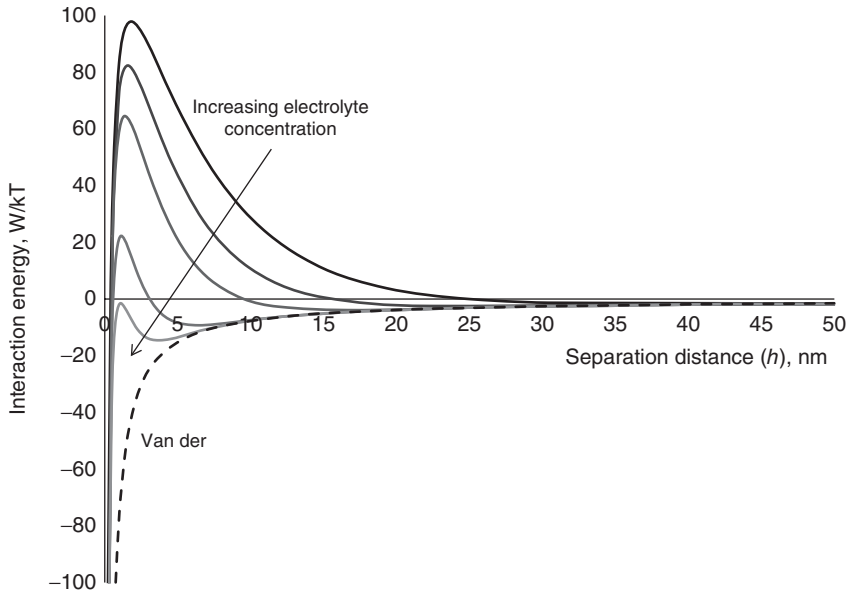


**Figure 6.4** Effect of electrolyte concentration on colloidal stability, calculated for 150 nm spherical silica particles with a surface potential of 40 mV. The salt concentrations used for these calculations are 0.0025, 0.005, 0.01, 0.04, and 0.08 M.

systems, a secondary minimum exists. Within this shallow minimum, the particle aggregation is weak and thus reversible; it can be easily overcome by applying a small amount of energy (e.g., agitation or sonication) to redisperse the particles.

The net interaction energy curve can be altered by modifying the environment in which the particles are suspended through changes in ionic strength (varies the electric double layer thickness), pH (affects the particle surface charge), or addition of surface active materials (also affects the particle surface charge). Typically, at low electrolyte levels and/or high surface charge densities, the electrostatic repulsive forces dominate the net interaction. As the electrolyte concentration increases and/or the surface charge density is lowered, the attractive vdW interaction dominates and induces particle aggregation. As an example, Figure 6.4 demonstrates the evolution of interaction energy profiles as a function of electrolyte concentration.

At a specific electrolyte concentration, the energy barrier against further particle–particle approach is zero, which induces a strong aggregation of the particles as the interaction energy falls into a deep minimum. The electrolyte concentration at this point is known as critical coagulation concentration (ccc). For a given colloidal system, the electrolyte valency (i.e., mono-, di-, or trivalent ions) will affect the ccc value, whereby, for example, smaller concentration of trivalent electrolyte is sufficient to induce aggregation. The Debye screening length described,  $K^{-1}$ , can be used to predict the effect of electrolyte concentration on colloidal stability.



The DLVO theory describes the net interaction on the basis of an ideal system where particles are suspended in a simple electrolyte solution. However, most real systems, including inkjet inks, contain additional components that may also affect the particle interactions. The following sections briefly describe the influence of these other components, starting with describing the particle behavior in the presence of polymers.

## 6.4

### Particle–Polymer Interactions

Ink formulations typically include different types of polymers (cf. Chapter 5), which can influence the stability of pigment particles. Interactions between colloids and polymers are typically complex and highly dependent upon the type and molecular weight of polymers, their concentration with respect to that of the particles, and whether they are likely to adsorb on the particle surface. The different conditions give rise to three main typical interactions, which we briefly describe in the next sections.

#### 6.4.1

##### Steric Stabilization

An often desired outcome of the addition of polymers in a colloidal suspension is an enhancement of particle stability. This is typically the case when the polymers are able to strongly adsorb to the particle surface and extend away from the surface when solvated by the continuous phase. Under these conditions, the particles are coated with a polymeric sheath, which offers a steric barrier to the approach/contact between two particles. The origin of the repulsive forces here stems from the increase in the local polymer concentration when polymer chains on the surface of two approaching particles overlap. The corresponding demixing increases the free energy in the system, which gives rise to a repulsive osmotic force. This is augmented by reductions in the configurational degrees of freedom in the overlap region, which also contributes to the separation force. A schematic of two approaching surfaces coated with a stabilizing polymeric sheath is included in Figure 6.5 [10].

Several methods can possibly obtain a colloidal suspension efficiently coated with a stabilizing polymer sheath ranging from using the polymer as stabilizer during particle synthesis to physical adsorption of the polymer on the bare particle surface. Polymers provide the most efficient steric stabilization when they possess two distinct moieties respectively designed for preferentially adsorbing onto the particle surface (i.e., anchoring groups) and for extending into the continuous phase to provide a thick layer/film around the particle (i.e., stabilizing groups). Such polymers can potentially be in the form of statistical copolymers, graft copolymers, or diblock (or more) copolymers. However, homopolymers such as those most often present in ink formulations can also act as efficient steric

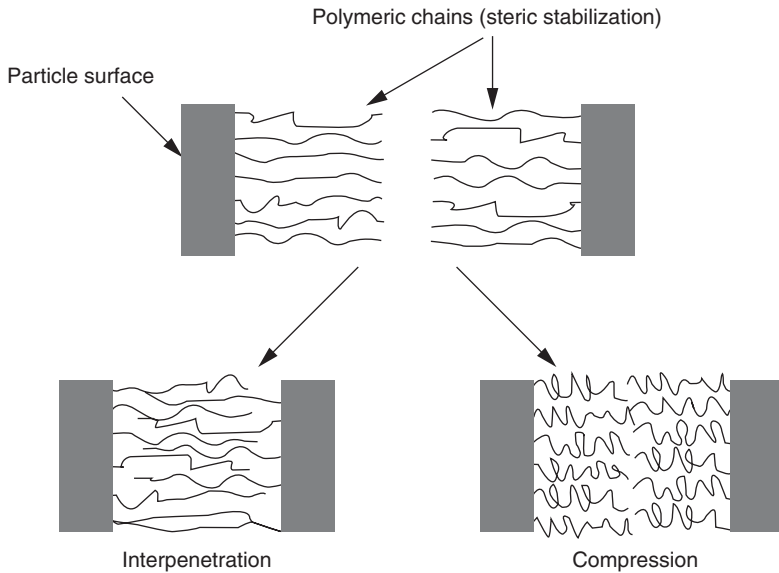


**Figure 6.5** Mechanisms leading to a repulsive force between two approaching sterically stabilized surfaces via changes from the equilibrium state of the polymer on the surface [10].

stabilizers, as only a small energy of adsorption is typically required to facilitate polymer adsorption. In addition, the polymer configuration on the particle surface, once adsorbed, is partly dictated by steric crowding, thus allowing for extended layers to be present on the particle surface at high adsorption densities.

The variables influencing the interaction,  $W_{\text{steric}}$ , between sterically stabilized particles can be understood from Eq. (6.9), derived by Fischer for two identical particles of radius  $r$  [11].

$$W_{\text{steric}} = \frac{4\pi r \delta^2 RT}{V_M} (P_C)^2 \left( \frac{1}{2} - \chi \right) \left( \frac{h}{2\delta} - \frac{1}{4} - \ln \frac{h}{\delta} \right) \quad (6.9)$$

where  $\delta$  is the thickness of the adsorbed polymer layer,  $V_M$  is the molar volume of solvent molecules,  $P_C$  is the polymer concentration in the adsorbate layer, and  $\chi$  is the Flory–Huggins parameter (essentially a measure of the quality of solvent for the polymer).

Clearly, the thickness of the polymer sheath, the solvent quality for the adsorbed polymer, and the density of polymer chains on the particle surface are key parameters, which must be optimized to obtain stable colloidal systems.

#### 6.4.2

#### Bridging Flocculation

Interactions between polymers and colloidal particles can also be detrimental to the stability of the colloids. This section and the next describe two common

examples of colloid particle destabilization upon addition of adsorbing and nonadsorbing polymers, respectively.

Bridging flocculation can occur as a result of individual polymer chains adsorbing on the surface of numerous particles at once, resulting in the creation of particle flocs. These flocs are maintained throughout the system by the presence of such molecular bridges between adjacent particles and are typically facilitated by the presence of low molecular coverage of polymer on the particle surface.

### 6.4.3

#### Depletion Flocculation

A nonadsorbing polymer can also drastically affect the behavior of colloidal particles in suspension. Under the appropriate conditions, a volume exclusion mechanism can lead to a net attraction between two hard, parallel plates (as initially described by Asakura and Oosawa [12]) and accordingly between two hard spheres or colloidal particles. This is a result of the presence of a volume around the colloidal particles that exclude the polymer solvated in the continuous phase. This volume is generally called the depletion zone (or depletion layer), and its width is referred to as the *depletion thickness*.

In simple terms, upon addition of a nonadsorbing polymer in a suspension of colloidal particles, the structuring of the resulting mixed system (on the basis of formation of depletion zone near the particle surface) can lead to two different interactions. Firstly, it can create a long-range repulsive force that is typically difficult to observe but is often present at high polymer concentrations. Secondly, short-range interaction, more often detected (and commonly known as the *depletion interaction*), can induce flocculation of the system. The latter mechanism stems from the overlap of the depletion zones of two approaching particles, which induces an attraction caused by an unbalanced osmotic pressure. In fact, the overlap region in this case experiences no osmotic pressure due to the absence of polymer chains. The osmotic pressure difference between the continuous phase (where the polymer is present and efficiently solvated) and the overlap region drives the formation of particle flocs. These flocs can be easily redispersed into single particles through gentle agitation.

The expression of the interaction energy as derived by Fleer *et al.* [13] is shown as follows:

$$W_{\text{dep}} = 2\pi r \left( \frac{\mu_1 - \mu_1^0}{V_M} \right) \left( \Delta - \frac{h}{2} \right)^2 \left( 1 + \frac{2\Delta}{3r} + \frac{h}{6r} \right) \quad (6.10)$$

where  $\mu_1$  and  $\mu_1^0$  are the chemical potentials of polymer solution and pure solvent, respectively, and  $\Delta$  is the depletion zone thickness.

Practically, the parameters that are most influential on the strength of depletion flocculation are the concentrations and hydrodynamic diameters of both the particles and polymers within the system. For the polymers, these parameters are also influenced by the choice of solvent, which dictates the volume fraction occupied by the polymer in the continuous phase.

In the case of ink formulations, polymers play a crucial role in modifying the interactions between the particles, and formulators must be aware of the interactions described to devise the most efficient inks. The other multiple components within common ink formulations can also have an influence on the stability of colloidal pigments. The next section briefly describes some of these additional components and their possible effects.

## 6.5

### Effect of Other Ink Components on Colloidal Interactions

Table 6.2 lists the most common components encountered when searching the patent literature for inkjet ink formulations. This table lists typical concentrations of the additional components, their purpose in the ink formulation. It is intended to be used as a guide for the following discussion.

#### 6.5.1

##### Surfactants

Surfactants are used in the majority of formulated products within a broad range of sectors including home and personal care, coatings, textile processing [14], cosmetics [15], and pharmaceuticals [16]. In an ink formulation, they are included to manipulate the surface tension of the liquids to be printed. This is typically required to achieve a good control over the behavior of the droplets as they form at the nozzle and in flight before reaching the substrate. Surfactants are also important during the deposition and subsequent drying of the droplet. For example, surfactants will influence the wetting and spreading of the droplet onto the substrate and their presence on the droplet surface is responsible for electrohydrodynamic flows within the liquid (cf. Chapter 11).

The ink in a printhead experiences a wide variety of shear rates; for channel refilling and ink flow, this can be approximately  $1\text{ s}^{-1}$ , but this can reach as high as  $10^6\text{ s}^{-1}$  as a droplet is ejected from the printhead nozzle. The addition of a surfactant would also fulfill these requirements. However, the addition of

**Table 6.2** Typical ink components and their purpose.

Component	Amount (wt%)	Purpose
Dye or pigment	2–6	Color
Diethylene glycol	5–15	Water-miscible solvent
Glycerol	0–10	Humectant
2-Pyrrolidone	0–10	Humectant/dye solubility
Surfynol 465	0.5–2	Surfactant
Proxel GXL	0.2	Biocide
Buffer	0.5–2	pH control
Water	Balance	Solvent

surfactants can cause foaming, which would be a major problem in terms of printhead functionality; therefore requiring use of, a low-foaming surfactant.

Additionally, within the pigment suspension, surfactants can have various effects due to their propensity to adsorb onto surfaces. Adsorption of the surfactants onto the surface of the pigments will modify the particle surface properties and will influence the interactions dictating colloidal stability as described earlier. For charged surfactants, for example, it is possible that their adsorption will modify the net charge density on the particle surface and possibly even reverse the surface charge. Nonadsorbing surfactants can also potentially induce depletion flocculation, for example, in the case where surfactants and particles have the same charge. Such constraints mean that most surfactants used in formulation of inks are nonionic and fast diffusing to allow for fast adsorption but poor foam ability.

### 6.5.2

#### **Viscosity Modifiers**

Another key physical property of the formulated inks, that requires close management is viscosity. Typically, the viscosity of inkjet inks is in the range 1–20 mPa·s. If the ink viscosity is too low, it will contribute to droplet breakup upon jetting. This then leads to formation of satellite drops, which will reduce the overall quality of the print. This is an effect that is further increased if the surface tension of the dispersion is relatively low. However, if the viscosity is too high, then the nozzle will be unable to refill within the required rate. For office/desktop printers, a broad range of ink viscosities is acceptable and thus does not require significant attention. However, the more demanding industrial printheads necessitate a need for very good control over ink viscosity to maintain the optimum printhead performance.

Typical viscosity modifiers used in the formulation of inkjet inks are nonadsorbing polymers. An example is high-molecular-weight poly (ethylene glycol). The polymer concentration is typically adjusted depending on the type of printhead. On the basis of polymer/particle interactions described earlier, care must be taken to operate under conditions where depletion flocculation is unlikely to occur so that pigment stability is maintained throughout the entire printing process. However, as we will see in the last section of this chapter, the particle aggregation phenomenon can be utilized to the user's benefit to enhance the resolution of the dried deposits.

### 6.5.3

#### **Humectants**

Across the different timescales of inkjet ink usage, several conditions such as storage and printer idle time or the printing process can lead to significant solvent evaporation, causing the ink to dry out in the reservoir. This is a concern as in most commercial applications, the printing conditions and environment are uncontrolled. Inks tend to dry out and form a hard crust on the nozzle, which if jetted could damage the printhead.

Humectants are added to minimize solvent evaporation. In this case should an ink dry out in the nozzle, the humectant assists in the formation of a soft crust instead, which upon printing will be less harmful to the printhead and print quality. The presence of a humectant forms a stronger hydrogen-bonded network, which minimizes evaporation and therefore slows down the drying out process. Urea is an excellent humectant and is most prevalent in the textile inkjet printing industry. Glycerol is another excellent humectant, forming a very soft plug as water evaporates (in the nozzle), whereby the “plug” can be easily blown out upon jetting.

High concentrations of humectants in the formulation are not desirable as this could lead to a undesirable increase in viscosity and also significantly long drying times. Therefore, a balance must be achieved, where the humectant content aids formation of a soft plug in the nozzle, drives an appropriate drying time without affecting the viscosity significantly.

#### 6.5.4

##### **Glycol Ethers**

Glycol ethers, such as ethylene- and diethylene glycols, are found in some ink formulations. They are used to modify the spreading and wetting behavior of ink, as well as aiding the ink penetration onto the printed media, and thus reducing the drying time. Glycol ethers are moderately surface-active, and as a result, they can be used as a supplement or alternative to surfactants. In spite of these desirable properties, their usage can lead to a reduction in print color strength as well as excessive penetration. All of which reduce the final image quality. Care must be taken then, in terms of concentration, when adding these to an ink formulation.

#### 6.5.5

##### **Storage – Buffers and Biocides**

Pigment-based inks are frequently stabilized with ionic polyacrylates, which become insoluble below pH 6. The pH of a given dispersion (ink) is found to decrease with time, due to the absorption of CO<sub>2</sub>, leading to destabilization. This can be a significant problem, because commercial inks have to be stable over long periods, ranging from months to years. The addition of a buffer into inks will negate this effect by maintaining a stable pH over the ink shelf life. Generally, simple phosphate (pH 6–8) or organic buffers, such as Trizma (pH 7–9), are used in commercial inks. Since buffers typically contain a significant proportion of electrolyte, care must be taken in this instance not to significantly affect the thickness of the electric double layer or the solvency of the continuous phase for a stabilizing polymer, which could affect the colloidal stability of the pigments.

Inkjet inks are also susceptible to bacterial and fungal growth, when stored over long periods. This is mainly in systems that incorporate glycerol or similar materials in the formulation, which are found to encourage organism growth. For this reason, biocide is commonly added into most ink formulations.

## 6.5.6

**Other Additives**

Sequestering agents (or chelating agents) are sometimes included in ink formulations for complexation with metal ion impurities within the inks [5]. They are commonly used to treat hard water. They have also been included in formulations to prevent thickening and/or gelling; generally, EDTA (Ethylenediaminetetraacetic acid) salts are used for this purpose. Other sequestering agents can also be used for this purpose, including nitrilotriacetic acid and pentetic acid salts; however, selection of an appropriate agent is determined by the pH and conditions of use. Protonation of the sequestering agent should be avoided (by controlling the pH) since the efficiency of the agent is otherwise compromised [6].

Anti-kogation agents are used when there is a risk from the ink to carbonize or cause scaling during printing [7]. Scaling can lead to the formation of a thermally insulating layer on the nozzle that prevents bubble formation. In general, these are not required, as the use of highly pure components during formulation minimizes scaling issues.

## 6.6

**Characterization of Colloidal Dispersions**

Understanding the behavior of inkjet inks throughout the printing process is important if we are to enable higher resolution and faster printing. In addition to the different techniques presented in this book, to analyze the behavior of the droplets and pigment particles during the printing process (i.e., during jetting and drying), an important topic is the characterization of colloidal particle suspensions, which can help predict and optimize the behavior of the pigments in the ink and of the ink droplets. Here, we present three main standard methods, particularly relevant to inkjet fluids, for achieving this.

## 6.6.1

**Dynamic Light Scattering (DLS)**

Dynamic light scattering (DLS) is a powerful and important technique, originally designed to determine size and size distribution of particle dispersions, but can now also be used to analyze polymer dispersions. The measurements are based on the light intensity fluctuations caused by Brownian motion. The intensity of the light scattered by the particles and polymers in the dispersion is measured, and the time-dependent fluctuation (due to Brownian motion) is related to the constructive and destructive interference. This is then time-correlated and used to determine the translational diffusion coefficient ( $D$ ) of the particles/polymers. The Stokes–Einstein equation can then be used to determine the hydrodynamic diameter,  $d_H$ , of the scattering objects,

$$D = \frac{k_B T}{3\pi\eta d_H} \quad (6.11)$$

where  $k_B$  is the Boltzmann constant,  $T$  is the absolute temperature, and  $\eta$  the viscosity.

Note that the size measured in DLS, referred to as  $d_H$ , is the diameter of a sphere that has the same translational diffusion coefficient as the particle. For colloidal particle systems, this generally means that there exists a volume of associated solvent (along with adsorbed ions and polymers) that moves with the particle. The hydrodynamic diameter values obtained from these measurements thus include the thickness of these layers. The measured hydrodynamic diameter of a polymer-coated particle is therefore a function of the chain length, grafting density of the polymer, and its solvent quality. Equally, for charged-stabilized particles,  $d_H$  is a function of the electrolyte concentration as the volume of water bound to the particle is dependent on the electric double layer thickness.

### 6.6.2

#### Electrophoretic Mobility (Zeta Potential)

The surface charge of a colloidal particle can be estimated through measurements of the zeta potential, which is the potential measured close to the surface of a charged particle as it moves within a fluid. The surface charge, moderated by any tightly bound surface ions, will respond to an applied electric field by diffusing toward the oppositely charged electrode. The rate of diffusion is dependent upon the strength of the electric field, the net charge at the shear plane close to the surface, and the size of the particle.

The velocity of the particles moving toward the oppositely charged electrode in an applied electric field can be measured and is referred to as the *electrophoretic mobility*  $U_E$ , which is converted to zeta potential, ( $\zeta$ ) via

$$U_E = -\frac{2\varepsilon\zeta f(\kappa r)}{3\eta} \quad (6.12)$$

where  $\varepsilon$  is the dielectric constant and  $f(\kappa a)$  is Henry's function of the ratio of the particle radius,  $r$ , to electrical double layer thickness,  $\kappa^{-1}$ . The measurements are commonly based on diluted dispersion similarly to the determination of hydrodynamic diameter in suspensions through DLS experiments.

Zeta potential is a proxy measure of dispersion stability as it is related to the surface charge, which is one of the key parameters needed to describe the electrical double layer. The value of the zeta potential is typically affected by pH for an aqueous dispersion. A plot of zeta potential against pH usually has, at a certain pH, a value of zero: This is known as the *isoelectric point* (iep) and is the pH at which the dispersion is expected to be least stable (i.e., where the repulsive forces induced by electrostatic interactions are the weakest). On either side of the iep, the zeta potential will increase in magnitude as the pH changes with more acidic media leading to positive surface charges and more alkaline continuous phases inducing negative surface charges. The exact pH for the iep depends upon the acid/base character of surface moieties on the particles, the Debye length, and any adsorption phenomena that may take place on the particle surface. As an example, silica



particles in an aqueous suspension typically have an iep around pH 2, while the iep for alumina particles is generally closer to pH 9.

### 6.6.3

#### Rheology

Knowledge of the rheological behavior (i.e., the flow and deformation) of an ink is essential, since it gives rise to the jetting behavior and printability of the ink. For a simple colloidal dispersion, comprising of latex particles suspended within a solvent, the rheological properties are dependent upon solvent viscosity, particle concentration, and particle size and shape [17, 18]. In more complex systems such as ink formulations, the additives introduced in Section 6.3.4 (in particular, polymer additives) have a drastic influence on the rheological properties (see Chapter 13). The specific rheology requirements of the fluid are dictated by the processing conditions upon jetting in the printer nozzle, that is, deformation kinematics (e.g., shear or extensional flows) and deformation rate (or stress), and so on.

### 6.6.4

#### Bulk Colloidal Dispersion

In a colloidal dispersion, forces acting between particles, whether attractive or repulsive (including Brownian motion, hydrodynamic effects, electrostatic, steric repulsion, and vdW forces), contribute to the shear stress and hence to the overall rheology. For the sake of simplicity, a dispersion of hard spherical particles in a Newtonian medium is considered here, where only Brownian motion and hydrodynamic effects (at high concentration) are taken into account. However, even under these simple conditions, the rheology still remains rather complex. The shear viscosity behavior of poly(styrene-ethylacrylate) particles in water, as a function of shear stress at various particle volume fractions, is displayed in Figure 6.6. At low particle volume fraction,  $\phi$ , the shear viscosity,  $\eta$ , is nearly independent of shear stress and is only marginally higher than the solvent viscosity,  $\eta_s$ , and can be described by Eq. (6.13):

$$\eta = \eta_s(1 + 2.5\phi) \quad (6.13)$$

This is valid only for the dilute suspension where a single sphere is not appreciably affected by the neighboring spheres. With increasing volume fraction, multi-body (two or more) spheres interact with each other simultaneously, causing the viscosity to increase with sphere concentration. The shear viscosity also becomes sensitive to shear stress,  $\sigma$  (equivalently shear rate,  $\dot{\gamma}$ ), with remarkable *shear-thinning* behavior occurring at intermediate shear stresses before reaching a secondary Newtonian plateau.

The Krieger–Dougherty equation [19] is an empirical expression often used to describe the volume fraction dependence of the plateau shear viscosity:

$$\eta_x = \eta_s \left( 1 - \frac{\phi}{\phi_m} \right)^{-2.5\phi_m} \quad (6.14)$$

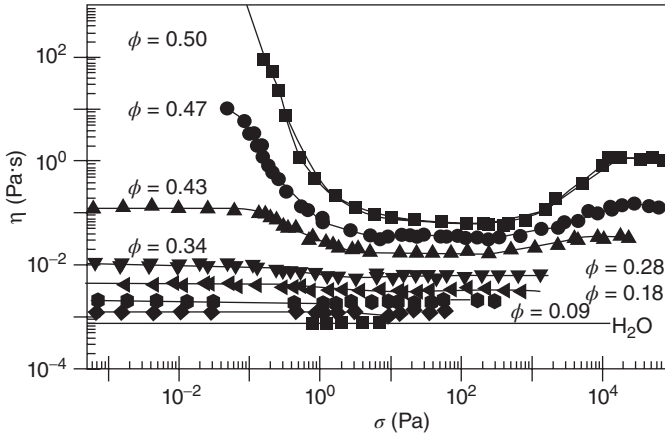


**Figure 6.6** The shear viscosity of charge-stabilized poly (styrene-ethylacrylate) particles in water, as a function of the applied shear stress and particle volume fraction [17]. Copyright Wiley-VCH Verlag GmbH & Co. KGaA. Reproduced with permission.

where  $x = 0$  (low shear plateau) or  $\infty$  (high shear plateau).  $\phi_m$  is the maximum packing volume fraction at which the viscosity diverges, with  $\phi_{m0} = 0.63$  for the low limiting shear viscosity  $\eta_0$  and  $\phi_{m\infty} = 0.71$  for the high limiting shear viscosity  $\eta_\infty$ .

In general, for a Brownian hard sphere in between these plateau regions, there exists a dimensionless shear rate, known as the Péclet number,  $Pe$ .  $Pe$  is defined as a balance between the particle diffusivity and flow:

$$Pe = \dot{\gamma} t_D = \frac{6\pi\eta_s r^3 \dot{\gamma}}{k_B T} \quad (6.15)$$

where  $t_D$  is a characteristic time taken for a particle to diffuse a distance equal to its radius,  $r$ . Reduced shear stress, a dimensionless group that is more commonly used, is defined as:

$$\sigma_r = \frac{\sigma r^3}{k_B T} \quad (6.16)$$

Hence, the relative shear viscosity  $\eta_r \equiv \frac{\eta}{\eta_s}$  is a universal function of two dimensionless quantities,  $\phi$  and  $\sigma_r$  (or  $Pe$ ). In this regard, one popular semi-empirical relation used in the literature to describe the viscosity in this region is as follows:

$$\frac{\eta - \eta_\infty}{\eta_0 - \eta_\infty} = \frac{1}{1 + \sigma_r / \sigma_c} \quad (6.17)$$

where  $\sigma_c$  is the critical reduced stress for shear thinning.

The mechanism of shear thinning in hard-sphere dispersions is reasoned to be due to the significantly lower Brownian contribution to shear stress under high shear stress conditions, leaving only the hydrodynamic effects, which results in a reduction of viscosity.

At increased shear stresses and for higher volume fractions, *shear thickening* may be observed, where the viscosity increases significantly with stress. This is thought to be a consequence of the formation of particle clusters, driven by shear into close proximity, as a consequence of hydrodynamic lubrication forces [20]. This behavior is undesirable for processing purposes. However, this typically occurs at particle concentrations (>50 vol%) much larger than what is found in inkjet inks.

Furthermore, weak elasticity (when storage modulus,  $G'$ , is nonzero) is observed in a hard-sphere dispersion, due to a relaxation in Brownian motion. The relaxation time, fundamentally set by the particle diffusivity, tends to restore equilibrium to the shear-distorted particle configuration. At low shear frequency, Brownian motion is relatively fast and therefore restores equilibrium conditions to the microstructure, thereby affecting the viscosity. At high frequency, Brownian motion does not have sufficient time to affect the viscosity. The hydrodynamic interactions are proportional to the rate of deformation and therefore contribute, at all frequencies, directly to the viscosity. As for  $\phi$  dependence, a plot of  $G'$ ,  $G''$  (loss modulus) versus  $\omega$  (angular frequency) will shift toward lower frequencies and higher moduli.

More relevant to the ink fluid, rheology of dispersions stabilized via electrostatic, steric (polymeric), or electrosteric repulsions can often be understood by defining an effective hard-sphere particle size and mapping onto the behavior of hard-sphere dispersions, with some additional necessary contributions incorporated or some adjustments made. Structural factors including particle size distribution, particle shape, and Debye length, significantly affect suspension rheology. Particle dispersions with a varied size distribution, such as bimodal or multimodal, drastically increases the maximum packing and therefore reduces viscosity. Rheology of nonspherical particles will depend on particle orientation with respect to the flow direction. These factors are of more importance, practically, in terms of formulating inks than the ideal hard-sphere dispersion.

### 6.6.5

#### Jetting

In a DoD printhead with a nozzle diameter  $\sim 50 \mu\text{m}$ , when a fluid is jetted at a speed of  $\sim 6 \text{ m s}^{-1}$ , shear rates in the nozzle exceed  $\sim 10^6 \text{ s}^{-1}$ . This is many orders of magnitude greater than the frequency limit attainable in conventional rheometers. As such, a piezo axial vibrator (PAV) technique and a torsion resonator rheometer with relevant high shear rate domains, or other specialised techniques accessible for inkjet fluids, are employed to characterize their linear viscoelastic rheology [21].

The printhead drive voltage, large pressure drop within the small nozzle diameter, as well technical problems of nozzle clogging, and so on govern the upper viscosity limit for jettable fluids to  $\sim 20 \text{ mPa}\cdot\text{s}$ . However, at these jetting speeds, satellite drops are quite easily produced (see Chapter 7); therefore, high-shear-thinning behavior with considerable elasticity, whereby a fast recovery of

viscoelasticity is observed within a short timescale after exiting the nozzle, is desirable for inkjet inks.

Certain amounts of polymer are commonly introduced into ink formulations to stabilize particle dispersions and to introduce or strengthen the shear-thinning behavior (particularly to increase the elasticity of the inks). The use of an elastic polymer is highly favorable for single drop formation, satellite drops suppression, and later, jet ligament breakup. The time taken for the drops to break off from the nozzle is comparable with the relaxation times of long-chain polymers, so that elastic effects can produce dramatic changes to the way the drops form [22]. Elastic stress can act to contract the trailing ligament into the main drop before capillary breakup. Hoath *et al.* [23] have demonstrated a direct link between jetting behavior and fluid elasticity, expressed in terms of the ratio  $G'/G^*$  (where  $G'$  and  $G^*$  are the elastic (storage) modulus and complex modulus of the fluid, respectively). The jet break-off time, the time at which the ligament detaches from the nozzle, increases roughly linearly with the ratio  $G'/G^*$ , while too high elasticity might prevent ligament break-off, encouraging retraction back inside the nozzle.

As extensional flow behavior of the fluid within the neck of the nozzle makes more sense in determining jet speed in practice, nonlinear fluid rheology is often explored using filament-stretching experiments (which is more analogous to real inkjet drop formation, to correlate with its jettability). The extensional viscosity increment due to polymer addition markedly prevents the filaments from breaking up, suppressing the satellite drops in capillary breakup, despite being at a very low concentration. It has been found that it is the strain hardening during stretching that is the key rheological property responsible for satellite drop suppression. Furthermore, the fluid relaxation time has a strong relation in controlling the satellite drop formation [24]. Moreover, dependence of jetting behavior on the jet Weissenberg number  $Wi$  (i.e., a dimensionless parameter defined by Hencky strain rate times the fluid relaxation time) and extensibility of the polymer molecules can be described in three different regimes [25]. In addition, where ink deposition is concerned, the elasticity acts more effectively than the viscosity in reducing radial flow, thus suppressing the ring stain during drying of fluid droplet [26].

Overall, it is the non-Newtonian characteristics of polymers that are crucial to the jetting behavior, and these are associated with its concentration and molecular weight and so on. Thus, to optimize the jetting conditions, it is vital to consider carefully the choice of polymer with suitable chain length, concentration, and solvent that satisfy the rheological requirements.

## 6.7 Sedimentation/Settling

When a particle is dispersed in a medium, three forces act on the particle; gravitational, buoyancy, and drag forces, (see Figure 6.7). Depending on the properties of the particle and dispersing medium, the balance of forces will dictate whether

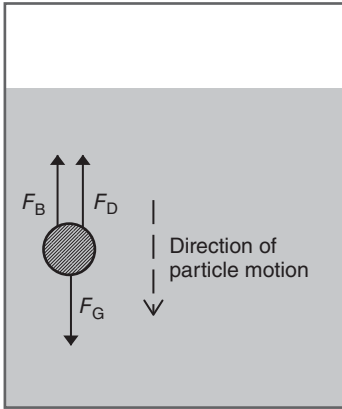


**Figure 6.7** Schematic of forces acting on a dispersed particle.

a particle will cream, sediment, or remain in dispersion. For a colloiddally stable dispersion, the particles are to remain in suspension during the product shelf life in order to guarantee its quality.

The three forces acting on the dispersed particle are as follow:

- 1) Gravitational force,  $F_G$ , is due to the Earth's gravity, which acts on any body on the Earth's surface.

$$F_G = \frac{4}{3}\pi r^3 \rho_p g \quad (6.18)$$

where  $r$  is the particle radius,  $\rho_p$  is the particle density, and  $g$  is the gravitational acceleration.

- 2) Buoyancy force,  $F_B$ , is the upward force exerted by the medium when a particle is placed into it.

$$F_B = \frac{4}{3}\pi r^3 \rho_m g \quad (6.19)$$

where  $\rho_m$  is the density of the dispersing medium.

- 3) Drag force,  $F_D$ , is the frictional force experienced by a particle when it is in motion. This force is due to the viscosity of the medium and is governed by Stokes' law as follows:

$$F_D = 6\pi r \eta_s v \quad (6.20)$$

where  $\eta_s$  is the solvent viscosity and  $v$  is the particle velocity.

Therefore, as a particle is dispersed in a medium, it immediately experiences a downward gravitational force, which is balanced by the upward buoyancy force. By assuming that the particle has a density greater than that of the medium, the particle will fall. As soon as the particle moves, the medium drag will impose an opposing force to the motion. At some point, the particle reaches a terminal velocity,  $v_t$ , when the drag force balances the difference between gravitational and buoyancy forces:

$$F_G - F_B = F_D \quad (6.21)$$

$$\frac{4}{3}\pi r^3(\rho_p - \rho_m)g = 6\pi r\eta_m v_t \quad (6.22)$$

$$v_t = \frac{2r^2(\rho_p - \rho_m)g}{9\eta_m} \quad (6.23)$$

Thus, this allows the colloidal stability (as well as shelf life) of a particle dispersion to be predicted. However, in reality, this estimation will be affected by the wall effect and particle concentration as follows:

- 1) Wall effect considers additional retardation force on the falling particle due to the influence of the container walls [27, 28]. This influence can be compensated with a correction factor:

$$f_w = \frac{v_{t(b)}}{v_{t(\infty)}} \quad (6.24)$$

where  $f_w$  is the wall correction factor and  $v_{t(b)}$  and  $v_{t(\infty)}$  are the terminal velocities in a bounded and unbounded fluid, respectively.

Generally, the wall correction factor is a function of the ratio of particle to container diameters,  $\beta = 2r/D_c$ . However, the wall correction factor becomes more complex as the flow regime and fluid type deviate from the ideal cases [29, 30].

- 2) As the particle concentration increases, the settling behavior switches from single particle to batch settling. The interparticle interaction induces a slower moving particle cloud [31, 32]. This is generally known as *hindered settling*, as governed by:

$$v_{tc} = v_t(1 - \phi)^n \quad (6.25)$$

where  $v_{tc}$  is the terminal velocity of a uniformly sized particle dispersion at volume fraction  $\phi$  and  $n$  is a particle-specific empirically determined exponent.  $n$  is governed by the particle Reynolds number at  $v_{tc}$ .

### 6.7.1

#### Sedimentation Characterization Techniques

Sedimentation characterization relies on the tracking of batch settling over time. This can be achieved by:

- 1) Physical measurement of sedimentation height change at predetermined times, together with concurrent sampling to determine particle concentration [33, 34]. This method tends to be intrusive and may suffer from sample destruction.
- 2) Using X-ray techniques to measure change in sample's X-ray density with time and sedimentation height. This method can be applied at high temperatures and pressures but is limited to materials with high atomic mass [35].
- 3) Using photo techniques, which rely on either a light point or a line beam to monitor the change in sample's turbidity with time and sedimentation height.

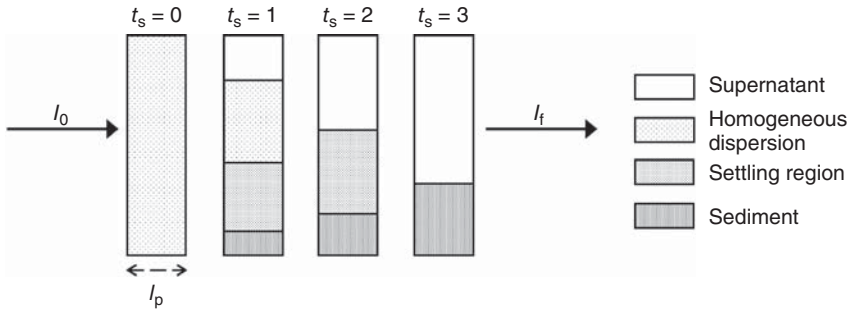


**Figure 6.8** Schematic of differences in particle concentration for a sedimenting colloidal dispersion.

The sample's transmission is directly correlated to the change in particle concentration. This method is simple, nonintrusive, and reliable, provided the sample preparation and experimental conditions are consistent [36–39].

The following discussions will concentrate on photo-based techniques. For accurate measurement, the sample has to be well dispersed at the beginning and maintained under constant temperature during measurement. As sedimentation takes place, the turbidity change in the dispersing medium is related to the particle concentration according to Beer–Lambert law (see Figure 6.8). Equation 6.26 describes the extent of attenuation of light beam as it passes through the sample. The intensity of incident beam reduces exponentially as it passes through the dispersion and the amount of transmission is a function of sample absorptivity and concentration, as well as path length of light through the sample.

$$Tr = \frac{I_f}{I_0} = e^{-\varepsilon_a l_p c_p} \quad (6.26)$$

where  $Tr$  is the transmission of light through the sample,  $I_0$  and  $I_f$  are the intensities of the incident and transmitted light, respectively,  $\varepsilon_a$  is the sample absorptivity (function of size and number of particles),  $l_p$  is the path length of light through the sample, and  $c_p$  is the sample concentration.

The photo-based measurements can be divided into three types:

- 1) UV–Visible spectroscopy (see Figure 6.9a), which is a light point measurement that allows monitoring of turbidity change at a particular sample height over time [40, 41].
- 2) Gravitational sedimentation, for example, Turbiscan<sup>®</sup> [36, 42] and LUMiReader<sup>®</sup> [43], which uses a light source to scan the sample as a function of sedimentation time and height. The light is scattered by the dispersed particles. Depending on the turbidity at a particular height, the scattered light will be detected either by transmission (Turbiscan<sup>®</sup>, LUMiReader<sup>®</sup>) or by backscatter detectors (Turbiscan<sup>®</sup> – see Figure 6.9b).
- 3) Centrifugal sedimentation, for example, LUMiSizer<sup>®</sup> (see Figure 6.9c), which applies a centrifugal force to accelerate the particle sedimentation while using

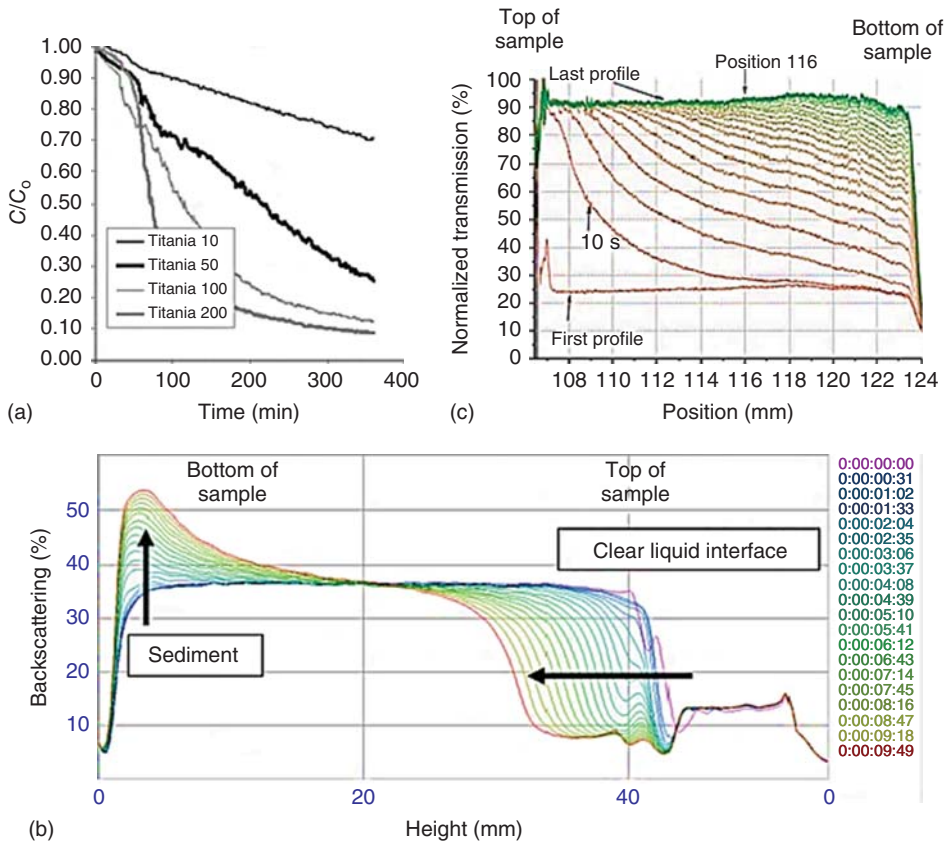


**Figure 6.9** Examples of sedimentation measurements via: a) UV-visible spectroscopy for effect of initial particle concentration (in 10, 50, 100 and 200 mg/L) on sedimentation of titania dispersions in sea water plotted against normalised concentration [40]. b) Turbiscan for the settling profiles of a uniformly sized particle dispersion plotted

against backscattering intensity, whereby the sedimenting interface propagates down the vessel and the sediments build up at the base [42]. c) LUMISizer for sedimentation profiles of a silican dispersion (without any addition of free polymer to induce particle aggregation) plotted against normalised transmission intensity [39].

a line beam to scan the sample as a function of sedimentation time and height. This allows examination of samples with small density differences between the particles and the dispersing medium.

An advantage of centrifugal sedimentation is the ability to gradually increase the centrifugal force acting on the sediments. This allows probing of the sediment bed response, which correlates to the stability of colloidal particles. Stable dispersions lead to a smooth constant profile irrespective of the applied force, while aggregates show a stepwise compression with increasing force (see Figure 6.10) [44]. This method will allow efficient investigation during ink formulation to



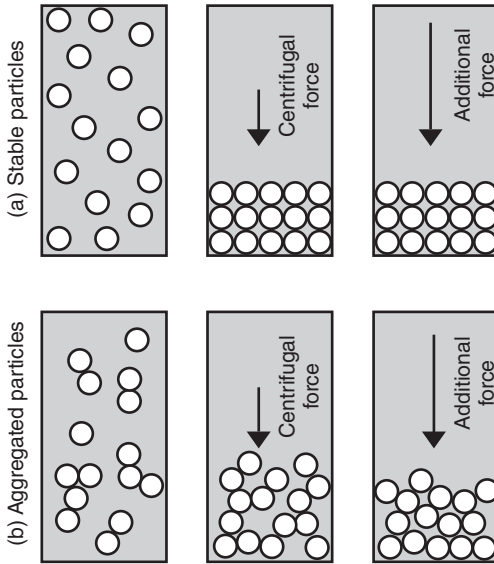


**Figure 6.10** Schematic of effect of centrifugal force on sedimentation of: (a) stable particles and (b) aggregates [44].

determine suitability of any added component into the “new” ink and hence the effect on colloidal/dispersion stability.

## 6.8

### Conclusions/Outlook

Formulation of inkjet fluids is an important part of future improvement of inkjet printing processes, notably in enabling the use of a wider range of materials and the preparation of inks with higher solid content to improve the overall print quality. As inkjet printing technologies are adapted to deposit drugs, electronic components, and other presently non-standard materials, colloidal forces will play a crucial role in ensuring stability of these novel ink designs.

Future formulations may take advantage of the knowledge of the governing colloidal forces to design functional inks that adapt their behavior along the timeline of the printing process. A recent example of such a functional design [45] induced particle aggregation on the printed substrate during the drying process. Here, the fact that particle and polymer concentrations increase during the drying time was used to induce depletion flocculation and freeze the position of the particles in suspension. This procedure relied on differential evaporation of the ethanol and water solvents forming the mixed continuous phase, which leads to particle accumulation within the droplet center. As can be seen from Figure 6.11, this mechanism combined with the induced depletion flocculation led to a final dry deposit consisting of a small concentrated central area of aggregated particles while the

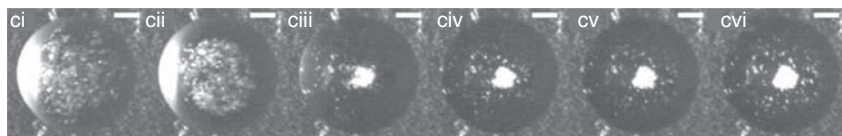


**Figure 6.11** Drying droplets of 50 vol% ethanol containing 0.1 vol% of 755 nm polystyrene model latex particles and 1 wt% nonadsorbing polymer of 70 kDa. Left to

right corresponds to: 10% of the drying time (ci) to a fully dried droplet (cvi) [45]. Reprinted with permission from Ref. [45]. Copyright (2015) American Chemical Society.

rest of the initial droplet footprint was almost entirely devoid of particles. The suspension composition was thus designed to induce depletion flocculation of the particles, in a timely manner, so that the particles would flocculate in the droplet center before full evaporation of the solvents. This design resulted in the ability to deposit small dots from large droplets, thus increasing the potential printing resolution.

This example of novel formulation/inkjet design exemplifies the possibility of formulating inks that can adapt their behavior throughout the printing process. As more materials are incorporated within inkjet inks, formulators will have an increasing amount of choices available to tailor such functionality into their designs.

## References

- Derby, B. (2010) Inkjet printing of functional and structural materials – fluid property requirements, feature stability and resolution. *Annu. Rev. Mater. Res.*, **40**, 395–414.
- Lamminmaki, T.T., Kettle, J.P., and Gane, P.A.C. (2011) Absorption and adsorption of dye-based inkjet inks by coating layer components and the implications for print quality. *Colloids Surf., A*, **380**, 79–88.
- Sousa, S., Gamelas, J.A., Mendes, A.D., Fiadeiro, P.T., and Ramos, A. (2013) Interactions of ink colourants with chemically modified paper surfaces concerning inkjet print improvement. *Mater. Chem. Phys.*, **139**, 877–884.
- Koo, H.S., Chen, M., Pan, P.C., Chou, L.T., Wu, F.M., Chang, S.J., and Kawai, T. (2006) Fabrication and chromatic characteristics of the greenish LCD colour-filter layer with nano-particle ink using inkjet printing technique. *Displays*, **27**, 124–129.
- Sadlar, R.A., Bruinsma, P.J., Chatterjee, A.K., Doumaux, H.A., Lassar, N.C., and Giere, M.D. (Hewlett-Packard Development Company), Inkjet inks which prevent kogation and prolong resistor life in inkjet pens. US6610129 B1.
- Guistina, R.A., Santilli, D., and Bugner, D.E. (Eastman Kodak Company), Aqueous pigment dispersions containing sequestering agents for use as inkjet printing inks. US5611847 A.
- Lindstrom, B.L., Bernal, A., Nelson, D.J., Sowinski, A.F., Jeanmaire, D.L., and Griffin, T.R. (Eastman Kodak Company), Ink composition for continuous inkjet printer. WO2013039941 A1.
- Derjaguin, B. and Landau, L. (1941) Theory of the stability of strongly charged lyophobic sols and of the adhesion of strongly charged particles in solutions of electrolytes. *Acta Phys. Chim.*, **14**, 633–662.
- Verwey, E. and Overbeek, J. (1948) *Theory of the Stability of Lyophobic Colloids*, Elsevier, Amsterdam, p. 205.

10. Cosgrove, T. (2010) *Colloid Science: Principles, Methods and Applications*, John Wiley & Sons, Inc., Hoboken, NJ.
11. Fischer, E.W. (1958) Elektronenmikroskopische untersuchungen zur stabilität von suspensionen in makromolekularen lösungen. *Kolloid Z.*, **160**, 120–141.
12. (a) Asakura, S. and Oosawa, F. (1954) On interaction between two bodies immersed in a solution of macromolecules. *J. Chem. Phys.*, **22**, 1255; (b) Asakura, S. and Oosawa, F. (1958) Interactions between particles suspended in solutions of macromolecules. *J. Polym. Sci.*, **33**, 183.
13. Fler, G.J., Scheutjens, J.M.H.M., and Vincent, B. (1984) Polymer adsorption and dispersion stability. *Am. Chem. Soc. Symp. Ser.*, **240**, 245.
14. Miao, Z., Yang, J., Wang, L., Liu, Y., Zhang, L., Li, X., and Peng, L. (2007) Synthesis of biodegradable lauric acid ester quaternary ammonium salt cationic surfactant and its utilization as calico softener. *Mater. Lett.*, **62**, 3450–3452.
15. Ran, G., Zhang, Y., Song, Q., Wang, Y., and Cao, D. (2009) The adsorption behavior of cationic surfactant onto human hair fibers. *Colloids Surf., B*, **68**, 106–110.
16. Cardoso, A.M.S., Faneca, H., Almeida, J.A.S., Pais, A.A.C.C., Marques, E.F., Pedroso de Lima, M.C., and Jurado, A.S. (2011) Gemini surfactant dimethylene-1,2-bis(tetradecyldimethylammonium bromide)-based gene vectors: a biophysical approach to transfection efficiency. *Biochim. Biophys. Acta*, **1808**, 341–351.
17. Mewis, J. and Wagner, N.J. (2012) *Colloidal Suspension Rheology*, Cambridge University Press.
18. Larson, R.G. (1999) *The Structure and Rheology of Complex Fluids*, Oxford University Press.
19. Krieger, I.M. and Dougherty, T.J. (1959) A mechanism to non-Newtonian flow in suspensions of rigid spheres. *Trans. Soc. Rheol.*, **3**, 137.
20. Brady, J.F. (1996) Model hard-sphere dispersions – statistical-mechanical theory, simulations, and experiments. *Curr. Opin. Colloid Interface Sci.*, **1**, 472.
21. Vadhilo, D.C., Tuladhar, T.R., Mulji, A.C., and Mackley, M.R. (2010) The rheological characterization of linear viscoelasticity for ink jet fluids using piezo axial vibrator and torsion resonator rheometers. *J. Rheol.*, **54**, 781.
22. Castrejon-Pita, J.R., Baxter, W.R.S., Morgan, J., Temple, S., Martin, G.D., and Hutchings, I.M. (2013) Future, opportunities and challenges of inkjet technologies. *Atomization Sprays*, **23**, 541.
23. Hoath, S.D., Hutchings, I.M., Martin, G.D., Tuladhar, T.R., Mackley, M.R., and Vadhilo, D. (2009) Links between ink rheology, drop-on-demand jet formation, and printability. *J. Imaging Sci. Technol.*, **53**, 041208.
24. Christanti, Y. and Walker, L.M. (2002) Effect of fluid relaxation time of dilute polymer solutions on jet break up due to a forced disturbance. *J. Rheol.*, **46**, 733.
25. Hoath, S.D., Harlen, O.G., and Hutchings, I.M. (2012) Jetting behaviour of polymer solutions in drop-on-demand inkjet printing. *J. Rheol.*, **56**, 1109–1127.
26. Talbot, E.L., Yang, L., Berson, A., and Bain, C. (2014) Control of the particle distribution in inkjet printing through an evaporation-driven sol-gel transition. *ACS Appl. Mater. Interfaces*, **6**, 9572–9583.
27. Brenner, H. (1961) The slow motion of a sphere through a viscous fluid towards a plane surface. *Chem. Eng. Sci.*, **16**, 242–251.
28. Faxén, H. (1922) Der Widerstand gegen die Bewegung einer starren Kugel in einer zähen Flüssigkeit, die zwischen zwei parallelen ebenen Wänden eingeschlossen ist (The resistance to movement of a rigid sphere in a viscous fluid, which is enclosed between two parallel flat walls). *Ann. Phys.-Berlin*, **37**, 89–119.
29. Strnadel, J., Simon, M., and Machač, I. (2011) Wall effects on terminal falling velocity of spherical particles moving in a Carreau model fluid. *Chem. Pap.*, **65**, 177–184.
30. Ataíde, C., Pereira, F., and Barrozo, M. (1999) Wall effects on the terminal

- velocity of spherical particles in Newtonian and non-Newtonian fluids. *Braz. J. Chem. Eng.*, **16**, 387–394.
31. Richardson, J. and Zaki, W. (1954) Sedimentation and fluidisation: part 1. *Trans. Inst. Chem. Eng.*, **32**, S82–S100.
  32. Baldock, T., Tomkins, M., Nielsen, P., and Hughes, M. (2004) Settling velocity of sediments at high concentrations. *Coastal Eng.*, **51**, 91–100.
  33. Andreasen, A., Jensen, W., and Lundberg, J. (1929) Ein Apparat für die Dispersoidanalyse und einige Untersuchungen damit (An apparatus for dispersion analysis and some research thereby). *Kolloid-Z.*, **39**, 253–265.
  34. Miller, K., Melant, R., and Zukoski, C. (1996) Comparison of the compressive yield response of aggregated suspensions: pressure filtration, centrifugation and osmotic consolidation. *J. Am. Ceram. Soc.*, **79**, 2545–2556.
  35. Vaidyanathan, K., Henry, J. Jr., and Verhoff, F. (1981) Indirect measurement of inclined sedimentation for ash in coal liquids at high temperature and pressure by x-ray photography. *Ind. Eng. Chem. Fundam.*, **20**, 165–168.
  36. Mengual, O., Meunier, G., Cayré, I., Puech, K., and Snabre, P. (1999) Turbiscan MA 2000: multiple light scattering measurement for concentrated emulsion and suspension instability analysis. *Talanta*, **50**, 445–456.
  37. Celia, C., Trapasso, E., Cosco, D., Paolino, D., and Fresta, M. (2009) Turbiscan Lab<sup>®</sup>: expert analysis of the stability of ethosomes<sup>®</sup> and ultradeformable liposomes containing a bilayer fluidizing agent. *Colloids Surf. B*, **72**, 155–160.
  38. Lerche, D. and Sobisch, T. (2007) Consolidation of concentrated dispersions of nano- and microparticles determined by analytical centrifugation. *Powder Technol.*, **174**, 46–49.
  39. Petzold, G., Goltzsche, C., Mende, M., Schwarz, S., and Jaeger, W. (2009) Monitoring the stability of nanosized silica dispersions in presence of polycations by a novel centrifugal sedimentation method. *J. Appl. Polym. Sci.*, **114**, 696–704.
  40. Keller, A., Wang, H., Zhou, D., Lenihan, H., Cherr, G., Cardinale, B., Miller, R., and Ji, Z. (2010) Stability and aggregation of metal oxide nanoparticles in natural aqueous matrices. *Environ. Sci. Technol.*, **44**, 1962–1967.
  41. Sillanpää, M., Paunu, T.-M., and Sainio, P. (2011) Aggregation and deposition of engineered TiO<sub>2</sub> nanoparticles in natural fresh and brackish waters. *J. Phys. Conf. Ser.*, **304**, 012018.
  42. Haywood, A. (2011) The effect of polymer solutions on the settling behaviour of sand particles. Dissertation. University of Manchester, p. 74.
  43. Sadat-Shojai, M., Atai, M., Nodehi, A., and Khanlar, L. (2010) Hydroxyapatite nanorods as novel fillers for improving the properties of dental adhesives: synthesis and application. *Dent. Mater.*, **26**, 471–482.
  44. Yow, H. and Biggs, S. (2013) Probing the stability of sterically stabilized polystyrene particles by centrifugal sedimentation. *Soft Matter*, **9**, 10031–10041.
  45. Talbot, E.L., Yow, H.N., Yang, L., Berson, A., Biggs, S.R., and Bain, C.D. (2015) Printing small dots from large drops. *ACS Appl. Mater. Interfaces*, **7**, 3782–3790.

## 7

### Jetting Simulations

*Neil F. Morrison, Claire McIlroy, and Oliver G. Harlen*

#### 7.1

##### Introduction

In the last fifteen years there has been a steady rise of interest in the simulation of inkjet flows. Industrial researchers now have a variety of computational tools at their disposal, along with the processing power to apply them to real problems, while academic groups have found the topic of jetting and breakup to be a rich seam abundant with diverse and delicate scientific phenomena suitable for study by numerical modelling.

Laboratory investigations of inkjet flows have proved highly challenging; advanced experimental techniques are required to achieve accurate visualization of the jetting dynamics on a sufficiently small scale. Nozzles are typically of order  $50\ \mu\text{m}$  in diameter while droplets of ink are ejected with velocities of up to  $20\ \text{m s}^{-1}$ , and so it is necessary to capture high-resolution images at frequencies of over a megahertz in order to capture individual breakup events in a continuous inkjet (CIJ) or to follow the evolution of a single drop-on-demand (DOD) ink ligament as it undergoes capillary thinning.

Furthermore, the inaccessibility of the flow within the print-head typically means that certain aspects of the jetting process are extremely difficult to assess by unobtrusive measurement. For example, the first pinch-off point of an ejected DOD ligament (i.e., the location at which the ligament detaches from the remaining ink in the print-head) normally lies marginally inside the nozzle chamber, and consequently the trailing rear end of the ligament cannot be observed in the earliest stages after pinch-off. Similarly, the full extent to which the meniscus is drawn back into the nozzle chamber by the driving modulation is difficult to visualize through experiments alone.

Because of the challenges involved in obtaining accurate and relevant experimental data, computational models have often been employed to provide researchers with additional insights into the flow dynamics of inkjet printing beyond those that are apparent in practice, and to aid developers in the pursuit of new technological innovations. Computer simulations can provide new insights

into various detailed mechanisms involved in the generation and breakup of jets, ranging from the fluid dynamics of the flow and the ink composition to the precise shape of the nozzle and the waveform of the driving modulation. They allow scientists to focus on specific parts of the flow, to assess the relative importance of parameters which might be impossible to isolate in practice, and to make alterations to the process without the need to build new prototype apparatus.

Although there are many tangible advantages to the use of numerical simulations in inkjet research and development, there are, of course, many potential difficulties to be considered. Commercial software packages can be expensive and cumbersome to use and may require a substantial amount of training, while the creation of a bespoke code is painstaking and may require several months even if the expertise is readily available. A programme of validation (benchmarking) is also necessary to ensure that the results are meaningful, and there may also be a certain degree of calibration involved in order to find a satisfactory balance between accuracy and runtime, for each particular application.

It is important, therefore, to have a clear set of objectives in mind before embarking on a computational investigation of an inkjet process. Several key questions should be discussed in advance, just as with any experimental study.

- Which parts of the process are of greatest interest?
- What can simulations add to the overall understanding?
- How can we best combine the insights gained from experiments and simulations?
- What tests can be conducted to assess the validity of the results?
- How will the results be factored into product design and development?
- Which parts of the process are fixed and which are variable?
- Where can simplifications be made?
- Can the previous work be adapted?
- Is it to be an empirical study, or do we wish to understand the underlying science?
- Are there in-house employees (or contacts thereof) who have relevant knowledge or experience?
- Are there academic links that could be beneficial?
- What are the time constraints for the investigation?
- What is the financial budget?

The answers to such questions may vary considerably based on the particular needs of each set of investigators, and the overall balance of priorities will strongly influence the scope of the study. Broadly speaking, commercial software packages are usually preferred by industrial research and development scientists, whereas academic investigators normally prefer to develop their own bespoke code. This is a generalization, of course, but it is based on several typical observations, which are pertinent to the discussion here in order to illustrate how the priorities may vary.

For example, industrialists usually wish to simulate a real process in full, with very specific geometry based on real manufactured part specifications, whereas academics are often interested in idealized sub-processes with simplified geometry but perhaps with more versatility. Industrial researchers might wish to use simulations as a proof of concept in developing new technology or to complement the results from ongoing experimental studies, while in an academic investigation, the actual industrial process may be a means to an end, with the real interest focused on the underlying science. In an academic study, sometimes, the development of the numerical method may be the objective in itself and the application to a real process may be used as a means of validation, whereas in industry, it is, of course, the opposite, and the focus is likely to be on obtaining meaningful results quickly.

Depending on the motivations behind the study, simplifications may be possible a priori, which could save time not only in the development of the numerical model but also in the runtime of each simulation. Although, nowadays, the processing power available to researchers is increasing at an exponential rate, it can still require several days of running on multicore machines to produce a sufficiently accurate simulation of an inkjet flow. However, it is often possible to take advantage of convenient symmetries in the flow domain, or to neglect certain aspects of the real process, and thereby enable computational resources to be spent where they would be most beneficial.

In the studies conducted in previous decades, such simplifications were fundamentally necessary. The pioneering numerical study by Fromm [1] showed for the first time the detailed evolution of a DOD jet from ejection to breakup, although at a computational time cost that was deemed unacceptably high to permit an exploration of the parameter space. With the aim of decreasing the runtime of simulations, Shield *et al.* [2] provided an early comparison of one-dimensional models and discussed the extent to which the full fluid dynamics may be simplified while maintaining relevant representative results. Constituent sub-processes of inkjet flows were also analyzed in isolation, for example, the breakup of contracting filaments (e.g., Schulkes [3] and Notz and Basaran [4]).

Subsequent improvements in computational power and the associated refinement of numerical methods allowed for the overall flow to be studied in greater detail, both in the case of slow pendant drop formation (e.g. Wilkes *et al.* [5]), and for industrial-speed jetting (e.g. Feng [6]). The emergence of commercially available computational fluid dynamics (CFD) software packages enabled non-specialists to create numerical models of their specific processes without incurring unacceptable overhead costs in time and resources. The relative merits of such software packages have been examined by Fawehinmi [7] in the context of drop formation.

Nowadays, computational modelling forms a staple part of most major industrial investigations into inkjet research and development, and there are dozens of academic groups around the world studying various aspects of jetting and breakup, many with direct links to industry and technology companies.



## 7.2

**Key Considerations for Modelling**

Inkjet processes are challenging to model directly. Flows are fully three-dimensional and transient. Geometries are often complex and asymmetric with many moving parts, sharp edges, and narrow constrictions. The high-speed ejection of liquid, often a multiphase suspension with thixotropic and/or viscoelastic properties, through tiny nozzle apertures leads to a severe test of the robustness of any numerical method. The effects of surfactants, air entrainment, temperature fluctuations, nozzle-plate wetting, crosstalk between adjacent nozzles, and electrostatic deflection of charged droplets are also factors that may be important or desirable to include in the modelling.

Even if some of these factors can be affordably neglected in the simulations, the idealized problem is often a tough application for computational tools. The fundamental scientific principle behind inkjet technology is the breakup of fluid jets or ligaments under surface tension, which involves the growth of infinitesimal perturbations along the free surface of the jet. Thus, in any computational model, it is imperative that the free surface is resolved accurately throughout the duration of the simulation – the detailed dynamics of jet breakup are highly sensitive, and the thinning of a fluid ligament must be followed right through until pinch-off and beyond. This demand imposes severe restrictions on the design of a numerical method. Non-uniform grid/mesh structures are necessary to ensure sufficient resolution in the thinnest parts of the jet, and this resolution must be adjusted adaptively over time to reflect the highly transient nature of the flow.

The schematic diagram of an idealized CIJ, shown in Figure 7.1, illustrates several important simplifications or assumptions that can potentially be made before designing a simulation. Firstly, the majority of the print-head structure and the interior of the nozzle chamber have been stripped off, leaving a single nozzle with a simple conical geometry. Secondly, an assumption of cylindrical symmetry has been made, which typically saves considerable computational time as compared to a fully three-dimensional model. Thirdly, an artificial inlet has been imposed (on the extreme left in Figure 7.1) to represent the continual replenishment of the ink in the nozzle chamber – the modulation of the jet at the desired frequency and amplitude may be represented by applying a time-dependent boundary condition on this inlet, based on the oscillation of pressure or fluid velocity caused in the nozzle chamber by the driving modulation. The resulting jet is assumed to emerge directly from the nozzle outlet with no wetting of the nozzle plate nor any slip of the contact line where the fluid meniscus meets the edge of the nozzle outlet.



**Figure 7.1** A schematic diagram for simplified continuous inkjet flow.



Similar simplifications are also applicable when developing a simulation of a DOD process. In this case, the principal distinction would be that instead of an inlet boundary condition of a small harmonic oscillation about an ongoing mean flow (as in CIJ models), there would be a temporary transient waveform of much larger amplitude, which ejects the ink ligament and then decays while the ligament detaches from the print-head. Consideration might also be given to which parts of the flow domain should be most well-resolved numerically in terms of the local mesh resolution. For instance, the most sensitive regions in CIJ are typically in fixed spatial locations due to the periodic nature of the flow (after initial startup). These locations are specifically (i) in the immediate vicinity of the nozzle outlet, where the modulation is imposed as an initial perturbation along the surface of the jet, and (ii) in the expected region of jet breakup where there may be a delicate borderline between the coalescence and detachment of satellite drops. By contrast, in a DOD flow, the key events are more transient in nature and thus the mesh resolution must update and evolve with the flow. During the ejection phase, the nozzle outlet region is most important, then subsequently, the focus of attention shifts to the point of break-off (typically inside the nozzle chamber) – thereafter, the thinning of the ejected ligament must be well-resolved, whereas the nozzle could be dispensed with altogether unless the modeller wishes to incorporate multiple ejection cycles.

Some examples of further assumptions that are commonly made, but are not illustrated in the diagram, are that the liquid being jetted is a homogeneous Newtonian fluid, that the airflow outside the jet may be represented simply by a constant coefficient of surface tension on the jet/air interface, that air resistance and perhaps also gravity may be neglected (depending on the physical dimensions of the process being modelled), and that any variations in temperature are insignificant. These and other simplifications are often made not only for convenience, in the sense that they save time in the computations, but also to permit the influence of variations of individual fluid parameters (e.g., density, viscosity, coefficient of surface tension) or other elements of the problem (e.g., nozzle shape, driving waveform) to be studied in isolation in a way that is often difficult in practice.

It should be noted that in Figure 7.1, there is no illustration of the impact of the jet (or drops) upon a substrate. In this chapter, we focus instead on simulating the generation of jets and drops, and the dynamics of breakup behaviour, rather than post-breakup events. Simulations of deposition and spreading are discussed by Wilson and Kubiak (see Chapter 11).

Similarly, in some applications, it may be that just one specific part of the overall jetting flow is the objective of a computational modelling programme and that the other parts are not the main focus of the investigation. For example, a researcher might wish to study the fluid dynamics occurring within the nozzle chamber, without devoting much attention to the external jet downstream. In such cases, it would be advisable to incorporate this focus into the design of the simulation in advance, in order to avoid spending time computing superfluous results, which will ultimately not provide a relevant contribution to the investigation. Conversely, if it is likely that various extensions and diversifications of the process will be

simulated, then it would be percipient to incorporate flexibility in order to avoid multiple stages of development and testing.

When first developing a simulation of an inkjet flow, the initial consideration is normally whether it should be a fully three-dimensional simulation or whether there are symmetries that can be exploited to reduce the spatial complexity. Jets are generally cylindrically symmetric, but nozzles and print-head geometries often are not, so a trade-off might be considered regarding the representation of the asymmetric components. In other words, how far back upstream behind the nozzle outlet should the model extend?

The boundaries of the initial fluid domain are specified by the physical dimensions of the interior of the nozzle chamber (and possibly the ambient air in the vicinity of the nozzle outlet). In a simulation, these might be defined via a simplified representation, for example, just a disembodied nozzle cone, or they could be based on importing a fully detailed blueprint into the model. There may even be additional elements incorporated into the initial domain beyond the part specification, for example, dimples or notches in the nozzle representing hypothetical manufacturing defects.

In the example illustrated in Figure 7.2, the initial fluid domain is bounded by an idealized axisymmetric nozzle chamber, so that the full 3D nozzle is a solid of revolution formed by rotating the pictured cross-section about the  $z$ -axis. The interior walls of the chamber are represented as line segments (edges, some curved) joining a number of distinguished points around the perimeter. These points are effectively the corners of the domain and may be given as inputs to a bespoke mesh

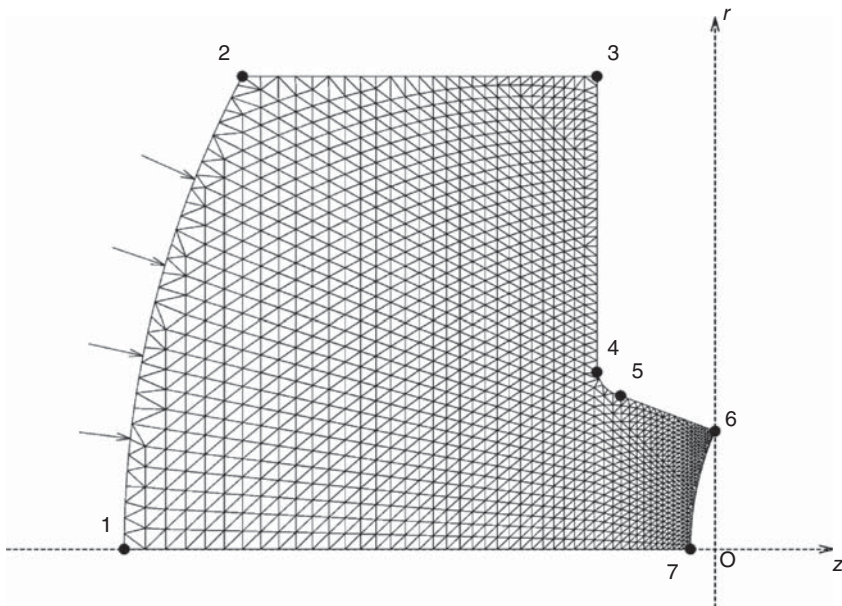


Figure 7.2 An example of how the initial fluid domain may be specified.

generator. In the case shown, the corners and connecting edges have the following properties: point 1 is a central pole on an artificial inlet, which runs between points 1 and 2, and this is the edge along which the driving waveform or modulation would be applied as a time-dependent boundary condition. Point 2 defines the join between the inlet and the interior walls of the nozzle chamber, and the edges between points 2 and 6 inclusive are considered as fixed rigid boundaries of the ink domain. Point 6 is situated at the nozzle outlet aperture, and the ink meniscus spans from points 6 to 7, with a curvature based on a prescribed initial condition. In Figure 7.2, the meniscus is assumed to be pinned at the outlet (point 6). Nozzle-plate wetting is not included in the diagram, but one could make adjustments to incorporate a wetting layer by pinning the meniscus further along the  $r$ -axis. Similarly, there is assumed to be no motion of the contact line between the meniscus and the nozzle edge. The resolution (i.e., the density of vertices) along the edges of the domain should be chosen appropriately to reflect the sensitivity of the flow to those components of the geometry and to ensure that the key boundary features of the intended geometry are captured.

Once the initial flow geometry has been defined, it must then be meshed, either in full 3D or as a cross-section, meaning that discrete vertices (or nodes) are defined throughout the fluid domain and its boundaries in order to subdivide it into a large number of small cells (or elements). The governing equations, typically non-linear partial differential equations, are then recast into a discrete formulation suitable for iterative solution by numerical algorithms designed for linear algebra. Meshing the initial fluid domain can be performed either by working inward from the boundary (e.g., the “advancing front” algorithm) or by overlaying a uniform grid and trimming away the vertices lying outside the domain. For more complex geometries, it may be expedient to use online software to automate this procedure.

In Figure 7.2, for example, the initial mesh resolution varies smoothly along the  $z$ -direction with a greater concentration of vertices in the neighbourhood of the nozzle outlet and the free surface of the fluid. Once the simulation is underway, it may be beneficial to have the mesh resolution vary dynamically in different regions of the flow, with the addition of vertices in areas of greatest importance and the removal of vertices in less important areas where a reduced accuracy is sufficient – this is known as *adaptive mesh refinement*.

The details of the nozzle geometry being modelled also determine the boundary conditions to be imposed on each edge of the boundary of the fluid domain. Jetting is normally induced by a driving velocity or pressure oscillation at the inlet, or by the deformation of moving parts of the nozzle chamber, and jet breakup is caused by the action of surface tension along the jet/air interface. Consequently, there are significant differences in the nature of the boundary conditions to be applied in the corresponding parts of the domain boundary. Along rigid interior walls, a no-slip condition (zero lateral fluid velocity) is usually imposed. If there are moving parts or other fluctuations of the nozzle chamber walls, then there would be a time-dependent normal velocity along those surfaces. If, as in Figure 7.2, symmetry has been assumed, then there is also a corresponding symmetric boundary

condition along the axis. On the free surface of the jet, there is a condition of zero shear stress and also the interfacial pressure discontinuity due to the surface curvature – the precise nature of the latter condition might depend on the extent to which the ambient airflow is included in the modelling and on whether any aspect of dynamic surface tension or the effect of surfactants is being considered.

The inlet boundary condition is the one where the modeller has the most choice, a reflection of the diversity of jetting mechanisms in real devices. If the jetting is being induced by deformation of the nozzle chamber walls, then the model might include a direct replication of this deformation, in which case the inlet serves principally to replenish the fluid in the chamber at an appropriate rate. Conversely, if the jetting is induced further upstream by the expansion of a bubble, or the oscillation of a membrane or some other physical construction that is not incorporated in the model, then the inlet boundary condition may instead be a representative oscillation of fluid velocity or pressure. In the simulation, this oscillation would be imposed either as a continuous function of time or as a smooth interpolation of discrete data based on measurements of the actual device. This type of implementation is likely to require substantial calibration in order to justify the assumptions made.

Another major consideration is the spectrum of fluids to be incorporated in the model. The applicability of any particular numerical method may depend strongly upon whether the fluids are constrained to be Newtonian or whether more complex fluids are being jetted. Non-Newtonian fluids, particularly viscoelastic fluids, have traditionally proved rather difficult to simulate even in straightforward geometries due to the hyperbolic nature of certain constitutive equations, and thus it is important to establish which rheological models are relevant and to take this into account when choosing the method. Similarly, if it is desired to simulate multiphase fluids, either as a continuum or with tracking of individual particles, then there are likely to be restrictions imposed on which algorithms are appropriate for the numerical discretization.

In applications relevant to inkjet flows, the most frequently used numerical methods in computational fluid dynamics software are the finite element method, the finite volume method, and the volume of fluid method. The finite difference method is also used in one-dimensional models where strong assumptions are imposed on the flow. It is not our aim here to give a full description of these methods in general, but rather to discuss their advantages briefly in the context of inkjet simulation.

The finite element method is popular in many industrial applications, particularly those with complex geometry and/or where unstructured meshing is desirable. It is also often favoured by academic researchers writing bespoke code for specific problems. In the extended case where the mesh nodes are Lagrangian material points in the fluid (i.e., they advect with the flow), it is also particularly suitable for the simulation of viscoelastic fluid models with free surfaces, provided that a mesh reconnection algorithm is also implemented. The finite volume method has been popular in generic CFD software due to its speed and flexibility, as it also permits unstructured meshes and is typically faster (but less stable) than

the finite element method, although its solutions are less accurate for equivalent mesh resolutions. The volume of fluid method is favoured in some commercial CFD packages as an enhancement for handling free surface flows, and it also has the potential capacity to enable some multiphase fluids to be simulated. However, it does not in itself provide a full solution for the flow within the fluid, and it must be coupled to another method (typically, the finite difference method).

In summary, regardless of whether the modelling is being performed via a bespoke code or a commercial software package, the choice of numerical method should be made carefully with consideration given not only to each method's generic computational speed and accuracy but also to its suitability for the intended study. There is not always a single "correct" choice, and indeed, it might be preferable to consider more than one option if possible. Major requirements for most inkjet simulations include the following:

- Accurate representation of jet breakup on small scales
- Accurate capture of the free surface dynamics of jets and thin ligaments
- Adaptive resolution in space and time
- Capacity to model the print-head geometry
- Capacity to include non-Newtonian fluid models.

## 7.3

### One-Dimensional Modelling

#### 7.3.1

##### The Long-Wavelength Approximation

Solving the full Navier-Stokes equations can be computationally expensive. Thus, in order to simplify the problem, the slender-jet approximation is often invoked for modelling jet breakup (for example, Eggers [8]). Based on the Reynolds lubrication theory, the wavelength of the jet is assumed to be sufficiently long such that the jet's velocity is independent of its cross-sectional area. Therefore, the kinematics of the motion are approximated as one-dimensional, depending only on the axial coordinate  $z$  (and the time  $t$ ) but independent of the radial and azimuthal coordinates.

By denoting the jet radius as  $h(z, t)$  and velocity as  $v(z, t)$ , the conservation of mass and momentum are given, respectively, by

$$\frac{\partial h^2}{\partial t} + \frac{\partial}{\partial z}(h^2 v) = 0$$

$$\frac{\partial}{\partial t}(h^2 v) + \frac{\partial}{\partial z}(h^2 v^2) = \frac{\partial}{\partial z} \left( h^2 \left( K + 3Oh \frac{\partial v}{\partial z} \right) \right)$$

where  $K$  is a curvature term discussed below, and the dimensionless Ohnesorge number is defined as

$$Oh = \frac{\mu}{\sqrt{\rho \gamma R}}$$

for a fluid with viscosity  $\mu$ , density  $\rho$ , and surface tension  $\gamma$ . For CIJ applications, inks generally have a low viscosity and are dominated by inertial effects with  $Oh \ll 1$ . The jet velocity is non-dimensionalized with respect to the nozzle outlet radius  $R$  and the Rayleigh capillary timescale  $\sqrt{\rho R^3/\gamma}$ , so that the initial dimensionless jet velocity is defined by the Weber number

$$We = \frac{\rho U^2 R}{\gamma}$$

for mean jet velocity  $U$ . Although, to leading order, the curvature term is  $K \sim 1/h$ , in order to include the effects of longitudinal curvature and retain the accuracy of the curvature beyond the limit in which  $h_z \ll 1$ , the full curvature expression

$$K = \frac{1}{h(1+h_z^2)^{1/2}} + \frac{h_{zz}}{(1+h_z^2)^{3/2}}$$

is used, where the  $z$ -subscript denotes differentiation with respect to  $z$ . Note that  $K$  has the same form as mean curvature, but both the axial and radial contributions to this curvature term are positive.

The validity of this approximation becomes questionable in the vicinity of large gradients, for example, in the neck regions connecting thin filaments of fluid to larger drops. However, this description remains surprisingly accurate, even if the long-wavelength assumption is not strictly valid [9]; results under this approximation are found to be highly quantitative, often representing the exact solution near to breakup. In particular, Ambravaneswaran *et al.* [10] have carried out a detailed comparison with the full Navier-Stokes solution, with excellent agreement for a wide range of parameters. This approximation can be expanded to higher order, which in principle could lead to a better description of non-linear jet dynamics. However, due to the increasing orders of spatial derivatives, which are difficult to compute, generally this has not been pursued.

Models based on these one-dimensional equations have been developed for their simplicity and computational efficiency and have been used with much success in modelling the thinning of liquid jets and filaments [11, 12] and the formation of droplets [10, 13]. These equations form the foundation for the simple CIJ model discussed throughout the remainder of this section.

### 7.3.2

#### A Simple CIJ Model

For simple idealized modelling, the details of the nozzle geometry are neglected altogether and only the dynamics at the nozzle exit are considered. In particular, for one-dimensional models, the driving velocity is assumed to have a plug-flow profile, where the fluid velocity is uniform across the jet radius. However, in real inkjets, the extrusion through the nozzle generates a Poiseuille flow so that the velocity profile is parabolic across the radius; shear at the nozzle wall slows down the outer fluid, so that the central section of the jet moves faster. Nonetheless, it has been shown that, beyond a sufficient distance downstream of the nozzle exit,



the velocity relaxes to a uniform profile [14]. Consequently, a one-dimensional model is expected to be sufficient for capturing the downstream dynamics of a CIJ.

Since spherically shaped drops are produced upon breakup, the downstream boundary condition is assumed to be an advancing spherical cap, for which  $K = 0$ . For an Eulerian coordinate system, material flows through the mesh so that an algorithm for “switching on” grid nodes as the jet advances along the grid is implemented. Additionally, a breakup criterion is defined when  $h$  becomes smaller than a specified cut-off radius  $h_c$ ; if  $h = h_c$ , then the fluid ahead of the break point is separated from the remaining jet and evolves to form a drop. The distance from the nozzle exit to this point of breakup defines the overall breakup length of the jet. Typically, the cut-off radius is set below 1% of the nozzle radius, and it should be ensured that  $h$  is greater than the spatial error incurred by the numerical scheme used for solving the governing equations.

The use of an adaptive meshing scheme is beneficial to the CIJ problem. Neck regions, where pinching of the free surface occurs, require a sufficiently fine mesh in order to obtain an accurately resolved solution, whereas dynamics upstream near the nozzle exit and in the larger drops are comparatively simple and so may be computed on a much coarser mesh. Thus, an adaptive mesh that, by construction, automatically refines in areas of high curvature can provide a resolved solution in a reduced computation time.

In order to drive the jetting, two methods may be used. Firstly, the jet radius at the nozzle exit may be varied such that

$$h(0, t) = 1 + \varepsilon \sin(2\pi ft) \quad (7.1)$$

for amplitude  $\varepsilon$  and jetting frequency  $f$ . Modulations in the radius mimic thermal fluctuations in the nozzle, and a similar approach has been used by van Hoeve *et al.* [15]. For small amplitudes ( $\varepsilon \leq 0.01$ ), a Rayleigh-type instability wave is propagated downstream from the nozzle exit. Although these waves are closely related to Rayleigh waves, they grow with spatial distance from the nozzle exit rather than time, and they are only equivalent to Rayleigh waves in the limit of infinite Weber number [16]. Since CIJs typically operate in the large Weber number limit ( $We \sim 400$ ), Rayleigh’s temporal theory is considered to be valid for describing the linear dynamics during the jetting process.

More realistically, inkjets are usually driven by a pressure modulation that translates to a variation in the mean jet velocity at the nozzle outlet. Thus, a second method is to impose a time-dependent velocity perturbation such that

$$v(0, t) = \sqrt{We}(1 + \varepsilon \sin(2\pi ft)) \quad (7.2)$$

Modulations of the velocity profile do not necessarily translate to a sinusoidal variation of the free-surface height, and so, the instability is not necessarily related to a typical Rayleigh wave. Furthermore, for industrial applications, large amplitudes ( $\varepsilon > 0.1$ ) of the driving velocity are applied, meaning that nonlinear interactions are important, which again are not accounted for by Rayleigh’s stability theory.

To compute the evolving free surface profile predicted by this one-dimensional CIJ model, a simple explicit second-order finite difference approach may be used

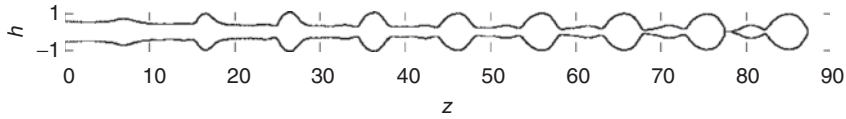


**Figure 7.3** Free surface of a continuous inkjet using a one-dimensional numerical model.

to solve the slender-jet equations [17]. It is important to choose the time step and mesh size in tandem to ensure stability of the difference scheme and accuracy of the computed solution. For example, Figure 7.3 shows a typical jet shape and breakup pattern predicted by this simple CIJ model, based on realistic fluid parameters.

### 7.3.3

#### Error Analysis for Simple Jetting

It is important to test the accuracy of the simple model in relation to the time stepping and mesh size implemented by the numerical scheme. For the simple CIJ model, numerical errors can be analyzed by considering the variation in breakup length for various time steps  $dt$  and mesh sizes  $dz$ . In Figure 7.4 the dimensionless breakup length, calculated as an average over 10 drops, is plotted with error bars representing the standard deviation from the average.

Figure 7.4a shows the breakup length calculated for a range of time steps  $dt$  with fixed mesh spacing  $dz = 0.025$ . The variation in breakup length is small (as compared to the jet wavelength, which in this case is set equal to 9) and is approximately constant ( $\approx 2.3$ ) for decreasing time step, despite the numerical scheme admitting second-order temporal accuracy. Thus, the deviations from the average jet length must originate from the mesh resolution.

For decreasing mesh size  $dz$  and fixed time step  $dt = 10^{-5}$ , Figure 7.4b shows that the dimensionless breakup length of the jet converges to approximately 104, and again, the standard deviation remains within one jet wavelength. However, as the mesh size is increased, the calculation becomes less accurate, departing from the converged value; as expected, the mean breakup length decreases linearly with  $dz^2$  due to the second-order spatial accuracy of the numerical scheme used. Somewhat counterintuitively, the size of the error bar decreases for coarser mesh sizes. Whereas fine meshes capture all of the features of breakup, low resolution does not capture the appearance of small satellite drops, which cause variation in the breakup length. Thus, since only the formation of the main drops is accounted for, there is a smaller deviation from the mean for larger mesh sizes.

### 7.3.4

#### Validation of the Model by Rayleigh's Theory

In order to test whether the model predictions are physically accurate, it is important to validate the results against a reference benchmark. This can be done by



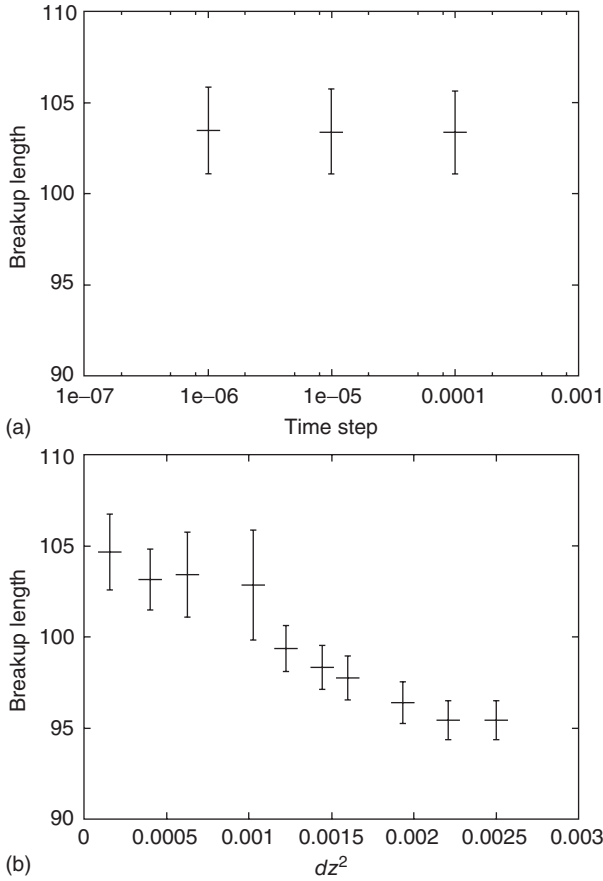


**Figure 7.4** Jet breakup length calculated by a simple CIJ model for a range of values of (a) time step and (b) mesh size.

comparing the model results to experimental observations or theoretical calculations. For jetting applications, it is common to validate models against the classical linear stability theory, first derived by Rayleigh [18].

In the long-wavelength approximation, the dispersion relation for a Newtonian fluid is given by

$$\alpha^2 + \frac{3\mu k^2}{\rho}\alpha - \frac{\gamma k^2}{2\rho R}(1 - k^2 R^2) = 0 \quad (7.3)$$

for growth rate  $\alpha$  and wave number  $k (= 2\pi/\lambda)$ . Thus, a jet is unstable provided that  $kR < 1$ , which is to say that the jet wavelength  $\lambda$  is greater than the circumference of the jet. Furthermore, solving Eq. (7.3) for the maximum growth rate yields the most amplified wave number, which, for jets dominated by inertial effects, corresponds to the most unstable wavelength  $\lambda^* \approx 9R$ . The inverse of the dispersion relation, multiplied by an arbitrary constant to account for the initial disturbance,

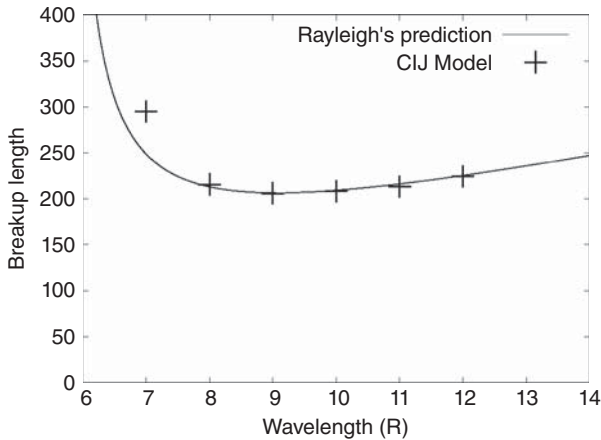


**Figure 7.5** Jet breakup length calculated by the simple CIJ model as compared to the prediction of Rayleigh's theory, for a range of wavelengths.

gives a theoretical breakup curve, predicting the ultimate breakup length of the jet for a particular wavelength.

In order to validate the simple CIJ model described, we drive the jet by applying a sinusoidal variation to its radius at the nozzle outlet as in Eq. (7.1) to create a Rayleigh instability wave. It is important to note that Rayleigh's theory is valid only in the limit of large Weber number – so that the spatial structure of disturbances growing along the jet is periodic – and for small driving amplitudes, so that the linear analysis is applicable. In Figure 7.5, the breakup length predicted by the simple CIJ model is compared to the inverse of Rayleigh's dispersion relation for theoretical validation.

The one-dimensional model results are in agreement with Rayleigh's theory for a range of wavelengths. Indeed, the shortest jets are produced by the most unstable wavelength  $\lambda^*$  and longer jets may be generated by imposing a different frequency due to the increased stability of the disturbance wave. As expected, there is a slight discrepancy for  $\lambda = 7R$  due to the validity of the slender-jet approximation for short wavelengths. Thus, the results of the simple CIJ model are considered physically correct in this linear regime.

Further validation tests which may be conducted include: ensuring that the growth rate  $\alpha$  of the applied perturbation agrees with that predicted by the theoretical dispersion relation for a particular wavelength; testing the effect of varying the Ohnesorge number. For larger Ohnesorge numbers, the maximum growth rate of the perturbation is reduced, due to viscosity retarding the disturbance wave. Thus, the wavelength of the most unstable wave should increase for higher viscosity jets.

Although linear theory provides a powerful validation tool, typical applications of CIJ operate at much larger amplitudes, inducing non-linear interactions in the dynamics which are not as well understood theoretically. Therefore, simulations

offer a valuable tool to explore this non-linear behaviour; however, comparable experiments are essential for validation.

### 7.3.5

#### Exploring the Parameter Space

Numerical simulation is now often considered equally as important as experimental data in analyzing the CIJ process, allowing a wide range of conditions and parameters to be tested which may be difficult to access experimentally. For the simple one-dimensional CIJ model, it is possible to explore the effect of varying different fluid properties by modifying the Ohnesorge number and the Weber number, as well as different jetting conditions by adjusting the driving boundary condition imposed at the nozzle outlet. In this sense, numerical simulation provides a simple tool for establishing breakup behaviour, and therefore optimum jetting conditions, without requiring the use of expensive consumables such as ink.

As an example, Figure 7.6 shows how changing the amplitude of a velocity-modulated jet can affect the type of breakup behaviour observed. In general, an ejected liquid jet forms a series of main drops connected by thinner filaments; however, the first pinch-off event depends on the amplitude of the driving velocity modulation. For small amplitude  $\varepsilon = 0.05$ , pinch-off first occurs downstream of the connecting filament, and similar breakup patterns have been observed by van Hove *et al.* [15]. Yet, increasing the amplitude to  $\varepsilon = 0.1$  causes the breakup to become “inverted” with the first pinch-off occurring upstream of the connecting filament, a phenomenon that is commonly observed both experimentally and in industrial applications (e.g., Chaudhary and Redekopp [19] and Kalaaji *et al.* [20]). However, increasing the amplitude further to  $\varepsilon = 0.15$  causes the breakup to revert back to downstream pinch-off.

For most CIJ applications, it is important to establish the optimum operational window for which satellite-free jetting is generated. Inverted pinch-off is generally

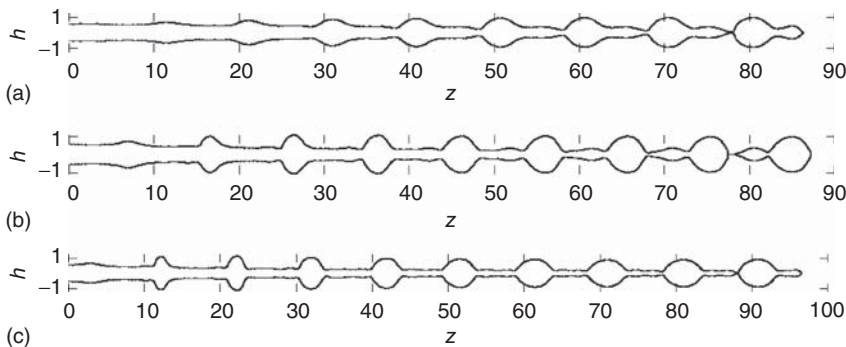


**Figure 7.6** Jet shapes predicted by the simple CIJ model for three different values of the modulation amplitude:  $\varepsilon = 0.05$  (a),  $\varepsilon = 0.1$  (b), and  $\varepsilon = 0.15$  (c).

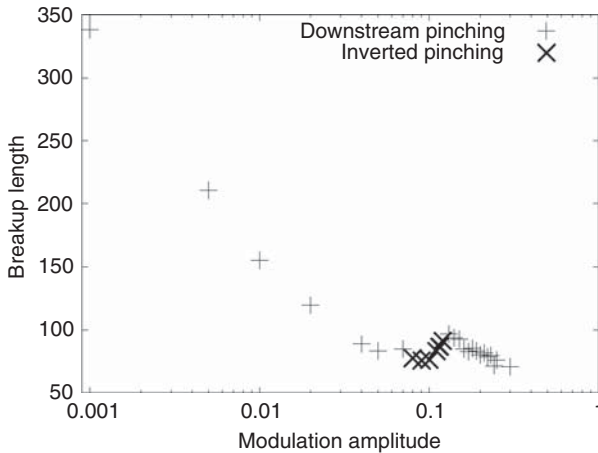


**Figure 7.7** Dependence of the jet breakup length upon the modulation amplitude.

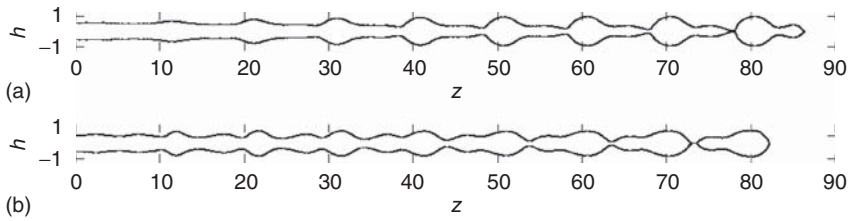
considered preferable for CIJ printing, since satellite drops can be completely eliminated by forward merging with the leading drop. On the other hand, downstream breakup is less desirable although satellite drops may be managed by rear-merging. By conducting a series of numerical simulations with increasing values of the modulation amplitude  $\varepsilon$ , the critical window for which this preferable inverted breakup occurs may be identified.

Figure 7.7 demonstrates a typical breakup curve, with jet breakup length plotted against modulation amplitude, predicted by the simple CIJ model; the X symbols indicate where inverted breakup is observed. As well as highlighting the optimum operational window, breakup curves (such as that shown in Figure 7.7) give an indication of the jetting behaviour. For example, at small amplitudes, Figure 7.7 shows an exponential decay in the breakup length, as would be expected by a linear instability, indicating the amplitude range for which the jet behaviour can be successfully described by linear theory. Deviation from this exponential behaviour demonstrates where non-linear interactions become important. It is in this non-linear regime, at approximately 10% of the driving velocity, that the ideal driving conditions for the specified fluid parameters are achieved. The effects that fluid properties have on this operational window can be explored readily via one-dimensional simulations.

### 7.3.6

#### A Numerical Experiment

As well as the capacity to explore a broad parameter space, one advantage of simulation is the ability to conduct numerical experiments and test scenarios that may not be possible with current technology. For example, the simple CIJ model allows the driving signal to be readily adapted via a straightforward change of the relevant boundary condition. In particular, it is known that the addition of higher



**Figure 7.8** Jet shapes calculated by a one-dimensional CIJ model with two different modulations – (a) first harmonic only and (b) with a second harmonic added.

order harmonics to the velocity modulation can have a significant effect on the breakup behaviour of a CIJ; Chaudhary and Maxworthy [21] have shown theoretically that the formation of satellite drops can be controlled by modulating the jet with a suitable harmonic added to the fundamental mode.

As an example, we examine the effect of adding a second harmonic to the driving velocity modulation in the form

$$v(0, t) = \sqrt{We}(1 + \varepsilon \sin(2\pi ft) + \varepsilon \sin(4\pi ft + \theta)) \quad (7.4)$$

Figure 7.8 shows how adding this second harmonic component affects the free-surface shape calculated by the simple CIJ model. In particular, the downstream pinch-off that is usually observed in this case is inverted to the preferred behaviour by modifying the driving signal in this way. Thus, it is possible to shift the optimum operational window to smaller amplitudes.

Although it is possible to add higher order harmonics to the driving modulation signal in current CIJ technology, in order to achieve the inversion of breakup to the desired behaviour, the simulation suggests that a phase shift is also required in order to induce asymmetry and that the coefficients of the two harmonics should be of the same order of magnitude. These conditions may be difficult to obtain within current CIJ print-heads.

## 7.4

### Axisymmetric Modelling

In order to incorporate more realistic nozzle structures and more diverse boundary conditions in the driving waveform (in particular for DOD processes) some of the simplifications discussed in the previous section must be dropped; the flow fields may no longer be assumed to be independent of the radial coordinate, and so, the governing equations of the flow must be solved in full. However, in a substantial majority of inkjet scenarios, the cylindrical symmetry of the jet about its axis may be exploited as an assumption in simulations without loss of generality, provided that the print-head geometry can also be represented in a cylindrically symmetric way. With this assumption, the modelling is axisymmetric; the jet and the print-head geometry may be fully described by a cylindrical coordinate system consisting of an axial coordinate  $z$  and a radial coordinate  $r$ , with the flow fields

being independent of the azimuthal (angular) coordinate. The coordinate origin may be taken at the centre of the nozzle outlet. The governing equations may then be solved numerically by applying one of the staple techniques of CFD depending on which is most suitable for the problems being considered.

In this section, we present various results obtained via an axisymmetric model of this form, to illustrate some of the aspects of inkjet which can be studied by computer simulations. The simulations shown here used a Lagrangian finite element method first developed for the study of creeping flow of dilute polymer solutions by Harlen *et al.* [22]. This method has since been extended to inertial flows and has been applied to study inkjet printing of Newtonian fluids (e.g., Castrejón Pita *et al.* [23, 24]) and viscoelastic and shear-thinning fluids (e.g., Morrison and Harlen [25, 26] and Morrison *et al.* [27]). Further details of the computational method may be found in these references; in brief, with regard to inkjet flows, the chief advantages of this particular Lagrangian finite element method are in capturing the free surface of the jet without numerical diffusion and in permitting a wide range of non-Newtonian constitutive relations to be modelled in an appropriate co-deforming reference frame.

#### 7.4.1

##### Continuous Inkjet

Figure 7.9 shows a comparison of the CIJ surface shapes observed in large-scale experiments (via shadowgraph imaging) by Castrejón-Pita *et al.* [23] and those computed by numerical simulations using the same jetting conditions and fluid parameters, for two different values of the modulation amplitude. Each image has been cropped to show only the neighbourhood of jet breakup. There is a close similarity between the simulated and experimental jets; analogous agreement was found over a range of parameters. Slightly longer droplet tails are visible in the simulation snapshots as compared to the corresponding shadowgraph pictures due to a small relative time lag between the two images.

The comparison shown in Figure 7.9 formed part of a programme of validation of the axisymmetric numerical method and its applicability to the modelling of jetting flows. In the simulations, the print-head geometry was simplified down to a straightforward nozzle cone not unlike that shown in Figure 7.1, and this was found to be sufficient to replicate the experimental jet. No significant differences to the computed jet were observed when using a more detailed model of the interior of the experimental print-head.

For a given fluid, the breakup pattern of a CIJ depends both on the amplitude of modulation and on the aspect ratio  $L/D$  of the straight section of the nozzle outlet, where  $L$  is the length and  $D$  the diameter. Whereas in one-dimensional models, a plug-flow velocity profile is assumed at the nozzle outlet, in reality, flow through a narrow constriction leads to a non-uniform profile upon emergence (typically a power law), with longer nozzles yielding a more Poiseuille-like variation across the jet radius. In axisymmetric simulations, it is normally a trivial adjustment to

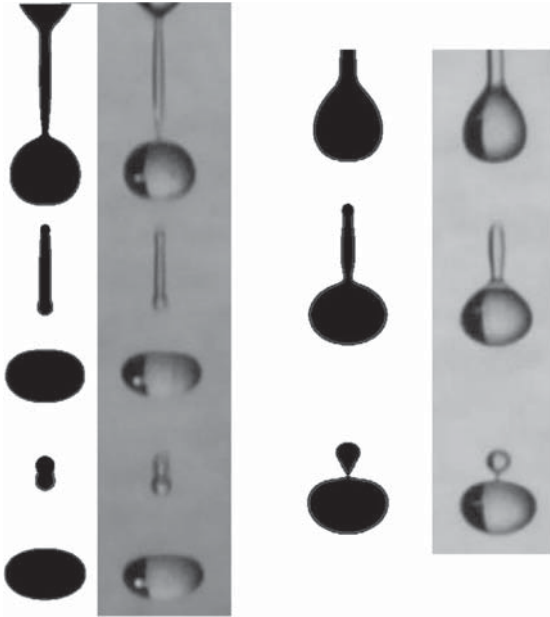


**Figure 7.9** Comparison of CIJ breakup in axisymmetric simulations and large-scale experiments for two different values of the modulation amplitude [23]. Reprinted (Figure 8) with permission from Ref. [23]. Copyright (2011) by the American Physical Society.

change the aspect ratio of the nozzle and thus explore a parameter space, which may be inconvenient to study with experiments alone.

Results from such an exploration are shown in Figure 7.10. Both the length of the nozzle outlet and the modulation amplitude were varied with all other parameters held fixed, and the breakup patterns of the resulting jets were classified according to whether or not satellite droplets were formed between consecutive main drops and whether the pinch-off of the connecting filaments first occurred at the upstream or downstream end (the latter is known as *reversal*). Images of the simulated jets are shown for selected points in the parameter space, illustrating the strong dependence of breakup behaviour upon both the nozzle length and the modulation amplitude. In this particular study, the modulation was applied as a nozzle vibration; in simulations, an equivalence was found (for simple sinusoidal modulations) between the two actuation methods of nozzle vibration and inlet flow rate modulation of equal frequency, with a simple rule for conversion between the corresponding amplitudes.

A numerical exploration of parameter space such as that shown in Figure 7.10 may involve hundreds of separate cases to be simulated in order to cover the range of possible outcomes with sufficient resolution. However, since a full axisymmetric CIJ simulation is computationally expensive relative to the one-dimensional model, it is desirable to develop a hybrid model that includes aspects

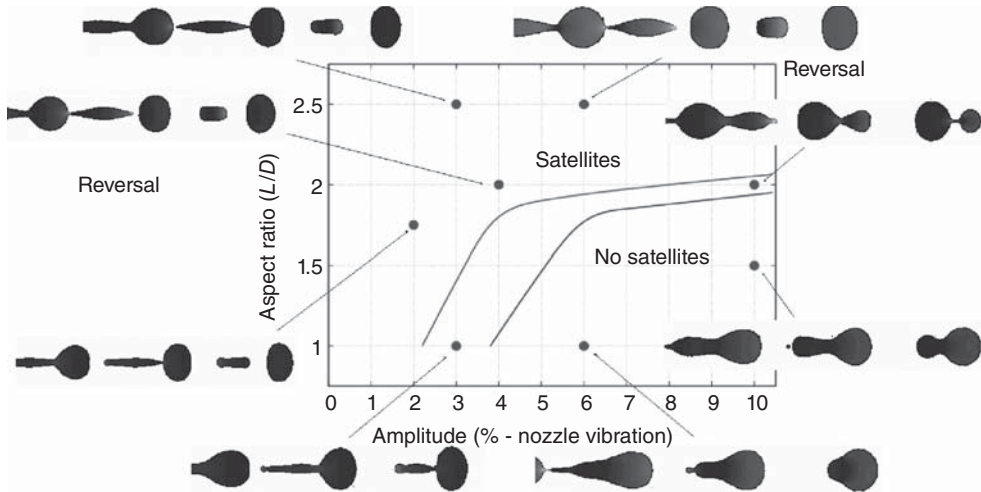


**Figure 7.10** Dependence of CIJ breakup pattern upon nozzle aspect ratio and modulation amplitude. The parameter space is partitioned based on whether satellite drops were observed.

of both methods. Indeed, it is possible to incorporate the dynamics of the jet surface instability generated in an axisymmetric model as an input modulation in the simpler one-dimensional model described earlier, in effect splicing the two models together. To generate the input data, the jet's radius and cross-section-averaged velocity are recorded in the early stages of an axisymmetric simulation at some fixed measuring point downstream of the nozzle outlet. The location of the measuring point must be sufficiently far downstream that the cross-sectional velocity profile of the jet is approximately uniform, since the one-dimensional model assumes a simple plug-flow profile. The recorded data are then interpolated by fitting a Fourier series containing three harmonic components, and the resulting waveform is employed as the “nozzle” boundary condition of the one-dimensional CIJ model. This approach creates both a height and velocity perturbation in the simpler model, which mimics the effects of flow through different nozzles without requiring the full axisymmetric model to be followed all the way to breakup. Figure 7.11 shows an example of the jet surface shape predicted by the “spliced” model as compared to the full axisymmetric simulation

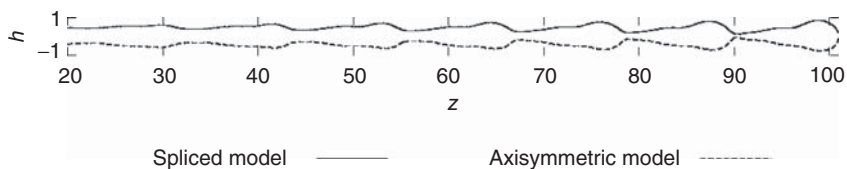


**Figure 7.11** Comparison of jet surface shapes computed by the spliced model and the full axisymmetric simulation.



**Table 7.1** Computational time required for the full axisymmetric simulation as compared to the spliced model, on a Dell workstation with 2.4 GHz processor.

	Hours	Minutes	Seconds
<b>Spliced model (total)</b>	<b>2</b>	<b>31</b>	<b>20</b>
Axisymmetric input	1	48	55
One-dimensional model	0	42	25
<b>Full axisymmetric model</b>	<b>55</b>	<b>8</b>	<b>12</b>

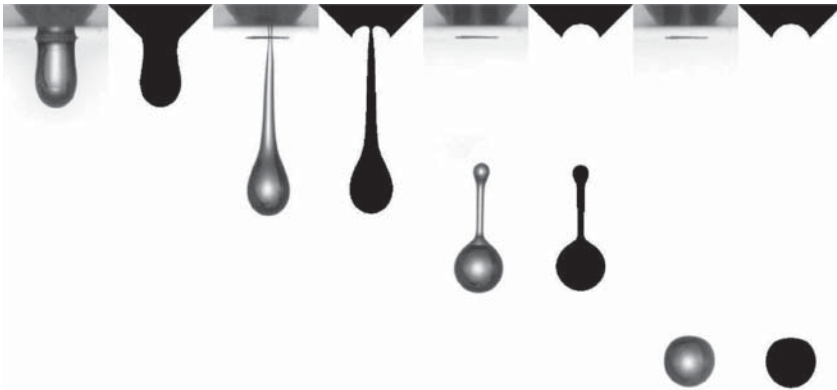
of the same case. The spliced model is able to reproduce, both qualitatively and quantitatively, the elongated surface pattern generated by the nozzle flow in agreement with the full simulation.

Table 7.1 summarizes the computational runtime used by both models. For the spliced model, the total runtime is broken down into the time taken to generate the input data via the early stages of the axisymmetric simulation and the time taken to run the one-dimensional model with that input. The overall runtime is reduced by a factor of  $\sim 22$  by the spliced model, while still capturing the effects of the specific nozzle geometry on the development of the surface instability along the jet.

#### 7.4.2

##### Drop-on-Demand

For DOD processes, a one-dimensional model is inappropriate due to the large flow oscillations in the nozzle chamber and the nature of the breakup events;

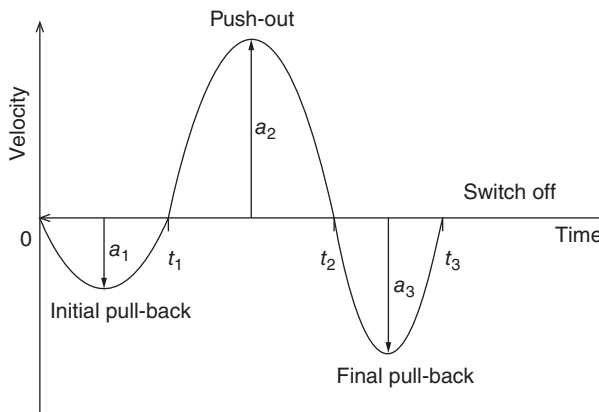


**Figure 7.12** Comparison of drop formation in axisymmetric simulations and large-scale experiments [24]. Reprinted (Figure 10) with permission from Ref. [24]. Copyright (2011) by the American Physical Society.

indeed, the first detachment of an ejected ink ligament from the print-head generally occurs inside the nozzle with a concave meniscus. Therefore, an axisymmetric model is more suitable for simulating DOD flows. In Figure 7.12, four different stages of drop formation are shown with comparison between simulations and large-scale experiments by Castrejón Pita *et al.* [24], with the same fluid parameters. In the corresponding study, the driving waveform in the simulation was based directly on measurements of the experimental flow within the nozzle chamber (using laser anemometry and a Perspex nozzle). This study contributed to the validation of the axisymmetric model and also informed the experimental group on the success of their flow measurement techniques.

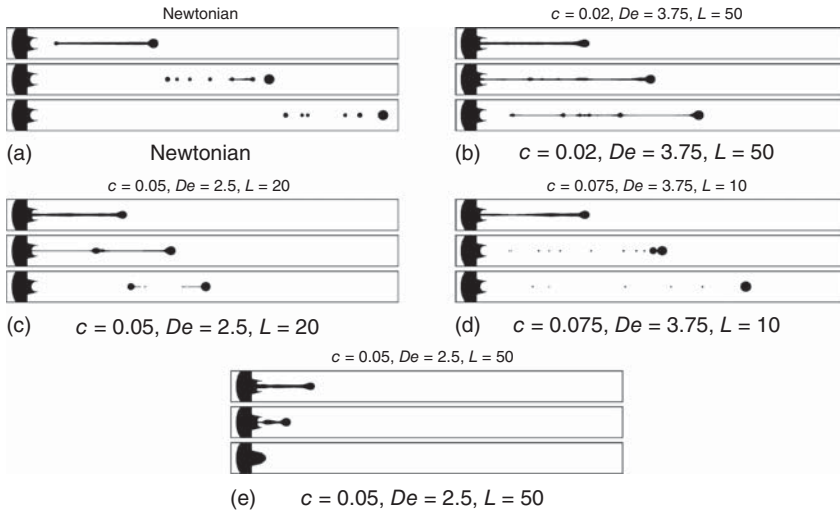
In any DOD simulation, the most sensitive part of the problem specification is the description of the driving waveform and how it may be incorporated in the model based on data derived from the real process. For example, in a print-head, the flow might be induced by an electrical signal fed to a transducer or piezoelectric component, which then generates a pressure and velocity oscillation in the nozzle chamber. Ideally, in a simulation, one would like to have an accurate measurement of this flow oscillation to provide the boundary condition on the nozzle inlet and maintain the axisymmetry of the simplified nozzle geometry used in the model. As the flow in the nozzle chamber is not always well known in the real process, some aspect of feedback and calibration may be needed in order to ensure that the simulations provide relevant results. In general, however, one may assume that a fairly simple square-wave electrical input gives rise to a roughly sinusoidal oscillation of decaying amplitude; deviations from this simple description form part of the finesse of each application.

Figure 7.13 shows a simplified waveform consisting of three parabolic sections, based on a smoothed fit to industrial data. This waveform consists of three main



**Figure 7.13** A canonical driving waveform applied as an inlet boundary condition in axisymmetric DOD simulations [25]. The driving signal, as a function of time. The

driving is imposed as a velocity boundary condition over the nozzle inlet. Copyright Springer-Verlag (2009), with kind permission from Springer Science and Business Media.



**Figure 7.14** Axisymmetric DOD simulations for five viscoelastic fluids; images of each case shown at three different times [25]. Copyright Springer-Verlag (2009), with kind permission from Springer Science and Business Media.

phases, a “pull/push/pull” structure; variations to this template may easily be considered. In a real nozzle chamber, the flow would continue indefinitely as further decaying oscillations, but in simulations, it was found to be sufficient to “switch off” the inlet flow after the three phases illustrated because pinch-off of the ink ligament had already occurred. The amplitudes and durations of the three phases are adjustable parameters, allowing different cases to be considered within the same canonical waveform. This generic waveform shape was found to produce simulated jets that agree quantitatively with ligament shapes, break-off times, and drop volumes measured in industrial apparatus.

The Lagrangian finite element method of Harlen *et al.* [22] was originally developed to handle the constitutive relations of certain viscoelastic fluid models, and therefore, it is particularly suitable for application to inkjet flows of complex fluids. In Figure 7.14, ligament breakup results are shown for five different sets of values of the parameters in a FENE-CR fluid model, with  $c$  being the effective concentration,  $De$  the Deborah number (cf. the relaxation time of the polymer), and  $L$  the extensibility of the polymer; these parameters are related naturally to the molecular weight and elastic modulus of a dilute polymer solution. In the corresponding study, the nozzle geometry and driving waveform were kept constant in all the simulated cases, and thus, the resulting drops are of different speeds; indeed, in the extreme case (e), the elasticity of the fluid does not permit breakup at all and the ligament retracts back into the nozzle, referred to as a *bungee* case.

The five specific cases shown in Figure 7.14 represent (qualitatively) the diverse family of breakup behaviours observed in experimental studies of viscoelastic jets [28, 29]. In general, the breakup may be classified into several prominent types and the parameter space partitioned accordingly. In Figure 7.15, the variation of

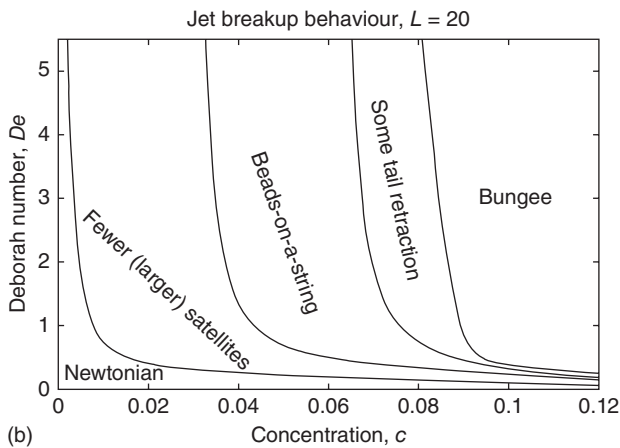
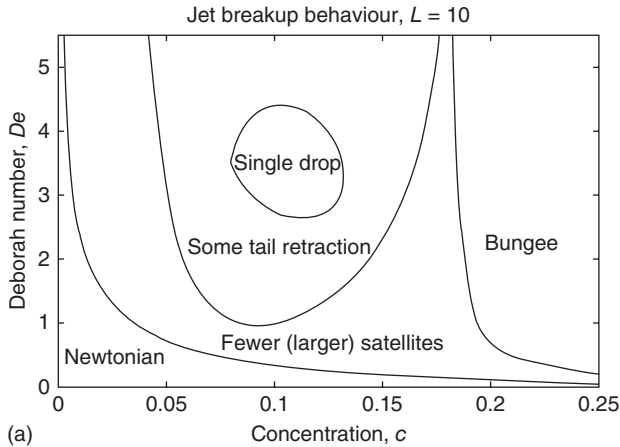


**Figure 7.15** Dependence of breakup behaviour upon the viscoelastic parameters (FENE-CR model) [25] Copyright Springer-Verlag (2009), with kind permission from Springer Science and Business Media.

the breakup with the viscoelastic parameters in the FENE-CR model ( $c$ ,  $De$ ,  $L$ ) is shown via two contour maps each with a fixed value of  $L$ . The full parameter space is three-dimensional, although as  $L$  increases, the picture continues to resemble the contour map in Figure 7.15b, but with the partition boundaries compressed further toward the Newtonian axes, reflecting the increased difficulty in ejecting strongly viscoelastic fluids.

The parameter maps shown in Figure 7.15 illustrate again the value that simulations may add to an investigation of inkjet processes; hundreds of separate sets of viscoelastic parameters were modelled corresponding to hundreds of different fluids, many of which might be difficult and/or expensive to synthesize in a laboratory and some of which might also be dangerous to use in a real apparatus. For the

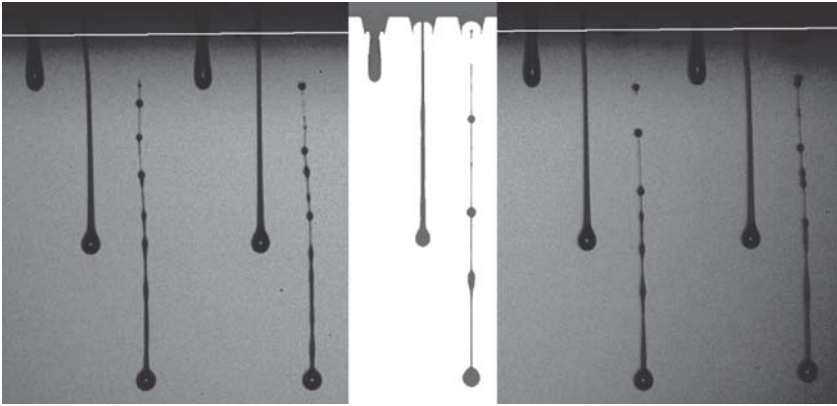


**Figure 7.16** Simulation results overlaid on an experimental image (SD Hoath) for 1000 ppm PS210 in DEP [26]. Reprinted with permission of IS&T: The Society for Imaging Science and Technology sole copyright owners of Ref. [26], Figure 5.

cases presented in Figures 7.14 and 7.15, the driving waveform was kept constant, and consequently, the drop speed was rather slower in many of the viscoelastic cases than the Newtonian reference case. General qualitative agreement was discussed, but one might wish to consider establishing quantitative agreement between simulations and experiments for a given fluid at a given jetting speed. Such an agreement is illustrated in Figures 7.16 and 7.17. Linear viscoelastic moduli were measured using rheometry (see Chapter 1) for two solutions of monodisperse polystyrene (PS210) in diethyl phthalate (DEP), and the Zimm

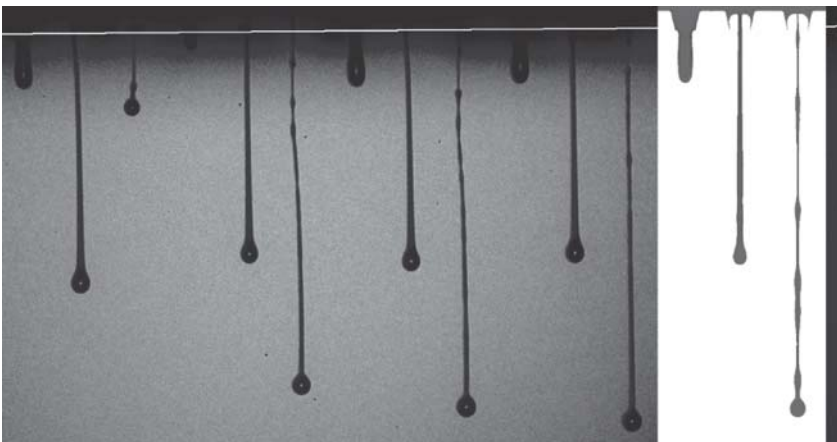


**Figure 7.17** Simulation results overlaid on an experimental image (SD Hoath) for 2000 ppm PS210 in DEP [26]. Reprinted with permission of IS&T: The Society for Imaging Science and Technology sole copyright owners of Ref. [26], Figure 6.

theory was applied to obtain values for the FENE-CR model parameters as follows:  $L = 20$ ,  $De = 4.8$ , and  $c = 0.023$  and  $0.046$  for 1000 and 2000 ppm solutions, respectively. Simulation results using these parameters are overlaid in Figures 7.16 and 7.17 on photographs of the real fluids jetted from a DOD print-head with an array of periodically synchronized nozzles. The close similarity between jet shapes and lengths demonstrates the capacity of the axisymmetric model to quantitatively represent viscoelastic inkjet printing.

## 7.5

### Three-Dimensional Simulation

While an axisymmetric simulation allows for a wide variety of inkjet processes to be studied, its inherent assumption of cylindrical symmetry of both the jet and the nozzle geometry might be too restrictive for some problems of interest to industrial researchers. In the cases where such symmetry cannot be assumed, it is instead necessary to employ a fully three-dimensional simulation in order to allow for variation in all coordinates separately. Although it is possible to extend the axisymmetric model outlined previously in order to study asymmetric phenomena (e.g., Morrison and Rallison [30]), when beginning a program of 3D inkjet simulation from scratch, it is likely to be preferable (initially at least) to make use of commercial CFD software packages designed for multiphysics applications in industrial contexts.

At printing conferences it is common, nowadays, to see reports on the use of such software to investigate design and development issues, such as the influence of external airflow, the effects of adjacent jets merging with each other, or to model potential defects in the manufacture of the print-head. For example, Figure 7.18 shows results from a DOD study of “tail-hooking,” where the tail of the ejected ligament is deflected away from the vertical axis of the nozzle. In this case, the nozzle plate was deliberately angled at  $7^\circ$  from the horizontal axis. Simulations using the

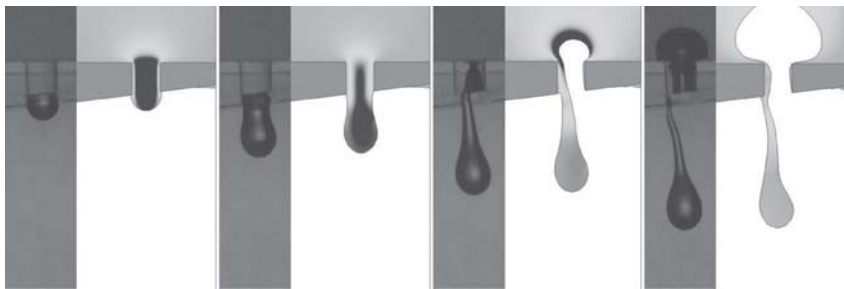


**Figure 7.18** A study of tail-hooking in DOD with an angled nozzle plate ( $7^\circ$ ); images from large-scale experiments and simulations (Flow-3D) at four different

times during the flow [31]. Reprinted with permission of IS&T: The Society for Imaging Science and Technology sole copyright owners of Ref. [31], Figure 6.

commercial software Flow-3D are shown alongside images obtained from large-scale experiments, which were conducted using a Perspex nozzle chamber to permit visualization of the meniscus inside the print-head. These images illustrate how simulations might be used to provide some insight into relevant problems in inkjet applications.

When using a commercial software package, one does not always have full access to all the nuts and bolts of the numerical algorithms used within, for example, the control of adaptive time-stepping and mesh resolution. Therefore, it is important to test the software's suitability for the problem and ensure that the results produced show convergence within acceptable tolerance levels, before relying upon the results as a true representation of a real flow. The default settings might not be adequate for the purpose, and a certain degree of adjustment may be necessary to establish a trade-off between the accuracy of the output and the runtime required by the simulations. Figure 7.19 shows a simple qualitative comparison of the results of a DOD simulation using Flow-3D with three different degrees of mesh refinement ("coarse," "medium," and "fine"), with all other parameters and settings being equal. For each case, images of the resulting

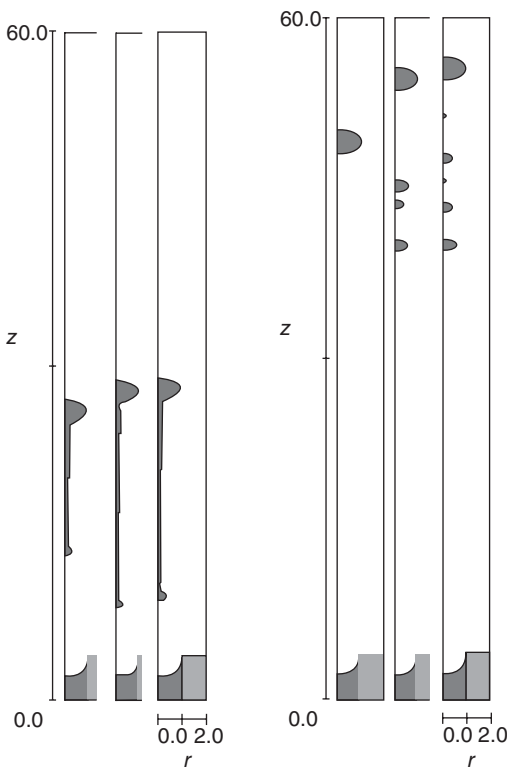


**Figure 7.19** Comparison of a DOD simulation at two different times using Flow-3D with three different mesh resolutions: coarse (left), medium (centre), and fine (right).

jets are compared at two different times. It is immediately apparent that the ink ligament produced using the “coarse” mesh is significantly shorter and does not break up into satellite drops, which disagrees entirely with the outcome of using the “medium” and “fine” meshes where multiple satellite drops were formed. The smaller differences between “medium” and “fine” may or may not be considered negligible, depending on the particular requirements. A comparison of this nature forms a simple convergence test and gives an idea of what level of mesh resolution is necessary in a particular software package to achieve meaningful results for a particular flow.

## References

- Fromm, J.E. (1984) Numerical calculation of the fluid dynamics of drop-on-demand jets. *IBM J. Res. Dev.*, **28** (3), 322.
- Shield, T.W., Bogy, D.B., and Talke, F.E. (1986) A numerical comparison of one-dimensional fluid jet models applied to drop-on-demand printing. *J. Comput. Phys.*, **67** (2), 327–347.
- Schulkes, R.M.S.M. (1996) The contraction of liquid filaments. *J. Fluid Mech.*, **309**, 277–300.
- Notz, P.K. and Basaran, O.A. (2004) Dynamics and breakup of a contracting liquid filament. *J. Fluid Mech.*, **512**, 223–256.
- Wilkes, E.D., Phillips, S.D., and Basaran, O.A. (1999) Computational and experimental analysis of dynamics of drop formation. *Phys. Fluids*, **11**, 3577.
- Feng, J.Q. (2002) A general fluid dynamic analysis of drop ejection in drop-on-demand ink jet devices. *J. Imaging Sci. Technol.*, **46** (5), 398.
- Fawehinmi, O., Gaskell, P., Jimack, P.K., Kapur, N., and Thompson, H. (2005) A combined experimental and computational fluid dynamics analysis of the dynamics of drop formation. *Phys. Fluids*, **11** (12), 3577.
- Eggers, J. (1997) Nonlinear dynamics and breakup of free-surface flows. *Rev. Mod. Phys.*, **69**, 865.
- Eggers, J. and Villermaux, E. (2008) Physics of liquid jets. *Rep. Prog. Phys.*, **71**, 036601.
- Ambravaneswaran, B., Wilkes, E.D., and Basaran, O.A. (2002) Drop formation from a capillary tube: comparison of one-dimensional and two-dimensional analysis and occurrence of satellite drops. *Phys. Fluids*, **14**, 2606–2621.
- Li, J. and Fontelos, M.A. (2003) Drop dynamics on the beads-on-string structure for viscoelastic jets: a numerical study. *Phys. Fluids*, **15**, 922–937.
- Clasen, C., Eggers, J., Fontelos, M.A., Li, J., and McKinley, G.H. (2006) The beads-on-string structure of viscoelastic threads. *J. Fluid Mech.*, **556**, 283.
- Ardekani, A.M., Sharma, V., and McKinley, G.H. (2010) Dynamics of bead formation, filament thinning and breakup in weakly viscoelastic jets. *J. Fluid Mech.*, **665**, 46.
- Castrejón Pita, J.R., Hoath, S.D., and Hutchings, I.M. (2012) Velocity profiles in a cylindrical liquid jet by reconstructed velocimetry. *ASME J. Fluids Eng.*, **134**, 011201-1.
- van Hoeve, W., Gekle, S., Snoeijer, J.H., Versluis, M., Brenner, M.P., and Lohse, D. (2010) Break-up of diminutive Rayleigh jets. *Phys. Fluids*, **22**, 122033.
- Keller, J.B., Rubinow, S.I., and Tu, Y.O. (1973) Spatial instability of a jet. *Phys. Fluids*, **16**, 12.
- Press, W.H., Teukolsky, S.A., Vetterling, W.T., and Flannery, B.P. (1992) *Numerical Recipes in Fortran 77*, 2nd edn, Cambridge University Press.
- Rayleigh, L. (1878) On the instability of jets. *Proc. London Math. Soc.*, **10**, 4–13.
- Chaudhary, K.C. and Redekopp, L.G. (1980) The nonlinear capillary instability of a liquid jet. Part 1. Theory. *J. Fluid Mech.*, **96**, 257–274.



20. Kalaaji, A., Lopez, B., Attané, P., and Soucemarianadin, A. (2003) Break-up length of forced liquid jets. *Phys. Fluids*, **15**, 2469.
21. Chaudhary, K.C. and Maxworthy, T. (1980) The nonlinear capillary instability of a liquid jet. Part 3. Experiments on satellite drop formation and control. *J. Fluid Mech.*, **96**, 287–297.
22. Harlen, O.G., Rallison, J.M., and Szabó, P. (1995) A split Lagrangian-Eulerian method for simulating transient viscoelastic flows. *J. Non-Newtonian Fluid Mech.*, **60**, 81.
23. Castrejón-Pita, J.R., Morrison, N.F., Harlen, O.G., Martin, G.D., and Hutchings, I.M. (2011) Experiments and Lagrangian simulations on the formation of droplets in continuous mode. *Phys. Rev. E*, **83**, 016301.
24. Castrejón Pita, J.R., Morrison, N.F., Harlen, O.G., Martin, G.D., and Hutchings, I.M. (2011) Experiments and Lagrangian simulations on the formation of droplets in drop-on-demand mode. *Phys. Rev. E*, **83**, 036306.
25. Morrison, N.F. and Harlen, O.G. (2010) Viscoelasticity in inkjet printing. *Rheol. Acta*, **49**, 619.
26. Morrison, N.F. and Harlen, O.G. (2011) Inkjet printing of non-Newtonian fluids. Proceedings of NIP27, p. 360.
27. Morrison, N.F., Harlen, O.G., and Hoath, S.D. (2014) Towards satellite free drop-on-demand printing of complex fluids. Proceedings of NIP30, p. 162.
28. Goldin, M., Yerushalmi, J., Pfeffer, R., and Shinnar, R. (1969) Breakup of a laminar capillary jet of a viscoelastic fluid. *J. Fluid Mech.*, **38**, 689.
29. Bazilevskii, A.V., Meyer, J.D., and Rozhkov, A.N. (2005) Dynamics and breakup of pulse microjets of polymeric liquids. *Fluid Dyn.*, **40**, 376.
30. Morrison, N.F. and Rallison, J.M. (2010) Transient 3D flow of polymer solutions: a Lagrangian computational method. *J. Non-Newtonian Fluid Mech.*, **165**, 1241–1257.
31. Harlen, O.G., Castrejón-Pita, J.R., and Castrejón-Pita, A.A. (2013) Asymmetric detachment from angled nozzle plates in drop-on-demand inkjet printing. IS&T's NIP29: International Conference on Digital Printing Technologies and Digital Fabrication 2013, pp. 277–280.



## 8

## Drops on Substrates

Sungjune Jung, Hyung Ju Hwang, and Seok Hyun Hong

## 8.1

## Introduction

The dynamics of a fluid drop impacting on a solid nonporous surface is a classical subject of interfacial hydrodynamics, which occurs in many industrial and environmental situations such as coating, rapid spray cooling of hot surfaces, quenching of aluminum alloys and steels, motor jet, rain drop, pesticides, and inkjet printing. The impact of liquid drops on dry surfaces creates various flow patterns depending on the properties of the liquid and the surface. Liquids vary in density, viscosity, elasticity, and surface tension. The velocity and the size of a droplet also have a significant influence on the resulting behaviors. The solid surface may be rough or smooth, hydrophobic or hydrophilic, chemically homogeneous or heterogeneous, planar or nonplanar, and normal or oblique. There are six possible consequences of a droplet falling on to a dry surface: deposition, prompt splash, corona splash, receding breakup, partial rebound, and complete rebound as seen in Figure 8.1, from [1].

The extent to which a drop wets the surface is usually described by its equilibrium contact angle ( $\theta_{eq}$ ), which is defined as the angle between the liquid/vapor interface as it meets the solid surface (Figure 8.2). The liquid drop takes a shape, which minimizes the free energy of the system by minimizing the surface area of the drop in the absence of gravity. Gibbs demonstrated that minimizing the free energy requires minimization of the sum ( $\psi$ ) of three energies contributed by the three interfaces

$$\psi = \sigma_{LF}A_{LF} + \sigma_{SL}A_{SL} + \sigma_{SF}A_{SF} \quad (8.1)$$

where  $\sigma$  is the surface tension,  $A$  is the area, and the subscripts LF, SL, SF refer to liquid–fluid, solid–liquid, solid–fluid interfaces, respectively. For a plane, homogeneous surface, the minimization yields,

$$\cos \theta = \frac{\sigma_{SF} - \sigma_{SL}}{\sigma_{LF}} \quad (8.2)$$

This is known as *Young's equation*. The wetting behavior of a liquid drop according to the contact angle is illustrated in Figure 8.3.

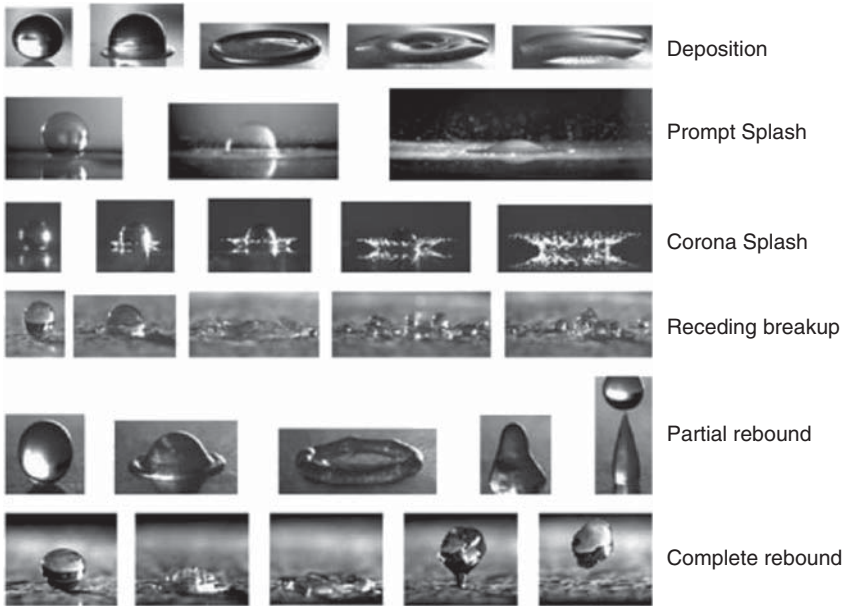


**Figure 8.1** A variety of morphologies of liquid drop impact on to a dry surface. Rioboo *et al.* [1].

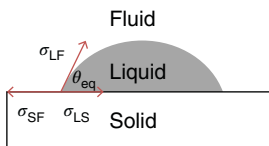


**Figure 8.2** A liquid drop on a solid with an ideal contact angle ( $\theta_{eq}$ ).

In an ideal situation of a liquid spreading on a uniform plane solid, there is only one equilibrium contact angle ( $\theta_{eq}$ ). But, in practice, a number of stable angles can be measured. Two relatively reproducible angles are the largest, called the *advancing contact angle* ( $\theta_a$ ), and the smallest, called the *receding contact angle* ( $\theta_r$ ). The advancing angle can be measured by pushing the periphery of a drop over a surface, and the receding angle can be measured by pulling it back. The difference between the two angles ( $\theta_a - \theta_r$ ) is often called the *contact angle hysteresis* [2].

A substantial number of experimental, numerical, and theoretical studies have been conducted to identify the important parameters influencing the wetting process and the final outcome of drop impact, for practical applications such as coating, painting, rapid spray cooling of hot surfaces, and splat quenching of metallic alloys. Many of these applications require a comprehensive understanding of the wetting process (e.g., to predict how quickly a deposited drop will wet a given area of the substrate). This chapter aims to achieve a fuller understanding of the mechanics of the liquid drop impact on a solid substrate. To this end, we will start with observing the process of inkjet-printed drop impact on a solid

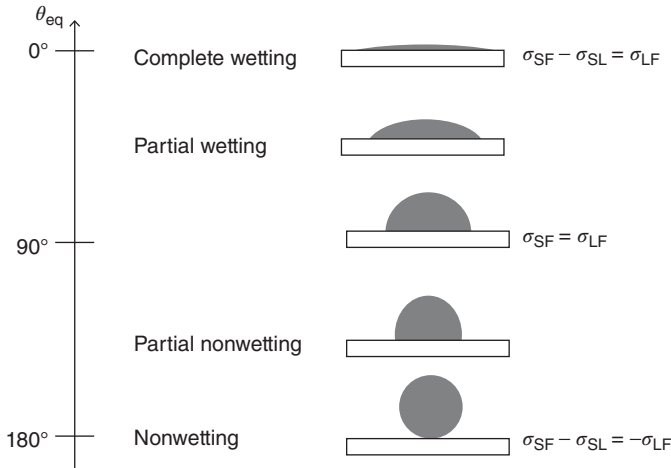


**Figure 8.3** Wetting behavior of a liquid drop according to the contact angle ( $\theta_{eq}$ ).

substrate. Then, dimensional analysis based on the Buckingham Pi theorem will be introduced, which helps us to predict the behavior of the drop on the surface.

## 8.2

### Experimental Observation of Newtonian Drop Impact on Wettable Surface

Drop-on-demand inkjet printing process involves the spreading of a liquid drop on a smooth, dry, solid surface, which can be described as a sequence of five successive phases: kinematic, spreading, relaxation, wetting, and equilibrium. Here are the experimental observations of an inkjet-printed drop impact. Drops of diethyl phthalate (DEP, a model ink) of  $28\ \mu\text{m}$  diameter were printed from an inkjet nozzle and were deposited on to a highly wettable indium tin oxide (ITO) coated glass substrate at  $6\ \text{m s}^{-1}$ . Sequential images of successive events were captured by a high-speed imaging apparatus with a series of time intervals from 100 ns at the earliest stages to 1 s for the final wetting phase. The evolution of the drop shape, its contact diameter and maximum height can be traced through Figures 8.4 and 8.5.

Figure 8.5a shows the variation in the contact diameter  $D$  with time  $t$  after impact. In Figure 8.5b, these quantities are plotted in dimensionless form, in terms of the spreading factor  $\beta$  ( $\beta = D/D_0$ ) and reduced time  $\tau$  (where  $\tau = tV_0/D_0$ ); the plot also shows the maximum height of the deposited drop  $h$ , also reduced as  $h/D_0$ . As the drop collided with the substrate, it initially formed a truncated sphere (up to about  $1\ \mu\text{s}$  after impact). Over the next few microseconds, the contact circle expanded radially from the impact point, with the drop changing its shape to a flat disk as shown in the image at  $4\ \mu\text{s}$  (in Figure 8.4). The drop then continued to spread until the kinetic energy momentarily became zero (at a spreading factor of  $\beta^*$ ) after  $\sim 4\ \mu\text{s}$ . At this point, the drop height reached a minimum. The relaxation

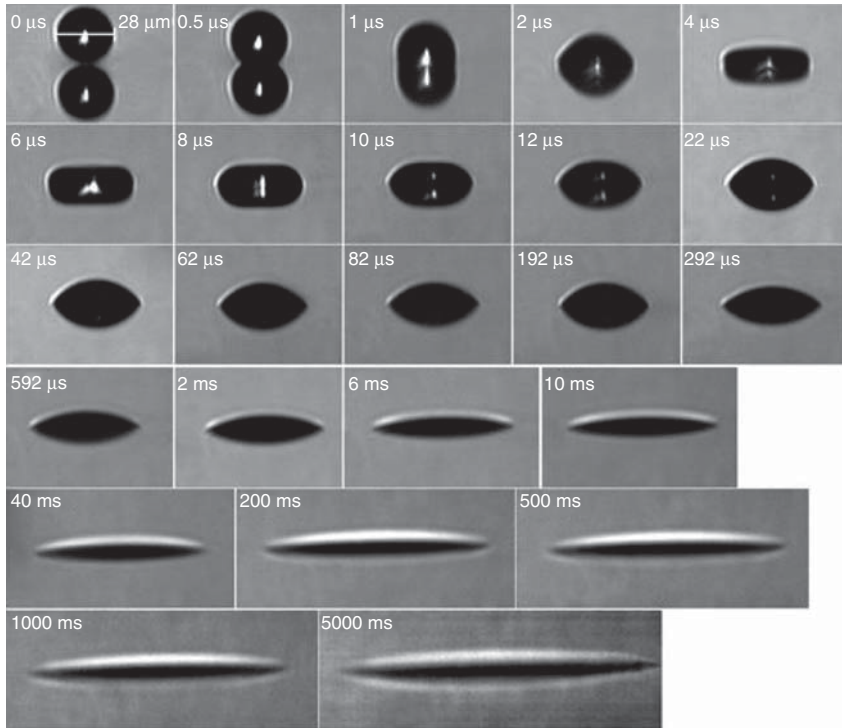


**Figure 8.4** Images showing the evolution of DEP drops impacting a corona-treated ITO-coated glass substrate at  $6 \text{ m s}^{-1}$ . Each image, captured with a single ultrashort flash, shows a different impact event at the time shown after initial impact, but the

reproducibility of the phenomena allows these images to be used to establish the variation in deposit shape and size with time. Each frame shows the image of the drop/deposit, together with its reflection in the horizontal surface of the substrate.

phase followed for the next  $\sim 50 \mu\text{s}$ , during which the edges of the drop showed little movement but its height changed significantly. As shown in Figure 8.4, the contact angle reduced progressively between  $\sim 4$  and  $\sim 20 \mu\text{s}$ . The lamella that had stretched during the spreading phase relaxed to form a spherical cap shape at this point (as seen in the images at 22 and 42  $\mu\text{s}$ ). Next, wetting phenomena occurred from  $\sim 55 \mu\text{s}$  onward, with the capillary force driving the liquid to spread further until its equilibrium state was reached. This process took a much longer time than the earlier phases, with the drop spreading for  $\sim 5 \text{ s}$  to reach a final diameter of  $\sim 140 \mu\text{m}$ , about five times the diameter of the original impacting drop.

### 8.2.1

#### Effect of Initial Speed on Drop Impact and Spreading

The drop speed at impact is varied between  $3$  and  $8 \text{ m s}^{-1}$  by changing the amplitude of the driving pulse for the inkjet nozzle. The speed could not be reduced

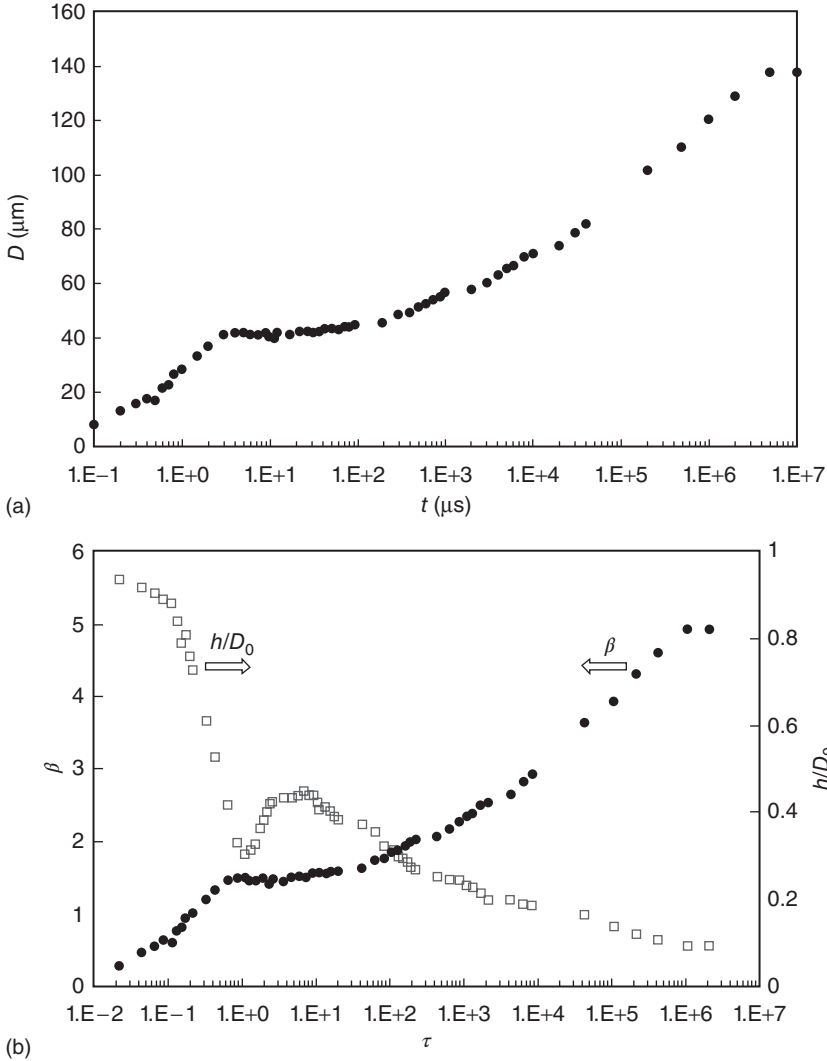


**Figure 8.5** Full history of spreading of DEP drops impacting a corona-treated ITO-coated glass substrate at  $6 \text{ m s}^{-1}$ : (a) contact diameter  $D$  as a function of time  $t$  ( $\mu\text{s}$ ) and (b) spreading factor  $\beta$  and dimensionless height  $h/D_0$  versus dimensionless time  $\tau$  ( $=tV_0/D_0$ ).

further as jetting became less repeatable below  $3 \text{ m s}^{-1}$ , and the voltage pulse available limited the maximum speed. The initial drop diameter increased slightly with speed from  $25 \mu\text{m}$  at  $3 \text{ m s}^{-1}$  to  $28 \mu\text{m}$  at  $8 \text{ m s}^{-1}$ . No satellite drops were observed at 3 and  $6 \text{ m s}^{-1}$ , but a secondary drop followed the main drop at  $8 \text{ m s}^{-1}$ .

Figure 8.6 shows the evolution of the spreading factor in the kinematic phase ( $\tau < 0.25$ ).

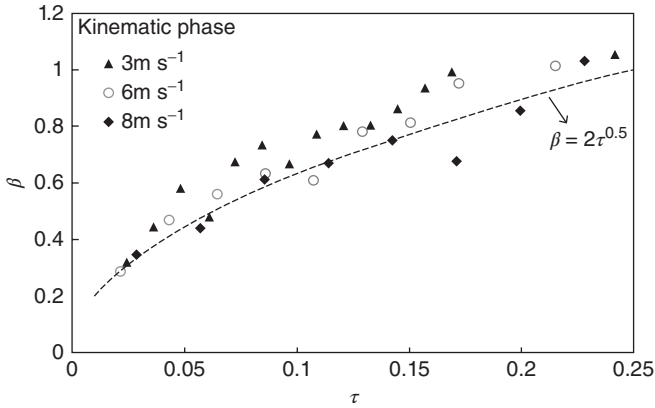


**Figure 8.6** The effect of impact speed on time evolution of spreading factor  $\beta$  during the kinematic phase for DEP drops impacting a corona-treated ITO-coated glass substrate, shown as a function of dimensionless time  $\tau$ .

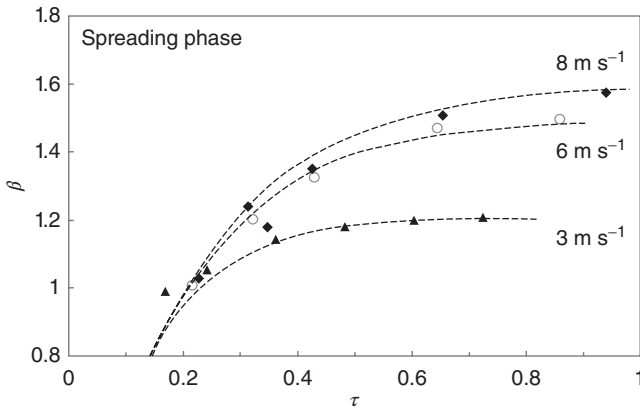


**Figure 8.7** The effect of impact speed on time evolution of spreading factor  $\beta$  during the spreading phase for DEP drops impacting a corona-treated ITO-glass substrate.

Regardless of the impact speed, all the drops reached  $\beta = 1$  at  $\tau \approx 0.2$ . Moreover, the diameter followed the same power law with  $\tau$  for all three speeds, with the points falling close to a single curve with an exponent of  $0.5 \pm 0.03$ . The evolution of the deposit diameter during the spreading phase ( $0.2 < \tau < \sim 1$ ) is shown in Figure 8.7. The spreading factor increased steadily to a maximum value  $\beta^*$  at a time  $\tau^*$ . A greater impact speed resulted in a higher value of  $\beta^*$  and a greater value for  $\tau^*$ .

The evolution of the spreading factor and the dynamic contact angle  $\theta_d$  during the relaxation phase ( $\tau^* \approx 1 < \tau < 10$ ) is illustrated in Figure 8.8, for the three different impact speeds. At early times,  $\theta_d$  fell as the fluid at the edges of the drop relaxed inward, a process that took longer for higher impact speeds. In the wetting phase ( $10 < \tau < 10^6$ ), the contact line moved slowly outward over the surface and the contact diameter increased as shown in Figure 8.9. For all three impact speeds,



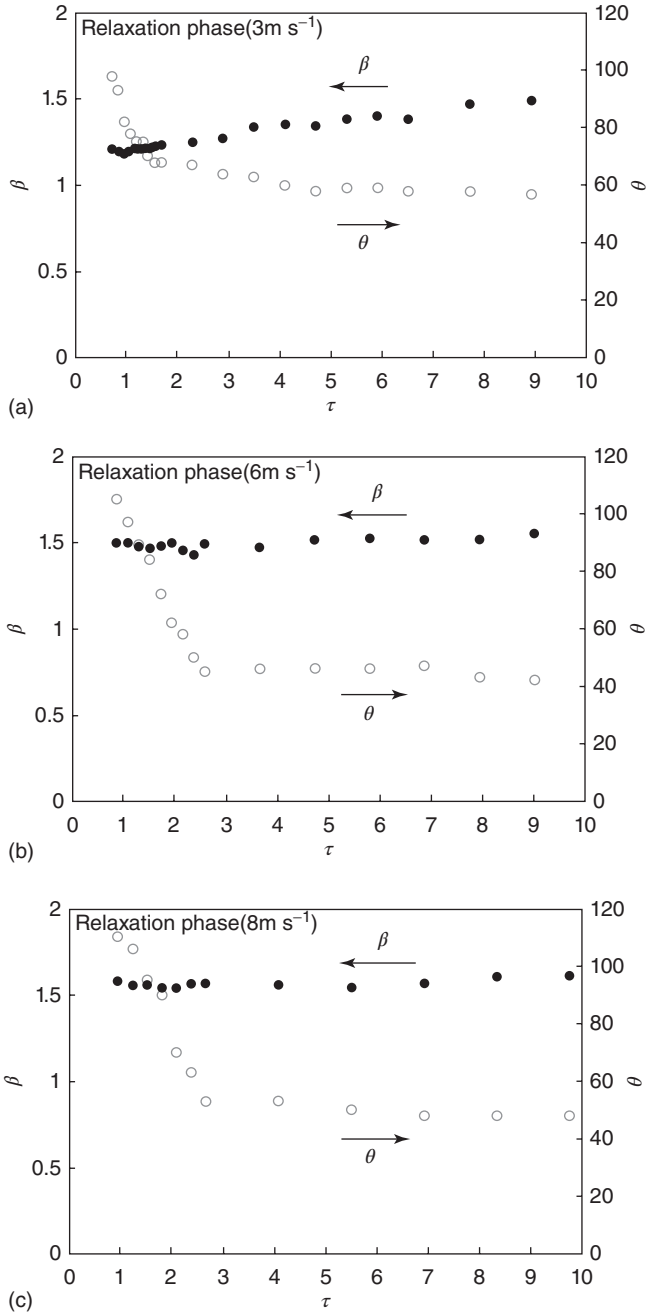


**Figure 8.8** The effect of impact speed on time evolution of spreading factor  $\beta$  and dynamic contact angle  $\theta_d$  during the relaxation phase for DEP drops impacting a corona-treated ITO-coated glass substrate at the three different speeds: (a)  $3\text{ m s}^{-1}$ ; (b)  $6\text{ m s}^{-1}$ ; and (c)  $8\text{ m s}^{-1}$ .

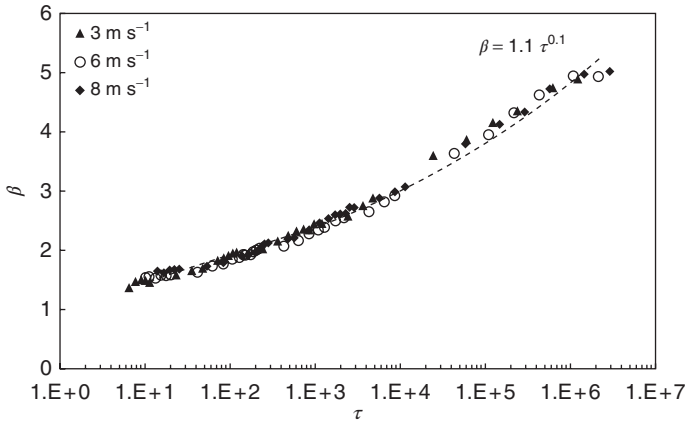


**Figure 8.9** The effect of impact speed on time evolution of spreading factor  $\beta$  during the wetting phase for DEP drops impacting a corona-treated ITO-coated glass substrate.

the diameter increased in the same way, following Tanner's power law prediction (shown by the dashed line) with exponents between 0.103 and 0.108. Finally, in the equilibrium phase, capillary-driven movement continued for about 5 s (to  $\tau \approx 2 \times 10^6$ ) until the contact line became pinned in the final equilibrium state. Although the drops had initially impacted the substrate with substantially different kinetic energies (by a factor of  $\sim 7$  between the drops at 3 and 8  $\text{m s}^{-1}$ ) and had spread over the surface at different speeds during the spreading phase, they all achieved essentially the same final spreading ratio  $\beta^\infty$  ( $\beta^\infty \approx 4.9$ ) at the same dimensionless time ( $\tau \approx 2 \times 10^6$ ).

### 8.2.2

#### Effect of Surface Wettability on Drop Impact and Spreading

In order to investigate the effect of surface wettability, a series of experiments was performed with an indium tin oxide (ITO)-coated glass substrate, a corona-treated ITO-coated glass substrate, and a polytetrafluoroethylene (PTFE)-coated glass substrate. Except for the treatment of the substrate, all the other conditions such as drop speed, shape of the driving waveform, and fluid properties remained the same. The evolution of the spreading factor for DEP drops at impact speeds of 6  $\text{m s}^{-1}$  on these three substrates is shown in Figure 8.10.

Sequential images of drop evolution for drop impact on an as-received ITO-glass substrate and PTFE-coated glass substrate are shown Figures 8.11 and 8.12. The spreading factor increased during the kinematic phase with a power-law relationship,  $\beta \propto \tau^{0.5}$ , and the durations of the first three phases were the same for all the substrates.

However, a significant influence of the surface wettability was observed during the wetting phase. Despite the fact that the drop experienced capillary-driven propagation from the same value of  $\tau$  as for the treated ITO-glass substrate,

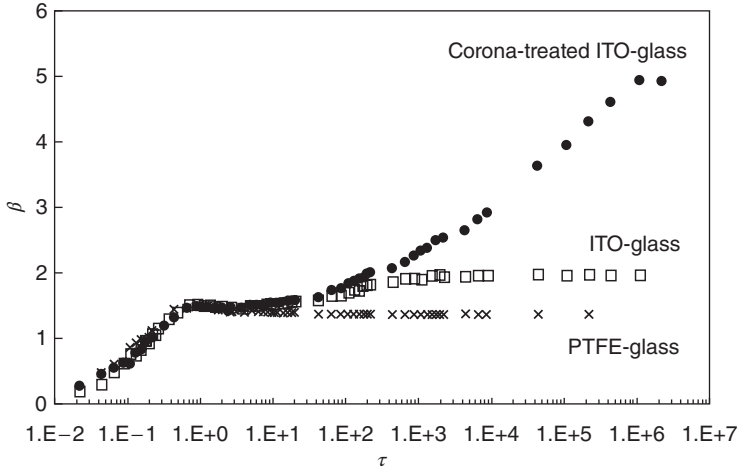


**Figure 8.10** Full history of spreading of drops of DEP drops impacting at  $6\text{ m s}^{-1}$  on to corona-treated ITO-coated, as-received ITO-coated, and PTFE-coated glass substrates.

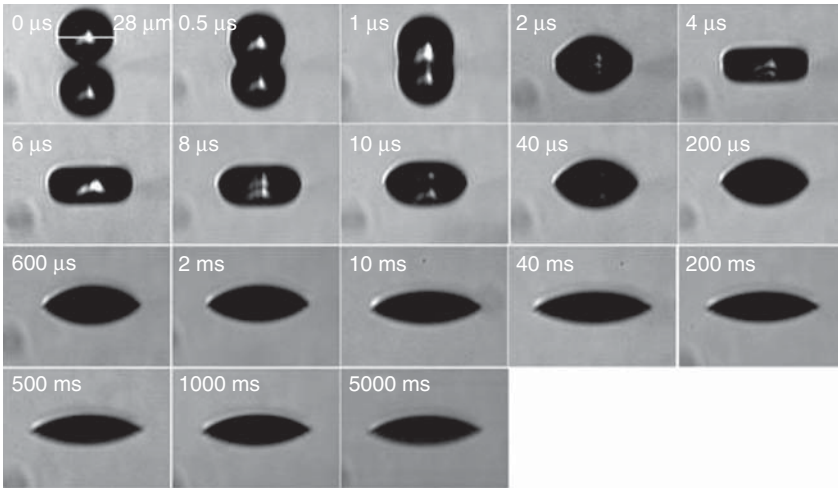


**Figure 8.11** Images showing the evolution of DEP drops impacting as-received ITO-coated glass substrate at  $6\text{ m s}^{-1}$ .

the wetting process on the nontreated ITO-glass substrate persisted only up to  $\tau \approx 10^3$ . It also deviated from Tanner’s law, with an exponent of  $0.06 \pm 0.003$ . Because of the short wetting time and the lower speed of movement,  $\beta^\infty$  was much smaller ( $\beta^\infty \approx 2$ ) than that on the more wettable surface. A moderate change in surface wettability (from  $\theta_{\text{eq}} = \sim 4^\circ$  to  $\sim 32^\circ$ ) resulted in a large difference in wetting time and in final drop diameter. On the other hand, for impact on a PTFE-coated substrate, a wetting phase was not observed and the value of  $\beta^\infty$  was smaller than  $\beta^*$ .

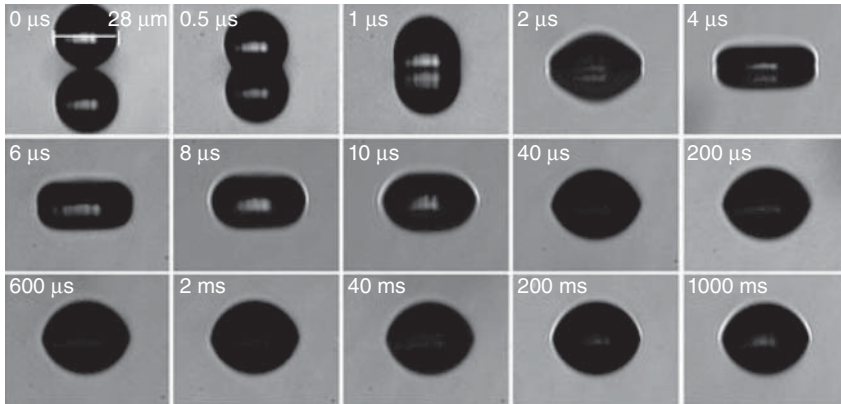


**Figure 8.12** Images showing the evolution of DEP drops impacting PTFE-coated glass substrate at  $6 \text{ m s}^{-1}$ .

### 8.2.3

#### Effect of Fluid Properties on Drop Impact and Spreading

The influence of fluid viscosity and surface tension were investigated by using drops of two glycerol–water mixtures (GW) as well as of DEP, deposited on to a treated-ITO glass substrate at  $6 \text{ m s}^{-1}$ . These were chosen to allow a comparison between a pair of fluids with essentially the same viscosity but different surface tensions (DEP and GW 60:40) and a pair with essentially the same surface tension but different viscosities (GW 60:40 and GW 50:50). The results are shown in Figure 8.13. The value of surface tension had no effect on the kinematic,

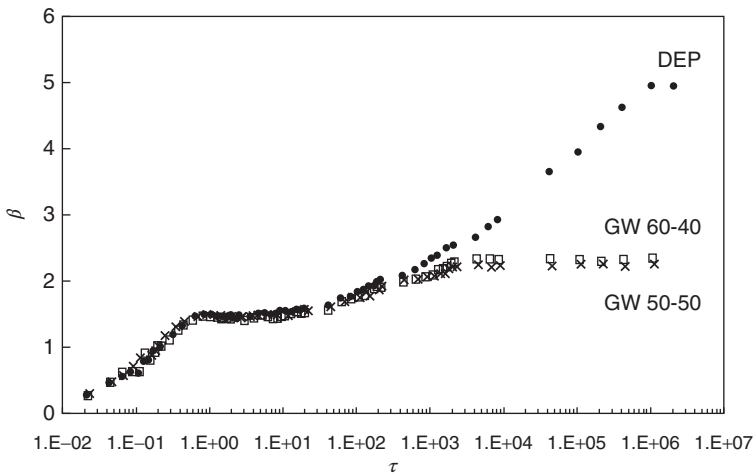


**Figure 8.13** Variation of spreading factor  $\beta$  with time  $\tau$  for three Newtonian solutions, with viscosity (DEP and GW 60:40) and surface tension (GW 60:40 and GW 50:50) paired values, impacting at  $6 \text{ m s}^{-1}$  on treated-ITO glass substrate.

spreading, or relaxation phases, but a marked influence on the wetting phase, in terms of the speed of expansion of the contact diameter and the final spreading factor. In contrast, the effect of viscosity was negligible throughout the deposition process, with no significant difference, within the experimental error, between the spreading curves.

### 8.3

#### Dimensional Analysis: The Buckingham Pi Theorem

In this section, we briefly introduce dimensional analysis. For a pedagogical reason, we start from a simple example to explain what dimensional analysis means. Consider a projectile problem. A ball is thrown upward. In this situation, we want to find the maximum height of the ball. By using Newton's second law with Newton's law of universal gravitation, we deduce a differential equation. Since the radius of the Earth is much larger than the height, we finally arrive at

$$\frac{d^2}{dt^2}h(t) = -g, \quad t > 0 \quad (8.3)$$

where  $h(t)$  is the height of the projectile and  $g$  is the gravitational constant. We solve the differential equation (8.3) with

$$h(t) = -\frac{1}{2}gt^2 + u_0t$$

where  $u_0$  is the initial velocity of the ball. The maximum height occurs at  $t = t_m = u_0/g$ , since then  $\frac{d}{dx}h(t) = -gt + u_0 = 0$ . Then, we conclude that the maximum height is

$$h_m = h\left(\frac{u_0}{g}\right) = \frac{u_0^2}{g} \quad (8.4)$$

Now we approach the projectile problem by reducing it to a simpler one by means of dimensional analysis. When solving the problem in the aforementioned manner, we follow two steps: model a differential equation and solve the equation. However, we illustrate in the following how the dimensional reduction provides a shortcut to arrive at an answer for the same problem without any differential equation. Assume that the maximum height is determined by the mass  $m$  of the ball, the initial velocity  $u_0$ , and the gravitational acceleration constant  $g$ . Therefore, we write  $h_m = F(m, u_0, g)$  for a suitable function  $F$ . We now investigate its dimension.

We introduce the fundamental dimensions  $M$ : mass;  $L$ : length; and  $T$ : time.

Then, the equation  $h_m = F(m, u_0, g)$  consists of a combination of these fundamental dimensions:

$$[h_m] = [m^a u_0^b g^c] \quad (8.5)$$

which is equivalent to

$$L = M^a \left(\frac{L}{T}\right)^b \left(\frac{L}{T^2}\right)^c = M^a L^{b+c} T^{-b-2c} \quad (8.6)$$

Here, we use the definitions of velocity as length over time and of acceleration as velocity over time. By comparing the exponents on both sides of Eq. (8.6), we find the following linear system:  $a = 0$ ,  $b + c = 1$ , and  $-b - 2c = 0$ . Solving this system requires that  $a = 0$ ,  $b = 2$ , and  $c = -1$ . Applying this solution to Eq. (8.3), we are immediately led to

$$h_m = C \frac{u_0^2}{g} \quad (8.7)$$

where  $C$  is a dimensionless constant. We have obtained a result similar to Eq. (8.4) without solving a differential equation. As compared to a differential equation method, the dimensional analysis leads to a much more convenient methodology, because even though all we know are the corresponding physical quantities of a given physics problem, we can deduce a reasonable result without much effort. On the other hand, this dimensional analysis has a limitation. Indeed, in general, only with the dimensional analysis, we may not find a specific solution  $F$ , and to obtain  $F$ , we need to derive differential equations or some physical laws. Unlike the projectile problem in which we readily found a solution by the dimensional analysis, we may not expect such fortune to hold for other problems. Nevertheless, we note that the advantage of the dimensional analysis is to reduce the original problem to a much simpler one. We will discuss more on the limitations and advantages in the next section.

However, here one natural question follows: if one has a dimensional problem (for instance, the projectile problem in the aforementioned case), can the problem always have a dimensional reduction form? Indeed, this dimensional reduction always exists by the Buckingham Pi theorem [3]. The Buckingham Pi theorem can be stated as follows. A natural phenomenon is described by the following general equation:

$$a = F(a_1, \dots, a_k, b_1, \dots, b_m) \quad (8.8)$$

where  $a$  is the unknown quantity (for instance, velocity, height, temperature, charge, and width), and  $a_1, \dots, a_k, b_1, \dots, b_m$  are the governing parameters such that  $a_1, \dots, a_k$  have independent dimensions. Then, Eq. (8.8) can be reduced to the form of the dimensionless equation:

$$\frac{a}{a_1^s, \dots, a_k^t} = \Phi \left( \prod_1 = \frac{b_1}{a_1^{s_1}, \dots, a_k^{t_1}}, \dots, \prod_m = \frac{b_m}{a_1^{s_m}, \dots, a_k^{t_m}} \right) \quad (8.9)$$

where  $\prod_1, \dots, \prod_m$  and  $\frac{a}{a_1^s, \dots, a_k^t}$  are dimensionless quantities.

We now apply the Buckingham Pi theorem to the aforementioned projectile problem. The projectile problem has an equation of the implicit form  $0 = F(m, u_0, g, h_m)$ . This equation corresponds to Eq. (8.8). As described earlier, the parameters  $m, u_0, g$  have independent dimensions. Thus, we obtain a dimensionless quantity with  $m, u_0, g, h_m$ , so that  $\prod_1 = \frac{h_m}{u_0^2/g}$ . The detailed calculation

was provided to solve Eq. (8.6). Finally, we have a dimensionless equation

$$0 = \Phi \left( \prod_1 = \frac{h_m}{u_0^2/g} \right)$$

corresponding to Eq. (8.9). But this means that  $\prod_1 = \frac{h_m}{u_0^2/g}$  must be a constant, that is,

$$h_m = C \frac{u_0^2}{g} \quad (8.10)$$

Note that Eq. (8.10) is exactly equal to the solution Eq. (8.7). As noted, the projectile problem has some luck such that  $\prod_1 = C$  corresponds to the solution obtained by solving the differential equation (8.3). In general, using the Buckingham Pi theorem directly may not find the exact expression of the function  $\Phi$  (see, e.g., [4]). More detailed application of the Buckingham Pi theorem is discussed in the next section. In this chapter, we apply the Pi theorem to deduce the maximum spreading diameter of a drop after impact, and we discuss an application of the Pi theorem to the problem of evaporating drops on a solid substrate, in which a scaling exponent of the radius of the drop will be deduced.

## 8.4

### Drop Impact Dynamics: The Maximum Spreading Diameter

In this section, we give concrete examples for the purpose of introducing applications of the Buckingham Pi theorem. When a liquid drop impacts on a substrate, the maximum spreading diameter  $R_{\max}$  can be described by the following equation:

$$R_{\max} = F(\rho, R_0, V_0, \sigma, \mu, h_m, g) \quad (8.11)$$

where  $\rho$  is the liquid density,  $R_0$  is the initial diameter,  $V_0$  is the velocity at the moment of impact,  $\sigma$  is the surface tension,  $\mu$  is the dynamic viscosity,  $h_m$  is the final thickness of the impacting drop at the impact stage, and  $g$  is the acceleration of gravity. The dimensions of the parameters are as follows:

$$\begin{aligned} [\rho] &= ML^{-3}, & [R_0] &= L, & [V_0] &= LT^{-1}, & [\sigma] &= MT^{-2}, & [\mu] &= ML^{-1}T^{-1}, \\ [h_m] &= L, & [g] &= LT^{-2} \end{aligned}$$

Now we apply the Pi theorem. However, there is no unique way to choose parameters that have independent dimensions. For instance,  $\rho$ ,  $R_0$ , and  $V_0$  have independent dimensions, but  $\sigma$ ,  $h_m$ , and  $g$  also have independent dimensions. Therefore, we choose parameters carefully to achieve reasonable results for specific purposes. One perspective is to select parameters that can be handled at the initial stage. When we have a liquid drop, we can adjust its initial velocity or size. Moreover, the surface tension  $\sigma$  or the dynamic viscosity  $\mu$  also can be

customized. A main emphasis is that we want to deduce meaningful output data, which depend continuously on the input data. One question arising from physics is how  $R_{\max}$  depends continuously on the properties of a liquid drop, for instance, the surface tension or the dynamic viscosity. Therefore, we choose  $\rho$ ,  $R_0$ , and  $V_0$  as independent parameters so that the reduced dimensionless form has dimensionless variables that can involve  $\sigma$  and  $\mu$  separately. In other words, in the notations of Eq. (8.8), we take as  $a$ 's:  $\rho$ ,  $R_0$ , and  $V_0$ , and as  $b$ 's:  $\sigma$ ,  $h_m$ ,  $\mu$ , and  $g$ . We now know that, by the Buckingham Pi theorem, there exists a reduced dimensionless form similar to Eq. (8.9). Note that the statement of the Pi theorem does not propose how to find an exact dimensionless form. We thus perform a detailed calculation to deduce a dimensionless form. Eq. (8.11) consists of combinations of the fundamental dimensions:

$$[R_{\max}] = [\rho^a R_0^b V_0^c \sigma^d \mu^e h_m^f g^i] \quad (8.12)$$

so that

$$\begin{aligned} L &= M^a L^{-3a} L^b L^c T^{-c} M^d T^{-2d} M^e L^{-e} T^{-e} L^f L^i T^{-i} \\ &= M^{a+d+e} L^{-3a+b+c-e+f+i} T^{-c-2d-e-2i} \end{aligned}$$

which gives rise to the following equivalent linear system by comparing the exponents on both sides of the given equation:

$$\begin{pmatrix} 1 & 0 & 0 & 1 & 1 & 0 & 0 \\ -3 & 1 & 1 & 0 & -1 & 1 & 1 \\ 0 & 0 & -1 & -2 & -1 & 0 & -2 \end{pmatrix} \begin{pmatrix} a \\ b \\ c \\ d \\ e \\ f \\ i \end{pmatrix} = \begin{pmatrix} 0 \\ 1 \\ 1 \end{pmatrix} \quad (8.13)$$

Here, we have considered  $\rho$ ,  $R_0$ , and  $V_0$  as independent parameters. We now deduce the row-reduced form of Eq. (8.13) using standard matrix methods:

$$\begin{pmatrix} 1 & 0 & 0 & 1 & 1 & 0 & 0 & | & 0 \\ -3 & 1 & 1 & 0 & -1 & 1 & 1 & | & 1 \\ 0 & 0 & -1 & -2 & -1 & 0 & -2 & | & 0 \end{pmatrix} \rightarrow \begin{pmatrix} 1 & 0 & 0 & 1 & 1 & 0 & 0 & | & 0 \\ 0 & 1 & 0 & 1 & 1 & 1 & -1 & | & 1 \\ 0 & 0 & 1 & 2 & 1 & 0 & 2 & | & 0 \end{pmatrix} \quad (8.14)$$

By Eq. (8.14), we have that  $a = -d - e$ ,  $b = -d - e - f + i + 1$ , and  $c = -2d - e - 2i$ . Therefore, we rewrite Eq. (8.12) as follows:

$$\begin{aligned} [R_{\max}] &= \left[ \rho^{-d-e} R_0^{-d-e-f+i+1} V_0^{-2d-e-2i} \sigma^d \mu^e h_m^f g^i \right] \\ &= \left[ R_0 \left( \frac{\sigma}{\rho R_0 V_0^2} \right)^d, \left( \frac{\mu}{\rho R_0 V_0} \right)^e, \left( \frac{h_m}{R_0} \right)^f, \left( \frac{g R_0}{V_0^2} \right)^i \right] \end{aligned}$$

This leads (since exponents  $d$ ,  $e$ ,  $f$ , and  $i$  are undetermined) to the dimensionless form

$$\frac{R_{\max}}{R_0} = \Phi \left( \frac{\sigma}{\rho R_0 V_0^2}, \frac{\mu}{\rho R_0 V_0}, \frac{h_m}{R_0}, \frac{g R_0}{V_0^2} \right) \quad (8.15)$$



An interesting remark is that the Reynolds number  $Re$  and the Weber number  $We$  are

$$Re = \frac{\rho R_0 V_0}{\mu}, \quad We = \frac{\rho R_0 V_0^2}{\sigma}$$

At the starting point, we have wanted to deduce the output data, which depends on the properties of the impacting drop, the surface tension  $\sigma$ , and the dynamic viscosity  $\mu$ . The dimensionless form Eq. (8.15) contains the dimensionless variables  $Re = \frac{\rho R_0 V_0}{\mu}$  and  $We = \frac{\rho R_0 V_0^2}{\sigma}$ . This coincides with our purpose at the starting point. Thus, the remaining question is how  $\frac{R_{\max}}{R_0}$  depends continuously on  $Re$  or  $We$  and how to find  $\Phi$ . There are two ways to deduce  $\Phi$ : experiments and modeling (fundamental physics laws or more concrete modeling, e.g., differential equations). We introduce examples to find  $\Phi$  in the next subsections.

#### 8.4.1

##### Viscous Dissipation Dominates Surface Tension

When we find a solution  $\Phi$ , to examine all the variables involved is by no means a trivial task. Instead, we often focus on a dominant physical property over others and conduct a corresponding asymptotic approximation. Therefore, we first assume that there is a regime where the viscous dissipation dominates the surface tension after the drop impacts. This implies that the kinetic energy of the impacting drop is dissipated by viscosity. Specifically, the kinetic energy of the drop, which is given at the initial stage by  $\frac{2}{3}\pi\rho R_0^3 V_0^2$ , is almost completely transferred into viscous dissipation. Therefore, by the law of energy conservation, we deduce

$$\frac{1}{2}\rho R_0^3 V_0^2 - E_{k,R_{\max}} \sim \frac{1}{2}\rho R_0^3 V_0^2 \sim (\text{the viscous force}) \cdot R_{\max}$$

where  $E_{k,R_{\max}}$  is the kinematic energy when the diameter is equal to  $R_{\max}$ . Moreover, by the definition of the viscous force, we have the viscous force  $\sim \mu R_{\max}^2 \frac{V_0}{h_m}$ . We finally conclude that

$$\rho R_0^3 V_0^2 \sim \mu \frac{V_0}{h_m} R_{\max}^3 \quad (8.16)$$

We also have another physics law of volume conservation:

$$R_0^3 \sim h_m R_{\max}^2 \quad (8.17)$$

By combining these physics laws Eqs. (8.16) and (8.17), we are led to  $\left(\frac{R_{\max}}{R_0}\right)^3 \sim \frac{\rho V_0 h_m}{\mu R_{\max}^2} \sim \frac{\rho V_0 R_0^3}{\mu R_{\max}^2}$  implies that  $\frac{R_{\max}}{R_0} \sim \left(\frac{\rho R_0 V_0}{\mu}\right)^{1/5}$ , so that  $\Phi \sim Re^{1/5}$ .

We have assumed that there is a regime where the viscous dissipation dominates the surface tension. Therefore, we can neglect the variable  $We$  of  $\Phi$  in Eq. (8.15). Moreover, the final thickness is much less than the initial diameter, so that we can also neglect the variable  $\frac{h_m}{R_0}$ . Hence, we deduce  $\Phi \sim Re^{1/5}$  upon further

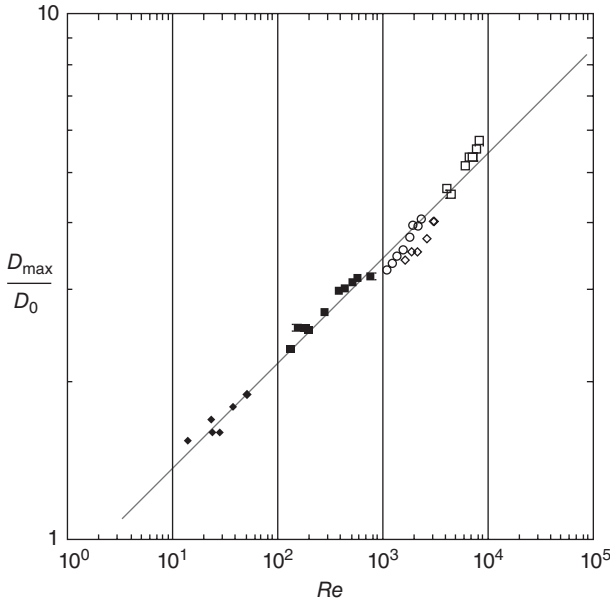


**Figure 8.14** Relative deformation of viscous drops as a function of the Reynolds number  $Re$  for silicone oils ( $\blacklozenge = 300 \text{ mPa}\cdot\text{s}$ ;  $\blacksquare = 20 \text{ mPa}\cdot\text{s}$ ) and viscous water–glycerol

mixtures (open symbols). The points are fitted well by the law  $D_{\max} = D_0 Re^{1/5}$ , represented as a solid line. Copyright C. Clanet *et al.* [5].

neglecting the gravity effect. For more detailed arguments, see the following and references therein.

Let us take an example of the drop impact of a viscous fluid. The experimental data from some viscous drops of silicone oils ( $\blacklozenge = 300 \text{ mPa}\cdot\text{s}$ ;  $\blacksquare = 20 \text{ mPa}\cdot\text{s}$ ) and viscous water–glycerol mixtures (open symbols) are shown in a plot in Figure 8.14 [5], where the relative maximal deformation ( $D_{\max}/D_0$ ) increases with Reynolds number, and follow the law  $D_{\max} \sim D_0 Re^{1/5}$ .

#### 8.4.2

##### The Flattened-Pancake Model

So far, we have deduced the model for the case in which  $Re$  dominates over the others. Contrary to the Section 8.4.1, we now introduce a scenario for a regime with  $We$  being dominant. One can consider that the gravity induced by acceleration overcomes surface tension, so that the drop is flattened. This is the case where the drop is larger than the capillary length. Here, the induced gravity can be expressed as  $V_0^2/R_0$ . Therefore, the so-called *impact capillary length* is

$$\sqrt{\frac{\sigma}{\rho V_0^2/R_0}} \sim h_m$$

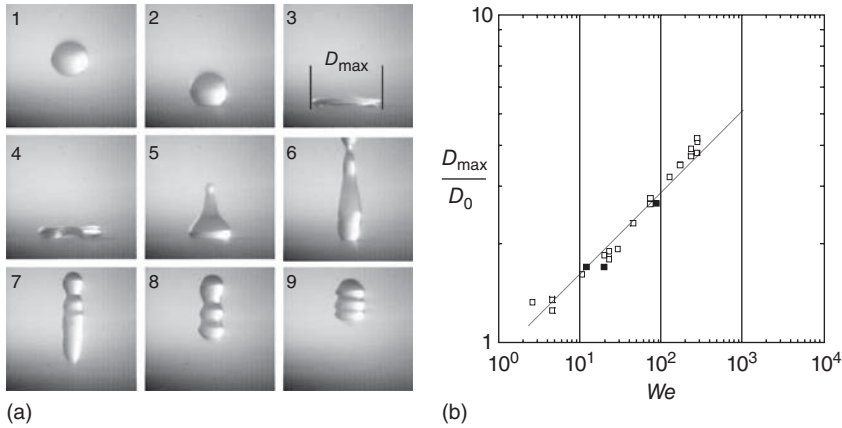


**Figure 8.15** (a) High-speed imaging of a water drop impact on a superhydrophobic surface. (Time interval between the images: 2.7 ms.) (b) Maximum diameter of the spreading drop normalized by the drop radius (spreading factor) as a function

of the Weber number. The open squares correspond to those obtained with water drops and the filled ones correspond to those obtained with mercury drops. The solid line indicates the slope 1/4. Copyright C. Clanet *et al.* [5].

Now, using this in the volume conservation law  $R_0^3 \sim h_m R_{\max}^2$ , we deduce  $\Phi \sim We^{1/4}$ .

Let us take an example of a water drop falling on a hydrophobic substrate [5]. The snapshot images in Figure 8.15 display the impact of a water drop ( $D_0 = 2.5$  mm) on a hydrophobic solid substrate ( $\theta_{\text{eq}} = 170^\circ$ ) at a speed  $V_0 = 0.83$  m s $^{-1}$ , which yields  $We = 24$ . The second image shows the drop when impacting at  $t = 0$ . In the third image taken at  $t = 2.7$  ms, the drop forms a flatted disk shape as it reaches its maximal extension  $D_{\max} \sim 2D_0$ . Then, it retracts and takes off (image 7). Our aim here is to describe the size of the disk-shaped drop at the maximum spreading,  $D_{\max}$ . The maximum diameter  $D_{\max}$  was measured from the images and then normalized with the initial diameter  $D_0$ .

### 8.4.3

#### The Kinetic Energy Transfers Completely into Surface Energy

Further, we introduce a regime where the viscosity may be neglected. Experiments can be conducted such that a liquid drop impacts on a superhydrophobic substrate. The superhydrophobic property allows for a high contact angle, so that it minimizes viscous dissipation. Therefore, the initial kinetic energy transfers totally into the surface energy of the drop. This is the case where we can neglect the variable  $Re$  of  $\Phi$  in Eq. (8.15). From the definition of the surface energy, we conclude the following law of energy conservation with our assumption:

$$\rho R_0^3 V_0^2 \sim \sigma R_{\max}^2$$

This implies  $\Phi \sim We^{1/2}$ . For more detailed arguments, see the following Refs. [6–8]. Collings *et al.* [6] predicted an upper bound on the maximum spreading diameter by neglecting the viscous dissipation:

$$\frac{R_{\max}}{R_0} = \left( \frac{We + 12}{3(1 - \cos \theta_{\text{eq}})} \right)^{1/2}$$

where  $\theta_{\text{eq}}$  is the equilibrium contact angle between the liquid and the solid surface. Here, if  $We$  is sufficiently large and  $1 - \cos \theta_{\text{eq}}$  is not close to zero (e.g., a liquid drop impacts on a superhydrophobic substrate), we deduce  $\Phi \sim We^{1/2}$ . However, there are limitations to the Collings *et al.* [6] model. For instance, viscous dissipation can be neglected only for very special cases and  $\theta_{\text{eq}}$  from Young's equation can be applied only to the case of a drop at rest. Therefore, an alternative model evolves to treat these problems, in the paper by Pasandideh-Fard *et al.* [8]. They use the advancing contact angle  $\theta_{\text{av}}$  to estimate the surface energy when the drop is at the maximum spreading diameter  $R_{\max}$ . They showed that

$$\frac{R_{\max}}{R_0} = \left( \frac{We + 12}{3(1 - \cos \theta_{\text{av}}) + \frac{4We}{\sqrt{Re}}} \right)^{1/2}$$

Here, in the limit  $We \rightarrow \infty$ , we deduce  $\frac{R_{\max}}{R_0} \sim Re^{1/4}$ . This result implies that combination of the surface tension effect and viscous dissipation yields a different scaling law from the viscosity dominant case (Section 8.4.1).

#### 8.4.3.1 Evaporation: A Scaling Exponent of the Radius

At the end of the full history of the impacting drop, the drop remains with an equilibrium shape on the substrate, which follows Young's angle. At this stage, evaporation of the drop occurs, and the drop will vanish. In this section, we apply the Pi theorem to investigate the behavior of the radius of the evaporating drop. We are interested in the limit  $\Delta t = t_0 - t$  that is close to zero, where  $t_0$  is the extinction time of the drop volume. Thus, the parameters that determine the radius of an evaporating drop are  $\Delta t$ , diffusion coefficient  $D$ , and vapor density  $\emptyset$ . The relation between these parameters and the radius  $R$  can be expressed implicitly as follows:

$$0 = F(\Delta t, D, \emptyset, R)$$

Here, the dimensions are

$$[\Delta t] = T, \quad [D] = L^2 T^{-1}, \quad [\emptyset] = M L^{-3}, \quad [R] = L$$

The variables  $\Delta t$ ,  $D$ ,  $\Phi$ , have independent dimensions. We now perform the detailed calculation. We deduce

$$[R] = [(\Delta t)^a D^b \emptyset^c], \quad L = T^a L^{2b} T^{-b} M^c L^{-3c} = M^c L^{2b-3c} T^{a-b}$$

with the following linear system:

$$\begin{pmatrix} 0 & 0 & 1 \\ 0 & 2 & -3 \\ 1 & -1 & 0 \end{pmatrix} \begin{pmatrix} a \\ b \\ c \end{pmatrix} = \begin{pmatrix} 0 \\ 1 \\ 0 \end{pmatrix}$$

so that the solution is easily found as  $(a, b, c) = (\frac{1}{2}, \frac{1}{2}, 0)$ . Then, we finally conclude that

$$0 = \Phi \left( \prod_1 = \frac{R}{\sqrt{D\Delta t}} \right)$$

This means that  $\prod_1 = \frac{R}{\sqrt{D\Delta t}}$  must be a constant, so that  $R \propto (t_0 - t)^{1/2}$ . Therefore, a critical exponent of the radius variation near the extinction time is  $1/2$ . This is the case for the evaporating drop whose contact angle is  $90^\circ$  on a solid substrate. It can be seen as a final asymptotic behavior. For more detailed arguments, see Ref. [9].

Let us take an example of an evaporating water drop on a substrate. The drop is confined in a tiny ( $1.5^3$  cm) box with a small opening at the top. The experimental data are shown in Figure 8.16 as a log–log graph of the radius  $R$  as a function of  $\Delta t = t_0 - t$ . For this evaporating drop, experimental data follow a dotted line representing the law  $R \propto (t_0 - t)^{1/2}$ .

Further essential reading for drops on substrates is provided by Ref. [10] and in Chapters 9–11 in this book.

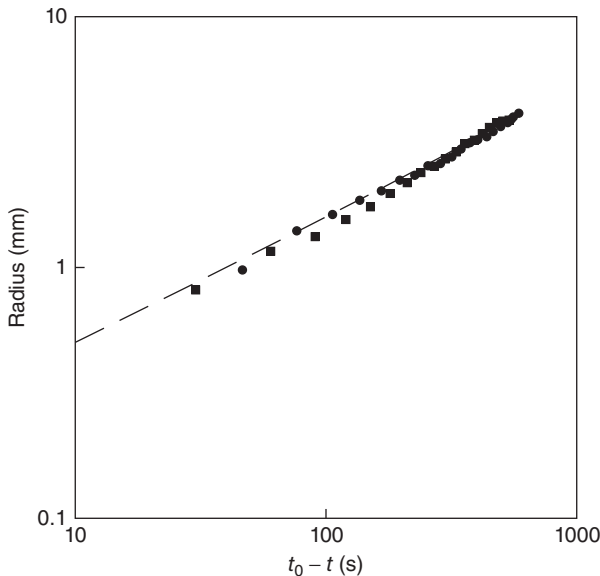


**Figure 8.16** Radius of a confined evaporating water drop as a function of time to extinction. Figure 5 of Ref. [9].

## References

1. Rioboo, R., Marengo, M., and Tropea, C. (2002) Time evolution of liquid drop impact onto solid, dry surfaces. *Exp. Fluids*, **33**, 112–124.
2. Blake, T.D. and Haynes, J.M. (1973) in *Progress in Surface and Membrane Science*, vol. 6 (eds J.F. Danielli, M.D. Rosenberg, and D.A. Cadenhead), Academic Press, pp. 125–138; e-book: (2013), Elsevier.
3. Buckingham, E. (1914) On physically similar systems: illustrations of the use of dimensional equations. *Phys. Rev.*, **4** (4), 345–376.
4. Butterfield, R. (1999) Dimensional analysis for geotechnical engineers. *Géotechnique*, **49** (3), 357–366.
5. Clanet, C., Béguin, C., Richard, D., and Quéré, D. (2004) Maximal deformation of an impacting drop. *J. Fluid Mech.*, **517**, 199–208.
6. Collings, E.W., Markworth, A.J., McCoy, J.K., and Saunders, J.H. (1990) Splat-quench solidification of freely falling liquid-metal drops by impact on a planar substrate. *J. Mater. Sci.*, **25**, 3677–3681.
7. Bennett, T. and Poulidakos, D. (1993) Splat-quench solidification: estimating the maximum spreading of a droplet impacting a solid surface. *J. Mater. Sci.*, **28** (4), 963–970.
8. Pasandideh-Fard, M., Qiao, Y.M., Chandra, S., and Mostaghimi, J. (1996) Capillary effects during droplet impact on a solid surface. *Phys. Fluids*, **8** (3), 650–659.
9. Shahidzadeh-Bonn, N., Rafai, S., Azouni, A., and Bonn, D. (2006) Evaporating droplets. *J. Fluid Mech.*, **549**, 307–313.
10. Bonn, D., Eggers, J., Indekeu, J., and Rolley, E. (2009) Wetting and spreading. *Rev. Mod. Phys.*, **81**, 739–805.

## 9

# Coalescence and Line Formation

Wen-Kai Hsiao and Eleanor S. Betton

### 9.1

#### Implication of Drop Coalescence on Printed Image Formation

Industrial inkjet printing has been an advanced process for large-format image reproduction, ceramic decoration, and other small- to mid-volume graphic printing applications. Similarly to other halftone and process color printing processes, inkjet printing relies on depositing tiny drops of inks in the primary cyan, magenta, yellow, and key (black) or CMYK colors to subtractively create the desired color gamut. Therefore, accurate placement of the printed dots is essential for good feature resolution and color reproduction. One may further argue that since the sizes of the individual printed dots produced by the current generation of industrial inkjet print heads are, in general, below the resolving limit of human eyes, our perception of the “print quality” of the inkjet-printed features is determined by the relative position of these printed dots and their morphology *en masse*.

A unique feature of inkjet printing is that the printed features are formed without physical contact between the printheads and the receiving media. Whereas this is a distinctive advantage when dealing with fragile or highly structured surfaces, it can present a limitation in regard to dot placement accuracy and more chance for deposited drops to overlap. Moreover, as inkjet printing migrates to high-speed, high-throughput processes such as single-pass Web printing applications (e.g., high-speed label print press), there is an increasing trend of printing over low or nonabsorbing substrates. As there is minimal ink absorption to limit the ink spread after drop deposition in these scenarios, there is an increased risk of uncontrolled drop coalescence and mixing on surface. In addition, as the printing rate and substrate speed increase, there is a greater likelihood of later deposited ink drops landing on wet drops and layers deposited previously. Some of the more drastic examples of the effect of such behavior on print quality can be seen in Figure 9.1.

In practice, the drop coalescence and mixing issues can often be minimized by optimizing the printing parameters and introducing measures such as substrate heating and UV pinning to reduce unwanted post-deposition drop spreading. However, as demand for higher printing speed continues to grow,

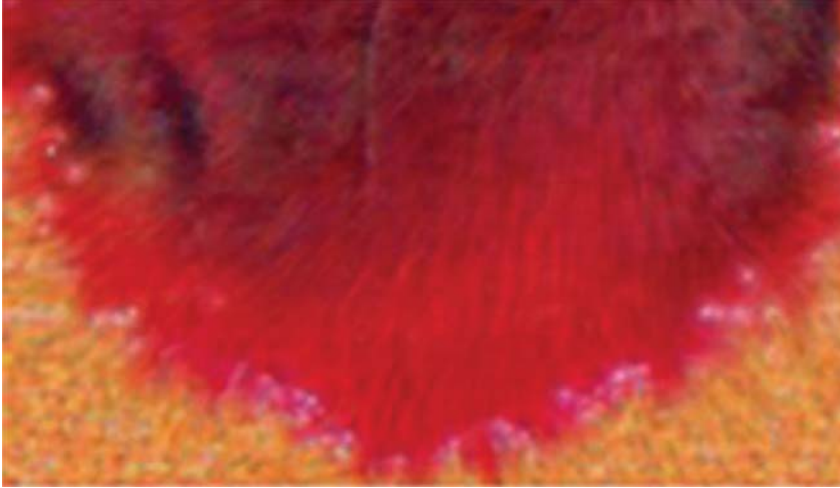


**Figure 9.1** Close-up view of an inkjet printed label with excessive drop coalescence issues.

these compensation strategies will eventually reach their limits. Therefore, a comprehensive understanding of the dynamics of printed drop coalescence is essential for optimizing the print quality in the next generation of industrial printing applications.

## 9.2

### Implication of Drop Coalescence on Functional and 3D Printing

As a flexible material deposition process, inkjet printing is also a promising technique used to fabricate functional features such as organic optical devices and transistors and organic or inorganic conductive tracks. However, bulge formation and capillary breakup have been plaguing the efforts of printing precise free-form linear and 2D features on surfaces using inkjet technology. Hebner *et al.* [1] have successfully used a standard desktop inkjet printer to pattern luminescent, doped polymers and fabricated organic light-emitting diodes (OLEDs). However, they have commented on the difficulty of aligning the shadow mask for metallization over the printed polymer dots directly, and their images of irregularly shaped printed dots suggested that this is likely a result of nonoptimized coalescence of the printed drops. Shimoda *et al.* [2] and Sirringhaus *et al.* [3] addressed the printed feature accuracy issue by using alternating hydrophilic and hydrophobic regions on the surfaces to limit spreading and coalescence of inkjet-printed functional fluids. Although their approaches have succeeded in producing functional organic light-emitting pixels and all-polymer transistor circuits, their processes limited the inherent flexibility of inkjet printing by requiring prepatterned substrates. Significantly, Sirringhaus and colleagues recognized that without the patterning and selective printing strategy, their printed features would have suffered issues such as bulge formation and capillary breakup. Gao and Sonin



[4] have demonstrated the potential of free-form inkjet printing as a fabrication technique by printing molten wax droplets to form pillars, lines, and walls. However, their results showed that careful control of the printing parameters is necessary to prevent bulges in their printed lines. Schiaffino and Sonin [5] further defined the regimes where bulge-free lines can be printed.

The mechanism of bulge formation has been well described by Davis [6] in regard to an unconstrained liquid rivulet and later by Duineveld [7] specifically for inkjet printing of continuous lines on surfaces. The criteria and dynamics described, such as that a liquid line is potentially unstable when the contact line is free to move and the number of bulges formed is inversely correlated to drop spacing, are well qualified by later works by van den Berg *et al.* [8] and van Osch *et al.* [9]. In both later works, the printing parameters, for example, drop spacing, were carefully tailored in accordance to the surface energy of the substrates used, that is, wetting property, to avoid the undesired results of either discontinuous line (drop spacing too large) or bulge formation (drop spacing too small), as shown in Figure 9.2.

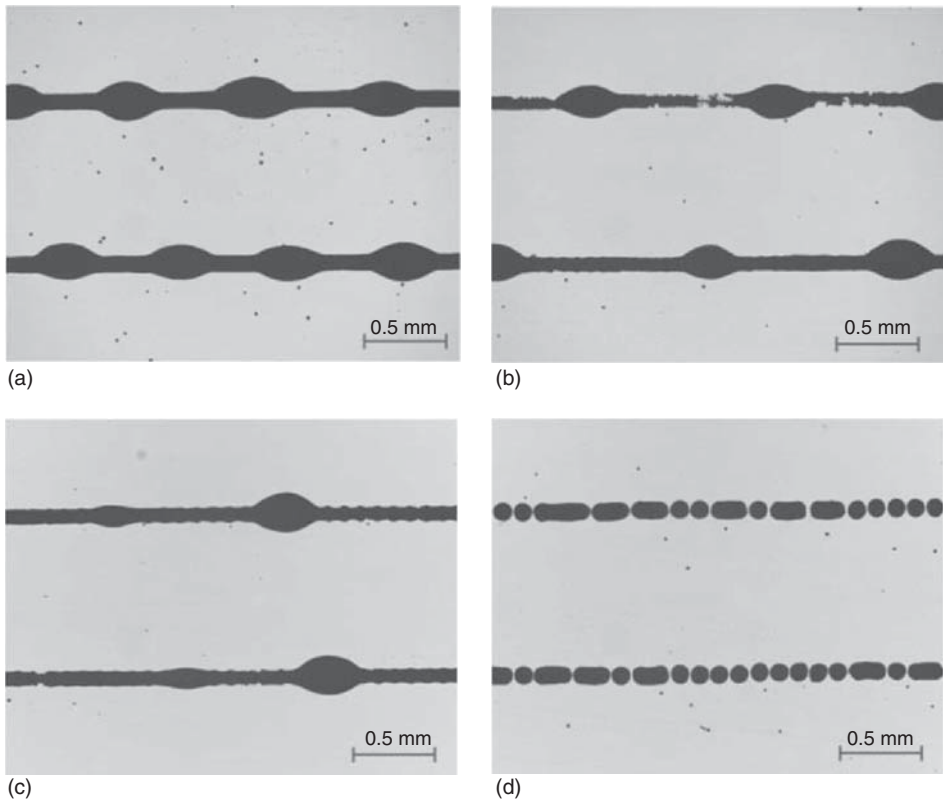


**Figure 9.2** Images of printed lines transit from bulging to discontinuing as the drop spacing increases from (a) to (d). (Reproduced with permission from van den Berg *et al.* [8].)

While further studies were conducted by Soltman and Subramanian [10] and Stringer and Derby [11] to model the line formation dynamics and predict the line stability regimes, in practice, the optimization of the printed line features is still performed on a trial-and-error, iterative basis. Therefore, additional empirical studies on inkjet drop coalescence and line printing dynamics, specifically those focused on validating analytical models, are particularly valuable. Two such studies are outlined in the following sections.

### 9.3

#### Coalescence of Inkjet-Printed Drops

##### 9.3.1

##### Coalescence of a Pair of Liquid Drops on Surface

The coalescence of 3D drops on a 2D surface by condensation has been investigated and modeled for a variety of fluids and surfaces since the 1980s. A detailed summary of this work is given by Meakin [12]. Although this work is useful for predicting drop size and distribution under certain circumstances, its applications are limited to predicting the behavior of bulk drops. Narhe *et al.* [13] and Andrieu *et al.* [14] also studied drop condensation but restricted their analysis to a single coalescence event between two drops and addressed the change in the length and width of the resultant single drop.

There has been additional work studying the necking behavior occurring during the early stages of coalescence between two free drops suspended from needles and brought into contact [15, 16]. Menchaca-Rocha *et al.* [17] used a second drop spreading at very low velocity until it coalesced with a stationary first drop. If the spreading velocity remains slow, the kinetic energy is negligible in comparison to surface tension forces. By using mercury drops, surface wetting effects could be ignored, due to the static contact angle of approximately  $160^\circ$ . The drops could also be moved together mechanically, avoiding the need for drop growth, and image capture could be triggered by the change in electric charge as the drops meet.

The coalescence of drops on a 2D substrate for wetting fluids was investigated by Kapur and Gaskell [18]. They placed a single drop of water–glycerol mixture on a glass slide and expanded a second drop until coalescence occurred, as shown in Figure 9.3.

The drops used were 3 mm in diameter, and images of the coalescence were captured at 13 500 fps from the side and above. The growth rate of the neck width was measured for a range of fluids with different viscosities. They found empirical coefficients  $k$  and  $n$  for the spreading relationship  $A = kt^n$ , where  $A$  is the area of the drop in contact with the substrate. They found the values of  $n$  to vary between 0.62 and 0.8, which showed that the coalescing drop was spreading at the upper rates seen for a single drop, suggesting that single drop impact and drop coalescence occur over similar timescales.

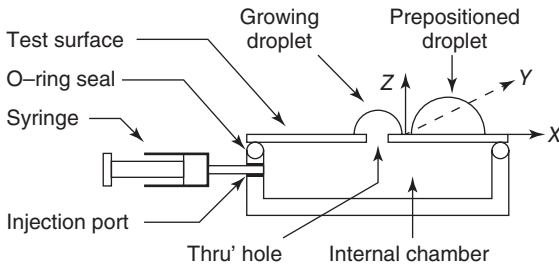


**Figure 9.3** Drop injection method for studying the coalescence of two sessile drops by Kapur and Gaskell [18].

The coalescence process for static drops is divided into three stages by Sellier and Trelluyer [19] as follows:

- 1) *Initial Stage*: The contact line does not move, the neck nucleates, and the neck width increases as  $t^{1/2}$ .
- 2) *Intermediate Stage*: The neck relaxes, and the contact line moves.
- 3) *Final Stage*: Limited movement of the contact line. The combined drop relaxes into a spherical cap.

As shown in Figure 9.4, the physical change in the coalescing drops is dominated by the dynamics of neck nucleation and expansion. When two drops are brought together at the beginning of coalescence, a tiny liquid bridge forms between them. For drops with negligible initial velocity, the van der Waals forces cause the initial formation of the bridge. Once the bridge, or the neck, has formed, it has high local surface curvature, causing high interfacial stress. This draws fluid into the necking region to reduce the surface energy. Eventually, the two drops become one, and the drop reaches equilibrium.

Case and Nagel [15] carried out experiments where a drop is suspended from a needle in air, while a second drop is expanded slowly until coalescence occurs. The bridging behavior between the two drops was compared with the viscous length

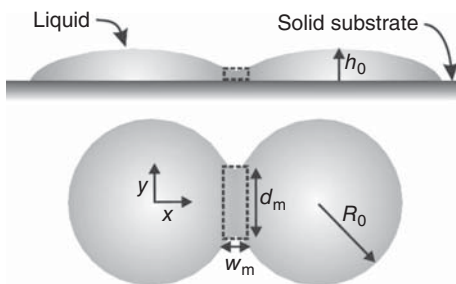


**Figure 9.4** Side and top views of neck formation during coalescence.

scale  $l_v = \eta^2 / (\rho\gamma_1)$ . Balancing the interfacial tension of the drops with inertia gives:

$$\left(\frac{\gamma_1}{\rho\nu}\right)^{1/2} \propto \frac{dr}{dt} \quad (9.1)$$

For two semihemispherical drops,  $\nu = r_n^2 / R_0$  where  $r_n$  is the bridge radius and  $\nu$  is the characteristic length scale. The solution of the differential equation is:

$$r_n = C \left(\frac{4\gamma_1 r}{\rho}\right)^{1/4} (t - t_0)^{1/2} = C \left(\frac{4\gamma_1 r}{\rho}\right)^{1/4} \tau^{1/2} \quad (9.2)$$

where  $t_0$  is the instant of coalescence,  $r$  is the drop radius, and  $C$  is a constant of the order of 1. This yields a scaling law of  $r_n \propto \tau^{1/2}$ , in agreement with the prediction of Eggers *et al.* [20]. This model is supported by the results of Menchaca-Rocha *et al.* [17], who found that the neck width for mercury drops on roughened glass increased as  $\tau^{0.41}$ . Ristenpart *et al.* [21] found that the neck width for silicone oil drops on polystyrene grew at a rate proportional to  $\tau^{0.53}$ .

Kapur and Gaskell [18] estimated the nondimensional time by  $\tau_2 = t\eta R_0 / \gamma_1$  and the semiwidth of the neck using  $d_n = r / (2R_0)$  to find the scaling relationship  $d_n \propto \tau_2^\alpha$ . From their experiments, it was found that  $\alpha$  had values between 0.42 and 0.57. When imaging the side view of drop coalescence, they observed fluid from the drops passing into the necking region and developing a capillary wave, which travels along the length of the drop, as shown in Figure 9.5. As the height of the drops does not decrease initially during necking, they suggest that the negative pressure in the neck, instead of hydrostatic pressure from the fluid above the neck, is

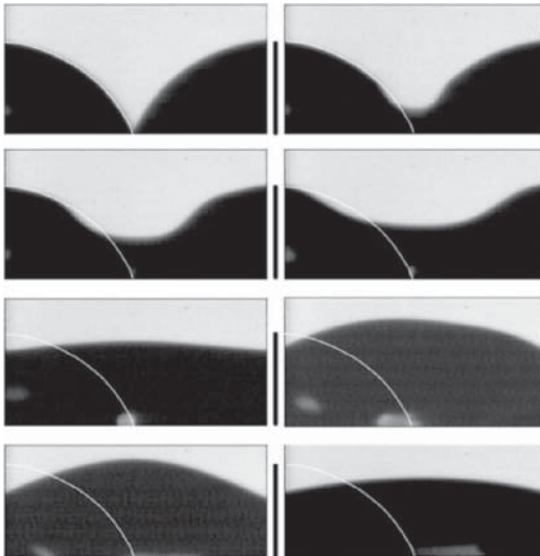


**Figure 9.5** Necking dynamics during coalescence of 2 mm size water drops. Taken by Kapur and Gaskell [18]. The initial profile of the first drop is marked on all images and the vertical scale bar represents 1.6 mm.

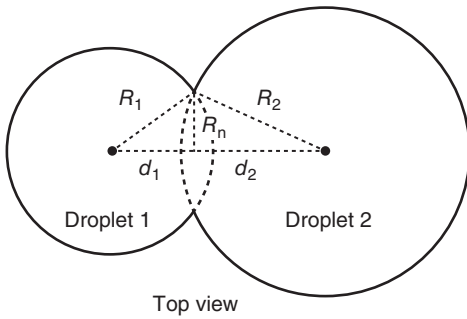


**Figure 9.6** Geometric setup for measuring drop coalescence by Sellier and Trelluyer [19].

driving the flow. The neck height then exceeds the initial drop height due to fluid inertia, causing oscillations. Similar oscillations were observed by Wang *et al.* [22] for water drops coalescing on an inclined surface. The amplitude of oscillations decreased with more viscous fluids and decayed faster. The decay rate was similar to that for freely suspended drops.

Diez and Kondic [23] carried out computer simulations based on the Navier–Stokes equations with the lubrication approximation to model the coalescence of two drops that completely wet the surface. In their model, they included a precursor film, which ejects a minidroplet at the necking point. Roisman *et al.* [24] and Sellier and Trelluyer [19] used a simple geometric model for finding the neck width based on Figure 9.6.

For drops of radius  $R_1$  and  $R_2$ , the Pythagoras theorem gives the semiwidth of the neck as:

$$R_n^2 = R_1^2 - d_1^2 = R_2^2 - d_2^2 \quad (9.3)$$

It is assumed that the spread length of the drop is approximately constant, so  $\Delta X = d_1 + d_2$ . Combining this into a nonlinear equation:

$$R_1^2 + R_2^2 - 2R_n^2 - \Delta X^2 + 2(R_1^2 - R_0^2)(R_2^2 - R_0^2) = 0 \quad (9.4)$$

The approximations used by Sellier and Trelluyer [19] were similar to that by Diez and Kondic [23]. However, the earlier work applied to completely wetting systems did not take into account the contact angle hysteresis and pinning or a nonspherical final shape. Diez and Kondic [23] investigated the influence of spacing between drops and concluded that as drop spacing decreases, the effect of surface energy increases, which accelerates the coalescence dynamics. This causes an increase in the neck width with smaller gaps between drops. Sellier and Trelluyer [19] expanded their work with an experiment whereby they placed a drop of one color on a surface and expanded a second drop of the same fluid but of a different color until coalescence began. In addition to supporting their model, the images taken showed that there is very little mixing occurring between the two drops during the early necking stage of coalescence.

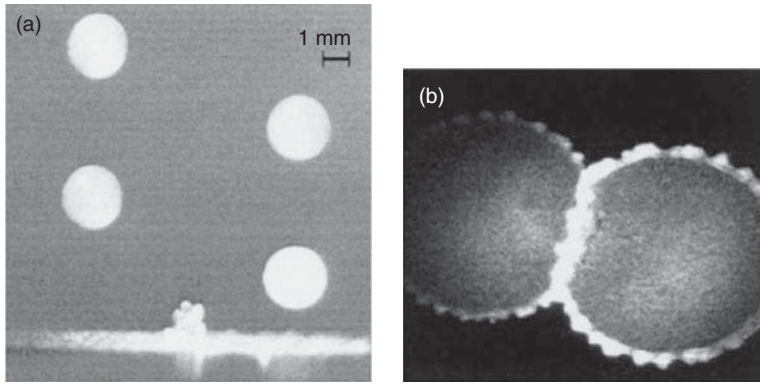


**Figure 9.7** (a) Side view and (b) bottom view of the sequential impact of 2.5 mm diameter water drops impacting at  $3.36 \text{ m s}^{-1}$  with an offset of 8.4 mm and time delay between impacts of 0.9 ms, by Roisman *et al.* [24].

### 9.3.2

#### Coalescence with Drop Impact

In inkjet printing coalescence occurs between drops that are still spreading after impact. There are considerably fewer studies in the literature considering the case where one or both drops are in motion during coalescence.

The events involved in one drop landing sequentially after a first drop was investigated by Roisman *et al.* [24] for millimeter-sized water drops. The offset between the centers of the two drops was varied, as was the time delay between depositions. Drop impact was imaged from above and from the side, as shown in Figure 9.7ab. Due to the high impact speed and large drop size, the impact regime is considerably different from that for the impact of inkjet size drops. Instead, splashing occurs, and a large sheet of fluid is ejected. The authors used a geometric model similar to that by Sellier and Trelluyer [19] to track the motion of the collision line between the drops and the uprising of the sheet of fluid, with good agreement with their experimental results.

This work has been expanded in a more recent work by Li *et al.* [25]. They investigated the effects of drop spacing on the final position of a drop formed by coalescence for lower impact velocities, where splashing does not occur. This work is aimed at the printing industry, where line thickness and consistency are affected by the drop spacing. The “drawback” process is thought to cause line bulging when a second drop draws an adjacent stationary drop toward it. Their experiments were carried out using millimeter-sized drops of water and ethylene glycol (EG). The first drop was deposited using a syringe and left until it had reached equilibrium. The substrate was then moved a controlled distance before a second drop was deposited at a velocity between  $0.2$  and  $1 \text{ m s}^{-1}$ . The coalescence of the drops was captured at 2000 fps, so it was not fast enough to capture the necking behavior in detail. For this system, reticulation occurred, leading to a maximum and a minimum spread length, as shown in Figure 9.8.

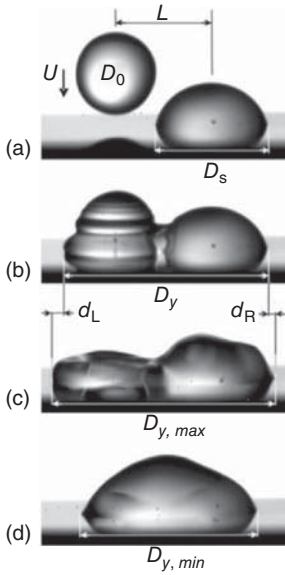


**Figure 9.8** Impact and coalescence of drops by Li *et al.* [25], showing (a) the incident drop diameter  $D_0$  and static diameter  $D_s$ , (b) the spread length  $D_y$ , (c) the maximum spread length  $D_{y,max}$ , and (d) the minimum spread length  $D_{y,min}$ .

Li *et al.* [25] describe the amount of overlap using an overlap value  $\lambda$  between the two drops defined as:

$$\lambda = 1 - \frac{\Delta x}{D_s} \quad (9.5)$$

where  $D_s$  is the static diameter of the first drop and  $\Delta x$  is the offset between drop centers (as shown in Figure 9.8), so  $\lambda = 1$  corresponds to drop on drop, while  $\lambda = 0$  is when the edges of the two drops are just touching.

The nondimensionalized spread length  $\psi$  is defined as

$$\psi = \frac{D_y}{D_s + \Delta x} \quad (9.6)$$

where  $D_y$  is the drop length measured after coalescence.

The maximum and minimum nondimensional spread lengths are defined in Eqs. (9.7) and (9.8), respectively, where  $D_{y,max}$  is the maximum spread length measured during coalescence and  $D_{y,min}$  is the minimum measured spread length.

$$\psi_{max} = \frac{D_{y,max}}{D_s + \Delta x} \quad (9.7)$$

$$\psi_{min} = \frac{D_{y,min}}{D_s + \Delta x} \quad (9.8)$$

For drops coalescing completely and forming a spherical cap at equilibrium,  $D_y = \sqrt[3]{2D_s}$ . Substituting for  $D_y$  gives Eq. (9.10), which corresponds to the equilibrium spread length,

$$\psi_e = \frac{\sqrt[3]{2}}{2 - \lambda} \quad (9.10)$$

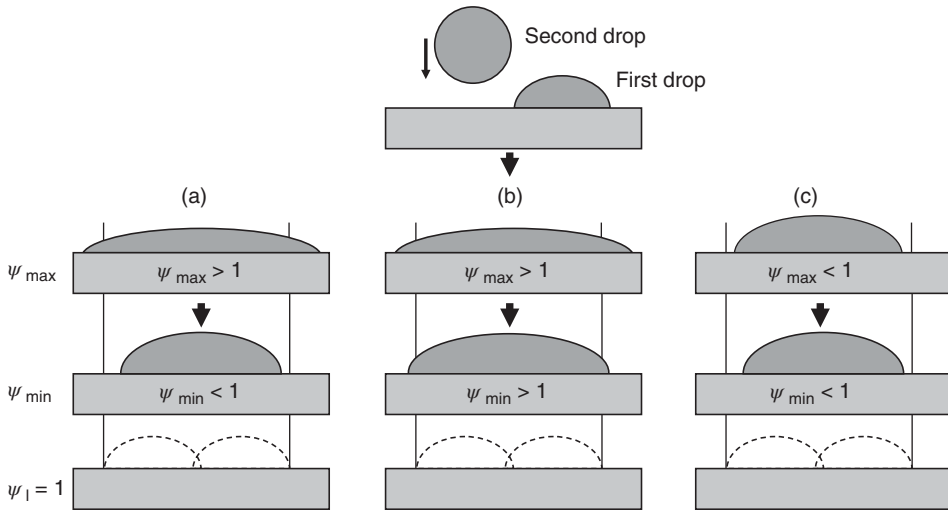


**Figure 9.9** Schematic of three possible outcomes after drop coalescence by Li *et al.* [25]. Showing (a) drawback due to retraction, (b) additional spread, and (c) drawback *not* due to retraction.

The ideal drop length,  $\Psi_i = 1$ , occurs when the second drop does not cause any retraction of the first drop and the contact lines do not move inward, such that  $D_y = D_s + \Delta x$ .

Figure 9.9 shows the three possible outcomes from coalescence: additional spread (the drops spread outward); drawback due to retraction when the combined drop length does not exceed the ideal spread length; or drawback not due to retraction when the drop retracts after the combined drop length exceeds the ideal spread length. These outcomes can be used to calculate an upper and a lower limit for the spread diameter after coalescence.

For printing purposes,  $\Psi_i$  is the optimum length, since there is no retraction. Figure 9.10 shows a graph that can be used to estimate when drawback will occur. This is divided into three sections: drawback due to retraction (gray area above the  $\Psi_e$  line); drawback not due to retraction (gray area below the  $\Psi_e$  line), and additional spread (white areas). The final spread length is related to the Weber and Ohnesorge numbers.

The authors also define a critical spread length required for printing a continuous line as:

$$\Psi_c = \frac{2(1 - \lambda)}{2 - \lambda} \quad (9.11)$$

This work represents an important contribution to the understanding of drop coalescence dynamics. However, while the effect of drop spacing was investigated, the drop size studied was much too large for the results to be directly applicable to inkjet printing. It also neglected the necking behavior and did not consider how this can affect the spread factor. The experimental study outlined in the next section aims to address some of these issues.



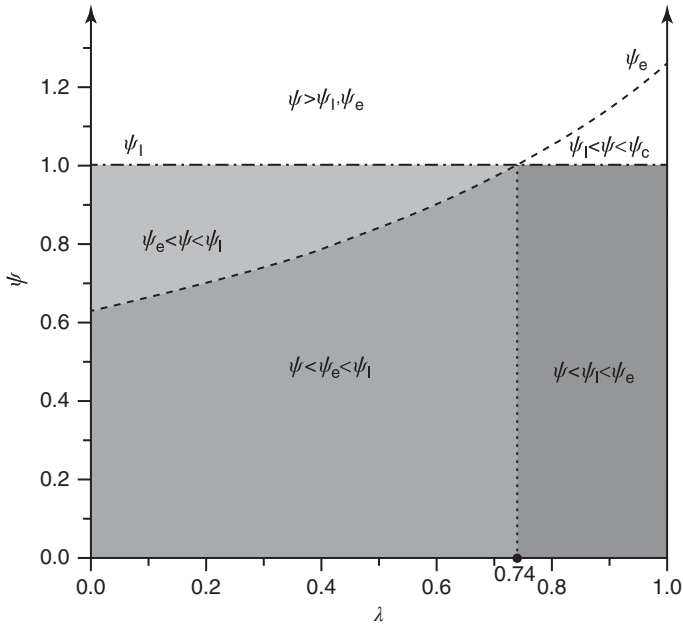


**Figure 9.10** Ideal spread length  $\psi$  as a function of the overlapping ratio  $\lambda$  as developed by Li *et al.* [25].

### 9.3.3

#### Coalescence of a Pair of Inkjet-Printed Drops

As mentioned in the previous sections, the models describing the coalescence dynamics of a pair of impacting drops were primarily developed and validated by experiments using millimeter-sized liquid drops. While these earlier works provided useful insights, it is far from clear that they can be applied directly to micrometer-sized ink drops used in inkjet printing applications. In addition, print quality issues observed in practice suggested that the coalescence dynamics may be affected by drop spacing.

As previously described, the coalescence of two drops on a surface initiates with the formation of a liquid bridge between the drops. This neck expands radially at a rate of  $\tau^{1/2}$ . The position of the neck between two static drops can be found from basic geometry, as shown in Figure 9.6. The liquid viscosity and contact angle should determine the spread length of coalescing sessile drops. Investigations into coalescence, where the second drop has a significant impact velocity, have shown that the final, combined drops are free to either expand or retract. The maximum and minimum drop lengths can be estimated for the amount of offset (overlap or underlap), as shown in Figure 9.11, between the two drops.

The work to be presented in the following sections investigated the coalescence of two inkjet-printed drops in real time. It addressed the effects of changing

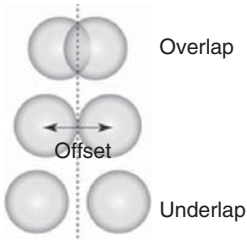


**Figure 9.11** Example of overlap and underlap of drop coalescence.

the offset between the two drops and also looked at the early necking stages for coalescence.

### 9.3.3.1 Experimental Setup

Coalescence experiments were carried out with  $39\ \mu\text{m}$  diameter inkjet drops at the two different frame rates; 500 000 fps for the impact stage and 20 000 fps for the wetting stage of drop spreading. Two drops were printed in short succession. The first drop was allowed to impact and spread before a second drop was deposited next to it. The impact velocity was constant at  $2.7\ \text{m s}^{-1}$ . The substrate was mounted on a linear stage and by varying the stage traversing speed, the drop offset could be accurately controlled. The actual drop offset was validated from the individual video frame as the distance from the center of the first drop to the center of the second drop the instant before it landed. The time delay between drop depositions was controlled by changing the print frequency of the printhead.

### 9.3.3.2 Necking Stage Dynamics

The impact stage was imaged at  $2\ \mu\text{s}$  time intervals to capture the necking dynamics between the two drops as they merge and spread. Figure 9.12 shows the early necking stages at increasing offsets between the first and the second drop.

The drop length is the distance measured between the left and the right edge of the combined drops. The drop length is normalized by the impact drop diameter to obtain the composite spread factor  $\xi = D_y/D_0$ , where  $D_y$  is the total width of the coalesced drops and  $D_0$  is the diameter of the impact drop. As expected,  $\xi$  for the two drops increases with the offset between drops.

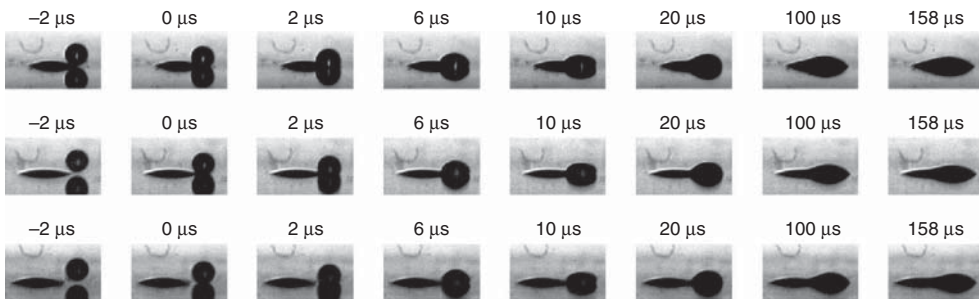


**Figure 9.12** Images of drop coalescence for drops impacting with a 12 ms time delay between impacts for gaps of: (a)  $41\ \mu\text{m}$ , (b)  $56\ \mu\text{m}$ , and (c)  $67\ \mu\text{m}$ .

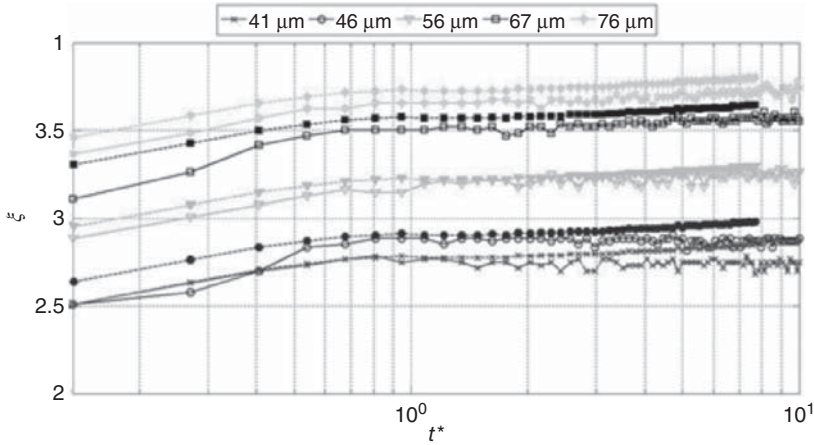


**Figure 9.13** Composite spread factor,  $\xi$ , measured during the necking stages of coalescence for different offsets; solid lines: experimental data; and dash lines: model predictions versus the nondimensional time  $t^* = tU_0/D_0$ , where  $U_0$  is the drop impact velocity.

When compared to the geometric model by Sellier and Trelluyer [19], there is reasonable agreement for the early kinematic phase of the second drop, even for small offsets. In general, the accuracy of the model prediction improved significantly in the later relaxation stage, as shown in Figure 9.13 in terms of  $\xi$  versus the nondimensional time  $t^* = tU_0/D_0$ .

The maximum height of the combined drop was found to be similar across the different drop offsets, as shown in Figure 9.14. As the maximum height during

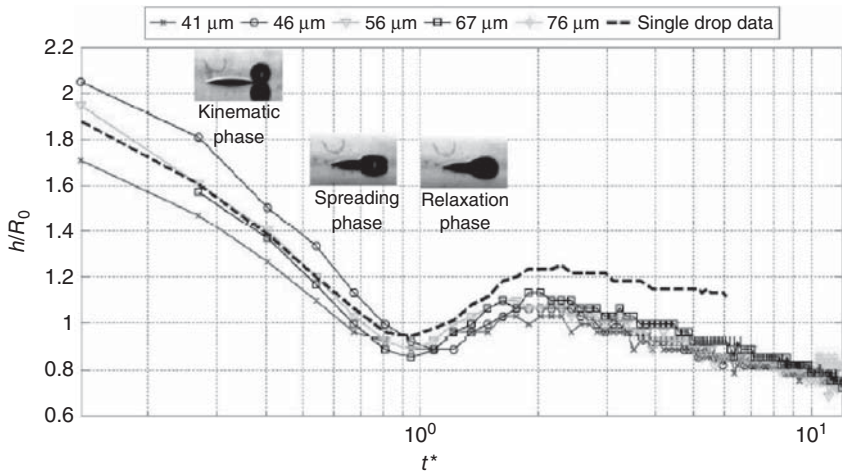


**Figure 9.14** Normalized drop height measured during the necking stages of coalescence for different offsets between drops (solid lines) as compared with drop height measured from single drop impact (dashed line).

impact/coalescence is primarily associated with the collapsing and spreading of the second drop, it suggests that the spreading of the later drop is not affected by the offset between drops in its early stage. The hypothesis is further supported by the fact that the typical maximum height recorded was similar to that of a single drop impacting a dry surface throughout the different spreading phases. Only during the final wetting phase does the height differ between a single impacting drop and a drop impacting alongside another.

In order to distinguish which drop is contributing most to the change in drop length, the left and right edge positions of the coalescing drops were extracted from the video frames. The drop length increases significantly in the direction of the second drop as it impacts and spreads. The left-hand side of the first drop is

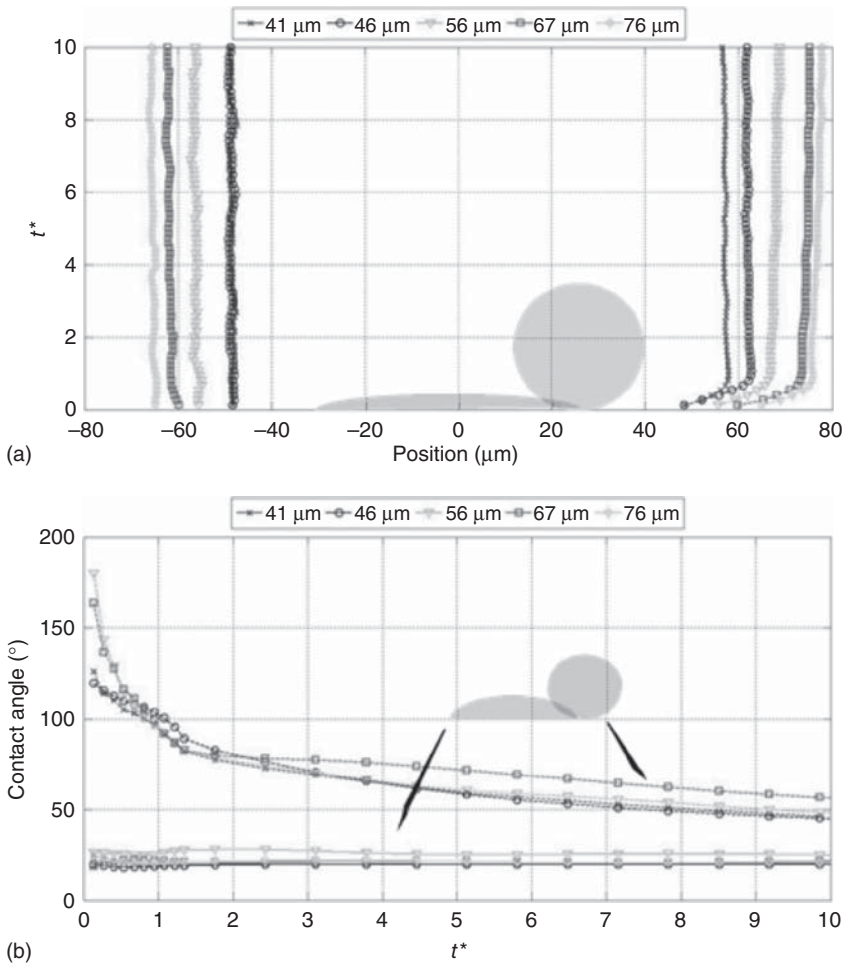


**Figure 9.15** The real-time dynamics of the left/right edge positions and contact angles at different drop offsets.

not displaced during the impact of the second drop for all offsets. In addition, the difference in offset between the two drops does not appear to significantly affect the dynamic values of the left and right contact angles of the combined drop, as shown in Figure 9.15.

In addition, the geometric model was used to calculate the position of the neck from the center of each drop, as shown in Figure 9.16. The results revealed a significant decrease in distance from the neck to the center of the first drop,  $d_1$ , as the drop offset increased. A decrease in  $d_1$  could be a result of either the neck moving toward the first drop or the peak of the first drop moving toward the neck. However as the radius of the first drop, determined by the distance from the drop

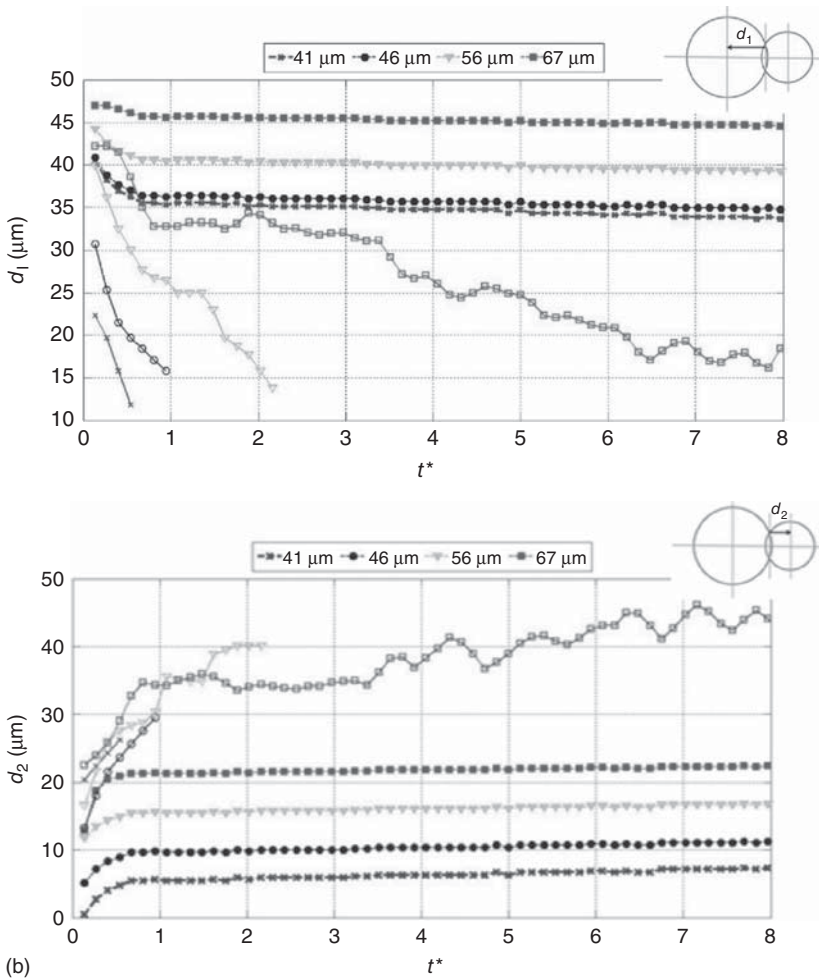


**Figure 9.16** Distances from the centers of both drop 1 and drop 2 to the necking region,  $d_1$  and  $d_2$ , respectively, for coalescence with a range of offsets. The open markers represent the measured results, whereas the solid markers give the model predictions.

peak to the left edge, does not increase as much as  $d_1$  decreases; the decrease most likely signifies the necking point moving toward the first drop. However, the geometric model does not predict the rapid decrease in  $d_1$  dynamically as seen experimentally and hence overestimates  $d_1$ , particularly in the later spreading stage. Furthermore, the model also fails to show the large increase in the measured distance from the center of the second drop to the neck,  $d_2$ . The increase in  $d_2$  most likely suggests that the neck was moving away from the second drop as the drops coalesced, since the radius dynamics of drop two is well predicted by the geometric model.

### 9.3.3.3 Discussion

The experimental results show a direct correlation between the composite spread factor  $\xi$  and the offset between the coalescing drops. While the correlation is expected and correct for small amounts of drop overlap, it becomes less accurate as overlap increases. Specifically,  $\xi$  values for the two smallest offsets tested in the experiments were nearly identical despite a significant difference in the amount of offset. One potential implication of this observation is that until the offset is sufficiently large to allow the second drop to dissipate its impact kinetic energy on the target surface, the coalescence of the inkjet-printed droplets will be dominated by the initial inertial force and hence independent to drop spacing and other interdrop effects.

### 9.3.3.4 Summary

To optimize print quality for many industrial printing and coating applications, ink drops being deposited from printheads must spread and coalesce with their surrounding drops controllably in order to produce either a continuous line or a consistent film thickness. As drop coalescence depends strongly on drop spacing, it is important to optimize the amount of offset so the best print quality is achieved with a minimum volume of ink.

Imaging studies of the drop impacting adjacent to an earlier deposited drop have shown that the spreading of the second drop was not affected by the interdrop interaction. A simple geometric model was adapted to compare with the early stages of coalescence dynamics. The model assumes that the diameter of the first drop remained constant during the impact of the second drop and that the diameter of the second drop spread at the same rate as that of a single drop impacting a clean surface. Essentially, the model assumes no interaction between the first and the second drop during impact and coalescence. The predicted drop height and length during the impact, spreading, and relaxation stages for the second drop showed good-to-reasonable agreement with the experiment results obtained with a 12 ms delay between drop impacts. However, the agreement between the model prediction and experimental data appeared to deteriorate significantly during the later wetting stage of spreading.

During the wetting stages, the spreading rate of drop length varied with the offset between the two drops. If the offset was large enough that the second drop impacted and spread before coalescence, the spreading rate increased. Overall, the

final composite spread factor increased with a larger offset between the first and second drops. This increase in the length of the drop appears to be mainly due to the offset for a time delay of 12 ms between the drop impacts.

## 9.4

### 2D Features and Line Printing

The experimental work described earlier shows that the coalescence of a pair of inkjet-printed drops exhibits predictable behavior in accordance to drop spacings. Furthermore, the lateral movement of the necking point of the coalescing drops suggested that fluid is transported between drops in a preferential direction. This particular phenomenon is significant when we try to inkjet-print linear or 2D features.

As indicated in the introduction section, bulges formation in printed lines and nonuniform printed features represent significant quality issues in the functional printing applications. While the stability (or instability) of an elongated bead of liquid on surface is a well-studied subject, Duineveld [7] produced one of the first systematic studies on the formation dynamics of the inkjet-printed lines. Specific to the phenomenon of bulge instability, he proposed that the bulges are formed when the pressure-driven flow along the liquid line is sufficiently large to transport fluid into regularly spaced bulges. As this fluid-driven pressure originates from the local curvature variation of the liquid surface, the flow created is preferential from the newly deposited drops to the existing liquid bead. While the mechanism is fundamentally similar to fluid transport around the neck region of a pair of coalescing drops, direct comparison is not appropriate as the initial condition is quite different. Essentially, the onset of the line bulging as studied by Duineveld [7] occurs when too many drops are deposited too quickly: the frequency of the bulges was shown to increase with either a decrease in drop spacing or an increase in deposition rate. This is, therefore, relevant when a maximum stable line width is desired. However, many functional printing applications aim to create small and precise features, and hence, a minimal line width may be more relevant. By using a volume conservation model and assuming a pinned contact line, Stringer and Derby [11] explored the lower bound of line stability when the drop spacing is just small enough to avoid scalloped edges. By incorporating the findings of Duineveld [7], they further mapped the region of stability defined by the equilibrium contact angle, drop spacing, and print velocity.

While the works outlined have established the fundamental criteria to create a stable printed line, most previous analyses and experiments do not adequately investigate the transient dynamics of line formation. Specifically, while drop spacing and print speed (i.e., drop deposition intervals) are used to define the line stability regimes in most studies, few have investigated the dynamics between a newly deposited drop and an existing liquid bead. Soltman and Subramanian [10] have provided a simple model to consider such dynamics. By assuming that a newly landed drop will preferentially flow into an existing bead on contact and that the



liquid–solid contact line cannot retract (zero receding contact angle), their model compares the free-spreading radius of a drop on the surface and the bead radius to determine the drop spacing threshold for the onset of scalloped lines. While their concept is attractively simple and simulations were performed to support the model, no attempt was made to verify the predicted dynamics experimentally.

The following sections outline a recent study carried out specifically to validate the Soltman and Subramanian model empirically [26] and contain excerpts from the referenced publication. By inkjet-printing aqueous model fluid (water and ethylene glycol (EG) mixture) on a glass surface, the effects of drop spacing and printing interval on the stability of the printed beads were studied. In addition, as the fluid/solid combination used has a nonzero receding contact angle, the results obtained were more broadly applicable in contrast to the usual prerequisite of a unidirectionally pinned contact line (i.e., contact line cannot recede).

#### 9.4.1

##### Model of Drop–Bead Coalescence

The model proposed by Soltman and Subramanian [10], which assumes a geometry such that sequentially deposited liquid drops form a linear bead on a nonabsorbing surface, is shown in Figure 9.17.

With further assumptions of a nonreceding contact line and that it is energetically favorable for the fluid in an overlapped drop to flow into a pre-existing liquid bead, Soltman and Subramanian [10] developed a geometrical description of the interaction between an impacting drop and a bead formed from previously deposited drops. If drops with radius  $R_d$  combine to form a cylindrical liquid bead on a surface, the radius of the resultant bead  $R_1$  is an inverse square function of the spacing between drops  $\Delta x$

$$R_1 = \sqrt{\frac{8}{3} \left( \frac{R_d^3 \Psi}{\Delta x} \right)} \quad (9.12)$$

where  $\Psi$  is a geometric function of the apparent static contact angle  $\theta_s$  expressed as

$$\Psi = \frac{\pi}{2} \left( \frac{\sin^2 \theta_s}{\theta_s - \sin \theta_s \cos \theta_s} \right) \quad (9.13)$$

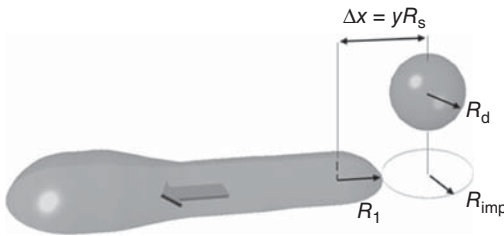


Figure 9.17 Schematic of the line formation by drop deposition model by Hsiao *et al.* [26].



By assuming that the radius of the end of the bead is  $R_1$ , the maximum contact radius to which a newly landed drop can spread before contacting the existing bead is

$$R_{\text{imp}} = \Delta x - R_1 \quad (9.14)$$

$R_1$  decreases and  $R_{\text{imp}}$  increases as  $\Delta x$  greatly increases, according to Eqs. (9.12) and (9.14). When  $R_{\text{imp}}$  becomes greater than  $R_1$ , a scalloped line is possible. As  $\Delta x$  increases further and  $R_{\text{imp}}$  approaches its steady-state (maximum) value of  $R_s$ , the landed drops will start to merge in pairs before finally forming individual isolated deposits. By plotting dimensionless radii  $R_1^* = R_1/R_s$  and  $R_{\text{imp}}^* = R_{\text{imp}}/R_s$  against the nondimensional drop spacing  $y = \Delta x/R_s$ , Soltman and Subramanian [10] were able to identify four theoretical regimes: continuous line with straight edges, scalloped line, pairwise bead formation, and isolated drop deposition.

While Soltman and Subramanian [10] have provided simulation results using Flow-3D to support their model, no empirical data was available to confirm the proposed drop–bead interaction dynamically. Although their observed printed line morphology generally mapped to the predicted regimes, qualitative adjustments were required to account for the effect of drying and impact inertia. Furthermore, their model did not consider the effect of the fluid inflow from subsequent drops on the morphology of an existing bead, which may be significant when printing shorter tracks or attempting to minimize the bulging-end effect observed by Duineveld [7]. By visualizing the drop–bead interaction dynamics in real time and considering the case of a mobile contact line, the following results aim to validate the hypotheses made in Soltman and Subramanian’s model and to broaden its application to the formation of continuous tracks by inkjet printing on any impermeable surface.

#### 9.4.2

##### Experiment and Observations

Droplets of a mixture of EG and deionized (DI) water (82.5 wt% EG) were printed from a MicroFab printhead consisting of a glass capillary, surrounded by a piezoelectric driving element, which tapers to an 80  $\mu\text{m}$  nozzle. A custom pneumatic controller was used to control the meniscus position within the nozzle by adjusting the pressure in the fluid reservoir. A tailored bipolar waveform amplified by a dedicated controller was applied to produce drops with a nominal diameter and velocity of 75  $\mu\text{m}$  and 2  $\text{m s}^{-1}$ , respectively. The distance between the nozzle outlet and the substrate was maintained at 1.5 mm. The substrates used were standard glass slides cleaned by handwashing in detergent, followed by rinsing sequentially with DI water, filtered acetone, and isopropyl alcohol, before final drying in an oven at 120  $^\circ\text{C}$  for >2 h. The fluid properties as well as the measured static, advancing, and receding contact angles on the cleaned glass surfaces,  $\theta_s$ ,  $\theta_a$ , and  $\theta_r$ , respectively, are listed in Table 9.1.

The printing experiments were carried out with a custom printing and imaging apparatus. The printhead was mounted in a temperature-controlled holder

**Table 9.1** Fluid and interfacial properties of 82.5/17.5 wt% ethylene glycol and deionized water mixture on glass as listed in Hsiao *et al.* [26].

$\rho$ (kg m <sup>-3</sup> )	$\mu$ (mPa·s)	$\gamma$ (N m <sup>-1</sup> )	$\theta_s$ (°)	$\theta_a$ (°)	$\theta_r$ (°)	$\psi$	$R_s$ (μm)
1016	10	0.054	34 ± 5	44 ± 5	20 ± 5	0.26	70 ± 3

positioned by a linear motor stage with 50 mm of travel. The substrates were mounted on a manual X–Y stage with a traveling range of 55 mm × 75 mm. The printhead and substrate stages were mounted on separated pivoting bases, so the substrate was isolated from any motor stage vibration during the head movement. The imaging area was back-illuminated by a metal-halide light source. The Shadowgraphs of the line formation were recorded initially at 21 052 fps up to 308 ms, then at a lower rate of 1000 fps for a further 3.5 s using a high-speed video camera (Phantom v7.3, Vision Research) equipped with high-magnification optics (12× Zoom lens, Navitar and 15× Plan Apo infinity-corrected long WD objective, Mitutoyo).

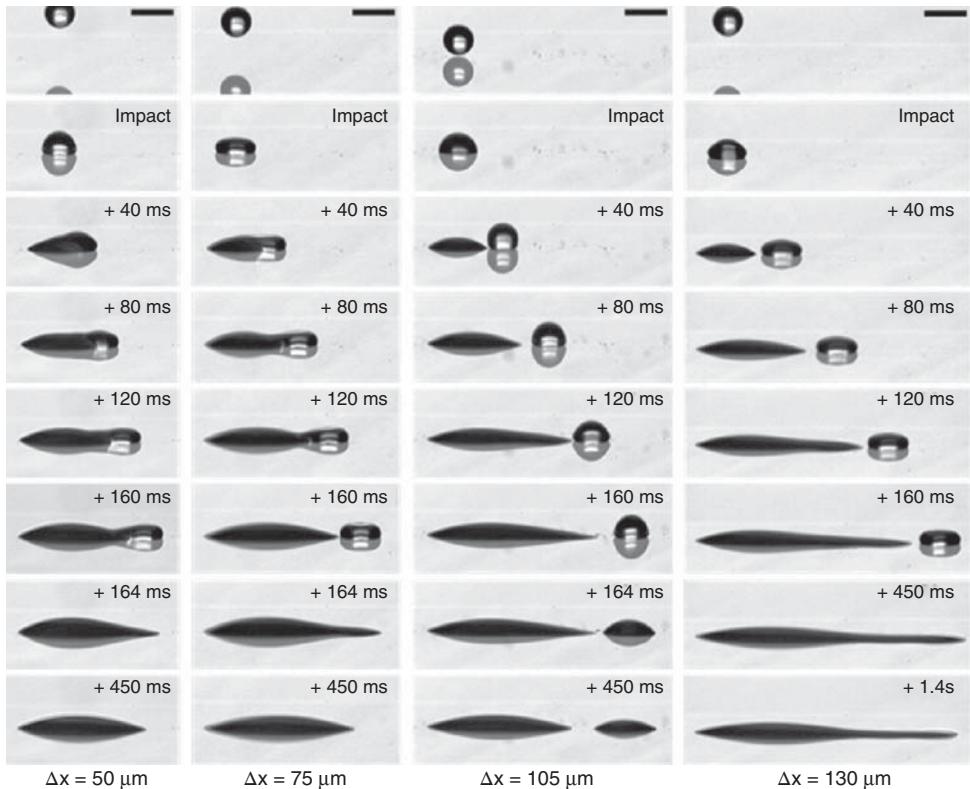
Printed tracks were formed by traversing the printhead across the substrate while it dispensed five drops at a set time interval. The drop spacing and time interval could be adjusted independently by altering the head stage velocity and the drop ejection frequency. The high-speed video recordings were converted into individual images before being processed with a custom MATLAB routine.

#### 9.4.2.1 Effect of Drop Spacing

The formation process for five-drop tracks of the EG–water mixture deposited on to glass with different drop spacing values is illustrated in Figure 9.18. As these images were captured at a nonzero angle of incidence, reflections of the liquid bead and drops on the substrate surface are visible in each frame.

The drop deposition interval  $\Delta t$  was held constant at 40 ms as the drop spacing  $\Delta x$  was increased from 50 to 130 μm. At smaller drop spacings ( $\Delta x = 50$  and 75 μm), the deposited drops formed continuous tracks on the glass surface despite the mobility of the contact line. Specifically, the right edges or “tails” of the tracks were observed to retract during and after printing. However, the drop spacings were sufficiently small to allow the sequential drops to bridge the gap and maintain the track continuity. The threshold of continuity was reached at  $\Delta x = 105$  μm when the last and fifth drop can no longer bridge the enlarged gap due to contact line retraction. However, and perhaps more interestingly, when the drop spacing was increased further to 130 μm, the printed track became stable and continuous again. The possible mechanism of this dynamics is discussed further in the later sections.

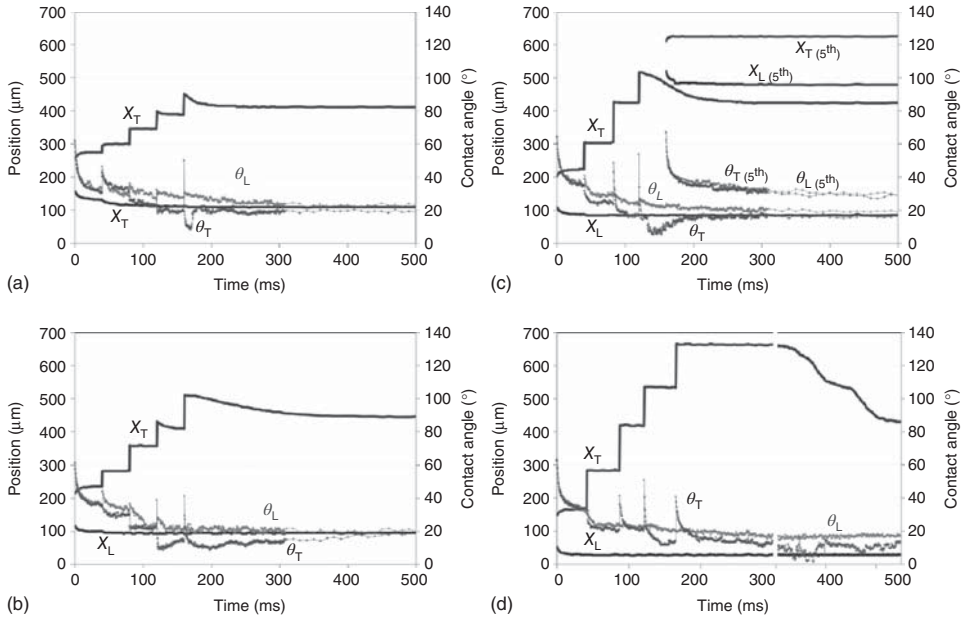
In order to quantify our observation, the track forming dynamics were first analyzed to show the movement of the track edges (left or “leading” verse right or “trailing”) and the associated contact angle dynamics, as shown in Figure 9.19. Note that an outward expansion of an edge is marked by either an increase of



**Figure 9.18** Track formation dynamics at different drop spacing (interdrop time,  $\Delta t = 40$  ms) taken by Hsiao *et al.* [26]; scale bars indicate  $100\ \mu\text{m}$ .

the position of the trailing edge,  $X_T$ , or a decrease of the position of the leading edge,  $X_L$ . As expected, the trailing edge  $X_T$  always increased stepwise in accordance to each impacting drop. On the other hand, the leading edges  $X_L$  remained mostly steady besides the initial expansions (spreading of the first drops) and some minor perturbations at the impact of the second drops for the smaller drop spacings ( $\Delta x = 50$  and  $75\ \mu\text{m}$ ). The contact line movement of the leading and trailing edges suggested that impact inertia affects the fluid movement locally (trailing edge) instead of globally (leading edge). This hypothesis is further supported by the edge contact angle dynamics, whereas only the trailing contact angles,  $\theta_T$ , perturbed significantly at each drop impact.

Additionally, retractions of the trailing edges are clearly visible for any drop spacing. As a general rule, the retraction did not become significant until the fourth drops, and it is clear how it has resulted in the discontinuous track observed at  $\Delta x = 105\ \mu\text{m}$ . In contrast, the trailing contact line remained pinned at  $\Delta x = 130\ \mu\text{m}$  within the same timescale as in the smaller drop spacings and only began to retract after 1 s. The lack of trailing edge retracting can be described

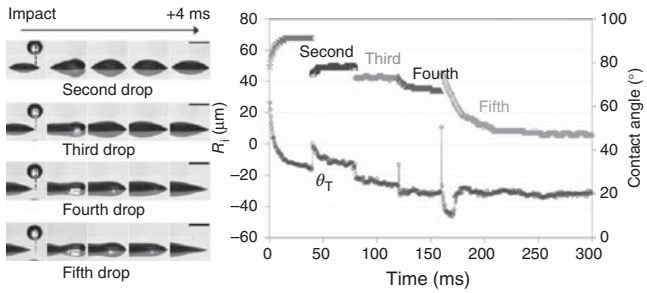
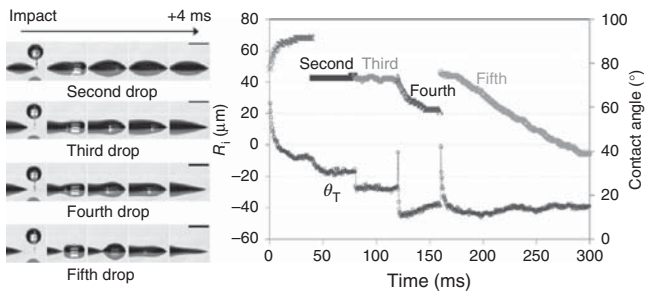
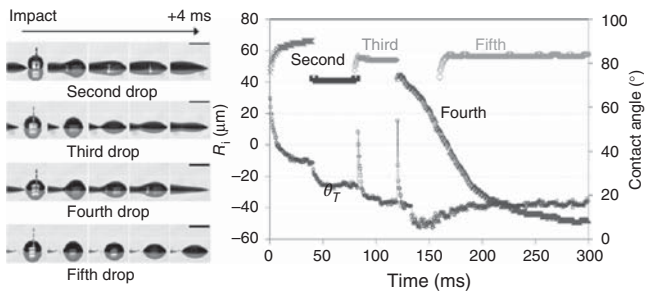
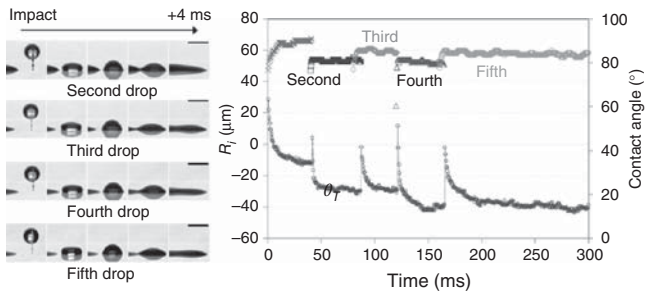


**Figure 9.19** Dynamics of bead edges ( $X_L$  and  $X_T$ ) and contact angles ( $\theta_L$  and  $\theta_T$ ) as described by Hsiao *et al.* [26]: (a)  $\Delta x = 50 \mu\text{m}$ ; (b)  $\Delta x = 75 \mu\text{m}$ ; (c)  $\Delta x = 105 \mu\text{m}$ ; and (d)  $\Delta x = 130 \mu\text{m}$ .

in terms of trailing contact angle  $\theta_T$  dynamics. In the case of smaller drop spacings,  $\theta_T$  decreased rapidly and in step with each impacting drop. The trailing edge retraction began when  $\theta_T$  became equal to or less than the receding contact angle  $\theta_r$ . In the case of  $\Delta x = 130 \mu\text{m}$ ,  $\theta_T$  never dropped below  $\theta_r$  during printing, and therefore, contact line retraction was absent.

While the correlation between  $X_T$  and  $\theta_T$  explained the observation, it does not reveal the underlying mechanism. Furthermore, the step increases of  $X_T$  were notably uneven as shown in Figure 9.19. Specifically, the increases at the impacts of the second drops were significantly smaller than the ones caused by the subsequent drops. It was unclear initially whether this was a result of the variation of drop placement due to the “first drop effect” or it represented the dynamics of drop–bead interaction. Therefore, the image data were reprocessed to study the drop landing events in detail. Figure 9.20 shows the drop landing positions and images of the drop–bead junctions during coalescence. In addition, the instantaneous drop radii  $R_i$ , determined by the differences between  $X_T$  and the landing positions, were plotted with the associated  $\theta_T$  against time. Note that the maximum value of  $R_i$ , or  $R_{i,\text{max}}$ , is equivalent to  $R_{\text{imp}}$  as defined in Eq. (9.14).

Based on the analysis of the drop landing positions, it was confirmed that the variations in the  $X_T$  step increments were not due to the jittering of the landing position (drop spacing variation was determined to have a standard deviation

(a) Drop-bead snapshots and  $R_i - \theta_T$  dynamics for  $\Delta x = 50 \mu\text{m}$ (b) Drop-bead snapshots and  $R_i - \theta_T$  dynamics for  $\Delta x = 75 \mu\text{m}$ (c) Drop-bead snapshots and  $R_i - \theta_T$  dynamics for  $\Delta x = 105 \mu\text{m}$ (d) Drop-bead snapshots and  $R_i - \theta_T$  dynamics for  $\Delta x = 130 \mu\text{m}$ 

**Figure 9.20** Snapshots of drop-bead junction at  $\Delta x =$  (a)  $50 \mu\text{m}$  (b)  $75 \mu\text{m}$  (c)  $105 \mu\text{m}$  (d)  $130 \mu\text{m}$  up to 4 ms postimpact with dynamics of drop spreading radius and contact angle ( $R_i$  and  $\theta_{RH}$ ) as shown by Hsiao *et al.* [26]; scale bars indicate  $100 \mu\text{m}$ .

less than  $5.6\ \mu\text{m}$ ). Therefore, the data suggested that the drop–bead interaction affected the postimpact drop spreading directly.

At  $\Delta x = 50\ \mu\text{m}$ , Figure 9.20a shows that  $R_i$  for the drops varied as the track grew. Specifically, the second drop expanded after landing, but the radius of the third drop remained constant. The images show that the second drop landed directly on to the liquid from the first drop. Therefore, its expansion was driven by undissipated impact inertia. In contrast, the third drop landed on the dry surface first and the majority of its impact inertia was dissipated to reach  $R_{\text{max}}$ . The landing event of the fourth drop was nearly identical to the third (hence, the similar initial  $R_i$ ) before contact line retraction, when  $\theta_T$  dropped close to  $\theta_r$ . As the drop–bead gap was increased by this retraction, the fifth drop was able to reach a greater  $R_i$  on impact before a large fall in  $\theta_T$  brought on a rapid retraction.

The dynamics of  $R_i$  for the drops with  $\Delta x = 75\ \mu\text{m}$ , as shown in Figure 9.20b, were mostly similar to the behavior with  $\Delta x = 50\ \mu\text{m}$ . The main differences were the lack of expansion after impact of the second drop and a slower retraction of the fifth drop. Both observations are consistent with the effects of the greater dissipation of drop inertia on the surface and the longer time needed for the liquid to flow across the larger distances.

For  $\Delta x = 105\ \mu\text{m}$ ,  $R_i$  for successive drops varied upward and downward as shown in Figure 9.20c. The drop spacing was just enough for the second drop to contact the liquid from the first drop immediately after reaching its  $R_{\text{max}}$ . As the spreading of the second drop was arrested close to  $R_{\text{max}}$ , the third drop had additional surface on which to spread beyond  $R_{\text{max}}$  under capillary force before contacting the previously deposited liquid. The greater expansion of the third drop, conversely, limited the spreading of the fourth drop. If the fourth drop did not retract before the landing of the fifth drop, we would see this pattern of alternating values of  $R_i$  continue indefinitely.

For  $\Delta x = 130\ \mu\text{m}$ , the drop spacing was sufficiently large that all the drops spread under capillary force before contacting the existing drop or bead, as shown in the images in Figure 9.20d. Therefore, the extents of spreading for the second and fourth drops were notably greater than in the previous case. While  $R_i$  still alternated up and down as described earlier, the magnitude of this effect was approximately halved as a result. Although  $\theta_T$  spiked at the landing of the second and fourth drops, its subsequent drops never brought it close to  $\theta_r$  as it did for the smaller drop spacing. Significantly, the curvature near the right bead edge, as shown in the images, never became concave during the relaxation of  $\theta_T$ . As a concave local curvature always preceded contact line retraction at the smaller drop spacing, it was suggested that such a feature directly correlated to a decrease in drop-to-bead flow, which could make a significant contribution to the track stability.

#### 9.4.2.2 Effect of Drop Deposition Interval

The empirical evidence presented suggests that track formation and stability are at least partly related to the process of liquid flow from the impacting drops to the pre-existing bead. While no analytical solution is available to predict this flow, its



direction and magnitude are often approximated by the pressure variation along a nonuniform track. Duineveld [7] has described schematically the growth of a track-end bulge as a result of fluid flow driven by the higher pressure at the drop landing end due to its extra curvature (smaller radius). This suggests that by reducing the curvature difference, the drop-to-bead flow may be reduced to improve the track stability and symmetry. One potential approach is to reduce the drop deposition interval in order to minimize the difference between the shapes of sequentially deposited drops during their coalescence.

Two tracks formed with the same drop spacing ( $\Delta x = 130 \mu\text{m}$ ) but with different drop deposition time intervals of 40 and 1 ms are shown in Figure 9.21a,b, respectively. For the shorter deposition interval, shown in Figure 9.21b, all the drops formed individual sessile deposits before merging. In addition, merging did not occur first between the earliest pair of drops (the first and second drops). Instead, the second and third drops merged first, quickly followed by the first drop, before being joined

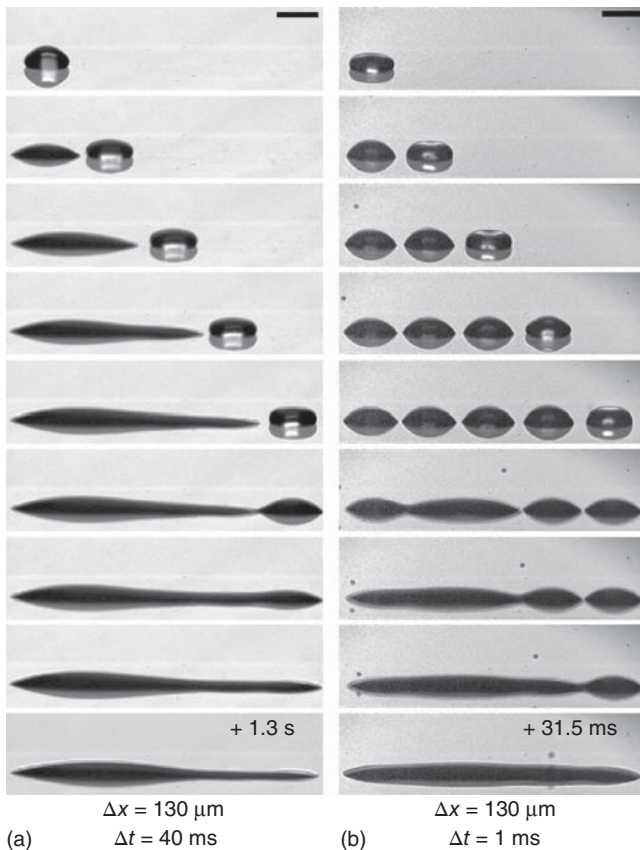


**Figure 9.21** Effect of drop deposition intervals ( $\Delta t$ ) on printed track morphology: (a) 40 ms and (b) 1 ms as shown by Hsiao *et al.* [26]. Scale bars indicate  $100 \mu\text{m}$ .

with the fourth and fifth drops in sequence. As no preferential fluid flow direction was established during track formation, the resultant track geometry was significantly more symmetrical than that of the track formed with the longer intervals (Figure 9.21a).

### 9.4.3

#### Stability Regimes and Discussion

Since the average  $R_s$  for these liquid drops on glass was approximately  $70 \mu\text{m}$ , the nondimensional drop spacing,  $y$ , in these experiments ranged from 0.71 to 1.86. As shown in Figure 9.22, the printed track morphology and values of dimensionless radius  $R_{i,\text{max}}^* = R_{i,\text{max}}/R_s$  of the later drops (second to fifth drops) can be mapped directly on to the regime map proposed by Soltman and Subramanian [10].

For  $\Delta x = 50$  and  $75 \mu\text{m}$  ( $y = 0.71$  and  $1.07$ ), the observations agree with their prediction that forming a continuous track is possible in this regime. Given that the liquid used showed a nonzero  $\theta_r$  on glass, the retractions of the trailing contact lines (CL) during and after track formation were expected and consistent with their hypothesis of a preferential drop-to-bead fluid flow. However, the average values of  $R_{i,\text{max}}^*$  were significantly greater than the values of  $R_{\text{imp}}^*$  predicted by the model and plotted on the graph. Soltman and Subramanian [10] conceded that while their model was effective in qualitatively predicting line morphology, it may not be sufficient to predict dimensions such as line width, due to effects such as impact inertia, which were not

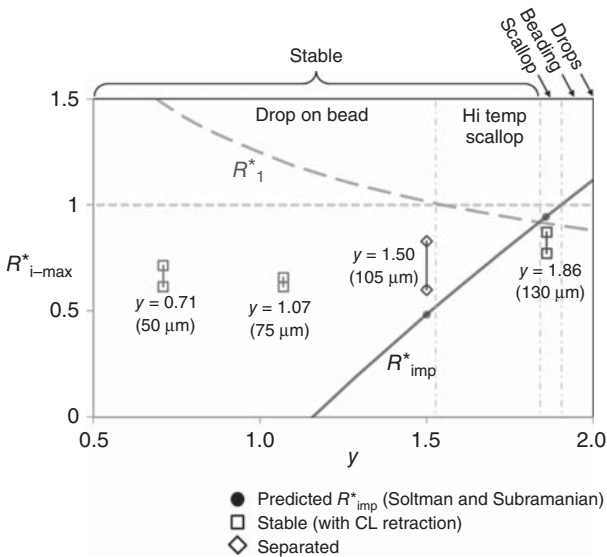


**Figure 9.22** Experimental results by Hsiao *et al.* [26] mapped onto line stability regimes as defined by Soltman and Subramanian [10]. Symbols: ●  $R_{\text{imp}}^*$  prediction, □ stable (with contact line retraction), and ◇ separated.



accounted for. The high-speed imaging results clearly corroborated their view by demonstrating that during track printing, the initial, often maximum, spreading of a deposited drop is influenced by impact inertia in addition to drop spacing.

For  $\Delta x = 105 \mu\text{m}$  ( $\gamma = 1.50$ ), a closer agreement between the experimental  $R_{i,\text{max}}^*$  and the predicted  $R_{\text{imp}}^*$  was found. In addition, the coalescence dynamics resulting in the step difference between  $R_{i,\text{max}}^*$  of second–fourth and third–fifth drops match the pairwise bead formation mechanism as proposed by Soltman and Subramanian [10]. Due to the receding contact line, the printed track assumed separated bead morphology instead of a stable or slightly scalloped track as predicted. However, it is easy to imagine a scalloped formation arising from the pairwise coalescence if the contact line is pinned rapidly, that is, colloidal track dried under high temperature.

The most intriguing comparison between the experimental results and the model arises for  $\Delta x = 130 \mu\text{m}$  ( $\gamma = 1.86$ ). While all tracks printed at smaller  $\Delta x$  exhibited the destabilizing effect of the receding contact line, instead, a stable track with well-matched  $R_{i,\text{max}}^*$  and  $R_{\text{imp}}^*$  was observed. Although the track ultimately contracted after more than 1 s, the period of stability was an order of magnitude longer than for tracks printed with smaller  $\Delta x$ , signifying a change in the underlying interaction.

One potential explanation arises from how  $R_1^*$  and  $R_{\text{imp}}^*$  were determined. Specifically, whereas  $R_1^*$  was determined based on volume conservation, which requires a mobile contact line, a nonreceding contact line is a prerequisite for determining  $R_{\text{imp}}^*$  as proposed by Soltman and Subramanian [10]. The difference in the assumed state of the contact line may explain the tendency for the experimental results, based on a receding and mobile contact line, to be consistently greater than  $R_{\text{imp}}^*$  and approaching  $R_1^*$  instead. At  $\Delta x = 130 \mu\text{m}$  ( $\gamma = 1.86$ ), the predicted  $R_{\text{imp}}^*$  and  $R_1^*$  converge, and therefore, the effect of the receding contact line is minimal.

Based on the observation of the drop–bead coalescence dynamics, another stabilization mechanism may also be involved. As shown in the images in Figure 9.20d, the neck regions during coalescence at  $\Delta x = 130 \mu\text{m}$  were considerably thinner than those with smaller drop spacings. For Poiseuille flow in a liquid film on a plane, the viscous pressure loss per unit length along the neck follows Eq. (9.15):

$$\Delta P_1 \propto \frac{\mu U}{h^2} \quad (9.15)$$

where  $\mu$ ,  $U$ , and  $h$  are the dynamic viscosity, flow velocity, and film thickness, respectively. Therefore, a decrease in the film thickness will increase the pressure loss in the neck region and can reduce drop-to-bead fluid flow and stabilize the printed track.

Whereas the internal fluid flow between a liquid bead and a deposited drop appears to affect the stability of a printed track, it may also represent an opportunity to optimize track geometry. As, according to Duineveld's model [7], the

internal fluid flow of a liquid bead is primarily a function of the regional curvature differences, reducing or tailoring such differences should offer us control over the internal fluid flow and, as a result, the morphology of the printed tracks. This hypothesis is supported by the observation that, when drops with similar sessile shapes coalesced, they formed a stable track with symmetrical morphology, as shown in Figure 9.21 for drops deposited at 1 ms intervals. Although the result is preliminary and at the moment only tested at one drop spacing, albeit a more representative one as the effect of the receding contact line appeared to be minimal, this is a fertile area for future investigation.

Although the effects of viscous dissipation at the neck region and curvature variation were discussed separately, it is likely that both operate together to affect the stability and geometry of a printed track. In addition, by approximating the neck region as an infinite thin film and considering only the profile curvature of the drop–bead junction, we risk oversimplifying the complexity of drop–bead interaction. Although quantifying this interaction is beyond the scope of the presented work, it may be an interesting area to explore in detail. Specifically, a future area of interest would be to observe both bottom and side profiles simultaneously during printing to define the drop–bead junction curvature in three dimensions and quantify its correlation to the internal fluid flow using techniques such as holographic imaging of seeding particles in the fluid.

#### 9.4.4

##### Summary

A high-speed imaging study was carried out to investigate the dynamics of liquid track formation on a surface with a nonzero receding contact angle to explore the broader validity of the line stability model proposed by Soltman and Subramanian [10]. The study found that at small drop spacing, where the deposited drops coalesced during their early inertia-driven and relaxation spreading phases, the tracks were potentially stable as predicted by the model. The tracks were ultimately destabilized by contact line retraction during and after printing, but the uniform direction of retraction confirmed the hypothesis of a preferential fluid flow from the landing drops to the pre-existing liquid bead. Although the model appears to predict the track formation dynamics and its mechanism of destabilization well, the study results showed that without considering the effect of drop impact inertia, it significantly underestimates the spreading of the deposited drops and, hence, underestimates the instantaneous width of the track as it grows. The best agreement between the empirical data and the model prediction occurred at the predicted transition from continuous to scalloped line. A good match was expected as at this drop spacing as (i) a deposited drop can dissipate its impact inertia fully on the surface before coming into contact with the previously deposited bead and (ii) the effect of the receding contact line is minimal. Furthermore, the data also confirmed the pairwise variation of the maximum drop spreading radii predicted by the model. For greater drop spacing, the experiments suggested that a slower drop-to-bead fluid flow may be responsible for stabilizing the printed track. The

slower flow was proposed to be caused either by an increase in viscous dissipation in the thinner neck region or by a reduction in the driving pressure due to the smaller curvature variations between the deposited drops and the previously deposited liquid bead. The latter hypothesis found good support from the observation of stable and symmetrical tracks printed with short time intervals, which allow similarly shaped drops to coalesce with minimal curvature variations in the neck regions. The effect of printing interval, independently of drop spacing, on track stability may have significant research and practical implications and should be investigated further.

## 9.5

### Summary and Concluding Remarks

While inkjet printing has great potential as a flexible patterning and material additive process, it is essential for the process designers to have a good understanding of the relevant physics and its limitations. While its noncontact nature may be a strength in many applications, it also limits the options we have to influence the drop placement once the materials left the inkjet nozzles. While drop placement accuracy is affected by many factors (e.g., jet and drop formation, surface properties), the greater print resolution (smaller drop spacing) and the demands of printing functional features (overlapping drops) mean that managing the interactions between deposited drops on surfaces will become more important than ever.

The coalescence between a pair of sessile drops is fundamental to these interactions, and this chapter has provided a comprehensive overview of the investigations conducted to characterize its dynamics and the underlying mechanisms. While these studies give us a better understanding of the physics involved, they are often conducted at much larger temporal and dimensional scales. Therefore, the overview also included remarks on the extents of how these results and conclusions are applicable to inkjet printing. In addition, a drop coalescence study conducted with parameters specific to industrial inkjet printing was presented. The study investigated the effects of drop spacing (offset) and print interval (delay) on the coalescence dynamics of a pair of inkjet-deposited drops. The results show that the drop coalescence is strongly influence by the neck region between drops. Early onset of necking, as a result of overlapping drop deposition, significantly limits the individual drop spreading extend and rate. Moreover, there is evidence of fluid being drawn from the later (second) drop into the earlier (first) drop based on the neck movement of the coalescing drops. This dynamics is significant not only to the image printing quality but also to functional applications such as line printing.

Being able to successfully inkjet-print linear features with consistent geometries is fundamental to many coating, functional printing, and material additive applications. Review of the literature showed that, whereas there were a good number of studies conducted to empirically determine the process regimes to

produce bulge-free continuous lines for applications such as printing conductive tracks, relatively few were focused on the mechanisms of the bulge formation and line destabilization. The consensus developed was that for a thick line, that is, width much greater than the diameter of a printed drop, fluid flow driven by the curvature variation of the free liquid surface is responsible for the bulge formation. For a thin line, that is, width similar to the diameter of a printed drop, the dynamics interaction between the existing liquid bead and the deposited drop determines whether the printed line is continuous, scalloped, or discontinuous. Although a geometric model exists to predict these regimes for a thin printed line, data to validate it empirically was incomplete. An experimental study was presented to investigate the real-time dynamics of the drop–bead interaction when liquid–solid contact line was not pinned. The results confirmed the existence of a preferential flow from the deposited drops into the liquid beads on surface, which destabilize and distorted the printed tracks. Surprisingly, when the drop spacing was increased over a threshold, the print track restabilized. Mapping the results onto the proposed regime map revealed that the restabilization occurred at the point where the predictions based on volume conservation (mobile contact line) and geometric model (pinned contact line) converge, that is, the effect of the contact line movement is minimal. Additionally, there were evidences suggesting that either an increase in viscous dissipation within the thinning liquid bridge or a reduction of the curvature different at the neck region is slowing the drop–bead flow and stabilizing the printed tracks. The latter mechanism has been demonstrated to help producing stable tracks with uniform widths when the print interval, that is, interdrop deposition time, was reduced.

## 9.6

### Working Questions

#### 9.6.1

Select a current generation of industrial inkjet printhead (e.g., Xaar 1002 and Dimatix StarFire) by assuming that it will be mounted on a one-pass inkjet print press producing 300 dpi labels on polymeric, nonabsorbing stocks. Assuming that the deposited UV ink drops will spread to three times their original spherical diameter in 100 ms and the stock feed for the print press is running at  $2 \text{ m s}^{-1}$ , how close will you need to place the UV pinning lamp to arrest the spreading to avoid drop coalescence? Justify your answer based on the specification of the printhead you selected.

#### 9.6.2

You are trying to print back electrodes for polymer solar cells using functional ink with silver nanoparticles. Sessile drop test has revealed that the ink has a mobile contact line and a static contact angle of  $32^\circ$  on your

working surface. What drop diameter will you select to print your conductive tracks in order to minimize the risk of line discontinuity due to contact line receding during printing?

## References

1. Hebner, T.R., Wu, C.C., Marcy, D., Lu, M.H., and Sturm, J.C. (1998) Ink-jet printing of doped polymers for organic light emitting devices. *Appl. Phys. Lett.*, **72** (5), 519–521.
2. Shimoda, T., Kanbe, S., Kobayashi, H., Seki, S., Kiguchi, H., Yudasaka, I., Kimura, M., and Miyashita, S. (1999) Multicolor pixel patterning of light-emitting polymers by ink-jet printing. Technical Digest of SID, pp. 376–379.
3. Sirringhaus, H., Kawase, T., Friend, R.H., Shimoda, T., Inbasekaran, M., Wu, W., and Woo, E.P. (2000) High-resolution inkjet printing of all-polymer transistor circuits. *Science*, **290**, 2123–2126.
4. Gao, F. and Sonin, A.A. (1994) Precise deposition of molten microdrops: the physics of digital microfabrication. *Proc. R. Soc. London, Ser. A*, **444**, 533–554.
5. Schiaffino, S. and Sonin, A.A. (1997) Formation and stability of liquid and molten beads on a solid surface. *J. Fluid Mech.*, **343**, 95–110.
6. Davis, S.H. (1980) Moving contact lines and rivulet instabilities – 1. The static rivulet. *J. Fluid Mech.*, **98**, 225–242.
7. Duineveld, P.C. (2003) The stability of ink-jet printed lines of liquid with zero receding contact angle on a homogeneous substrate. *J. Fluid Mech.*, **477**, 175–200.
8. van den Berg, A.M.J., de Laat, A.W.M., Smith, P.J., Perelaer, J., and Schubert, U.S. (2007) Geometric control of inkjet printed features using a gelating polymer. *J. Mater. Chem.*, **17**, 677–683.
9. van Osch, T.H., Perelaer, J., de Laat, A.W.M., and Schubert, U.S. (2008) Inkjet printing of narrow conductive tracks on untreated polymeric substrates. *Adv. Mater.*, **20**, 343–345.
10. Soltman, D. and Subramanian, V. (2008) Inkjet-printed line morphologies and temperature control of the coffee ring effect. *Langmuir*, **24**, 2224–2231.
11. Stringer, J. and Derby, B. (2010) Formation and stability of lines produced by inkjet printing. *Langmuir*, **26**, 10365–10372.
12. Meakin, P. (1992) Droplet deposition growth and coalescence. *Rep. Prog. Phys.*, **55** (2), 157–240.
13. Narhe, R., Beysens, D.A., and Nikolayev, V.S. (2004) Contact line dynamics in drop coalescence and spreading. *Langmuir*, **20**, 1213–1221.
14. Andrieu, C., Beysens, D.A., Nikolayev, V.S., and Pomeau, Y. (2002) Coalescence of sessile drops. *J. Fluid Mech.*, **453**, 427–438.
15. Case, S.C. and Nagel, S.R. (2008) Coalescence in low-viscosity liquids. *Phys. Rev. Lett.*, **100**, 084503.
16. Wu, M., Cubaud, T., and Ho, C.-M. (2004) Scaling law in liquid drop coalescence driven by surface tension. *Phys. Fluids*, **16** (7), 51–54.
17. Menchaca-Rocha, A., Martínez-Dávalos, A., Núñez, R., Popinet, S., and Zaleski, S. (2001) Coalescence of liquid drops by surface tension. *Phys. Rev. E*, **63** (4), 046309.
18. Kapur, N. and Gaskell, P.H. (2007) Morphology and dynamics of droplet coalescence on a surface. *Phys. Rev. E*, **75** (5), 056315.
19. Sellier, M. and Treluyer, E. (2009) Modeling the coalescence of sessile droplets. *Biomicrofluidics*, **3** (2), 022412.
20. Eggers, J., Lister, J.R., and Stone, H.A. (1999) Coalescence of liquid drops. *J. Fluid Mech.*, **401**, 293–310.
21. Ristenpart, W.D., McCalla, P.M., Roy, R.V., and Stone, H.A. (2006) Coalescence of spreading droplets on a wettable substrate. *Phys. Rev. Lett.*, **97** (6), 064501.
22. Wang, H., Liao, Q., Zhu, X., Li, J., and Tian, X. (2010) Experimental studies of liquid droplet coalescence on a gradient surface. *J. Supercond. Novel Magn.*, **23** (6), 1165–1168.

23. Diez, J.A. and Kondic, L. (2002) Computing three-dimensional thin film flows including contact lines. *J. Comput. Phys.*, **183** (1), 274–306.
24. Roisman, I.V., Prunet-Foch, B., Tropea, C., and Vignes-Adler, M. (2002) Multiple drop impact onto a dry solid substrate. *J. Colloid Interface Sci.*, **256**, 396–410.
25. Li, R., Ashgriz, N., Chandra, S., Andrews, J.R., and Drappel, S. (2010) Coalescence of two droplets impacting a solid surface. *Exp. Fluids*, **48**, 1025–1035.
26. Hsiao, W.-K., Martin, G.D., and Hutchings, I.M. (2014) Printing stable liquid tracks on a surface with finite receding contact angle. *Langmuir*, **30** (41), 12447–12455.

## 10 Droplets Drying on Surfaces

*Emma Talbot, Colin Bain, Raf De Dier, Wouter Sempels, and Jan Vermant*

### 10.1

#### Overview

The drying of a droplet on a surface is a natural phenomenon that we see around us every day, but it is also exploited by human beings in numerous technological applications, such as spray painting, inkjet printing, crop spraying, and spray cooling.

A complete description of droplet drying involves many different aspects: which is the most important depends on the application. For example, the evaporative cooling of a surface requires accurate predictions of the drying time, which depends on the contact angle of the droplet and whether the contact line is free to move. For coating applications, droplet coalescence is important as is uniformity of the deposited film. For inkjet printing, control is needed over the deposit morphology, particle distribution, and surface finish, as all these determine the print quality and the functioning of printed devices. For graphics applications, a uniform deposit requires the minimum amount of ink for a given color density. The deposition is influenced by the motion of the contact line following impact (i.e., does the droplet spread to cover an appropriate area of the substrate?) and during drying (i.e., does the contact line retract and drag the material along with it?) and by internal flows, which are responsible for the transport of suspended particles within the droplet. Assembly within a droplet (e.g., colloidal crystals) and micromanipulation (e.g., size sorting [1] or DNA stretching [2]) also rely on the internal flows to construct the desired output.

There is no such thing as a “typical ink,” due to the wide range of printable fluids targeted at numerous applications far exceeding the standard inkjet office printer. Examples include metallic nanoparticles for microcircuitry [3, 4], conducting/semiconducting polymers for organic electronic devices [5, 6], biological samples for microassays [7, 8], and ceramics for 3D printing [9, 10]. Many inks comprise complex fluids containing multiple solvents, which are often laden with surfactants and/or polymers as dispersants for a particulate pigment. Heat transfer, mixtures of solvents, surfactants, or even neighboring drops or obstacles can lead to surface tension gradients that induce internal flows (known as

*Marangoni effects*) [11]. Transport of particles inside droplets largely depends on the internal flow, resulting in a catalog of morphologies and microstructures in the deposit. Different internal flows produce a range of deposits including ring stains, uniform films, pillars, and arches. This chapter primarily focuses on the radial convective flow due to evaporation in droplets with a fixed contact line (commonly termed the *coffee ring effect*) and Marangoni flows resulting from surface tension gradients.

Substrates used in inkjet printing may be porous or impermeable, rough or smooth, rigid or flexible, flat or shaped in three dimensions. The wetting behavior, thermal properties, temperature, and patterning of the substrate all influence the end deposit. A droplet that spreads and then maintains a pinned contact line at a constant radius is desirable to produce a well-defined edge to the deposit but may cause the formation of a ring stain with poor optical density. Contact lines that retract during drying often lead to irregular deposits and poor control. However, with the correct substrate wetting, controlled retraction is capable of forming highly periodic and reproducible structures (e.g., photonic crystals [12]).

To optimize the performance of the dried droplets, a careful choice of ink and matching substrate is required. Particle–particle and particle–substrate interactions can cause unexpected changes in ink behavior. Manipulating ink stability during drying and accounting for changes in local particle or polymer concentration, viscosity, and elasticity can alter the resulting deposit structure. Similarly, a careful choice of the combination of solvents in a mixture or addition of surfactant can result in recirculating flows that suppress ring stains.

## 10.2

### Evaporation of Single Solvents

This section sets out a simple yet accurate model for the evaporation of a small droplet, accounting for the droplet geometry and contact line motion.

Here, we consider an axisymmetric sessile drop as shown in Figure 10.1a [13]. A static sessile droplet takes the shape of a spherical cap unless the droplet is significantly deformed by gravitational forces. The ratio of gravitational effects to surface tension effects is determined by the Bond number,

$$Bo = \rho g h_0 R / \sigma \quad (10.1)$$

where  $\rho$  is the fluid density,  $g$  is the acceleration due to gravity,  $R$  is the contact radius of the droplet,  $h_0$  is the apex height, and  $\sigma$  is the surface tension. Gravity can be neglected if  $Bo \ll 1$ . Inkjet droplets fulfill this condition, so can usually be modeled by a spherical cap. For evaporating droplets, we also have to consider dynamical effects. The Capillary number,  $Ca$ , indicates the ratio of viscous forces to surface tension forces:

$$Ca = \mu u / \sigma \quad (10.2)$$

where  $\mu$  is the fluid viscosity and  $u$  is the characteristic flow velocity. For low capillary numbers, internal flow is facile and surface tension ensures that the drying



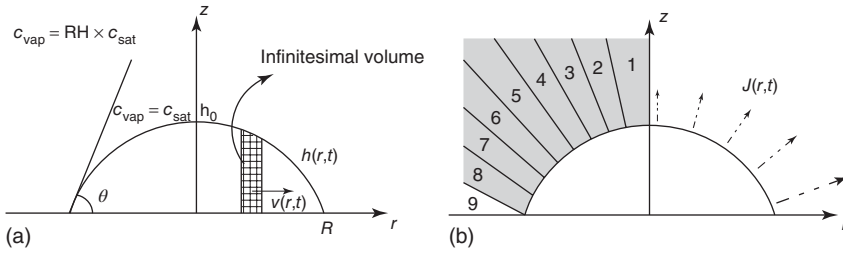


**Figure 10.1** The modeling of diffusion-limited evaporation from a droplet: (a) droplet shape indicating the apex height  $h_0$ , the height of the liquid–vapor interface  $h(r,t)$ , the contact radius  $R$ , the contact angle  $\theta$ , and the vapor concentration  $c_{\text{vap}}$ , which is equal to the saturation vapor concentration  $c_{\text{sat}}$  at the liquid–vapor interface, and the ambient vapor concentration (related to

the relative humidity,  $RH$ ) far from the free surface and (b) evaporation along the normal direction supplies vapor to regions 1–8 due to diffusion along the radial concentration gradient. Diffusion across the normal occurs toward region 9, causing an increase in the vapor concentration gradient closer to the contact line, enhancing the evaporative flux,  $J(r,t)$ .

droplet always has spherical curvature at the air–liquid interface. However, if the fluid is highly viscous, or particles/polymers enhance the viscosity during drying, then  $Ca > 1$  may be possible. In this scenario, the internal flows cannot keep pace with evaporation, and the droplet geometry may deviate from a spherical cap.

For  $Bo \ll 1$  and  $Ca \ll 1$ , the height of a droplet with contact angle  $\theta$  at a radial distance  $r$  is described by [14]

$$h(r, t) = \sqrt{\frac{R^2(t)}{\sin^2 \theta(t)} - r^2} - R(t) \cot \theta(t) \quad (10.3)$$

where  $h$  is the interface height at radial coordinate  $r$  and time  $t$  and  $\theta$  is the contact angle (refer to Figure 10.1a). The droplet contact angle and volume,  $V$ , can be expressed as

$$\theta = 2 \tan^{-1} \left( \frac{h_0}{R} \right) \quad (10.4)$$

and

$$V = \frac{\pi h_0}{6} (3R^2 + h_0^2) = \pi R^3 \frac{\cos^3 \theta - 3 \cos \theta + 2}{3 \sin^3 \theta} \quad (10.5)$$

Evaporation is an endothermic process, requiring energy for the phase change from liquid to vapor. To transfer from the liquid to the vapor, molecules must have sufficient kinetic energy to overcome this energy barrier. Molecules with higher thermal energy inherently have higher kinetic energy and so have a higher probability of transferral. The droplet then becomes cooler as the molecules with higher thermal energy are depleted. This process is known as *evaporative cooling*. Heat transfer to the liquid–vapor interface is then required before molecules in the vicinity of the interface gain enough energy to transfer into the vapor phase. The

evaporation rate can be limited by diffusion, the kinetics of transfer of molecules across the interface, or the transfer of heat to the liquid–vapor interface [15, 16].

Molecules transfer to and from the liquid by evaporation and condensation. At equilibrium, the rates of evaporation and condensation are equal. Vapor molecules colliding with the liquid can either enter the liquid or stay in the vapor. The proportion of molecules entering the liquid is described by the accommodation coefficient,  $\gamma$ , where  $0 < \gamma < 1$ , that is,  $\gamma = 0.05$  corresponds to 5% of the molecules that collide with the liquid entering. The flux entering (or leaving) the liquid at equilibrium is then

$$J_Z = Z_w \gamma \quad (10.6)$$

which has units of  $\text{m}^{-2} \text{s}^{-1}$ , where  $Z_w$  is the collisional flux,

$$Z_w = \frac{1}{4} \bar{u} \frac{N}{V} = \frac{1}{4} \bar{u} \frac{p^*}{k_B T} = \frac{1}{4} \frac{p_i p^*}{k_B T} \sqrt{\frac{8R_u T}{\pi M}} = p^* N_A \sqrt{\frac{1}{2\pi R_u T M}} \quad (10.7)$$

Here,  $\bar{u}$  is the mean velocity,  $k_B$  is the Boltzmann constant,  $R_u$  is the universal molar gas constant,  $N_A$  is Avogadro's constant,  $N/V$  is the number of molecules per unit volume,  $p^*$  is the equilibrium vapor pressure of the liquid, and  $M$  is the molar mass. For a water droplet at 293 K, the maximum evaporative flux (i.e., when  $\gamma = 1$ ) is  $J_Z \sim 10^{22} p^*$ .

The problem is then the transport of the vapor away from the liquid–vapor interface, which can occur either ballistically [17] or by diffusion [18, 19] (sometimes in conjunction with convection of the surrounding vapor [20, 21]). For macroscopic droplets at atmospheric pressure, diffusion is almost always rate-limiting. Ballistic evaporation requires nanoscale droplets or reduced pressures and occurs when the Knudsen number,  $Kn > 1$ . The Knudsen number is defined as  $Kn = \lambda/R$ , where  $\lambda$  is the mean free path length and  $R$  is the droplet radius. For nitrogen at ambient temperature and pressure,  $\lambda = 68 \text{ nm}$ . If  $Kn \gg 1$ , molecules travel many times the droplet size before they collide with other gas molecules, and the chance of them re-entering the droplet is negligible, that is, there is no condensation. Alternatively, diffusion transports molecules away from the liquid–vapor interface, but there must be a concentration gradient in the vapor phase.

The vapor pressure decays with radial distance from the liquid–vapor interface (where the vapor pressure at the surface is  $p_{\text{surf}}$ ). The integrated flux through a spherical surface,  $s$ , at distance,  $r$ , from the center of the droplet is given by Fick's first law

$$\int J_D ds = -4\pi r^2 D \frac{dc}{dr} \quad (10.8)$$

At steady state,  $\int J_D ds$  is independent of  $r$ . Integrating Eq. (10.8) and using the boundary conditions  $c(r = \infty) = 0$  and  $c(r = R) = c_{\text{surf}}$  gives the evaporative flux as

$$J_D = \frac{c_{\text{surf}} D}{R} = \frac{p_{\text{surf}} D}{R k_B T} \quad (10.9)$$

For a water droplet at 293 K,  $J_D \sim 10^{15} p_{\text{surf}}/R$ . If evaporation is diffusion-limited, the surface is locally at equilibrium and  $J_D \sim 10^{15} p^*/R$ . Evaporation is only kinetically limited if  $J_D > J_Z$ , which requires a droplet radius  $< 100$  nm at ambient temperature and pressure. Thus, evaporation is limited by diffusion for macroscopic droplets unless the total ambient pressure (not the vapor pressure!) is reduced.

To calculate the height-averaged radial flow velocity,  $\bar{v}$ , inside the droplet, a mass balance is written over an infinitesimal annular part of the droplet (Figure 10.1a), where the accumulated liquid per unit surface area per unit time equals the net influx of liquid minus the solvent evaporated from the surface [22]:

$$\rho \frac{dh}{dt} = -\rho \frac{1}{r} \frac{d}{dr} (rh\bar{v}) - J_s(r, t) \sqrt{1 + \left(\frac{dh}{dr}\right)^2} \quad (10.10)$$

A description for the evaporation rate,  $J_s$ , and the height profile of the droplet as function of time is required to solve this equation for the average velocity. For diffusion-limited evaporation, the evaporative flux is strongly enhanced near the edge of the droplet (for  $\theta < 90^\circ$ ) [23]. To see why this is, divide the region above the droplet into equal segments (i.e., Sections 1–9 in Figure 10.1b), each with diffusive transport normal to the liquid–vapor interface due to the gradient in vapor concentration (from  $c_{\text{sat}}$  at the interface to  $c_{\text{sat}} \times \text{RH}$  far from the interface). For central regions (e.g., 1 on the left-hand side in Figure 10.1b), diffusion across the normal (between numbered regions) can replenish molecules lost due to evaporation from the interface. For  $\theta = 90^\circ$ , each slice would be identical and evaporation would be uniform. However, for  $\theta < 90^\circ$ , there is a region (labeled 9 in Figure 10.1b) whose normal does not intersect the liquid surface. Consequently, vapor diffuses into this region from the neighboring region 8, increasing the concentration gradient and hence the evaporation rate in that region. Diffusion from region 7 into region 8 helps to replenish molecules lost into region 9 and so on. Thus, the evaporation rate is highest at the contact line and decreases monotonically toward the apex.

During evaporation, the droplet shrinks, and the position of the liquid–vapor interface changes. The time-dependent vapor concentration near the liquid–vapor interface is then governed by the unsteady diffusion equation,

$$\frac{dc}{dt} = D\nabla^2 c \quad (10.11)$$

where  $c$  is the vapor concentration,  $D$  is the diffusion coefficient of vapor in the ambient atmosphere, and  $t$  is the time. Diffusion can be considered as a quasi-steady process if the timescale required for a concentration profile to build up at the liquid–vapor interface is much faster than the drying time. If this is the case, the time-dependent terms in Eq. (10.11) can be ignored and the vapor concentration profile obeys the Laplace equation,

$$\nabla^2 c = 0. \quad (10.12)$$

The boundary conditions to solve this Laplace equation are that: (i) far from the droplet surface, the vapor concentration equals the ambient vapor concentration

(defined by the relative humidity of the environment if the liquid is water) and (ii) the vapor concentration at the liquid–vapor interface is the saturation concentration. As a result, the evaporative flux for contact angles  $<90^\circ$  can be approximated by [22, 24, 25]

$$J_s(r, t) = J_0 \left( 1 - \left( \frac{r}{R} \right)^2 \right)^{-\lambda} \quad (10.13)$$

where  $\lambda = (\pi - 2\theta)/(2\pi - 2\theta)$  is a function of the contact angle. Note that the factor  $(1 - (r/R)^2)^{-\lambda}$  causes the evaporative flux to diverge at the contact line. In practice, the assumption of diffusion-controlled evaporation will break down very close to the contact line (within a distance of roughly the mean free path) and the flux is then limited by the evaporation kinetics. The prefactor,  $J_0$ , is just the evaporation rate from a spherical droplet with a correction for the finite contact angle. To a good approximation

$$J_0 = \frac{D_{c,\text{sat}}(1 - \text{RH})}{R} (0.27\theta^2 + 1.30) \left( 0.6381 - 0.2239 \left( \theta - \frac{\pi}{4} \right)^2 \right) \quad (10.14)$$

where RH is the relative humidity [14]. Once the evaporation rate is known, the height profile of the liquid droplet can be calculated as a function of time. The change in the mass of the droplet needs to equal the rate of loss by evaporation [22]:

$$\rho \frac{dV}{dt} = \rho \frac{d}{dt} \int_0^R 2\pi r' h(r', t) dr' = \int_0^R 2\pi r' J_s(r', t) \sqrt{1 + \left( \frac{d}{dr'} h(r', t) \right)^2} dr' \quad (10.15)$$

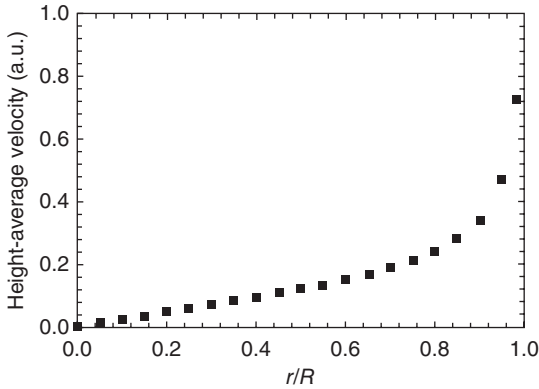
By combining Eqs. (10.10, 10.13), and (10.15), the height-averaged radial velocity of the liquid inside the droplet can be expressed as [24, 26]

$$\bar{v} = \frac{R^2}{4r(t_f - t)} \left[ \left( 1 - \left( \frac{r}{R} \right)^2 \right)^{-\lambda} - \left( 1 - \left( \frac{r}{R} \right)^2 \right) \right] \quad (10.16)$$

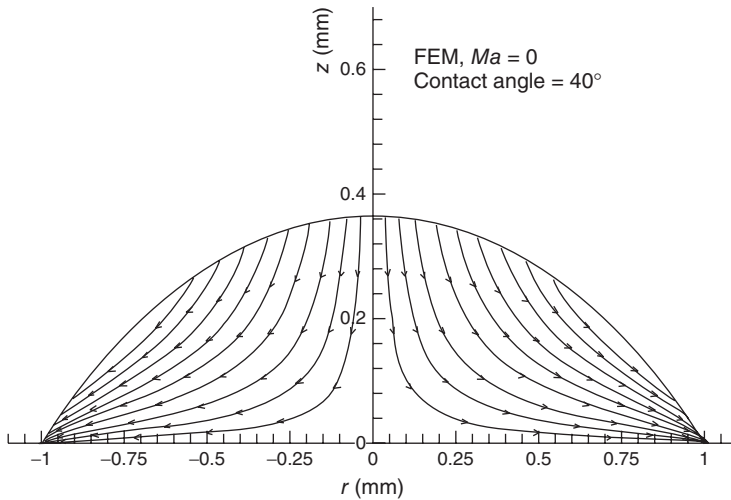
where  $t_f$  is the drying time.

Figure 10.2 shows the predicted average velocity in the evaporating droplet. Due to the pinning of the droplet, an *outward* flow is set up, as characterized by a positive velocity value. To calculate the full three-dimensional velocity field, one is required to solve a set of partial differential equations or simulate the drop with a finite element model (FEM) [24, 27, 28]. No analytical solution exists, and so the solution is restricted to a numerical or approximate description (see Figure 10.3).

There are two limiting modes of evaporation: the constant contact angle mode (receding contact line) and the constant contact area mode (pinned contact line). For the constant contact angle mode, the contact radius decreases throughout drying (Figure 10.4a). For the constant contact area mode, the droplet evaporates with a fixed contact radius and a decreasing contact angle (Figure 10.4b). Intermediate modes exist such as stick-slip recession of the contact line [29]. Often, there



**Figure 10.2** Simulated results for the radial height-averaged velocity within an evaporating water droplet (initial radius 1 mm, initial contact angle  $20^\circ$ ), which leads to an outward motion of the liquid with the velocity diverging near the contact line.



**Figure 10.3** Streamline plot of the flow field due to evaporation inside a water droplet with a contact angle of  $40^\circ$  from the finite element model [24]. Reprinted with

permission from (Analysis of the microfluidic flow in an evaporating sessile droplet, Ref. [24]). Copyright (2005) American Chemical Society.

is a transition from constant contact area mode to constant contact angle mode, when the contact angle falls below the receding contact angle.

If a droplet dries with a pinned contact line, there is no reduction in the droplet diameter. In order to replenish the solvent that has evaporated at the contact line (to maintain the pinning), while retaining the spherical cap shape imposed by the surface tension, a radial flow is established [30–32] (see Figure 10.3). The liquid in the center of the droplet acts as a reservoir for the outward flow. For droplets

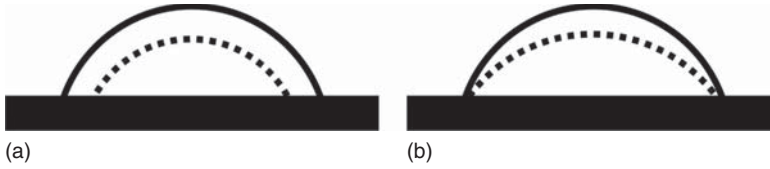


**Figure 10.4** The limiting modes of evaporation for a sessile droplet. Drying with (a) a moving contact line in constant contact angle mode and (b) a pinned contact line in constant contact area mode. The dotted line indicates the new liquid–vapor interface following a period of evaporation.

with a moving contact line, the internal convective flow viewed from above is no longer always toward the contact line [33].

A number of evaporative models have been proposed for limiting mode evaporation (and an intermediate slip mode) based on the assumption that evaporation is diffusion-limited [18, 19, 24, 30, 34, 35]. These models also assume that the droplet is isothermal with a spherical cap shape. Popov [19] solved the Laplace equation to yield a rate of mass loss over time for a sessile droplet of

$$\frac{dM}{dt} = -4\pi R(t)D(n_s - n_\infty) \times \left[ \frac{\sin \theta(t)}{4(1 + \cos \theta(t))} + \int_0^\infty \frac{1 + \cosh 2\theta(t)\tau}{\sinh 2\pi\tau} \tanh[(\pi - \theta(t)\tau)]d\tau \right] \quad (10.17)$$

where  $M$  is the mass,  $n_s$  is the saturation vapor density, and  $n_\infty$  is the ambient vapor density ( $n_\infty = n_s \times \text{RH}$ ). The term outside of the square bracket describes the evaporation rate for a spherical droplet. The terms inside the square bracket account for the nonuniform evaporation rate along the liquid–vapor interface.

The wetting behavior of a droplet on a substrate can strongly influence the drying time (Figure 10.5). Typically, pinned droplets of single solvents dry faster than those whose contact line is free to move (until the contact angle

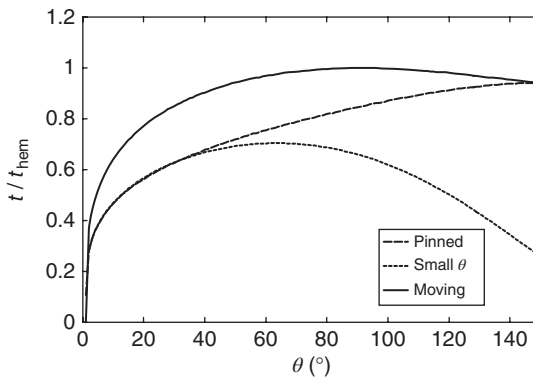


**Figure 10.5** Drying time predictions for diffusion-limited drying with pinned or moving contact line modes (including pinned drying in the limit of small contact angles), normalized by the time for a free hemisphere of equivalent volume to dry.

reaches  $\sim 140^\circ$ ). Higher contact angles resulting from hydrophobic substrates also lengthen the drying time. On hydrophilic substrates, where the contact angle is  $< 90^\circ$ , the difference in drying times between limiting modes is reduced. For contact angles  $< 90^\circ$ , a pinned contact line results in a linear mass loss with time. For a moving contact line (or  $\theta > 90^\circ$ ), the mass loss with time is nonlinear, with the evaporation rate slowing down toward the end of drying.

The aforementioned equations (and the model predictions in Figure 10.5) for diffusion-limited evaporation are valid only in the isothermal case: when evaporative cooling is significant, the evaporation times can be appreciably underpredicted by the model, due to the reduction of the saturated vapor pressure at lower temperatures. The thermal conductivity of the substrate can have a strong impact on the evaporation rate [34, 36–38]. If the substrate is a good thermal conductor, then heat transfer between the substrate and the contact area of the droplet can negate evaporative cooling. If the substrate is an insulator (e.g., Teflon), then a droplet of the same fluid may show significant evaporative cooling and a longer drying lifetime.

### 10.3

#### Evaporation of Mixed Solvents

The evaporation of binary-solvent mixtures can differ greatly from the evaporation of the single-solvent components [39]. For mixtures where the component solvents have very different evaporation rates, the initial evaporation rate often closely matches that of the more volatile component. A transition period follows, and then the evaporation rate closely matches that of the least volatile component. For a freely moving contact line, the contact angle may also increase during drying if the surface tension of the mixture increases as more of the volatile (low surface tension) component is lost.

At the liquid–vapor interface, the vapor exists in equilibrium with the liquid if evaporation is diffusion-controlled. The pressure exerted by the vapor on the liquid phase is known as the *vapor pressure*. In a solvent mixture, the vapor pressure depends on the partial vapor pressures of the components. For an ideal mixture (in which each component fluid interacts with itself and the other component identically), the vapor pressure is described by Raoult's law, whereby the total vapor pressure,  $p_s$ , depends on the molar ratios of the component fluids ( $x_A$  and  $x_B$ ), as

$$p_s = p_A + p_B = p_A^* x_A + p_B^* x_B \quad (10.18)$$

where  $p_A$  and  $p_B$  are the partial vapor pressures of component A and B, and  $p_A^*$  and  $p_B^*$  are the vapor pressures of component A and B, respectively. Note that the evaporative flux  $J_A \propto p_A D_A$ , so the diffusion coefficient is equally as important as the vapor pressure for estimating relative evaporation rates of components.

Few mixtures behave in a near-ideal manner; hence, simple relationships such as Raoult's law cannot be used for model predictions. For example, azeotropes are mixtures that deviate from Raoult's law sufficiently to give a maximum

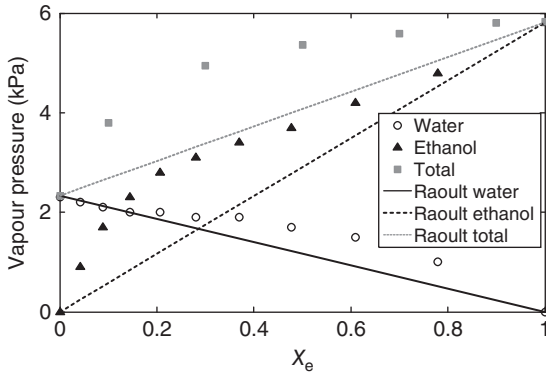


**Figure 10.6** Variation of the partial vapor pressures and total vapor pressure of an ethanol/water mixture with a mole fraction of ethanol,  $x_e$  [40, 41]. The lines indicate predictions from Raoult's law for comparison.

or minimum in the vapor pressure with composition. Ethanol/water has an azeotrope at a mole fraction of ethanol,  $x_e$ , of 0.90 (at room temperature and pressure). Figure 10.6 shows the deviation in the partial and total vapor pressures from Raoult's law. Note that the evaporation of ethanol is enhanced by the deviation from Raoult's law, particularly at low ethanol concentrations.

### 10.3.1

#### Marangoni Flows

Marangoni flows originate when there is an imbalance of the surface tension at the free surface and have been observed since classical times as “tears of wine” [42]. In a sessile droplet, a surface tension gradient along the liquid–vapor interface drives internal Marangoni recirculation cells. The fluid flows from low to high surface tension in order to balance tangential stresses at the liquid–vapor interface, causing cells within the droplet. A surface tension gradient along the liquid–vapor interface,  $d\sigma/d\hat{t}$ , results in a flow along the interface with velocity,  $u$ , determined by

$$\frac{d\sigma}{d\hat{t}} = -\mu \frac{du}{d\hat{n}} \quad (10.19)$$

assuming a lubrication approximation, where  $\hat{t}$  is a unit vector tangent to the liquid–vapor interface and  $\hat{n}$  is the unit vector outward normal to the liquid–vapor interface.

#### 10.3.1.1 Thermal Marangoni Flows

Thermal Marangoni flows arise due to temperature gradients within the droplet, resulting in recirculation cells (Figure 10.7). Hu and Larson calculated the thermal Marangoni flow in a water droplet using a finite element method for an axisymmetric drop [28]. Temperature fields were found by applying a finite



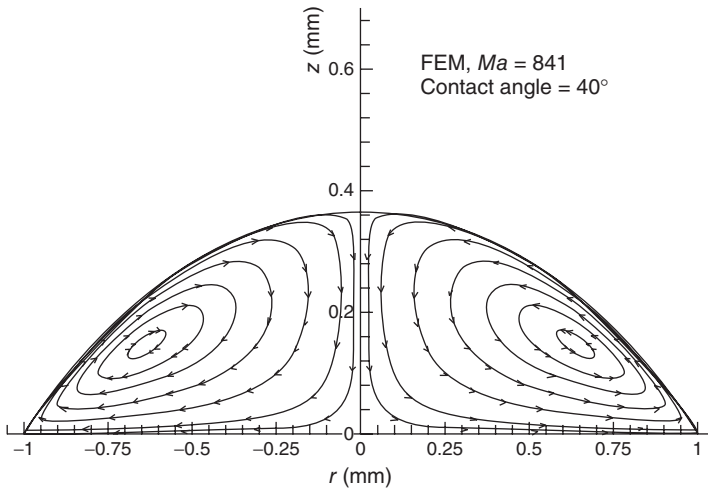


**Figure 10.7** Streamline plot of the flow field inside a water droplet with a thermal Marangoni number of 841 and contact angle of  $40^\circ$  from the finite element model solution to the Marangoni stress boundary

condition [28]. Reprinted (adapted) with permission from (Analysis of the effects of Marangoni stresses on the microflow in an evaporating sessile droplet, Ref. [28]). Copyright (2005) American Chemical Society.

element analysis to the heat equation, from which the surface temperature profile was obtained. The model results compared favorably with experiments, despite no coupling between the flow and temperature [43]. Due to the nonuniform evaporative flux across the droplet ( $\theta < 90^\circ$ ), enhanced evaporation at the contact line causes more evaporative cooling in this region as compared to the apex of the droplet. The resulting temperature gradient along the liquid–vapor interface drives Marangoni flow. Particles transported to the contact line by evaporation-driven radial flow are then transported back toward the center of the droplet along the liquid–vapor interface, reducing buildup of a ring stain.

Ristenpart *et al.* [25] investigated the effect of the thermal conductivity of the substrate ( $\kappa_S$ ) relative to the liquid ( $\kappa_L$ ) and the contact angle on the direction of thermal Marangoni flow. If the relative thermal conductivity of the substrate as compared to the liquid ( $\kappa_R = \kappa_S/\kappa_L$ ) is above a critical value ( $\kappa_R > 2$ ), then energy transfer to the droplet makes the droplet warmest at the contact line (where the conduction pathway is smallest) and colder at the droplet apex (where the conduction pathway is longest). If the substrate is a poor conductor and the relative conductivity falls below a critical value ( $\kappa_R < 1.45$ ), then little energy is available to maintain the droplet temperature and the contact line becomes colder than the rest of the droplet, as the evaporative flux is largest here. In this case, Marangoni flow is directed from the apex toward the contact line along the liquid–vapor interface. The critical ratio of thermal conductivities is given by

$$\kappa_R = \tan \theta_c \cot \left( \frac{\theta_c}{2} + \frac{\theta_c^2}{\pi} \right) \quad (10.20)$$

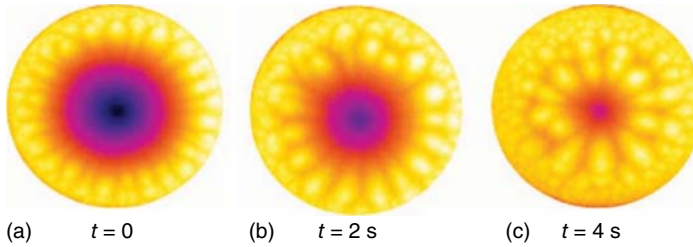


**Figure 10.8** Evolution of the patterns observed during the evaporation of a millimetre-scale FC-72 drop on a titanium substrate by infrared thermography.

Dark purple indicates cooler regions and yellow/white warmer regions [46]. Reprinted with permission from Ref. [46]. Copyright 2008, AIP Publishing LLC.

where  $\theta_C$  is a critical contact angle. For intermediate values of  $\kappa_R$  (i.e.,  $1.45 < \kappa_R < 2$ ), the Marangoni flow direction depends on the contact angle, reversing direction at  $\theta_C$ .

In many industrial settings, the substrate is heated, which can also induce thermal gradients [44, 45]. Infrared thermography has revealed the thermal waves and temperature gradients associated with evaporating droplets (on heated substrates) and where evaporative cooling is significant [45–47]. Note that thermal waves are not included in the model by Hu and Larson [28] due to the assumption that the drop is axisymmetric. The droplets exhibited a cool center relative to the contact line region, with thermal waves processing around the droplet (Figure 10.8a-c). In some cases, such as thin droplets, cellular structures formed with length scales depending on the local thickness.

### 10.3.1.2 Solutal Marangoni Flows

Compositional variation along the liquid–vapor interface can also result in solutal Marangoni flows. An example is given next (Figure 10.9) for a binary solvent mixture, where differential evaporation of the components (with different surface tensions) causes the surface tension gradient. Preferential evaporation of the more

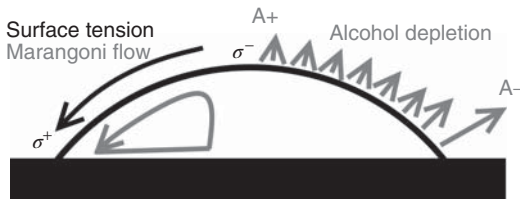


**Figure 10.9** Cartoon example of the alcohol depletion along the liquid–vapor interface of an alcohol/water droplet (where the alcohol is more volatile and has the lower surface tension). A– indicates regions of

lower alcohol composition at the contact line, and A+ regions less depleted in alcohol. The direction of the Marangoni flow is also indicated.

volatile alcohol, combined with enhanced evaporation at the contact line ( $\theta < 90^\circ$ ), results in a higher depletion of the alcohol from the contact line as compared to the apex. The water-rich contact line then has a higher surface tension than the apex, generating a Marangoni flow along the liquid–vapor interface toward the contact line.

Surfactants or surface-active polymers can also cause solutal Marangoni flow [11, 48–51]. In millimeter-scale water droplets, Still *et al.* [48] observed surfactant eddies near the contact line even when the surfactant concentration exceeded the critical micelle concentration (above which a monolayer is expected). Surfactant is transported toward the contact line by the evaporation-driven flow within droplets of water, resulting in a build-up of surfactant near the contact line, which lowers the surface tension in this region. By using surfactant-producing bacteria, Sempels *et al.* [52] were able to switch these Marangoni-driven eddies on or off.

In printed lines of multicomponent droplets, the time delay between each droplet deposition can allow a surface tension gradient along the direction of the printed line. If the least volatile component has the higher surface tension, then the first droplet will have a higher surface tension than the incoming second droplet (which is undepleted). The surface tension gradient in the coalesced droplet will cause fluid to flow toward the initial droplet, thus depleting the second. This effect can cause droplets printed earlier to dry later than subsequent droplets.

## 10.4

### Particle Transport in Drying Droplets

The previous sections considered the evaporation and flows within solvent droplets. This section covers the effects of particle transport within such droplets and discusses the resulting deposits. Particular attention is paid to the “coffee ring effect.”

#### 10.4.1

##### The “Coffee Ring Effect”

The drying of droplets is a simple experiment to perform, but some of the physics involved are encountered in other applications such as coating flows and drying films. Despite the simplicity of the experiment, the physical phenomena that come into play are actually quite diverse. The well-known coffee stain, a thick dark ring that marks the original shape of the droplet (Figure 10.10), is caused by an interplay of phenomena. The dissolved solute precipitates at the edge of the spill where the concentration of the coffee exceeds the saturation level, giving rise to the dark ring at the droplet edge and an absence of coffee grounds in the middle. Although this is an everyday occurrence, it was only in 1997 that coffee rings were explained [18, 22]. Of course, the production of a ring-shaped pattern is not limited to the

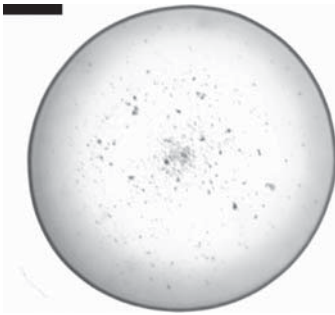


**Figure 10.10** A coffee stain: top view of a ring-shaped deposit of coffee grounds (scale bar 5 mm).

evaporation of coffee. Rather, numerous substrates (e.g., glass, metal, platinum, and roughened polytetrafluoroethylene (PTFE) and solvents (e.g., water, acetone, methanol, toluene, and ethanol) have been tested and have been shown to produce the coffee ring effect [22]. Time-resolved microscopy experiments on the evaporation of water droplets containing suspended particles showed an internal flow in the droplet radially outward from the center toward the contact line (Figure 10.3). This flow transports any suspended particles or dissolved solute to the contact line and forms a concentrated ring [24, 27]. The size of matter concentrated at the contact line ranges from micrometer-sized cells and colloids [18, 53, 54] to nanoparticles [55] and even individual molecules [48, 52, 53, 56]. In all cases, the outward flow that causes the ring stain is controlled by the evaporation rate, which determines the thickness of the final deposition pattern.

For the formation of ring stains, the contact line must be pinned, that is, the receding contact angle  $\theta_r = 0$ . Young's equation states that the equilibrium contact angle is given by  $\cos \theta = (\sigma_{sv} - \sigma_{sl})/\sigma_{lv}$ , where the subscripts s, v, and l refer to solid, vapor, and liquid, respectively. If there are strong attractive interactions between the liquid and the solid, then the numerator in Young's equation is large and the contact angle is small or zero. Few surfaces display a single thermodynamic contact angle: it is more common for the angle to be different depending on whether the droplet is advancing or receding across the surface. The difference between the advancing and receding contact angles is referred to as the contact angle hysteresis (CAH), usually expressed as  $\cos \theta_r - \cos \theta_a$ . The higher the CAH, the more likely that the receding contact angle is zero and the contact line is pinned. For a given CAH, the lower the value of the equilibrium contact angle,  $\theta_{eq}$ , the more likely it is that  $\theta_r = 0$ . Hence, strong attractive interactions between the liquid and the substrate tend to favor contact line pinning, even for liquids that do not wet the substrate ( $\theta_a > 0$ ) [57–59]. Other factors increasing CAH are porosity, roughness, and chemical heterogeneity. Porous surfaces retain liquid due to retain liquid due to the negative Laplace pressure associated with the small dimensions of the pores. The contact angle on rough surfaces is given by Wenzel's equation [60]  $\cos \theta = r_w (\sigma_{sv} - \sigma_{sl})/\sigma_{lv}$ , where  $r_w (>1)$  is the ratio of the true surface area to the geometric area. For surfaces with equilibrium contact angles  $<90^\circ$ , roughness increases  $\cos \theta$  and therefore reduces the contact angle. Rough surfaces also show increased CAH: the microscopic contact angle is greater or

less than the macroscopic contact angle depending on whether the local slope of the surface is toward or away from the droplet. The receding contact line tends to be pinned by ridges and indentations [61]. For chemically heterogeneous surfaces, the most wettable patches determine  $\theta_r$ , while the least wettable determine  $\theta_a$  [62]. Particles deposited at the contact line behave as a rough, porous surface and tend to pin the contact line even on smooth, homogeneous substrates. This “self-pinning” increases the chance of the coffee ring effect, even if the attractions between the solvent and the surface are not very strong [18, 22, 63].

Numerous applications make use of evaporating droplets to pattern surfaces. Droplet evaporation is a low-cost and simple technique for delivering suspended material to a substrate, but it is confronted with the inhomogeneous distribution of the deposited material. In most cases, the resulting circular deposit is considered a strong disadvantage to the technique of droplet evaporation. However, some applications have turned this property into a valuable asset.

#### 10.4.1.1 Disadvantages to the Ring-Shaped Pattern

- 1) *Inkjet Printing and Coatings*: Inkjet printing is generally carried out by depositing small droplets containing pigment onto a surface and allowing the ink to dry; a different technique to industrial coating or painting processes [64–66] but with similar results. Ink can be extremely expensive, especially when considering the price per unit volume. In order to be used as a protective coating or simply having an esthetic function, the smallest amount of ink or paint should be used to get the job done, but the performance and lifetime are critically dependent on the uniformity of the printed films. Hence, inhomogeneous films will be detrimental to the functionality of the coated surfaces. By understanding the coffee ring effect and knowing how to control or inhibit it, the solid content of the ink could be decreased together with the overall price of the coating process [67].
- 2) *3D Printing*: This is a technique used for rapid prototyping or for the manufacturing of ceramic components. In a layerwise manner, small droplets containing ceramic or polymeric structures are deposited onto each other on a substrate to create an object [68, 69]. In some cases, this is carried out from a solution or a suspension. The three-dimensional structure of the printed object requires a continuous distribution of material to secure the shape and the appropriate mechanical strength of the printed object. Additionally, this necessitates contact and adhesion between the individual drops [70]. An inhomogeneous dispersal can warp the layered structure.
- 3) *DNA Grafting*: A technique where specific sequences in DNA strands are removed and replaced with sequences of other DNA for use in genetic modification. During the grafting process, thousands of small picoliter droplets are deposited onto a substrate, all acting as individual nanoreactors, each droplet differing slightly from the adjacent droplet with respect to the DNA solutes.

The solvent in the droplets is allowed to evaporate to concentrate the DNA, which increases the speed of the grafting process and the result after evaporation is examined using microscopical techniques. Inhomogeneous deposits in the coffee stains impede correct data processing and subsequent interpretation of the grafting results [71, 72].

#### 10.4.1.2 Exploiting the Coffee Ring Effect

- 1) *Nanowire Assembly*: The inhomogeneous deposition opens up a pathway to create 1D structures with circular or even linear patterns [73, 74]. Metallic particles get jammed at the contact line, creating a conductive ring-shaped pattern due to the dense particle packing, yielding a “nanowire” with an electrical conductivity that can go up to 15% of the bulk material [75]. This allows for microfabrication of low-cost electronic devices at dimensions comparable to those achieved with modern lithographic techniques. Additionally, transparent conductive layers can be obtained by the overlap of multiple metallic rings that span the entire coating area: the rings that are in contact with each other guide the electrical current, yet the coating is transparent as the metallic material is not spread out evenly across the surface and light is allowed to pass through [76].
- 2) *Nanochromatography*: Health-care diagnostics requires the accurate detection of pathogens. Detection can be facilitated by separation by size of the biological material (e.g., cells) using the coffee ring effect. The smallest cells are dragged further outward toward the contact line by the radial flow before their size prevents further outward motion. Much larger cells, however, remain excluded further inward due to the height restriction near the contact line [1]. This size segregation is known as the *confinement effect*. This allows separation of cells in multiple rings at the edge of the droplet (see Figure 10.11) and

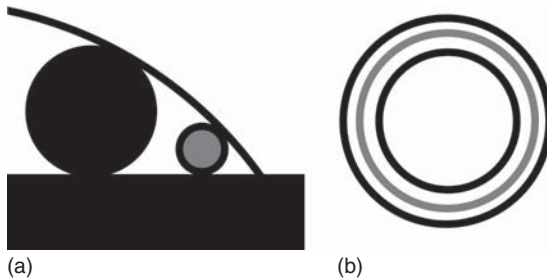


**Figure 10.11** Cartoon of size-sorting within a drying droplet showing: (a) the side profile and (b) the drop from above. Smaller particles (gray) are transported closer to the contact line by evaporation driven flow where the droplet height is smaller. Larger

particles (black) are confined further inward due to the size restriction imposed by the height of the liquid–vapor interface. As a result, smaller particles form an outer ring and larger particles an inner ring deposit.

therefore aids in the detection of specific biological markers. All nonrelevant particles, which have sizes different from those of the markers of interest, are collected in a different ring stain and can be ignored, improving the signal-to-noise ratio of the markers of interest [53].

- 3) *DNA Stretching*: Optical gene mapping is a technique where the entire sequence of a DNA strand is determined, hence providing access to information on DNA structure and properties. By using the specific binding of enzymes to a DNA motif and visualizing where along the strand these are found, together with the testing of different binding enzymes, the entire DNA strand sequence can be fully mapped. In order to determine the location of the enzymes in an accurate way, the DNA molecules need to be stretched completely. By using the outward flow field in an evaporating droplet, which applies an extensional shear flow, the DNA molecules are dragged along and are subsequently stretched as they get deposited on a substrate suitable for adhesion [2, 77]. After stretching, the strand is ready for sequence analysis.

#### 10.4.1.3 Avoiding the Coffee Ring Effect

Two conditions must be met for the coffee ring effect to occur: first, the contact line must be pinned and second, there must be evaporation from the contact line region. If one of these conditions is not met, it is possible to obtain particle deposits that deviate from the ring-shaped pattern.

When the contact line of the droplet is not pinned, there is no need for replenishment of liquid evaporated along the contact line in order to keep a spherical cap shape. The flows inside droplets with a receding contact line need not be radially outward [33], in which case particles do not accumulate at the periphery (unless gathered by the receding contact line). One route to circumvent contact line pinning is electrowetting: for a sessile droplet, the presence of an electric field elongates the droplet along the field direction, overcoming the surface tension that tries to induce the spherical cap geometry of the droplet [78]. By applying an alternating voltage to the droplet via the insertion of an electrode tip, the electrowetting technique oscillates the contact line. The motion of the droplet edge eliminates the pinning of the droplet [79]. Note that electrowetting requires the application of a high-frequency alternating voltage, which is a difficult technique to perform on an industrial scale.

Alternatively, the second prerequisite for the coffee ring effect can be addressed: in the free evaporative state, there is enhanced evaporation near the contact line (for  $\theta < 90^\circ$ ), amplifying the outward flow. Implementing a reduction of the evaporative flux near the contact line changes the internal flow field. As an example, the evaporation of a droplet in a closed environment with a hole above the center of the droplet increases the evaporation rate at the apex and decreases evaporation from the edge. Depending on the strength of the increased central evaporation rate, a reduced, less distinctive coffee ring pattern can occur, up to even an inward flow followed by a central heap-up of particles [22, 80].



Another way to remove the ring stain while maintaining the prerequisites for the coffee ring effect is to alter the internal flow within the droplet such that radial flow does not dominate. For example, introducing a surface tension gradient along the liquid–vapor interface by simply adding surfactant can recirculate particles inside the droplet and prevent the incorporation of particles (or polymers) in a ring stain at the contact line [50, 64, 81]. Note that if Marangoni flow ends during the drying lifetime, or convective flow becomes stronger than the Marangoni flow, then radial flow will once more transport particles to the contact line, which will develop a ring stain.

As a last resort, there is the influence of the droplet size on the deposition pattern. It is found that for very small droplets, on the order of  $\leq 10\ \mu\text{m}$  in diameter, the coffee ring effect is not observed. Two timescales govern the deposition pattern: the droplet lifetime and the time to induce solute-based self-pinning. If the droplet is small enough, the time for evaporation of the droplet is so small that the droplet has already evaporated before the particles can be set in motion by the outward flow, thus resulting in a random homogeneous deposition. Additionally, the particle size has an influence and dictates the second timescale. To obtain a pronounced pinning of the contact line during evaporation, the self-pinning effect of the contact line by the particles that accumulate at the interface is extremely important. If the particles in the droplet are small enough, the time for two nearby particles to collide and form an arrested structure that could increase the pinning strength of the contact line is too long with respect to the evaporation time. For very small particles, therefore, no coffee ring effect is seen if the pinning of the droplet is strongly dependent on a physical obstruction [82].

#### 10.4.2

##### Particle Migration

In addition to following the flow along fluid streamlines, particles can migrate across streamlines if an external force is present. For example, picoliter droplets of ethanol/water (with  $\leq 50\ \text{vol}\%$  ethanol) exhibit particle migration toward the center of the droplets during drying [50]. The migration forms a concentrated central group and depleted contact line for the duration of the Marangoni flow period. Potential mechanisms for such migration include thermophoresis, chemophoresis, and shear-induced migration.

#### 10.5

##### Drying of Complex Fluids

The patterns resulting from dried colloidal droplets can be beautiful and incredibly complex [83], with the resulting morphology dependent on a number of variables. This section discusses the influence of the contact line motion (pinned, moving, or stick-slip motion), particle character (size, shape, volume fraction), segregation of solids during drying (skin formation, cracking, and buckling effects), viscosity,



elasticity, local environment (relative humidity and local humidity gradients), and the destabilization of colloids during drying.

### 10.5.1

#### Contact Line Motion

The velocity of the contact line (coupled with the particle concentration) can have a large influence on the resulting fine structure. For example, Deegan [84] observed rings, grid-like structures, radial spokes, or sawtooth (triangular) patterns depending on whether the contact line remained completely pinned, moved in places but remained fixed in others, or built up multiple layers at higher particle concentrations following a moving contact line (see Figure 10.12). During periods where the contact line is pinned, radial flow to the contact line builds up a ring deposit. If the contact line remains fixed at a constant radius throughout drying, the resulting deposit is a single ring stain. Consecutive pinning and depinning events can allow stick-slip motion of the contact line, forming rings where the droplet pinned. This can result in a deposit consisting of multiple concentric rings, or internally tangent rings centered on a single point at the contact line, which remained pinned throughout the entire drying lifetime.

Large structural differences can occur between the particle packing at the contact line and at the center of the deposit (Figure 10.13). Often, the contact line exhibits a highly ordered, “crystalline” deposit structure, whereas the center of the deposit may be looser in structure. This results from the speed of radial flow throughout the drying lifetime: particle speeds toward the contact line are slower at the start of drying [85], allowing more time for particle rearrangement and alignment into a close-packed structure at the contact line [26]. Later in the drying lifetime when the droplet is thinner and flow speeds are faster, the comparative rush of particles toward the contact line leaves greater disorder centrally, where the deposit builds inward. As the droplet thins, dewetting causes the final “lacy” fine structure at the center of the droplet due to capillary immersion forces.

Often, a receding contact line results in unpredictable dewetting and drags particles to form an irregular edge to the deposit. However, if the recession of the contact line can be adequately controlled, then the motion can be used to self-assemble highly ordered structures: photonic crystals are one example of highly periodic structures that can be formed from inkjet droplets [64]. In special cases, motion of the contact line can allow the droplet to “climb” the deposit during drying. For example, polyethylene oxide solutions have been shown to pile up during drying to form monolithic structures at particular concentrations [86].

### 10.5.2

#### Particle Character

The shape, size, and rigidity of particulates within a droplet can play a significant role in the deposit structure. Additionally, particle–particle and/or particle–substrate interactions can be used to alter the deposit morphology.

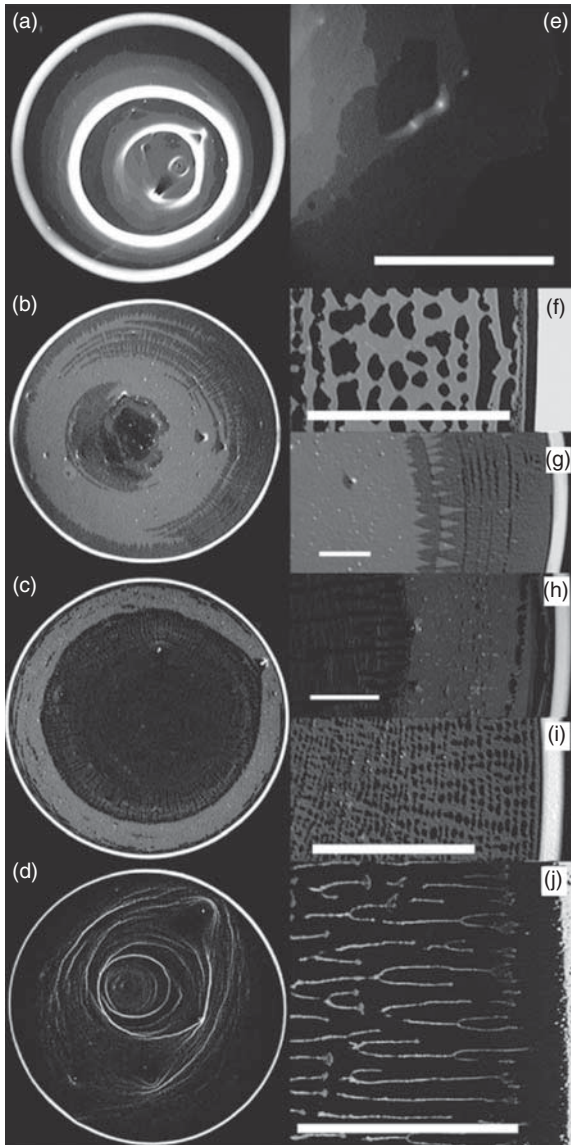


**Figure 10.12** Deposits of  $0.1\ \mu\text{m}$  microspheres at volume fraction: (a) 1%, (b) 0.25%, (c) 0.13%, (d) 0.063%. Corresponding zooms are given (e–j) to the right of each whole deposit ( $\sim 6\ \text{mm}$  in diameter). Scale

bars are  $500\ \mu\text{m}$  for (e–i) and  $250\ \mu\text{m}$  for (j). [84]. (Reprinted (figure) with permission from “Pattern formation in drying drops,” Ref. [84]. Copyright (2000) by the American Physical Society.)

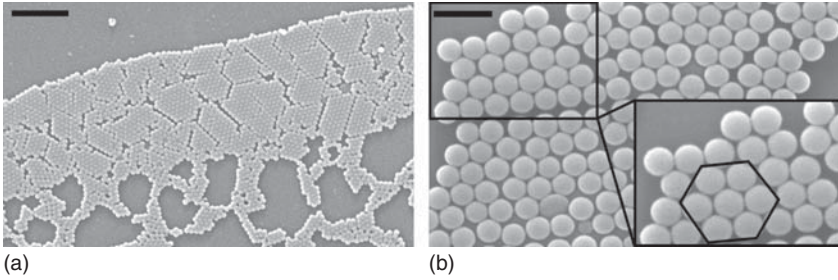


**Figure 10.13** Deposit structure near the contact line for water droplets with: (a) 1 vol% 200 nm polystyrene beads and (b) 0.1 vol% 1  $\mu\text{m}$  polystyrene beads. Close-packed arrays are formed immediately at

the contact line with fractures evident. Further toward the deposit center (inside the ring), loose “lacy” structure builds up on dewetting.

The packing or stacking affinity of particulates is reflected in the height and width of the ring stains produced due to the coffee ring effect. Hodges *et al.* noticed that the stacking of disks at the contact line formed a higher ring stain than spherical particles of comparable size [87]. The higher ring results from the enhanced stacking affinity of the disks.

At the liquid–vapor interface, the shape of particles plays another role: shape-dependent capillary interactions are capable of inhibiting the coffee ring effect [88, 89], allowing the deposition pattern to be tuned to a full homogeneous deposit for highly elongated particles. Once carried to the liquid–vapor interface by radial flow, anisotropic particles (e.g., ellipsoids) cause significant deformation of the free interface, resulting in strong long-range interparticle interactions. These interparticle interactions lead to the formation of loosely packed aggregate structures at the liquid–vapor interface, keeping particles in a raft and preventing buildup at the contact line. The raft stretches across the liquid–vapor interface, spanning the free surface, and dries downward to produce a uniform deposit. Similarly, Bigioni *et al.* [55] utilized attractive particle interactions between surface active spherical particles to grow a film at the liquid–vapor interface. The film then dried vertically downward to form a more uniform deposit than the ring stain observed when particle interactions were not present.

Particle size can enable segregation within a droplet due to the confinement effect (see Section 10.4.1.2). Larger particles may also settle, rather than following internal flows. The settling velocity,  $v_s$ , can be determined by balancing the particle buoyancy with Stokes’ drag, giving

$$v_s = \frac{2}{9} \frac{(\rho_p - \rho_f)ga^2}{\mu} \quad (10.21)$$

where  $a$  is the radius of a spherical particle,  $\rho_f$  is the fluid density, and  $\rho_p$  is the particle density.

Particle–substrate interactions can also play a key role in the deposit morphology (e.g., van der Waals interactions and electrostatic interactions) [90]. If the

signs of the charges of both the particles and the substrate are opposite, the mobility of the particles can be hindered, reducing the “coffee ring effect.” Particles “stick” to the substrate, forming a disordered structure at the contact line [91]. When particles have the same charge as the substrate, there is no attraction, and radial flow builds up a ring stain with an ordered structure.

### 10.5.3

#### Segregation of Solids

As a droplet evaporates, and the free surface moves downward, the material within the droplet may gather at the liquid–vapor interface. If the material is not able to diffuse away from the free surface, then the concentration may reach a level where a skin or “crust” is formed. Often, these particulates pin the contact line, so as the droplet continues evaporating, the radius of curvature,  $r_c$ , decreases. The pressure,  $P$ , inside a droplet described by a spherical cap is determined by the Laplace equation,

$$P = 2\sigma/r_c \quad (10.22)$$

When the pressure inside the droplet becomes too low, the crust buckles, sagging inward at the center where the skin is the thinnest [51]. Alternatively, if the polymer concentration becomes high enough, the outer skin undergoes a glass transition and a buckling instability occurs, forming a “Mexican hat” deposit, where the apex height is raised during drying [92].

Cracks can develop in surface films or skins to allow the relaxation of stress [93, 94], often exhibiting a regular spacing. For elastic materials, the elastic energy gained by relaxation must be at least equivalent to the energy required for the formation of the new surface. The cracking of such a skin can lead to a poor-quality surface finish (Figure 10.14b,c).

Segregation of solids can also occur at the contact line due to the coffee ring effect. This may raise the local viscosity or elasticity or cause supersaturation,

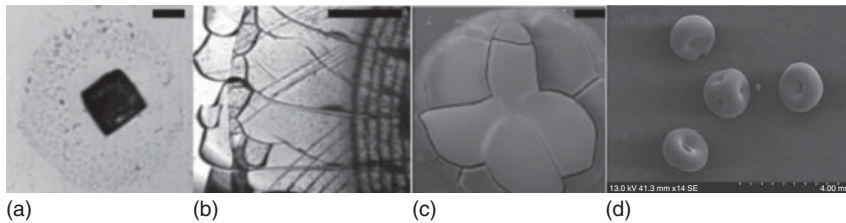


**Figure 10.14** (a) Cubic crystal deposited from a dried drop of 0.3 M NaCl solution, scale bar 20  $\mu\text{m}$ . (b) Regularly spaced fractures at the contact line of a silica deposit, scale bar 1 mm. (c) Cracking due to the formation of a skin during the drying of a silica suspension. Scale bar 20  $\mu\text{m}$ .

(d) Arched deposits left by drying droplets of colloidal alumina due to the raise in local humidity by neighboring droplets [10]. Reprinted with permission from (Arched structures created by colloidal droplets as they dry, Ref. [10]). Copyright (2009) American Chemical Society.

which results in crystallization. If the viscosity increase is sufficient, then the droplet profile may be deformed from a spherical cap. To maintain a pinned contact line, radial flow throughout the droplet is no longer necessary, as the droplet can deform from the spherical cap shape otherwise imposed by the surface tension. Hence, ring stains can be inhibited. Similarly, Talbot *et al.* [95] used the concentration of Laponite clay at the contact line due to the larger evaporative flux in this region to induce a sol–gel transition. The elasticity of the gel was able to overcome capillary flow toward the contact line. By adjusting the initial Laponite concentration, the amount of radial motion could be controlled, allowing the deposit formed to be tailored from a ring stain to a uniform deposit or even a dome.

#### 10.5.4

##### **Local Environment**

Deliberate manipulation of the local evaporation rate via control of the local relative humidity can lead to the formation of unusual structures such as arches, boats, and cups. A wall or second droplet placed close to the initial droplet can raise the local humidity and reduce the evaporation rate on that side. Transport of particulates to the contact line due to evaporation-driven flow is then reduced on the wall side, resulting in a cavity (see Figure 10.14d).

Deegan *et al.* [22] modified the local humidity across a droplet to determine the effect of the evaporative flux on the deposit. By raising the droplet on a pedestal, surrounded by a pool of water, a uniform evaporative flux was acquired across the droplet. Similar to an ambient environment with enhanced evaporation at the contact line, the resulting deposit was a ring stain. By containing the droplet in a chamber with a small opening above the center of the droplet, the evaporative flux was enhanced at the center of the droplet as compared to the edge (with a profile similar to the droplet shape). Due to the largely reduced evaporation from the contact line as compared to the apex, radial flow was significantly reduced, forming a uniform deposit.

#### 10.5.5

##### **Substrate Patterning**

By patterning substrates with hydrophilic and hydrophobic regions, the wetting of droplets over separate regions of the same substrate can be controlled to form straight lines (without bulging instabilities) or a variety of shapes from single droplets such as squares [96], lozenges, or butterflies [97].

The geometry of the surface is as important as patterned surface wetting. Droplet spread across a surface can be hindered by protuberances of controlled size and shape [98]. Pillars or posts raised above the surface have also been implemented to attain noncircular contact lines [99].

## 10.5.6

**Destabilization of Colloids during Drying**

Concentration of solute within the droplet during drying can cause destabilization of an ink by decreasing the Debye length,

$$r_D = \sqrt{\frac{\epsilon_r \epsilon_0 k_B T}{2N_A e^2 I}} \quad (10.23)$$

where  $N_A$  is Avogadro's constant,  $e$  is the elementary charge,  $I$  is the ionic strength,  $\epsilon_r$  is the dielectric constant,  $\epsilon_0$  is the relative permittivity of free space,  $k_B$  is the Boltzmann constant, and  $T$  is the temperature. A smaller Debye length indicates a shorter distance over which the electrical double layer screens repulsions between particles. Particles are then able to approach one another more closely, which can result in aggregation. Concentration of salts due to solvent evaporation can increase the ionic strength, decreasing the Debye length. In some cases, the salts crystallize to form cubic crystals in the deposit or fractal-like fingers [56] (Figure 10.14a). Solvent mixtures can also influence the Debye length through depletion of the more volatile solvent. For example, in an ethanol/water mixture, the dielectric constant increases throughout drying (as  $\epsilon_{r,\text{ethanol}} < \epsilon_{r,\text{water}}$ ) as the ethanol is depleted. The Debye length then increases, ensuring stability.

Polymers may cause flocculation of particulate inks by bridging flocculation, or charge–patch interactions for adsorbing polymers, and through depletion flocculation for nonadsorbing polymers. Often, destabilization is undesirable, but in some cases, it can be useful for “locking” together the structure in a single aggregate or causing sedimentation of aggregates to result in a more uniform deposit (rather than allowing transport by radial flow to form a ring stain). Flocculated and interconnected networked structures can present alternative rheological behavior that can be useful for direct write applications [100].

In summary, the drying of a sessile droplet is a complex process involving heat and mass transfer. Radial flow driven by evaporation in pinned droplets often results in a ring stain. By using Marangoni flows, anisotropic particles, viscosity-related deformation of the liquid–vapor interface, or elasticity of the fluid, uniform deposits can be obtained. Segregation of solids may result in cracking or buckling of a surface skin, affecting quality control. The substrate's thermal properties, wetting properties, and patterning/roughness all contribute to the dried result. Careful thought is required to tailor an ink to a given application and provide the desired deposited output.

**10.6****Problems****10.6.1**

A sessile water droplet is drying on a glass substrate at 25°C. Calculate the contact angle below which the Marangoni flow direction switches. What



direction does the Marangoni flow take along the liquid–vapor interface for a contact angle of  $20^\circ$ ?

**Working** The thermal conductivity of glass ( $0.96 \text{ Wm}^{-1} \text{ K}^{-1}$ ) and water ( $0.58 \text{ Wm}^{-1} \text{ K}^{-1}$ ) gives a relative thermal conductivity of  $\kappa_R = 1.66$ . Using Eq. (10.20) to plot and find the root corresponding to the critical contact angle yields  $22^\circ$  ( $0.39 \text{ rad}$ ). At a contact angle of  $20^\circ$ , the contact line will be cooler, giving Marangoni from the apex toward the contact line along the liquid–vapor interface.

### 10.6.2

Spherical polystyrene beads are being used as tracer particles for tracking flow within a water droplet (at  $25^\circ \text{C}$ ). What is the particle size limit within a fluid flowing at a velocity of  $5 \mu\text{m s}^{-1}$ , at which the flow velocity is equal to the settling velocity? How does this differ for an ethanol droplet?

**Working** The densities of polystyrene, water, and ethanol are  $1050$ ,  $998$ , and  $790 \text{ kg m}^{-3}$ , respectively. The viscosities of water and ethanol are  $0.89$  and  $1.09 \text{ mPa}\cdot\text{s}$ , respectively. Using Eq. (10.21), the particle radius limit for a water droplet is  $6.3 \mu\text{m}$  and for an ethanol droplet, it is  $3.1 \mu\text{m}$ .

### References

1. Monteux, C. and Lequeux, F. (2011) Packing and sorting colloids at the contact line of a drying drop. *Langmuir*, **27** (6), 2917–2922.
2. Abramchuk, S.S., Khokhlov, A.R., Iwataki, T., Oana, H., and Yoshikawa, K. (2001) Direct observation of DNA molecules in a convection flow of a drying droplet. *Europhys. Lett.*, **55** (2), 294–300.
3. Fuller, S.B., Wilhelm, E.J., and Jacobson, J.M. (2002) Ink-jet printed nanoparticle microelectromechanical systems. *J. Microelectromech. Syst.*, **11** (1), 54–60.
4. Kim, D. and Moon, J. (2005) Highly conductive ink jet printed films of nanosilver particles for printed electronics. *Electrochem. Solid-State Lett.*, **8** (11), J30–J33.
5. Hebner, T.R., Wu, C.C., Marcy, D., Lu, M.H., and Sturm, J.C. (1998) Ink-jet printing of doped polymers for organic light emitting devices. *Appl. Phys. Lett.*, **72** (5), 519–521.
6. Sirringhaus, H., Kawase, T., Friend, R.H., Shimoda, T., Inbasekaran, M., Wu, W., and Woo, E.P. (2000) High-resolution inkjet printing of all-polymer transistor circuits. *Science*, **290** (5499), 2123–2126.
7. Okamoto, T., Suzuki, T., and Yamamoto, N. (2000) Microarray fabrication with covalent attachment of DNA using Bubble Jet technology. *Nat. Biotechnol.*, **18** (5), 438–441.
8. Roth, E.A., Xu, T., Das, M., Gregory, C., Hickman, J.J., and Boland, T. (2004) Inkjet printing for high-throughput cell patterning. *Biomaterials*, **25** (17), 3707–3715.
9. Mott, M., Song, J.-H., and Evans, J.R.G. (1999) Microengineering of ceramics by direct ink-jet printing. *J. Am. Ceram. Soc.*, **82** (7), 1653–1658.
10. Chen, L. and Evans, J.R.G. (2009) Arched structures created by colloidal droplets as they dry. *Langmuir*, **25** (19), 11299–11301.
11. Hamamoto, Y., Christy, J.R.E., and Sefiane, K. (2012) The flow characteristics of an evaporating ethanol water mixture droplet on a glass substrate. *J. Therm. Sci. Technol.*, **7** (3), 425–436.

12. Kuang, M., Wang, J., Bao, B., Li, F., Wang, L., Jiang, L., and Song, Y. (2014) Inkjet printing patterned photonic crystal domes for wide viewing-angle displays by controlling the sliding three phase contact line. *Adv. Opt. Mater.*, **2**, 34–38.
13. Larson, R.G. (2014) Transport and deposition patterns in drying sessile droplets. *Am. Inst. Chem. Eng. J.*, **60**, 1538–1571.
14. Hu, H. and Larson, R.G. (2002) Evaporation of a sessile droplet on a substrate. *J. Phys. Chem. B*, **106**, 1334–1344.
15. Cazabat, A.M. and Guéna, G. (2010) Evaporation of macroscopic sessile droplets. *Soft Matter*, **6** (12), 2591–2612.
16. Murisic, N. and Kondic, L. (2011) On evaporation of sessile drops with moving contact lines. *J. Fluid Mech.*, **679**, 219–246.
17. Smith, J.D., Cappa, C.D., Drisdell, W.S., Cohen, R.C., and Saykally, R.J. (2006) Raman thermometry measurements of free evaporation from liquid water droplets. *J. Am. Chem. Soc.*, **128**, 12892–12898.
18. Deegan, R.D., Bakajin, O., Dupont, T.F., Huber, G., Nagel, S.R., and Witten, T.A. (1997) Capillary flow as the cause of ring stains from dried liquid drops. *Nature*, **389**, 827–829.
19. Popov, Y.O. (2005) Evaporative deposition patterns: spatial dimensions of the deposit. *Phys. Rev. E*, **71** (3), 036313.
20. Shahidzadeh-Bonn, N., Rafai, S., Azouni, A., and Bonn, D. (2006) Evaporating droplets. *J. Fluid Mech.*, **549**, 307–313.
21. Kelly-Zion, P.L., Pursell, C.J., Vaidya, S., and Batra, J. (2011) Evaporation of sessile drops under combined diffusion and natural convection. *Colloids Surf., A: Physicochem. Eng. Aspects*, **381** (1–3), 31–36.
22. Deegan, R.D., Bakajin, O., Dupont, T.F., Huber, G., Nagel, S.R., and Witten, T.A. (2000) Contact line deposits in an evaporating drop. *Phys. Rev. E*, **62** (1), 756–765.
23. Poulard, C., Guéna, G., and Cazabat, A.M. (2005) Diffusion-driven evaporation of sessile droplets. *J. Phys.: Condens. Matter*, **17**, S4213–S4227.
24. Hu, H. and Larson, R.G. (2005) Analysis of the microfluid flow in an evaporating sessile droplet. *Langmuir*, **21** (9), 3963–3971.
25. Ristenpart, W.D., Kim, P.G., Domingues, C., Wan, J., and Stone, H.A. (2007) Influence of substrate conductivity on circulation reversal in evaporating drops. *Phys. Rev. Lett.*, **99** (23), 234502.
26. Marín, Á.G., Gelderblom, H., Lohse, D., and Snoeijer, J.H. (2011) Order-to-disorder transition in ring-shaped colloidal stains. *Phys. Rev. Lett.*, **107**, 085502.
27. Fischer, B.J. (2002) Particle convection in an evaporating colloidal droplet. *Langmuir*, **18**, 60–67.
28. Hu, H. and Larson, R.G. (2005) Analysis of the effects of Marangoni stresses on the microflow in an evaporating sessile droplet. *Langmuir*, **21** (9), 3972–3980.
29. Shanahan, M., Sefiane, K., and Moffat, J. (2011) Dependence of volatile droplet lifetime on the hydrophobicity of the substrate. *Langmuir*, **27** (8), 4572–4577.
30. Picknett, R.G. and Bexon, R. (1977) Evaporation of sessile or pendant drops in still air. *J. Colloid Interface Sci.*, **61** (2), 336–350.
31. Birdi, K.S. and Vu, D.T. (1989) A study of the evaporation rates of small water drops placed on a solid surface. *J. Phys. Chem.*, **93**, 3702–3703.
32. Bourgès-Monnier, C. and Shanahan, M.E.R. (1995) Influence of evaporation on contact angle. *Langmuir*, **11**, 2820–2829.
33. Masoud, H. and Felske, J.D. (2009) Analytical solution for inviscid flow inside an evaporating sessile drop. *Phys. Rev. E*, **79**, 016301.
34. Talbot, E.L., Berson, A., Brown, P.S., and Bain, C.D. (2012) Evaporation of picoliter droplets on surfaces with a range of wettabilities and thermal conductivities. *Phys. Rev. E*, **83**, 061604.



35. Stauber, J.M., Wilson, S.K., Duffy, B.R., and Sefiane, K. (2014) On the lifetimes of evaporating droplets. *J. Fluid Mech.*, **744**, R2.
36. David, S., Sefiane, K., and Tadrist, L. (2007) Experimental investigation of the effect of thermal properties of the substrate in the wetting and evaporation of sessile drops. *Colloids Surf., A: Physicochem. Eng. Aspects*, **298** (1–2), 108–114.
37. Dunn, G.J., Wilson, S.K., Duffy, B.R., David, S., and Sefiane, K. (2009) The strong influence of substrate conductivity on droplet evaporation. *J. Fluid Mech.*, **623**, 329–351.
38. Sefiane, K. and Bennacer, R. (2011) An expression for droplet evaporation incorporating thermal effects. *J. Fluid Mech.*, **667**, 260–271.
39. Sefiane, K., Tadrist, L., and Douglas, M. (2003) Experimental study of evaporating water-ethanol mixture sessile drop: influence of concentration. *Int. J. Heat Mass Transfer*, **46** (23), 4527–4534.
40. Washburn, E.W. (1928) *The International Critical Tables*, vol. **3**, McGraw-Hill Book Co., New York.
41. D'Avila, S.G. and Silva, R.S.F. (1970) Isothermal vapor-liquid equilibrium data by total pressure method. Systems acetaldehyde-ethanol, acetaldehyde-water, and ethanol-water. *J. Chem. Eng. Data*, **15** (3), 421–424.
42. Thompson, J. (1855) On certain curious motions observable at the surface of wines and other alcoholic liquors. *Philos. Mag. J. Sci. (London, Edinburgh and Dublin)*, **10**, 330–333.
43. Hu, H. and Larson, R.G. (2006) Marangoni effect reverses coffee-ring depositions. *J. Phys. Chem. B*, **110** (14), 7090–7094.
44. Girard, E., Antoni, M., Faure, S., and Steinchen, A. (2006) Evaporation and Marangoni driven convection in small heated water droplets. *Langmuir*, **22** (26), 11085–11091.
45. Sefiane, K., Fukatani, Y., Takata, Y., and Kim, J. (2013) Thermal patterns and hydrothermal waves (HTWs) in volatile drops. *Langmuir*, **29** (31), 9750–9760.
46. Sefiane, K., Moffat, J.R., Matar, O.K., and Craster, R.V. (2008) Self-excited hydrothermal waves in evaporating sessile drops. *Appl. Phys. Lett.*, **93** (7), 074103.
47. Fabien, G., Antoni, M., and Sefiane, K. (2010) Infrared thermography investigation of an evaporating sessile water droplet on heated substrates. *Langmuir*, **26** (7), 4576–4580.
48. Still, T., Yunker, P.J., and Yodh, A.G. (2012) Surfactant-induced Marangoni eddies alter the coffee-rings of evaporating colloidal drops. *Langmuir*, **28** (11), 4984–4988.
49. Truskett, V.N. and Stebe, K.J. (2003) Influence of surfactants on an evaporating drop: fluorescence images and particle deposition patterns. *Langmuir*, **19** (20), 8271–8279.
50. Talbot, E.L., Berson, A., and Bain, C.D. (2013) Internal flows and particle transport inside picoliter droplets of binary solvent mixtures. NIP29: 29th International Conference on Digital Printing Technologies, and Digital Fabrication 2013, September/October, 2013, pp. 307–312, ISSN: 978-0-89208-307-7.
51. Kajiyi, T., Nishitani, E., Yamaue, T., and Doi, M. (2006) Piling-to-buckling transition in the drying process of polymer solution drop on substrate having a large contact angle. *Phys. Rev. E*, **73**, 011601.
52. Sempels, W., de Dier, R., Mizuno, H., Hofkens, J., and Vermant, J. (2013) Auto-production of biosurfactants reverses the coffee ring effect in a bacterial system. *Nat. Commun.*, **4** (1757), 1–8.
53. Wong, T., Chen, T., Shen, X., and Ho, C. (2011) Nanochromatography driven by the coffee ring effect. *Anal. Chem.*, **83**, 1871–1873.
54. Kruglova, O., Demeyer, P.-J., Zhong, K., Zhou, Y., and Clays, K. (2013) Wonders of colloidal assembly. *Soft Matter*, **9**, 9072–9087.
55. Bigioni, T.P., Lin, X.-M., Nguyen, T.T., Corwin, E.I., Witten, T.A., and Jager, H.M. (2006) Kinetically driven self assembly of highly ordered nanoparticles monolayers. *Nat. Mater.*, **5**, 265–270.
56. Kaya, D., Belyi, V.A., and Muthukumar, M. (2010) Pattern formation in drying

- droplets of polyelectrolyte and salt. *J. Chem. Phys.*, **133**, 114905.
57. Sefiane, K. (2004) Effect of nonionic surfactant on wetting behavior of an evaporating drop under a reduced pressure environment. *J. Colloid Interface Sci.*, **272**, 411–419.
  58. Innocenzi, P., Malfatti, L., and Falcaro, P. (2014) *Water Droplets to Nanotechnology: A Journey Through Self-Assembly*, RSC Publishing, Reviewed by Ian Hamley.
  59. Xu, W. and Choi, C.-H. (2012) From sticky to slippery droplets: dynamics of contact line deepening on superhydrophobic surfaces. *Phys. Rev. Lett.*, **109**, 024504.
  60. Adamson, A.W. and Gast, A.P. (1997) *Physical Chemistry of Surfaces*, 6th edn, John Wiley & Sons, Inc..
  61. Oliver, J.F., Huh, C., and Mason, S.G. (1976) Resistance to spreading of liquids by sharp edges. *J. Colloid Interface Sci.*, **59**, 568–581.
  62. Raphaël, E. and de Gennes, P.G. (1989) Dynamics of wetting with nonideal surfaces. *J. Chem. Phys.*, **90**, 7577–7584.
  63. Weon, B.M. and Je, J.H. (2013) Self-pinning by colloids confined at a contact line. *Phys. Rev. Lett.*, **110**, 028303.
  64. Park, J. and Moon, J. (2006) Control of colloidal particle deposit patterns within picolitre droplets ejected by ink-jet printing. *Langmuir*, **28** (8), 3506–3513.
  65. Prevo, B.G. and Velez, O.D. (2004) Controlled, rapid deposition of structured coatings from micro- and nanoparticle suspensions. *Langmuir*, **20**, 2099–2107.
  66. Mix, A.W., Chen, Z.B., Johnson, L.M., and Giacomini, A.J. (2011) Blotching in roll coating. *J. Coat. Technol. Res.*, **8**, 67–74.
  67. Cawse, J.N., Olson, D., Chisholm, B.J., Brennan, M., Sun, T., Flanagan, W., Akhave, J., Mehrabi, A., and Saunders, D. (2003) Combinatorial chemistry methods for coating development V: generating a combinatorial array of uniform coatings samples. *Prog. Org. Coat.*, **47**, 128–135.
  68. Derby, B. (2011) Inkjet printing ceramics: from drops to solid. *J. Eur. Ceram. Soc.*, **31**, 2543–2550.
  69. de Gans, B.-J., Duineveld, P.C., and Schubert, U.S. (2004) Inkjet printing of polymers: state of the art and future developments. *Adv. Mater.*, **16**, 203–213.
  70. Dou, R. and Derby, B. (2012) Formation of coffee stains on porous surfaces. *Langmuir*, **28**, 5331–5338.
  71. Dugas, V., Broutin, J., and Souteyrand, E. (2005) Droplet evaporation study applied to DNA chip manufacturing. *Langmuir*, **21**, 9130–9136.
  72. Fang, X., Li, B., Petersen, E., Seo, Y.-S., Samuilov, V.A., Chen, Y., Sokolov, J.C., Shew, C.-Y., and Rafailovich, M.H. (2006) Drying of DNA droplets. *Langmuir*, **22**, 6308–6312.
  73. Huang, J., Tao, A.R., Connor, S., He, R., and Yang, P. (2006) A general method for assembling single colloidal particle lines. *Nano Lett.*, **6**, 524–529.
  74. Cuk, T., Troian, S.M., Hong, C.M., and Wagner, S. (2000) Using convective flow splitting for the direct printing of fine copper lines. *Appl. Phys. Lett.*, **77**, 2063–2065.
  75. Magdassi, S., Grouchko, M., Toker, D., Kamyshny, A., Balberg, I., and Millo, O. (2005) Ring stain effect at room temperature in silver nanoparticles yields high electrical conductivity. *Langmuir*, **21**, 10264–10267.
  76. Layani, M., Gruchko, M., Milo, O., Balberg, I., Azulay, D., and Magdassi, S. (2009) Transparent conductive coatings by printing coffee ring arrays obtained at room temperature. *ACS Nano*, **3** (11), 3537–3542.
  77. Levy-Sakin, M. and Ebenstein, Y. (2013) Beyond sequencing: optical mapping of DNA in the age of nanotechnology and nanoscopy. *Curr. Opin. Biotechnol.*, **24**, 690–698.
  78. Vancauwenberghe, V., Di Marco, P., and Brutin, D. (2013) Wetting and evaporation of a sessile drop under an external electrical field: a review. *Colloids Surf., A: Physicochem. Eng. Aspects*, **432**, 50–56.
  79. Eral, H.B., Mampallil Augustine, D., Duits, M.H.G., and Mugele, F. (2011)

- Suppressing the coffee stain effect: how to control colloidal self-assembly in evaporating drops using electrowetting. *Soft Matter*, **7**, 4954–4958.
80. Tamaddon, A.H., Mertens, P.W., Vermant, J., Vereecke, G., Holsteyns, F., Heyns, M., and De Gendt, S. (2014) Role of ambient composition on the formation and shape of watermarks on a bare silicon substrate. *ECS J. Solid State Sci. Technol.*, **3**, N3081–N3086.
  81. Kajiya, T., Kobayashi, W., Okuzono, T., and Doi, M. (2009) Controlling the drying and film formation processes of polymer solution droplets with addition of small amount of surfactants. *J. Phys. Chem. B*, **113**, 15460–15466.
  82. Shen, X., Ho, C.-M., and Wong, T.-S. (2010) Minimal size of coffee ring structure. *J. Phys. Chem. B*, **114**, 5269–5274.
  83. Takhistov, P. and Chang, H.-C. (2002) Complex stain morphologies. *Ind. Eng. Chem. Res.*, **41**, 6256–6269.
  84. Deegan, R.D. (2000) Pattern formation in drying drops. *Phys. Rev. E*, **61** (1), 475–485.
  85. Marín, Á.G., Gelderblom, H., Lohse, D., and Snoeijer, J.H. (2011) Rush-hour in evaporating coffee drops. *Phys. Fluids*, **23**, 091111.
  86. Baldwin, K.A., Granjard, M., Willmer, D.I., Sefiane, K., and Fairhurst, D.J. (2011) Drying and deposition of poly(ethylene oxide) droplets determined by Peclet number. *Soft Matter*, **7**, 7819–7826.
  87. Hodges, C.S., Ding, Y., and Biggs, S. (2010) The influence of nanoparticle shape on the drying of colloidal suspensions. *J. Colloid Interface Sci.*, **352** (1), 99–106.
  88. Yunker, P.J., Still, T., Lohr, M.A., and Yodh, A.G. (2011) Suppression of the coffee-ring effect by shape-dependent capillary interactions. *Nature*, **476** (7360), 308–311.
  89. Dugyala, V.R. and Basavaraj, M.G. (2014) Control over coffee-ring formation in evaporating liquid drops containing ellipsoids. *Langmuir*, **30**, 8680–8686.
  90. Jung, J.-Y., Kim, Y.W., Yoo, J.Y., Koo, J., and Kang, Y.T. (2010) Forces acting on a single particle in an evaporating sessile droplet on a hydrophilic surface. *Anal. Chem.*, **82** (3), 784–788.
  91. Yan, Q., Gao, L., Sharma, V., Chiang, Y.-M., and Wong, C.C. (2008) Particle and substrate charge effects on colloidal self-assembly in a sessile drop. *Langmuir*, **24** (20), 11518–11522.
  92. Pauchard, L. and Allain, C. (2003) Buckling instability induced by polymer solution drying. *Europhys. Lett.*, **62** (6), 897–903.
  93. Sobac, B. and Brutin, D. (2014) Desiccation of a sessile drop of blood: cracks, folds formation and delamination. *Colloids Surf., A: Physicochem. Eng. Aspects*, **448**, 34–44.
  94. Routh, A.F. (2013) Drying of thin colloidal films. *Rep. Prog. Phys.*, **76**, 046603.
  95. Talbot, E.L., Yang, L., Berson, A., and Bain, C.D. (2014) Control of the particle distribution in inkjet printing through an evaporation-driven sol-gel transition. *Appl. Mater. Interfaces*, **6** (12), 9572–9583.
  96. Fan, F. (2004) Assembly of colloidal particles by evaporation on surfaces with patterned hydrophobicity. *Langmuir*, **20** (8), 3062–3067.
  97. Léopoldès, J., Dupuis, A., Bucknall, D.G., and Yeomans, J.M. (2003) Jetting micron-scale droplets onto chemically heterogeneous surfaces. *Langmuir*, **19** (23), 9818–9822.
  98. Alam, P., Toivakka, M., Backfolk, K., and Sirviö, P. (2007) Impact spreading and absorption of Newtonian droplets on topographically irregular porous materials. *Chem. Eng. Sci.*, **62** (12), 3142–3158.
  99. Vrancken, R.J., Blow, M.L., Kusumaatmaja, H., Hermans, K., Prenen, A.M., Bastiaansen, C.W.M., Broer, D.J., and Yeomans, J.M. (2013) Anisotropic wetting and de-wetting of drops on substrates patterned with polygonal posts. *Soft Matter*, **9** (3), 674–683.
  100. Lewis, J.A. (2002) Direct-write assembly of ceramics from colloidal inks. *Curr. Opin. Solid State Mater. Sci.*, **6**, 245–250.



# 11

## Simulation of Drops on Surfaces

*Mark C T Wilson and Krzysztof J Kubiak*

### 11.1

#### Introduction

This chapter explores ways in which the interactions of liquid drops with solid surfaces can be simulated using numerical methods. Simulations are desirable for a number of reasons, for example: (i) to provide additional insight to complement what can be achieved experimentally, (ii) to explore new (potentially far-fetched) ideas before performing experiments, and hence “steering” experiments efficiently, and (iii) to provide an optimization tool, possibly exploiting formal mathematical/computational optimization methods or automated approaches, for identifying the optimal system design and operating parameters.

Given the success and accuracy with which drop formation can be simulated (see Chapter 7), one could be forgiven for thinking that simulating the spreading of a simple, nonspashing drop on a smooth, uniform solid surface is a straightforward undertaking. In fact, even this seemingly simple scenario is rather challenging to model, and genuinely predictive simulations of such systems are still not well established. The key issue is in dealing with the moving contact line, that is, the line at which the surface of the drop meets the solid surface, and this is discussed in detail in later sections.

Simulations are built upon mathematical models that attempt to capture the physics governing the behavior of the system of interest. Indeed, a simulation is essentially an implementation of a mathematical model, using appropriate numerical approximations of either the equations (as in finite-difference-based methods) or the solution of the equations (as in the finite element method) to allow one to include complicated geometries and to solve nonlinear equations and boundary conditions and so on. For a simulation to be useful, validation of its predictions against experimental observations is crucial. If a system can be simulated in a reliable way, this supports the conclusion that the physical mechanisms and models in the underlying theory are correct and indicates that the system is well understood. The simulation can then be used as a tool for exploration, design, and optimization as mentioned.

There are essentially two sources of error in a simulation. Firstly, there are discretization errors, which arise from the approximations made in solving the relevant equations numerically. Most simulations involve some form of computational mesh comprising cells or elements, and the predictions of the simulation can be sensitive to the size, shape, and distribution of such elements. The second, and more fundamental, source of error is in the mathematical model itself, that is, does the model include sufficient physics to represent properly the problem of interest? The challenge posed by moving contact lines is that their behavior is a result of simultaneous effects at both molecular and macroscopic length scales. In other words, wetting is a multiscale phenomenon.

## 11.2

### Continuum-Based Modeling of Drop Dynamics

The usual approach to simulating fluid flows is to consider the fluids involved as continuous media, that is, without an underlying molecular composition. Under this continuum hypothesis, molecular length and time scales become zero, and so the representation of the surface of a drop – the liquid–air interface – is a mathematical surface of zero thickness. In reality, this interface has a nonzero thickness typically of a few molecules, but on the scale of even a tiny inkjet drop, this is still very small. As explained in Chapter 2, the fact that molecules at the liquid–air interface experience asymmetric cohesive intermolecular forces gives rise to the surface (or interfacial) tension. In the continuum model, the surface tension, denoted by  $\gamma$ , is a property of the zero-thickness surface.

In the bulk of the liquid, the flow is governed by the Navier–Stokes and continuity equations described in Chapter 2 for the velocity and pressure fields,  $\mathbf{u}(\mathbf{x})$  and  $p(\mathbf{x})$ , respectively, where  $\mathbf{x} = (x, y, z)$  is position in space. These nonlinear, continuous partial differential equations are solved numerically by discretizing them into a large set of simultaneous algebraic equations using one of a number of well-established approaches such as finite element or finite volume methods, which involve dividing the simulation volume (or “domain”) into small elements or cells. Solving this large matrix system produces values of the velocity components and pressure at a set of “nodes” throughout the flow domain.

#### 11.2.1

##### Finite Element Analysis

The numerical method most suited to the zero-thickness “sharp”-interface model described is the finite element method (described in Chapter 2). In that approach, the liquid domain is divided into contiguous elements, which can have linear or curved edges and surfaces. Figure 11.1a shows a two-dimensional representation. Over each element, the velocity components and the pressure field are approximated by low-order (typically linear or quadratic) polynomial functions, which interpolate the variables between the nodes in the element. The edges (in 2D) or

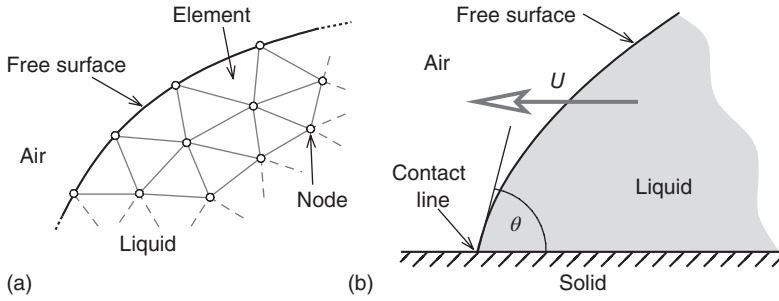


**Figure 11.1** (a) Representation of a liquid volume by a mesh of finite elements fitted to the free-surface shape and (b) a liquid volume spreading from right to left across a solid surface.

surfaces (in 3D) of the elements adjacent to the free surface of the liquid actually define that surface, and so the finite element mesh is always fitted to the shape of the drop and evolves with it. Note that, since inkjet printing normally occurs in air, which has a much lower density and viscosity than liquid, the air surrounding the liquid is typically not modeled explicitly but represented as an inviscid, passive ambient medium of constant pressure. An early example of using finite element analysis for an impacting and spreading drop is the work of Fukai *et al.* [1].

### 11.2.2

#### Finite Element Boundary Conditions for Free Surfaces

To illustrate the boundary conditions, we will consider a two-dimensional representation of a free-surface flow in which a body of liquid is advancing at speed  $U$  from right to left across a solid surface (see Figure 11.1b). Let us assume that all variables are made dimensionless by dividing all lengths by a characteristic length,  $L$ , all velocities by  $U$ , time by  $L/U$ , and pressure by  $\mu U/L$  where  $\mu$  is the dynamic viscosity of the liquid. Along the free surface of the liquid, the so-called kinematic condition,

$$(\mathbf{u} - \dot{\mathbf{x}}_{fs}) \cdot \hat{\mathbf{n}} = 0 \quad (11.1)$$

applies, where  $\mathbf{x}_{fs}$  represents the coordinates of a point on the free surface and  $\hat{\mathbf{n}}$  is the normal to the surface. This condition is usually used to update the position of the free surface as the simulation progresses. The conditions on stress at the free surface can be written as

$$\hat{\mathbf{n}} \cdot \boldsymbol{\sigma} = \frac{1}{Ca} \frac{d\hat{\mathbf{t}}}{ds} \quad (11.2)$$

where  $\boldsymbol{\sigma}$  is the dimensionless stress tensor with components  $\sigma_{\alpha\beta} = -p\delta_{\alpha\beta} + \partial u_\alpha / \partial x_\beta + \partial u_\beta / \partial x_\alpha$ ,  $\hat{\mathbf{t}}$  is the tangent to the free surface,  $s$  is the distance (arc length) along the surface, and  $Ca = \mu U / \gamma$  is the capillary number. Equation (11.2) captures both the condition on the normal stress, that is, Laplace's law relating the pressure jump at the interface to the surface tension and curvature of the

interface, and the condition that the tangential stress is zero. Note that the pressure is usually expressed relative to the ambient pressure, meaning that  $p = 0$  outside the drop. The 11.2 conditions can be incorporated very naturally in the finite element method, because the derivation of the finite element equations (i.e., the system of simultaneous algebraic equations) involves integration over the fluid volume, and this in turn involves an integration of  $\hat{\mathbf{n}} \cdot \boldsymbol{\sigma}$  over the surface of the domain. The surface integrand can hence be replaced using Eq. (11.2).

### 11.2.3

#### The Moving Contact-Line Problem

When a fluid is in contact with a solid surface, the well-established boundary condition applied in the standard fluid mechanics framework is the so-called no-slip condition, that is, the velocity of the fluid at the solid surface is equal to the velocity of the solid. In the case of inkjet printing, though the substrate being printed might be moving through the printer, if we take our frame of reference to be the substrate, so that we move with it, the solid surface in our simulation becomes a stationary surface, that is,  $\mathbf{u} = 0$ . Now consider a liquid drop impacting and spreading on the substrate. As mentioned in the introduction, the “contact line” is where the free surface of the liquid drop meets the solid surface. As the drop spreads out, this contact line is clearly moving over the stationary substrate. The velocity at the contact is therefore in violation of the no-slip condition.

To explore this (in)famous fluid mechanics problem further, it is easier to change our frame of reference so that we move with the contact line. To simplify the problem further, we will consider for now a steady two-dimensional flow, as shown in Figure 11.2.

Here, the contact line appears as a point at a fixed position, and the solid surface now has a speed  $U$  relative to the contact line. This arrangement can be realized practically in the steady plunging of a tape into a bath of liquid [2, 3]. The free surface now has a steady shape, and the kinematic condition 11.1 simplifies to

$$\mathbf{u} \cdot \hat{\mathbf{n}} = 0 \quad (11.3)$$

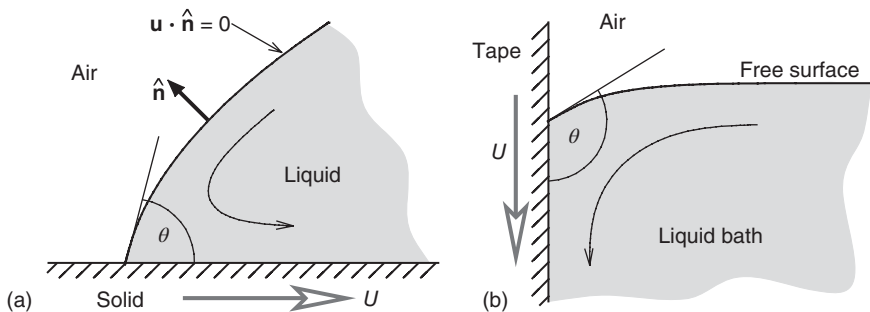


**Figure 11.2** (a) A steadily advancing contact line viewed from a frame of reference moving with the contact line and (b) schematic of a plunging tape experiment in which the free surface has a fixed shape and location with respect to the laboratory.



The no-slip condition becomes

$$\mathbf{u} = U\hat{\mathbf{t}}_s \quad (11.4)$$

where  $\hat{\mathbf{t}}_s$  is the tangent to the solid surface. Hence, on each interface, the velocity is along the tangent to the interface. If the contact angle,  $\theta$ , has a value of  $180^\circ$ , the free surface meets the solid at a cusp; the two tangents then match, and the liquid traveling along the free surface can accelerate smoothly to reach the speed of the solid. However, a problem arises if (as is usually the case)  $\theta < 180^\circ$ . In that case, there is a finite corner and the tangents to the free surface and the solid surface are not parallel. Clearly, it is not possible to satisfy both Eqs. 11.3 and 11.4. The liquid would have to experience an infinite acceleration at the contact line, resulting in a singularity in the shear stress.

The usual approach to circumventing this problem is to replace the no-slip condition (11.4) with some form of velocity condition that allows for slip between the liquid and the solid. This can take the form of a specific velocity distribution, such as  $\mathbf{u} = U[1 - \exp(-x/\lambda)]\hat{\mathbf{t}}_s$ , where  $x$  is distance from the contact line and  $\lambda$  is a specified “slip length,” or the Navier condition, which relates the liquid velocity at the solid surface to the shear stress on the solid:

$$u - U = \frac{\mu}{\beta} \frac{\partial u}{\partial y} \quad (11.5)$$

where  $\mu$  is the liquid viscosity and  $\beta$  is a coefficient of sliding friction. Such conditions remove the problem of the incompatibility of the boundary conditions, and the associated shear-stress singularity, though there is still an integrable singularity in the pressure field [4].

#### 11.2.3.1 The Contact Angle as a Boundary Condition

In order to complete the mathematical model described, the contact angle needs to be specified. In the finite element framework, this can be done by substituting the appropriate value of the tangent to the free surface at the contact line where it appears in the finite element equations [5] or the condition on the tangent can be used to update the position of the contact line. Note that the contact angle is the only way in which the particular surface chemistry of the liquid and solid enters the mathematical model.

The need to impose the contact angle as an input to the simulation substantially degrades the predictive power of the simulation, particularly as the contact angle can exhibit complex behavior, as explored further in Section 11.3.

#### 11.2.3.2 An Interface Formation Model

An important development in the modeling of moving contact lines is the “interface formation model” of Shikhmurzaev [6]. This model recognizes that as a contact line advances across a solid, the solid–air interface is replaced by a solid–liquid interface, that is, a new solid–liquid interface is created. The supposition is that the molecules in this interface do not achieve their equilibrium state instantaneously but take time to do so. Since the new interface starts at the contact line, which moves across the solid, this implies that the interfacial tension

of the solid–liquid interface has a nonequilibrium value at the contact line and that it relaxes toward its equilibrium value away from the contact line. Experiments [7] have shown that as a contact line advances across a solid, the liquid “rolls” over the solid, so that liquid molecules that were part of the liquid–air interface pass through the contact-line region and into the solid–liquid interface. Hence, as these molecules approach the contact line, it can be expected that their equilibrium arrangement at the liquid–air interface will start to adjust as part of the process of becoming liquid–solid molecules. (Of course, this is a simple, ensemble-based view; in practice, individual molecules are continuously exchanged between interfaces and the bulk in a dynamic equilibrium that results in observed interfacial properties such as surface tension.)

Now, for a static drop sitting at rest on a flat solid, the contact angle satisfies Young’s equation, which is a force balance at the contact line in the direction parallel to the solid surface:

$$\gamma \cos \theta = \gamma_{SG} - \gamma_{SL} \quad (11.6)$$

where  $\gamma_{SG}$  and  $\gamma_{SL}$  are the interfacial tensions of the solid–gas (i.e., solid–air) and solid–liquid interfaces, respectively. Recall that  $\gamma$  is the surface tension of the liquid–air interface. A cornerstone of the interface formation model is the assumption that Eq. (11.6) also holds in the dynamic case, that is, when the contact line is moving. As mentioned, when the contact line moves, the interfacial tensions at the contact line are expected to have different values from their equilibrium ones, and Eq. (11.6) provides the means by which the contact angle can be determined.

The interface formation model includes additional boundary conditions on the interfaces that account for a net mass flux between the interfaces and the bulk, as part of the interface formation/destruction process, and generalizations of standard boundary conditions, together with equations of state for the interfaces, which account for the effects of varying interfacial tensions. Together, these form a complete model of the wetting process, which is the only sharp-interface model that does not require the contact angle to be specified as a boundary condition; it is determined as part of the solution. Given the mathematical complexity of the model, implementation is only feasible within the finite element framework, where the interfaces are well represented. For details of such implementation, see Sprittles and Shikhmurzaev [8], [9]. The model has recently been applied to axisymmetric drop impact and spreading [10].

#### 11.2.4

##### The Volume of Fluid Method

A very popular method for modeling free-surface flows is the so-called *volume-of-fluid* (VOF) approach [11]. Unlike the finite element approach described, where the computational mesh is fitted to the free-surface shape, in the VOF method, a fixed mesh is used and the free surface moves through the mesh. The position of the free surface is represented by means of a function,  $F$ , which, at each point in

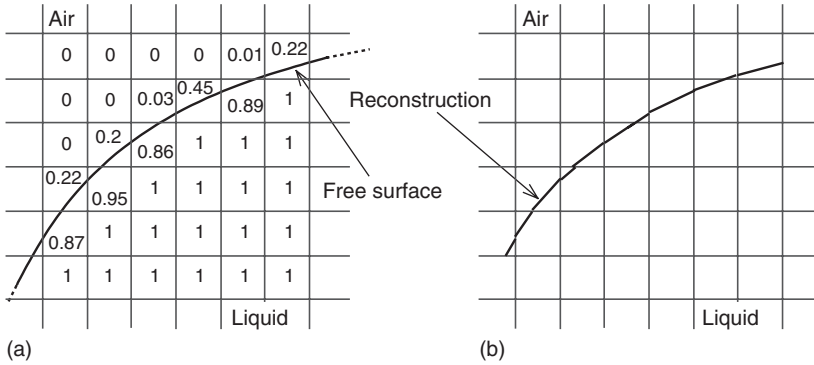


**Figure 11.3** Volume-of-fluid representation of a free surface via a fixed mesh defining cells having a volume fraction indicating how much of the cell is occupied by liquid. In (a), the same free surface as in

Figure 11.1a is shown with corresponding volume fractions, while (b) shows a piecewise linear reconstruction of the free surface from the volume fractions.

space, has a value of 1 if the point is occupied by liquid and zero if not. Averaging over a cell within the mesh, this gives the fraction of the volume of the cell that is filled with liquid. Hence, each cell has associated with it a volume fraction,  $C$ , such that  $0 \leq C \leq 1$ , see Figure 11.3.

The movement of the free surface is determined by the advection of  $F$  with the flow:

$$\frac{\partial F}{\partial t} + \nabla \cdot (\mathbf{u}F) = 0 \quad (11.7)$$

The governing equations for the flow are the Navier–Stokes equations, which are typically solved using the finite volume method. Representing the position of the interface as a collection of volume fractions is computationally efficient, but the detailed shape of the free surface is lost. Hence, a key step in the VOF approach is the reconstruction of the interface shape, so that the boundary conditions on stress (in particular, that the pressure on the free boundary is equal to the curvature of the boundary multiplied by the surface tension) can be determined and applied. By approximating the free surface as a straight line within a partially filled cell, it is possible to use the volume fractions in neighboring cells to determine the slope of this line and then to position the line within the cell to match its volume fraction. Careful calculations of the curvature can then also be made. Contact angles can be imposed directly as a geometric constraint on the interface.

Since the VOF method first appeared, there have been many developments of it. A popular approach is to model the liquid and the surrounding fluid in a two-fluid model, with the surface tension being included via the “continuum surface force” (CSF) approach [12]. In that approach, the surface tension is included as a source term in the Navier–Stokes equations as [13]:

$$f_\gamma = \gamma \left[ -\nabla \cdot \left( \frac{\nabla C}{|\nabla C|} \right) \right] \nabla C \quad (11.8)$$

Away from the free surface, the gradient of the volume fraction  $C$  is zero, so Eq. (11.8) only provides a contribution close to the free surface.

VOF-based methods have been applied to drop impact and spreading in many works, see, for example, Šikalo *et al.* [13], Pasandideh-Fard *et al.* [14], Bussman *et al.* [15], Nikolopoulos [16], and Yokoi *et al.* [17]. All of these require the contact angle to be specified. Though the VOF method is based on a sharp-interface representation of the liquid–air interface, in practice, the cell-based volume fraction inevitably leads to a blurring of the interface over several cells. The size of free-surface features that can be resolved is limited by the size of the cells in the mesh. The VOF algorithms dealing with the interface reconstruction and advection can be rather intricate, but VOF-based simulations are generally less computationally intensive than finite element simulations, especially in three dimensions.

The commercial software FLOW-3D is built upon the VOF method and includes both the single-fluid and two-fluid models. Other commercial and open-source computational fluid dynamics programs also feature a VOF capability for two-phase flow, for example, ANSYS Fluent, STAR-CCM+, and OpenFOAM.

### 11.3

#### Challenging Contact Angle Phenomena

An essential stage in the development of a successful – and useful – simulation is to validate the predictions of the simulation against experimental observations of the same system. Given the reliance of the previously described simulation approaches on the contact angle as an input parameter, here, we explore some of the features and phenomena related to contact angles that make predictive simulation of drops on surfaces so challenging.

#### 11.3.1

##### Apparent Contact Angles

The first point to note in comparing simulation and experiments is that, while the sharp-interface mathematical model includes a precise contact angle at a specific point, experimentally, it is impossible to measure the contact angle so precisely. There is always a finite resolution. Direct measurements of the contact angle are therefore actually measurements of the tangent to the free surface close to, but not precisely at, the contact line. One can refer to such measured contact angles as “apparent contact angles” to acknowledge the finite resolution of the observation (see Figure 11.4a).

An alternative approach is to measure the positions of key features of the free surface and to deduce the contact angle by assuming a particular geometrical form for the surface. For an inkjet-sized drop sitting in equilibrium on a substrate, the assumption that the free surface is a spherical cap is a reasonable one, since gravity will have a negligible effect on the shape at that length scale. By measuring the

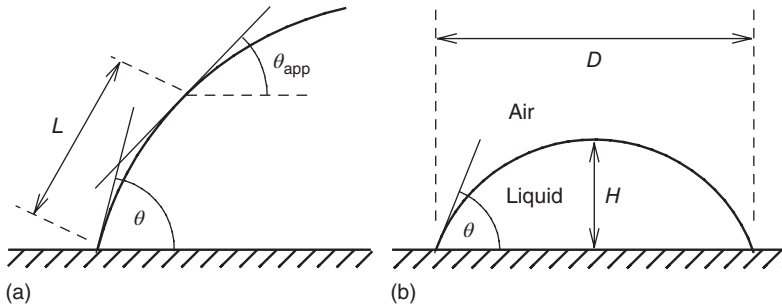


**Figure 11.4** (a) In a direct measurement of a contact angle, there is inevitably a finite resolution of the experimental image, meaning that the “apparent contact angle” measured is actually the tangent to the free surface at some distance  $L$  from the contact

line; and (b) for small drops, where the free surface is well captured by a circular arc, the contact angle can be calculated from measurements of the height and contact diameter.

height  $H$  of the drop and the diameter  $D$  of its contact with the solid, one can calculate the contact angle using (see Figure 11.4b)

$$\theta = 2 \tan^{-1} \left( \frac{2H}{D} \right) \quad (11.9)$$

As an exercise, verify Eq. (11.9) and compute error  $\theta - \theta_{\text{app}}$  versus  $(L, D, \theta)$ . Such contact angles are also referred to as *apparent contact angles*. There are still errors associated with this approach – even when the geometrical assumption is a good one – because it can sometimes be difficult to identify clearly where the contact line is and, hence, evaluate the diameter  $D$ . The discrepancy between the “real” and “mathematical” contact angle and the apparent contact angle becomes much more evident when the contact line is moving, as discussed in Section 11.3.3.

### 11.3.2

#### Contact Angle Hysteresis

When a drop is sitting at equilibrium on a horizontal solid surface, the contact angle observed is referred to as the *static* or *equilibrium* contact angle. For a given liquid, its value will depend on the material the substrate is composed of. However, the static contact angle is rarely unique – most solid surfaces feature heterogeneities that give rise to a range of possible static contact angles, which means that the static contact angle observed depends on the history of the drop, that is, how it was deposited on the solid. This is known as *contact angle hysteresis*, and the limiting values of the static contact angle that can be observed are known as the *advancing* contact angle,  $\theta_A$ , and the *receding* angle,  $\theta_R$ .

To illustrate the significance of this, consider the controlled experiment shown in Figure 11.5a, in which liquid is ejected slowly through a small circular hole in a horizontal substrate out onto the solid surface. As the free surface emerges from the orifice, the contact line will stay “pinned” to the rim until the contact angle

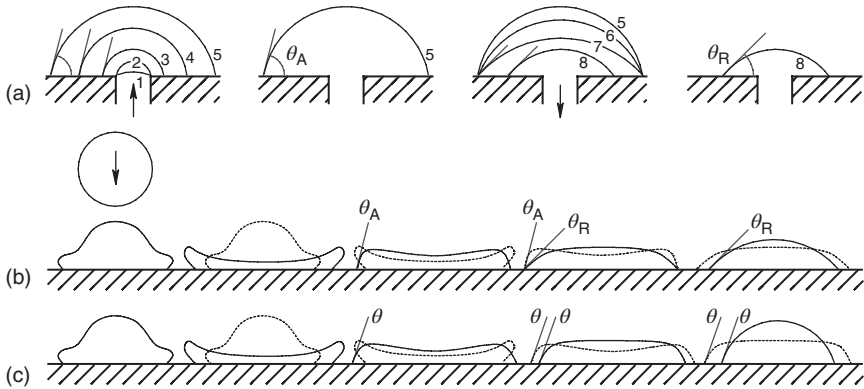


**Figure 11.5** Contact angle hysteresis: (a) sketch of an experiment in which a liquid drop is grown and subsequently shrunk, resulting in different observed static contact angles; drop impact and spreading on a surface with (b) substantial hysteresis, showing the pinning of the contact line, and (c) no hysteresis, showing the lack of pinning.

between the free surface and the horizontal surface reaches a critical value. If the ejection is very slow, the drop will then expand and spread over the solid, maintaining the same contact angle, that is, the advancing contact angle. Suppose that the ejection is then stopped. The drop will remain in its final state, and the static contact angle observed will be  $\theta_A$ .

Now suppose that we extract liquid from the expanded drop through the hole. Instead of reversing its movement, the contact line will stay pinned in place while the drop shrinks in height and the contact angle reduces until it reaches another critical value, that is,  $\theta_R$ . If the extraction occurs very slowly, the contact line will then shrink and recede from the surface, maintaining the contact angle at  $\theta_R$ . If the extraction then stops again, the drop will remain in the configuration where the contact angle is equal to the receding value.

To see how contact angle hysteresis relates to drop deposition on a surface, Figure 11.5b shows a schematic of a drop being deposited on a surface with large contact angle hysteresis and one with small hysteresis. After the initial contact, the drop spreads with a contact angle greater than or equal to  $\theta_A$ . Once the drop reaches its maximum extent, the contact line is pinned while the free surface rises as surface tension causes the recoil of the drop, and the contact angle reduces. If  $\theta_R$  is small enough that the contact angle of the drop never falls below it, the contact line will remain pinned, and this will be its final configuration. On the other hand, if the contact angle falls below  $\theta_R$ , driven by the dynamics of the free surface, the contact line will contract. If  $\theta_A = \theta_R = \theta$ , that is, there is no hysteresis, the contact line will immediately start contracting to produce a final sessile drop with a contact angle of  $\theta$ , see Figure 11.5c.

Contact angle hysteresis is particularly important when consecutively printed drops coalesce [18]. In practice, two drops printed a short distance apart will end up with a “peanut”-shaped footprint. A simulation that does not take into account

contact angle hysteresis will incorrectly produce a combined drop with a circular footprint.

### 11.3.3

#### Dynamic Contact Angles

When a contact line moves, the apparent contact angle generally changes from the static contact angle, and the angle observed is referred to as the *dynamic contact angle*. If the contact line is advancing across the solid, as in a drop spreading, the dynamic contact angle generally increases with the speed of the contact line, while for receding contact lines, the dynamic contact angle generally decreases. The literature on dynamic contact angles is very extensive, stretching back several decades, and includes various attempts at determining empirical and theoretical models that capture the variation of the dynamic contact angle with the wetting speed.

An important contribution was made by Hoffman [19], who conducted systematic experiments with various oils spreading along glass capillaries. By using measurements of the positions of points on the meniscus and the assumption of a constant radius of curvature, he obtained apparent dynamic contact angles  $\theta_d$  over a wide range of capillary numbers. Plotting the contact angle data from the different oils against the capillary number showed that the data collapsed onto a single master curve. Though Hoffman did not provide an explicit form for this curve, Kistler [20] expresses it as

$$\theta_d = f_H(Ca) = \cos^{-1} \left\{ 1 - 2 \tanh \left[ 5.16 \left( \frac{Ca}{1 + 1.31Ca^{0.99}} \right)^{0.706} \right] \right\} \quad (11.10)$$

which is valid for perfectly wetting systems, that is, where the static contact angle  $\theta_s$  is zero. Hoffman suggested that this universal curve also applies when  $\theta_s > 0$  if a shift factor is included to take into account  $\theta_s$ , giving

$$\theta_d = f_H(Ca + f^{-1}(\theta_s)) \quad (11.11)$$

An alternative expression representing Hoffman's data was given by Jiang *et al.* [21] as

$$\frac{\cos \theta_s - \cos \theta_d}{\cos \theta_s + 1} = \tanh (4.96 Ca^{0.702}) \quad (11.12)$$

which was also tested against other published data. For small  $Ca$ , these expressions are also consistent with a theoretical result derived under the assumption  $Ca \ll 1$  and known as the *Hoffman–Voinov–Tanner law*:

$$\theta_d^3 - \theta_s^3 \cong c_T Ca \quad (11.13)$$

where  $c_T$  is approximately 72. A comprehensive asymptotic analysis of the dynamic contact angle during spreading of liquids was developed by Cox [22], from which various functional forms for  $\theta_d = f(U, \dots)$  can be obtained.

Note that all the aforementioned expressions stem from investigations of well-controlled and essentially two-dimensional wetting configurations, where

the contact line moves steadily over the substrate and viscous effects dominate. In drop impact and spreading, the movement of the contact line is determined by competition among inertial, viscous, and surface tension effects, and measurements of apparent contact angles during drop impact and spreading – even in axisymmetric cases – have shown very complicated behavior (e.g., Vadillo *et al.* [23] and Šikalo *et al.* [24]). Indeed, the experiments of Šikalo *et al.* [24] indicate that the dynamic contact angle is not only a function of the wetting speed but also a function of the flow field near to the contact line. A nonlocal hydrodynamic influence on the dynamic contact angle has also been reported in continuous wetting systems [4, 25] and clearly poses a problem for predictive simulations based just on expressions such as Eqs. (11.10–11.13).

Two other approaches to understanding the phenomena of dynamic contact angles are worth noting. One is the “molecular kinetic” theory first described by Blake and Haynes [26]. This is based on the statistical dynamics of the molecules in the region close to the contact line (which, on a molecular scale, is more of a region) and the adsorption and desorption of molecules from each fluid as the contact line moves. The expression relating the contact line speed to the dynamic contact angle that arises from the theory is

$$\cos \theta_d = \cos \theta_s \mp \frac{2kT}{\gamma \lambda^2} \sinh^{-1} \left( \frac{U}{2\kappa_0 \lambda} \right) \quad (11.14)$$

where  $k$  is the Boltzmann constant,  $T$  is the absolute temperature,  $\kappa_0$  is the equilibrium frequency of molecular displacements, and  $\lambda$  is the average distance of each displacement. The positive/negative signs refer to advancing or receding movement of the contact line.

The other approach is the “interface formation model” of Shikhmurzaev [6] described in Section 11.2.3.2. The full model produces the dynamic contact angle as part of a complete solution of the whole flow and does not, therefore, involve a specific relationship between  $\theta_d$  and  $U$ . The model, therefore, has the potential to capture the nonlocal effects on  $\theta_d$  as mentioned earlier. An asymptotic form of the model has also been derived by Shikhmurzaev [27], which does provide an expression for  $\theta_d$ , but interestingly even this includes a term involving the speed of the liquid on the free surface at a finite (i.e., nonlocal) distance away from the contact line.

#### 11.3.4

#### Dynamic Contact Angles in Numerical Simulations

As mentioned earlier, in sharp-interface-based simulations, the contact angle is required as a boundary condition. The simplest approach in specifying the dynamic contact angle is to set it equal to the static contact angle. The rationale is that the free surface will “bend” substantially due to viscous effects in the region very close to the contact line, below the resolution of experiments, and that experimentally observed behaviors of the apparent contact angle are a result of this. However, high-resolution finite element calculations performed by Wilson



*et al.* [4] to capture this “viscous bending” showed that, in the continuous wetting problem they considered, it was impossible to match the experimentally observed apparent contact angle using the condition  $\theta_a = \theta_s$ .

A challenge in dealing with fully three-dimensional simulations of printed drops (as is required, e.g., in simulating consecutively printed drops or printing onto nonuniform substrates) is that the dynamic contact angle varies along the contact line; indeed, parts of the contact line can be advancing while others are receding. Bussman *et al.* [15] performed 3D simulations of drop impact onto a step and used values of the dynamic contact angle interpolated from experimental photographs. This produced good agreement with the experiments but clearly provided no predictive capability. To improve the prediction value of the simulation, they also tested a contact angle model in which they applied a typical “leading” contact angle value at all points on the contact line that were calculated to be advancing and a typical “trailing” value at receding points. Poorer but “reasonable” agreement with the experimental observations was claimed.

In their axisymmetric level set–VOF simulations, Yokoi *et al.* [17] tested several different contact angle models, including one based on Eq. (11.13) and others based on maximum/minimum dynamic contact angles and equilibrium angles. Their results highlighted the sensitivity of the predictions to the contact angle model. The models based on maximum/minimum dynamic angles and equilibrium angles showed poor agreement with experimental observations. However, their model that involved using Eq. (11.13) to approximate experimental measurements showed good agreement.

A popular approach to deal with the variation of the dynamic contact angle is to choose one of the relationships in the previous section and apply it during the simulation, by taking into account the instantaneous contact-line speed. However, determining the correct value of the contact-line speed involves its own subtleties. For example, Roisman *et al.* [28] illustrate that it cannot be reliably approximated by the velocity of a material point close to the contact line. There are several examples in the literature illustrating that the predictions of drop deposition simulations are sensitive to the contact angle imposed, with some concluding that good agreement between simulation and experiment can only be achieved if the experimentally observed contact angle is used.

### 11.3.5

#### Resting Time Effect

A further complication in dealing with contact angles is the potential for the advancing and receding contact angles of a sessile liquid drop to be a function of the time that the drop has spent in contact with the solid. Tadmor *et al.* [29] presented careful experiments to measure the retention force of drops on surfaces – that is, the force required to make a drop slide on a surface. This was performed by depositing drops onto a horizontal surface, waiting for different lengths of time (with appropriate measures to avoid evaporation), and then tilting the surface until the drops began to move. The lateral retention force (which can

be related to the advancing and receding contact angles) was determined from the drops' volume and density and the component of gravitational acceleration along the surface.

Results showed that this force increased substantially over typically 10–15 min for glass/mica surfaces and over longer times for Teflon surfaces. Measurements of the advancing and receding contact angles at the point of motion show an increase (decrease) in the advancing (receding) contact angle with time waited before tilting. The cause of the effect is attributed to deformation of the solid surface caused by the normal component of the surface tension or reconfiguration of the surface molecules.

The aforementioned timescales are much longer than the typical inkjet timescales. However, the initial rate of change of the force is large, and this may have a role to play in the “drawback” phenomenon seen when a drop is printed onto, but offset from, a previously deposited drop [30, 31]. In that scenario, the two drops are pulled together by surface tension forces in the liquid bridge (or “neck”) that forms between them. However, the first drop remains in place and the second drop is pulled into it [32]. This has important implications for the printing of continuous lines [33].

#### 11.4 Diffuse-Interface Models

In contrast with the sharp-interface models described in Section 11.2, diffuse-interface models begin with the perspective that liquid interfaces have a finite thickness over which thermodynamic variables change smoothly but rapidly between the bulk values on either side. Figure 11.6 compares the density profile through an interface in the sharp- and diffuse-interface representations. van der Waals introduced the first diffuse-interface theory, based on his equation of state, to explain why interfaces have surface tension, and these ideas have been developed over the ensuing century and more.

A key difference from the sharp-interface approach is that in the diffuse-interface model, the two phases are inherently included in the model. This means that to simulate drops impinging and interacting with a surface, it is necessary to

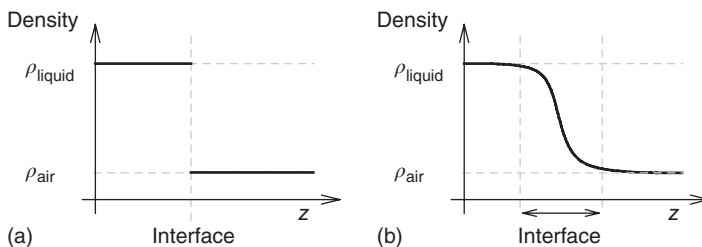


**Figure 11.6** Density profile through a liquid–air interface in (a) a sharp-interface and (b) a diffuse-interface representation. The coordinate  $z$  lies normal to the interface.

extend the computational domain to include sufficient ambient space, making the calculation more time-consuming. The liquid and surrounding fluid are modeled as a single fluid existing as different phases in different parts of the domain. The phases are identified by means of an “order parameter,” which could be the fluid density (for a single-component liquid–vapor system), the composition or mass fraction (for a two-component system), or, in general, a “phase field” function having constant values (e.g., +1 and –1) in the two phases and changing smoothly but rapidly in the interface region [34]. If necessary, the fluid properties such as viscosity can be interpolated between the bulk values using the local value of the phase field function. Indeed, diffuse-interface methods are also known as *phase field methods*.

The partial differential equations describing the two-phase system derive from the specific free energy of the system, which can be written as [35]

$$f = \frac{1}{4}\beta c^4 - \frac{1}{2}\alpha c^2 + \frac{1}{2}\varepsilon|\nabla c|^2 \quad (11.15)$$

where  $c$  is the mass fraction of one component and  $\alpha$ ,  $\beta$ , and  $\varepsilon$  are constants (for an isothermal system). The first two terms on the right-hand side are the Ginzburg–Landau free energy, representing the homogeneous free energy of a system having two coexisting stable states. The gradient term arises from a mean-field approximation [36] accounting for the finite range of intermolecular forces. For a planar interface at equilibrium, the concentration profile through the interface has the form

$$c(z) = \pm\sqrt{\alpha/\beta} \tanh\left(\frac{z}{\sqrt{2\varepsilon/\alpha}}\right) \quad (11.16)$$

where  $z$  is the coordinate through the interface. The quantity  $\sqrt{\varepsilon/\alpha}$  gives a measure of the thickness of the interface, and the surface tension of this interface is given by [37]

$$\gamma = \varepsilon \int_{-\infty}^{\infty} \left(\frac{dc}{dz}\right)^2 dz \quad (11.17)$$

From Eq. (11.15), equations governing the interface dynamics as well as force contributions to the Navier–Stokes equations, can be derived. These are quite complicated and are not listed here, but example applications and discussion relevant to simulating drop dynamics on surfaces can be found in Khatavkar *et al.* [35] and [38].

The presence of the solid surface in the domain is accounted for by modifying the free energy to include a “wetting potential,” which leads to a boundary condition for the gradient of the concentration at the solid. By the choice of the wetting potential, different contact angles can be included. Hence, in the diffuse-interface approach, the (static) contact angle is imposed in terms of an equilibrium surface energy rather than a geometrical constraint on the free surface. Note that the diffuse nature of the interface avoids the stress singularity in the moving contact-line problem, since it is possible to impose the no-slip condition on the solid surface,

and the contact line can move through diffusion [39]. Similarly to VOF models, phase field methods use a fixed computational mesh and the interface moves through the mesh. The commercial (finite-element-based) simulation software COMSOL Multiphysics includes an implementation of a phase field formulation for 2D or 3D two-phase flow, including wetting flows.

## 11.5

### Lattice Boltzmann Simulations of Drop Dynamics

All the numerical simulation methods described so far in this chapter involve some form of discretization of the continuous Navier–Stokes equations into a (very) large set of simultaneous algebraic equations to be solved for the values of velocity components and pressure at each node in the computational mesh. This could be described as a “top-down” approach, starting from macroscopically observable variables obeying continuous partial differential equations. At the other extreme, it is possible to model liquids at the atomic scale, through molecular dynamics (MD) simulations in which the movement of individual atoms is captured. Inevitably, MD simulations are severely limited in the length- and timescales that can be achieved, and such an approach is not of practical use for simulating real drops – even tiny inkjet drops.

Lying between these two extremes is a class of simulation methods known as *mesoscopic* methods, which attempt to preserve some of the molecular nature of the fluid, but in a statistical mechanics approach that enables simulations to access larger length- and timescales than MD. Arguably the most popular of these mesoscopic methods is the lattice Boltzmann (LB) method, which has been applied to a very diverse range of problems including many studies of drop dynamics and wetting. In the remainder of this chapter, we present some of our own simulations of drop dynamics using this approach.

#### 11.5.1

##### Background and Advantages of the Method

The lattice Boltzmann method is a very different approach from that of discretizing the Navier–Stokes equations. It has its origins in the kinetic theory of gases, and the lattice Boltzmann equation stems from the continuous Boltzmann equation,

$$\frac{\partial f}{\partial t} + \xi \cdot \nabla f + \mathbf{F} \cdot \left[ \frac{\partial f}{\partial \xi} \right] = \Omega(f) \quad (11.18)$$

describing the evolution of a single-particle probability distribution function,  $f(\mathbf{x}, \xi, t)$ . This function represents the probability of finding a fluid particle near to position  $\mathbf{x}$  that is moving with a velocity close to  $\xi$  at time  $t$ . The term on the right-hand side is a collision function that captures the relaxation of the system toward a local (Maxwellian) equilibrium distribution, and  $\mathbf{F}$  is an external force.

A simple form of the collision operator, proposed by Bhatnagar *et al.* [40], is

$$\Omega(f) = -\frac{1}{\tau}(f - f^{\text{eq}}) \quad (11.19)$$

where  $\tau$  is a relaxation time, and the equilibrium distribution function is given by

$$f^{\text{eq}} = \frac{\rho}{\sqrt{(2\pi RT)^3}} \exp\left[-\frac{(\boldsymbol{\xi} - \mathbf{u})^2}{RT}\right]. \quad (11.20)$$

In Eq. (11.20),  $\rho$  and  $\mathbf{u}$  are the macroscopic density and velocity of the fluid,  $R$  is the universal gas constant, and  $T$  is the absolute temperature. Relaxation toward this local equilibrium distribution takes place on the timescale of molecular flight between collisions, and the relaxation time is related to the viscosity of the fluid. The macroscopic quantities are determined from moments of  $f$ :

$$\rho(\mathbf{x}, t) = \int f(\mathbf{x}, \boldsymbol{\xi}, t) d\boldsymbol{\xi} \quad \rho(\mathbf{x}, t)\mathbf{u}(\mathbf{x}, t) = \int \boldsymbol{\xi} f(\mathbf{x}, \boldsymbol{\xi}, t) d\boldsymbol{\xi} \quad (11.21)$$

that is, by integration over velocity space. These integrals are approximated using quadrature, for example,

$$\int \omega(\boldsymbol{\xi}) f(\mathbf{x}, \boldsymbol{\xi}, t) d\boldsymbol{\xi} = \sum_i W_i \omega(\boldsymbol{\xi}_i) f(\mathbf{x}, \boldsymbol{\xi}_i, t) \quad (11.22)$$

where  $\omega$  is an arbitrary function and  $W_i$  are the weights. This process discretizes the continuous spectrum of molecular velocity by introducing a finite set of specific molecular velocities –  $\boldsymbol{\xi}_i$  in Eq. (11.22) – and gives rise to the structure of the “lattice,” since the links between nodes in the lattice correspond to  $\boldsymbol{\xi}_i$ .

For an isothermal 3D simulation, a popular (and the most stable) set of  $\boldsymbol{\xi}_i$  involves 19 vectors as shown in Figure 11.7. These vectors are given by the

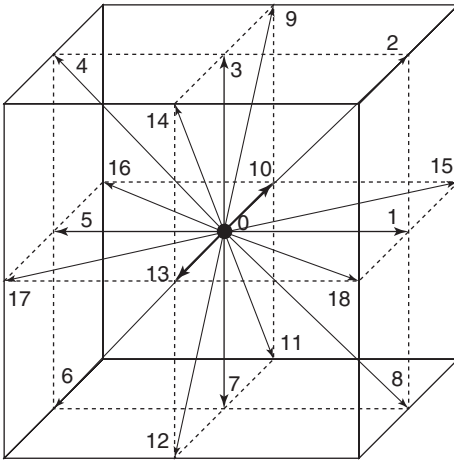


**Figure 11.7** Scheme of lattice node links for the “D3Q19” structure; this lattice is a standard lattice used in 3D simulations.

displacement from any node to all its nearest neighbors and all its next-nearest neighbors, plus the zero vector (note that the numbering in Figure 11.7 starts at zero, corresponding to the zero vector). Each link  $\xi_i$  in the lattice has associated with it a discrete distribution function,  $f_i \equiv W_i f_i^{\text{eq}}$ . Each node in the lattice, therefore, has a collection of 19 values  $f_i$  and, with each time step,  $\Delta t$ , these values propagate along the associated link to the next node. Note that the regular Cartesian lattice is the computational mesh of the LB method but, in addition to discretizing space as in other methods, it also embodies the discretization of the molecular velocities. For this reason, the lattice spacing,  $\Delta x$ , influences the kinematic viscosity,  $\nu$ , of the fluid being simulated, as seen in the relationship between the viscosity and the relaxation time:

$$\nu = \frac{1}{6}(2\tau - 1)(\Delta x)^2 / \Delta t \quad (11.23)$$

The discrete form of Eqs. (11.18) and (11.20) arrived at are

$$f_i(\mathbf{x} + \xi_i \Delta t, t + \Delta t) = f_i(\mathbf{x}, t) - \frac{1}{\tau} [f_i(\mathbf{x}, t) - f_i^{\text{eq}}(\mathbf{x}, t)] \quad (11.24)$$

$$f_i^{\text{eq}} = W_i \rho \left[ 1 + \frac{(\xi_i \cdot \mathbf{u})}{RT} + \frac{(\xi_i \cdot \mathbf{u})^2}{2(RT)^2} - \frac{(\mathbf{u} \cdot \mathbf{u})}{2(RT)} \right] \quad (11.25)$$

The  $f_i$  values are the primitive variables of the lattice Boltzmann method, that is, the unknowns to be determined at each time step. The macroscopic quantities are calculated from them via

$$\rho(\mathbf{x}, t) = \sum_{i=0}^{18} f_i$$

and

$$\mathbf{u}(\mathbf{x}, t) = \frac{1}{\rho(\mathbf{x}, t)} \sum_{i=0}^{18} f_i \xi_i \quad (11.26)$$

plus the equation of state to determine the pressure.

Remarkably, it can be shown (see, e.g., Nourgaliev *et al.* [41]) that the Navier–Stokes equations can be derived from (11.24) to (11.26) via a “Chapman–Enskog” procedure involving a special expansion in terms of the Knudsen number. The incompressible Navier–Stokes equations are obtained plus “error” terms that result from the compressibility of the lattice Boltzmann approach. These can be made negligible by an appropriate choice of the lattice spacing, time step size, and relaxation time. Hence, the lattice Boltzmann method can be seen as an alternative means of “solving” the Navier–Stokes equations. (In fact, by an appropriate choice of equilibrium distribution function and lattice structure, the dynamics governed by any advection-/diffusion-based partial differential equation can be simulated in this way.)

Unlike “traditional” Navier–Stokes solvers, the lattice Boltzmann method is algorithmically very simple. After initialization, which usually involves setting

$f_i = f_i^{\text{eq}}$  with appropriate choice of  $\rho$  and  $\mathbf{u}$ , there are essentially just two main steps repeated at each time step:

- 1) *Streaming*: each  $f_i$  value moves to the next node along its associated link.
- 2) *Collision*: at each node, the  $f_i$  values relax toward the local Maxwellian distribution.

These can be thought of as representing molecular motion and molecular collision. In the “collision” step, at each lattice node, the macroscopic quantities are updated using Eq. (11.26) and then used to update  $f_i^{\text{eq}}$  via Eq. (11.25). The right-hand side of Eq. (11.24) can then be evaluated, which corresponds to the new values of  $f_i$  at each node. The “streaming” step is then effected by simply assigning the new  $f_i$  values to the corresponding lattice link of the appropriate neighboring node.

Notice that this algorithm is highly localized: exchange of information occurs only between neighboring nodes. There is no matrix to invert. This localized nature provides a key advantage of the LB approach, namely that it is easy to implement in a highly parallel manner with excellent scalability to many cores. Indeed, it is now very popular to execute LB simulations on graphical processing units (GPUs), whose highly parallel architecture is very well suited to LB algorithms and can result in execution speeds that are several hundreds of times faster than CPU-based implementations.

### 11.5.2

#### Multiphase Flow and Wetting

There are several ways in which the basic LB structure outlined has been extended to include two-phase flow, and most of these result in a diffuse-interface representation of the liquid–air interface in which the fluid properties vary over (typically) about four lattice nodes or more. Perhaps, the two most popular approaches are the so-called free-energy model of Swift *et al.* [42] and the “pseudopotential” model of Shan and Chen [43] and their later variants.

The free-energy model is based on the same physics as the diffuse-interface methods discussed in Section 11.4. The pressure tensor derived from the free-energy functional is coupled to the LB system by constraining the moments of  $f_i$  to ensure conservation of mass, momentum, and energy. In a way similar to that mentioned in Section 11.4, the presence of the solid surface can be accounted for by the addition of a contribution to the total free energy of the system. This results in a boundary condition in which the gradient of density normal to the surface is specified in terms of a “wetting potential” that is chosen to achieve the desired static contact angle [44].

The pseudopotential model is the most computationally efficient multiphase LB method and, in our experience, achieved the best match with experimental observations for a drop impinging on a previously deposited drop. In this model, a fluid interaction force,

$$\mathbf{F}(\mathbf{x}, t) = -G\psi(\mathbf{x}, t) \sum_{a=0}^{18} W_i(\mathbf{x}, \boldsymbol{\xi}_i, t) \boldsymbol{\xi}_i \quad (11.27)$$

is added to the velocity field to account for interparticle forces. Here,  $G$  is an interparticle potential strength parameter, which has a negative value for fluid attraction and positive value for fluid repulsion, and  $\psi$  is a potential function that depends on density:

$$\psi(\rho) = \rho_0 [1 - \exp(-\rho/\rho_0)] \quad (11.28)$$

where  $\rho_0 = 1$ . This model produces a nonideal equation of state that supports the coexistence of a heavy phase of density  $\rho_h$  and a light phase of density  $\rho_l$ . To capture the viscosities of the two phases, a different bulk relaxation time is used for each, that is,  $\tau_h$  (liquid) and  $\tau_l$  (gas), and in the interface region, linear interpolation based on the local density is used to achieve a smooth transition between the two.

In order to simulate the solid–fluid interactions, a surface wetting model must also be introduced. One approach, which lends itself to the treatment of contact angle hysteresis described in the next section, is to specify the fluid density on the solid surface via a “surface affinity” parameter [45, 46] defined in a range from 0 to 1 by:

$$\eta = \frac{\rho_s - \rho_l}{\rho_h - \rho_l} \quad (11.29)$$

where  $\rho_s$  is the density at the solid surface. The  $\eta$  parameter is a convenient way to control the surface density to achieve a static contact angle between  $0^\circ$  ( $\eta = 1$ ) and  $180^\circ$  ( $\eta = 0$ ). Unfortunately, the relation  $\theta = f(\eta)$  is not a linear function; in fact (unlike in the free-energy model), there is no analytical expression for this relationship. However, it is possible to perform calibration simulations of sessile drops to determine a tabular or graphical representation that can be used for future simulations. Figure 11.8 shows the result of such a calibration for different values of the interparticle interaction parameter  $G$ .

The main limitation of the multiphase Shan–Chen LB model is that surface tension and density are controlled by the same fluid–fluid interaction parameter  $G$ ,

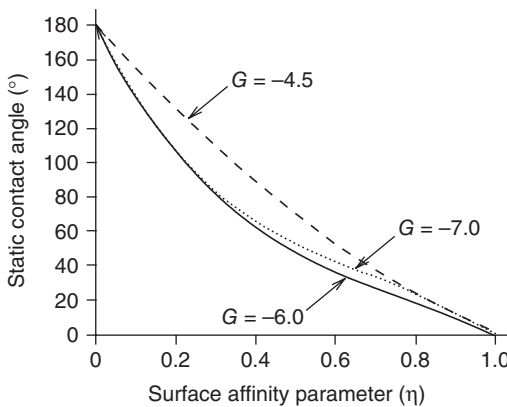


**Figure 11.8** Static contact angle achieved for different surface affinity parameter values in sessile drop simulations using the Shan–Chen model.



and this can make matching experimental parameters difficult. Similarly to other diffuse-interface approaches, it is also difficult to achieve stable simulations when the density ratio between the phases is large. Several extensions to the model have been proposed to extend the density ratios achievable by the model and to provide more control over surface tension [47]. Yuan and Schaefer [48] proposed modifications to the equation of state, and for example, by using the Carnahan–Starling equation of state

$$p = \rho RT \frac{1 + (b\rho/4) + (b\rho/4)^2 - (b\rho/4)^3}{(b\rho/4)^3} - a\rho^2 \quad (11.30)$$

where  $a$  and  $b$  are specified constants, it is possible to extend the density ratio  $\rho_h/\rho_l$  up to 1000, achieving the density ratio of water/air.

Note that a key feature of the LB wetting models is that the surface wettability is specified (via the relevant “wetting parameter” – e.g., surface affinity or wetting potential) in terms of the *static* contact angle. The *dynamic* contact angle is not required as a boundary condition. This is a significant advantage over methods requiring the dynamic contact angle to be specified, because static contact angles can be measured experimentally much more easily, using a configuration that can be independent of the flow of interest. For example, an experiment based on Figure 11.5a could be used to establish the static contact angle(s), and this information could then be used in a simulation of drop impact and spreading. Note also that, being diffuse-interface-based, the LB models do not suffer from the stress singularity described in Section 11.2.3.

### 11.5.3

#### Capturing Contact Angle Hysteresis

The wetting model described in the previous section is sufficient to simulate drops on a perfectly smooth, hysteresis-free surface. However, as noted in Section 11.3.2, most surfaces exhibit contact angle hysteresis, and this strongly influences the dynamics and final printed shape of drops on surfaces. There are essentially two fundamental approaches to dealing with contact angle hysteresis: (i) capture the cause (and, hence, effect) of the hysteresis, by including representations of the chemical and physical nonuniformities of the surface, or (ii) just capture the effect. Most simulations of wetting adopt the second, pragmatic approach.

In “traditional” approaches, such as VOF, where the dynamic contact angle must be specified as a boundary condition, the treatment of contact angle hysteresis relies on calculating the speed of the contact line to identify whether or not the liquid–air interface is advancing or receding and whether or not the current value of the contact angle is above or below the hysteresis range, and then appropriate action can be taken. This includes actively immobilizing the contact line where necessary to represent contact-line pinning.

The LB framework provides the opportunity for a simpler approach, such as that proposed by Castrejón-Pita *et al.* [18] and [32]. Instead of relying on the angle and speed of the liquid–air interface, the model is based on identifying parts of

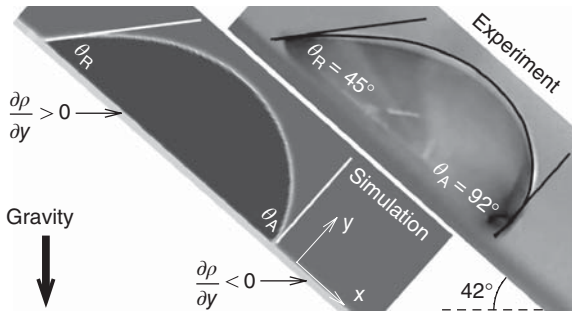


**Figure 11.9** Photograph of a water drop on a steadily inclined polycarbonate plastic surface at the moment when the drop starts to move, together with the corresponding lattice Boltzmann simulation. This experiment

is used to tune the parameters of the hysteresis model and, hence, calibrate the code for use in other simulations of the same liquid and solid.

the solid surface that have been recently wetted or dewetted. By using the “surface affinity” model of Section 11.5.2, it is easy to identify which parts of the solid surface are covered with liquid, simply by calculating the normal gradient of the density at the surface. Since the density at the surface lies between the liquid and gas bulk densities, parts of the solid where the density gradient is positive are wetted and parts where it is negative are not (see Figure 11.9). Initially, the surface affinity is set to correspond to the advancing contact angle  $\theta_A$ . Once the surface at a given location is wetted, the local value of  $\eta$  changes over time  $T_a$  to correspond to the receding static contact angle  $\theta_R$ . The time  $T_a$  represents the physical time needed for the retention force (see Section 11.3.5) to saturate. On the other hand, if a location becomes dewetted, the surface at that location starts to recover its initial properties, that is, the value of  $\eta$  is adjusted so that the local static contact angle reverts to  $\theta_A$  over a time  $T_e$ , which corresponds to the physical time needed for evaporation of liquid molecules from the dewetted surface. A linear interpolation is used to adjust  $\eta$  over the required period.

For a given liquid and solid, the parameters in the hysteresis model can be determined by simulating the experimental configuration used to measure the contact angle hysteresis of the surface – for example, a drop on a plate whose inclination is gradually increased until the drop starts to move. An example of such a calibration is shown in Figure 11.9, showing good agreement with the drop shape. Once calibrated, for this liquid and solid combination, the code can then be used in a different flow – for example, the deposition and spreading of a drop on a surface.

A drop deposition scenario that is particularly sensitive to contact angle hysteresis is that of printing a drop onto a sessile, predeposited drop at an offset between the drop centers, as shown in Figure 11.10a. If the offset is not too large, the drops will coalesce to form a composite drop. However, the combined drop will not have a circular final footprint – its final shape will be peanut-like as a result of

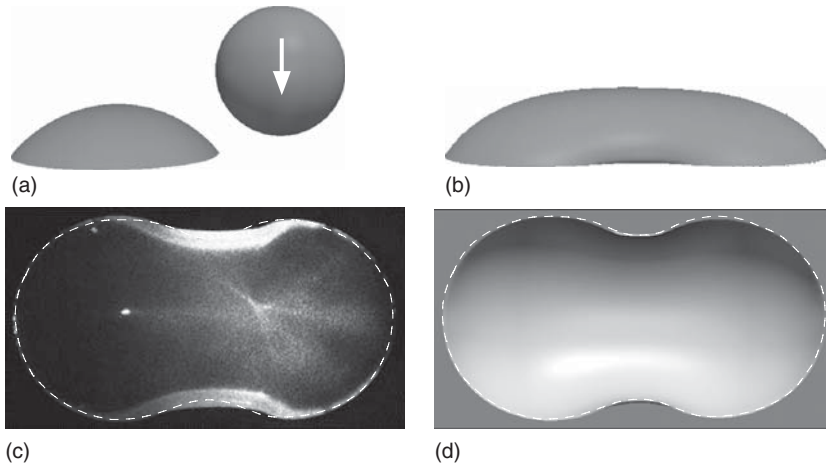


**Figure 11.10** Simulation of a drop impacting on previously deposited sessile drop and comparison with experiment: (a) simulation initial state; (b) simulation final state, side view; and (c) experimental view from below, through the Perspex substrate, of the

final state. (d) Top view of the final state predicted by the simulation. See the main text for experimental conditions. The white dashed line shows the predicted footprint of the composite drop. (Courtesy of J.R. Castrejón-Pita, University of Cambridge.)

contact angle hysteresis. During the coalescence, there is simultaneous advancement of the contact line (in the “neck” region between the two original drops) and recession (at the furthest extreme of the second drop). These two processes cease once the local contact angle falls within the hysteresis range, thus pinning the contact line and leaving the elongated configuration. Simulating this process, therefore, makes a particularly good test for the hysteresis model.

It is important to note that, in contrast to other methods that intentionally pin the contact line, there is no mechanism in the LB model to intervene and artificially prevent the contact line from moving. Once calibrated, the code is used without further tweaking, and any prediction of contact-line pinning is a result of a local equilibrium state having been reached.

Figure 11.10c shows the final printed footprint observed experimentally after an 85% : 15% glycerol–water drop coalesced with a predeposited drop of the same liquid. The center-to-center lateral separation of the drops was 3.8 mm, with their (in-flight) diameters being 2.38 mm. The impact speed was  $1.1 \text{ m s}^{-1}$ , and the liquid density, viscosity, and surface tension were  $1222 \text{ kg m}^{-3}$ ,  $100 \text{ mPa}\cdot\text{s}$ , and  $64 \text{ mN m}^{-1}$ , respectively. The substrate was Perspex, and the advancing and receding contact angles were  $85^\circ$  and  $54^\circ$ , respectively. The image shows the composite drop viewed from below, through the substrate. The experiments were conducted by J.R. Castrejón-Pita at the University of Cambridge. A top view of the final composite drop predicted by the corresponding simulation is shown in Figure 11.10d, and the footprint agrees very well with the experiment. Further comparisons of the simulation and experiments can be found in Castrejón-Pita *et al.* [18], showing excellent agreement.

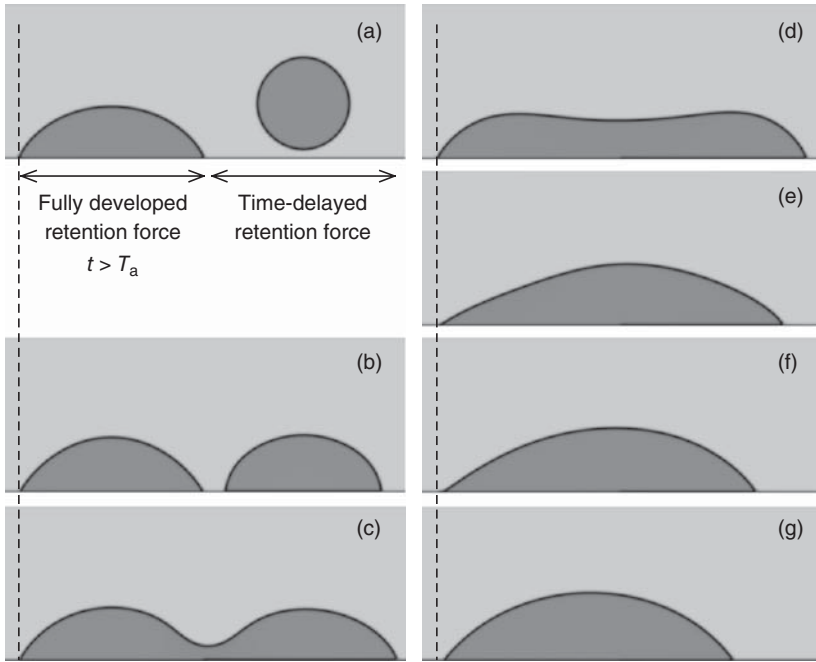


**Figure 11.11** Simulation of a drop impacting sufficiently close to a previously deposited sessile drop to allow coalescence of the two. The images show side-view snapshots as time increases from (a) to (g). The interaction between the first drop and the solid is fully saturated, whereas that

between the second drop and the solid develops over a finite time. This results in a lower local value of the receding contact angle on the left than on the right, and the consequential pinning of the left-hand edge of the contact line at its initial position, indicated by the vertical dashed line.

As mentioned in Section 11.3.5, when consecutively printed drops coalesce, the second drop tends to be pulled into the first drop, with the contact line of the first drop remaining pinned on the side opposite to the impact. This results in the part of the composite footprint corresponding to the second drop having a slightly smaller diameter than that corresponding to the first drop. On close examination, this can be seen in Figure 11.10. This “drawback” phenomenon is explored further in Figure 11.11, which shows a sequence of cross-sectional side views of an impacting and sessile drop coalescing (under conditions different from those shown in Figure 11.10, chosen to illustrate the behavior more obviously).

In Figure 11.11a, the drop on the left-hand side has been allowed to settle, such that the surface underneath it has a surface affinity ( $\eta$ ) value corresponding to the receding contact angle. The unwetted parts of the solid have a surface affinity value corresponding to the advancing contact angle. The second drop (of the same volume) impacts to the right of the first on a dry part of the solid, and as it spreads, the value of  $\eta$  on the newly wetted solid surface is gradually adjusted as per the

hysteresis model described. However, the timescale on which this occurs is longer than the time required for the second drop to make contact with the first. Where the drops meet, a “neck” grows rapidly (Figure 11.11c,d), and at stage (d), the composite drop shape appears symmetrical. As the center of the composite drop rises further, the contact angles at the left- and right-hand sides of the drop decrease. Since the surface affinity at the right-hand edge is still lower than that at the left, exhibiting a higher static contact angle, the right-hand contact angle falls below the local receding contact angle first, and the right-hand edge of the drop starts to recede to the left (Figure 11.11e). At this point, the left-hand contact angle is still larger than the local receding contact angle, so the left-hand edge of the contact line remains pinned. However, the dynamics in the bulk of the composite drop do eventually cause the left-hand contact angle to dip below the local receding contact angle, and the left-hand edge of the drop does recede very slightly from its initial position (Figure 11.11f). The resulting effect (Figure 11.11g) is that the second drop is drawn into the first.

It should be stressed again that there is no artificial or intentional pinning of contact lines in the lattice Boltzmann simulation shown in Figure 11.11; the behavior develops naturally as a result of the evolution of the local *static* contact angle values when the surface becomes wetted. This is a significant advantage over alternative methods, such as VOF, which require the local *dynamic* contact angle to be specified at all times. The parameters of the LB model are chosen based on independent calibration experiments to determine the contact angle hysteresis for a given liquid and solid surface, then used without further tweaking.

#### 11.5.4

##### Rough Surfaces

The local nature of the interactions between the nodes and the nearest neighbors makes the lattice Boltzmann approach well suited to simulating flows involving complex geometries such as porous media and rough surfaces, which is useful for certain applications of inkjet printing. Implementation of topographical features is relatively straightforward, and therefore, real surface maps (obtained, e.g., by interferometry) can be directly imported into the computational space and aligned with the lattice nodes to create a virtual representation of the real surface. The fidelity of the constructed surface will, of course, depend on the lattice resolution; however, using 3D space of  $128 \times 128 \times 128$  nodes is sufficient to achieve satisfactory results for the inkjet printing purposes illustrated here. An example simulation of printing onto a rough surface is shown in Figure 11.12, which clearly shows the local deformations of the contact line and the resulting asymmetrical footprint. Indeed, surface roughness is one cause of contact angle hysteresis.

In the case shown in Figure 11.12, the surface is a ceramic, deliberately roughened anisotropically as part of the investigation of correlations between contact-line motion and topographical surface parameters reported in Kubiak *et al.* [49]. On rough surfaces, spreading is affected by local pinning of the contact line at surface asperities. When the dominant roughness is unidirectional, capillary action

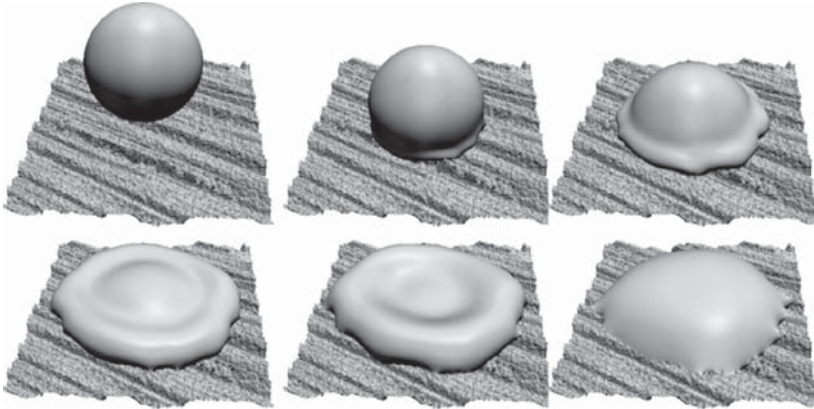


**Figure 11.12** Lattice Boltzmann simulation of a drop impacting on a virtual representation of a real rough ceramic surface.

can promote spreading along roughness grooves, while contact-line motion in the lateral direction is impeded by the roughness peaks.

#### 11.5.5

##### **Chemically Inhomogeneous Surfaces**

Another aspect heavily influencing contact angle hysteresis and drop deposition dynamics is inhomogeneity in the chemical composition of the substrate surface, which leads to a spatially varying surface energy and hence wettability. The local intrinsic static contact angle may therefore vary significantly across the surface, which will affect the macroscopic behavior of the liquid on such a surface. As with surface roughness, chemical inhomogeneity of the surface is readily included in lattice Boltzmann simulations, since the wetting parameter (e.g., surface affinity or wetting potential) can be set to have a different value at each lattice node on the surface.

Figure 11.13 shows an example in which a random pattern generator was used to create a flat but chemically nonuniform surface. Circles of random size with random surface energy were placed in random positions on the solid boundary, to create the surface shown in Figure 11.13. The shading on the surface indicates the wettability of each patch, with darker patches corresponding to higher static contact angles. Note that, in this case, the hysteresis model described in Section 11.5.3 is not used; each patch has a single, constant value of  $\eta$ . As can be seen in the figure, there are local deformations of the contact line and variations in the contact angle around the contact line. This effect is similar to that of surface roughness, but via a different mechanism. Chemical inhomogeneity is also a cause of contact angle hysteresis.

In the situations presented in Figures 11.12 and 11.13, the length scale of the surface nonuniformity is quite large relative to the drop size, and in such cases, it is



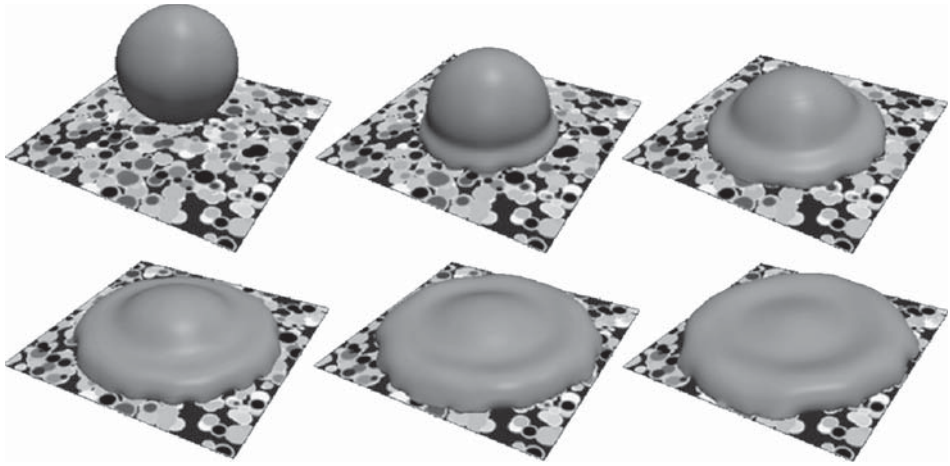


**Figure 11.13** Lattice Boltzmann simulation of a drop impacting on a flat but chemically inhomogeneous surface. The circular patches on the substrate are randomly generated areas of different wettability. Darker patches have a higher static contact angle.

difficult to capture the dynamics using macroscopic or “averaged” representations of the contact angle behavior. The nontrivial variations in contact angle around the contact lines seen in Figures 11.12 and 11.13, and especially the transitions between areas of different contact angle, highlight the difficulty in simulating 3D drop dynamics on complex surfaces using other methods that require the local dynamic contact angle to be specified at all times and all points on the contact line.

Armed with a simulation tool that can predict drop dynamics on complex surfaces, it is possible to explore ideas for enhancing printing results. A final example is shown in Figure 11.14, where a deliberate regular chemical patterning of the substrate has been created to see the effect on controlling continuous line printing for conductive tracks. The gray squares have a lower static contact angle than the surrounding substrate, and this promotes pinning of the contact line along the rows of the pattern, maintaining a straight thin track.

## 11.6

### Conclusion and Outlook

This chapter has explored various methods for simulating drop dynamics on solid surfaces and has highlighted that the key challenge in predictive modeling of such systems is in capturing the complex behavior of moving contact lines and the associated contact angles.

In terms of modeling general free-surface dynamics, sharp-interface models have the advantage that the free surface is well defined, and the finite element method is particularly well suited to numerical analysis based on such models; indeed, it has been used with much success for the simulation of inkjet

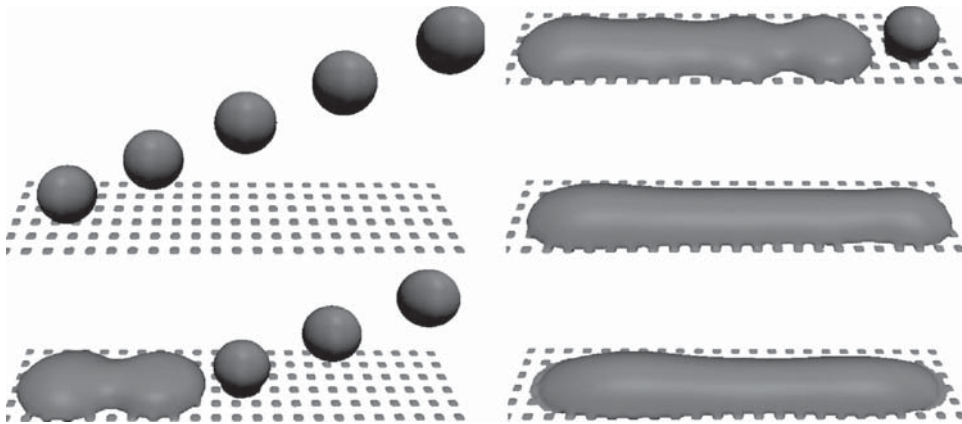


**Figure 11.14** Lattice Boltzmann simulation of a sequence of drops impacting and coalescing on a regular chemically patterned surface. The gray squares have lower static contact angle than the surrounding white substrate.

drop formation. The VOF method is also a popular and efficient approach for simulating free-surface flows, particularly in 3D.

For the simulation of flows involving moving contact lines, sharp-interface models have the serious drawback that the (dynamic) contact angle between the free surface and the solid must be specified as a boundary condition. This is problematic for genuinely predictive simulations because, as highlighted in this chapter, the contact angle exhibits complex behavior including hysteresis (which may be time-dependent), nontrivial variations with contact-line speed, and even influences from the flow field near the contact line. Several studies have illustrated the sensitivity of simulation results to the representation of the contact angle behavior.

A more desirable approach is one that does not require the dynamic contact angle to be explicitly prescribed. One such approach is the lattice Boltzmann method illustrated in Section 11.5. Apart from algorithmic benefits that make the method very amenable to large-scale parallel computations, the method has the clear advantage that only the *static* contact angle(s) need to be specified; the dynamic contact angle emerges through the simulation. This is significant, since for the liquid and solid combination of interest, the static contact angle (or more precisely, the advancing and receding static contact angles) can be determined in an independent experiment (e.g., a tilting plate) and used to calibrate the parameters in the model. A simulation of the flow of interest (e.g., drop impact and spreading) can then be performed without further tweaking of parameters. Comparisons of lattice Boltzmann simulations with experiments show good agreement, especially in the final footprint of deposited drops.

In this chapter, only simulations of the hydrodynamics of drop deposition have been discussed. In practice, of course, once an inkjet drop is deposited, it undergoes drying or curing. Simulating these effects evidently involves additional complexities, particularly when considering drops composed of colloidal



suspensions. Modeling developments in this area have primarily been in the context of the sharp-interface continuum framework, using simplifications such as the lubrication approximation of the Navier–Stokes equations [50–52] or assuming, for example, a spherical drop shape and applying conservation of mass arguments [53]. Axisymmetric finite element simulations that combine fluid dynamics and heat and mass transfer for the evaporation of single drops [54, 55] have also been reported. Inevitably, these involve simplifications of the contact-angle and contact-line dynamics.

Lattice Boltzmann simulations of inkjet drop drying have yet to be established, although encouraging developments have recently been made, for example, in the extension of the Shan–Chen multiphase model used here to model evaporation and nucleate boiling [56]. Albernaz *et al.* [57] have also successfully simulated the evaporation of a freely suspended/falling hexane drop using a lattice Boltzmann model.

It is clear that genuinely predictive, direct numerical simulations of the complete process of inkjet drop impact, spreading, coalescence, and drying have yet to be achieved. However, recent developments show that the key ingredients for such simulations are ripening, and complete simulations should be expected in the near future.

### Acknowledgment

The lattice Boltzmann work presented in this chapter was conducted as part of the Innovation in Industrial Inkjet Technology (I<sup>4</sup>T) Programme Grant (EP/H018913/1) funded by the Engineering and Physical Sciences Research Council.

### References

1. Fukai, J., Zhao, Z., Poulikakos, D., Megaridis, C.M., and Miyatake, O. (1993) Modeling of the deformation of a liquid droplet impinging upon a flat surface. *Phys. Fluids A*, **5** (11), 2588–2599.
2. Blake, T.D. and Ruschak, K.J. (1979) A maximum speed of wetting. *Nature*, **282**, 489–491.
3. Benkreira, H. (2004) The effect of substrate roughness on air entrainment in dip coating. *Chem. Eng. Sci.*, **59** (13), 2745–2751.
4. Wilson, M.C.T., Summers, J.L., Shikhmurzaev, Y.D., Clarke, A., and Blake, T.D. (2006) Nonlocal hydrodynamic influence on the dynamic contact angle: slip models versus experiment. *Phys. Rev. E*, **73**, 041606.
5. Bach, P. and Hassager, O. (1985) An algorithm for the use of the Lagrangian specification in Newtonian fluid mechanics and applications to free-surface flow. *J. Fluid Mech.*, **152**, 173–190.
6. Shikhmurzaev, Y.D. (2008) *Capillary Flows with Forming Interfaces*, Chapman & Hall/CRC.
7. Dussan, E.B. V. and Davis, S.H. (1974) On the motion of a fluid-fluid interface along a solid surface. *J. Fluid Mech.*, **65**, 71–95.
8. Sprittles, J.E. and Shikhmurzaev, Y.D. (2013) Finite element simulation of

- dynamic wetting flows as an interface formation process. *J. Comput. Phys.*, **233**, 34–65.
9. Sprittles, J.E. and Shikhmurzaev, Y.D. (2012) Finite element framework for describing dynamic wetting phenomena. *Int. J. Numer. Methods Fluids*, **68** (10), 1257–1298.
  10. Sprittles, J.E. and Shikhmurzaev, Y.D. (2012) The dynamics of liquid drops and their interaction with solids of varying wettabilities. *Phys. Fluids*, **24**, 082001.
  11. Hirt, C.W. and Nichols, B.D. (1981) Volume of fluid (VOF) method for the dynamics of free boundaries. *J. Comput. Phys.*, **39**, 201–225.
  12. Brackbill, J.U., Kothe, D.B., and Zemach, C. (1992) A continuum method for modeling surface tension. *J. Comput. Phys.*, **100**, 335–354.
  13. Šikalo, Š., Wilhelm, H.-D., Roisman, I.V., Jakirlić, S., and Tropea, C. (2005) Dynamic contact angle of spreading droplets: experiments and simulations. *Phys. Fluids*, **17**, 062103.
  14. Pasandideh-Fard, M., Qiao, Y.M., Chandra, S., and Mostaghimi, J. (1996) Capillary effects during droplet impact on a solid surface. *Phys. Fluids*, **8**, 650–659.
  15. Bussman, M., Mostaghimi, J., and Chandra, S. (1999) On a three-dimensional volume tracking model of droplet impact. *Phys. Fluids*, **11** (6), 1406–1417.
  16. Nikolopoulos, N., Theodorakakos, A., and Bergeles, G. (2007) Three-dimensional numerical investigation of a droplet impinging normally onto a wall film. *J. Comput. Phys.*, **225**, 322–341.
  17. Yokoi, K., Vadillo, D., Hinch, J., and Hutchings, I. (2009) Numerical studies of the influence of the dynamic contact angle on a droplet impacting on a dry surface. *Phys. Fluids*, **21**, 072102.
  18. Castrejón-Pita, J.R., Kubiak, K.J., Castrejón-Pita, A.A., Wilson, M.C.T., and Hutchings, I.M. (2013) Mixing and internal dynamics of droplets impacting and coalescing on a solid surface. *Phys. Rev. E*, **88**, 023023.
  19. Hoffman, R.L. (1975) A study of the advancing interface. I. Interface shape in liquid-gas systems. *J. Colloid Interface Sci.*, **50** (2), 228–241.
  20. Kistler, S.F. (1993) The hydrodynamics of wetting, in *Wettability* (ed J.C. Berg), Marcel Dekker.
  21. Jiang, T.-S., Oh, S.-G., and Slattery, J.C. (1979) Correlation for dynamic contact angle. *J. Colloid Interface Sci.*, **69** (1), 74–77.
  22. Cox, R.G. (1986) The dynamics of the spreading of liquids on a solid surface. Part 1. Viscous flow. *J. Fluid Mech.*, **168**, 169–194.
  23. Vadillo, D.C., Soucemarianadin, A., Delattre, C., and Roux, D.C.D. (2009) Dynamic contact angle effects onto the maximum drop impact spreading on solid surfaces. *Phys. Fluids*, **21**, 12202.
  24. Šikalo, Š., Tropea, C., and Ganić, E.N. (2005) Dynamic wetting angle of a spreading droplet. *Exp. Therm. Fluid Sci.*, **29**, 795–802.
  25. Blake, T.D., Bracke, M., and Shikhmurzaev, Y.D. (1999) Experimental evidence of nonlocal hydrodynamic influence on the dynamic contact angle. *Phys. Fluids*, **11** (8), 1995–2007.
  26. Blake, T.D. and Haynes, J.M. (1969) Kinetics of liquid/liquid displacement. *J. Colloid Interface Sci.*, **30** (3), 421–423.
  27. Shikhmurzaev, Y.D. (1993) The moving contact line on a smooth solid surface. *Int. J. Multiphase Flow*, **19** (4), 589–610.
  28. Roisman, I.V., Opfer, L., Tropea, C., Raessi, M., Mostaghimi, J., and Chandra, S. (2008) Drop impact onto a dry surface: role of the dynamic contact angle. *Colloids Surf, A*, **322**, 183–191.
  29. Tadmor, R., Chaurasia, K., Yadav, P.S., Leh, A., Bahadur, P., Dang, L., and Hoffer, W.R. (2008) Drop retention force as a function of resting time. *Langmuir*, **24**, 9370–9374.
  30. Lee, M.W., Kim, N.Y., Chandra, S., and Yoon, S.S. (2013) Coalescence of sessile droplets of varying viscosities for line printing. *Int. J. Multiphase Flow*, **56**, 138–148.
  31. Li, R., Ashgriz, N., Chandra, S., Andrews, J.R., and Williams, J. (2008) Drawback during deposition of overlapping molten wax droplets. *J. Manuf. Sci. Eng. Trans. ASME*, **130**, 041011.

32. Castrejón-Pita, J.R., Betton, E.S., Kubiak, K.J., Wilson, M.C.T., and Hutchings, I.M. (2011) The dynamics of the impact and coalescence of droplets on a solid surface. *Biomicrofluidics*, **5**, 014112.
33. Hsiao, W.-K., Martin, G.D., and Hutchings, I.M. (2014) Printing stable liquid tracks on a surface with finite receding contact angle. *Langmuir*, **30**, 12447–12455.
34. Anderson, D.M., McFadden, G.B., and Wheeler, A.A. (1998) Diffuse-interface methods in fluid mechanics. *Annu. Rev. Fluid Mech.*, **30**, 139–165.
35. Khatavkar, V.V., Anderson, P.D., Duineveld, P.C., and Meijer, H.E.H. (2007) Diffuse interface modeling of droplet impact. *J. Fluid Mech.*, **581**, 97–127.
36. Cahn, J.W. and Hilliard, J.E. (1958) Free energy of a non-uniform system. I. Interfacial energy. *J. Chem. Phys.*, **28** (2), 258–267.
37. Rowlinson, J.S. and Widom, B. (1989) *Molecular Theory of Capillarity*, Clarendon Press.
38. Khatavkar, V.V., Anderson, P.D., Duineveld, P.C., and Meijer, H.E.H. (2005) Diffuse interface modelling of droplet impact on a pre-patterned solid surface. *Macromol. Rapid Commun.*, **26**, 298–303.
39. Jacqmin, D. (2000) Contact-line dynamics of a diffuse fluid interface. *J. Fluid Mech.*, **402**, 57–88.
40. Bhatnagar, P.L., Gross, E.P., and Krook, M. (1954) A model for collision processes in gases. I. Small amplitude processes in charged and neutral one-component systems. *Phys. Rev.*, **94**, 511–525.
41. Nourgaliev, R.R., Dinh, T.N., Theofanous, T.G., and Joseph, D. (2003) The lattice Boltzmann equation method: theoretical interpretation, numeric and implications. *Int. J. Multiphase Flow*, **29**, 117–169.
42. Swift, M.R., Osborn, W.R., and Yeomans, J.M. (1995) Lattice Boltzmann simulation of nonideal fluids. *Phys. Rev. Lett.*, **75**, 830–833.
43. Shan, X. and Chen, H. (1994) Simulation of nonideal gases and liquid-gas phase transitions by the lattice Boltzmann equation. *Phys. Rev. E*, **49**, 2941–2948.
44. Briant, A.J., Wagner, A.J., and Yeomans, J.M. (2004) Lattice Boltzmann simulations of contact line motion. I. Liquid-gas systems. *Phys. Rev. E*, **69**, 031602.
45. Iwahara, D., Shinto, H., Miyahara, M., and Higashitani, K. (2003) Liquid drops on homogeneous and chemically heterogeneous surfaces: a two-dimensional lattice Boltzmann study. *Langmuir*, **19** (21), 9086–9093.
46. Davies, A.R., Summers, J.L., and Wilson, M.C.T. (2006) On a dynamic wetting model for the finite-density multiphase lattice Boltzmann method. *Int. J. Comput. Fluid Dyn.*, **20** (6), 415–425.
47. Kuzmin, A. and Mohamad, A.A. (2010) Multirange multi-relaxation time Shan-Chen model with extended equilibrium. *Comput. Math. Appl.*, **59**, 2260–2270.
48. Yuan, P. and Schaefer, L. (2006) Equations of state in a lattice Boltzmann model. *Phys. Fluids*, **18**, 042101.
49. Kubiak, K.J., Wilson, M.C.T., Mathia, T.G., and Carras, S. (2011) Dynamics of contact line motion during the wetting of rough surfaces and correlation with topographical surface parameters. *Scanning*, **33** (5), 370–377.
50. Fischer, B.J. (2002) Particle convection in an evaporating colloidal droplet. *Langmuir*, **18**, 60–67.
51. van Dam, D.B. and Kuerten, J.G.M. (2008) Modeling the drying of ink-jet-printed structures and experimental verification. *Langmuir*, **24**, 582–589.
52. Siregar, D.P., Kuerten, J.G.M., and van der Geld, C.W.M. (2013) Numerical simulation of the drying of inkjet-printed droplets. *J. Colloid Interface Sci.*, **392**, 388–395.
53. Deegan, R.D., Bakajin, O., Dupont, T.F., Huber, G., Nagel, S.R., and Witten, T.A. (2000) Contact line deposits in an evaporating drop. *Phys. Rev. E*, **62**, 756–765.
54. Bhardwaj, R., Fang, X., and Attinger, D. (2009) Pattern formation during the evaporation of a colloidal nanoliter drop: a numerical and experimental study. *New J. Phys.*, **11**, 075020.

55. Fukai, J., Kubo, K., Tanigawa, T., and Nakaso, K. (2014) Numerical simulation on drying process of an inkjet droplet using Lagrangian FEM. Presented to the 10th International Conference on Heat Transfer, Fluid Mechanics and Thermodynamics, Orlando, FL, July 14–16, 2014.
56. Márkus, A. and Házi, G. (2011) Simulation of evaporation by an extension of the pseudopotential lattice Boltzmann method: a quantitative analysis. *Phys. Rev. E*, **83**, 046705.
57. Albernaz, D.L., Do-Quang, M., and Amberg, G. (2013) Lattice Boltzmann method for the evaporation of a suspended droplet. *Interfacial Phenom. Heat Transfer*, **1** (3), 245–258.

## 12

# Visualization and Measurement

*Kye Si Kwon, Lisong Yang, Graham D. Martin, Rafael Castrejón-García, Alfonso A. Castrejón-Pita, and J. Rafael Castrejón-Pita*

### 12.1

#### Introduction

Drop formation is an important natural process with significant repercussions in the inkjet industry. While the study of this field started in the eighteenth century with the works of Rayleigh, it is generally accepted that it is a topic yet to be fully understood. Most methods aiming to model and predict droplet behavior are either inaccurate or have not been successfully validated. In fact, most numerical methods are still unsuitable to accurately predict drop formation, which limits their use in industrial environments. While experimental studies have been strongly limited by technology, numerical models have been limited by computational power, cost, and resolution. Currently, many experimental studies rely on high-speed imaging where the spatial resolution is inversely proportional to the temporal resolution, for example, most high-speed cameras can either record very fast at low resolutions or visualize with high resolution at low speeds. This is a major difficulty in experiments where high-spatial and -temporal resolutions are required to resolve very small features at very high speeds and also macroscopic events at longer times. A similar issue affects numerical methods where liquid boundaries and their dynamics are modeled by finite elements; high-spatial or -temporal resolutions imply long and costly computational times [1]. In fact, theoretical studies are also complicated when tackling the dynamics of fluid surfaces. Up to the point of breakup, and from the point of coalescence, the dynamics of fluids are described as a continuous medium (the Navier–Stokes equation), but, theoretically, both the breakup and the coalescence points are described as mathematical singularities [1]. As a consequence, the majority of theoretical models only deal with asymptotic behavior, where transitional aspects are often not considered. These limitations have restricted our understanding of droplet phenomena, which carry great industrial relevance. As a consequence, the industry often relies on empirical trial-and-error testing when developing and optimizing inkjet product. Currently, to overcome these problems, most of the research in the field of droplet dynamics has focused on the development of experimental rigs to

characterize and image the processes of drop formation, coalescence, mixing, and splashing. Undoubtedly, some of these limitations are being overcome by new generation technologies, that is, better sensors and faster computational power, and by scientist artfulness. These efforts aim to provide a firm experimental platform to validate both numerical and theoretical models.

These days a large variety of technologies are used to study droplets. Advances in visualization technologies are allowing the observation of fast-occurring phenomena in drops, such as droplet pinch-off or coalescence; nevertheless, most of these methods are still to be tested under practical conditions. Higher speeds of processing are permitting the agile modeling of droplet coalescence, yet much validation work needs to be done to obtain a set of reliable predicting methods. Experimental techniques used in this field range from traditional photographic methods and high-speed imaging to holography. Most of these methods by themselves do not provide quantitative data and need to be combined to image analysis or other approaches to obtain measurable values that can be appropriately compared with numerical or theoretical models. Alternatively, validation is often also achieved by combining imaging and instrumentation. The aim of this chapter is to provide the reader with a broad perspective of some of the techniques currently used in the field of droplets; further details are at hand from the references.

## 12.2

### Basic Imaging of Droplets and Jets

Many aspects on the study of droplet formation, drop mixing, substrate absorption, and splashing are being progressed further by the recording and analysis of images. One of the simplest forms of visualization is shadowgraphy, where the object under investigation is placed between a light source and a sensor (commonly a camera or a charge-coupled device (CCD)). In fact, the works carried out with shadowgraph setups have been seminal in the field of droplets, where the first photographic record of a droplet was taken by this technology in 1891 [1]. The basic arrangement for shadowgraphy is presented in Figure 12.1, where the illumination often consists of two important components: an optical diffuser and a collimation or light condenser element. The collimator aims to collect the maximum amount of light possible from the source and direct it to the diffuser that in turn produces a uniform background. Both the position and characteristics of the collimator and the diffuser are critically important for the development of an effective setup, especially the ones for image analysis that require a high contrast between the visualized objects and their background. Further details of this technology can be found in [2].

The technology of shadowgraph offers, as any other method, advantages and disadvantages to a particular application. While the shadowgraph technology uses most of the light provided by its source and produces a good contrast between objects and their background, it is a method that cannot differentiate between multiple fluids and/or objects with different optical properties or those

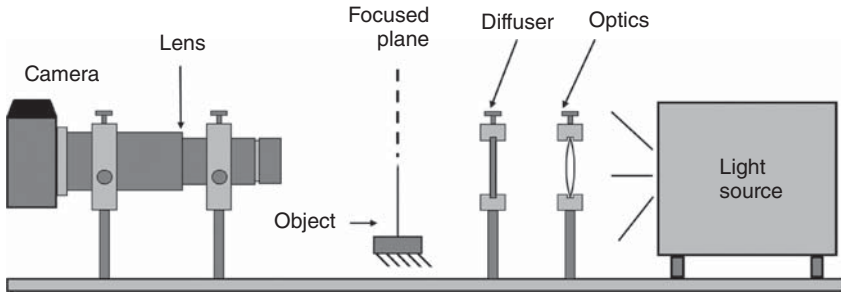


Figure 12.1 Schematic view of a shadowgraph system.

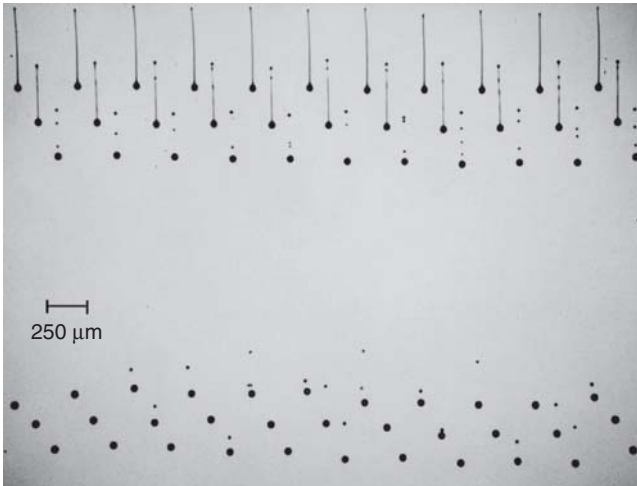


Figure 12.2 Shadowgraph imaging of the jetting of  $50\ \mu\text{m}$  droplets at approximately  $5\ \text{m s}^{-1}$ , details in [3].

of different color, as only their “shadows” are acquired. This is clearly exemplified in Figure 12.2, where droplets of colorless ink are shown in a light-gray background. A good contrast is much desired in image analysis to facilitate the identification of fluid or object boundaries, and an efficient lightening is critical with low-sensitivity sensors. However, the lack of discrimination between liquids implies that a vast amount of information is discarded, preventing the study of other aspects of fluid dynamics such as droplet mixing or chemistry.

The study of the contact-line dynamics of a droplet advancing or receding over a solid substrate are ideal conditions for shadowgraphy. These dynamics depend on the properties of the liquid, the solid, and the surrounding gas phase and importantly on the surface quality. These triple-phase dynamics fulfill all the conditions for shadowgraph: it is a rapid phenomenon that requires fast speeds of recording (i.e., short exposure times and low-light conditions), and all the phases have drastically different optical properties. Examples of the shadowgraph imaging of

droplet impact are shown in Figure 12.3. Given that most light from the source (100 W light emitting diode (LED) continuous light) is collected, a high-speed camera (in this case, a Phantom V310) can readily acquire at exposure times of  $1\ \mu\text{s}$  to produce sharp images. As a consequence, shadowgraph should be used under the conditions of: low light, low-sensitivity sensors, and two-phase systems with large differences in refractive indexes (e.g., drops on air).

A different case is the mixing of droplets, as is a phenomenon driven by diffusion, which lasts few hundreds of milliseconds. It has been proven that color imaging techniques, such as high-speed imaging, can be used to track the progression of mixing during drop deposition and drop coalescence; examples of these are shown in Figure 12.4.

In the case of color imaging, the light source is not placed at the back but at the front of the object. This way, the light received by the sensor is reflected and not dispersed away from it. The major disadvantage of this approach is that only a fraction of the light is collected by the sensor. In fact, color cameras are generally less sensitive than their monochrome counterparts (typically a factor of 3), so color imaging is only applicable under conditions of high-intensity illumination or long exposure times. This is exemplified in Figure 12.4, where the exposure time has

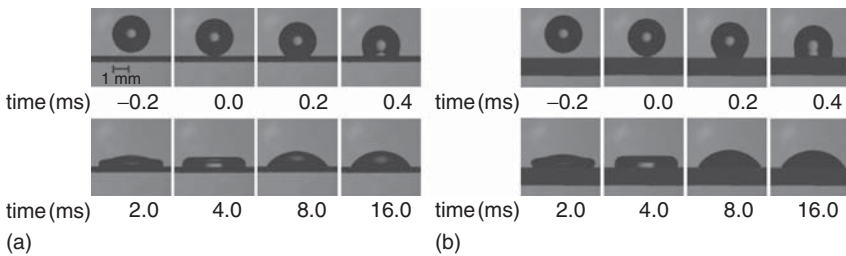


**Figure 12.3** The impact of 100 cP glycerine and water drops of 2.5 mm diameter onto (a) aluminum and (b) Perplex at  $1.0\ \text{m s}^{-1}$ . Exposure time of  $1\ \mu\text{s}$ .

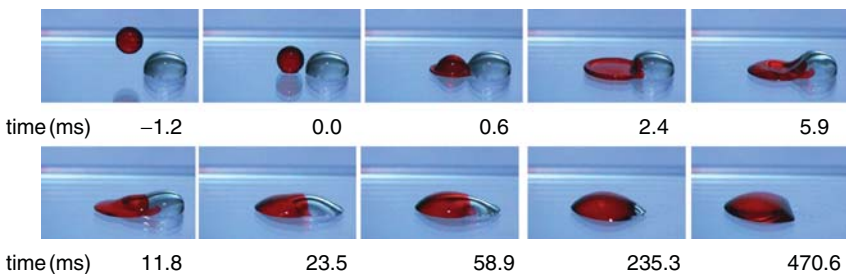


**Figure 12.4** The impact of a 100 cP glycerine and water drop of 2.5 mm diameter at  $1.4\ \text{m s}^{-1}$  onto a colorless droplet twice its size resting on a solid substrate with a

divided wettability. The left-hand side of the substrate is wettable, while the right-hand side is hydrophobic. Exposure time of  $100\ \mu\text{s}$ .



been increased by a factor of 100 to obtain reasonable results. Regardless of this limitation, color imaging is a technique with great potential in the area of reactive inkjet, where acidity or pH indicators could be added to droplets to monitor the progress of a chemical reaction. The use of one or several colored fluorescent dyes and tracer particles can potentially boost the lighting and track the migration of different “parcels” of fluid within a drop.

High-speed and single-frame imaging setups require much specialized equipment as they are commonly used in applications where high-intensity light sources or fast flashes are available. Alternative options exist to study the dynamic of droplets, but these methods also have advantages and disadvantages according to the particular application. Some of these techniques are discussed in the following subsections.

### 12.3

#### Strobe Illumination

As inkjet applications broaden, various types of jetting materials are required to be precisely dispensed from inkjet heads. Droplet behavior from the inkjet head must be measured properly to evaluate and control jetting behavior. Vision-based measurement techniques based on strobe illumination have been used to gain physical insight into jetting behavior by acquiring droplet images. The droplet jetting speed and droplet volume are the most frequently measured jetting performance parameters from the acquired droplet images [4–7]. The use of strobe illumination has an advantage here because droplet visualization can be implemented inexpensively and the jetting behavior can be analyzed via real-time image processing. However, the method of strobe illumination has a drawback because drop-by-drop variations in the jetting behavior cannot be measured unlike in high-speed imaging technology [6].

Figure 12.5 shows a schematic view of a jetting visualization setup based on strobe illumination. To acquire droplet image, the standard low-cost CCD cameras with dozens of frames per second is used. The diameter of an ink droplet from the inkjet head can vary from 20 to 100  $\mu\text{m}$ , depending on the jetting conditions and nozzle diameter. Therefore, a zoom lens with an amplification factor of about 4–8 $\times$  must be used to magnify the image of the droplet. An adequate lighting should be provided because the acquired image is likely to be very obscure due to the high magnification (the small field of view) reducing the amount of lighting. For the strobe lighting, a LED light with a short-time duration (less than few microseconds), which is synchronized to the firing signal, is used to obtain sharp droplet images.

For the light synchronization, a driving pulse voltage signal for the LED light is triggered from a jetting trigger signal with an adjustable time delay, for example,  $t_1$  and  $t_2$ , as seen in Figure 12.6.

The use of a trigger delay in the LED light is important because different droplet images can be obtained as the delay time is varied, as seen in Figure 12.7. For

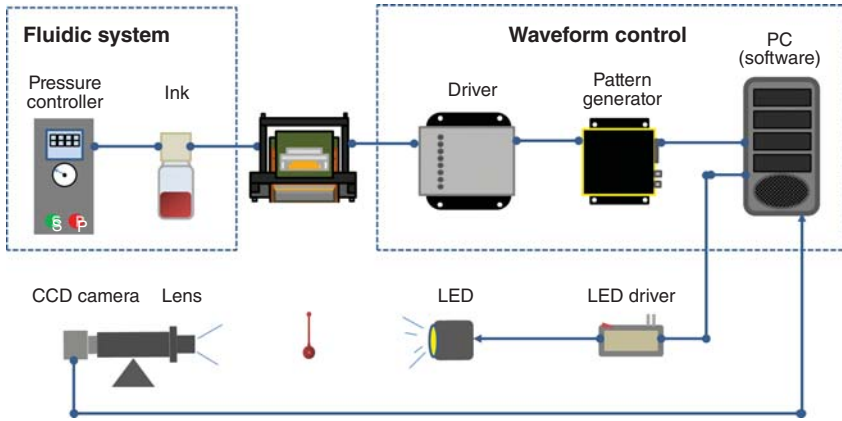


Figure 12.5 Schematic of vision measurement system based on the strobe illumination.

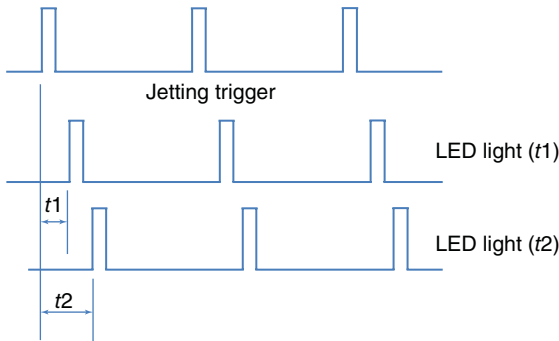
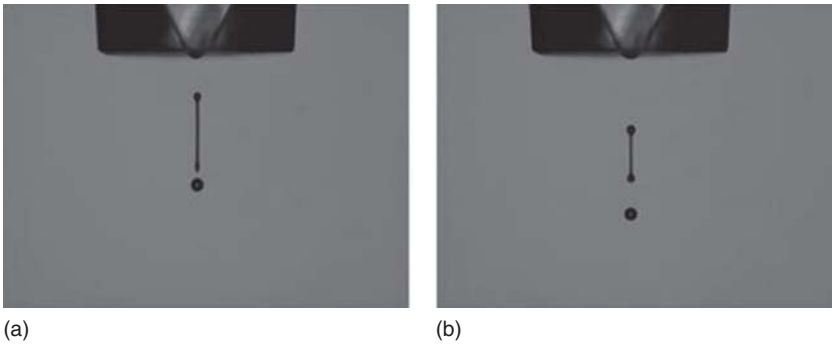


Figure 12.6 LED lighting control.

example, by using two different triggers, as shown in Figure 12.7a,b, the jetting speed can be obtained by using the droplet travel distance during the time interval [4, 5, 8]. Also, sequential images of drop formation measurement can be obtained by increasing the trigger delay of the LED light from zero to a time of interest ( $\sim 500 \mu\text{s}$ ) with a predetermined time interval ( $\sim 10 \mu\text{s}$ ) [6, 7, 9].

In addition to the trigger delay, the on time ( $T_{\text{on}}$ ) of LED light is important. A short  $T_{\text{on}}$  is generally recommended, less than  $1 \mu\text{s}$ , to avoid possible droplet image blurring due to droplet movement during the LED on time. However, short  $T_{\text{on}}$  can also result in a darker image in the case of low-frequency jetting due to low duty ratio of the LED light. The duty ratio can be defined by  $T_{\text{on}}/T$  ranging from 0 to 1. Here,  $T$  is the period of LED light, which is the inverse of jetting frequency. Both  $T_{\text{on}}$  and the jetting frequency effect the quality of recorded images, to understand better these effects three different cases of strobe illumination (shown in Figure 12.8) are presented in Figure 12.9. As shown in Figure 12.9a,b, the use of longer  $T_{\text{on}}$  ( $5 \mu\text{s}$ ) produces brighter image. However, the droplet image becomes blurred because of droplet movement effect during  $T_{\text{on}}$ .



**Figure 12.7** Images with different trigger delay: (a)  $t_1 = \mu\text{s}$  and (b)  $t_2 = 180 \mu\text{s}$ .

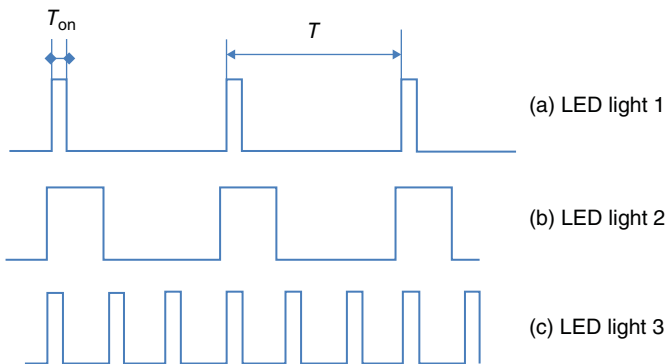


**Figure 12.8** Brightness effect of LED light control: (a) low duty ratio; (b) high duty ratio; and (c) higher jetting frequency (high duty ratio).

The image brightness is also related to jetting frequency. The higher jetting frequency can increase duty ratio of LED light, which results in brighter lighting conditions for vision measurement. For example, Figure 12.9a–c show the jetting frequency effect on image brightness when  $T_{\text{on}} = 1 \mu\text{s}$ . Note that jetting image of 5 kHz is brighter than that of 1 kHz due to the higher duty ratio. Nonetheless, the image blur is not observed due to the short on time of LED ( $T_{\text{on}} = 1 \mu\text{s}$ ), unlike the image using longer on time ( $T_{\text{on}} = 5 \mu\text{s}$ ) as shown in Figure 12.9b.

In practice, image analysis of droplet with jetting frequency of less than 500 Hz might be difficult to measure due to the following reasons: (i) the acquired image may not be bright enough due to low duty ratio ( $<1.0 \times 10^{-4}$  in the case of  $T_{\text{on}} = 1 \mu\text{s}$ ) unless the light intensity of LED is high and (ii) the acquired image is likely to blink because the number of LED lighting pulses (or lighting amount) in each image might be different due to low-frequency lighting. In general terms, image analysis with strobe illumination is more suitable to droplet jetting frequency higher than 500 Hz. On the other hand, it should be noted that image analysis of high-frequency jetting (more than 5 kHz) might be complex due to many subsequent images appearing on the image [9].

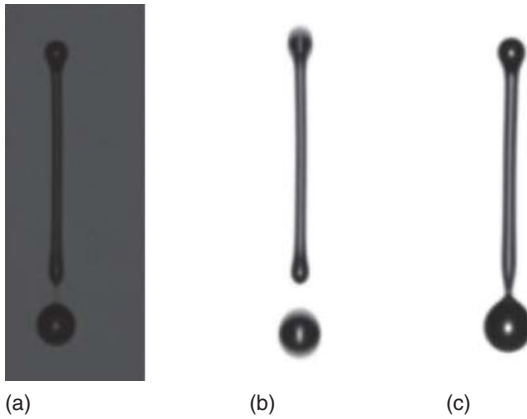


**Figure 12.9** Brightness effect of LED light control: (a) 1 kHz jetting with  $T_{\text{on}} = 1 \mu\text{s}$ ; (b) 1 kHz jetting with  $T_{\text{on}} = 5 \mu\text{s}$ ; and (c) 5 kHz jetting with  $T_{\text{on}} = 1 \mu\text{s}$ .

## 12.4

### Holographic Methods

Conventional observation techniques, as described elsewhere in this chapter, suffer from a number of limitations, which include:

- They are two-dimensional. Information about position and velocity of drops and jets in the direction of the lens axis is not easy to obtain.
- To achieve high accuracy in drop placement or size measurement, a very small field of view is required. Hence, it is difficult to compare many drops. Normally, only one or a few drops are in the field of view at one time, and to gather more information, the imaging system has to be translated relative to the printer. For example, to analyze the performance of a printhead, it is common to observe drops from one nozzle at a time and then mechanically shift to the next and so on.
- The depth of field is small, which can lead to inaccuracy if, for example, the drop trajectory from a particular nozzle is out of alignment in the lens axis direction.
- Evaluation of the position and particularly the size (volume) of the drop is dependent on an accurate estimation of the edge of the drop.
- If drops and drop trajectories are being evaluated over a frame, then optical distortions in the lens system may introduce errors.

Holography offers an alternative technique, which can overcome some of these issues [10]. As illustrated next, it is particularly suited to simultaneous measurement of large numbers of drops and, with suitable techniques, can offer high (submicron) positional and size measurements over a field of view of several centimeters.

A hologram is a recording, on photographic film, or on a digital sensor, of an interference pattern, which encodes both intensity and phase information about the light reflected or transmitted by a subject. This is achieved by using a coherent

light beam split into two paths. One beam illuminates the subject on its way to the recording device while the other is directed to the recorder without interacting with the subject (the reference beam). These beams interfere, and the resultant pattern is recorded by the sensor. The illuminating beam is usually a visible light laser with sufficient coherence to produce the desired interference pattern. It can be shown that this pattern contains enough information about the subject to reconstruct a three-dimensional image. If a photographic plate has been used, the reconstruction can be performed optically by illuminating the developed plate with the reference beam alone. A digital recording can be digitally reconstructed using the results of the theoretical analysis of the holographic process.

While the aforementioned arrangement describes the general holographic process, there is a simpler arrangement that can be used if certain conditions are met. The beam that illuminates the subject(s) can be used as the reference beam if the subject takes up only a small part of the volume probed. A field of drops ejected from an inkjet printhead would fulfill this condition. These days it is common to use a digital sensor in which case this technique is known as *in-line* digital holography. Figure 12.10 illustrates this concept.

A short pulse of collimated, coherent laser light illuminates the drops that have been ejected into the sample region. Light interacting with the sample interferes with the undisturbed light and forms a pattern on the sensor producing a ring pattern for each drop, which encodes its position (in three dimensions) and its size. As drops are moving at several meters per second, then the duration of the pulse needs to be quite short to avoid smearing the image, typically a few nanoseconds. As the beam is a parallel beam, then the field of view seen by the sensor is the size of the sensor itself. However, as light scattered from drops outside this area will also reach the sensor and record an interference pattern, it is possible to obtain information about those drops as well.

Figure 12.11 illustrates an experimental arrangement used to compare holographic results with those obtained using a more conventional shadowgraph image. Here, a beam splitter is used to transmit light to both a sensor to capture the hologram and a normal camera with a 1 : 1 magnification lens producing a

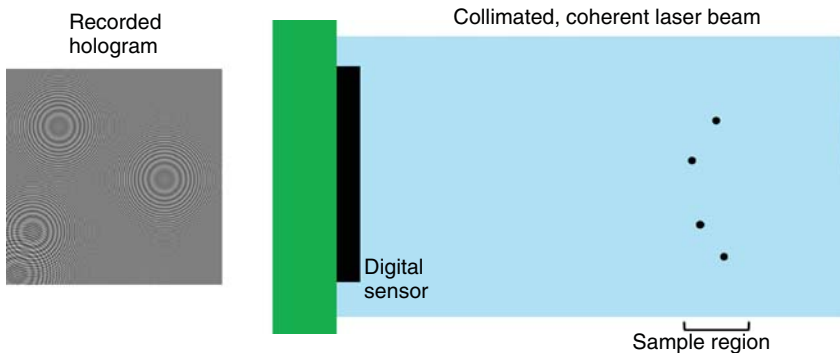
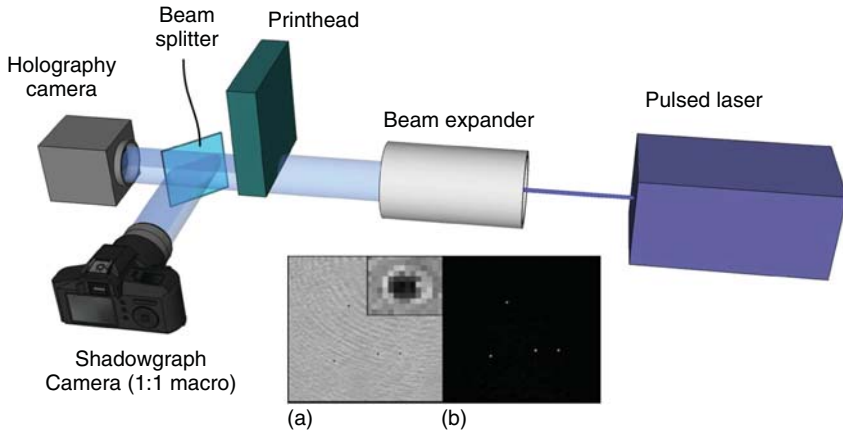
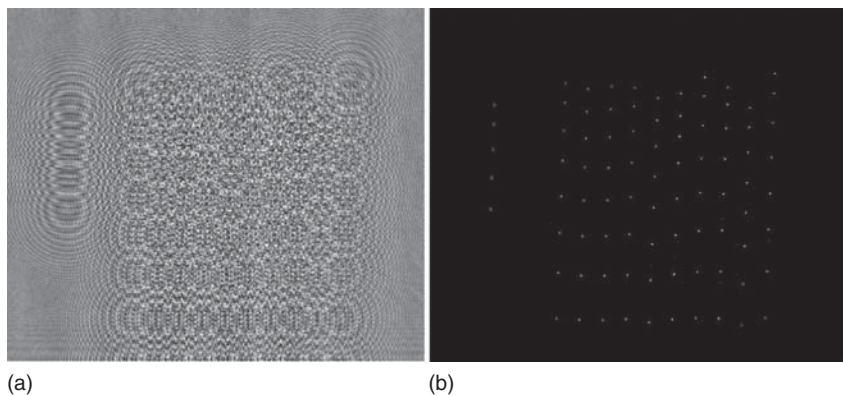


Figure 12.10 Schematic view of an in-line digital holography setup.



**Figure 12.11** Schematic view of a combined shadowgraphy–holographic setup. Image comparison of shadowgraphy (a) with holography (b).



**Figure 12.12** Processing of a hologram, (a) hologram obtained from a succession eight of drops from 10 nozzles of a Dimatix Spectra printhead printing drops at 5 kHz. (b) One  $x$ - $y$  plane from the reconstruction.

life-size shadowgraph of the sample area. In Figure 12.12, the images of a few particular drops are reproduced from the shadowgraph (a) and by means of digital holographic reconstruction (b) [11]. As can be seen, in this case, the shadowgraph images are only a few pixels across, and consequently, the accuracy of position and, particularly, size measurements will not be high. The digital reconstruction of the drops is the first step in an analysis, which will enable submicron accuracy for the position and the size of the drop.

Figure 12.13 is an example of a hologram (a) and one of the planes perpendicular to the optical axis from its three-dimensional reconstruction (b). Each drop produces a ring pattern in the hologram (a) corresponding to a reconstructed drop image in (b). The full reconstruction includes a number of planes spaced along

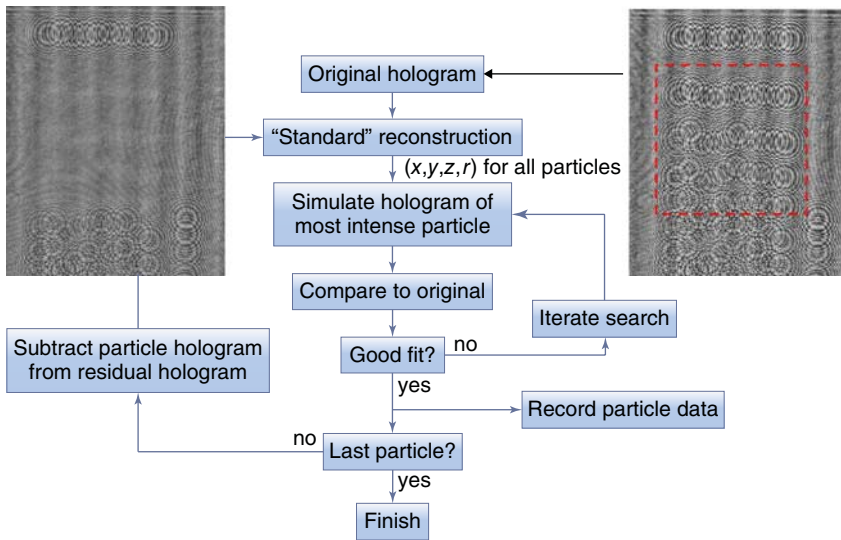


Figure 12.13 Inverse-problem optimization for high-resolution reconstruction.

the optical ( $z$ ) axis. The image shows 10 nozzles (plus one extra for positioning purposes) of a Dimatix Spectra SE-128 printhead firing at a frequency of 5 kHz. In this particular arrangement, the nozzle array was at approximately  $45^\circ$  to the  $z$ -axis, so some of the drops in the reconstruction (b) are “in focus” and some are not. Inspection of other planes in the reconstruction would reveal the  $z$  position of each drop.

There are several enhancements to the basic in-line holographic technique, which provide more information or enhance the accuracy of measurement. Velocity information can be obtained if two images are taken with a short time interval between them. The movement of the drops between these two images will enable obtaining an estimate of the velocity. Clearly, this requires that the laser system can produce two pulses in quick succession; one way of achieving this is to arrange for two lasers to fire along the same axis. The other requirement is that the camera needs to be capable of capturing at least two images in quick succession. Fortunately, the well-known technique of particle imaging velocimetry (of which this a special example) has stimulated the development of such cameras.

The ability to distinguish the patterns produced by the drops is much improved by subtracting an “empty” hologram taken perhaps a few seconds prior to the capture of the printed drops. This removes imperfections in the image produced, for example, by dust particles on the optics.

A major improvement to accuracy is enabled by making the assumption that the drops are round. This is a reasonable assumption to make except close to the nozzle where the drops are still forming from the “extruded” inkjet. With this assumption then, the pattern produced by each drop in the hologram can be exactly calculated if its position and diameter are known. Hence, if the “approximate” position and size are known as a *starting point* (e.g., by carrying out a standard

holographic reconstruction as that illustrated in Figure 12.13), then an iterative search can be made to find a best fit between the actual hologram and a hologram calculated from the position and size [11, 12]. Once a best fit has been found, then the parameters used to form the calculated hologram are very close to those of the real drop.

Figure 12.13 shows the algorithm employed. A standard reconstruction is performed on the original hologram after background subtraction. The largest drop image is selected, and its position and size are used as the starting point to find a good fit. Once found, the parameters are recorded, and the calculated pattern is subtracted from the real hologram, thus removing it before going around the loop again until all drops have been found. In Figure 12.13, the hologram image on the right is the original hologram with an area in which drops are to be found as marked by the dashed box. The hologram on the left is the original hologram with all the calculated drop diffraction patterns subtracted.

While this technique can produce good results for the estimation of the  $x$  and  $y$  positions and the drop size (i.e., to be  $>1\ \mu\text{m}$ ), the location in  $z$  is not so good. One further improvement that would resolve this would be to add a second camera perpendicular to the first as illustrated in Figure 12.14. In this arrangement, a beam splitter transmits part of the laser beam through another path to pass through the sample area at right angles to the first beam. The second camera records the hologram produced by this beam.

This has several advantages:

- The poor  $z$  position estimate from camera 1 can be replaced by the better  $x$  estimate from camera 2.
- The  $y$  estimates can be used to discover any systematic differences between the results from the two cameras.
- Four estimates (two Particle Image Velocimetry (PIV) images from each camera) of the size of each drop are obtained per experiment, which improves the accuracy.

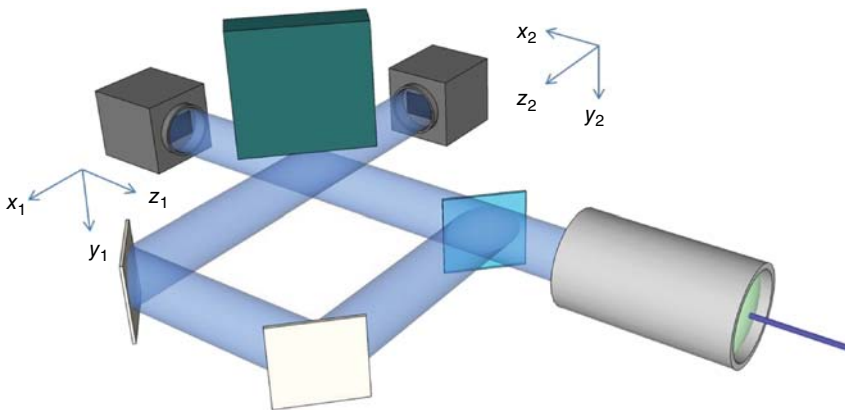


Figure 12.14 Two-camera arrangement for holography.



While this technique can provide very good estimates of the position and size of many drops at once, it does have some drawbacks:

- Distorted drops close to the nozzle cannot be measured in this way.
- Successive drops from any one nozzle are at different positions in the drop “life cycle,” so comparisons can be difficult.
- Significant time is required to complete the reconstruction and analysis, and so, with currently available normal computing power, real-time or near-real-time analysis is not possible.
- The equipment is expensive and requires careful operation.

Potential applications for systems such as this include:

- Investigation of the variation in drop size and velocity with position in the drop sequence.
- The effects of the gap between successive drop groups on the size and velocity (the so-called first drop effects).
- The variation in size between all nozzles in an array.
- Variations in alignment including those that not normally measured (i.e., in the optical axis direction).
- Variations in array performance over time.

## 12.5

### Confocal Microscopy

Stroboscopic method is commonly used for studying drop formation in a fast-moving jet where pulsed illumination is synchronized with drop generation. A single-flash imaging technique has been reported in which a 20 ns flash light with high intensity gives a frozen image with much less blur [13]. Alternatively, high-speed cameras can be used to study the evolution of single drops with a frame rate of a million frames per second for a resolution of 1 million pixels [14]. Recent advances in the speed and resolution of jet imaging have followed on the heels of improvements in sensor and camera technology. A conventional microscope is, however, invariably used to magnify the image of micron-sized jets or drops. The spatial lateral resolution  $RL$  depends on the optical system and is diffraction-limited to  $0.61 \lambda L/NA$ , while  $\lambda L$  is the wavelength of the illumination and  $NA$  is the numerical aperture of the objective lens, which give us a typical submicron resolution. Recently, confocal microscopy is used to study liquid microjet instability [15]. The temporal resolution of a confocal imaging system is limited by the response time of the photomultiplier tube and by the oscilloscope bandwidth, typically to 1 ns. It has been reported that the surface profile of a periodically disturbed jet can be determined from nozzle to breakup with a resolution of 4 nm.

Confocal microscopy was invented by Marvin Minsky [16]. Figure 12.15 shows the principle of confocal microscopy. A pinhole is placed conjugate to the focus of the objective lens so that out-of-focus signal is efficiently suppressed and depth

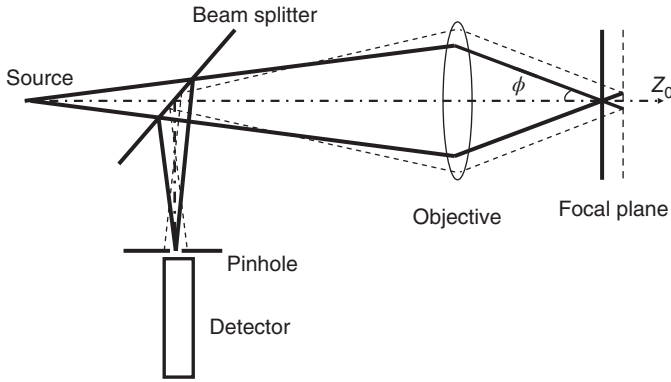


Figure 12.15 Principle of confocal microscopy.

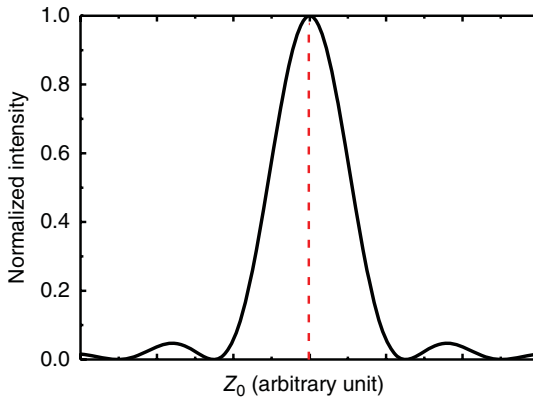
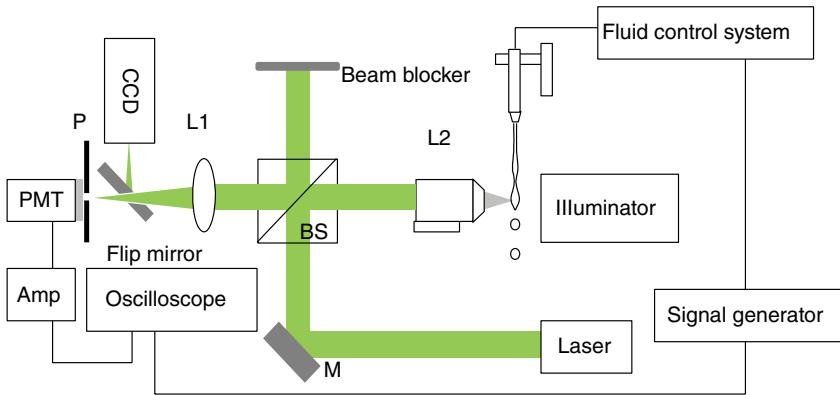


Figure 12.16 Axial response of a perfect mirror in confocal microscopy. The dotted line shows the focus position in  $Z_0$ .

discrimination can be achieved. Theoretical analysis shows that a confocal microscope has a lateral resolution 30% better than a conventional one, that is,  $RL_{\text{confocal}} = 0.44 \lambda L/NA$  [17].

Figure 12.16 shows the axial response of a perfect mirror scanning across optical axis. The peak corresponds to the position when the mirror is in the focal plane. The theoretical full-width half-maximum (FWHM) of the idealized confocal system with an infinitely small pinhole is  $\sim 0.4\lambda L/NA$ . Confocal imaging provides us depth discrimination as a method to profile surface roughness with nanometer resolution by both interferometric and noninterferometric methods [18, 19].

Figure 12.17 shows a schematic of the experimental apparatus for the measurement of jet instabilities by confocal and conventional imaging. The pressurized liquid is fed from a reservoir into a dispenser head. A laminar jet emerges vertically from the dispenser head typically with a circular funnel-shaped glass nozzle of sub-100  $\mu\text{m}$  internal diameter. The aqueous jet runs at a mean speed



**Figure 12.17** Schematic of confocal and conventional imaging setup for studying liquid microjet. M: mirror; BS: beam splitter; L1 and L2: lenses; PMT: photomultiplier tube; Amp: amplifier; and P: pinhole.

of  $6 \text{ m s}^{-1}$ . The jet is mounted on a three-axis motorized, translation stage. A perturbation signal is applied to the dispenser head with a frequency of 10–12 kHz. Confocal and conventional imaging systems share the same objective and tube lenses, with a flip mirror to switch between the two modes. A laser light is used as a light source for confocal imaging, which is focused onto the jet. The backscattered light from the sample is collected by the same objective and then focused onto a pinhole through a tube lens. The pinhole is positioned conjugate to the focus of the objective lens so that the signals that arise from the focus pass through the pinhole and the signals from the out-of-focus regions are largely blocked. The pinhole size matches the Airy disc of the focusing beam to achieve the best signal-to-noise ratio. The signal is detected by a photomultiplier tube and transmitted to an oscilloscope for data processing. For conventional imaging, a white light can be used as light source. A CCD camera with a short exposure time of  $1 \mu\text{s}$  records the shadow image of the jet with single shot.

Figure 12.18 shows conventional images of the water jet with a perturbation frequency,  $f = 11.8 \text{ kHz}$ , and a wavelength of the induced perturbation,  $\lambda = 480 \mu\text{m}$ . The perturbation applied to the flow rate generates swells and necks. As the Laplace pressure varies inversely as the radius of curvature of the jet, the internal pressure increases at the neck and decreases at the swell, causing the fluid to flow from the neck to the swell. This flow exacerbates the instability and eventually causes the jet to break at the neck and form drops.

According to Rayleigh's linear stability analysis [20], the radial displacement  $\delta$  of a cylindrical jet of an incompressible inviscid liquid subject to infinitesimal axisymmetric oscillations of the surface grows exponentially if  $2\pi a/\lambda < 1$ , where  $a$  is the radius of the unperturbed jet and  $\lambda$  is the wavelength of the perturbation. It has the form of

$$\delta(z, t) = \delta \cos [k(z - u_0 t)] = \delta_0 e^{\alpha t} \cos [k(z - u_0 t)] \quad (12.1)$$

where  $\delta_0$  is the initial amplitude of the disturbance,  $u_0 = \lambda f$  is the jet velocity,  $\alpha$  is the growth rate coefficient, and wave number  $k = 2\pi/\lambda$ . Donnelly and Glaberson derived the growth rate by measuring the amplitude,  $\delta$ , of successive oscillations, from half of the difference in radius difference between neighboring swell and neck, where the surface age,  $\tau$ , is related to the distance from the nozzle by  $\tau = z/u_0$  [21]. They showed that the perturbation grows exponentially to within one wavelength of the disengagement of the drop from the jet. The growth rate was within 10% of the value predicted by Rayleigh's linear theory. Bellizia *et al.* pointed out that in order to remove second-order effects on the growth rate measurement, the radius of necks and swells should have been measured at the same axial location,  $z$ , on the jet [22], which is not possible with frozen images of the type shown in Figure 12.18.

With confocal imaging, when the oscillation amplitude is in a few microns, one could locate the swell and neck confocally and at the same jet axial location. The principle is shown in Figure 12.18. By scanning the jet along the optical axis of the confocal imaging system, the confocal response curve can be obtained, as shown in the inset in Figure 12.19. The time base of the oscilloscope and speed of the stage should be adjusted to avoid aliasing of the wave. The top envelope of the signal from the confocal pinhole is extracted as shown in the main graph in Figure 12.19, and a polynomial is fitted to the two maxima to obtain the locations of the swell and the neck, respectively. The displacement between the swell and the neck can be determined with an accuracy of  $0.2 \mu\text{m}$ . To achieve a higher resolution in surface profiling, the quasilinear slope of the confocal response with respect to position along the optical axis can be used. Figure 12.19 shows that the intensity signal is well approximated by a linear function of  $Z_0$  over a range of  $-7$  to  $-4 \mu\text{m}$  from the front surface reflection of an unperturbed jet. Within this linear range, the displacement  $\Delta D$  between two surfaces is proportional to the intensity difference of the detected signals  $\Delta I$ , that is,  $\Delta D = \Delta I/S$ , where  $S$  is the gradient of the plot in Figure 12.19. The resolution is limited by the mechanical stability of the nozzle, fluctuation of the light source, and electronic noise. The experimental

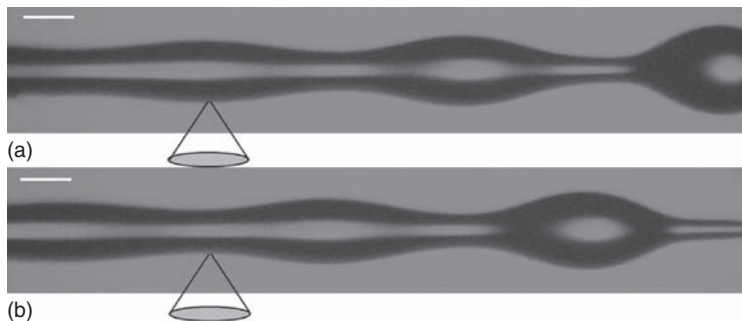


**Figure 12.18** Images that are conventionally used to determine the growth rate of the jet: (a) and (b) have an exposure time of  $1 \mu\text{s}$  and are separated by an interval of  $42 \mu\text{s}$ . Scale bar in  $100 \mu\text{m}$ . The sketched

lens and beams in (a) and (b) focusing on the surface of the swell and the neck illustrate how the growth rate of the jet is determined by confocal microscopy.

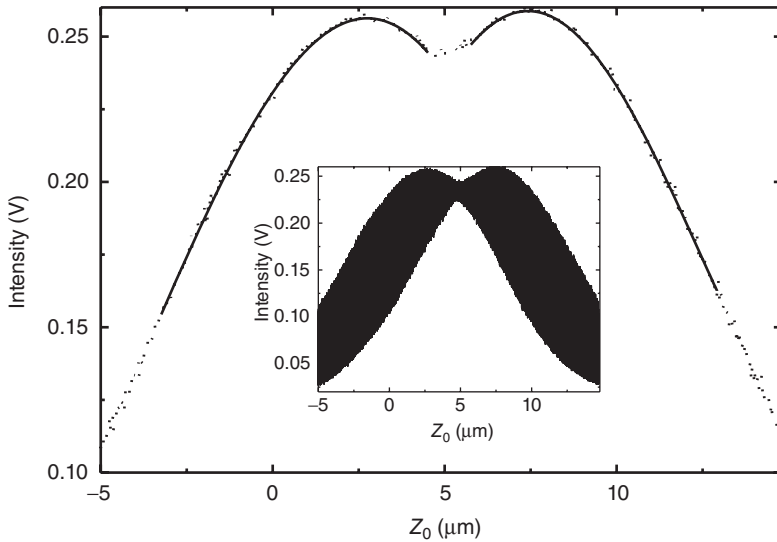


**Figure 12.19** Principle of the determination of the displacement of swell and neck by confocal scan method. Inset: confocal response from the oscillating jet.

approach is as follows. When the surface displacement of the corresponding neck and swell is less than that of the linear dynamic region, which is normally the case for the first four wavelengths in a microjet, the front surface of the jet can be placed from the focal plane of the objective lens such that both the neck and the swell are within the quasilinear intensity response range. The oscillating wave is detected in the time domain as shown in Figure 12.20.

The crest and trough of the sinusoidal wave correspond to the swell and the neck, respectively, for the same jet axial position. The amplitude of oscillation  $\delta$  can be readily derived from  $\Delta I/2S$ , where  $\Delta I$  is the intensity difference between crest and trough. For an ideal sinusoidal oscillation, the fast Fourier transform (FFT) amplitude is proportional to the oscillation amplitude. The FFT amplitude of the fundamental signal can be recorded to give us the resolution of the displacement,  $2\delta$ , as small as 4 nm [15].

Figure 12.21 plots values of  $2\delta$  as a function of  $Z_0$  (on a semi-log plot) over 2 orders of magnitude in the oscillation amplitude with three confocal methods [15]. From Eq. (12.1), the slope of this curve is equal to  $\log_{10}(e) \times \alpha/u_0$ , (where  $\alpha$  is the growth rate and  $u_0 = z/t$  is the jet velocity) and is expected to be independent of  $z$  for a jet of constant velocity (see Chapter 4). While the data are accurately linear from  $z = 2.5$ – $4.0$  mm. The growth rate of the Rayleigh instability is then used to deduce the dynamic surface tension (DST) of the liquid, following an existing linear, axisymmetric, constant-property model [23]. The DSTs of the pure water and ethanol/water mixture were reported from the measured growth rate at a surface age of 0.6–0.9 ms [15]. Preliminary data on surfactant solutions, in which the DST cannot be assumed to be constant, have also been presented [24].

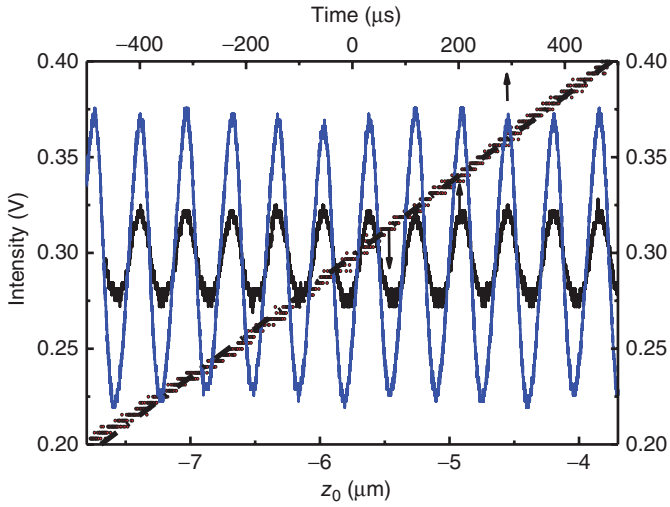


**Figure 12.20** Oscillation of a perturbed jet as a function of time (upper scale) at  $z = 1$  mm (small amplitude wave) and  $z = 2$  mm (large amplitude wave). Quasilinear confocal response (points) of an unperturbed jet as a function of the position of the surface along.

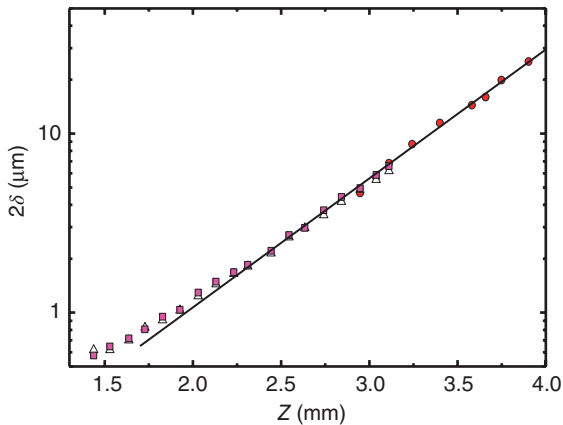


**Figure 12.21** Jet oscillation amplitude measured by three methods [15]. The solid line is a linear fit to data for  $2.5 \text{ mm} < z < 3.9 \text{ mm}$ .

## 12.6

### Image Analysis

#### 12.6.1

##### Binary Image Analysis Method

Generally speaking, recorded droplet images from a CCD camera have eight-bit format pixels that produce gray-scale images with intensity values ranging

from 0 to 255, and the final values are determined by the brightness of the image [8]. Most inkjet image analysis focuses on extracting droplet location and size information using binary droplet image. When using strobe shadowgraph illumination, a droplet image appears as a dark object on a lighter background. To extract the droplet information based on converted binary images, it is preferred that the droplet has a value of 1 and the background has a value of 0. Therefore, we recommend that image values that are higher than the threshold value for binary conversion are mapped to 0, and the image values lower than the threshold value are mapped to 1 in the converted binary image [4]. Here, proper selection of the threshold value is important to obtain the binary image of droplet to extract droplet information such as the location and size. The advantage of using binary image is that a morphology function can be used to obtain droplet images by deleting and modifying the binary droplet image in presence of image noise or other objects.

By using the binary image analysis of droplet, jetting speed as well as a drop formation curve (or droplet trajectory) can be calculated [9]. In addition, droplet volume can be obtained from binary image analysis by assuming that droplet shape is spherical in shape [4]. However, the droplet shape is not likely to be spherical, as it often has long ligaments. Another critical issue is that it is difficult to measure droplet volume accurately because the CCD camera has limited pixel resolution and the image size of droplet can be very sensitive to lighting conditions and the threshold value required to convert gray-scale to binary images.

Two examples of these methods are described for LabVIEW and MATLAB.

#### 12.6.1.1 Edge Detection Method (Droplet Volume Calculation Using LabVIEW)

As discussed, droplet volume could be difficult to measure using binary image analysis if there is a long tail in the droplet. Recently, Hutchings *et al.* have developed image processing techniques to obtain the volume of ink droplets with ligaments [25]. The sliced width of a ligament of a droplet image in the lateral direction was used for their droplet volume measurement as shown in Figure 12.22.

To obtain the sliced width, edge detection techniques can be used to detect the droplet boundary information. A set of horizontal ROI (Region of Interest) lines

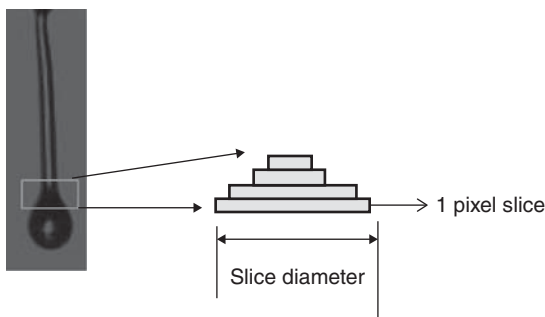


Figure 12.22 Droplet volume measurement with a long ligament, details in [25].

can be used to define the image processing area and obtain the edge information of the droplet. Then, the diameter of each cylinder can be calculated by using the detected edge, and then the droplet volume is just the addition of all the sliced cylinder volumes.

In this section, LabVIEW is used to calculate the volume of a droplet with a long ligament by extracting the boundary information (edge locations). For easy programming, the use of **Vision Assistant** tool is recommended for **LabVIEW** beginners. Various vision functionalities provided by **LabVIEW** are easily accessed by the **Vision Assistant**. For details, the reader may refer to [10].

After launching the **Vision Assistant**, the droplet images to be analyzed can be read from image files or directly acquired from a camera. As a next step, **Clamp (Rake)** function from **Processing Function: Machine Vision** is selected (Figure 12.23). The image processing area (droplet of interest) can be selected by using ROI from the processing window of the vision assistant as seen in Figure 12.24-1. From the clamp setup menu, proper parameters for edge detection can be selected (Figure 12.24-2). For example, gap (current value is 5) can be further reduced to increase the number of horizontal lines within the ROI.

As a result of **Clamp (Rake)** function, the detected edges are seen along the horizontal ROI line, which is indicated as a small yellow circle on the image, as seen in Figure 12.24.

If the detected edges are acceptable, then a standard VI file can be created by selecting **Create LabVIEW VI** from **Tools** in the menu bar of **Vision Assistant**. When the created VI is run, the edge detection results from the standard VI should be automatically shown, as seen in Figure 12.25. In fact, the image can be magnified to confirm the edge detection points.

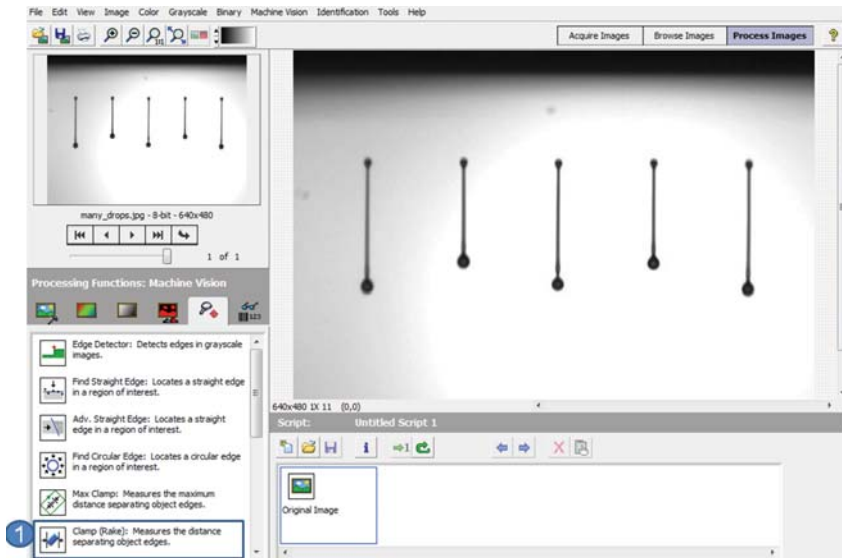


Figure 12.23 Vision assistant to open droplet image.



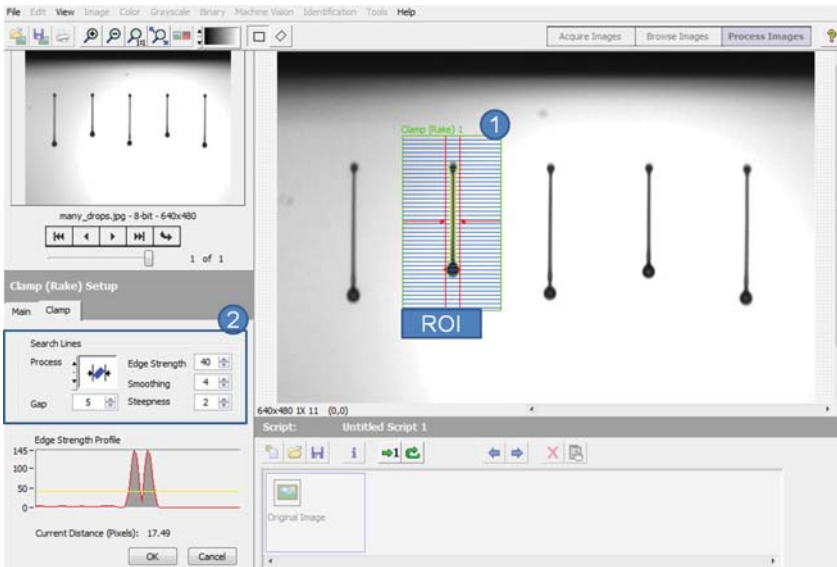


Figure 12.24 Clamp (Rake) setup.

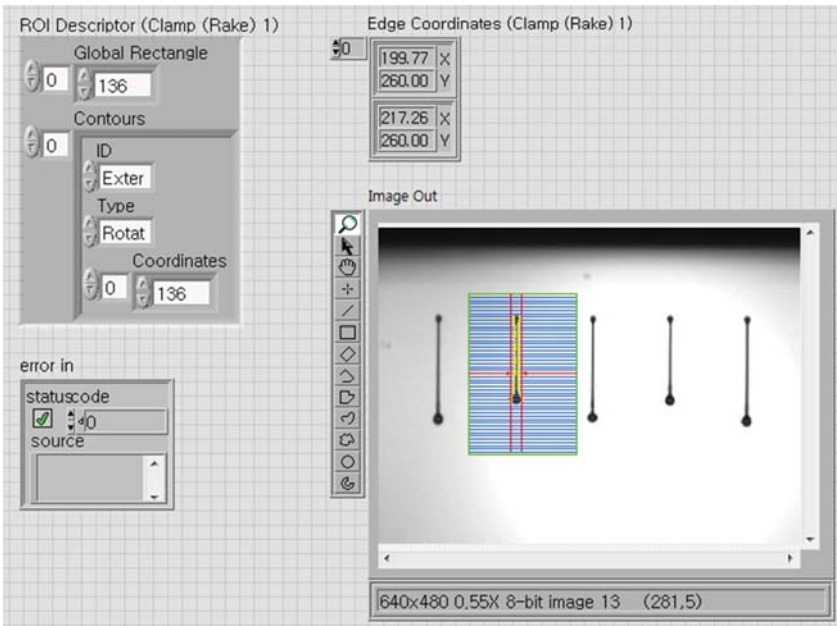


Figure 12.25 Created standard VI using Vision Assistant.

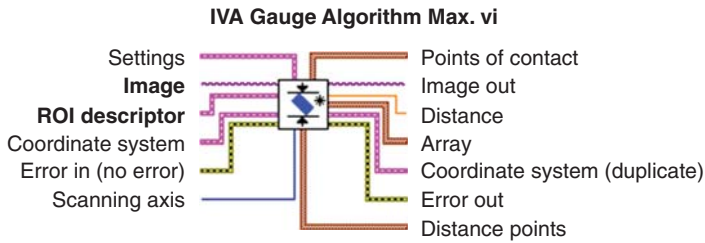


Figure 12.26 Modified IVA Gauge Algorithm Max.vi.

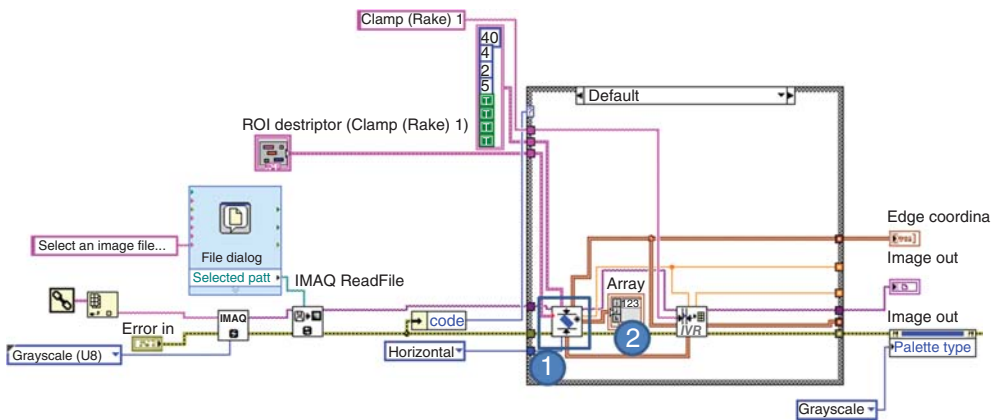


Figure 12.27 Modified VI to obtain all edge information.

Note that the VI created using Vision Assistant does not provide the final solution and should be modified according to one's requirement. For example, to access the edge points from the VI, one needs to modify one of the subVIs named **IVA Gauge Algorithm Max.vi** (Figure 12.26). For this purpose, a double click on the subVI (Figure 12.26) should present all the edge information including the details of the **Array**. This indicator is connected to the output terminal as seen in Figure 12.27. Note that the initially created VI does not have any output terminal for all edge information. As a next step, all edge location (array in Figure 12.27) is used to calculate droplet volume by adding all the sliced cylinder volumes together.

All further programming details are not be covered in this chapter but left as an exercise problem. For further details, the reader is referred to the machine vision textbook [8].

### 12.6.1.2 Edge Detection Method (Threshold Detection Using MATLAB)

A less user-friendly but equally useful way of detecting the boundary of liquids or objects is through MATLAB. This approach has been successfully used on the study of filament breakup where in combination with high-speed imaging can produce submicron resolutions. A fully functional example is given next. The first step is to digitally scan the upper image of the thinning filament as shown in Figure 12.28a; the full algorithm is presented in Figure 12.29. The steps in the algorithm are as follow: the raw image ( $I_m$ ) is loaded into MATLAB, which is then converted to a gray-scale intensity image ( $G$ ). In order to increase the accuracy of the method, a simple background subtraction step is added. This removes any possible persistent, unwanted features (unrelated to the phenomenon under consideration) and inhomogeneities in the background illumination. In the case under consideration here, the background image (BGNF) is, as the name indicates, a picture of the system without any liquid filaments. For practical reasons, this background image can also be a blank image. As before, this image is firstly converted from a true color RGB image to a gray-scale map. An extra optional step consists of the application of some degree (variable) of blurring; this is particularly useful when manipulating images with inhomogeneous lighting. Then, the two intensity maps are subtracted and the background-free image is obtained ( $sIM$ ). The resultant gray-scale image is then converted into a Black and White binary image ( $bw$ ). The intensity threshold chosen for this conversion is judiciously chosen as to obtain a true  $bw$  representation of the filament. A common feature observed in objects with curvatures (drops and filaments) is the generation of “bright spots” due to the optical focusing and unwanted reflections of the background light onto the sensor of the camera. In order to remove these “false” structures being detected as “true” boundaries by the code, an elimination of holes step is added ( $ImNH$ ). The boundary of the remaining object is then extracted (i.e., the coordinates of each point of the boundary), as shown in Figure 12.28b (blue line). Finally, the Euclidian distance between every pair of points belonging to the boundary is computed (represented by the double search loop), with the minimum value corresponding to the neck diameter. Figure 12.28b shows an example of the effectiveness of the code in extracting not only the minimum neck diameter but also its position along the axis of symmetry (in red).

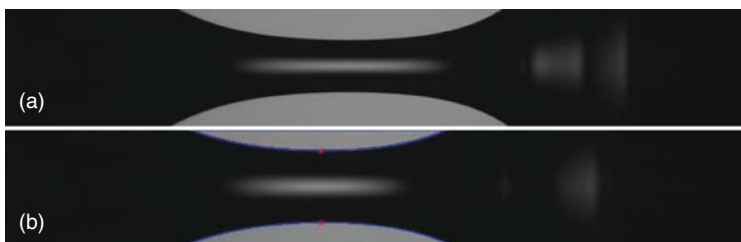


**Figure 12.28** Pictures for image analysis: (a) shows a thinning liquid filament as taken by high-speed imaging shadowgraphy; (b) presents the boundary detection as output from the algorithm in Figure 12.29.

```

Im = imread('Image_filename'); %Original Image
BGND=imread('Background_filename'); %Image of the background, without obstructions
G = rgb2gray(Im);
BGND = rgb2gray(BGND);
mIM=imfilter(BGND,fspecial('average',30),'replicate'); %Smoothing of the background
sIM=mIM-G; %Background subtraction
level = 0.10; %setting a threshold for the grey scale to B&W conversion
bww = im2bw(Im2,level);
bw=(~bww);
Im3a = bwareaopen(bw, 30); %removing holes
boundary=bwboundaries(Im3a);
d=10000; % set an initial value, d will be shorter for the line we want to find
point1=0; % initialize the points to check later if we found the points
point2=0;
ab=boundary{1}; % first boundary
bb=boundary{2}; % second boundary
%cb=boundary{3}; % third boundary, in case it is needed
for k=1:size(bb,1) % loop through all points on first boundary
    for i=1:size(ab,1) % loop through all points on second/third or 'n' boundary
        dist=sqrt((ab(i,1)-bb(k,1))^2+(ab(i,2)-bb(k,2))^2); % calculate distance
        if(dist<d) % check if distance found is shorter than previously found
            d=dist; % save new shortest distance
            point1=k; % save index of point on first boundary
            point2=i; % save index of point on second boundary
        end
    end
end
distance=d %Minimum Neck
figure(1) %Showing the position of the minimum neck
imshow(Im)
hold on
plot(ab(:,2),ab(:,1), 'b', 'LineWidth', 2)
plot(bb(:,2),bb(:,1), 'b', 'LineWidth', 2)
plot(ab(point2,2),ab(point2,1),'-ro')
plot(bb(point1,2),bb(point1,1),'-ro')

```

Figure 12.29 MATLAB example for boundary detection.

## References

1. Eggers, J. and Villermaux, E. (2008) Physics of liquid jets. *Rep. Prog. Phys.*, **71**, 036601.
2. Settles, G.S. (2012) Schlieren and shadowgraph techniques: visualizing phenomena, in *Transparent Media*, Springer, Berlin.
3. Castrejon-Pita, J.R., Martin, G.D., and Hutchings, I.M. (2011) Experimental study of the influence of nozzle defects on drop-on-demand ink jets. *J. Imaging Sci. Technol.*, **55**, 040305.
4. Kwon, K.S. (2009) Speed measurement of ink droplet by using edge detection techniques. *Measurement*, **42** (1), 44.
5. Kipman, Y. (2009) Three methods of measuring velocity of drops in flight using jetxpert. Proceedings of NIP25 and Digital Fabrication, Kentucky, pp. 71–74.
6. Kwon, K.S. (2012) Vision monitoring, in *Inkjet-Based Micromanufacturing*, Wiley-VCH Verlag GmbH & Co. KGaA, Weinheim. doi: 10.1002/9783527647101.ch9
7. Kwon, K.S. (2010) Experimental analysis of waveform effects on satellite and ligament behaviour via in situ measurement of the drop-on-demand drop formation curve and the instantaneous jetting speed curve. *J. Micromech. Microeng.*, **20**, 115005.

8. Kwon, K.S. and Ready, S. (2015) *Practical Guide to Machine Vision Software: An Introduction with LabVIEW*, Wiley.
9. Kwon, K.S. *et al.* (2014) An inkjet vision measurement technique for high frequency jetting. *Rev. Sci. Instrum.*, **85**, 065101.
10. Gabor, D. (1948) A new microscopic principle. *Nature*, **161**, 777–778.
11. Gire, J., Denis, L., Fournier, C., Thiébaud, E., Soulez, F., and Ducottet, C. (2008) Digital holography of particles: benefits of the “inverse problem” approach. *Meas. Sci. Technol.*, **19** (7), 074005.
12. Soulez, F., Denis, L., Fournier, C., Thiébaud, E., and Goepfert, C. (2007) Inverse-problem approach for particle digital holography: accurate location based on local optimization. *J. Opt. Soc. Am. A*, **24** (4), 1164–1171.
13. Martin, G.D., Hoath, S.D., and Hutchings, I.M. (2008) Inkjet printing - the physics of manipulating liquid jets and drops. *J. Phys.*, **105**, 012001.
14. Etoh, T.G., Son, D.V.T., Akino, T.K., Akino, T., Nishi, K., Kureta, M., and Arai, M. (2010) Ultra-high-speed image signal accumulation sensor. *Sensors*, **10**, 4100.
15. Yang, L., Adamson, L.J., and Bain, C.D. (2012) Study of liquid jet instability by confocal microscopy. *Rev. Sci. Instrum.*, **83**, 073104.
16. Minsky, M. (1961) US Patent 3013467, *Microscopy apparatus*.
17. Wilson, T. and Sheppard, C.J.R. (1984) *Theory and Practice of Scanning Optical Microscopy*, Academic Press, London.
18. Hamilton, D.K. and Matthews, H.J. (1985) The confocal interference microscope as a surface profilometer. *Optik*, **71**, 31.
19. Lee, C. and Wang, J. (1997) Noninterferometric differential confocal microscopy with 2 nm – depth resolution. *Opt. Commun.*, **135**, 233.
20. Rayleigh, L. (1966) On the capillary phenomena of jets. *Proc. R. Soc. London*, **29**, 71 (1879).
21. Donnelly, R.J. and Gaberson, W. (1966) Experiments on the capillary instability of a liquid jet. *Proc. R. Soc. London, Ser. A*, **290**, 547.
22. Bellizia, G., Megaridis, C.M., McNallan, M., and Wallace, D.B. (2003) A capillary-jet instability method for measuring dynamic surface tension of liquid metals. *Proc. R. Soc. London, Ser. A*, **459**, 2195.
23. Weber, C. (1931) Zum Zerfall eines Flüssigkeitssrahles. *Z. Angew. Math. Mech.*, **11**, 136.
24. Yang, L. and Bain, C.D. (2009) Liquid jet instability and dynamic surface tension effect on breakup. Proceedings of NIP25 and Digital Fabrication, Kentucky, pp. 78–82.
25. Hutchings, I.M., Martin, G.D., and Hoath, S.D. (2007) High speed imaging and analysis of jet and drop formation. *J. Imaging Sci. Technol.*, **51**, 438.



## 13 Inkjet Fluid Characterization

*Malcolm R. Mackley, Damien C. Vadillo, and Tri R. Tuladhar*

### 13.1

#### Introduction

This chapter is concerned with developing an understanding of the way inkjet fluid properties can be characterized. Inkjet processing involves forcing an inkjet fluid through very small nozzles, which are typically of order 30  $\mu\text{m}$  in diameter. The driving force can be provided, for example, by bubble-jet solvent evaporation (see, e.g., Vaught *et al.* [1] and Hawkins [2]), by pump and piezoelectric modulation using continuous inkjet (CIJ) [3] or piezo activation drop-on-demand (DOD) technology [4, 5]. In all the cases, the driving force is relatively low, and therefore, in order to obtain jetting velocities of meters per second, the viscosity of the inkjet fluid also needs to be low and typically below, say, 40 mPa·s. Fluids of this low viscosity are normally considered to be Newtonian, however, because jetting velocities are high and also involve significant extensional deformations. Non-Newtonian, inertial, and viscoelasticity effects have become important in terms of controlled high-quality jetting.

The whole jetting process is extremely delicate and sensitive to a wide range of variables, some of which are summarized as follows.

- Jetting drive device
  - Geometry and material of construction of overall jetting nozzle
  - Effect of adjacent jets in jetting arrays
  - Timescale and characteristics of jetting driving force
  - External jetting environment
  - Jetting temperature profile
- Formulation of the inkjet fluid
  - Speed of sound and bulk modulus
  - Rheology and fluid history of inkjet fluid
  - Surface tension of fluid – static and dynamic
  - Particle size and concentration
  - Contact angle of fluid

Recent innovative ideas in inkjet printhead (PH) designs capable of improved print speed, quality, and resolution for a wider range of inks and advances in inkjet ink chemistry and physics have extended inkjet technology to newly emerging markets and to applications such as display fabrication, ceramic components, microarrays for biological screening, controlled-release drug delivery, anticounterfeiting, and 3D printing. New and existing applications demand increased drop velocity, high print frequency, controlled drop size, and improved directionality. However, increased mist or satellite drop formation and reliability issues can work against the achievement of these requirements.

Despite recent advances in ink chemistry and physics, one of the key challenges in ink formulation is to develop inks that are consistent. Ink formulations are maintained to keep key parameters within specifications, yet it is often noticed that there are marked differences in the jetting performance between batches or between colors of a set of apparently identical inks. As a consequence, extensive and time-consuming ink reformulation and validation (optimization and/or separate waveform development) need to be carried out for each batch or between colors to achieve satisfactory jetting. This issue is further complicated when developing inks for niche applications, which could contain special pigments/particles with high loading concentration and density, polymers/binders of high molecular weight, and carrier fluid with different physical and chemical properties. Any variation in the composition could change fluid physical properties (such as density, surface tension, viscoelasticity, speed of sound) beyond the existing printhead operating windows.

A fundamental understanding of ink chemistry and the influence of individual components, as well as the ink as a whole, on the overall dynamic flow behavior and on substrate during printing is necessary in order to achieve targeted drop size, reduced satellite/mist formation, high print speed, frequency, and print reliability.

## 13.2

### The Influence of Ink Properties on Printhead and Jetting

Printing ink is subject to a wide range of dynamic and thermal perturbations. In the case of the DOD system, an ink supply, whether a gravity-fed bottle or a sophisticated ink supply system, serves two principal purposes; to deliver ink to the printhead inlet and to control meniscus pressure. From the inlet, a manifold distributes ink to the channels, its optimized design ensuring that each channel is supplied with the same pressure and flow rate. The active channel size defines the final drop volume while its geometry can define its operation mode and ultimately the sort of ink that can be used. Activation of the channel walls dictates the type of drop that is ejected. The nozzle holds the ink in while not printing and controls the drop formation process while drops are ejected [6].



Ejection of ink and subsequent drop formation are influenced by the physical properties of the fluid. For piezoelectric inkjet devices, high-frequency voltage pulses (waveform) are applied to a piezoelectric element. This causes an ink-filled channel to deform, thereby creating a fluctuating pressure profile. Through fluid acoustics, two or more consecutive waves are superpositioned, which guide the pressure pulses toward the nozzle [7]. The required superposition is achieved via adjustment to the electrical signals driving the piezoelectric actuator, that is, waveform frequency, voltage amplitude, and pulse duration [8]. As a result, a strong acceleration of fluid occurs inside the nozzle, which overcomes the viscous dissipation and the energy associated with forming a new surface so that fluid is jetted at high speed. The propagation and reflection of acoustic pressure waves are a function of fluid properties, printhead design, and constituent materials. The amplitude of the applied voltage pulse modifies the fluid acceleration in the channel and hence velocity of the jet ejected from the printhead. The presence of any dissolved gas or bubbles slows down the acoustic wave propagation and hence the jetting characteristics. Speed of sound, bulk modulus, density, pigment size, and distribution influence acoustic waves and are important parameters for optimization of drive waveform. Surface tension is also another very important factor in relation to drop formation; however, this chapter concentrates on one area alone, namely the rheology of the inkjet fluid.

### 13.3

#### The Rheology of Inkjet Fluids

The introduction of pigments to the carrier fluid can produce considerable deviation from the Newtonian behavior. This is due to particle association (by chemical bonds and/or physical interaction) during flow. The size and concentration of the pigment particles affect the viscosity and the likelihood of nozzle blockage. Dispersants are added to stabilize the pigments. Additives such as resins and polymers are often present to bind other components of the ink and contribute to the properties of the ink once on the substrate (e.g., grip/adhesiveness, gloss, resistance to heat, chemicals, and water). All of these additives influence the ink properties such as viscosity of the fluid and also elasticity due to their potential polymeric nature.

During printing, the fluid is subjected to high-frequency pressure fluctuations in the channel during actuation and high shear at the nozzle wall. As the jet emerges from the nozzle, the viscosity and elastic stresses resist the necking motion of the liquid filament, whereas surface tension and inertia influence the resulting shape and form of the emerging drop. These opposing forces result in high extensional deformation of the jet and subsequently into a spherical drop. The optimum values of the surface tension and viscoelasticity become a compromise of what is required upstream (in the channel) and downstream (in-flight).

## 13.3.1

**Base Viscosity**

The starting point of inkjet fluid characterization is the Newtonian viscosity of the fluid. A fluid is Newtonian if it obeys the linear relationship of Eq. (13.1).

$$\tau = \eta \dot{\gamma} \quad (13.1)$$

where  $\tau$  is the shear stress,  $\eta$  the Newtonian viscosity, and  $\dot{\gamma}$  the applied shear rate. Water is Newtonian and has a viscosity at room temperature of about 1 mPa·s. Most organic inkjet solvents are also Newtonian, and they have Newtonian viscosities that are similar to that of water or slightly higher (3–6 mPa·s).

Some fluids can be non-Newtonian, where the apparent viscosity  $\eta_a$  can depend on the applied shear rate, as expressed by Eq. (13.2).

$$\tau = \eta_a(\dot{\gamma})\dot{\gamma} \quad (13.2)$$

This complicates matters a little in terms of characterization; however, most inkjet fluids will have a limiting “zero-shear-rate” Newtonian viscosity, where at low shear rate, the viscosity is independent of the shear rate. Figure 13.1 shows a schematic of a Newtonian fluid and a typical non-Newtonian shear-thinning fluid. In most cases, inkjet fluids, if not Newtonian, would be expected to follow a so-called cross equation of the form given in Eq. (13.3).

$$\tau = \eta_\infty \dot{\gamma} + \frac{(\eta_0 - \eta_\infty)}{(1 + \dot{\gamma}^n)} \dot{\gamma} \quad (13.3)$$

where  $\eta_0$  and  $\eta_\infty$  represent limiting low- and high-shear-rate viscosities, respectively, and  $n$  is a power-law index that controls the apparent viscosity change between the limits.

The addition of additives such as pigment particle into an inkjet fluid will increase the fluid viscosity, and a useful lower bound guide in terms of viscosity enhancement can be obtained using the Einstein equation (Eq. (13.4)), which is

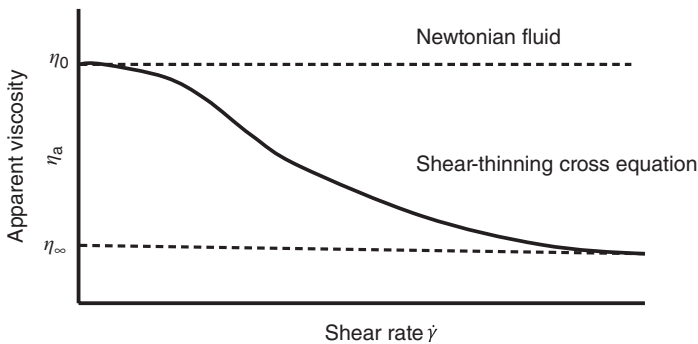


**Figure 13.1** Schematic graph of apparent viscosity as a function of shear rate for Newtonian and cross-equation fluids.

applicable only for low-concentration noninteracting particles.

$$\eta = \eta_0(1 + 2.5\phi) \quad (13.4)$$

where  $\eta_0$  is the viscosity of the base solvent and  $\phi$  the volume fraction of the added particles. This equation is plotted in Figure 13.2, and it can be seen, for example, that a 10% volume fraction of particles will increase the viscosity by only a factor of order 1.3. While this could be significant in terms of jetting performance, the predicted increase is less than a factor of 2 even for a 20% loading. The Einstein relation is valid for low concentration of noninteracting spheres in Newtonian solvent. For such low-concentration particles, the Einstein relation predicts that the suspension rheology will be Newtonian and also independent of the particle size. Increasing particle loading above, say, 10% causes a nonlinear increase in the suspension viscosity well above the Einstein prediction.

The addition of polymer to the fluid can, however, have a much more dramatic effect and the effect of interparticle interaction when particles are present can also greatly influence the basic viscosity behavior.

Viscosities are usually measured in simple shearing flow, which is schematically depicted in Figure 13.3. Simple shear is the type of flow experienced within a capillary and within the parallel section of an inkjet nozzle where the velocity change is perpendicular to the direction of flow. There is, however, a second important form of fluid deformation, namely elongational flow, which occurs for inkjet processing when the fluid enters and leaves the jetting nozzle and during drop stretching and breakup. This type of deformation is also illustrated in Figure 13.3 and is where the velocity change is in the direction of the flow. There is a so-called extensional viscosity  $\eta_e$ , which for a Newtonian fluid is linked to the shear viscosity by a Trouton ratio (TR) of 3.

$$\text{Trouton ratio for Newtonian fluid } TR = \frac{\eta_e}{\eta_0} = 3 \quad (13.5)$$

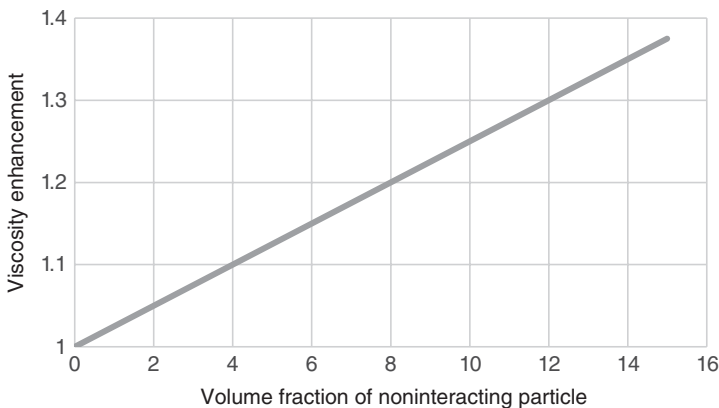


**Figure 13.2** Graph of Einstein equation viscosity enhancement as a function of volume fraction for noninteracting spheres.

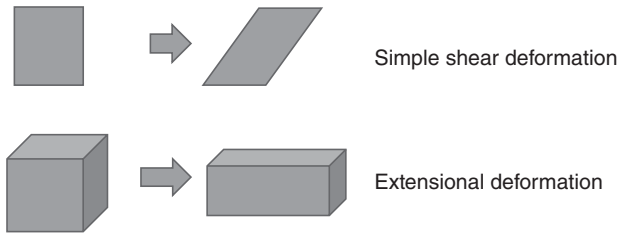


**Figure 13.3** Schematic diagram of deformation of simple shear and uniaxial extension.

Because of the low-shear viscosity values for inkjet fluids, the measurement of shear viscosity for printing inks is not necessarily straightforward, and in addition, the viscosities of inkjet fluids are very temperature-sensitive. Commercially, shear viscosities of inkjet fluids are normally measured by a number of techniques summarized as follows.

Measuring viscosities close to that of water presents difficulties. A classic way of measuring “watery” viscosities is to use an Oswald viscometer shown schematically in Figure 13.4. This “time-of-flight” device is accurate for Newtonian fluids but is not easily configured as a simple readout device. Commercial instruments such as the Seta KV6 Viscometer Bath (<http://www.stanhope-seta.co.uk>) require substantial temperature baths to achieve isothermal conditions and also are not easily automated. Rolling-ball viscometers such as Kittiwake FG-K1 ([www.kittiwake.com](http://www.kittiwake.com)), Grabner Minivis ([www.grabner-instruments.com](http://www.grabner-instruments.com)), and Anton Paar Lovis ([www.anton-paar.com](http://www.anton-paar.com)) are more compact and can work in the low-viscosity watery regime. Alternatively, *hydramotion.com* designed a handheld shear-wave portable viscometer, “Viscolite,” which can also measure low viscosities. Many rotational rheometers struggle to handle very low viscosities; however, for example, *malvern.com*, *tainstruments.com*, *anton-paar.com*, and *brookfieldengineering.com* all claim to have rotational rheometers of different forms that can operate in the inkjet fluid regime. A hybrid microfluidic and MEMS (microelectromechanical system) sensor-based instrument such as mVroc™ viscometer ([rheosense.com](http://rheosense.com)) is capable of measuring the viscosity over a shear rate range of  $1 - 106 \text{ s}^{-1}$ .

### 13.3.2

#### Viscoelasticity (LVE)

Inkjet fluid rheology is just one of the parameters that affect the whole inkjet process, and the rheology can interact with other parameters in a complex way. It is, therefore, no surprise that inkjet printing is still considered something of an art; however, in the last decade, systematic scientific investigation has been applied and there has been a progressive improvement in scientific understanding. Inkjet rheology has been a part of this development, and the purpose of this section is to review the current understanding of inkjet characterization in order to assist in the quantitative characterization and modeling of the industrial inkjet process.

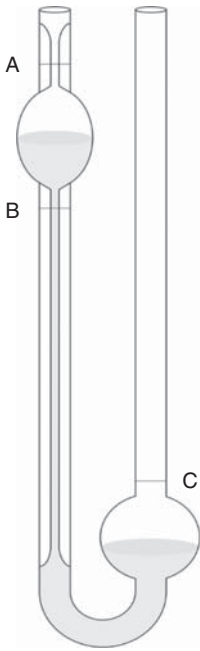


**Figure 13.4** Schematic diagram of an Oswald viscometer. The fluid initially in reservoir between A and B is timed when it fills reservoir C.

In the case of DOD, the acoustic waves that cause a droplet to be ejected are affected by ink viscosity. The acoustic waves will be dampened more with increased viscosity; therefore, the drive energy has to be increased in order to jet the fluid. In the channel, if the viscosity is too high, the ink may not flow through the printhead and too low viscosity may cause the ink to leak out of the printhead. Once the jet detaches from the nozzle, high viscosity is preferable to reduce satellite formation in-flight and to avoid drop splattering or bouncing during landing. The ink viscosity is mainly dictated by the choice of carrier fluid and pigment loading. The operating temperature is varied to bring the fluid viscosity down to optimum operating window of 3–40 mPa·s for most inkjet system and preferably between 10 and 20 mPa·s for most DOD printheads.

It is well known that addition of a small amount of polymer significantly influences the jetting behavior due to subtle changes in their elasticity (see, e.g., Hoath *et al.* [9] and Tuladhar *et al.* [10]). High elasticity influences the jetting velocity and forms a thin ligature, which may break up at multiple points, resulting in many satellites (or mist). In extreme cases, the jet does not detach from the nozzle and is either pulled back into the nozzle or floods the nozzle. Low or no elasticity can result in satellite formation at high jetting speed. The presence of some optimum elasticity is required, whereby the liquid filament connecting the main drop is instantly pulled into the main droplet after breaking from the nozzle, giving a satellite-free drop.

Viscoelastic effects are potentially important in relation to inkjet printing; however, accessing the viscoelastic properties of low viscosity inkjet fluids is not easy

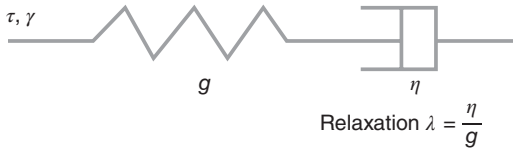


**Figure 13.5** Schematic diagram of spring and dashpot Maxwell model.

because the fluid relaxation times  $\lambda$  are usually of millisecond order or less, which is outside the normal measurement range of most rheometers.

A useful way of visualizing viscoelasticity is to consider the Maxwell spring and dashpot model, where the spring elastic modulus  $g$  represents the elastic component of the fluid and the viscous dashpot  $\eta$  is the viscous component. Figure 13.5 shows a schematic diagram of a Maxwell element, and the overall stress  $\tau$  and strain response  $\gamma$  of the model is controlled by the following differential equation where the relaxation time  $\lambda$  of the element is given by

$$g \frac{d\gamma}{dt} = \frac{d\tau}{dt} + \frac{\tau}{\lambda} \quad (13.6)$$

Small-strain oscillatory viscoelastic measurements are a powerful way of obtaining linear viscoelastic measurements of a fluid, and if a small sinusoidal strain displacement is made where the strain  $\gamma$  is given by  $\gamma = \gamma_0 \sin \omega t$ , where  $\omega$  is the angular frequency of oscillation, then from measurement of a torque response, three connected properties can be measured, as given in Eq. (13.7)

$$G' = \frac{g\lambda^2\omega^2}{(1 + \lambda^2\omega^2)}, \quad G'' = \frac{g\lambda\omega}{(1 + \lambda^2\omega^2)}, \quad \eta^* = \frac{g\lambda}{(1 + \lambda^2\omega^2)^{1/2}} \quad (13.7)$$

$G'$  is known as the *elastic storage modulus*,  $G''$  is known as the *viscous loss modulus*, and  $\eta^*$  is the complex viscosity.

A graphical representation of the  $G'$ ,  $G''$ , and  $\eta^*$  profiles for a Maxwell model fluid is shown in Figure 13.6, and this illustrates that at low frequency, the viscous loss modulus  $G''$  dominates and at high frequency, the elastic modulus  $G'$  dominates. The complex viscosity  $\eta^*$  for a Maxwell fluid remains independent of low frequency and then decreases at high frequency.

It is sometimes easier to measure a complex viscosity rather than a steady shear viscosity. In most cases, the two are equivalent. If the Cox–Merz rule is followed [11], a plot of complex viscosity as a function of angular frequency will be identical to a plot of apparent viscosity as a function of shear rate.

An inkjet fluid can, under certain situations, be modeled as a linear combination of a Newtonian solvent with an additional Maxwell element component [12]. In this case, the oscillatory linear viscoelastic or linear viscoelasticity (LVE) response will have a general form of the type shown in Figure 13.7. This graph shows that, at both low and high frequencies, the viscosity term  $G''$  dominates; however, at intermediate frequencies, the elastic term  $G'$  can become significant.

Because of the low viscosity for inkjet fluids, the associated relaxation times for the fluid are very low and may be of order of milliseconds or less. This in turn

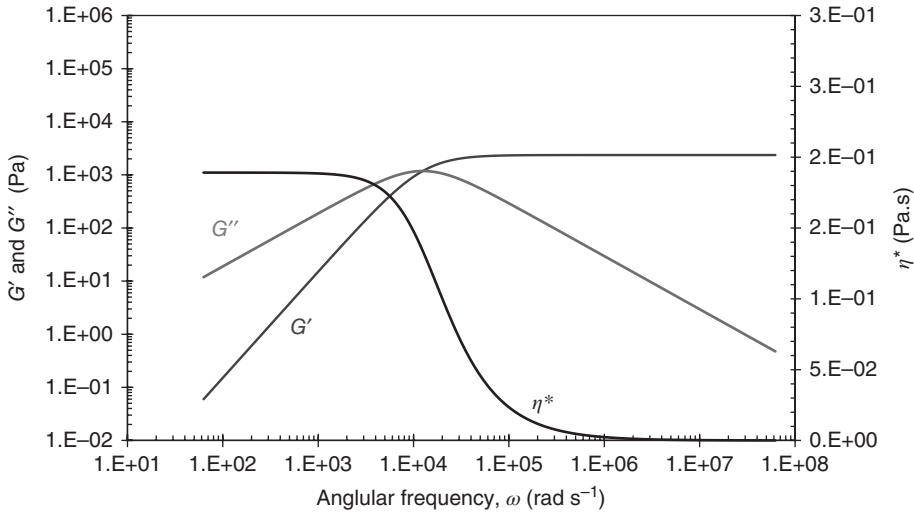


**Figure 13.6** Graph of linear viscoelastic oscillatory response  $G'$ ,  $G''$ , and  $\eta^*$  plotted as a function of applied angular frequency for the Maxwell fluid parameters used:  $\lambda = 80 \mu\text{s}$ ,  $g = 2364 \text{ Pa}$ , and  $\eta = 0 \text{ Pa}\cdot\text{s}$ .

requires specialized rheometers to access such high shear rates or equivalently high frequency of oscillation.

### 13.4

#### The Measurement of Linear Viscoelasticity for Inkjet Fluids

The steady-shear viscosity flow curve for inkjet fluids is difficult to obtain. Figure 13.8 illustrates some data for diethyl phthalate (DEP) solvent system with different concentrations of a monodisperse polystyrene (PS) [13]. At low concentrations, the base viscosity is very low and essentially Newtonian. The data shown in Figure 13.7 was obtained from two different rheometers. The low-shear-rate data was obtained from an Ares rotation viscometer [13] and the high-shear-rate data from small-bore capillary-flow pressure drop measurements using a Cambridge Multipass Rheometer [14]. The data show reasonable consistency between the shear rate regimes that both machine can access; however, shear thinning is only found for the higher concentration solutions. Inkjet fluids would show essentially the same behavior as the DEP solvent with no shear thinning.

Oscillatory  $G'$ ,  $G''$ , and  $\eta^*$  data are in principle generally easier to obtain for inkjet fluids than steady-shear flow curves. A difficulty arises here as well in that conventional oscillatory rheometers normally are unable to oscillate above a frequency of up to 50 Hz. While this is adequate for many polymer systems and structured fluids, the maximum frequency of the conventional rotational

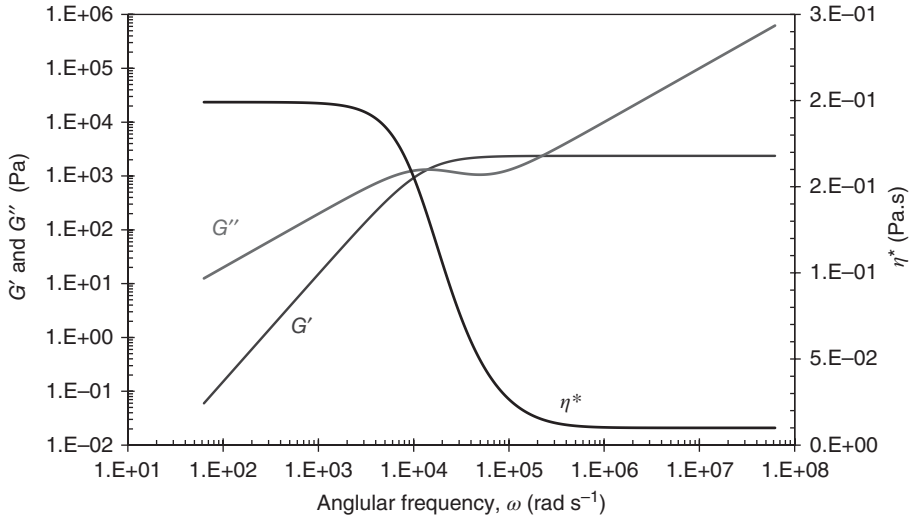


**Figure 13.7** Plot of  $G'$ ,  $G''$ , and  $\eta^*$  as a function of angular oscillation frequency for a combined Newtonian solvent fluid with an added Maxwell viscoelastic component. Parameters used:  $\lambda = 80 \mu\text{s}$ ,  $g = 2364 \text{ Pa}$ , and  $\eta = 10 \text{ mPa}\cdot\text{s}$ .

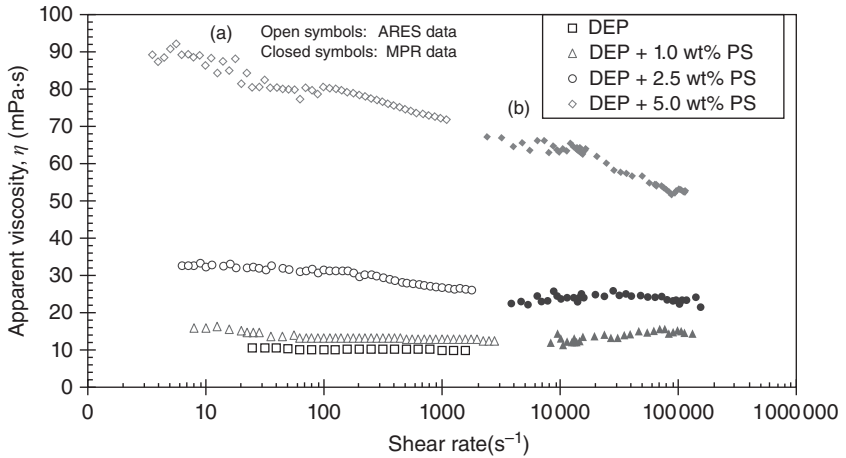


**Figure 13.8** The effect of polystyrene concentration on the apparent shear viscosity of DEP solvent and DEP-PS solutions for a range of shear rates at 25 °C using (a) ARES

parallel plate configuration for low-shear-rates (open symbols) and (b) MPR for high-shear-rate experiments (closed symbols) [13].



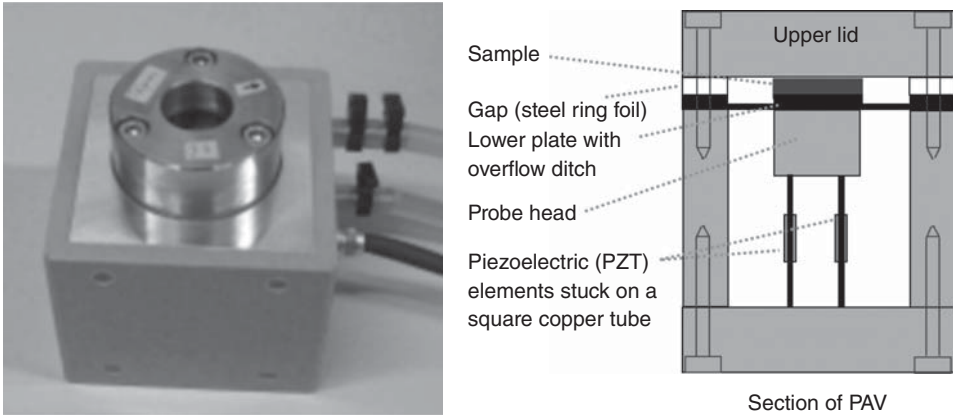


**Figure 13.9** Photograph and schematic diagram of the Piezo Axial Vibrator (PAV) rheometer.

rheometers is too low to detect any viscoelastic effects for the very low viscosity of inkjet fluids.

The late Professor Pechold from Ulm University spent many years developing a “Piezo Axial Vibrator” (PAV) rheometer [15] that was capable of measuring linear viscoelastic properties at very high frequencies. Figure 13.9 shows both a photograph and a schematic diagram of the device. A small quantity of fluid is held between two flat discs, and one of the discs is oscillated by a piezo actuator. The overall response of the system is followed using other piezo elements, and from the response,  $G'$ ,  $G''$ , and  $\eta^*$  can be determined. Figure 13.10 shows the LVE response for a polymer solution using both a conventional oscillatory rheometer and a PAV

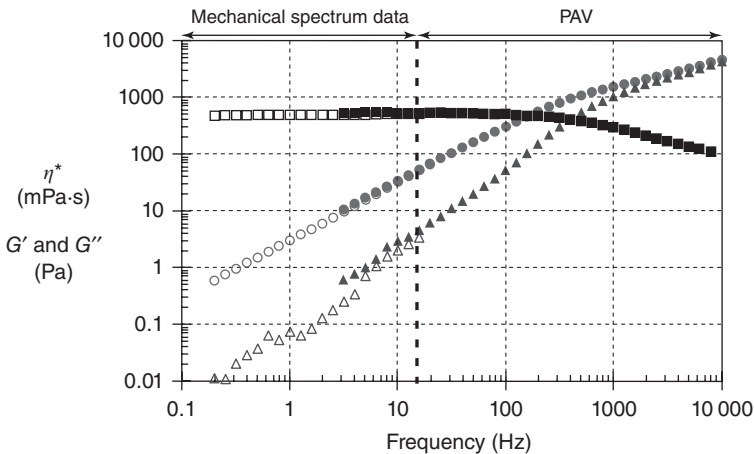


**Figure 13.10** Matching LVE mechanical spectrum data as a function of applied angular frequency (ARES, empty symbols) and PAV data (full symbols). Fluid: DEP – 10 wt% of monodisperse polystyrene  $210 \text{ kg mol}^{-1}$ . (■)  $\eta^*$ , (●)  $G''$ , and (▲)  $G'$  [16].

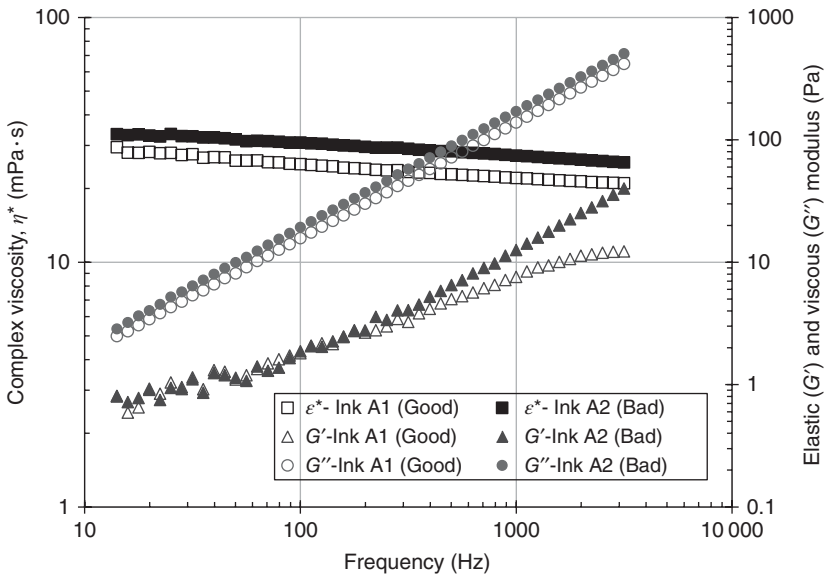


**Figure 13.11** PAV oscillatory LVE data as a function of frequency for a “good” and a “bad” printing ink.

[16]. Self-consistency between the two rheometers is good, and it can be seen that the frequency range of the data is greatly increased when the PAV is used.

The PAV can be used to access the LVE of inkjet fluids and as an example data for two inks are shown in Figure 13.11. One ink was found to jet satisfactorily and has been designated a “good” ink. A similar composition, but “bad ink” in terms of jetting, has been shown for comparison purposes. In both cases, the complex viscosity  $\eta^*$  is very similar. There are, however, differences in elastic  $G'$  response, and this may be related to the observed difference in process behavior.

A further example of PAV inkjet data is shown in Figure 13.12. Here, the influence of cellulose on the pigmented inks has been tested, and again, there is a detectable difference in the elastic  $G'$  behavior when a small percentage of elastic cellulose solution is added to the ink, although the inelastic, viscous  $G''$  behavior is very similar.

Other apparatuses exist for the measurement of high-frequency LVE data. A piezo-activated torsion resonator [16] can access even higher frequencies as compared to the PAV; however, it is a single-frequency device and very difficult to operate to obtain reliable and accurate data. Recently, multiple light scattering Diffusive-Wave Spectrometers (DWSs) [17] have been developed to access high-frequency data, but these apparatuses usually work in transmitted light, and this makes them unsuitable for most opaque pigmented inks. At present, the PAV appears as the only apparatus capable of measuring low-viscosity high-frequency LVE for inkjet fluids.

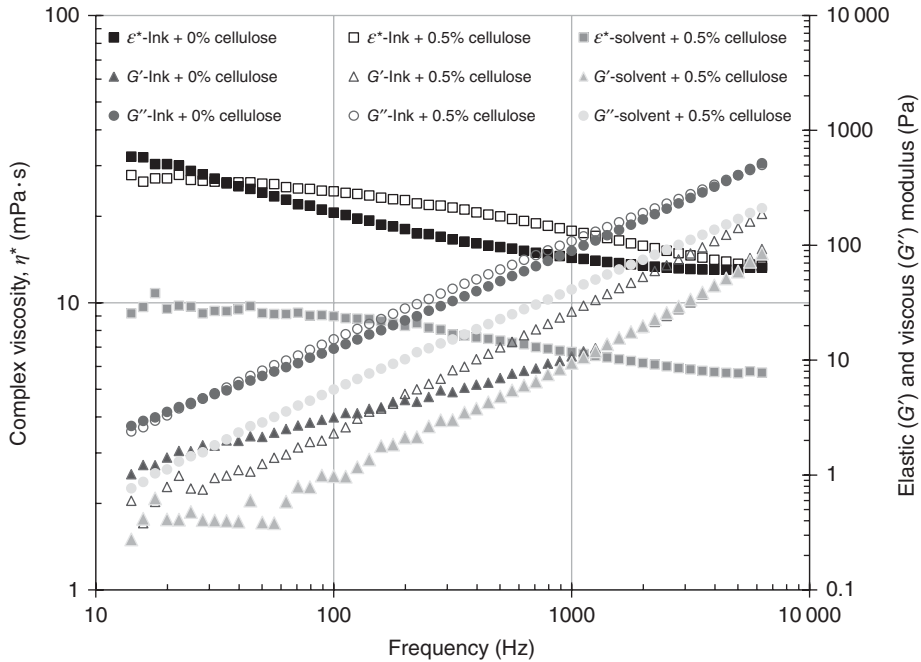


**Figure 13.12** PAV oscillatory LVE data as a function of frequency for a printing ink, with and without cellulose.

### 13.5

#### The Measurement of Extensional Behavior for Inkjet Fluids

When ink leaves the nozzle of an inkjet printer, the emerging ink is stretched and then forms a drop. This process involves jet velocities typically of meters per second and is dominantly an extensional flow deformation. The behavior of the stretching and breakup during this process can be very sensitive to the rheology of the inkjet fluid, and it is desirable to be able to measure the characteristics of inkjet fluids in this type of deformation. Stretching filaments of fluid to measure extensional viscosities goes back to the pioneering work of Trouton [18]. He studied the stretching behavior of high-viscosity tars. Later, extensive studies were carried out on the stretching behavior of polymer systems (see, e.g., McKinley [19] and McKinley and Sridhar [20]), although all systems investigated had very much higher viscosities as compared to inkjet fluids. The idea of using capillary thinning as a way of characterizing the extensional behavior of structured fluids was introduced by Bazilevsky *et al.* [21], who developed a device that involved rapid stretching of a fluid filament and then following the subsequent time evolution of capillary thinning.

Both the stretch and thinning behaviors of inkjet fluids can provide useful information about the extensional behavior of inkjet fluids. The experimental deformation situation is shown schematically in Figure 13.13, where the fluid is initially

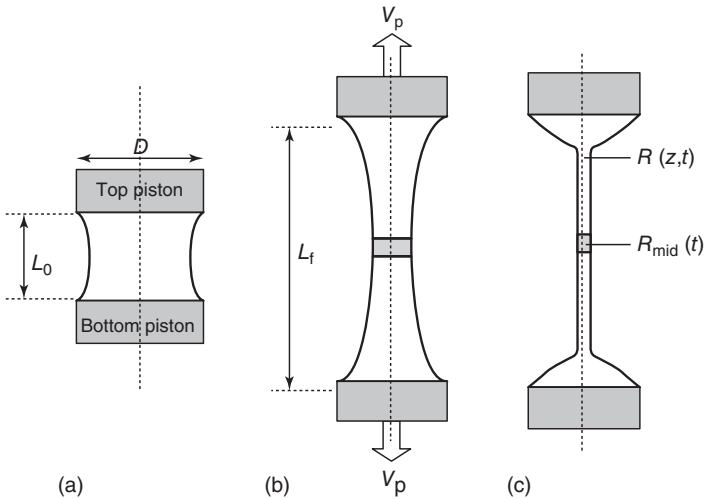


**Figure 13.13** Schematic diagram showing (a) initial position of filament, (b) filament stretching, and (c) filament shortening.

positioned between two pistons (Figure 13.13a). Either one or both pistons are then moved and stretching takes place (Figure 13.13b). During this period, it is possible to determine the transient extensional viscosity of the fluid using information on the capillary thinning at the center of the filament; see, for example, Sridhar *et al.* [22]. Subsequently, when the pistons stop moving (Figure 13.13c), capillary thinning takes place due to surface tension forces. Again, it is possible to derive a transient viscosity from this thinning action. See, for example, Anna and McKinley [23].

Filament breakup is very sensitive to a number of factors including the rheology of the fluid and the velocity with which the pistons are moved apart. High-viscosity fluids often survive the stretching process and filament thinning occurs on a timescale of seconds. Inkjet fluid behavior occurs with a much shorter timescale, and breakup can occur during the stretch or filament relaxation stage, depending on the fluid and the operating boundary conditions.

The only commercial filament stretch and thinning apparatus currently available is the Caber Apparatus (<http://www.thermoscientific.com/content/tfs/en/product/haake-caber-1-capillary-breakup-extensional-rheometer.html>), and the results of using this device are reported, for example, by Rodd *et al.* [24]. An alternative to the Caber instrument that is specifically relevant to the characterization of inkjet fluids is the Trimaster series developed at Cambridge University [25]. A schematic diagram of the Mk2 Trimaster is shown in Figure 13.14a, with a photograph in 13.14b. The device has two pistons that move in opposite directions, thereby keeping the center of the filament in the same central position. The piston movement for the Mk2 Trimaster is shown in Figure 13.15 and demonstrates that the moving period is essentially linear and that the final stretched position

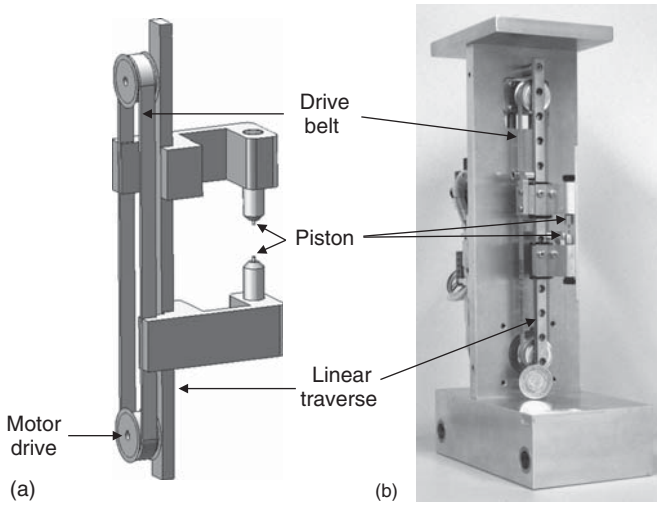


Figure 13.14 (a) Schematic diagram and (b) photograph of the Mk2 Cambridge Trimaster.

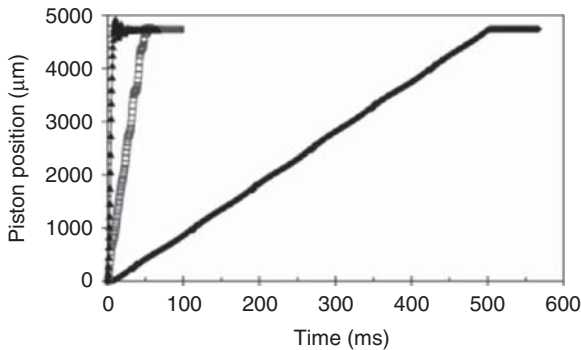
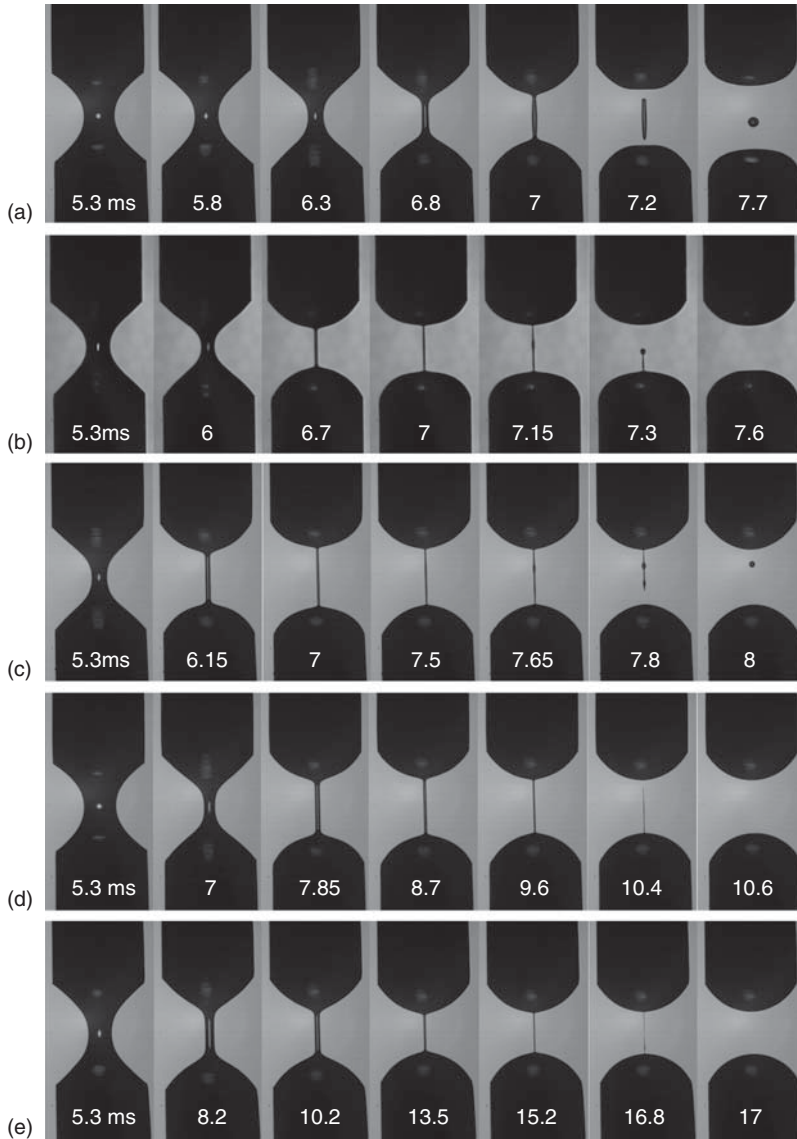


Figure 13.15 Piston positions as a function of time for the Mk2 Trimaster for different piston velocities, with diamonds denoting  $10 \text{ mm s}^{-1}$ , open squares  $100 \text{ mm s}^{-1}$ , and triangles  $500 \text{ mm s}^{-1}$ .

remains constant. The maximum useful velocity that can be achieved with this model is about  $500 \text{ mm s}^{-1}$ .

Representative photographic sequences obtained using the Mk2 Trimaster is shown in Figure 13.16. For all the cases, the piston motion stopped at  $1.5 \text{ ms}$ , and the photographs show the contour evolution after the pistons have stopped moving. Figure 13.16a shows a Newtonian DEP solvent, and in this case, the filament thinning is followed by end pinching, which occurs at either end of the filament and a single drop is formed from the end-pinched fluid. Figure 13.16b–e show the effect of progressively increasing polymer content. The breakup time increases with polymer concentration and also the form of breakup. The effect of end pinching is gradually attenuated and a thin parallel filament with longer life develops. At higher concentrations, the fluid within the filament is consumed into the ends and



**Figure 13.16** Photograph of the filament breakup captured with the Trimaster in the extensional viscometer modes [25] of (a) DEP; (b) DEP + 0.2 wt% PS110; (c) DEP + 0.5 wt% PS110; (d) DEP + 1 wt%

PS110; and (e) DEP + 2.5 wt% PS110. Initial gap size: 0.6 mm; stretching distance: 0.8 mm; and stretching velocity:  $150 \text{ mm s}^{-1}$ . Piston diameter: 1.2 mm.

no central drop is formed. While the viscosities of these solutions are generally greater than that of inkjet fluids, the basic features of end pinching or fine filament formation are the characteristic way in which different inkjet formulations behave.

Recently, a fast filament stretching variant, the Trimaster Mk4, has been developed, and a schematic diagram and a photograph of the apparatus are shown in Figure 13.17ab. Here, a rotating wheel is accelerated and then comes in contact with two metal arms that are separated by a wedge on the wheel. With this apparatus, piston separation velocities as shown in Figure 13.18 of  $2 \text{ m s}^{-1}$  are possible, which are close to the inkjet printing velocities. Depending on the diameter of the pistons, breakup for inkjet fluids can occur during or after movement of the

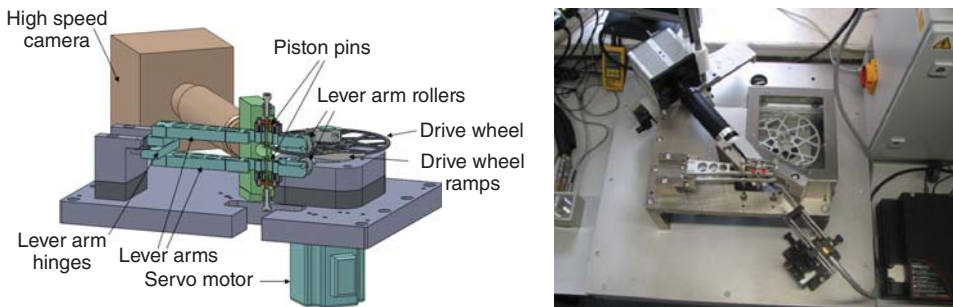


**Figure 13.17** Schematic diagram and photograph of Huxley Bertrum HB MK4 Cambridge Trimaster.

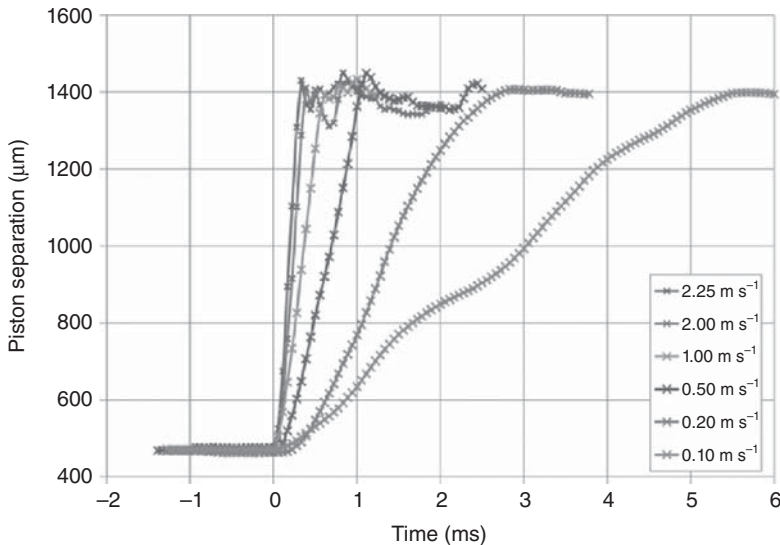


**Figure 13.18** Piston displacement as a function of time for Huxley Bertrum HB4 Cambridge Trimaster.

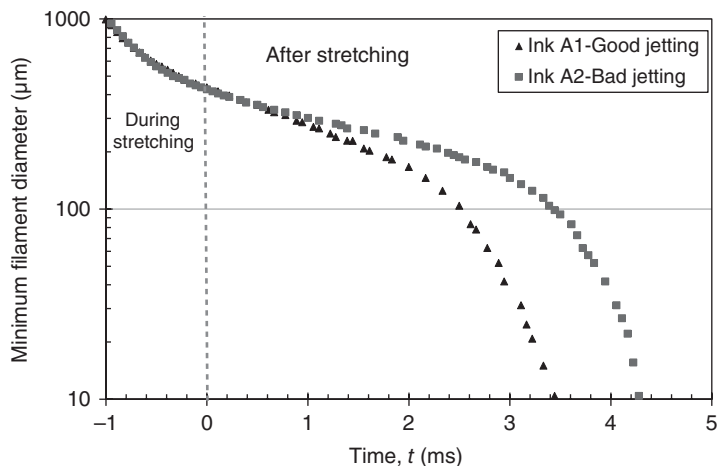


**Figure 13.19** Plot of filament diameter thinning during stretching and decay after stretching using HBMk4 for a “good” and a “bad” commercial ceramic inkjet printing ink. Initial sample height 0.5 mm, filament stretched speed  $1 \text{ m s}^{-1}$ , and final sample height 1.5 mm.

pistons. When using 1.0 mm diameter pistons, Figure 13.19 shows the behavior of a “good” and a “bad” printing ink during and after stretching. The figure plots the minimum thickness of the thread in the central region of the filament. By using a smaller diameter of piston, it is possible to observe breakup during the stretching phase of the motion for commercial inkjet fluids.

Filament stretching and filament thinning experiments have clear potential for carrying out rheological tests on small quantities of fluid for inkjet characterization. Achieving conditions close to that of inkjet processing is not easy; however, the Mk4 Trimaster deformation now comes close to providing matching controlled velocity and extensional deformations to existing inkjet printers.

### 13.6

#### Linking Inkjet Rheology to Printhead Performance

Small variations of polymeric additives (concentration and/or molecular weight) in low-viscosity inkjet inks ( $<50 \text{ mPa}\cdot\text{s}$ ) have a detrimental effect on the inkjet printing behavior to the extent that it may not jet at all even though the bulk properties are same. It is possible to encounter inkjet formulations that do not initially jet satisfactorily; however, after several subtle modifications to the formulations, it is able to jet reliably with minimal satellite formation, although all formulations have apparently identical base composition and physical properties.

The detailed understanding of the inks dynamic properties, printhead operating windows, and drive profile can be exploited to expand the ink envelope that exhibits good jetting characteristics (lower satellite/misting and good reliability) and also show insensitivity to temperature fluctuation and drive profile.



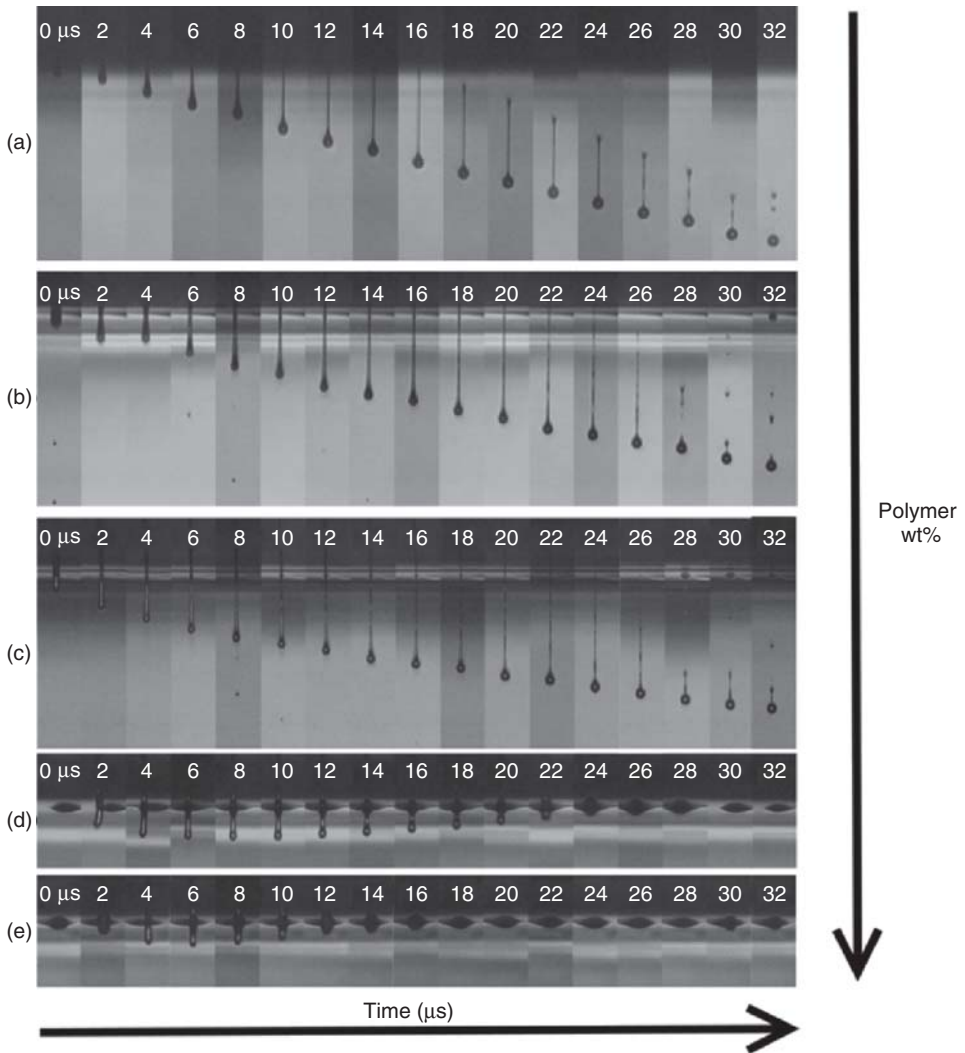


**Figure 13.20** Jetting photographs of five 17 mPa·s PS110 solutions of varying concentrations: (a) 0%; (b) 0.1%; (c) 0.2%; (d) 0.5%; and (e) 1.0%. In-flight jetting images obtained from Xaar 1001 PH using Spark Flash Rig.

Figure 13.20 shows the effect of increased polymer concentration on the jettability of five-model monodisperse Polystyrene PS110 (molecular weight of  $110\,000\text{ g mol}^{-1}$ ) solutions of different concentrations (0–1.0 wt%) but matched viscosity of 17 mPa·s [10]. The matched bulk viscosity was achieved by varying the proportion of high-viscosity dioctylphthalate, DOP (50 mPa·s) and low-viscosity DEP (10 mPa·s) as a carrier fluid. The jetting was carried out at 25 °C using a Xaar 1001 PH with the standard waveform. The drive amplitude was adjusted to

achieve a drop velocity of  $5 \text{ m s}^{-1}$  at 1 mm distance from the nozzle. Although the bulk physical properties were almost identical, the jetting behavior was found to be very different. The number of satellites reduced with increasing polymer concentration and negligible or satellite-free drops were obtained for 0.2% PS110 (Figure 13.20c). However, further increases in PS concentration resulted in no jetting even when the drive amplitude was significantly increased. Influence of polymer concentration and structure can be associated with the differences in elasticity.

Figure 13.21 shows the effect of increased polymer concentration on the dynamic rheology of the five-model PS110 solutions. Although the complex rheology and viscous modulus were apparently identical for all five solutions (Figure 13.20a,b), there were marked differences in the elastic moduli at higher frequencies (Figure 13.20c). Up to 100 Hz, there were hardly any elastic moduli for all solutions. The  $G'$  was not quantifiable up to 10 kHz

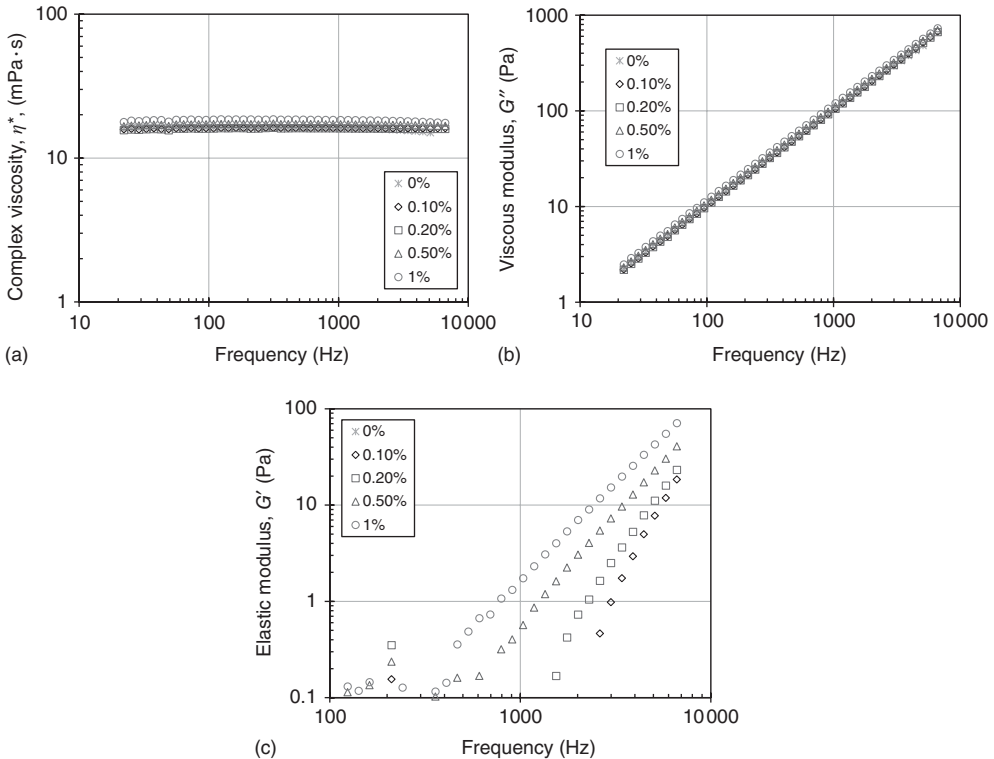


**Figure 13.21** PAV oscillatory LVE data as a function of frequency for PS110 solutions of varying concentrations 0–1.0%: (a) complex viscosity  $\eta^*$ ; (b) viscous modulus  $G''$ ; and (c) elastic modulus  $G'$ .

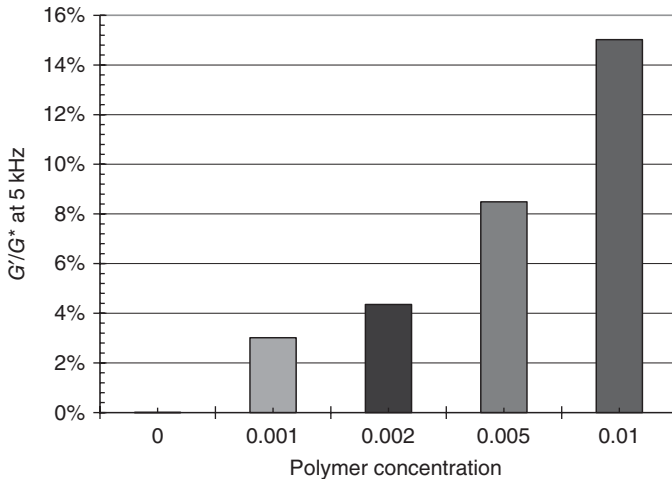


**Figure 13.22** Comparisons bulk viscosity and ratio  $G'/G^*$  at 5 kHz for the five-model solutions of varying PS110 concentrations.

for 0% PS110 solution. Above 1 kHz, a significant shift in the  $G'$  profile was seen for increased PS concentration. This clearly indicates that these fluids are not identical under printing conditions (10–100 kHz) and hence would expect a different printing behavior. From the ratio of elastic ( $G'$ ) to complex modulus ( $G^*$ ), obtained from the PAV measurements, the elasticity at high frequency can be deduced. Figure 13.22 shows the dimensionless elasticity (ratio of  $G'-G^*$ ) obtained at 5 kHz frequency. For the Newtonian (no elasticity) 0% PS20, satellite drops were evident during jetting (Figure 13.20). The 0.5–1.0% PS110 did not detach from the nozzle despite increasing the drive voltage and showed high elasticity. Fewer or negligible satellites were obtained between 0.1% and 0.2%, where it had some degree of elasticity but less than 0.5%, suggesting an optimum elasticity of 2–8% for these PH conditions for satellite-free jetting.

Filament stretching has been used as a quality control tool [13] and [25] to correlate and match the filament stretching behavior with the inkjet printing behavior of inkjet fluids. Close inspection of the filament shape of the thin ligature just before breakup can be linked to in-flight jet ejection and breakup mechanism.

Figure 13.23 shows the representative photographic sequence obtained using the Mk2 Trimaster for the PS solutions. The “optimum” breakup behavior for a DOD drop is a very subtle balance in relation to trailing filament formation and breakup. The 0% PS110 solution of Newtonian DEP/DOP solvent (Figure 13.23a) showed rapid thinning followed by end pinching, which occurred at either end of the filament and a single drop was formed from the end-pinched fluid.

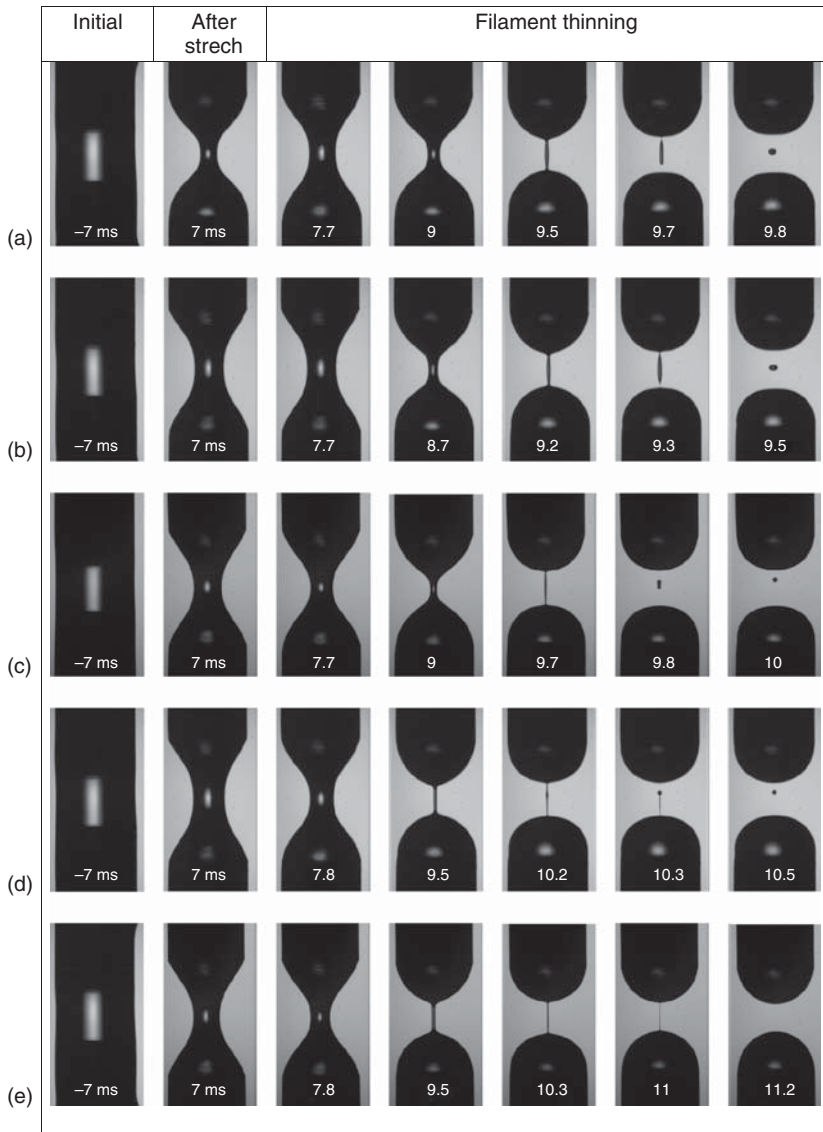


**Figure 13.23** Photographs of the filament stretch and breakup captured with the Trimaster in the filament breakup mode of five 17 mPa·s PS110 solutions of varying

concentrations: (a) 0%; (b) 0.1%; (c) 0.2%; (d) 0.5%; and (e) 1.0%. Initial gap size: 0.6 mm, stretching distance: 1.6 mm, and stretching velocity:  $150 \text{ mm s}^{-1}$ .

Figure 13.23b–e show the effect of progressively increasing polymer content. The breakup time increased with polymer concentration and also the form of breakup, similarly to that seen in Figure 13.16. At 1.0% PS110, the filament was consumed into the ends and no central drop was formed, although the viscosities of all these solutions were almost identical.

Vadillo *et al.* [25] illustrate that the ideal situation would be that breakup occurs at the tail and subsequently the trailing filament retracts back into the main drop, thereby not forming unwanted satellites. If end pinching occurs at both ends of the filament during filament thinning, a central droplet is formed. In terms of jetting, the filament may breakup into one or many satellite drops. If the filament thinning breakup is delayed too long, there is a potential for forming Rayleigh instabilities along the trailing thread, which subsequently breaks up into satellite drops. Finally, if the fluid is too viscoelastic, the consequent inkjet drop profile would be a filament, which (i) stretches without breakup, (ii) retracts into the jetting device, or (iii) cannot be released from the printhead.

Unlike viscosity, it is difficult to quantify the extensional behavior and the degree of elasticity of inkjet fluids (as a result of dispersant, binders, and other additives) using standard tools, and hence, it is difficult to control during formulation. There is clearly a benefit with high-frequency and extensional rheology to evaluate inkjet fluids before they are loaded into the printheads – either as a batch-to-batch quality assessment tool or as an aid in the development of fluid formulations.

Further examples linking the complex rheology and jetting behavior are illustrated by Hoath *et al.* [9], Tuladhar *et al.* [10], and Tuladhar *et al.* [26]. Further measuring techniques capable of detecting subtle changes in ink properties under conditions similar to those experienced during jetting, that is, high frequency (10–100 kHz) in the channel, high shear rates ( $10^5$ – $10^6$  s<sup>-1</sup>) in the nozzle, extensive extension in-flight, and high impact on landing, will allow one to predict the subtle difference in the jetting behavior by mimicking the fluid behavior to the real jetting process.

## 13.7

### Conclusions

This chapter has outlined some of the factors that control the droplet formation of inkjet printers and in particular has examined the effect of fluid rheology. The viscosity and viscoelasticity of inkjet fluids are not easy to measure because the base viscosity is low and generally close to that of water, and in addition, the viscoelasticity of the fluid is difficult to measure because the viscoelastic relaxation times of inkjet fluids are generally submillisecond. Another difficulty is the measurement of the extensional behavior of inkjet fluids where again the low viscosity and short timescales involved mean that a special apparatus is required.

In order to characterize the rheology of inkjet fluids, it has been necessary to develop a special experimental apparatus to access the required viscosity and time domain of these fluids. The authors of this chapter have found the Pechold PAV apparatus [15] particularly useful in order to measure both complex viscosity and elastic modulus components of inkjet and model fluids.

In addition, a Trimaster filament stretch apparatus [25] that can follow extensional behavior has been developed. Information from both apparatuses has helped characterize different fluids and establish a link between process behavior and formulation.

In general, it has been found that the presence of any polymeric component with a significant molecular weight can have a profound effect on inkjetting behavior. The presence of particles alone, while influencing the base viscosity, does not generally affect the jetting behavior significantly; however, the addition of particles in the presence of polymer can have a synergistic effect. Jetting is extremely formulation-sensitive with many factors combining to influence the final performance of a particular printhead. Successful inkjet printing still remains something of an art form, which in turn means that a full understanding and control of the process are not yet achieved. High-level rheology characterization of inkjet fluids of the type described in this chapter and also advanced numerical simulation of the process (see for example [27, 28]) have advanced the subject; however, at present, the only way to ensure that a particular formulation jets satisfactorily on a particular printhead is to carry out an experimental test.

### Acknowledgments

Much of the work described in this chapter has been carried out within the EPSRC/Industry project, Innovation in Industrial Inkjet Technology (I4T), and we are very grateful for their financial support. We are also grateful to Dr Simon Butler from the Department of Chemical Engineering and Biotechnology at the University of Cambridge for his patience and skill in obtaining many of the experimental results reported in this chapter.

### References

1. Vaught, J.L., Cloutier, F.L., and Donald, D.K. (1984) Thermal inkjet printer. US Patent 4,490,728.
2. Hawkins, W.G. (1985) Bubble jet printing device. US Patent 4,532,530.
3. Sweet, R. (1971) Fluid droplet recorder. US Patent 3,596,275.
4. Fischbeck, K.H. and Wright, A.T. (1986) Shear mode transducer for drop-on-demand liquid ejector. US Patent 4,584,590.
5. Brunahl, J. and Grishin, A.M. (2002) Piezoelectric shear mode drop on demand inkjet actuator. *Sens. Actuators, A*, **101**, 371–382.
6. Massucci, M., Boltryk, P., Tuladhar, T., and Drury, P. (2011) From ink bottle to ink drop: the flow environment in

- an inkjet print-head. NIP & Digital Fabrication Conference, Minneapolis, MN, ISBN 978-89208-296-4, pp. 54–58.
7. Beulen, B., de Jong, J., Reintem, H., van den Berg, M., Wijshoff, H., and van Dongen, M.H.A. (2007) Flows on the nozzle plate of an inkjet print-head. *Exp. Fluids*, **42**, 217–224.
  8. Reis, N., Ainsley, C., and Derby, B. (2005) Ink-jet delivery of particle suspensions by piezoelectric droplet ejectors. *J. Appl. Phys.*, **97**, 094903-1–094903-6.
  9. Hoath, S.D., Hutchings, I.M., Martin, G.D., Tuladhar, T.R., Mackley, M.R., and Vadillo, D. (2009) Links between ink rheology, drop on demand jet formation and printability. *J. Imaging Sci. Technol.*, **53** (4), 041208-1–041208-8.
  10. Tuladhar, T.R., Harvey, R., Tatum, J., and Drury, P. (2009) Understanding inkjet inks and factors influencing the jetting behavior. NIP & Digital Fabrication Conference, Kentucky, ISBN 978-089208-287-2, pp. 423–426.
  11. Cox, W.P. and Merz, E.H. (1958) Correlation of dynamic and steady flow viscosities. *J. Polym. Sci.*, **28**, 619–622.
  12. Yu, J.D., Sakai, S., and Sethian, J.A. (2007) Two-phase viscoelastic jetting. *J. Comput. Phys.*, **220**, 568–585.
  13. Tuladhar, T.R. and Mackley, M.R. (2008) Filament stretching rheometry and break-up of low viscosity polymer solutions and inkjet fluids. *J. Non-Newtonian Fluid Mech.*, **148**, 97–108.
  14. Mackley, M.R. and Hassell, D.G. (2011) The multipass rheometer; a review. *J. Non-Newtonian Fluid Mech.*, **166** (9–10), 421–456.
  15. Kirschenmann, L. (2003) Construction of two piezoelectric probes (PRV/PAV) for the viscoelastic properties of soft substances in frequencies 0.5 Hz – 2 kHz and 0.5 Hz-7kHz. PhD thesis. University of Ulm, Germany.
  16. Vadillo, D.C., Tuladhar, T.R., Mulji, A.C., and Mackley, M.R. (2010) The rheological characterization of linear viscoelasticity for ink jet fluids using piezo axial vibrator and torsion resonator rheometers. *J. Rheol.*, **54** (4), 781–795.
  17. Mason, T.G. and Weitz, D.A. (1995) Optical measurements of frequency-dependent linear viscoelastic moduli of complex fluids. *Phys. Rev. Lett.*, **74**, 1250–1253.
  18. Trouton, F.T. (1906) On the coefficient of viscous traction and its relation to that of viscosity. *Proc. R. Soc. London, Ser. A*, **77**, 426–439.
  19. McKinley, G.H. (2005) *Rheology Reviews*, The British Society of Rheology, pp. 1–49.
  20. McKinley, G.H. and Sridhar, T. (2002) Filament stretching rheometry of complex fluids. *Annu. Rev. Fluid Mech.*, **34**, 375–415.
  21. Bazilevsky, A.V., Entov, V.M., and Rozhkov, A.N. (1990) in *Liquid Filament Microrheometer and Some of its Applications*, Third European Rheology Conference (ed. D.R. Oliver), Elsevier Applied Science, pp. 41–43.
  22. (a) Sridhar, T., Tirtaatmadja, V., Nguyen, D.A., and Gupta, R.K. (1991) Measurement of extensional viscosity of polymer solutions. *J. Non-Newtonian Fluid Mech.*, **40**, 271–280; (b) Sridhar, T. (1990) An overview of the project M1. *J. Non-Newtonian Fluid Mech.*, **35**, 85–92.
  23. Anna, S.L. and McKinley, G.H. (2001) Elasto-capillary thinning and breakup of model elastic liquids. *J. Rheol.*, **45**, 115–138.
  24. Rodd, L.E., Scott, T.P., Cooper-White, J.J., and McKinley, G.H. (2005) Capillary breakup rheometry of low viscosity elastic fluids. *Appl. Rheol.*, **15** (1), 12–27.
  25. Vadillo, D.C., Tuladhar, T., Mulji, A.C., Jung, S., Hoath, S.D., and Mackley, M.R. (2010) Evaluation of the inkjet fluid's performance using the "Cambridge Tri-master" filament stretch and break-up device. *J. Rheol.*, **54**, 261–282.
  26. Tuladhar, T.R., Tatum, J., and Drury, P. (2011) Influence of print-head geometry, print conditions and fluid dynamic properties on the jetting behaviour. NIP & Digital Fabrication Conference,

- Minneapolis, MN, ISBN 978-89208-296-4, pp. 70–73.
27. Tembely, M., Vadillo, D., Mackley, M.R., and Soucemarianadin, A. (2012) The matching of a “one-dimensional” numerical simulation and experiment results for low viscosity Newtonian and non-Newtonian fluids during fast filament stretching and subsequent break-up. *J. Rheol.*, **56**, 159–184.
  28. Vadillo, D.C., Tembely, M., Morrison, N.F., Harlen, O.G., and Mackley, M.R. (2012) The matching of polymer solution fast filament stretching, relaxation, and break up experimental results with 1D and 2D numerical viscoelastic simulation. *J. Rheol.*, **56**, 1491–1516.



## 14 Surface Characterization

Ronan Daly

### 14.1

#### Introduction

The end goal of almost every application of inkjet printing is to deliver a new function or structure to an existing material surface. The first and still most successful and prevalent commercial application is printing of decorative patterns and text. This field rapidly evolved to a large manufacturing scale, as described in Chapter 1, with a wide range of surfaces such as paper, plastics, foils, fabric, and ceramic tiles. In the last 20 years, the applications of inkjet printing have diversified and the complexity of the delivered function has continuously increased. This is clear when tracking developments in inkjet printing of conductive tracks through to field effect transistor (FET) and microelectromechanical system (MEMS) and MEMS device printing, 3D printing of polymers, waxes, and metals, antibody and enzyme printing for biosensing, cell printing in regenerative medicine as well as combinatorial chemistry and high-throughput screening for pharmaceutical development. As we explore in this chapter, with each development, the role and integrity of the surface becomes more critical to ensuring successful and sustained delivery of the intended function. The original graphical applications require that the surface has the suitable properties to achieve a targeted print resolution and a pigment or dye adhesion appropriate to the application. More recent uses for inkjet technologies, for example, pharmaceutical printing, may require that the surface has the appropriate mechanical, chemical, and biocompatibility to ensure that highly repeatable crystallization processes will occur. The surface is no longer a passive underlying layer but is instead an active component that must be carefully monitored to ensure that the intended modification is achieved.

Surface science and surface characterization are vast fields of study with an immensely broad range of analytical techniques. Rather than try to introduce the reader to the full array of techniques, it is attempted in this chapter to provide a systematic approach to thinking about the needs of each application and a toolset of the most common techniques to help start to choose the right approach to qualify a robust and repeatable process.

## 14.1.1

**Understanding Surface Characterization Requirements**

Some of the current areas of rapid development in inkjet research and manufacturing literature are graphical printing, 3D fabrication, electronics/device fabrication, biological printing, and pharmaceutical printing. There is a process map presented in Figure 14.1 showing the main considerations when trying to define surface characterization needs for any of these applications. There are five different process steps over the lifetime of the printing process where the surface plays a key role. Each has specific characterization requirements to define (i) the original surface properties, (ii) the interaction of the ink with the surface, (iii) the delivery of the function from the ink to the surface, (iv) the properties of the final surface, and (v) the long-term stability of the functional surface. This map covers the full manufacturing system from the perspective of the underlying substrate to be coated and can be used to identify a list of properties to monitor at each stage. This systematic approach will enable a new inkjet user to identify the critical concerns for each application, and only after this is complete is it possible to choose the most appropriate characterization techniques.

In this chapter, we discuss each process step and build up a picture of the main categories of test that can be considered, namely chemical, physical/mechanical, electrical/thermal, optical, and biological characterization. The theory behind a few of the most relevant characterization techniques will then be explained in detail in Section 14.3.

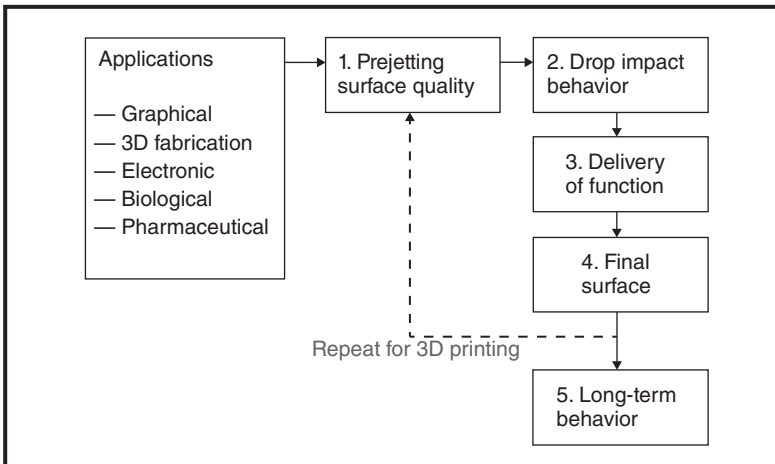


**Figure 14.1** Process map showing the steps that must be considered when defining the characterization techniques for any application of inkjet printing. At any stage (1–5),

there will be sets of chemical, physical, mechanical, electrical, thermal, optical, and biological tests that should be considered.

## 14.2

### Process Map to Define Characterization Needs

In this section, we go through each of the five separate steps shown in Figure 14.1. The drop formulation, ejection, and tuning are largely ignored at this stage but have been discussed in Chapters 3–7 and 13. Our focus is entirely on the characterization of inkjet-printed drops interacting with the surface. The first consideration is then quite intuitive and explores how we define the suitability of a surface for inkjet printing.

#### 14.2.1

##### Prejetting Surface Quality

When considering inkjet printing as the appropriate coating technique for any application, it is essential to define the required accuracy, resolution, and repeatability of the drop placement. With an increased demand for precise drop placement, there is an equivalent importance placed on ensuring a predictable surface quality. The initial prescreening of a starting material is often not discussed in detail in the literature but is in fact a critical step in manufacturing research. Characterization techniques and standards need to be defined to make sure the surface is within acceptable quality boundaries. This step is of great importance in research and large-scale fabrication because it occurs prior to the value-adding process of surface functionalization. Any errors at or after this stage reduce yield and are costly to the overall operation. Examples are discussed next relating to printed electronics and high-throughput screening applications, but firstly, the traditional application of graphical printing is discussed.

##### 14.2.1.1 Example 1: Graphical Printing

Graphical inkjet printing on fibrous materials is of enormous commercial importance, and so, we consider that system first. Printing to flat nonporous samples is considered in the second example. Printing onto fibrous materials such as paper and card is a major market for companies such as Hewlett-Packard. Inkjet-printed fabrics are also increasing in importance, with clothing industries identifying the importance of late-stage customization, such as minimization of batch size and responsiveness to the market. These are fibrous, porous materials, and in the case of paper specifically, there is a highly random structural combination of cellulose fibers, lignin, and functional coatings. Paper is formed by entanglement and subsequent bonding of fibers as they are separated from a dilute water suspension using a wire mesh. This wet, entangled material is pressed and dried to form the required sheets. Additional processes include coating with hydrophobic materials to improve resistance to water and bleaching to improve brightness. There is a rich history of inkjet printing to paper underpinning a range of major industries, and so, it is not surprising that the paper industry has developed quality standards that characterize the suitability of paper to an application. Here, we use this as an example to identify the questions that need to be asked and the chemical,

physical/mechanical, optical, and biological tests that should be considered when validating the surface prior to inkjet printing.

**14.2.1.1.1 Surface Chemistry Tests** For graphical printing onto paper, one of the key concepts is the control of ink imbibition and especially lateral spread in the porous bulk. This is influenced by a combination of the wettability and microstructure of the material. As can be seen in Figure 14.2a, an inkjet drop is estimated to be on the order of magnitude of the fibers. By increasing the volumetric dosage of ink per unit area, imbibition is seen both in the vertical access into the depth of the paper and horizontally, as shown in Figure 14.2b. Coupled with the random structure of paper, this immediately highlights the minimal control that will be available to drop placement. Figure 14.2c,d show the end of a single line of aqueous black ink printed along a paper surface. The images are of the same location but with increasing working distance of the microscope. This shows that ink drops can, firstly, miss the upper fibers of a paper surface and, secondly, spread along fibers in an effect that diffuses the edge profile of the line.

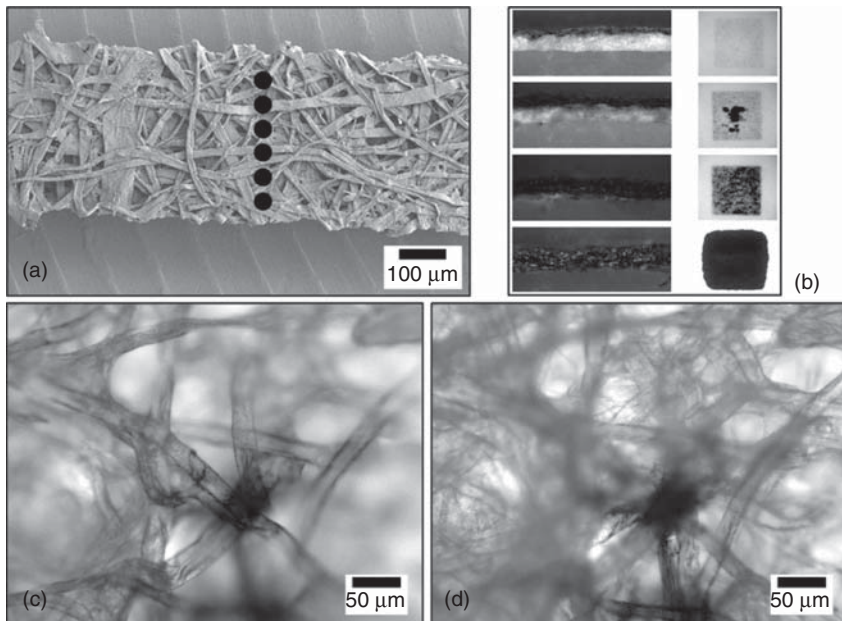


**Figure 14.2** (a) SEM of Whatman 1 chromatography paper with black circles drawn to illustrate approximate scale of standard inkjet drops; (b) increasing volumes of aqueous ink printed onto the same area of the paper with images of the paper cross section and the reverse side of the sample showing ink penetration; and (c,d) optical microscopy image of the same paper

material after printing a single line of black ink. With increasing working distance, it can be seen that ink can spread along fibers and is dosed to a number of fibers in the three-dimensional matrix due to the open porous structure. (Panel (a) by Ronan Daly, Panels (b–d) by Sze-Xian Lim, Department of Engineering, University of Cambridge.)

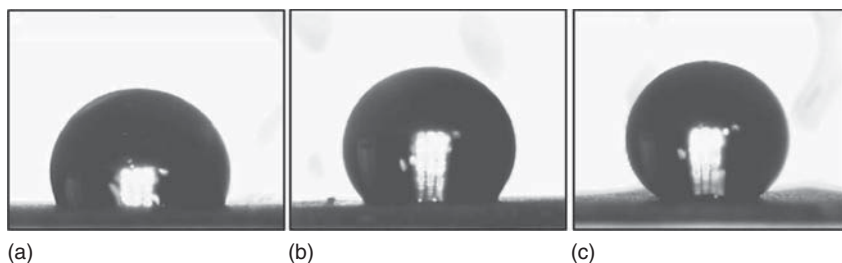


**Figure 14.3** (a–c) Water drop on Whatman 1 chromatography paper treated with increasing concentrations of AKD to show increased angles of contact between the drop and the surface.

The absorbance of the paper is, therefore, an important parameter that needs to be characterized and monitored. As discussed in Section 14.3.1.5, this is determined by the porosity and also the surface chemistry of the fibers. This can vary significantly in the manufacturing processes because the paper industry normally applies a dilute coating of hydrophobic material to the fiber surfaces, for example, alkyl ketene dimer. Upon drying, this material covalently bonds to the cellulose fibers, leaving hydrophobic groups exposed to air. This is used to reduce the naturally high absorbency of paper.

There are two standard approaches to testing the surface chemistry and wettability of paper in the industry. The first is to measure the time required for water to wick along the full length of an 8 mm wide and 40 mm long strip of paper. An excellent example of this work shows a change of 220 s to complete this wicking when moving from a birch to a flax-based paper [1]. This is a straightforward technique because the channel dimensions are significantly larger than the fiber size, allowing the assumption of an isotropic surface. In addition, the system is very easy to image because water imbibition prevents the significant light scattering due to the modification of the bulk refractive index, making the paper appear translucent. This approach is easily implemented in any industrial environment. A second technique is to measure the contact angle of a drop on the surface, as shown in Figure 14.3. The use of the naturally occurring angle of contact that a droplet makes with a surface to define the surface energy is detailed in Section 14.3.1.2. The droplet used is usually on the order of a millimeter in diameter rather than that of an inkjet drop. Because paper is so absorbent, the surface is usually densified through compaction to ensure that the angle is linked to the paper surface and not the porous flow.

**14.2.1.1.2 Physical/Mechanical Tests** The pore size varies drastically from standard printing paper (1–10  $\mu\text{m}$ ) to chromatography paper (10–100  $\mu\text{m}$ ). In the research literature, pore sizes are traditionally defined by mercury porosimetry, where the required pressure is measured to drive imbibition of mercury into the pores. This inversely correlates to the pore size. More recently, nondestructive X-ray tomography methods have been employed [2]. However, at an industrial

scale, it is standard to look at air permeation through the paper and deduce if any changes to the porosity have occurred (ISO 5636-3). This is described as “mean air flow rate through unit area under unit pressure difference in unit time, under specified conditions.” Identifying a change in this ability of air to permeate the paper will immediately signal a problem with a deviation from the standard porosity. The thickness and grammage (mass per unit area) are also recorded for paper to ensure a consistent density (ISO 534, ISO 536). The wet strength is important to ensure that the sheet will withstand handling even while the ink has not yet dried. This is measured by standard tensile techniques. The robustness of paper changes with fiber length and manufacturing processes. Again, identifying the deviation from standard behavior at this stage is crucial as it avoids mechanical failure of sheets or poor print quality with the significant additional value lost at this late stage.

**14.2.1.1.3 Optical Tests** When holding a paper up toward a light, the mottled effect or the variation in optical density is observed. This is the local variation in density due to fiber distribution. However, it is this density variation that can determine the paper strength and behavior upon printing and so must be quantified using standard techniques. Radiography techniques are normally used to define this “formation” of paper. In addition, optical tests are used to record the brightness of the paper upon reflection. This is carried out according to the standard ISO 2470 to ensure consistent and comparable results across material types. This is a critical parameter both for graphical printing, where poor contrast may lead to the failure of a barcode readout, and in new applications such as biosensor fabrication [1] where sufficient brightness is needed to enable clear readout of a color change. Brightness in paper originates from a combination of the number of layers that scatter light (at least 10 layers of fibers [1, 3]), the pore size (at least twice the wavelength of light [3]), and the optical brighteners added during the pulping process [4]. The result can be measured using a spectrophotometer, which quantifies the level of reflection across a range of specified wavelengths.

#### 14.2.1.2 Example 2: Printed Electronics

Inkjet printing has already made the leap to use in electronics, with initial research [5] and the main applications found in fabricating conductive tracks on surfaces (e.g., Printed Electronics, Ltd). MEMS and FET fabrication by inkjet printing is at an earlier stage of integration into manufacturing but is also a very active area of research. This approach is expected to rapidly increase in importance because of the benefits in moving to digital fabrication for low-volume niche applications. Smaller drop size capability and advances in functional ink development to include advanced materials such as graphene and carbon nanotubes ensure that printed electronics will increase in both complexity and breadth of application. Target surfaces for these devices include standard silicon wafer surfaces, sapphire-coated semiconductor surfaces, flexible polymer surfaces, and even ceramic tiles. The silicon fabrication industry, although relying on standard optical

and electron-beam lithography approaches, has defined a set of techniques appropriate for characterizing the initial surfaces for these applications. These techniques give an excellent starting point in the case of inkjet-printed applications, firstly, because many initial reports are using inkjet printing onto similar materials and, secondly, because the methods have already been tested at appropriate scales of manufacturing. In the silicon fabrication industry not only the functional inks but also the surfaces are considered high value materials, and so, it is even more critical to implement careful validation of surfaces prior to printing, to minimize expensive waste streams.

**14.2.1.2.1 Surface Chemistry Tests** As with paper, the surface chemistry is an essential component to understand to ensure a predictable drop spreading behavior. The optical measurement of the angle formed by a liquid when resting on a flat surface is detailed in Section 14.3.1.2 and is one of the key techniques for defining surface properties, but in essence, the contact angle on such flat surfaces is a balance of three surface energies, solid/air, liquid/air, and solid/liquid. The spreadability of a liquid on a surface is a useful factor, shown in Eq. (14.1) and known as the *Harkin coefficient of spreading*. This gives a quantitative result to the propensity of the system to lower its total energy by expanding or contracting the three-phase region. One complication of this approach is that it is not an inline positive validation technique, which is where optical methods show more promise.

$$S_{\text{liquid on solid/air interface}} = \gamma_{\text{solid/air}} - (\gamma_{\text{liquid/air}} + \gamma_{\text{solid/liquid}}) \quad (14.1)$$

For inkjet printing of electronics, it is essential that the wettability is adequate to drive ink spreading and avoid Rayleigh instabilities and breakup of printed linear features. Sufficiently poor spreading will drive retraction of liquids into spherical caps, as shown in Figure 14.4a. With a slightly reduced contact angle, the line remains stable, as shown in Figure 14.4b. With additional surface modification to drive near-perfect wetting, the lines again become lost, with spreading dominating the behavior, as seen in Figure 14.4c. It is important to mention, as noted by Hsiao *et al.* [6], that stability of the line is linked not only to the surfaces but also to

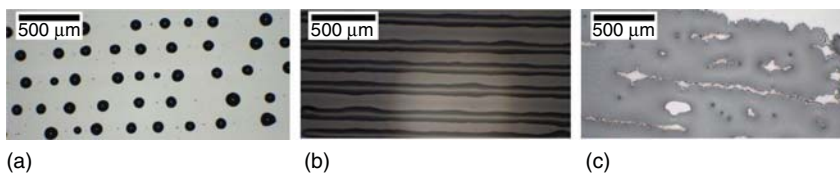


**Figure 14.4** (a) 1:1 water/glycerol ink is printed on a silicon wafer with silicon dioxide surface layer, resulting in Rayleigh instabilities of the line and breakup; (b) the same ink is printed on a microscope slide and remains in stable lines; and (c) the same

ink is printed on the first silicon wafer after exposure to intense UV radiation to drive higher wettability. This drives spreading and reduces the line definition. (Yoanna Shams, Department of Engineering, University of Cambridge.)



additional factors such as the drop spacing, drop impact velocity, and the timing of the drop print frequency.

**14.2.1.2.2 Optical Tests** Particulate contamination of the original surface is one of the main causes of low yields in the standard fabrication manufacturing facilities. This can clearly be seen to lead to challenges in inkjet printing as shown in Figure 14.5a, where 1 : 1 water–glycerol ink is printed onto a glass microscope slide. Particulate contamination resulting from a poor cleaning protocol leads to additional spreading and pinning of the lines. This deviation from the desired straight line can be important if it occurs in multiple locations, driving the two lines to coalesce, as shown in Figure 14.5b. While for graphical printing on flat surfaces, such as plastic packaging, this is not a critical error, it will however create a short circuit in an electronics application. As a result, advanced laser light scattering techniques have been developed, which are useful for surface characterization prior to printing electronics. Light reflection is disrupted or scattered by very low levels of particulate contamination.

Nano- and microscale layers of dielectric or conductive materials may already be present on the surface, with inkjet used to deliver additional functional components. In these cases, optical techniques are also used for validation. Ellipsometry, for example, measures the change in polarity of an incident light source upon reflection and uses this to determine the thickness of the layer it has passed through as well as a range of other properties, such as the crystallinity, roughness, or doping concentration. Infrared, ultraviolet/visible, and Raman spectroscopy are also essential optical tools that probe and analyze materials to identify their chemical composition at an even smaller scale. Printed electronics can also require very clean initial surfaces and even functional monolayers to improve electron mobility or surface adhesion. Optical techniques can identify the presence or quality of these layers by driving energy absorption by bond vibration, electron promotion,

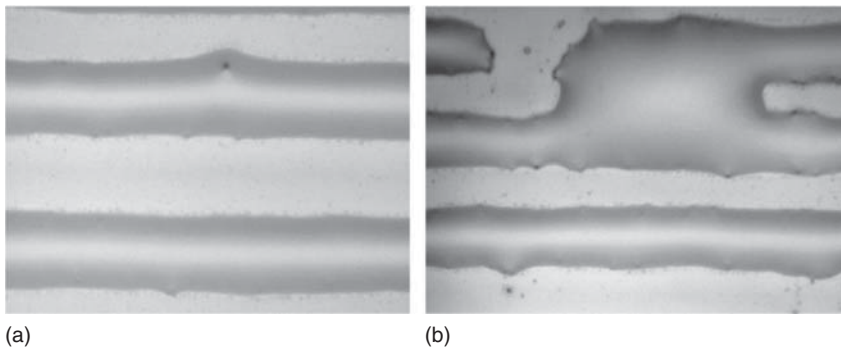


**Figure 14.5** (a) 1 : 1 water/glycerol ink is printed on a glass microscope slide. Particulate contamination can lead to pinning of the line. (b) If the pinning occurs while too

close to another feature, coalescence can occur. (Yoanna Shams, Department of Engineering, University of Cambridge.)



and even electron emission. Raman spectroscopy is also often used in the semiconductor industry not only for surface information but also for determining the nature of the particulate contamination to help track down the source of the problem.

**14.2.1.2.3 Electrical Techniques** As thin layers of conductive or insulating materials are routinely included on the surface to be printed, the quality of this is of great importance. Resistance can be measured for materials in the ohm to megaohm range using a standard ohmmeter. In this case, a constant current is used across two contacts and the voltage drop is recorded. This is, however, not sufficiently sensitive for thin semiconducting or highly conducting materials. Conductivity is essential to record and is the ability of a material to allow electron and hole flow [7]. Resistivity is the inverse of this, the ability to oppose electrical conductance. The key point about both measures is that they are defined per unit length. However, when examining silicon substrates, semiconducting layers with ion implantation or thin functional layers [7] (such as conductive tracks and carbon nanotube sensing layers), the sheet resistance is far more useful. This is simply resistivity divided by the thickness of the sample or layer. It is measured as “ohms per square” and is useful because it is scalable to the value of any sample size. This is measured most commonly using a four-point probe methodology, discussed in more detail in Section 14.3.3. These values are used to judge the quality not only of the initial surfaces but also of any cleaning stages that are used to remove the natural oxide layers.

#### 14.2.1.3 Summary

Significant emphasis has been given to this first section because ensuring that the original surface is suitable for printing is key to minimizing expensive waste streams. Also, when defects or printing issues arise, it is much easier to carry out root cause analysis when the initial surface is fully characterized and validated, allowing rapid decisions about the extent to which batch containment or recall is required. It is clear that the key properties that need to be considered are those that control droplet spread, imbibition, as well as the material’s chemical and physical integrity. Once the surface is prepared, the behavior of the drop upon printing is the essential behavior to understand. Again, this can be controlled partly by understanding of formulation and printing discussed in the previous chapters but also by characterizing the role of the surface, as discussed in the next section.

### 14.2.2

#### Drop Impact Behavior

The characterization of a surface prior to printing using contact angle measurements has already been noted. This normally involves millimeter-scale drops being deposited on the surface of interest at as slow a velocity as is feasible. However, with inkjet printing, very small drops (picoliter-scale) arrive at a very high velocity, often with the next drop already exiting the nozzle before the first

has hit the surface, and so, there is a much broader range of feasible behaviors upon impact. The most common set of behaviors that can occur are listed as follows:

- 1) the drop can bounce, recoiling completely from the surface;
- 2) the drop may spread to an equilibrium contact angle;
- 3) a phase transition may occur, with solidification at a nonequilibrium contact angle (e.g., wax printing, UV-curable inks);
- 4) a drop may coalesce with a second drop already on the surface and either retract into a single spherical cap or stabilize as an extended line;
- 5) imbibition can occur if the surface is porous and wetting;
- 6) when printing onto a liquid, the drop can bounce off the surface, coalesce, or remain as a stable colloid in the bulk or at the liquid/air interface (e.g., printing into high throughput screening (HTS) well plates containing buffer solutions and antibodies).

Again, understanding the surface rather than just the ink formulation is essential in driving controlled impact behavior as shown here by referring to application examples. The techniques for characterizing these events are necessarily mostly focused on imaging approaches of the dynamic process as it occurs and postprinting samples.

#### 14.2.2.1 Example 1: 3D Printing

Additive manufacturing by inkjet printing is carried out either by using digital patterning to bind a powder temporarily into a structure prior to sintering or by directly printing the structure, building drops one on top of the other while driving a phase change or cross-linking solidification with each layer. Additive manufacturing by inkjet printing is now a successful commercial tool capable of high-definition fabrication, but there are surface characterization approaches that should be considered as the technique is applied to broader applications other than standard rapid prototyping, for example, 3D electronic device fabrication [8].

**14.2.2.1.1 Optical and Imaging Techniques** Positive-confirmation techniques for drop tracking and real-time impact behavior are very difficult to implement on a manufacturing scale. For initial research and product development, there are a range of techniques, including (i) shadowgraphy using a short-duration strobe to enable image capture and also (ii) high-speed imaging. These can be achieved with white light or laser holography [9]. For 3D printing, postprinting analysis is still the most useful approach during the development stage. As shown in Figure 14.6, the impact and phase-change behavior of a line of wax drops is analyzed to find the optimum drop spacing to ensure straight lines and walls of wax. Similar approaches are needed for UV-curable inks. Figure 14.6a shows the instability of bulging lines, fixed due to a phase change. The drop frequency was too fast and Rayleigh instabilities began to take effect during solidification. The layers can be built in the height direction but each has the same instability (Figure 14.6b). Figure 14.6c,d show the equivalent behavior with a decreased drop frequency.

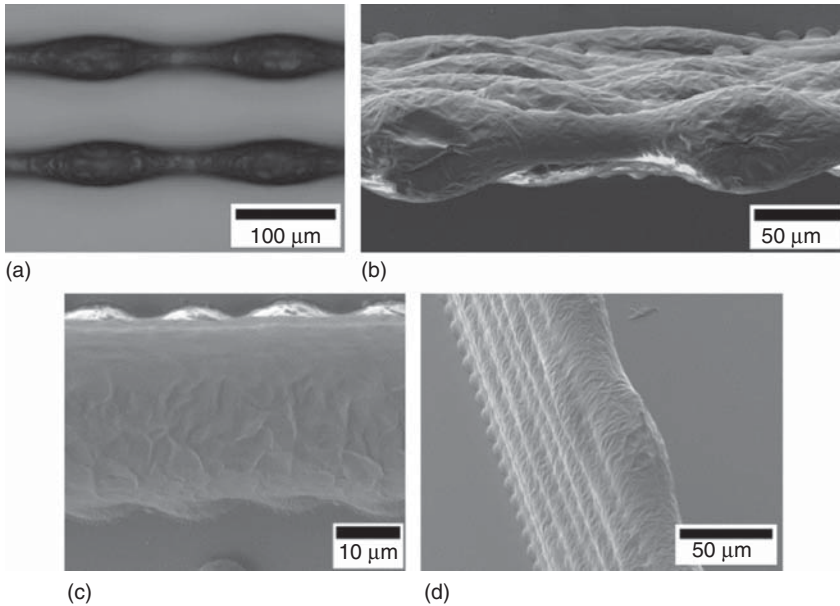


**Figure 14.6** (a) Paraffin wax printed using a  $20\ \mu\text{m}$  diameter inkjet nozzle at a drop spacing of  $5\ \mu\text{m}$ . The Rayleigh instability is halted before breakup due to solidification. (b) Ten layers are printed in a vertical wall using the same settings as (a). (c) A single

layer is printed at an increased drop spacing of  $15\ \mu\text{m}$  resulting in a much straighter line. (d) A 10-layer vertical wall is printed at the same settings, again showing a more regular shaped wall.

The key surface influence is again the surface chemistry to drive spreading of the still-molten wax. For 3D printing, however, the underlying surface is immediately replaced by the solid phase of wax for all subsequent layers. This highlights the main challenge of surface control for 3D printing. The subsequent layers must spread to the correct angle and solidify when interacting with their own solid phase of ink. Secondly, the surface temperature must remain constant despite (i) hot wax being deposited at a high frequency to the surface or (ii) UV-curable ink (often printed at elevated temperatures) undergoing intense optical energy that can lead to a buildup of thermal energy in the surface. Any buildup of thermal energy in the form of a temperature change will modify the phase-change behavior and drive an increase in the spread of the ink.

#### 14.2.2.2 Example 2: Reactive Inkjet Printing and High-Throughput Screening

A patent [10] in 1995 from Protogene Laboratories examined miniaturization of assays for pharmaceutical development. Since then, inkjet printing has been a major focus of research for developing high-throughput drug discovery techniques [11]. It is clear that for critical applications such as drug development, the stringent regulatory environment will demand precise data of the drop behavior upon impact.

**14.2.2.2.1 Optical Techniques** Again, optical imaging techniques are critical to validating an inkjet application. When examining inkjet printing of liquid drops onto a solid surface, it is important to know if the liquid is being repelled from the surface through charge effects or rebounding and landing elsewhere due to poor wettability. This is especially important for developing applications in high-throughput screening of pharmaceuticals. In such cases, the underlying surface is usually a liquid, in the form of a drop, spherical cap, or flat surface. It is essential to know if when a liquid drop lands on these surfaces, it will coalesce, alternatively land and remain separate, or, in fact, bounce away. These will be important considerations, for example, in combinatorial chemistry where inkjet is being explored for very small scale parallel synthesis of large numbers of new molecules. Figure 14.7a shows the coalescence of a liquid drop (water/glycerol) with a previously printed drop of the same fluid, and it is clear even in this case from the meniscus that instant mixing does not occur. Equally, imaging has shown (Figure 14.7b) that similarly to the work in [12] for millimeter scale drops noncoalescence of liquid drops can lead to rejection of the drop from the surface.

Droplet impact when printing any material in a pattern, similarly to graphical printing, can lead to instabilities in line formation. Figure 14.7c shows the printing of drops and their subsequent coalescence. Depending on the spacing and print frequency chosen, a range of line instabilities can occur, such as those shown in Figure 14.7c. These are also significantly influenced by the impact with the surface, the contact angle, and pinning of the drop edge.

#### 14.2.2.3 Summary

Droplet impact leads to a finite set of behaviors, as noted in the introduction to Section 14.2.2, the result of which will ultimately lead to the success or failure of the coating process. The droplet impact occurs at high speed and in a manufacturing environment over a range of conditions, making it inherently difficult to predict and also difficult to observe, especially with positive-confirmation techniques. While significant effort is required to define new measurement systems. The underlying effects are dominated by surface tension, viscosity, and elasticity of materials. This suggests careful mapping of behavior across a phase space of temperatures and materials will allow robust process boundaries to be defined where the surface will behave as expected. It is therefore vital during manufacturing to control the underlying surface through understanding of the inherent heat transfer and maintenance of the local conditions.

### 14.2.3

#### Delivery of Function

Once drops impact on a surface, they must also then deliver their intended function. This section introduces the role of the surface in allowing the function to be transferred from the droplet. This can occur through simple drop drying, where solvent evaporation leads to precipitation of the functional material onto the

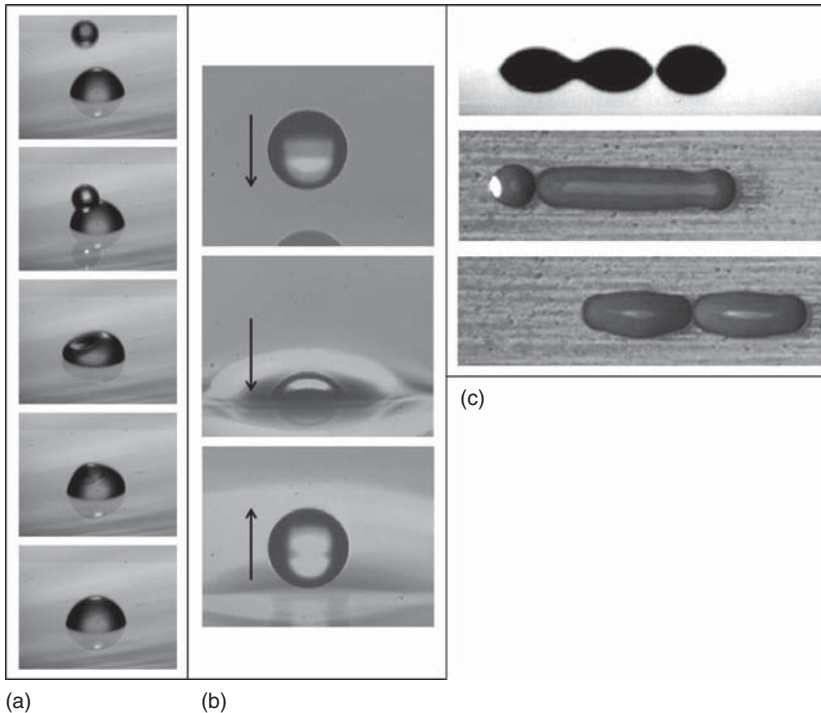


**Figure 14.7** (a) Water-glycerol ink drop printed onto a previously deposited drop. Coalescence occurs without complete mixing. (Qingxin Zhang, Department of Engineering, University of Cambridge.) (b) A water-glycerol drop bounces off an organic solvent surface due to an

air cushion trapped between the liquid surfaces. (c) Capture of line-printing midcoalescence and postprinting images of the line breakup that can occur. (Wen-Kai Hsiao, Inkjet Research Centre, Department of Engineering, University of Cambridge.)

surface. Alternatively, cross-linking can be initiated to drive solidification if the function is the adherence of a polymer gel in, for example, graphical applications. For biosensor or pharmaceutical developments, the function is often the transfer of active biomolecules to a surface or liquid reservoir for subsequent reactions. The role of the ink formulation is studied in the literature for all of these areas, but for manufacturing, it is also vital to ensure that the surface is maintained under the appropriate conditions to achieve functionalization.

#### 14.2.3.1 Example 1: Graphical Printing

UV-curable inks, often acrylate-based polymer systems with initiators and monomers included in the formulation, are an incredibly important elements of the inkjet printing industry due to the robustness of the coating, good adhesion to a broad range of nonporous materials, and excellent print resolution that can be

achieved. These inks are formulated to combine high viscosity with rapid fixing to ensure minimum spread and a high print resolution.

**14.2.3.1.1 Chemistry Techniques** If a surface to be printed has water or other solvents trapped within the matrix, especially at the surface, even at very low levels, these may continue to outgas during the delivery of the ink. It is known that UV-curable reaction chemistry can be sensitive to outgassing chemicals, often inhibiting the solidification. Two techniques that can be used to validate a material are differential scanning calorimetry (DSC) and thermogravimetric analysis (TGA). DSC details the specific heat capacity of a sample, which is effected by its purity, and TGA is able to break down and remove the material through heat, noting to a high degree of accuracy how this progresses with temperature. This enables identification of both different trapped solvents and other impurities.

**14.2.3.1.2 Optical Techniques** Optical techniques such as high-speed imaging are excellent for understanding the solidification process. Again, this is not a positive validation technique, but it is important to firstly confirm the repeatable printing of drops that solidify at nonequilibrium contact angles. This is influenced by the surface chemistry, thermal conductivity, and also the environmental conditions and so can be linked to the change in drop behavior.

#### 14.2.3.2 Example 2: Advanced Functional Materials

Inkjet printing of biological or pharmaceutical materials and functional micro- and nanomaterials is of enormous importance in the research literature. The actual jetting of materials such as nanometallic inks, carbon nanotubes, graphene, and etch-resist waxes is quite straightforward. However, interaction with the surface and delivery of the function to the surface is much more complex to control. The function can be delivered by slow adsorption (chemical or physical), simple precipitation, or crystallization of the material from the solution onto the surface.

**14.2.3.2.1 Physical/Mechanical Techniques** Ultrasensitive measurements of mass change over time can be used to quantify drop deposition [13]. However, far more sensitivity is needed to show delivery of a function, for example, quartz crystal microbalance studies can be used to observe the adsorption of proteins to surfaces [14]. These coatings are not representative of *in situ* printing but allow mapping of the robustness and sensitivity. Similarly, microresonators can be coated with an appropriate material and used [15] to understand adsorption behavior and positioning of ink components, validating the delivery mechanism. These work by monitoring the change in oscillating frequencies by infinitesimal increases in mass. It is hoped that, as these (and also lateral bulk acoustic resonators) are already approaching industrial-scale use, surface functionalization by soft matter or thin solid layers will obtain a representative surface to have as an *in situ* alternative to drop watching.

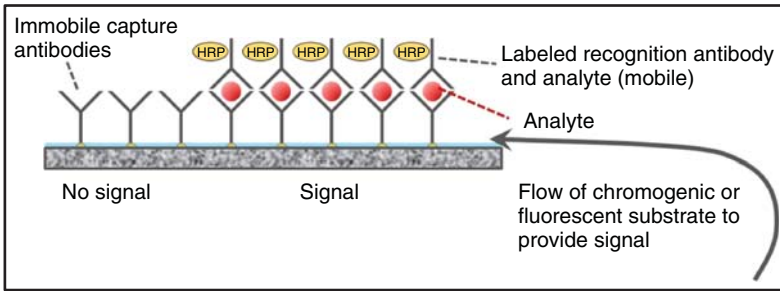


**Figure 14.8** Enzyme-linked immunosorbent assay (ELISA) where capture antibodies are successfully deposited onto a surface to enable capture of labeled recognition ligands. Development with a substrate provides an optical readout of successful binding.

**14.2.3.2.2 Biological Techniques** Often, when delivering biological materials to a surface, it is with the intention of driving a lock-and-key reaction between two components for sensing purposes, as discussed in Section 14.3.5. The delivery of the function still requires much more detailed knowledge as to the thermodynamic journey of the molecules. Each surface needs to be tested to understand how the properties such as surface functionality and surface roughness interact with the target analyte reaction while avoiding nonspecific binding of the analyte to the surface. These conditions can be tested using, for example, small samples of the surfaces of interest in well plates. To handle the large number of variants when examining both new surfaces and dosing technologies, it is best to use a multiplex approach, for example, 96-well-plate automatic reader. As shown in Figure 14.8, this may be carried out using an enzyme-linked immunosorbent assay (ELISA), where the successful adhesion of an antibody to a surface is noted by reacting it with subsequent identification steps to obtain an optical signal. The capture antibody reacts with an antigen, already linked to a labeled antibody in a “sandwich assay.” The label in Figure 14.8 is horseradish peroxidase (HRP), an enzyme that can catalyze a color change when developed with a substrate. This signal can confirm the delivery of the biological function to a surface.

#### 14.2.4

##### The Final Functionalized Surface

The final printed surface must be characterized and understood to ensure the successful delivery of the intended function. This could include achieving sufficient resolution and contrast for graphical applications, recording lasing behavior from printed liquid crystals [16], successful sensing of biological components in an assay, and measuring the required electrical properties in a printed circuit and mechanical properties for a printed flexible surface. For 3D printing, this surface achieved after one layer is in fact then considered as the underlying layer for the next iteration. It will therefore need to be considered in the first category and continue to circulate in the process map. This is a critical consideration because most



materials will spread or behave differently on an underlying surface as compared with spreading on top of the same material. The techniques for final validation of a function are entirely dependent on the application in mind and may include:

- *Atomic Force Microscopy*: A surface probe technique to map out the 3D structure of a surface at the nano- and microscale.
- *Scanning Electron Microscopy (SEM)*: 2D imaging at the nano- and microscale, often with additional backscattered X-ray spectroscopy.
- *Four-Point Probe Measurement*: Electrical measurements to ensure that the required sheet resistance or switching behavior has been achieved.
- *Spectroscopy*: Optical probing of surfaces to define the material's chemical structure.
- *Enzyme-Linked Immunosorbent Assay (ELISA)*: A very flexible technique for probing biological interactions at surfaces. Enzyme-catalyzed optical signals show where the target materials are positioned and the intensity can be quantified to give concentration information.
- *Nanoindentation*: A validation technique capable of defining the extent of solidification by probing the mechanical properties of thin films.

Some of these key surface characterization techniques are discussed in more detail in Section 14.3.

#### 14.2.5

##### Long-Term Behavior

Whether inkjet printing is used to apply a graphical pattern, for biological materials, or for conductive tracks, the long-term stability of the functionalized surface is an essential consideration. Stability testing is usually carried out by identifying the extreme conditions that may be faced by the surface and artificially recreating these in a laboratory environment. The surface is then regularly characterized to identify any change in the function.

##### 14.2.5.1 Example 1: Paper

Exposure of inkjet colorants to light drives photochemical reactions that lead to fading. UV/Vis spectroscopy can be used to identify changes in the absorbance of colorants as they degrade. Exposure to liquids can lead to an undesired redissolving of the dye, while abrasion can lead to dislodging of pigments, both also leading to a reduction in the color. Work is still going on to improve the permanence of color by improving surface charge balance or including polymers to drive adhesion [17].

##### 14.2.5.2 Example 2: Protein Printing

Proteins, enzymes, and antibodies are often printed to surfaces for biosensing applications. The natural environment for these materials is normally a biological system, and while they can be stabilized temporarily in salt buffer solutions or for longer periods by careful freezing, it is difficult to maintain biological activity



at room temperature. Also, buffer salts are normally present at a concentration higher than that of the biomolecules, and so, inkjet printing can quickly leave a surface with a very high concentration of crystallized salt. As noted previously, ELISA studies are carried out to test the stability of biological molecules that have adhered to a surface while (i) being maintained at refrigerated temperatures, (ii) room temperature, (iii) elevated temperatures (e.g., 40 °C), and (iv) repeated temperature cycles (e.g., freeze-thaw cycles).

#### 14.2.5.3 Example 3: Cured Ink Adhesion

Cross-linked or cured inks are more permanent and mechanically robust but still can have adhesion challenges over time. These can often be tested through mechanical means such as scratch testing, abrasion testing, tape testing, and nanoindentation. A tape test, for example, examines the adhesion of ink to a surface upon application and removal of an adhesive tape. As described in standard ASTM F1842, a lattice pattern is cut into the ink or coating to be tested. A pressure-sensitive adhesive tape is applied to the pattern and removed. The remaining pattern is semiquantitatively evaluated based on guidelines in the standard.

### 14.3

#### Surface Characterization Techniques

It is clear from the preceding discussion and examples that within the five process steps where surfaces need to be carefully considered and characterized that there are common tests that can be carried out, for a range of different purposes and focusing on different length scales. Some of the key techniques are discussed in more detail in this section, providing both the underlying principles and some examples of the technique in practice. This section introduces in more detail: surface chemistry tests, optical tests, mechanical tests, electrical tests, and biological tests.

#### 14.3.1

##### Chemical Analysis of Surfaces

In this section, we consider the most important parameter first: surface energy of the substrate material. This will be considered for solid, solid-porous, and liquid surfaces.

##### 14.3.1.1 Surface Tension and Wettability Studies

The concept of surface tension,  $\gamma$ , is often expressed as the force required when extending a surface by a unit length. Forces acting on the molecules in the bulk of the material are considered on average to be isotropic. Molecules at an interface, by the same argument, have an unbalanced resolution of forces. If we want to extend the surface, work is required to bring the molecules from the bulk to

the surface. This work is the surface tension ( $\text{N m}^{-1}$ ). To minimize this work, the molecules attempt to remain in the bulk and fight to minimize the surface area. The amount of work is related to the balance of intermolecular forces of the system in question.

By using an approach from [18], the breaking of a material to form two identical surfaces by overcoming these intermolecular forces is described in Eq. (14.2).

$$W = \frac{\pi C \rho^2}{12 D_0^2} = \frac{A}{12 \pi D_0^2} = 2\gamma \quad (14.2)$$

where  $\rho$  is the number density of molecules ( $\text{m}^{-3}$ ),  $C$  is the interaction constant ( $\text{J m}^6$ ),  $D_0$  is the initial distance, usually taken as the interatomic spacing,  $W$  is the interaction function, and “ $A$ ” is the Hamaker constant, a measure of the interaction forces involved for the system.

By convention, when overcoming the interactions involved in just a single component, 1, “ $W$ ” is called *work of cohesion*. Work of adhesion describes the work required to separate two planes of differing materials. Inkjet printing of drops on surfaces leads to three-phase interfaces, and a more complex balance of surface energies will now be introduced. The behavior of small drops of liquids on surfaces, their contact angle, and their behavior on rough materials have been of great interest for almost two centuries. Lord Rayleigh described their importance in determining the cleanliness and flatness of a photographic plate. The spreading of the solution on the substrate is a three-phase surface tension problem, as is the behavior of water droplets positioned at a liquid/air interface. There now follows a brief introduction to the topic of three-phase equilibrium, specifically as it occurs between (i) solid/liquid/air and (ii) liquid/liquid/air interfaces.

#### 14.3.1.2 Liquid Drops on Solid Surfaces

By using the interpretation we noted earlier where the work required to extend an interface is the work required to promote molecules from the bulk to the interface, the surface tension can then be understood as a force acting tangentially to the interface. These forces are shown for a sessile drop in Figure 14.9a, which is a three-phase system. For a system at equilibrium, the tangential forces will balance. Resolving these forces leads to the Young–Dupré equation, Eq. (14.3), and characteristic contact angle,  $\theta$  (Figure 14.9b). Another, often more useful, way to understand this equation is to consider a system that is driving to reduce its surface free energy. To do this, it will try to maximize the interfacial area with the lowest energy. If a drop perimeter is assumed to spread by a distance  $dx$  (as shown in Figure 14.9c), it will need to (i) promote molecules to the liquid solid interface and (ii) promote molecules to the liquid–solid interface. Both operations require energy, so it will only be possible if reducing the solid–vapor interfacial energy is of equal benefit.

$$\gamma_{S/L} - \gamma_{S/V} + \gamma_{L/V} \cos \theta = 0 \quad (14.3)$$

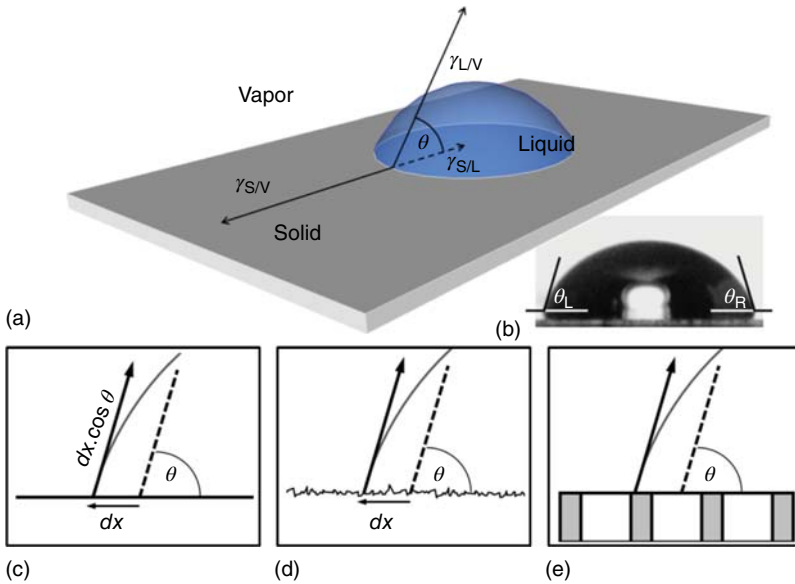


**Figure 14.9** (a) A liquid drop on a flat surface reaches its characteristic contact angle,  $\theta$ , due to the three-phase surface tension balance; (b) an example of a contact angle measurement is shown for water

on polystyrene; and (c–e) the effect of flat homogeneous surfaces, rough surfaces, and inhomogeneous surfaces are considered at the three-phase boundary.

This is usually represented as a free-energy minimization problem [19], as in Eq. (14.4).

$$dF = dx(\gamma_{S/L} - \gamma_{S/V}) + dx \gamma_{L/V} \cos \theta \tag{14.4}$$

At equilibrium, as  $\frac{dF}{dx}$  tends to 0, we return to the Young–Dupré equation. This approach helps understand the reason why surface roughness is a critical consideration. For rough surfaces, any change in the droplet perimeter needs to create a much larger interface with the solid for the same movement in  $x$  (Figure 14.9d). This additional interface can be included in the aforementioned approach by a scaling roughness factor,  $r$ . This is the ratio of actual to projected area. The roughness can be included to give Eq. (14.5) and subsequently compared with Eq. (14.3) to give a simplified Eq. (14.6) [19].

$$dF = r \cdot dx(\gamma_{S/L} - \gamma_{S/V}) + dx \gamma_{L/V} \cos \theta_{app} \tag{14.5}$$

$$\cos \theta = r \cdot \cos \theta_{app} \tag{14.6}$$

This means that if a liquid spreads on a flat surface with a contact angle less than  $90^\circ$ , then it is wetting, and any roughness will only enhance the wettability and drive a lower contact angle. Conversely, if you find that a flat material has a contact angle greater than  $90^\circ$ , then any surface roughness will only increase the nonwetting behavior.

While it is essential to understand the surface roughness prior to printing, it is equally important to know the surface chemical heterogeneity. If a surface, as shown in Figure 14.9e, has a simple bimaterial heterogeneity, then there will be a scaled contribution to wetting from both components, as shown in Eq. (14.7), based on the area fraction of each material ( $f_1$  and  $f_2$ ) and the overall or apparent contact angle ( $\theta_{\text{app}}$ ). In a similar step, in comparison to the Young–Dupré equation, this can be further simplified to Eq. (14.8).

$$dF = f_1 \cdot dx(\gamma_{S/L} - \gamma_{S/V})_1 + f_2 \cdot dx(\gamma_{S/L} - \gamma_{S/V})_2 + dx \gamma_{L/V} \cos \theta_{\text{app}} \quad (14.7)$$

$$\cos \theta_{\text{app}} = f_1 \cos \theta_1 + f_2 \cos \theta_2 \quad (14.8)$$

If a surface is made up of very thin pillars, but they are spaced close enough so the liquid drop can bridge the gap, capturing the air in between the pillars, then this same analysis is especially useful. The contact angle with air increases toward  $180^\circ$ , while the surface area fraction of solid reduces toward  $0^\circ$ . As in the case of a lotus leaf, where a hierarchy of micro- and nanostructures delivers exactly this scenario, we start to observe superhydrophobicity and a contact angle close to  $180^\circ$ .

It is clear that, to understand the drop behavior on a surface, the ink needs to be monitored (which is relatively easy to do with standard surface tension measurements) and also the surface needs to be fully characterized. Measuring the contact angle is often sufficient to ensure good control if consistent drop speeds, conditions, and control materials are employed. Quantifying the roughness is essential and is usually achieved by white light interferometry or atomic force microscopy. Estimating the surface energy of a material may assist with defining a system when different inks need to be used. Girifalco and Good [20] proposed a relationship between the interfacial tensions, shown in Eq. (14.9).

$$\gamma_{S/L} = \gamma_{S/V} + \gamma_{L/V} - 2\varphi(\gamma_{S/V} \cdot \gamma_{L/V})^{1/2} \quad (14.9)$$

where:

$$\varphi \approx \frac{4(V_S V_L)^{1/3}}{(V_S^{1/3} + V_L^{1/3})^2}$$

where  $V$  is the molar volume of each component. This can be simplified to allow estimation of the solid–vapor interfacial tension from the contact angle information using Eq. (14.10) [19].

$$\cos \theta = 2\varphi \left( \frac{\gamma_S}{\gamma_{L/V}} \right)^{1/2} - 1 \quad (14.10)$$

Such estimation techniques are crucial for rapid interpretation of wettability behavior and prediction of suitability of new surface materials to inkjet printing processes.

#### 14.3.1.3 Example of Contact Angle Measurement

A new, thin transparent polymer film is being tested for suitability for replacing current polycarbonate-printed electronics devices. The ink viscosity will remain the same, but a new ink formulation is expected to change the surface tension slightly. It is known from the current process that the best contact angle to ensure stable, continuous lines is  $44^\circ$ .

Droplet contact angle observation:

- Ensure that the polymer surface is clean and dry using only ultrapure solvents, clean air, and lint-free materials for preparation. Allow the sample to return to room temperature prior to measurement.
- Use a clean glass syringe and syringe pump to deliver a controlled volume at a regulated speed to the surface of your material.
- Record an image of the drop using a shadowgraphy technique with a collimated light source.
- Repeat for at least 10 drops.
- Fit the curve of the drop surface to calculate the contact angle using image analysis software.
- Use an average of the left and right contact angles (as noted in Figure 14.9b) and the 10 samples.

Option 1: Direct observation of contact angles coupled with iterative minor alterations to the formulation (trial and error) is performed.

Option 2: Known, characterized liquids can be deposited and contact angles recorded to allow the use of estimation techniques (e.g., Eq. (14.10)) to define the surface energy of the old and new polymer films. This will enable calculation of a target surface tension required of the ink to meet the demands of a  $44^\circ$  contact angle.

#### 14.3.1.4 Liquid Drops on Liquid Surfaces

Reactive inkjet printing and inkjet printing of pharmaceuticals, (of interest in for example pharmaceutical combinatorial chemistry) relies on inkjet deposited drops interacting with a previously printed liquid drop or a larger liquid reservoir. These liquid–liquid interfacial scenarios can lead to a range of behaviors, as shown in Figure 14.7, such as bouncing, sinking, or remaining stable at the interface. While bouncing of drops is beyond the scope of this chapter the other two scenarios rely on understanding the three-phase interfacial balance. For example, as shown in Figure 14.10a, the drop can form at the interface with two different radii of curvature. A liquid droplet is not always stable at the interface and can also sink into the other liquid. This is entirely due to surface tension as gravitational forces are insignificant at the scale of most inkjet drops. The stability of a drop at a liquid surface can be interpreted as a force triangle, known as *Neumann's Triangle* [21]. If the sum of any two sides (each of which is a vector representing an interfacial tension of the system) is greater than the final third vector, then the drop is unstable and will be rejected from the fluid. This is almost always by sinking into the fluid bulk. Figure 14.10b shows the triangle and the relationships.

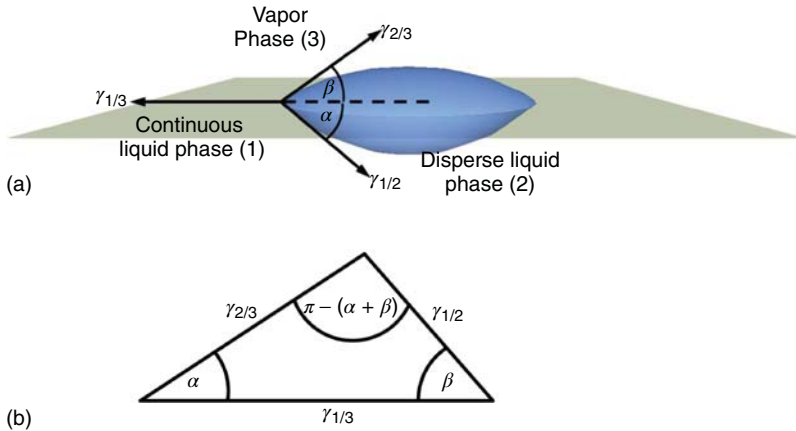


**Figure 14.10** (a) A liquid lens, formed at a liquid/air interface, where  $\gamma_{1/2}$ ,  $\gamma_{1/3}$ , and  $\gamma_{2/3}$  represent the liquid/lens, liquid/vapor, and lens/vapor surface tensions, respectively. Characteristic contact angles are formed above and below the liquid bulk

interface. (b) Neumann's triangle is shown, representing each surface tension as a vector. This is used along with the statements shown to predict the stability of a drop at a liquid interface.

#### 14.3.1.5 Role of Surface Chemistry on Imbibition

Whether inkjet printing onto paper or mopping up a spill with tissue paper, a fluid is absorbed rapidly into porous cellulose-based materials. However, it is clear that paper allows for a clear, legible script, whereas tissue is highly absorbent and does not allow fine control. The imbibition and spreading are due to the same minimization of surface energy as discussed for solid nonporous surfaces. The surface chemistry of the fibers as well as the porous structure can be understood through analyzing the absorbing behavior.

As shown in Figure 14.2, paper is highly porous and is made up of packed cellulose fibers. While fluid flow through a sequence of these small pores involves complex geometries and modeling, once we consider larger dimensions and can average over the behavior of many pores, it is much more straightforward to predict flow. In such cases, the flow of liquid through the pores can be analyzed using the assumption of an equivalent cylindrical capillary tube. The contact angle,  $\theta$ , of the liquid within a capillary leads to a meniscus. Any curved liquid/air interface gives a pressure differential, with the higher pressure on the concave side. This difference in pressure drives the fluid flow. Equation (14.11) describes the relationship between this pressure drop, the radius of the capillary tube, and the balance of surface tensions between the vapor, solid fibers, and liquid.

$$\Delta P = \frac{2(\gamma_{1/3} - \gamma_{1/2})}{r} \quad (14.11)$$

where  $r$  is the radius of the cylindrical capillary,  $\gamma_{1/3}$  is the paper/air surface energy,  $\gamma_{1/2}$  is the paper/liquid interfacial energy, and  $\Delta P$  is the pressure difference across the curved interface under static conditions. A positive value for

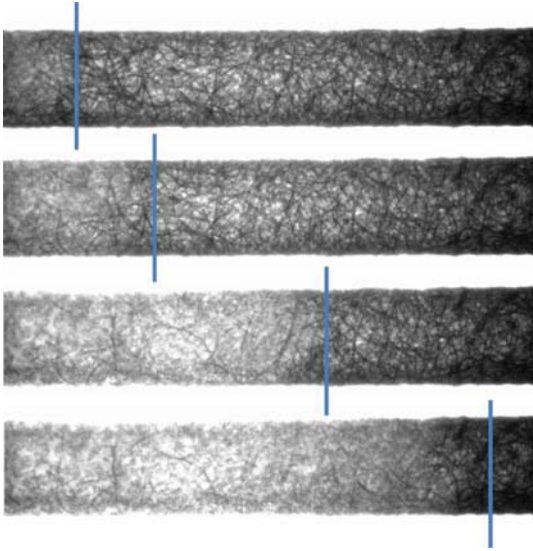


**Figure 14.11** A paper channel with water imbibing from the left, moving with each image to the point highlighted by the blue line.

the difference in pressure can be interpreted as a drive for the liquid to imbibe into the pore. The surface chemistry of paper is usually quickly understood by wettability or absorbance tests. The balance of surface energies that leads to absorption and porous flow is often defined by the Washburn equation Eq. (4.12). While Eq. (14.11) highlights the on/off flow prediction based on positive or negative capillary pressures, the Washburn equation can help understand the rate of imbibition into microfluidic channels or, for example, paper channels as shown in Figure 14.11.

$$h_p(t) = \sqrt{\frac{\gamma_{2/3} l r}{2\mu}} \cdot \sqrt{t}, \quad l = \frac{\gamma_{1/3} - \gamma_{1/2}}{\gamma_{2/3}} \quad (14.12)$$

where  $h_p$  is the depth of liquid penetration in time  $t$ ,  $r$  is the capillary radius, and  $\eta$  is the viscosity of the penetrating liquid. The basic understanding of surface-tension-driven imbibition into porous materials is contained within these equations. While more complex numerical approaches are often employed, these models still underpin many of the contemporary approaches [22–24]. The two equations illustrate very well the battle between the drive to minimize surface energy and the resistance to flow due to viscous forces.

#### 14.3.2

##### Mechanical Testing of Surfaces

A range of mechanical tests were noted in Section 14.2, two of which are rising rapidly in importance, namely atomic force microscopy and nanoindentation.

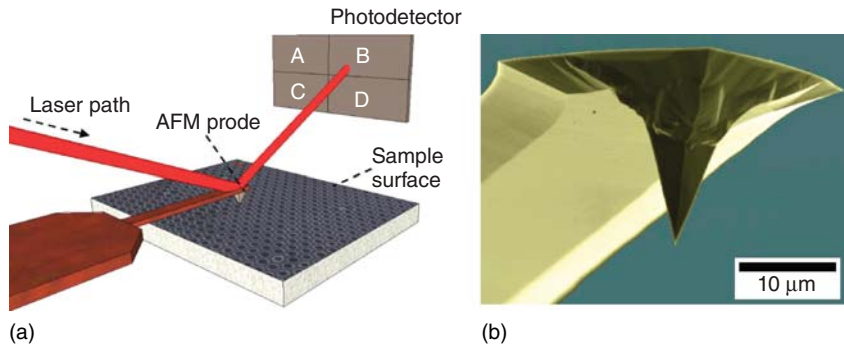


**Figure 14.12** (a) Illustration of the principle of AFM showing the cantilever and probe, the laser and photodetector and (b) SEM image of an AFM tip showing the sharp tip that contacts the surface of interest.

#### 14.3.2.1 Atomic Force Microscopy (AFM)

The importance of surface roughness and also the final distribution of materials are noted as key points in the science of inkjet printing to surfaces in Section 14.2. New advances require highly repeatable thin layers for photocatalysis or biological sensing. Atomic force microscopy is an essential tool for rapid, three-dimensional mapping of surfaces. As seen in Figure 14.12a,b, a sharp probe at the end of a cantilever is positioned slightly above the interface. The probe, most often made from silicon nitride or silicon, is raster-scanned across the sample. In “contact mode,” the cantilever is deflected from a user-defined set point due to surface topography. This deflection is recorded by a laser beam, aligned to reflect off the back of the cantilever, onto the photodetector, as shown in Figure 14.12a.

The combination of signals from the four quadrants allows information about the vertical and torsional forces to be calculated and fed back to the AFM head to compensate for the height change and maintain a chosen tip deflection. This forms a high-resolution three-dimensional image of the surface of the substrate. The alternative “tapping mode” oscillates the cantilever at its resonant frequency. The deflection of the laser mimics this oscillation, and on encountering a feature, both change accordingly. The feedback maintains the resonant frequency oscillation by moving the height as before and mapping out the topography of the surface.

While this approach is sensitive to nanoscale roughness, it is not suitable for larger topographies. An AFM will overcompensate for large topographical features providing repeatable artifacts that are difficult to interpret. Less sensitive probe techniques or optical interferometry can be used to get this information.

#### 14.3.2.2 Nanoindentation

Other physical measurement techniques include tensile testing and indentation. Nanoindentation is especially relevant as it is used for probing mechanical properties of thin films. Nanoscale movement is required to ensure that the stress field



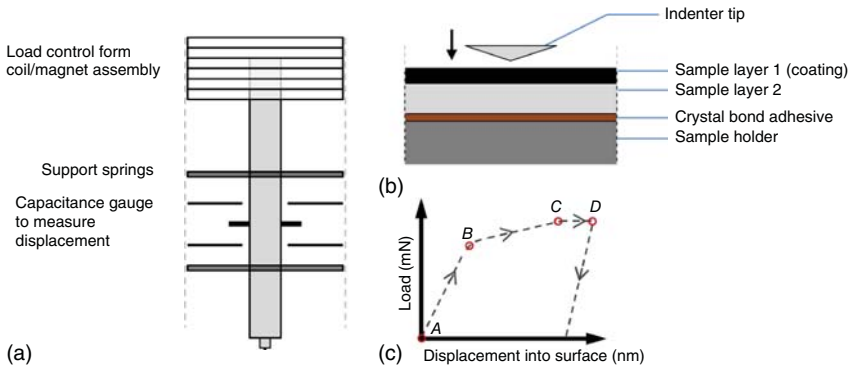


**Figure 14.13** (a) Illustration of a standard nanoindenter configuration; (b) example of layout of layers after sample preparation; and (c) indentation response example

including an elastic–plastic transition can be seen at *B*, a holding program is shown from *C* to *D* prior to retraction.

from a probe does not interact with the underlying layers to obtain an artificial reading. Nanoindentation traditionally applies a stress by way of a vertical loading force acting on a very well defined contact geometry. The loading force is carefully regulated and controlled, while the depth of indent is measured using a highly sensitive capacitive displacement meter with subnanometer resolution.

This produces force–displacement curves for the material, which are used to calculate the stiffness, hardness, and elasticity values of the material. Figure 14.13a shows an illustration of the key components of an indenter where an electric current running through a coil/magnet assembly induces a vertical movement with a force proportional to the current.

Samples must be mounted on rigid (usually metal) stubs indicated in Figure 14.13b. These are inserted and secured in a nanoindenter stage. It is essential in mechanical testing that the method of adhering the specimen to the stub does not interfere with the results. The stiffness value of the adhesive must be significantly higher than that of the material being tested. Normally, samples are attached using a crystallizing bonding agent. An example response to indentation is shown in Figure 14.13c, where an elastic–plastic transition can be seen at *B*, a constant load is shown from *C* to *D* prior to retraction.

### 14.3.3

#### Electrical Analysis of Surfaces

Materials are commonly grouped into one of three categories based on their electrical behavior, namely conductors, semiconductors, or insulators. The assignment of a material to a group depends on the ability of the electrons to occupy the valence and conduction bands. Insulators do not conduct electricity because there is such a large jump in energy required to promote electrons to the conduction band from the valence band. Once in the conduction band, the

electron is sufficiently mobile to enable delocalization and “flow.” Resistance ( $R$ ) to electron flow in a sample is generally measured as the ratio of the applied voltage ( $V$ ) and the measured current ( $I$ ) (Eq. (14.12)) and measured in ohms.

$$R = \frac{V}{I} \quad (14.13)$$

There is a more useful measure, resistivity ( $\rho$ ), which is a characteristic value of a bulk material and is the resistance corrected for the sample dimensions ( $t$ -thickness,  $W$ -width,  $L$ -length), as shown in Eq. (14.14) and measured in  $\Omega$ -cm.

$$\rho = \frac{RtW}{L} \quad (14.14)$$

Thin film measurements and sample measurements that are predominantly of interest for inkjet printing applications focus on the 2D equivalent, sheet resistance. If we rearrange Eq. (14.14) to solve for  $R$  and then assume that the  $x$ - $y$  dimensions are always equivalent (i.e.,  $W = L$ ), then the sheet resistance is clearly the resistivity for a known area, by taking into account the sample thickness, as shown in Eq. (14.15).

$$R_s = \frac{\rho}{t} \quad (14.15)$$

The sheet resistance is in units of ohms but is often described as ohms per square because of its scalability to the required sheet dimension. The prevalent technique discussed so far is the four-point probe measurement [25]. The general principle is to use a probe station configuration, as shown in Figure 14.14a, that enables manual placement of each sharp probe at the point of interest, or for industrial applications, a linear probe setup shown in Figure 14.14b is more often employed. In either case, a current flows across the outer two probes and the voltage drop across the inner two probes is measured. It is essential to ensure good contact between the metal probes and the surface of interest.

The probes need to be sufficiently large as to ensure a very low contact resistance and small or sharp enough in some cases to penetrate the natural oxide layers that build up on many surfaces. Equal spacing is critical for easy analysis with sheet resistance. Conductivity/resistivity measurements along with sheet resistance are essential starting points of electrical characterization. While out of the scope of this chapter, electrochemical biosensors are now being explored with inkjet printing and more complex measurements will then be required.

#### 14.3.4

##### Optical Analysis

There is a wide range of scales at which quantitative analytical tools use electromagnetic radiation to interact with solid surfaces. At a microscale, the semiconductor industry uses laser scanning of surfaces as a means of identifying particulate contamination. Particles and defects on the order of the laser wavelength drive scattering that stands out above the background noise due to microroughness. Standard ellipsometry tools also operate at nano and micro

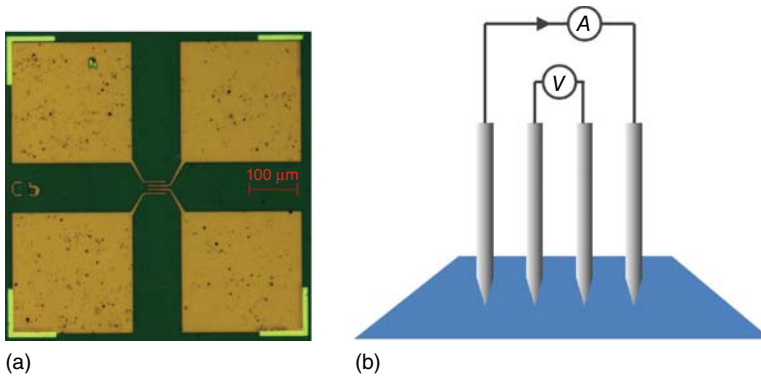


**Figure 14.14** (a) Four gold pads easily contacted by a metal probe for electrical measurement with one microelectrode extending from each to enable four-point probe measurement. (b) Linear arrays are

often employed in quick industrial measurements, but both use the same approach of measuring the voltage drop between two inner electrodes while flowing a current through the outer two electrodes.

length scales. These operate by reflecting a polarized incident beam at an angle from the surface. The change in polarization is a measure of the complex refractive index of the interface. Typical uses allow very accurate thickness measurements and optical constant definition for thin layers on the order of a few Angstroms up to several micrometers. While the data is relatively straightforward to collect, it is an indirect solution requiring fitting to a model. Comparisons of a number of techniques show that this is a satisfactory approach. Contamination or variation in thicknesses on these length scales is rarely acceptable for this industry, it is often important to also find out the source of the observed behavior by analysis of the material at the molecular level using another optical technique, spectroscopy. There is a wide range of complex and complimentary tools available using light to probe the chemical and electronic structure of materials including optical absorption and emission measurements as well as electron emission spectroscopy. The key step in understanding is that photon energy ( $h\nu$ ) can be absorbed during a jump in quantum state of an electron. The energy of the photon must match the jump energy precisely ( $de = h\nu$ ). Subsequently, emission can occur, as the excited state electron returns to its ground state, releasing a photon. The full spectrum of electromagnetic radiation has been explored in probing surfaces, from long wavelengths with lower frequencies (and hence energy) to very short wavelengths with higher frequencies (and energy). An example of the range is shown in Table 14.1, where the energy  $E = \frac{hc}{\lambda}$  is tabulated across a portion of the spectrum (Planck's constant  $h$  and velocity of light  $c$ ). This shows that we can measure molecular behavior, from vibrational excitation of molecules in the infrared range to changes in electronic states by electron promotion in the ultraviolet and visible range. This level of energy can also lead to complete removal of an electron at a specific energy as shown in Eq. (14.16).

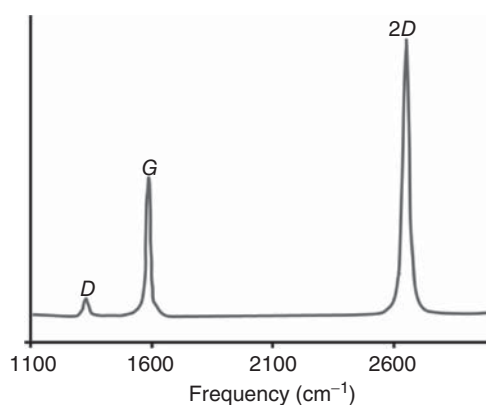
$$E_K = h\nu - E_B \quad (14.16)$$

**Table 14.1** Wavelength and energy across the electromagnetic spectrum most used in spectroscopy.

	$\lambda$ (nm)	$E$ (kJ mol <sup>-1</sup> )
Infrared	1 000 000-700	0.12–171
Visible	700-400	171–299
Ultraviolet	400-10	299–11 963
X-ray	10-0.01	11 963–11 962 673

where  $E_K$  is the kinetic energy of the photo-emitted electron and  $E_B$  is the binding energy of the electron in the material.

Alternatively, rather than absorption, samples can also drive scattering of the incoming radiation. While the bulk of scattering is elastic Rayleigh scattering, a small amount of inelastic scattering also occurs. Here, the energy changes due to interactions with the materials of interest. This inelastic scattering is often referred to as *Raman scattering*. The incident energy interacts with the molecules leading to vibrational changes. The scattered light has therefore lost a fixed amount of energy, leading to scattering of a photon with a longer wavelength. The spectrum is then useful to understand the vibrations that were triggered. The group functions have been carefully cataloged, characterized over the last 20 years, and enable detailed chemical analysis with incredible surface sensitivity. Examples common in the literature include examination of pharmaceutical polymorphs, the presence of single or multilayers of graphene, identification of the proteins on the surfaces of cells, and identification of contamination in high-precision processes [26–28]. One specific example, becoming more prevalent in manufacturing, is the tracking of clean graphene transferred as a single-layer flake to a surface. A sketch of an expected spectrum is shown in Figure 14.15.

**Figure 14.15** Sketch of a Raman spectrum from single-layer graphene showing the D, G, and 2D peaks.

## 14.3.5

**Biological Analysis**

Bioprinting is becoming an incredibly important route for sensor fabrication, for functional coating of biomaterials, and also for tissue engineering through dosing of cells and growth factors to scaffolds [29]. There are two key approaches we need to consider. The first is the identification of molecular-level behavior. Proteins are highly complex materials with a specific sequence of hundreds to thousands of amino acids, but the function is linked not just to the sequence but more to the folded geometry that this sequence drives. Each protein encourages molecular recognition through its charge, geometry, and associated “ligand” in a lock-and-key mechanism. To use inkjet printing for molecular sensing applications, the surfaces must not drive nonspecific binding of proteins. This is when molecules stick by physisorption to the substrate even where no capture protein exists. Secondly, after printing, the function of the antibody or protein must be proven to have survived the tortuous flow process through the nozzle, impact, and drying. Both tests most commonly use an ELISA detection technique. There are many variations of ELISA, but the shared theme is a sequence of lock-and-key recognition reactions and an enzyme label signaling the presence of the reactions. One example is the Direct Sandwich ELISA, shown earlier in Figure 14.8. In this case, a solid phase is functionalized with a capture antibody (by inkjet printing). Normally, free antibodies that have not attached are then removed by a washing step. The antigen of interest is then incubated with the capture antibody allowing a lock-and-key reaction to occur. Upon completion, the unreacted antigen is rinsed away. The sandwich is formed by a second recognition ligand, an antibody, for example, with an attached enzyme (e.g., HRP). This is quantified in a device such as a spectrophotometer. Activity of an inkjet-printed antibody layer or antigen sample can be recorded by the quantitative results achieved from these optical signals. ELISA can be used as testing of function but is also important for initial surface testing to ensure low levels of nonspecific binding.

At the cellular level, it is again important to characterize the suitability of a surface to cell growth prior to printing, simply to pull apart the variables in your experiment where the cell proliferation can be affected by the storage environment, printing process, surface incubation, and so on. There are standardized biocompatibility tests that are suitable for this work. Cytotoxicity results, for example, can be carried out, for example, using ISO 10993-5, which describes *in vitro* cytotoxicity tests for medical devices. In this case, tests include direct contact with the surface material, diffusion of toxins through a gel layer from the surface, and exposure of a cell layer to a liquid that has been exposed to the surface material (“fluid extract”). Cells are watched in culture for a limited period of time, that is, 3 days to observe their proliferation behavior and morphological response.

## 14.4

### Conclusion

Inkjet printing has become a new resource in both the process engineer's toolkit and the academic researcher's laboratory. This is ideal because research will find a clear translation route to an industrial process. It also means that just as we become more adventurous in the type of inks we are printing, for example, biological molecules and thin controlled layers of interconnected nanomaterials, we must also branch out and incorporate a broader range of underlying surfaces into the printing system. The research and development teams examining inkjet printing will need to understand the role of the surface to a much greater level of detail and call upon a wide range of analytical techniques. A successful researcher will therefore not necessarily be expert in a single approach but instead must build a library of different techniques for probing surface properties. With a shift toward these complex, high-value inks and surface materials (as compared with graphical inks and cellulose-based surfaces), the value of the final product increases dramatically throughout the manufacturing system. For a sustainable business model, this will also lead to a drive toward increased yields and initiatives to minimize errors or poor repeatability. From this chapter, it is clear that positive-confirmation techniques are lacking in this field and so will most likely be the next area to develop to keep up with the rapid pace of progress.

This chapter was formulated to give the reader a starting point for what questions need to be asked about surfaces used in inkjet printing applications. This is through a series of examples of applications and their recommended surface characterization techniques. Some additional detail is provided in Section 14.3 for a few of the key techniques to help build the basic knowledge to ensure when new surfaces or applications are explored, then the reader will quickly identify the required analytical approach. As part of this journey and finding out which questions need to be asked, it is also clear that a researcher must understand the targeted manufacturing system and start to build a picture of the upstream and downstream influences on the surfaces. With this knowledge and a library of analytical techniques, engineers and scientists will dramatically increase the breadth of technologies using inkjet printing that reach commercialization.

## 14.5

### Questions to Consider

1. How would you define and classify the complexity of an inkjet printing application?
2. How else would you approach the problem of ensuring stable lines of printed ink?
3. Rather than think about what material you would like to print, think about what materials you would like to print to. What are the key functions of these surfaces, and how would you measure them before and after printing?

## References

- Lappalainen, T., Teerinen, T., Vento, P., Hakalahti, L., and Erho, T. (2010) Cellulose as a novel substrate for lateral flow assay. *Nord. Pulp Pap. Res. J.*, **25** (4), 536–550.
- Alava, M. and Niskanen, K. (2006) The physics of paper. *Rep. Prog. Phys.*, **69**, 669–723.
- Carlsson, J., Hellentin, P., Malmqvist, L., Persson, A., Persson, W., and Wahlström, C.G. (1995) Time-resolved studies of light propagation in paper. *Appl. Opt.*, **34**, 1528.
- Roberts, J.C. (1996) *The Chemistry of Paper* Chapter 7, The Royal Society of Chemistry.
- Perelaer, J., de Gans, B.J., and Schubert, U.S. (2006) Ink-jet printing and microwave sintering of conductive silver tracks. *Adv. Mater.*, **18** (16), 2101–2104.
- Hsiao, W.K., Martin, G.D., and Hutchings, I.M. (2014) Printing stable liquid tracks on a surface with finite receding contact angle. *Langmuir*, **30** (41), 12447–12455.
- Johnson, W. and Yarling, C. (1993) Sheet resistance and the four point probe, in *Characterization in Silicon Processing*, Chapter 23 (ed Y.E. Strausser), Butterworth-Heinemann, Stoneham, MA.
- Lewis, J.A. and Ahn, B.Y. (2015) Device fabrication: three-dimensional printed electronics. *Nature*, **518** (7537), 42–43.
- Martin, G.D., Castrejon-Pita, J.R., and Hutchings, I.M. (2011) Holographic measurement of drop-on-demand drops in flight. NIP27: The 27th International Conference on Digital Printing Technologies and Digital Fabrication 2011, 2011 October 2 to 6, Minneapolis, Minnesota, pp. 620–623.
- Brennan, T.M. (1995) Method and apparatus for conducting an array of chemical reactions on a support surface. US Patent 5,474,796.
- Daly, R., Harrington, T., Martin, G., and Hutchings, I. (2015) Inkjet printing for pharmaceuticals – A review of research and manufacturing. *Int. J. Pharm.*, **494** (2), 554–567.
- Couder, Y., Fort, E., Gautier, C.-H., and Boudaoud, A. (2005) From bouncing to floating: noncoalescence of drops on a fluid bath. *Phys. Rev. Lett.*, **94** (17), 177801.
- Verkouteren, R.M. and Verkouteren, J.R. (2009) Inkjet metrology: high-accuracy mass measurements of microdroplets produced by a drop-on-demand dispenser. *Anal. Chem.*, **81** (20), 8577–8584.
- Höök, F., Rodahl, M., Brzezinski, P., and Kasemo, B. (1998) Energy dissipation kinetics for protein and antibody – antigen adsorption under shear oscillation on a quartz crystal microbalance. *Langmuir*, **14** (4), 729–734.
- Maloney, N., Lukacs, G., Jensen, J., and Hegner, M. (2014) Nanomechanical sensors for single microbial cell growth monitoring. *Nanoscale*, **6**, 8242–8249.
- Gardiner, D.J., Hsiao, W.-K., Morris, S.M., Hands, P.J.W., Wilkinson, T.D., Hutchings, I.M., and Coles, H.J. (2012) Printed photonic arrays from self-organized chiral nematic liquid crystals. *Soft Matter*, **8** (39), 9977–9980.
- Schmid, C. (2008) Formulation and properties of waterborne inkjet inks, in *The Chemistry of Inkjet Inks*, Chapter 7 (ed S. Magdassi), World Scientific Publishing Co. Pte. Ltd.
- Israelachvili, J.N. (2011) *Intermolecular and Surface Forces* Chapter 10, 11, 3rd edn, Academic Press.
- Berthier, J. (2013) The physics of droplets, in *Microdrops and Digital Microfluidics*, Chapter 3.3.2, 2nd edn, Elsevier.
- Girifalco, L.A. and Good, R.J. (1957) A theory for the estimation of surface and interfacial energies. I. Derivation and application to interfacial tension. *J. Chem. Phys.*, **61** (7), 904–909.
- Rowlinson, J.S. and Widom, B. (1982) *Molecular Theory of Capillarity*, Dover Publications Inc, New York.
- Hyväluoma, J., Raiskinmäki, P., Jäsberg, A., Koponen, A.I., Kataja, M., and

- Timonen, J. (2006) Simulation of liquid penetration in paper. *Phys. Rev. E*, **73** (3), 036705.
23. Mullins, B.J., Braddock, R.D., and Kasper, G. (2007) Capillarity in fibrous filter media: relationship to filter properties. *Chem. Eng. Sci.*, **62** (22), 6191–6198.
24. Jaganathan, S., Vahedi, T.H., and Pourdeyhimi, B. (2008) Modeling liquid porosimetry in modeled and imaged 3-D fibrous microstructures. *J. Colloid Interface Sci.*, **326** (1), 166–175.
25. Schumacher, B., Bach, H.-G., Spitzer, P., and Obrzut, J. (2006) Electrical properties, in *Springer Handbook of Materials Measurement Methods*, Chapter 9 (eds H. Czichos, T. Saito, and L. Smith), Springer.
26. Melendez, P.A., Kane, K.M., Ashvar, C.S., Albrecht, M., and Smith, P.A. (2008) Thermal inkjet application in the preparation of oral dosage forms: dispensing of prednisolone solutions and polymorphic characterization by solid-state spectroscopic techniques. *J. Pharm. Sci.*, **97**, 2619–2636.
27. Ferrari, A.C., Meyer, J.C., Scardaci, V., Casiraghi, C., Lazzeri, M., Mauri, F., Piscanec, S., Jiang, D., Novoselov, K.S., Roth, S., and Geim, A.K. (2006) Raman spectrum of graphene and graphene layers. *Phys. Rev. Lett.*, **97** (18) Article ID 187401.
28. Huh, Y.S., Chung, A.J., and Erickson, D. (2009) Surface enhanced Raman spectroscopy and its application to molecular and cellular analysis. *Microfluid. Nanofluid.*, **6** (3), 285–297.
29. Derby, B. (2008) Bioprinting: inkjet printing proteins and hybrid cell-containing materials and structures. *J. Mater. Chem.*, **18** (47), 5717–5721.



## 15 Applications in Inkjet Printing

*Patrick J. Smith and Jonathan Stringer*

### 15.1

#### Introduction

At its simplest, inkjet printing is a droplet deposition technique. Droplets are ejected from the printhead and precisely placed on a substrate at positions selected before the process began. As the droplets produced by inkjet are uniform and repeatable, they can be considered as building blocks, which allows a variety of structures to be built. A line is simply a linear sequence of droplets placed in such a way that they overlap for some applications or that have been positioned close enough together so as to convince the human eye that they form a continuous line. For a film, droplets are placed in the  $Y$ - as well as  $X$ -direction. Two-dimensional features as complex as a photograph are so often printed by inkjet printing means that the process has become routine and the beauty of the science and engineering necessary to obtain the print has been overlooked. The fact that droplets can now be positioned in the  $Z$ -direction (a process with a variety of names such as 3D printing or additive manufacture) has stimulated the public's imagination, but again, their interest lies in what can be produced and not how it is produced. The preceding chapters of this book have focused on the scientific and engineering aspects that need to be considered in order to eject droplets and to ensure that they are situated precisely where required. In this chapter, we provide a variety of answers to the questions "What can be printed?" and "Why choose inkjet printing to print this?" In short, this chapter is devoted to exploring the application areas where inkjet printing confers a distinct advantage.

The first section of the chapter discusses the use of inkjet in terms of graphics, which is by far the largest application area and the subject of a variety of publications. The use of inkjet printing in 3D applications is also discussed. The rest of the chapter focuses upon more exotic applications of inkjet printing and is structured into three main material application areas: inorganic, organic, and biological. Each application area will be discussed with reference to the ink type that is typically used for the material, the ink's printability, and how this affects the performance of the end device. Other factors that will be discussed are how changing printing and drying parameters can affect the final performance. The chapter also discusses

issues that can affect the inks, their resultant devices, and the most appropriate substrates to use with the inks. Each section also discusses the postprocessing that needs to be performed in order to achieve the desired performance, and the limits that are imposed because of this.

## 15.2

### Graphics

Without doubt, the largest application for inkjet printing is the graphics market. As an example of the market's size, the sales of inkjet ink for 2014 were projected to be \$6.2 billion [1]. As with all inkjet applications, the issue of functionality in graphic applications is affected by the interaction between the substrate and the droplet but is less dependent on the interaction between the droplets, as compared to printed electronics whereby a degree of overlap is essential. For graphics, the functional component is predominantly a pigment, although dyes are still used for low-end applications [2].

There are a range of factors that need to be considered with regard to the formation of a colored image on a substrate (which is usually paper); these include color fastness, drying time, ink printability, ink longevity (storage), safety, and cost. The factor of ink longevity is important due to the ink sitting in a reservoir for months at a time, such as is the case for small office printers that routinely perform small print runs. Of equal importance is that the ink should be ready to print at all times; the term *latency* is used to describe the length of time an ink can remain idle at the nozzle before ejection is no longer possible [3]. Inks are formulated to match the printhead rheology to ensure successful ejection over a long timescale.

A typical ink contains a pigment dispersed in carrier solvent, usually water, with a number of additives that enhance printability and longevity. The first additive is the surfactant species used to stabilize the dispersed pigment particles, preventing agglomeration. A viscosity modifier, such as ethylene glycol, is added to enhance ink jettability and reduce spreading on a substrate. Similarly, a component that modifies surface tension can be added, such as the addition of propanol to water. Surface tension contributes to droplet formation and droplet spreading [4]. Defoaming agents, such as tributyl phosphate, are added to inhibit the formation of bubbles. The term *latency* describes the length of time that an ink can idle at the printhead nozzle and still be successfully jetted. Humectants, such as diethylene glycol, are added to inhibit the evaporation of water for aqueous inks, thereby extending latency from seconds to days and weeks.

In order to be printable, inkjet inks typically have to have viscosities in the 2–20 mPa·s region. However, this has the converse consequence of imbuing the droplet with a high degree of mobility on the substrate, leading to poor print quality. The problem is compounded due to paper being the substrate of choice that is used for graphics. The porosity of paper causes an ink to be absorbed and spread, leading to poor color quality as well as poor definition. As such, a considerable degree of effort has gone into developing substrates that are suitable for inkjet printing.

The main strategy employed to obtain substrates that ensure high print quality for graphics application is to coat the paper with an ink-receiving layer that is either microporous or “swellable” [5]. The function of the ink-receiving layer is to rapidly absorb the ink and to fix its pigment, or dye, load at the surface. For microporous coatings, small porous particles of silica, calcium carbonate, and alumina are commonly used. Swellable coatings employ either natural polymers such as gelatin or synthetic polymers such as polyvinylalcohol (PVA) and poly(vinylpyrrolidone) (PVP).

An alternative approach to ensuring good print quality (which is growing in appeal and employment) is to use a UV-curable ink in which the polymerization of deposited droplets of monomers and/or oligomers is exploited to fix the ink to the surface of the substrate. As droplets of UV ink cure almost instantaneously on the substrate, absorbance by the substrate is less of an issue. Additional advantages are conferred as the curing lamps take up less space than conventional dryers and use less energy. A UV ink typically contains a mix of monomers/oligomers, usually acrylates; the colorant, either a dye or a pigment, although the latter is used more often due to its better lightfastness; a photoinitiator, which is essential to promote the polymerization of the monomer/oligomer mix; and additives that promote printability, latency, and shelf life [6].

As the UV ink droplet is cured at the surface, adhesion is much more critical than for traditional ink droplets that interact with ink-receiving layers. A balance also needs to be sought between increasing the functionality of the monomers and oligomers, which leads to increased cross-link density of the polymer (which in turn results in a film that is harder and more resistance to abrasion and solvents) and ensuring that adhesion is not lowered since an increase in functionality can cause curing shrinkage [6].

### 15.3

#### Inkjet Printing for Three-Dimensional Applications

All inkjet printing applications will produce, to a differing extent, a three-dimensional structure. For the majority of applications, however, the height of deposit has been either of negligible importance (such as graphical applications) or at least an order of magnitude smaller than the lateral dimensions of the deposit (such as printed electronics). The heights of deposits (or, alternatively, the amount of solid material deposited per unit area) in these applications do have significant impact upon the utility of the final product (e.g., color saturation in graphics or sheet resistance in printed conductors [4]), but they can primarily be viewed as two-dimensional techniques. This distinction can become more blurred when one considers the complexity in three dimensions that is required for, as an example, fabricating a thin-film transistor via inkjet printing [7]. For this section, however, the use of inkjet printing in the manufacture of three-dimensional components will consider only applications where the height of the manufactured component is of a similar magnitude to the lateral dimensions.

Manufacturing a component with a nonnegligible height by inkjet printing is not a trivial matter; it is necessary for:

- 1) The printed ink itself to have an appreciable solid component.
- 2) The ink to undergo a phase change from liquid to solid upon printing.
- 3) Or, for the ink to interact with another pre-existing material that enables the three-dimensional structure to be made (e.g., powder bed printing).

Each of the three cases mentioned, together with example applications and some of the challenges involved, will now be discussed.

To obtain an appreciable solid component within the ink, it is necessary either to suspend solid particles within the fluid to be printed or to dissolve a solid component within the fluid that will subsequently come out of solution upon evaporation of the carrier liquid. As shown in the previous chapters, for successful inkjet printing of a liquid, it is necessary to meet stringent fluid requirements, particularly in relation to viscosity. This has significant implications with regard to the amount of solid component that can be incorporated into a printing ink.

For particle suspensions, as the amount of particles increases, the probability of individual particles interacting with each other also increases, with particle loading above a small concentration by volume showing significant particle–particle interaction (see Chapter 6 for more details); it is, therefore, highly probable that any suspension-based ink used for making appreciably three-dimensional structures will show significant particle–particle interactions. Empirical relationships have been defined that predict the Newtonian rheological behavior for suspensions with significant particle–particle interactions [8, 9], with these models tending to predict a sharp rise in viscosity above approximately 40% by volume particle loading. Given the limits on viscosity for a printable liquid, it is therefore extremely challenging for the solid loading to be greater than approximately 40%.

Due to the high shear stresses experienced during droplet ejection in inkjet printing (see Chapters 2 and 13), it is important to consider any non-Newtonian rheological behavior of the ink. It is clearly beneficial that an ink exhibits shear thinning behavior (i.e., viscosity goes down as shear rate increases) rather than dilatant (or shear thickening) behavior, as this will increase the likelihood of successful droplet ejection. For particle suspensions that are well dispersed, this is often found to be the case [10], but any agglomeration within the printhead may lead to shear thickening behavior. For this reason, as well as straightforward mechanical blockage of the printhead, it is imperative that any ink used is well dispersed, made up of suitably sized particles (a maximum diameter at least an order of magnitude less than the nozzle size) and that any agglomerates are filtered before entering the printhead.

For an ink where the solid phase is in solution, there are two further limits upon the maximum achievable solid loading. For solutions of relatively small molecules (such as salts), the solid loading is limited by the concentration at which the carrier solvent becomes saturated and cannot dissolve any more solid phase. Above this concentration, there will be a solid phase present within the ink of an indeterminate size that may lead to blockages within the printhead. Due to the small size of

the nozzle, any localized evaporation at the nozzle is liable to result in an increased concentration of solute at the nozzle, which if greater than the saturation concentration will tend to block up the nozzle. For larger molecules, such as polymers and other macromolecules, there are also further issues due to non-Newtonian rheology within an extensional flow (see Chapters 5, 7, and 13). Due to these limitations on potential solid loading for both solutions and suspensions, most three-dimensional printing of this type has concentrated on relatively small features and has often been combined with other manufacturing techniques to produce a functional component. Due to the benefits from near-net-shape forming and the need for a subsequent sintering step, this type of three-dimensional printing has primarily been used for ceramic materials, most commonly suspensions. Examples of the types of material printed include zirconia-based suspensions for dental prostheses [11] and lead zirconate titanate (PZT) suspensions for structured ultrasonic transducers [12]. More detail about the various applications for three-dimensional printing of ceramics is given in Section 15.4.2. Examples of the use of polymeric systems include the printing of regenerated silk structures for biological applications [13].

It should be apparent that increasing the amount of solid phase within the printed ink is imperative for achieving a higher speed of manufacture. The first method by which this is achieved is by having a printing ink that dramatically changes phase from liquid to solid soon after printing. The earliest example of such three-dimensional printing was the use of wax that was heated until molten to make it printable, before subsequent solidification upon the substrate [14–16].

Due to the relatively short timescale necessary for solidification of each droplet (in comparison to spreading of the droplet, as discussed in Chapters 8 and 9), the resolution of the printed pattern is primarily controlled by the temperature of the substrate and the molten liquid, as this dictates the rate at which heat is removed from the molten ink and therefore at which phase change occurs [15]. By depositing subsequent droplets directly on top of preceding droplets, it is possible to build pillars of solidified material, with the maximum achievable height again dictated by the temperature difference between the layers and how quickly heat can be removed [14].

While direct deposition of molten wax and similar materials (e.g., very low molecular weight thermoplastics) enables the fabrication of relatively simple geometries such as pillars and walls, greater complexity is difficult due to the need for a self-supporting structure. To achieve such complexity, it is therefore necessary to deposit not one but two materials; one to fabricate the desired structure (or build material) and one to fabricate a temporary support structure that can be later removed (or support material). Such a two-component system is found in the range of 3D inkjet printers produced by Solidscape Inc., who use a thermoplastic-build material and a wax-based support material. Between each printed layer, the printed material is moved downward by a fixed amount and milled so as to provide a flat substrate for any subsequent droplets. The support material is removed after printing by dissolution in a suitable solvent. This

method of 3D printing provides very high resolution and accuracy, approximately 100  $\mu\text{m}$  in the  $X$ - $Y$  plane and approximately 10  $\mu\text{m}$  in the  $Z$  plane.

The limitations of such a technique, however, include very long build times (this is a trade-off with  $Z$ -plane resolution, as thinner layers mean we need more of them) and the fundamental limitations of using materials suitable for printing (e.g., wax). The parts produced are therefore fragile with poor mechanical integrity. They do, however, find uses for both prototyping and visualization of three-dimensional parts [17] and as molds for casting of both purely decorative items (such as jewelry) and more technical applications (such as tissue scaffolds [18]). By incorporating a solid phase, such as ceramic particles, into the build material, it is also possible to use this process to form green ceramic parts [10, 19, 20]. Similar techniques have also been investigated where solder is the ink, so as to deposit solder bump connections onto circuit boards [10].

Solidification by cooling is not the only phase change that is possible to exploit when trying to obtain solid features. It is also possible to use a resin-based system that polymerizes to form a solid object either by chemical reaction [21] or by application of an external energy such as light [22, 23]. By printing a material before polymerization (either a monomer or a prepolymer), the non-Newtonian rheological constraints associated within printing bulk polymers can be overcome. It should be noted, however, that the resin still has to meet other fluid characteristics typical of a jettable ink, and, as such, the materials are limited and often require elevated printing temperatures to be successfully printed.

The most widely used curing mechanism for printable resins is curing by ultraviolet light, as used in the commercially available printers produced by Objet Geometries [23] or the ProJet™ printers made by 3D Systems. The working principle of these printers is fundamentally similar to those of the Solidscape printers described, but with the critical addition of a UV-curing stage immediately after deposition of each layer. Both of these printers typically use acrylate prepolymers, which can produce a final component of controllable mechanical properties superior to the wax-based printers described previously. By careful control of the chemical structure of the prepolymer, it is possible to obtain a wide variety of mechanical properties, including both rigid components and elastomeric parts. It is also possible to deposit more than one acrylate-based prepolymer into each component, which can give rise to purposefully varied mechanical properties within a given part. It has also been demonstrated that using multiple materials can produce shape-memory materials (a material that changes to a preordained shape upon a change in environmental conditions), and by designing the structure of the rigid and flexible phases, the remembered shape can be controlled [24].

The printing of resins has also been exploited in conjunction with the tendency of liquid droplets to form a spherical cap to produce microlens arrays [22]. The optical properties of the lens, in particular focal length, are determined by the size and curvature of the lens. By controlling the curing of the prepolymer (and hence how far the droplet spreads) together with the volume of deposited resin (i.e., how many droplets are jetted at a given location), it is therefore possible to

vary the optical properties of the microlens with only a facile change in the manufacturing process. Due to the noncontact nature of this method of fabrication, it is possible to deposit lenses onto other delicate parts, such as MEMSs (microelectromechanical systems) without damage [25].

Curing of a prepolymer by chemical reaction has also been investigated for use in three-dimensional printing. These systems typically use a two-ink system so that the polymerization reaction only occurs where the two inks are in proximity; due to the need for two separate inks that react to form the final deposit, this technique is often referred to as *reactive inkjet* or *reactive jetting* [26]. One example of such a system is the reactive jetting of molten caprolactam, which is a prepolymer of nylon; this required two inks, one of which consisted of an activator dissolved in molten caprolactam and another consisting of a catalyst dissolved in molten caprolactam. However, the printability of the catalyst-containing ink was found to be suboptimal due to solid phases inducing instability and clogging [21]. Another such reactive system to be investigated was for the synthesis of polyurethane from a polyol-based ink and an isocyanate-based ink [27]. This was found to successfully produce polyurethane deposits, although the height of the deposits was minimal.

Until now, discussion has focused on three-dimensional printing whereby the solid phase is contained completely within the printed ink, and the constraints placed upon a three-dimensional process because of this. The alternative to this is to use inkjet printing to selectively pattern a supplementary material such that it can be bound together to form a three-dimensional part. Typically, this supplementary material takes the form of a powder, with the layer of powder acting in a similar manner to a piece of paper used in typical graphical printing. This method presents several potential advantages from a manufacturing perspective when compared to depositing the solid material directly. Firstly, and most apparent, it removes the necessity of having the solid phase in the ink. It also means that the build speed is controlled primarily by the powder layer thickness rather than the height of each deposited layer, although this may also result in a decreased resolution in the *Z*-plane. Finally, the selective binding of powder implies the presence of nonbound powder immediately surrounding fabricated object, which eliminates the need for a support material to be deposited contemporaneously.

Currently, the most commonly used powder bed inkjet printing process is that invented by Sachs *et al.* [28] and licensed to Z Corporation and other derivatives. It works by printing a binding ink (which acts as a glue) onto a powder bed. After deposition of the binding ink onto the powder bed, the platform onto which the item is printed is lowered and recoated with further powder. This process is repeated until the final part is made. Development of materials for these systems, both ink and powder, has been quite extensive and has led to a wide range of potential applications. Perhaps, the most straightforward variation is the use of binding inks of different colors that allow multicolored parts to be fabricated. Other examples include the use of elastomeric binders to produce flexible parts [29], the use of metal powder that can (after further processing via infiltration) produce solid metal parts [30], and the use of ceramic powders to act as casting molds or as near-net-shape forms [31].



In addition to powder binding, inkjet printing can also be used to selectively sensitize a powder bed to an external source of radiation. This has been demonstrated in a process called *High-Speed Sintering* [32] whereby an infrared absorbing ink is printed onto a polymer powder bed before exposure to an infrared lamp that heats up the powder where printed upon. By careful selection of powder and processing conditions, it is possible to use this localized rise in temperature to sinter the particles together locally and form a three-dimensional shape. Initially devised as a lower cost and more scalable form of laser sintering of polymeric powders (another additive manufacturing technique), it presents a number of advantages over other inkjet-based powder bed methods. It does not use a binding material, which may limit the mechanical properties of manufactured parts; this in turn reduces the need for subsequent processing to consolidate the part. By using the absorption of infrared energy at the surface of the powder bed as the means to consolidate material, it makes the properties of the component far less dependent upon how the ink interacts with the binder (i.e., the printed ink just has to be present, rather than completely wet the powder material). Finally, by varying the amount of infrared absorbing ink present at the surface, it is possible to vary the amount of energy absorbed and, hence, the degree of consolidation and melting achieved. This in turn means that it is possible to control the mechanical properties of the manufactured component locally [33].

## 15.4

### Inorganic Materials

This section mostly discusses metals that are used to produce conductors such as electrodes and their oxides, which have been used to produce ceramics. Materials used for magnetic application and quantum dot displays are also discussed.

#### 15.4.1

##### Metallic Inks for Contacts and Interconnects

Electrodes are essential components in all electronic circuits [34]. Although electrodes can be prepared using polymeric inks, metal-containing inks are preferred due to the much higher levels of conductivity and are commonly obtained [35, 36]. There are two forms a metal-containing ink can take. The first type of ink is based on a suspension of nanoparticles [37]. Nanoparticles have a larger surface-area-to-volume ratio than particles on the micron scale and upward [38], which means lower temperatures can be used to fuse the particles together. However, in order to prevent the nanoparticles fusing together at room temperature, they are coated with a stabilizer, which must be removed usually by thermal treatment. The advantages of nanoparticle inks tends to be that they have a higher degree of loading, that is, with each pass of a printhead, more metal is deposited than with the other ink type.



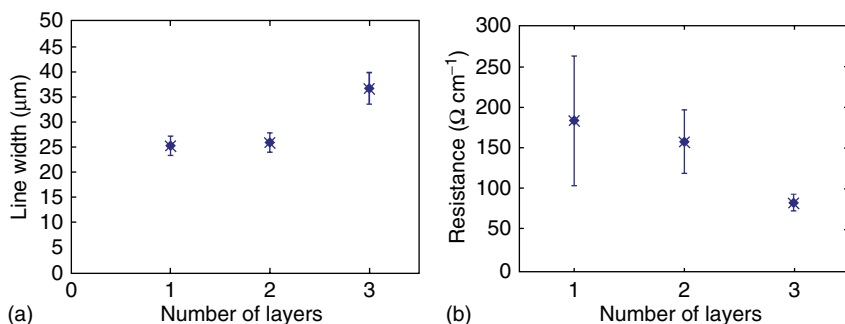


**Figure 15.1** (a) Average line width as a function of layer number, dot spacing was kept constant at  $20\ \mu\text{m}$ . As the number of layers increases, the width of the lines

becomes broader. (b) Resistance as a function of layer number, as can be seen by the triple layered lines are more conductive and have less variability in their values [37].

The second type of ink takes the form of a metal salt dissolved into an appropriate solvent; it is commonly known as a *metal–organic decomposition* (MOD) ink since it relies on the organic component of the salt decomposing to leave the metal [39, 40]. MOD inks tend to reduce nozzle clogging due to their solution nature; they also tend to result in much higher conductivities [39]. Although contact resistance has been reported as being higher [41], drying morphology is also noted to be better for nanoparticle inks [42]. Both types of ink can typically be thermally converted to produce conductive metal tracks, and there is a wide range of alternative conversion methods that have been and continue to be developed. As that discussion moves toward matters of materials science and is beyond the scope of this chapter, the interested reader is referred to other sources [36].

From an inkjet printing point of view, the end performance, that is, conductivity, can be improved by printing additional layers. Teng and Vest observed that the sheet resistances of their inkjet-printed silver MOD lines were similar to those of thin-film evaporated silver after four to five layers had been inkjet-printed [40]. Similarly, Meier *et al.* observed an increase in conductivity, as can be seen in Figure 15.1 and in reliability (i.e., the scatter in values was markedly reduced) for inkjet-printed nanoparticle inks [37]. One side effect of printing more layers is that line width increases, which may not be desirable for some applications. Conductivity can also be increased by decreasing the value of dot spacing. Although this also leads to an increase in line width, the increase in conductivity occurs as more ink and therefore more metal per unit area are deposited.

#### 15.4.2

##### Ceramic Inks

The inkjet printing of ceramics to form, in particular, three-dimensional objects is a growing area of research with applications ranging from artistic to dentistry; an example can be seen in Figure 15.2. Huson has reported on the fabrication of



**Figure 15.2** Ceramic artifacts that have been produced by 3D printing [31].

ceramic objects, in which the versatile geometries offered by additive manufacture are exploited with regard to producing objets d'art [31].

Derby and coworkers [10] have reported on the phase-change printing of a suspension of alumina particles in a hot wax matrix. Each droplet of molten wax solidified upon contact with a cool substrate, allowing excellent control over the forming product. The wax was then removed in the debinding step in a low temperature oven ( $\sim 50^\circ\text{C}$ ) before the green body was fired in a higher temperature furnace ( $1600^\circ\text{C}$ ). Although a measure of geometrical anisotropy was observed, printed objects shrink more in the  $Z$  direction than in the  $X$  and  $Y$  directions [19], a wide variety of objects have been produced [10]. The wax-based inks had an upper limit in terms of printability; 40% particle volume inks could be printed (and in some cases, 45%), but the large increase in relative viscosity that began just after 30–35% meant that each printed droplet contained more wax than functional material.

### 15.4.3

#### Quantum Dots

Quantum dots are semiconducting nanocrystals that are of interest due to their narrow spectral emission. The simplicity of fabricating devices based on quantum dots renders them attractive in a number of applications, such as lasers and displays [43]. A simple quantum dot light-emitting diode (QDLED) consists of a quantum dot layer that is positioned between two layers, one of which is the electron transport layer and the other is the hole transport layer, both of which can be composed of polymeric materials. Although the two transport layers can be deposited using vacuum deposition or solution processing, the quantum dots are typically deposited using a liquid handling process, such as spin coating [44]. However, although spin coating can deposit a thin uniform layer, it has the unfortunate

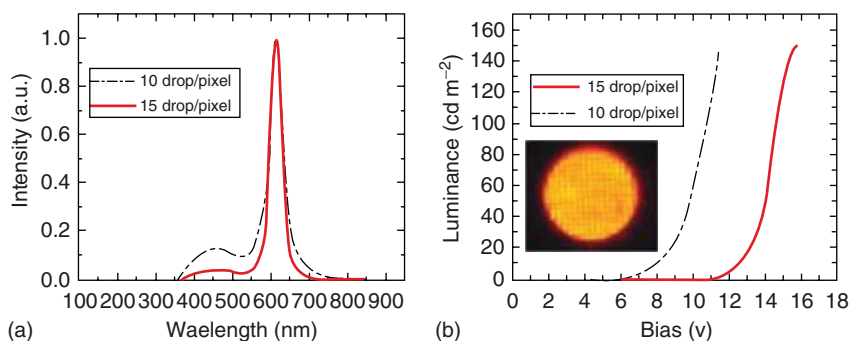


**Figure 15.3** (a) Emission of pixelated devices comparing devices with 10 drops per pixel (dashed curve) to those with 15 drops per pixel (solid curve). (b) Luminance versus applied voltage for the same two

devices, a noticeable increase in drive voltage is seen for the device with 15 drops per pixel. The inset is a photograph of pixelated QDLEDs 243 pixels with a common cathode operating at 12 V [45].

side effect of wasting up to 94% of the expensive quantum dots [45]. Haverinen *et al.* addressed this high level of wastage by employing inkjet printing to deposit the quantum dot layer [45]; the advantage of their approach being that inkjet is an additive technology and therefore levels of waste were greatly decreased. Of particular interest is the observation by Haverinen *et al.* that the purity of the emitted electroluminescent spectra of quantum dot light-emitting diodes was related to the number of printed drops per pixel (Figure 15.3), suggesting that a confident degree of tuning could be obtained, if so wished.

The approach employed by Haverinen *et al.* could be described as a nanoparticle ink approach since their quantum dots were composed of an ink before printing. An approach similar to the MOD ink technique has also been used. MOD inks can be used in an emerging field, termed *reactive inkjet printing* [26]. Chemical reactions require that precise control over dispensed aliquots is necessary so that the correct stoichiometry is obtained. Reactive inkjet printing builds on this principle since inkjet printing dispenses uniform droplets of known volume and concentration.

Ramos *et al.* [46] used an inkjet printer to deposit cadmium and sulfur precursors that were subsequently processed at 250 °C to form a CdS film for subsequent use as a thin-film transistor (TFT). As this approach did not use a nanoparticle ink, organic stabilizers, which can affect end device performance, were not needed. A scheme of the approach used by Ramos *et al.* is shown in Figure 15.4.

## 15.5 Organic Materials

Over the last 10 years, there has been a surge of interest in the possibilities offered by printed electronics, whereby a wide variety of devices can be fabricated

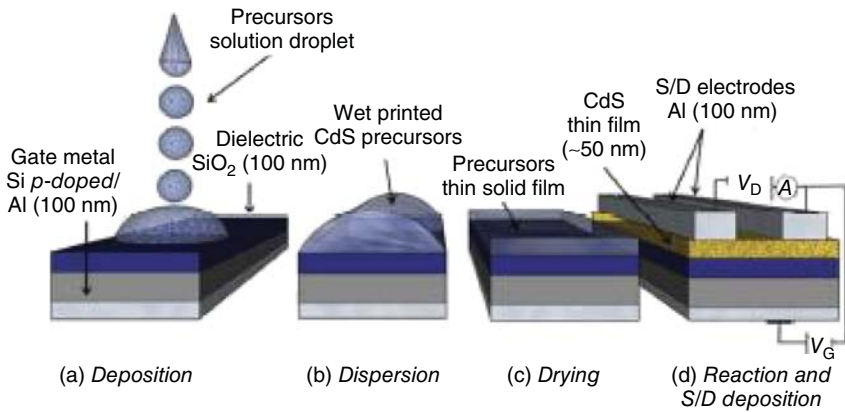


**Figure 15.4** The TFT device fabrication process employed by Ramos and colleagues; first, (a) the Cd and S precursors are printed; (b) dispersion of the solution; (c) solvent

evaporation then occurs before, and (d) a thermal reaction to produce the CdS thin film. Source and drain contacts are then deposited [47].

on flexible substrates using printing technologies [36]. Some of the envisioned examples are small electronic games on breakfast cereal packets, smart tags on supermarket produce, and bendable E-book readers [48]. Printed electronics are seen as primarily low-end applications where production volumes are large and overall processing costs are low. However, there is also considerable appeal in printed photovoltaic devices, due to the well-known attractions of solar power; here, printed electronics offers the opportunity to bring down the costs associated with large-area photovoltaic assemblies.

Conductive polymers have often been proposed as candidates for these applications due to their processability and low production costs. Also, polymer films can be stressed without breaking, which offers clear advantages for flexible electronic devices. Examples of such devices include field-effect transistors, thin-film transistors, passive elements, and radio frequency identification (RFID) tags, which have been printed [49, 50].

Inkjet has been considered as a processing technology for printed electronics. However, given the large production volumes or large areas that many applications demand, such as RFID tags, high-throughput techniques such as gravure printing are seen as the main options. Leenan and colleagues compare the charge carrier mobility requirements with print resolution for a range of patterning techniques; Figure 15.5 shows the comparison graphically. Leenan *et al.* say: “The higher the charge carrier mobility of the semiconductor, the lower are the resolution requirements of the printing methods that can be used to print products with increasing circuit complexity” [48]. As can be seen from Figure 15.5, the current resolution of inkjet printing is severely tested when organic semiconductors are used for a low resolution display (100 rows of pixels, 10 Hz). However, it should be noted that strident research efforts have been made in reducing inkjet’s droplet size from

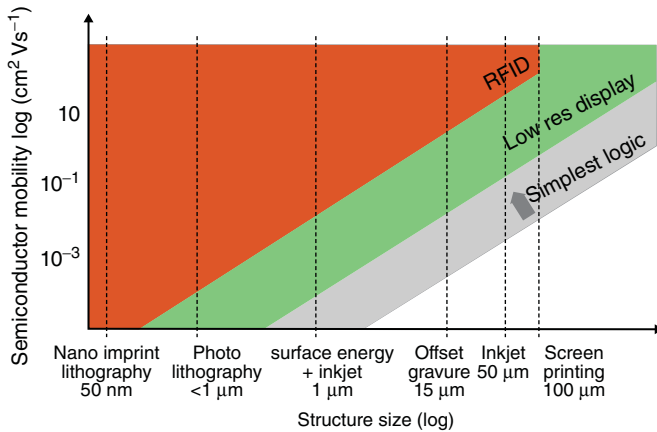


**Figure 15.5** Semiconductor charge carrier mobility versus print technique resolution requirements for printed electronics [48].

picoliters to femtoliters since Leenan’s article, and such systems are now commercially available [51].

Sirringhaus and colleagues have proposed an elegant approach to the manufacture of high-performance printed electronic devices with dimensions in the micron and submicron regimes by controlling the spread of inkjet-printed droplets [52]. They achieved this by using lithography to produce surface energy patterns that repel the deposited ink from specific regions of the substrate. Depending on the lithographic technique used, they were able to produce lines with widths that varied from 250 nm up to 20 μm (electron-beam lithography) or from 2 to 20 μm (optical lithography). Such an approach enabled the inkjet printing of polymer field-effect transistors that had channel lengths as narrow as 500 nm.

In subsequent work, Sirringhaus *et al.* were able to remove the lithography step [53] and achieve channel lengths that were 100 nm or smaller. The approach involved three steps, as illustrated in Figure 15.6, in which a conductive polymer poly(3,4-ethylenedioxythiophene) polystyrene sulfonate (PEDOT:PSS) feature was first printed and, then in a second step, had its surface energy reduced. The decrease in surface energy was achieved by either depositing carbon tetrafluoride via plasma treatment or by simply adding a surfactant to the first batch of PEDOT:PSS ink. In the third step, the second polymer feature was printed with a degree of overlap, but due to the surface energy difference, the new droplets slid off the original droplets forming a gap between the two.

A completely different application of the inkjet printing of polymers relates to recent work performed by Zhang *et al.*, in which they deposited simple polymers into carbon fiber composites [54, 55]. The manufacture of carbon fiber composites involves the stacking of sheets of “prepreg,” which is formed from an array, or weaving, of carbon fibers that have been surrounded and infused with an epoxy matrix. A pattern consisting of a simple polymer ink was printed onto

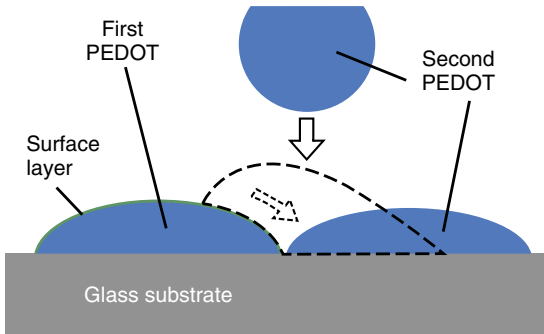


**Figure 15.6** The dewetting approach employed by Siringhaus *et al.* to successfully obtain channel lengths in the order of 100 nm [53].

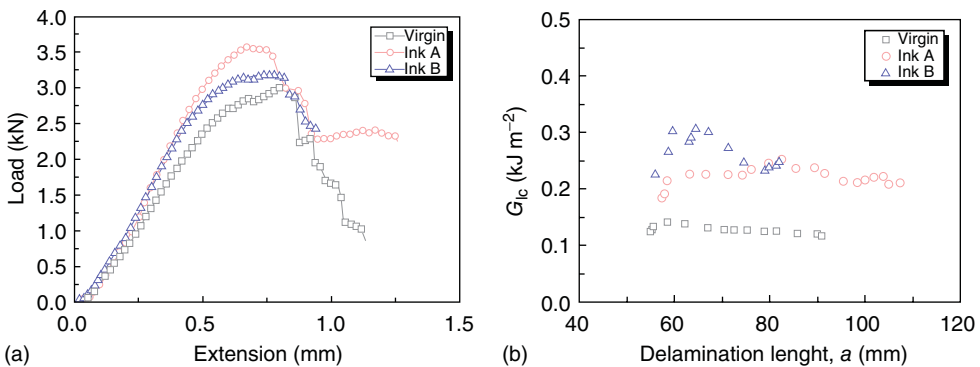


**Figure 15.7** (a) Load extension graph obtained by short-beam shear and (b) mode I critical strain energy release rate against delamination length obtained by double cantilever beam test, demonstrating

the increased interlaminar shear strength, stiffness, and toughness of samples printed with both ink A and ink B as compared to nonprinted (virgin) prepreg.

each sheet of prepreg. After printing and processing, a variety of mechanical tests were performed on the resultant carbon fiber composite; significant increases in strength, stiffness, and toughness of the final aerospace-grade composite systems were found, as shown in Figure 15.7 [54]. The significance of the results is that enhancements in the mechanical properties of the composite can be achieved for minimal weight increase (0.015 wt%) [55].

## 15.6

### Biological Materials

The ability of inkjet printing to dispense picoliter volumes of liquid at defined locations, combined with the inherently efficient use of material and noncontact nature of deposition, has led to considerable interest to use in biological

applications [56–58]. In addition to the constraints placed upon printing due to fluid properties, liquid–substrate interactions, and drying discussed in the previous chapters, biological materials tend to present their own unique challenges with regard to inkjet printing. The types of biologically relevant material will be dependent upon the application and can be loosely divided into two categories: biomacromolecules for analysis and sensing and tissue engineering. Both of these are discussed in more depth next.

### 15.6.1

#### **Biomacromolecules for Analysis and Sensing**

A biomacromolecule is a molecule of biological origin with a large molecular weight. Biomolecules include proteins, DNA, RNA, and polysaccharides. All of the biomacromolecules are critical in the function of living organisms, and an understanding of how they interact with other substances or organisms is of great importance in cell biology, tissue engineering, and health care.

Of current interest is the application of inkjet printing in the fabrication of arrays of biomacromolecules for subsequent analysis. This is intimately linked with the rise to prominence of high-throughput experimentation, where a series of regions of differing composition are patterned onto a surface so as to determine how a substance or organism interacts with each region [59]. Examples of this type of device being fabricated via inkjet printing include DNA microarrays for studying the gene expression [60] and protein microarrays [61].

Another area of significant development is fabrication of biosensors for health-care monitoring and diagnostic purposes [62]. These typically take the form of an electroactive protein (such as an enzyme), which is bound to associated electronic circuitry to produce an electrical signal in the presence of the detected species. A typical, and relatively well-known, example of such a sensor would be the use of glucose oxidase for monitoring blood sugar levels in diabetic patients. In this application, the main cost is associated with glucose oxidase enzyme, and this has acted as a significant motivation to use inkjet printing as compared to more widespread screen printing techniques that have higher inherent wastage of the enzyme material during processing [63]. Glucose-oxidase-based biosensors have been successfully fabricated using inkjet printing and have demonstrated effective performance [64, 65].

A number of issues associated with inkjet printing are also apparent in the printing of biomacromolecules, but due to their nature, it is often more challenging to address these issues. An example of this would be segregation of material to the periphery of a printed droplet upon drying (or “coffee ring staining,” see Chapter 10). This would be undesirable in both given examples of arrays and biosensors due to the uneven distribution of material affecting subsequent analysis. A common approach to control the segregation of material is to use two or more solvents of different volatilities within the ink to counteract the induced Marangoni currents within the drying droplet. With proteins and similar, it is important that great care is taken such that any chosen solvent does not lead to protein denaturing



and losing structure (e.g., a denatured enzyme would not be able to function). As most organic solvents (e.g., alcohols) will denature a protein molecule, it is generally preferable to use a relatively benign substance to achieve this, with some success having been found with the use of small amounts of low-molecular-weight polyethylene glycols [66].

The printing process is also a potential cause of denaturation of proteins, due to the stresses applied as the ink is forced through the nozzle, and in the case of thermal inkjet printing, the localized heating produces the pressure wave to eject a droplet. It has been found that the activity of enzymes that have been printed by both methods have shown an approximately 15–30% loss of activity, with the loss in activity being greater at higher actuation voltages (and therefore a higher strain [65]). To counteract this loss, it is necessary to add much smaller molecules that are able to temporarily surround the protein and act to “cushion” the biomacromolecule against the mechanical stresses experienced. An example of such an addition would be the addition of trehalose sugar, which forms hydrogen bonds with the protein and acts to stabilize the protein solution [67].

#### 15.6.2

##### Tissue Engineering

One of the principle motivations behind the printing of biological material is the potential to construct complex three-dimensional geometries of a biocompatible support material, cells, and other biological material so as to be able to culture new tissue for a desired medical application [58]. This requires the ability to accurately dispense a multitude of water-based solutions and suspensions in an arbitrary pattern, a task that inkjet printing is superficially well suited. There has therefore been a great deal of work toward achieving such a paradigm, as there could be significant benefits in health care, particularly associated with increasing the availability of new tissue for grafts and transplantation from the recipient patient, thus reducing the likelihood of the new tissue being rejected by the immune system. A brief overview of some of the work in this field is given here; for a more in-depth review of the area, the reader is referred to other materials [56, 68].

The use of inkjet printing, and other additive manufacturing techniques, in the field of tissue engineering has been termed *bioprinting* [69] and can be loosely divided into three areas: the printing of a suitable scaffold material, the patterning of cells, and the printing of other biological materials (typically proteins and polysaccharides) to direct the growth of cells [56]. Issues associated with the printing of proteins and polysaccharides have been discussed previously, and as such will only be mentioned in passing, with the focus being on cell patterning and scaffold materials.

The first example of inkjet printing being used to pattern cells was indirect and used a standard desktop printer cartridge that had a substitute ink of fibronectin, a protein that encourages adhesion of cells [70]. The fibronectin was then printed in a defined pattern, and after cell culture, it was shown that the cells preferentially attached to the printed regions. Similar work has been performed with patterns



of laminin [71], collagen [72], and growth factors [73, 74]. The work with growth factors has shown that the proliferation of cells is concentration-dependent [74], showing that cell growth can be controlled by printing gradients of relevant material. Recent work has shown that using similar techniques, it is possible to control the differentiation of stem cells, opening the potential of multiple cell types being patterned [75].

In addition to patterning cells via the printing of biomacromolecules, work was also conducted on direct inkjet printing of cells onto a substrate [76–78]. This has the potential advantage of being able to position multiple types of cell simultaneously, a requirement for all but the most basic of tissues [79]. For such a technique to be useful, it is imperative that the cells are not significantly affected by the printing process and the large strains that are experienced during ligament generation, detachment, and impact. To evaluate this, it is necessary to culture the cells over an extended period of time (typically weeks) to see whether there is immediate cell death due to printing and whether any damage to the cells caused by printing affects how the cells proliferate.

Works on several different types of cell have shown that viability is typically over 85% using both thermal and piezoelectric printheads [80, 81]. For piezoelectric printheads, the influence of printing parameters (actuation voltage and rise/fall time), and therefore the stresses experienced by the cell, on the viability has been investigated; with an increase in actuation voltage shown to lead to a statistically significant reduction in cell viability, although viability was still found to be over 95% [77].

A scaffold material is another integral part of engineered tissue that must fulfill a number of requirements to function. As well as having sufficient structural integrity, it must be biocompatible and nontoxic, be of a suitable geometry, produce an environment amenable to the necessary cell growth and development, and degrade over time in a benign way as the cells present are able to replace the scaffold with produced extracellular matrix. Initial attempts at using inkjet printing to generate such scaffolds did so indirectly, with a sacrificial mold printed in a wax-like material, followed by casting and freeze-drying of a collagen structure in the mold and subsequent removal of the mold [18]. While being successful, this approach is limited as the necessary subsequent processing means that biological material cannot be deposited simultaneously. This provides limitations in terms of patterning different types of cells on and within the scaffold.

Work has, therefore, focused on the direct printing of scaffold materials [79, 82–85]. For this to be achieved effectively, it is necessary to formulate an ink that has suitable fluid properties for printing yet is still able to form a structure of suitable mechanical integrity. This necessitates that the ink undergoes a phase change, and due to the limited range of conditions in which cells are viable and the necessity for cells to be fed and hydrated if they are to survive, this phase change is typically the formation of a water-based gel (or hydrogel). Besides the variation in the material used to achieve the hydrogel, the primary difference is the method of gelation (or cross-linking) used, with the three main groups being chemical gelation, thermal gelation, or photopolymerization, or a combination of the three.

Chemical gelation relies on diffusion of a chemical species into the gelling material that reacts to cross-link the gel. A typical example of this is sodium alginate with the addition of calcium chloride, where the divalent calcium ion replaces the monovalent sodium ion in the alginate to cross-link into a gel. The need for two components in chemical gelation means that for inkjet printing, either of the components can be printed. Due to the challenges in precisely depositing consecutive drops in a timescale over which the first drop has not evaporated, most work has focused on printing only one of these components. A typical method of achieving this is to selectively print one of the components into a liquid bath onto a platform that lowers into the bath between each layer. This has the advantage of keeping the scaffold in an appropriate environment for cell culture and hydration during the fabrication process. Printing of calcium chloride solution into a sodium alginate bath tends to produce a porous scaffold (with a void size of approximately 25  $\mu\text{m}$ ), due to the diffusion of calcium ions from the droplet into the surrounding alginate [79, 82]. The structure has correspondingly poorer mechanical properties than a dense sodium alginate scaffold [82]. However, such an approach has been used to successfully fabricate an implantable scaffold containing three different cell types that maintained their viability after printing and implantation [79]. The printing of sodium alginate into a calcium chloride bath has also been demonstrated [83, 84], which does not exhibit the porous structures obtained by the converse method due to the different direction in which the calcium ions diffuse. This technique has been used to successfully print alginate-encapsulated cells [84].

Thermal gelation relies on a change in temperature that rapidly increases the viscosity of a liquid to a gel (e.g., the setting of gelatin). This change is typically reversible and therefore requires an additional cross-linking stage. An example of this is the printing of a pluronic polymer that is of a lower viscosity at lower temperatures [85]; this meant that the refrigerated ink could be printed on a room-temperature substrate to form a suitably gelled material. To maintain the structure obtained by thermal gelation, a photopolymerization step followed.

Use of tandem thermal and chemical gelation has also been demonstrated [86], whereby an ink containing both sodium alginate and collagen (which undergoes a slow thermal gelation) was printed onto a substrate saturated in calcium chloride. The fast chemical gelation was used to hold the collagen in place while it underwent thermal gelation, and the alginate was then removed by chelating the calcium ions to leave a collagen hydrogel.

## References

1. Graphic Monthly Canada  
<http://www.graphicmonthly.ca/?id=68>  
(accessed 17 November 2014).
2. Shakhnovich, A. and Belmont, J. (2010) Pigments for inkjet applications, in *The Chemistry of Inkjet Inks* (ed S. Magdassi), World Scientific Publishing.
3. Pond, S.F., Wnek, W.J., Doll, P.F., and Andreottola, M.A. (2000) Ink design, in *Inkjet Technology and Product Development Strategies* (ed S.F. Pond), Torrey Pines Research.
4. Magdassi, S. (2010) Ink requirements and formulations guidelines, in *The*

- Chemistry of Inkjet Inks* (ed S. Magdassi), World Scientific Publishing.
5. Bugner, D. (2002) Papers and films for ink-jet printing, in *Handbook of Imaging Materials*, 2nd edn (eds A. Diamond and D. Weiss), Marcel Dekker.
  6. Edison, S.E. (2010) Formulating UV curable inkjet inks, in *The Chemistry of Inkjet Inks* (ed S. Magdassi), World Scientific Publishing.
  7. Hayes, D.J., Cox, W.R., and Grove, M.E. (2001) *J. Soc. Inf. Disp.*, **9** (1), 9–13.
  8. Bergstrom, L. (1996) *J. Mater. Sci.*, **31** (19), 5257–5270.
  9. Derby, B. and Reis, N. (2003) *MRS Bull.*, **28** (11), 815–818.
  10. Seerden, K.A.M., Reis, N., Evans, J.R.G., Grant, P.S., Halloran, J.W., and Derby, B. (2001) *J. Am. Ceram. Soc.*, **84** (11), 2514–2520.
  11. Ebert, J., Ozkol, E., Zeichner, A., Uibel, K., Weiss, O., Koops, U., Telle, R., and Fischer, H. (2009) *J. Dent. Res.*, **88** (7), 673–676.
  12. Noguera, R., Lejeune, M., and Chartier, T. (2005) *J. Eur. Ceram. Soc.*, **25** (12), 2055–2059.
  13. Suntivich, R., Drachuk, I., Calabrese, R., Kaplan, D.L., and Tsukruk, W. (2014) *Biomacromolecules*, **15** (4), 1428–1435.
  14. Gao, F. and Sonin, A.A. (1994) *Proc. R. Soc. London, Ser. A*, **444** (1922), 533–554.
  15. Schiaffino, S. and Sonin, A.A. (1997) *Phys. Fluids*, **9** (11), 3172–3187.
  16. Schiaffino, S. and Sonin, A.A. (1997) *J. Fluid Mech.*, **343** (7), 95–110.
  17. Kim, M.S., Hansgen, A.R., Wink, O., Quaipe, R.A., and Carroll, J.D. (2008) *Circulation*, **117**, 2388–2394.
  18. Sachlos, E., Reis, N., Ainsley, C., Derby, B., and Czernuszka, J.T. (2003) *Biomaterials*, **24** (8), 1487–1497.
  19. Smith, P.J., Derby, B., Reis, N., Wallwork, A., and Ainsley, C. (2004) *Key Eng. Mater.*, **264–268**, 693–696.
  20. Reis, N., Ainsley, C., and Derby, B. (2005) *J. Appl. Phys.*, **97** (9), 094903.
  21. Fathi, S., Dickens, P., and Hague, R. (2011) *Int. J. Adv. Manuf. Technol.*, **59** (1–4), 201–212.
  22. Pilipovic, A., Raos, P., and Sercer, M. (2009) *Int. J. Adv. Manuf. Technol.*, **40** (1–2), 105–115.
  23. Cox, W.R., Guan, C., Hayes, D.H., and Wallace, D.B. (2000) *Int. J. Microcircuits Electron Packag.*, **23** (3), 346–351.
  24. Ge, Q., Qi, H.J., and Dunn, M.L. (2013) *Appl. Phys. Lett.*, **103**, 131901.
  25. Cox, W.R. and Chen, T. (2001) *Opt. Photonics News*, **12** (6), 32–35.
  26. Smith, P.J. and Morrin, A. (2012) *J. Mater. Chem.*, **22**, 10965.
  27. Krober, P., Delaney, J.T., Perelaar, J., and Schubert, U.S. (2009) *J. Mater. Chem.*, **19**, 5234–5238.
  28. Sachs, E., Cima, M., Williams, P., Brancazio, D., and Cornie, J. (1992) *J. Eng. Ind.-Trans. ASME*, **114** (4), 481–488.
  29. Wang, L., Lau, J., Thomas, E.L., and Boyce, M.C. (2011) *Adv. Mater.*, **23** (13), 1524–1529.
  30. Crane, N.B., Wilkes, J., Sachs, E., and Allen, S.M. (2006) *Rapid Prototyping J.*, **12** (5), 266–274.
  31. Huson, D. (2007) Proceedings of Digital Fabrication, pp. 894 and (2008), pp. 283, <http://www.uwe.ac.uk/sca/research/cjpr/> (accessed 12 August 2014).
  32. Hopkinson, N. and Erasenthiran, P. (2004) Proceedings of the Solid Freeform Fabrication Symposium, University of Texas, Austin, TX, p. 312.
  33. Ellis, A., Noble, C.J., and Hopkinson, N. (2014) *Addit. Manuf.*, **1–4**, 48–51.
  34. Singh, M., Haverinen, H.M., Dhagat, P., and Jabbour, G.E. (2010) *Adv. Mater.*, **22**, 673.
  35. Tekin, E., Smith, P.J., and Schubert, U.S. (2008) *Soft Matter*, **4**, 703.
  36. Perelaer, J., Smith, P.J., Mager, D., Soltman, D., Volkman, S.K., Subramanian, V., Korvink, J.G., and Schubert, U.S. (2010) *J. Mater. Chem.*, **20**, 8446–8453.
  37. Meier, H., Löffelmann, U., Mager, D., Smith, P.J., and Korvink, J.G. (2009) *Phys. Status Solidi A*, **206**, 1626.
  38. Buffat, P. and Borel, J.-P. (1976) *Phys. Rev. A*, **13**, 2287.
  39. Dearden, A.L., Smith, P.J., Shin, D.-Y., Reis, N., Derby, B., and O'Brien, P. (2005) *Macromol. Rapid Commun.*, **26**, 315.
  40. Teng, K.F. and Vest, R.W. (1988) *IEEE Trans. Compon., Hybrids, Manuf. Technol.*, **11**, 291.

41. Gamerith, S., Klug, A., Schreiber, H., Scherf, U., Moderegger, E., and List, E.J.W. (2007) *Adv. Funct. Mater.*, **17**, 3111.
42. Choi, H.W., Zhou, T., Singh, M., and Jabbour, G.E. (2015) *Nanoscale*, **7**, 3338–3355.
43. Guerreiro, P.T., Ten, S., Borrelli, N.F., Butty, J., Jabbour, G.E., and Peyghambarian, N. (1997) *Appl. Phys. Lett.*, **71**, 1595.
44. Zhao, J., Bardecker, J.A., Munro, A.M., Liu, M.S., Noi, Y., Ding, I.-K., Luo, J., Chen, B., Jen, A., and Ginger, D.S. (2006) *Nano Lett.*, **6**, 463.
45. Haverinen, H.M., Myllylä, R.A., and Jabbour, G.E. (2009) *Appl. Phys. Lett.*, **94**, 073108.
46. Ramos, J.C., Kabir, D.L., Mejia, I., Mireles, M., Martinez, C.A., and Quevedo-Lopez, M.A. (2013) *ECS Solid-State Lett.*, **2** (9), 67.
47. Ramos, J.C., Mejia, I., Martinez, C.A., and Quevedo-López, M.A. (2013) *J. Mater. Chem. C*. doi: 10.1039/C3TC31475H
48. Leenen, M.A.M., Arning, V., Thiem, H., Steiger, J., and Anselmann, R. (2009) *Phys. Status Solidi A*, **206** (4), 588.
49. Sirringhaus, H., Kawase, T., Friend, R.H., Shimoda, T., Inbasekaran, M., Wu, W., and Woo, E.P. (2000) *Science*, **290**, 2123.
50. Zirkl, M., Sawatdee, A., Helbig, U., Krause, M., Scheipl, G., Kraker, E., Ersman, P.A., Nilsson, D., Platt, D., Bodö, P., Bauer, S., Domann, G., and Stadlober, B. (2011) *Adv. Mater.*, **23**, 2069.
51. SIJTechnology <http://www.sijtechnology.com> (accessed 11 September 2014).
52. Wang, J.Z., Zheng, Z.H., Li, H.W., Huck, W.T.S., and Sirringhaus, H. (2004) *Nat. Mater.*, **3**, 171.
53. Sele, C.W., von Werne, T., Friend, R.H., and Sirringhaus, H. (2005) *Adv. Mater.*, **17**, 997.
54. Zhang, Y., Stringer, J., Grainger, R., Smith, P.J., and Hodzic, A. (2014) *Phys. Status Solidi RRL*, **8**, 56.
55. Zhang, Y., Stringer, J., Grainger, R., Smith, P.J., and Hodzic, A. (2014) *J. Compos. Mater.*, 0021998314533715.
56. Derby, B. (2012) *Science*, **338** (6109), 921–926.
57. Mironov, V., Reis, N., and Derby, B. (2006) *Tissue Eng.*, **12** (4), 631–634.
58. Saunders, R.E. and Derby, B. (2014) *Int. Mater. Rev.*, **59** (8), 430–448.
59. Delaney, J.T. Jr., Smith, P.J., and Schubert, U.S. (2009) *Soft Matter*, **5**, 4866–4877.
60. Hughes, T.R., Mao, M., Jones, A.R., Burchard, J., Marton, M.J., Shannon, K.W., Lefkowitz, S.M., Ziman, M., Schelter, J.M., Meyer, M.R., Kobayashi, S., Davis, C., Dai, H., He, Y.D., Stephanians, S.B., Cavet, G., Walker, W.L., West, A., Coffey, E., Shoemaker, D.D., Stoughton, R., Blanchard, A.P., Friend, S.H., and Linsley, P.S. (2001) *Nat. Biotechnol.*, **19**, 342–347.
61. McWilliam, I., Chong, K.M., and Hall, D. (2011) *Methods Mol. Biol.*, **785**, 345–361.
62. Setti, L., Fraleoni-Morgera, A., Mencarelli, I., Filippini, A., Ballarin, B., and Biase, M. (2007) *Sens. Actuators, B: Chem.*, **126** (1), 252–257.
63. Chuang, M.C., Shen, J., Dudik, L., and Liu, C.C. (2005) Emerging Information Technology Conference (EITC), 2005.
64. Setti, L., Fraleoni-Morgera, A., Ballarin, B., Filippini, A., Frascaro, D., and Piana, C. (2005) *Biosens. Bioelectron.*, **20** (10), 2019–2026.
65. Cook, C.C., Wang, T.M., and Derby, B. (2010) *Chem. Commun.*, **46** (30), 5452–5454.
66. Setti, L., Piana, C., Bonazzi, S., Ballarin, B., Frascaro, D., Fraleoni-Morgera, A., and Giuliani, S. (2004) *Anal. Lett.*, **37** (8), 1559–1570.
67. Nishioka, G.M., Markey, A.A., and Holloway, C.K. (2004) *J. Am. Chem. Soc.*, **126** (50), 16320–16321.
68. Varghese, D., Deshpande, M., Kesari, P., Ohri, S., and Boland, T. (2005) *J. Thorac. Cardiovasc. Surg.*, **129** (2), 470–472.
69. Derby, B. (2008) *J. Mater. Chem.*, **18** (47), 5717–5721.
70. Klebe, R.J. (1988) *Exp. Cell. Res.*, **179** (2), 362–373.
71. Gustavsson, P., Johansson, F., Kanje, M., Wallman, L., and Linsmeier, C.E. (2007) *Biomaterials*, **28** (6), 1141–1151.
72. Roth, E.A., Xu, T., Das, M., Gregory, C., Hickman, J.J., and Boland, T. (2004) *Biomaterials*, **25** (17), 3707–3715.

73. Watanabe, K., Miyazaki, T., and Matsuda, R. (2003) *Zool. Sci.*, **20** (4), 429–434.
74. Miller, E.D., Fisher, G.W., Weiss, L.E., Walker, L.M., and Campbell, P.G. (2006) *Biomaterials*, **27** (10), 2213–2221.
75. Ker, E.D.F., Chu, B., Phillippi, J.A., Gharaibeh, B., Huard, J., Weiss, L.E., and Campbell, P.G. (2011) *Biomaterials*, **32** (13), 3413–3422.
76. Xu, T., Jin, J., Gregory, C., Hickman, J.J., and Boland, T. (2005) *Biomaterials*, **26** (1), 93–99.
77. Saunders, R.E., Gough, J.E., and Derby, B. (2008) *Biomaterials*, **29** (2), 193–203.
78. Lorber, B., Hsiao, W.K., Hutchings, I.M., and Martin, K.R. (2014) *Biofabrication*, **6** (1), 015001.
79. Xu, T., Zhao, W.X., Zhu, J.M., Albanna, M.Z., Yoo, J.J., and Atala, A. (2013) *Biomaterials*, **34** (1), 130–139.
80. Cui, X.F., Dean, D., Ruggeri, Z.M., and Boland, T. (2010) *Biotechnol. Bioeng.*, **106** (6), 963–969.
81. Saunders, R., Gough, J., and Derby, B. (2005) *Nanoscale Mater. Sci. Biol. Med.*, **845**, 57–62.
82. Xu, T., Baicu, C., Aho, M., Zile, M., and Boland, T. (2009) *Biofabrication*, **1** (3), 035001–035006.
83. Nakamura, M., Nishiyama, Y., Henmi, C., Yamaguchi, K., Mochizuki, S., Takiura, K., and Nakagawa, H. (2006) Digital Fabrication Proceedings, Denver, CO, 2006, pp. 89–92.
84. Nakamura, M., Nishiyama, Y., and Henmi, C. (2008) IEEE International Symposium on Micro-Nanomechatronics and Human Science. MHS 2008, Nagoya, Japan, November 6–9, 2008, pp. 451–456.
85. Di Biase, M., Saunders, R.E., Tirelli, N., and Derby, B. (2011) *Soft Matter*, **7** (6), 2639–2646.
86. Pataky, K., Braschler, T., Negro, A., Renaud, P., Lutolf, M.P., and Brugger, J. (2012) *Adv. Mater.*, **24** (3), 391–396.



## 16 Inkjet Technology: What Next?

*Graham D. Martin and Mike Willis*

### 16.1

#### Achievements So Far

The development of a variety of inkjet technologies and techniques seen today has, at the time of writing, taken perhaps 50 years or more. Continuous inkjet (CIJ) printers became established in the 1970s as a way to place variable information onto products and paper as part of a manufacturing process. The 1980s saw the introduction of home- and office-based drop-on-demand (DOD) printers to accompany the personal computers (and later digital cameras), which were also emerging at that time. With some niche exceptions (described next), the fundamental technologies of inkjet have remained the same since this initial period (CIJ): piezoelectric modulation of jets to produce drops followed by electrostatic selection; DOD: either thermal (bubble jet) or piezoelectric actuation to eject individual drops). However, much has changed in the way these techniques have been implemented and in the way the components, particularly print-heads, have been manufactured.

A number of new approaches have been developed recently or are being developed (discussed next), with some using unique mechanisms; one or more of these could provide a significant step change in performance.

Individual parts of print-heads such as nozzles and actuator arrays have always necessitated the use of fabrication techniques now known as MEMS (microelectromechanical systems) processes, not an acronym familiar to the early inkjet pioneers. A variety of MEMS fabrication techniques have been used for constructing critical parts, and the trend has been to integrate these processes so that more of the print-head structure is fabricated using one or more of these techniques in succession. Such techniques often require very significant investment in the development of appropriate tools and materials; hence, print-heads destined for large-volume home and office printers have been constructed this way for some time while industrial-use inkjet systems, which until recently have been produced in smaller numbers, have tended to be assembled more traditionally (although with some critical parts using MEMS). Now, MEMS fabrication is being more widely implemented to construct

print-heads destined for commercial printing and industrial applications. Some of the latest developments are to be discussed next. This evolution of manufacturing technique and material improvements have enabled smaller, higher density, higher throughput, more reliable nozzles in print-heads capable of being stacked in wider arrays. This has enabled the encroachment of inkjet powered systems into some commercial printing applications displacing conventional printing technology, particularly where the benefits of inkjet (e.g., variable and noncontact printing) translate into profitable advantages.

## 16.2

### The Inkjet Print-Head as a Delivery Device

The inkjet print-head (Figure 16.1) can be considered basically as a fluid delivery device, capable of generating drops of liquid of a precise size and in a controlled manner, subject of course to the properties of the liquid. As almost all kinds of current inkjet print-heads have been developed for printing text and images, the drop sizes they produce reflect those needed for impressive images at the viewing distances of the application. Therefore, standard drop volumes are in the range of 2–20 pl for print-heads designed for document printing and 5–50 pl for those intended for outdoor and industrial printing applications.

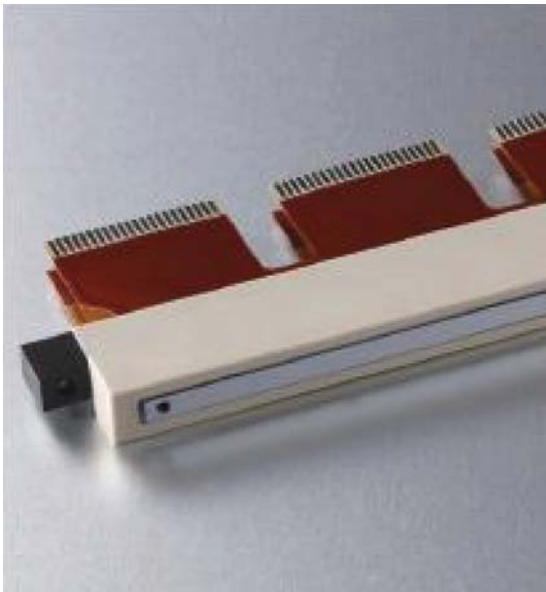


**Figure 16.1** FUJIFILM Endura SX-3 print-head. The SX3 is a compact and lightweight jetting assembly designed specifically for deposition applications requiring multiple

piezoelectric micropumps packed tightly together. There are 128 jets, and the nozzles are arranged in a single line with a 508  $\mu\text{m}$  spacing between nozzles.



At present, the production quantities of print-heads required for inkjet digital fabrication are quite small, so there is little incentive to produce special designs. Therefore, at this stage of the evolution of print-heads, the choice of dedicated heads available to developers for fabrication projects is quite small, and the products are adapted from graphics print-heads. However, we expect that as the market for digital fabrication grows, print-head suppliers will develop more custom heads with some of the special features required, such as smaller drop volumes and better control over drop velocity, drop volumes, and drive waveform.

## 16.3

### Limitations of Inkjet Technology

As described in Chapter 1, inkjet technology has some great advantages, including the complete flexibility of a digital process, and as a noncontact process, it can allow drop deposition onto nonplanar surfaces, onto wet surfaces, and onto surfaces already printed without the risk of removing the previous deposits. However, there are some drawbacks as well. Some of these are fundamental to the technology, while others are limitations for digital fabrication applications due to the print-heads being currently optimized for graphics printing.

#### 16.3.1

##### Jetting Fluid Constraints

Inkjet technology imposes limitations on the physical properties of the inks that can be used, in general to relatively low viscosities, normally below 20 mPa·s. Other parameters such as surface tension also need to be held within certain limits. To achieve a low viscosity, the jetting fluids are usually formulated with the functional materials dissolved or dispersed in a carrier liquid, such as water or organic solvent. If the volatility of the solvent is high, this can create operating problems within DOD inkjet print-heads due to the ink drying in the nozzles. The low dilution of active materials can also cause drying problems on the substrate, as a large amount of liquid is needed to deposit a small amount of material.

#### 16.3.2

##### Control of Drop Volume

There are many applications where it is desirable to vary the amount of material deposited at each pixel. Multiple drops can be filled at each position, but then the incremental amount is one drop. Most of today's technologies are binary: that is, they generate only a single drop volume. Some inkjet technologies allow direct control over the drop volume, but only over a small range. There are a couple of emerging technologies that can generate an infinitely variable range of fluid volumes.

## 16.3.3

**Variations in Drop Volume**

With multinozzle print-heads, there will be small channel-to-channel variations in drop generation performance introduced during manufacturing. These may be variations in actuator efficiency, alignment tolerances, and physical dimensions of the pressure chambers and nozzles. The result is variations in drop volume and velocity from channel to channel across an inkjet print-head. End effects can also occur, where the efficiency of channels at the ends of rows is different from those in the center. To overcome this, some print-heads are manufactured with dummy channels at each end.

To reduce these problems, some print-heads have the capability of adjusting the drive waveform on a channel-by-channel basis so that the variations between channels is minimized.

Variations in drop volume can also arise from the drop formation process according to the ink formulation. If particulates or high-molecular-weight

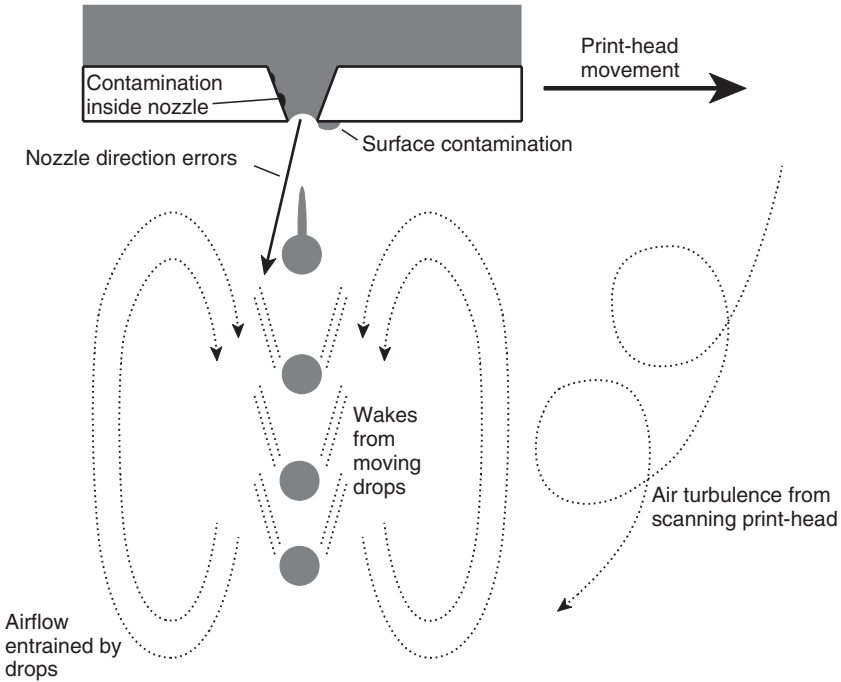


**Figure 16.2** Some of the factors that can affect the trajectory of drops in flight. Shown here are just some of the factors, due to manufacturing tolerances and finish of nozzles, contamination inside and around

the outer rim of the nozzles, airflows caused by the movement of the print-head and by the drops themselves. In addition, there are end effects at the ends of rows of nozzles.

polymers are included in the formulation, for instance, then these can introduce small variations in the break-off of the ligament at the nozzle.

#### 16.3.4

#### Jet Directionality and Drop Placement Errors

The flight path taken by drops from the print-head to the substrate is dependent on several factors (Figure 16.2), but, in particular, the nozzle exit shape and condition. There will be small variations in the jetting angle from nozzle to nozzle as a result of manufacturing processes. The quality of nozzles varies between different print-head types. In addition, further errors will be due to buildup of contamination inside and around the nozzle rim.

Further variations occur according to the way that drops break off from the nozzles. Several factors affect the size and shape of the ligament that connects the front of the ejected drop to the nozzle during the drop formation process, in particular the ink formulation and drive waveform. If the position at which the tail of the drop breaks from the nozzle varies, then variations in trajectory and landing position of the drop are also likely.

Once the trajectory of the drops has been determined by the print-head and drop break-off has occurred, then aerodynamic effects come into play.

For some digital fabrication applications where drop landing accuracy is paramount, for instance, the printing of flat-panel displays, a technique of pre patterning the substrate has been used (Figure 16.3). The patterning process locally changes the wettability of the substrate. The surface tension of the jetted fluid then causes the fluid to align and fill the spaces defined by the patterning.

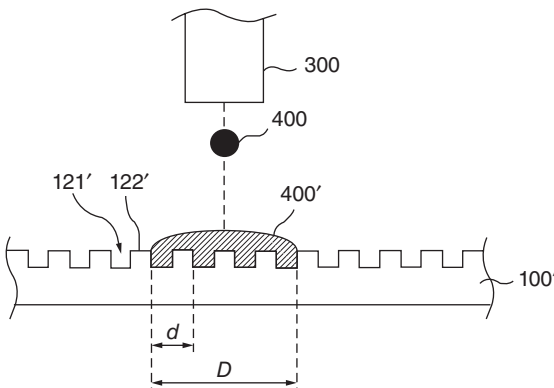


**Figure 16.3** Substrate patterning to improve drop placement. US 2010/0055396 method for high-resolution inkjet print using prepatterned substrate and conductive substrate manufactured using the same, LG Chemical, Ltd. A laser interferometric lithographic

method is used to prepattern a substrate coated with a photoresist. Conductive ink printed onto the substrate preferentially fills the valleys rather than the ridges, so the line width is constrained to a width  $D$ .

## 16.3.5

**Aerodynamic Effects**

As the drops pass through air on their way to the substrate, they encounter aerodynamic drag. At small drop volumes, perhaps 5 pl or less, the air drag is sufficient to decelerate the individual drops strongly, and depending on the spacing between the print-head and the substrate, they may not even reach the substrate. The situation is confusing, as when a series of drops is jetted from the same nozzle, the first drop is slowed by drag but the following drops slip-stream behind it and longer working distances are possible. In addition, if many drops are jetted simultaneously, air is entrained toward the substrate, which also helps to carry the drops toward it.

However, the greater the influence of the air, the worse the placement error of the drops is likely to be. Because of the differences in geometry at the ends of the print-heads, the airflows will be different from those in the center of a nozzle row. There have been some proposals to enclose inkjet systems within vacuum chambers in order to eliminate the influence of aerodynamic effects entirely (Figure 16.4).

## 16.3.6

**Impact and Surface Wetting Effects**

As the relatively low viscosity fluid impacts the substrate, it spreads and wets the surface. The amount of spreading varies according to the ink formulation, viscosity, and surface tension, the drops impact velocity and the substrate hardness, surface microprofile, and surface energy. If drops are jetted on to previously deposited wet drops, then splashing may occur. If printing the same or other materials has already patterned the surface, then the wetting behaviors may vary between the virgin substrate and the patterned regions.

If, during the jetting process, long ligaments are formed, then the ligament may not have been drawn into the main drop by the time of impact. If the print-head and substrate have relative motion, then the ligament may impact outside the main drop, misshaping the printed dot.

If satellite drops are formed in the jetting process, then these too may land outside the periphery of the main drop. Although not important for most graphics applications, drop debris outside the intended impact area may lead to an unacceptable image quality for some digital fabrication applications.

## 16.4

**Today's Dominant Technologies and Limitations**

Most inkjet devices in use today are of the DOD type, where each nozzle has its own actuator and drops are generated only as required, either as the print-head moves over the substrate or as the substrate moves under the print-head. For DOD

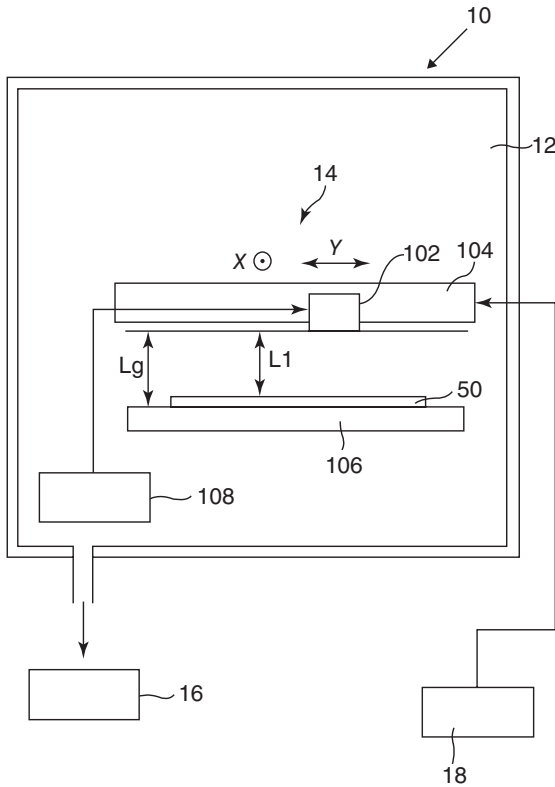


**Figure 16.4** Enclosing an inkjet system within a vacuum to reduce or eliminate aerodynamic effects of drops in flight. US 2009/0256880 printing system, inkjet printer, and method for printing, Mimaki

Engineering Co., Ltd. A decompressor is configured to reduce a pressure in an area between the medium and the nozzles to a pressure lower than atmospheric pressure.

print-heads, the two main actuator types are thermal or bubble-jet and piezoelectric, as described in Chapter 3.

#### 16.4.1

##### Thermal Drop-on-Demand Inkjet

We recall that in the thermal or bubble-jet process, a heater inside the actuator cavity is in contact with the liquid to be ejected. When an electrical pulse is applied to the heater, the surface temperature rises rapidly to around 350–400 °C. This initially causes the nucleation of bubbles, followed by coalescence into one large bubble. The rapid bubble growth has been likened to a microexplosion and causes a very rapid pressure increase within the actuator chamber. Most of this pressure is released by the flow of ink from the nozzle, although inevitably some flow occurs back into the ink manifold of the print-head. In addition, the print-head structure

will flex slightly. As the electrical pulse ends, the heater cools rapidly (as it has minimal thermal mass), the bubble collapses, and the pressure falls quickly within the actuator chamber. This stops the flow of ink through the nozzle, causing the ink already ejected to break away and fly toward the substrate.

Today's devices are designed and optimized for desktop graphics printing, which requires a high nozzle density and low manufacturing costs. To achieve a high nozzle density, thermal management within the print-head is key. Much of the heat generated during the actuation cycle is wasted, and the management of this waste heat is critical to continued operation of the print-head. By keeping the ink viscosity low, the required drop ejection energy is also kept low, reducing the thermal management problems. Therefore, thermal or bubble-jet print-heads are designed to operate with low-viscosity inks. For graphics printing, ink containing a small percentage by weight of a colorant is sufficient to form an acceptable image. Pigment-based inks also include some resins, but still the formulations of these inks have to be kept to tight viscosity specifications.

To use thermal or bubble-inkjet technology for nongraphic applications would ideally require:

- Redesign to allow higher viscosity fluids to be jetted
- Improvements to robustness and life
- Better stability and control: thermal inkjet tends toward the formation of long tails and satellite drops.

Both Canon and Hewlett-Packard began using new manufacturing processes around 2003–2004 where the nozzle plate is directly formed on the silicon substrate rather than added as a separate item. This allows all of the print-head to be manufactured in a serial production line, and allows for much greater freedom in changing the design for different applications. However, at the time of writing, little evidence of customization has emerged, although Hewlett-Packard has a series of patents on a small, replaceable dispensing-type print-head and drive module referred to as TIPS (*Thermal Inkjet Picofluidic System*) (Figure 16.5). A variety of fluids are claimed capable of being jetted, such as PEDOT, conductive polymers, and organic solvents. The drop volume is around 1 pl.

It is possible to redesign thermal or bubble-jet print-heads to jet higher viscosity fluids, and there have been reports on this.

Of course, materials within any jetted fluid need to be compatible with temperatures reached within the print-head. Only a very small amount of the ink is vaporized during the bubble-jet process, but over time, deposits may build up.

Although there are some nongraphics applications of the current technologies where low-viscosity fluids can be used, we think it is unlikely that special print-heads will be developed unless some high-volume applications emerge. The strength of thermal or bubble inkjet is that it can be manufactured in high volume at low cost. If home or personal dispensing uses could be found, then this could be the application to make it viable.

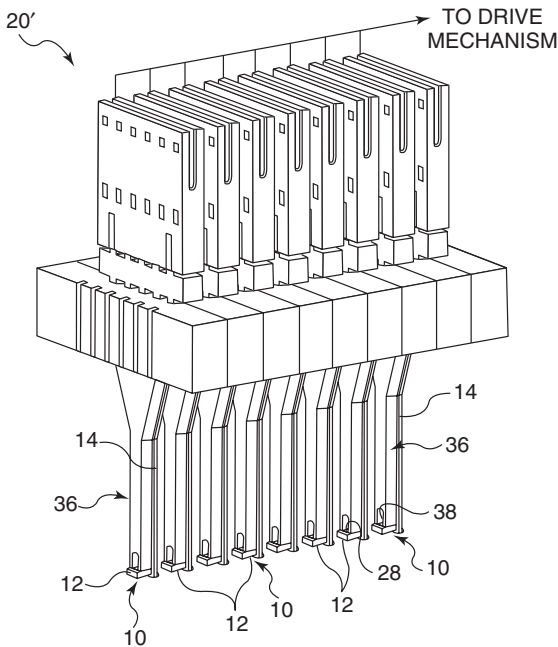


**Figure 16.5** Dispensing fluids using thermal inkjet. US 2009/0047440 fluid delivery system, Hewlett-Packard. The nozzles 10 are first immersed in the fluids, and a small

quantity wicks into the firing chambers and manifolds by capillary forces. Drops of the fluid can then be dispensed by firing drops.

#### 16.4.2

##### Piezoelectric Drop-on-Demand Inkjet

In a piezoelectric DOD print-head, drops are generated, as in bubble jet, by a rapid pressure increase of the ink inside the actuator chamber. The difference is that a small piezoelectric actuator, one for each chamber, generates the pressure. When a voltage is applied across the actuator, the piezoelectric material distorts, and this change in shape is used to displace the chamber wall or roof into the chamber to generate the required pressure for ink ejection. Because of limitations of the activity of piezo materials, practical drive voltages, and other considerations, the area of piezo material required to generate drops is much higher than the area of a bubble-jet heater. Therefore, the nozzle-to-nozzle spacing and the area of piezo print-heads tend to be greater, leading to a lower native print resolution.

Although heat is not used to generate drops, in operation, the piezo actuators generate waste heat, and removing this is a consideration for high-duty-cycle operation.

A challenge when designing piezo print-heads is how to manufacture the relatively complex ink paths from a central manifold to the actuator chambers and hence the nozzles. Traditionally, stacked layers of stainless steel or ceramic have

been separately patterned, then bonded together to achieve this. Recent advances in silicon fabrication techniques, particularly DRIE (deep reactive-ion etching), has led to a trend in the use of silicon MEMS techniques to fabricate these complex “channel” plates. The use of silicon enables stiffer structures, higher channel resolution, and higher drop frequencies.

In order to decrease the channel spacing, the actuator dimensions have to be reduced. To maintain useable drop volumes, this means that the displacement of the actuator into the chamber needs to be increased. This necessitates a reduction in the thickness of the actuator roof and also the piezo material.

In the past, print-heads used pieces of piezoelectric material such as ceramic PZT (lead zirconate titanate) sliced into wafers and then diced to form individual actuators. As the need for thinner piezo layers has grown, and also to aid cost savings for mass manufacturing, alternative means of forming piezo layers have been developed. Thick-film deposition of piezo layers has been used commercially since the mid-1990s, and more recently, thin-film deposition techniques have been used. Thin-film piezo layers can be moisture-sensitive when electric fields are applied, so the piezo material has to be protected in hermetically sealed covers.

Generally, it is possible to apply more energy to the ink in a piezo actuator than in a bubble-jet device and, hence, to jet higher viscosity materials. In addition, there is no need to include a volatile material within the ink for bubble generation, and the ink ingredients do not have to withstand high temperature excursions.

Most of today’s piezo print-heads use what is known as *roof-mode architecture*. One of the industrial print-head suppliers, Xaar uses a moving wall architecture where the channel walls are made from piezo material and flex to produce pressures on the ink.

## 16.5

### Other Current Technologies

Apart from bubble and piezo DOD inkjet, CIJ has been employed for many years for coding, marking, addressing, and form printing. In addition, development work has also been ongoing in the search for a way of generating drops from nozzles using electrostatic forces. We shall discuss these technologies here.

#### 16.5.1

##### Continuous Inkjet

In CIJ technology, as described in Chapter 3, drops are generated continuously, charged, and deflected to separate printing drops from nonprinting drops, which are then collected and recirculated. This technology does not lend itself to high channel densities, due to the high voltages required for charging the drops. The system is additionally complex and relatively expensive. An added drawback for some applications using expensive materials is the large volume of ink required within the feed and recirculating system.



However, Eastman Kodak has developed a new type of CIJ (called *Stream*), which we discuss next as an emerging technology (see also Chapters 2 and 3). This has the potential to offer higher nozzle densities, smaller drops, and faster print speeds than traditional CIJ, although it still retains a large-volume ink supply.

### 16.5.2

#### Electrostatic Drop-on-Demand

Methods of generating drops using electrostatic forces have been known for some time. An external electrostatic field is applied to a raised meniscus in a nozzle. Above a certain field strength, the meniscus forms a cone shape as the electrostatic forces reduce the surface tension forces of the liquid. Increasing the field still results in the emission of a thin thread of fluid from the tip of the cone. The drop size is controlled by the length of the field pulse and is infinitely variable.

There are several advantages of this technology. The drop diameter is only a fraction of the nozzle diameter and is not so affected by nozzle quality or contamination as in conventional DOD. It is also of great current interest because of its potential to create very small drop sizes, for instance, in the femtoliter range.

However, the process has some drawbacks. The high electric fields involved, together with the need for a bulging meniscus in the nozzle, means that nozzle densities are quite limited. The high voltages are more expensive to generate and switch than for piezo or bubble jet.

Several teams are working with this technology, for instance, AIST in Japan [1] and Queen Mary College, London, UK [2], aiming to develop it for direct writing electronic applications and for the dispensing of very small quantities of fluids (Figure 16.6).

### 16.5.3

#### Acoustic Drop Ejection

There are systems that produce drops directly from high-frequency acoustic generators. Xerox developed a nozzleless inkjet technology where the acoustic generators are submerged in the ink, with the acoustic energy focused on the ink surface. There are no nozzles or indeed a nozzle plate. Fine drops of ink are emitted in a stream at the points of focus.

Similar principles have been used by Picoliter Inc., now called *Labcyte*, to cause the noncontact transfer of fluids in volumes from 2 nl to 10  $\mu$ l. “Acoustic droplet ejection” (ADE) technology (Figure 16.7) is claimed to be a very gentle process. Labcyte has demonstrated that it can be used to transfer proteins, high-molecular-weight DNA, and live cells without damage or loss of viability.

Similarly to electrospray printing, it is capable of generating very small drops and the drive pulse width can directly control the amount of fluid deposited.

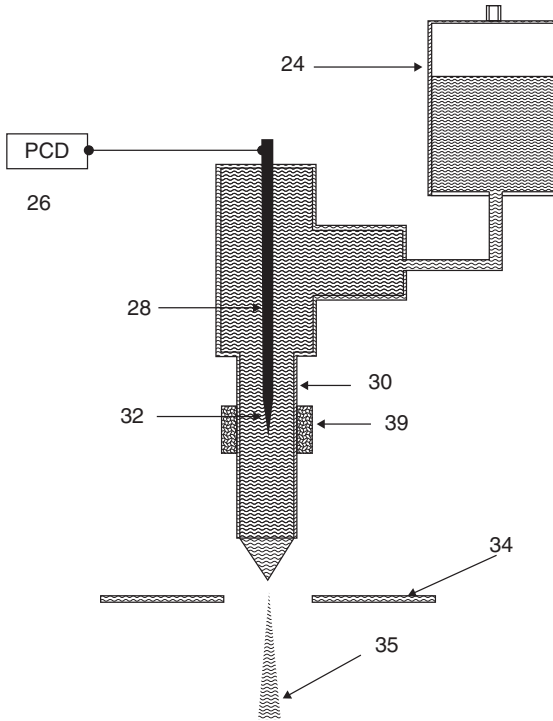


**Figure 16.6** Electrostatic spray jetting. WO 2008/142393 an electrostatic spraying device and a method of electrostatic spraying, Queen Mary and Westfield College. The liquid to be jetted, in this case silicone oil, fills the emitter tube 30. A piezoelectric

charging device is connected to electrode tip 32, and the resultant charged fluid forms a cone in the emitter nozzle where a highly asymmetric field is generated by aperture electrode 34. A stable cone of fluid is sprayed from the tip of the fluid cone.

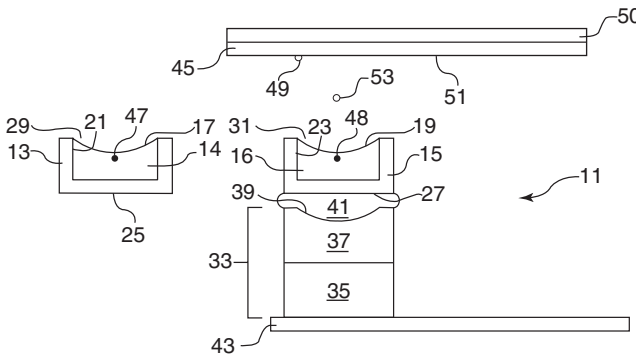


**Figure 16.7** Acoustic drop generation. EP 1 337 325 acoustic ejection of fluids from a plurality of reservoirs, PicoLiner Inc. Acoustic ejector 33 comprises an acoustic generator 35 and a focusing component 37. This is

acoustically coupled to a liquid reservoir 15 by fluid 41. The acoustic energy is focused to a point 48 just below the liquid surface, and drops 53 are ejected from the free surface of the liquid.

## 16.6

### Emerging Technologies and Techniques

For around a decade before 2010, there had been very little development of new inkjet technologies, the focus being on the evolution of piezo and bubble-jet DoD technology for office and graphics applications. But more recently, driven by the need for higher print speeds in the graphics area, and fine drops for digital fabrication applications, we are now seeing the introduction of new technologies and techniques. In most cases, these overcome some of the restrictions of today's inkjet devices.

#### 16.6.1

##### Stream

Eastman Kodak has been developing a new CIJ technology for a number of years. It has demonstrated printing at substrate speeds of  $200 \text{ m min}^{-1}$  ( $3.3 \text{ m s}^{-1}$ ) at 600 dpi with variable drop sizes in full color, using pigmented inks, and is the technology incorporated in the PROSPER range of high-volume digital printing systems. The print-head technology is considerably less complex as compared the traditional binary CIJ, consisting of annular ring heaters surrounding nozzles formed in a silicon nozzle plate.

As with other CIJ technologies, the ink is pressurized and flows continuously from the nozzles during operation. To stimulate the liquid flowing from each nozzle to break into regular-sized drops, the heater surrounding the nozzle exit is pulsed. The temperature of the ink surface is raised by just a few degrees, which changes the surface tension of the ink stream enough to provide discontinuities at which the stream can break up. In this way, a stream of drops is produced, and by turning off the heater pulses for three to four cycles, larger drops can be formed. In the current implementation, the larger drops pass into the substrate to print and the smaller drops are deflected by a transverse airflow, collected, and recirculated (Figure 16.8). The result is a print-head technology capable of high nozzle densities, and the nozzle heater drivers can be fabricated on the nozzle front face along with the heaters. The transverse airflow system can be built up as a structure directly on to the nozzle plate.

A key advantage of this technology may be its freedom to use a wide range of inks. It is believed that continuous jets of most inks can be broken up with thermal pulses without any special formulation being required, and the pump pressure can be adjusted to accommodate different ink viscosities. The breakup length of the ink stream can be adjusted by varying the amplitude of the heater pulse. Therefore, beyond the current graphics printing uses of Stream, it may have a future application in high-speed printing for manufacturing.

#### 16.6.2

##### Print-Head Manufacturing Techniques

MEMS technology has been commercialized for many applications during the past decade. MEMS devices, usually made by modified semiconductor processes

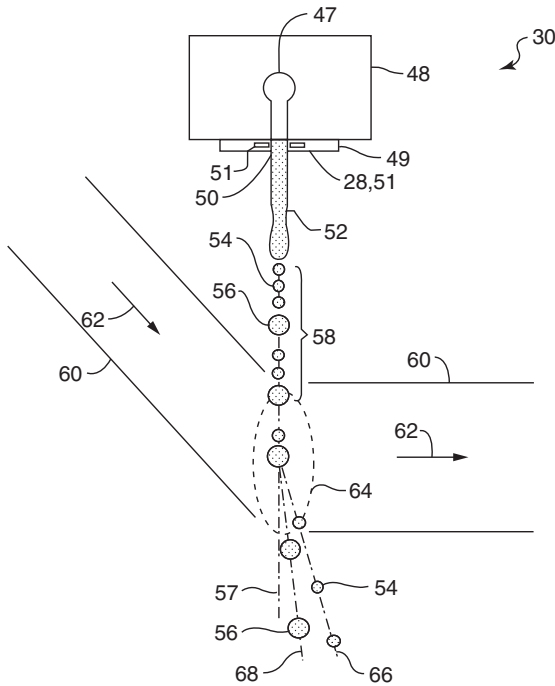


**Figure 16.8** Kodak stream technology. US 2011/0242169 continuous printer with actuator activation waveform, Eastman Kodak Company. Ink under pressure flows through nozzle 50 that is surrounded by heater 51. Pulses of heat stimulate the jet 52 to form

small drops 54. If the pulses cease for a few cycles, larger drops 56 are formed. A laminar transverse airflow 62 then deflects the smaller drops to a gutter, while the larger drops continue to the substrate.

such as wet etching, dry etching, and electrodischarge machining, also have application for the generation of liquid jets and drops.

On 15 July 1997, Silverbrook Research (now filing under Zamtek, with the patents controlled by Memjet) filed 372 patent applications on a single day at the US Patent and Trademark Office. By the end of July 2010, they had filed just over 5000 US patent applications. The majority of these applications relate to MEMS inkjet devices with around one quarter relating to the actuator design.

Initially, Silverbrook Research was pursuing a wide range of possible MEMS actuator designs, but the first one chosen for commercialization is based on a suspended heater thermal inkjet design. By suspending the heater within the chamber, the efficiency of the device is improved by around 1 order of magnitude as compared to conventional thermal inkjet devices with surface-mounted heaters. This high efficiency allows a very high density of actuators without thermal management problems, as the ink carries all of the excess heat away. However, we understand that this design as commercialized may be limited to relatively simple dye-based inks.

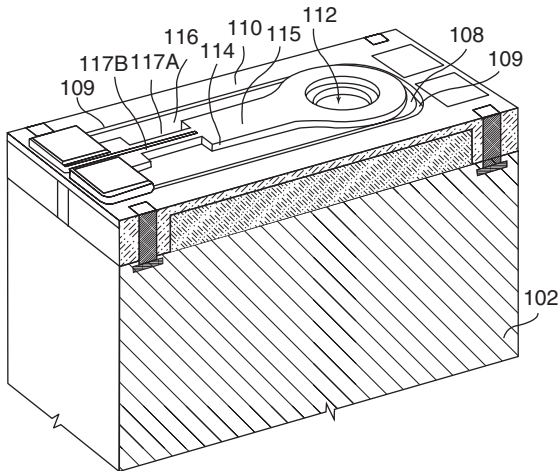


**Figure 16.9** MEMS print-head technology. US 2009/0278876 short pulse-width actuation of thermal bend actuator, Silverbrook Research Pty Ltd. Heaters 117 cause a deflection of nozzle plate 115 downward into the fluid chamber below (not shown).

This causes some of the fluid to be pushed up through nozzle 112 that forms a drop. The top surface is planarized with a compliant layer of polydimethylsiloxane PDMS (not shown) that also provides a nonwetting surface.

Another design Silverbrook has demonstrated is a moving nozzle operated by a thermal bend actuator (Figure 16.9). The nozzle is driven downward into the ink, displacing an equal volume from the nozzle. As compared to a conventional actuator, the pressure exerted on the ink is considerably less. Because there is no heating within the chamber, this method is probably suited for more complex inks. Until the technology is commercialized, it is too early to tell what role it may have for digital fabrication.

Other companies have also explored new print-head designs using MEMS and, in particular, silicon-based manufacturing techniques. For instance, in 2008, Xerox published a number of US patent applications covering a roof-mode actuator where the diaphragm is moved electrostatically (Figure 16.10). In 2012, Konica Minolta patented a silicon-based print-head structure (EP2716461) with a better means of electrical connection. Indeed, there have been more than 100 US inkjet patents and patent applications with the word “silicon” in the title, abstract or claims published every year since 2001, peaking at over 250 per year during the period 2007–2011.

An interesting manufacturing technique, which could involve an inkjet-based additive manufacturing process (i.e., using an inkjet to make an inkjet), is described in a patent application from Xerox (US2013/0215197). The additive manufacturing technique is used to create a sacrificial mold, out of wax, or PMMA, of the fluid paths within a print-head. This is then cast or coated with a suitable material such as an epoxy or a metal layer, and then, once coated, the sacrificial mold can be removed by melting or dissolved by a solvent. This

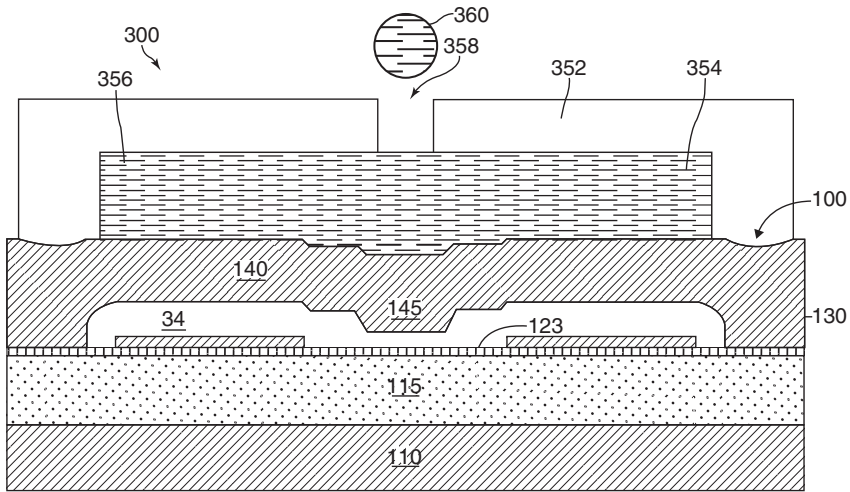


**Figure 16.10** Electrostatic diaphragm roof mode actuator. US 7942508 decreased actuation voltage in MEMS devices by constraining membrane displacement without using conductive “landing pad,” Xerox Corporation. Diaphragm 140 is attracted to ring electrode 130 by the electrostatic field

between them. The protrusion 145 restricts the diaphragm movement and prevents it shorting against the electrode. When the field is removed, the diaphragm springs back up and drop 360 is ejected from the nozzle.

structure can then be bonded to other components of the print-head. The advantage here is that several other forming and bonding steps are removed from the manufacturing process.

### 16.6.3

#### Flextensional

Flextensional devices consist of a piezo actuator coupled to a flexible mechanical device. Some of the MEMS devices proposed by Silverbrook are flextensional, and there have been other designs in the past from Hewlett-Packard.

The Technology Partnership also has a series of patent applications covering a flextensional design. The piezo ceramic is bonded to an electroformed nozzle plate. There are slots on each side of the piezo material allowing flexure of the nozzle layer (Figure 16.11). When a pulse is applied, a downward deflection of the nozzle occurs and ink is displaced out of the nozzle. A second pulse is applied to dampen the return movement. As the drop ejection takes place under relatively low pressures, then it should be possible to jet more difficult ink types, for instance, those containing heavy pigments.

In 2014, Toshiba TEC published patent applications describing an all-silicon version with a piezo actuator.

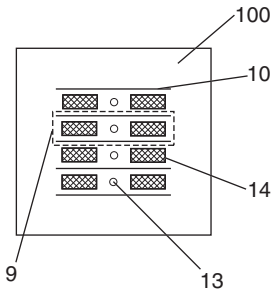


**Figure 16.11** Moving nozzle print-head. WO 2008/044069 liquid projection apparatus, The Technology Partnership plc. Piezo actuators (shaded) are fixed to a nozzle plate, which are able to move due to slits 10. The actuators cause the nozzle plate to move downward, forcing ink up through nozzles 13.

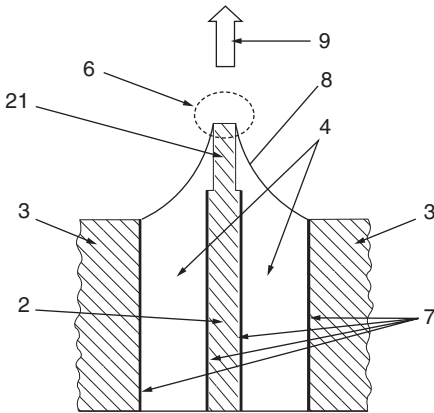


**Figure 16.12** Tonejet ejection site. WO 2011/154334 image and print-head control, Tonejet limited. Charged pigment particles 6 agglomerate at electrode tip 21 in response to an electric field and are then ejected 9 to the substrate.

#### 16.6.4

##### **Tonejet**

Tonejet ink is similar to liquid toner, consisting of charged pigments and polymers in solid form suspended in an insulating carrier liquid. The ink wicks up electrodes that also form ejection points (Figure 16.12). When a voltage is applied to these electrodes, the particles agglomerate at the electrode tips. Once the accumulated charge reaches a high enough level, the particles are ejected toward the substrate, with only a small amount of the carrier liquid being carried over.

Although for graphics applications the particles consist of pigmented polymer resins, it is also possible to fabricate toners as functional materials, as well as incorporating higher density pigments.

#### 16.6.5

##### **Ink Recirculation**

A constant flow of ink moving past the back of the nozzle plate in an inkjet print-head provides several benefits. The movement of ink reduces the likelihood of

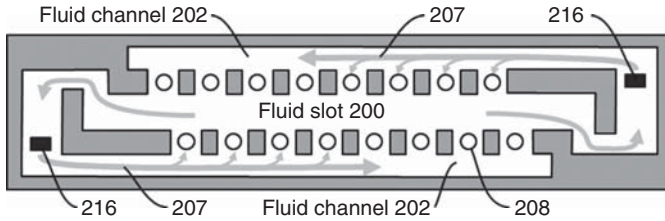


**Figure 16.13** On-chip ink recirculation. US 2012/0007921 fluid ejection device with circulation pump, Hewlett-Packard. Ink is circulated by the fluid circulation pump 216 through fluid channels 202 to each drop generator channel (e.g., 208), then to the fluid slot 200 as indicated by the gray arrows 207.

precipitation or flocculation of ink components. Any contaminating particles in the ink do not inevitably pass through a nozzle but are likely to be recirculated and filtered out, and any air bubbles present or ingested through the nozzle can also be swept away. These benefits are at the price of additional cost and complexity. Several companies now offer recirculating systems. The Xaar 1001 print-head was one of the first examples of this and has proved successful in applications with “difficult” inks such as those for ceramic printing. Hewlett-Packard has a patent application (US2012/0007921) that describes a print-head with a cross-flow generated using an on-chip “bubble” pump working on a principle similar to the nozzle actuation mechanisms (Figure 16.13). Lexmark has claimed a similar system (US2013/0182022). Samsung has an application (US2014/0078224) with two (or three) thin-film piezoelectric actuators per nozzle, which can either circulate ink or eject ink through the nozzle, depending on the timing of the actuations (Figure 16.14).

#### 16.6.6

#### Indirect Inkjet Printing

Indirect inkjet printing refers to the use of an intermediate substrate (belt) onto which ink drops are printed and then transferred by some means to the final surface. While not a new idea (Xerox has used it with phase-change inks for some time), the announcement of the Landa process (Nanography) has focused attention in this area.

The Landa process, still under development at the time of writing, claims to be a system that does not have the drawbacks associated with prior attempts at indirect printing. The claimed advantages derive from several technical features:

- The use of nanoparticles in a water-based ink (although many “conventional” inkjet inks contain such particles).
- The water content of the ink is substantially removed by heating it while it is on the transfer belt.



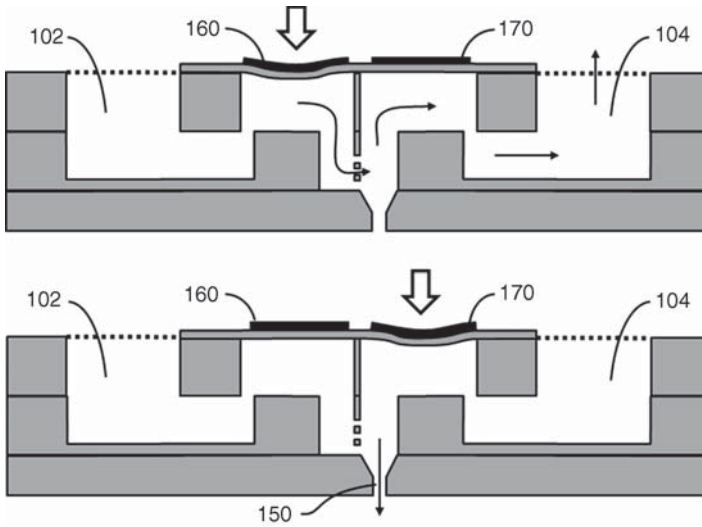


**Figure 16.14** Thin-film print-head with ink recirculation. US 2014/0078224 inkjet print head, Samsung. Ink is recirculated through chambers 102 and 104 or ejected through nozzle 150 by moving separate actuators 160 and 170 in appropriate sequences.

- The application of a cationic polymer by roller to the blanket prior to printing the anionic polymer containing ink allows drop spread on the otherwise hydrophobic surface long enough to remove carrier and increase viscosity, yet allowing 100% transfer to occur when the ink moves from the blanket to the receiving substrate.
- The ink film on the substrate is retained as a very thin film on the surface.

As well as the normal advantages of digital printing, these features lead to a number of claimed advantages over directly printing inkjet systems:

- Use of inexpensive water-based ink without soaking or distorting absorbent substrates
- More efficient drying using the heated blanket
- Extended color gamut (nanoparticles concentrated at surface)
- High gloss
- Media-friendly

These advantages are obtained at the expense of a complex system of belt and rollers (which may have a life) and a very specific chemistry and materials combination associated with the precoat, ink, and belt.

Other companies exploring indirect printing include: Canon, Ricoh, Hewlett-Packard, Seiko Epson, and Xerox.

## 16.6.7

**Wide Format Printing**

A significant shift in technique has been taking place, which enables the use of inkjet in applications previously the preserve of conventional offset processes. Ten to fifteen years ago, most inkjet printing was carried out by moving one or a few print-heads back and forth over substrates, which were generally wider than the print-heads. It is now becoming much more common to arrange print-heads so that print from one to the next is contiguous all the way across the width of the substrate. This shift has been enabled by a number of technical advances including:

- Features that have enhanced reliability, for example, ink recirculation.
- Heads designed specifically to fit together.
- The use of UV-curable and, more recently, latex inks, which allow drying/curing without removing large quantities of water or other carrier.
- A better understanding of how to deal with the joint between heads.
- Housekeeping and maintenance features that service print-heads, enabling them to keep operating or be swiftly replaced if faulty.
- Various forms of redundancy to allow for nozzle failure. This could involve additional printing from nozzles adjacent to a failed nozzle or extra print-heads.
- Enough computer power to process and move data to hundreds of thousands of nozzles in parallel.

## 16.6.8

**Failure Detection**

Inkjet printers with many thousands of nozzles require means to detect failure so that automatic or manual correction or intervention can be made. As inkjet printers become larger and are used in circumstances of continuous production, the detection of faults will become more and more important. One way of detecting problems is to observe test prints either by a human operator or by processing a captured image of the test print. This technique is usually used before a print run for a rough assessment of image quality or to trigger a cleaning cycle or print-head replacement. Observations of drops in flight using a strobe light and then processing captured images of drops in flight are often used to set up print-heads or assess print quality between print runs. Holographic observation of ink drops in flight [3], which can provide very accurate position and drop volume measurements over a large field of view, is a technique that may, in the future, provide an automated way of assessing print-head performance over time and under different circumstances. These techniques can provide valuable information about print-head performance and failure modes but, in the future, detection of an error as it occurs will be required. Two techniques are beginning to be implemented.

*In situ* optical drop detection can enable almost instant detection of error. Hewlett-Packard has recently introduced a system called *Backscatter Drop Detection* in which light from a surface-emitting diode illuminates the drops in flight and backscattered light from the drops is focused on a detector. The

detector signal is processed to assess the nozzle's fitness to print. If an error is detected, then adjacent nozzles can be used to at least partially compensate for the missing drops.

Another technique, developed by Océ, uses the piezoelectric transducer, used to eject the drop, also as a sensor [4]. Once a drop ejection has been actuated, the cavity behind the nozzle will display a characteristic acoustic response. The piezoelectric transducer, either the actuator or a second transducer, is used to detect this response. If the drop does not print properly, the acoustic response will change, and this can be used to take corrective action. This technique is sensitive enough to detect prefailure changes such as the presence of a small bubble within the print-head cavity.

## 16.7

### Future Trends for Print-Head Manufacturing

In the past, print-head manufacturers designed and manufactured their own print-heads. Print-head manufacturing requires a huge investment to provide capital equipment and establish production. With inkjet increasingly sharing the manufacturing technologies of the semiconductor industry, it is becoming possible to outsource at least part of the manufacturing process. As an example, it is believed that Hewlett-Packard now outsources over 50% of its thermal inkjet print-head dies from ST Microelectronics (STM).

This is particularly the case now that MEMS manufacturing processes can be incorporated into silicon processing as well as the fabrication of integrated circuitry. Therefore, there is the possibility of the emergence of fabless print-head companies, analogous to fabless chip companies. The Silverbrook Memjet print-head dies are made under a partnership with Taiwan Semiconductor: Silverbrook Research designs and models the print-head designs, which STM then produces.

At the moment, there are few print-head designs specifically for nongraphics applications. Print-head manufacturers are reluctant to invest in the design, development, tooling, and manufacture of devices specifically for digital fabrication applications as the customer base is fragmented and the market at present is unknown. Examples of current products include the FUJIFILM Dimatix D-128 DPN, Konica Minolta 128SNG-MB, and internal-use-only designs at Seiko Epson and Sharp.

Print-head manufacturers are addressing other issues for graphics applications. For piezoelectric print-heads, there is regulatory and environmental pressure to move toward using lead-free materials (instead of the current standard PZT). At the moment, it is difficult to achieve the current amount of piezoelectric activity from lead-free materials, but within a few years, we expect practical lead-free devices to become available.

Another trend is the development of thin-film piezo material deposition techniques enabling higher channel densities. Several of the existing print-head

manufacturers are using thin-film piezo, for instance, Seiko Epson, Panasonic, and Fujifilm, with others likely to follow.

## 16.8

### Future Requirements and Directions

Graphics applications for inkjet use inks suitable for printing on paper, both coated and uncoated, and nonporous substrates such as boards, ceramic tiles, plastics, and metals. Generally, the printed spot size needs to be correct for viewing at an appropriate working distance. The printed spot size is mainly a function of the ink interaction with the substrate.

For digital fabrication, the fluids used and the printed spot sizes required vary over a much wider range as compared to graphics applications. In some cases, the spot size must be very well controlled, for instance, when printing fine conductive tracks. For other applications, the drop volume is important, for instance, when printing microarrays for biomedical applications.

#### 16.8.1

##### Customization of Print-Heads for Nongraphics Applications

At present, little customization of print-head technology is practical or viable. Print-head manufacturers apply great development effort into improving their yields and manufacturing consistency and are reluctant to make even small changes. What is needed are print-heads designed for relatively easy customization in nozzle count and layout, drop size, fluid handling capability, and so on.

#### 16.8.2

##### Reduce Sensitivity of Jetting to Ink Characteristics

For virtually every print-head available at the moment, the fluid must be formulated to work within the chosen print-head. Substituting the print-head for a different model may well require changes to the fluid formulation to maintain acceptable jetting. This constrains the development of new applications.

When scientists focus on developing a new application, they wish to optimize the fluid for its function, not for the print-head. They are side-tracked into having to learn the special requirements of the inkjet process. Print-head manufacturers may supply a basic specification for fluids, for instance, the viscosity and surface tension limits, but this is often just a starting point on the way to satisfying the requirements for consistent jetting without satellite drops.

What is needed are print-heads that are much more tolerant of fluid formulation, both by the design of the print-head and by the control of its operating parameters. At the moment, there are some heads where the temperature of the print-head can be controlled to adjust the ink viscosity and bring it within the print-head operating range. In others, there may be control over the drive voltage

or the drive waveform shape. At present, experience and knowledge are required to find the best operating parameters for jetting fluids, but the hope is that at some stage in the future, this can be fully automated. In fact, research is ongoing in an attempt to predict the operating parameters directly from the fluid composition.

### 16.8.3

#### Higher Viscosities

A typical room-temperature viscosity that can be jetted with a piezo-based DOD inkjet print-head is 5–15 mPa·s. For some graphics applications, for instance, with UV-curable inks, it is not possible to formulate a suitable ink at such low viscosity. To overcome this limitation, some print-heads can be heated, for instance, to 50–100 °C, significantly reducing the fluid viscosity so that it can be successfully jetted.

However, this approach may not be suitable for some applications, where the materials in the formulation are temperature-sensitive. In addition, the fluid may be held within the heated print-head and fluid supply system for a considerable time, leading to accelerated aging or deterioration of the ingredients.

To eject higher viscosities from nozzles requires higher pumping pressures. It is possible to design print-heads to do this, but it adds to the cost per actuator and increases the nozzle-to-nozzle spacing. It also becomes more difficult to maintain a streamlined fluid flow through the nozzles, essential for consistent jetting.

Thermal or bubble inkjet is normally associated with low jetting viscosities, but some years ago, Canon developed a system incorporating a valve at the back of the channel to increase the jetting efficiency. Claims were made that fluid with a viscosity of 100 cP was jettable. The technology was not commercialized due to life issues – the valve was prone to breakage – but it did demonstrate that new designs could allow much higher viscosities.

There is perhaps more potential for CIJ systems to jet higher viscosities. At present, they are limited to 1–3 mPa·s. The patents for the Kodak Stream technology discussed in Section 16.5.1 suggest that 100 mPa·s may be possible, by using a suitable nozzle design and applied pressure to achieve the flow and increasing the “pinch” amplitude.

But, generally, today’s thinking is that the viscosity of jettable fluids will always need to be below about 100 mPa·s to satisfy the laws of physics for consistent jet breakup.

### 16.8.4

#### Higher Stability and Reliability

For graphics applications, it often does not matter if there are a few satellite drops, or if the jet breakup has some instability, causing small amounts of fluid to scatter around the main drop on the substrate.

Graphic images are often printed in such a way to deliberately mask jetting defects such as these, yet still produce acceptable image quality. However, this

may not apply to other inkjet and dispensing applications where fluid outside the “image” boundaries may be unacceptable and lead to low production yields.

With today’s devices, various tricks are used to enhance the jetting stability and performance, but with significant reductions in throughput. For instance, print-heads may be operated at a low drop frequency, at which the jetting will be more stable. To keep all of the nozzles working, drops may be fired from every nozzle and the print-head wiped after every scan of the substrate. Although this may succeed in maintaining jetting stability and the integrity of the image, excessive spitting of ink drops will be wasteful of fluid, and increased wiping of the nozzle plate may lead to excessive wear and a shortened print-head life.

#### 16.8.5

##### **Drop Volume Requirements**

The requirements for drop volume vary considerably for the current and future applications of inkjet. Today’s devices can jet drops from as small as 1–100 pl or more. But this is for different print-heads. At present, the range of drop sizes that can be jetted from the same nozzles is much smaller, and the number of drop-size increments is limited to five (Epson) or eight (Xaar).

Subpicoliter drops are needed for some applications. It is likely that current piezo print-head technology can generate drops down to 0.1 pl. More interesting is the electrostatic (electrospray) technology discussed in Section 16.4.2 that allows the formation of drop volumes down to 0.01 pl (10 fl); by adjusting the pulse width, it is also possible to continuously vary the amount of fluid deposited.

Perhaps, more important is not the precise drop volume but the stability of the drop production process and the variations from nozzle to nozzle. The drop volume from a single nozzle can also vary from drop to drop. The variation is likely to increase with the complexity of the ink formulation. Unfortunately, most methods used to measure drop volume, such as jetting many thousands of drops and then weighing them, measure only the average drop volume and not the variation.

The drop volume is also likely to vary from nozzle to nozzle due to small manufacturing variations that affect the efficiency of each drop generator and channel dimensions. In addition, crosstalk effects between channels can and will affect drop volumes according to the pattern of drops printed, and at the end of the print-heads, there may be end effects again causing variations in drop volume.

#### 16.8.6

##### **Lower Costs**

In most cases within a manufacturing or production environment, the inkjet system will be part of the overall factory processes and the print-heads will be used in a manner similar to that of machine tools. In this respect, the cost of the print-head will be amortized over its period of use.

However, there may be applications where the inkjet system is designed to be relatively low-cost, and installed and maintained by the user, in which case the cost of the print-head and its replacement becomes much more significant.

At present, the lowest print-head cost, in terms of cost per nozzle, is thermal or bubble inkjet. This has been taken to extremes by the Memjet technology from Silverbrook Research, where the very low cost per nozzle has been achieved by making the cell size (the area occupied by a single actuator, driver, and nozzle) as small as possible. Cell densities as high as  $48\,000\text{ cm}^{-2}$  are achieved. By assuming the rest of the print-head package is also low-cost, then this could be very valuable if high throughput using a relatively large number of nozzles is required.

There have also been proposals to use less expensive materials than silicon to construct print-heads. Eastman Kodak has proposed making a CIJ Stream head from sheets of polymers rather than silicon [5].

For the dominant technology outside home/small office – piezo DOD – a major way to reduce costs is to miniaturize the whole design. This is likely to require etched silicon channel plates and thin-film piezo. For relatively low-volume industrial print-heads, it is likely that the unit cost will remain the same or perhaps increase; the “cost saving” will be represented by an increase in the number of nozzles for the given price.

## 16.9

### Summary of Status of Inkjet Technology

As we have discussed here, inkjet technology has some key advantages for many applications, although there are some constraints. Some of the constraints are fundamental to inkjet, while others can be solved, provided there is sufficient incentive to fund the development and manufacture of new printing devices. Current trends in inkjet graphics printing are focused on achieving high image quality and high reliability, both welcome attributes.

We shall summarize here the improvements that might follow from our discussion of emerging technology.

First, let us consider the costs of inkjet technology. If the costs of the print-head and peripheral technology can be reduced, then almost certainly their use would become more widespread. Some would argue that the costs of inkjet are small as compared to that of an overall production system, with the benefit of flexible manufacturing and reduced waste. At present, the cost of even an off-the-shelf development system with a print-head, electronics, and ink system can approach USD 100 000.

When inkjet technology is capable of handling a wider range of fluids without extended fluid development, we will again see a greater market uptake for non-graphics applications. Such flexibility has not been required for graphics printing and only relatively recently has drawn the attention of research and development initiatives.

For some applications, a further breakthrough will occur when smaller drop volumes are available. Smaller drops are required to form narrower conductive tracks and finer feature sizes and deposit smaller amounts of functional materials. However, the ability to form smaller drops is only one step to a solution. To achieve the throughput possible with larger drops, the number of nozzles must be increased. It is also much harder to achieve controlled drop trajectories to the substrate with smaller drops.

Therefore, we shall hopefully see the day in the near future when scientists and engineers wishing to develop a new application do not have to become inkjet experts first. Print-heads, drive electronics and software, and ink supply systems can be sourced for graphics applications. What industry now needs are the tools for their world, enabling them to focus on the application rather than on inkjet development.

### References

1. Murata, K., Matsumoto, J., Tezuka, A., Matsuba, Y., and Yokoyama, H. (2005) Super-fine ink-jet printing: toward the minimal manufacturing system. *Microsyst. Technol. Micro-Nanosyst.-Inf. Storage Process. Syst.*, **12** (1–2), 2–7.
2. Paine, M.D., Alexander, M.S., Smith, K.L., Wang, M.J., and Stark, J.P.W. (2007) Controlled electrospray pulsation for deposition of femtoliter fluid droplets onto surfaces. *J. Aerosol Sci.*, **38**, 315–324.
3. Martin, G.D., Castrejón-Pita, J.R., and Hutchings, I.M. (2011) Holographic measurement of drop-on-demand drops in flight. Proceedings of the Society of Imaging Science and Technology NIP27: International Conference on Digital Printing Technologies and Digital Fabrication 2011, pp. 620–623.
4. Wijshoff, H. (2010) The dynamics of the piezo inkjet print-head operation. *Phys. Rep.*, **491** (4–5), 77–177.
5. Vaeth, K., DeMejo, D., Dokyi, E., Evans, M., Jech, J., Lehmann, M., Link, R., and Sechrist, J. (2007) MEMS-based inkjet drop generators fabricated from plastic substrates. Proceedings of the Society of Imaging Science and Technology NIP23: International Conference on Digital Printing Technologies and Digital Fabrication 2007, pp. 297–301.



## Index

### a

absorption 391  
 acoustic drop ejection (ADE) 429  
 acoustic pressure waves 341  
 adaptive mesh refinement 175  
 additive manufacturing 374  
 advanced functional materials 378–379  
 advancing contact angle 200  
 aerodynamic effects 47–48, 424  
 anti-kogation agents 155  
 apparent contact angles 288–289  
 atomic force microscopy 388  
 axisymmetric inkjet simulation  
 185–194

### b

back shooter structure 63  
 backscatter drop detection 438  
 base viscosity 342–344  
 binary image analysis method  
 330–331  
 binary solvent mixtures 259–263  
 biocides 154  
 biological analysis 393  
 biomacromolecule 411–412  
 bioprinting 393  
 block co-polymer 119  
 body force 19, 22  
 boiling mechanism 58–63  
 Bond number 252  
 bridging flocculation 150–151  
 Brownian motion 159  
 bubble formation 58  
 Buckingham Pi theorem 210–212  
 bulge formation 220–221  
 bulge instability 235  
 buoyancy force 161

### c

CAH, *see* contact angle hysteresis (CAH)  
 canonical driving waveform 189–190  
 capillary break-up 220  
 capillary deceleration 99–101  
 capillary number 252  
 carbon nanotube (CNT)–polymer composites  
 137  
 cavitation 59, 66–68  
 centrifugal sedimentation 164  
 ceramic inks 406  
 chain growth polymerization 118  
 chemical analysis 381  
 chemically inhomogeneous surfaces  
 306–307  
 CIJ printing, *see* continuous inkjet (CIJ)  
 printing  
 coefficients of viscosity 22  
 coffee-ring effect 252–268  
 colloidal particles 144–165, 274  
 commercial software packages 25–26, 170  
 commercialization process 31  
 complex actuation pulse design 85–88  
 computational fluid dynamics (CFD) 25–28,  
 176–177  
 computer simulations 225  
 condensation 222  
 confocal microscopy 325–326, 328–330  
 constrained actuation pulse design 84–85  
 contact angle hysteresis (CAH) 200, 264,  
 289–290, 301–305  
 contact angle observation 385  
 contact angle 285  
 contact line motion 269  
 continuous inkjet (CIJ) printing 2–5, 30–31,  
 43–45, 74–75, 93–102, 132–134, 186–189,  
 419, 428–429

- continuous jets 30–31
  - continuum surface force (CSF)
    - approach 287
  - continuum-based droplet simulation
    - modeling 282–284, 286–288
  - conventional printing methods 1
  - coordination polymerization 118
  - Cox Merz rule 346
  - critical spread length 227–228
  - crosstalk 45–47
  - cured ink adhesion 381
  - cytotoxicity tests 393
- d**
- deep reactive ion etching (DRIE) 428
  - density 15–16
  - depletion flocculation 151–152
  - Derjaguin, Landau, Vervey, and Overbeek theory (DLVO theory) 144, 147, 149
  - diffuse interface droplet simulation
    - models 294–296
  - Diffusive Wave Spectrometer (DWS) 350
  - digital printing process 2
  - dimensional analysis 211
  - dimensionless groups 8–9
  - dimensions 14–15
  - dispersions 155–161
  - DLS, *see* dynamic light scattering (DLS)
  - DNA grafting 265
  - DNA stretching 267
  - DOD printing, *see* drop-on-demand (DOD) inkjet printing
  - drag force 161
  - drop coalescence 220–222, 225–228, 230–234
  - drop deposition interval 242–244
  - drop formation 124, 340
  - drop impact behavior 226–228, 373, 375–376
  - drop placement errors 423
  - drop spacing 221, 234, 238–242
  - drop speed effect 203, 206
  - drop speeds 5
  - drop volume 421–424
  - drop–bead coalescence 236–237
  - droplet drying 251–275
  - drop-on-demand (DOD) inkjet printing
    - 2–5, 31, 94–95, 102–110, 131–132, 134, 189–194, 201, 419, 425–429
  - drops on substrates 199–217
  - Duineveld's model 245
  - dye-based inks 142–143
  - dynamic contact angle 291–293
  - dynamic light scattering (DLS) 155–156
  - dynamic viscosity 7
- e**
- edge detection method 331–336
  - electrical tests 373, 389–390
  - electrophoretic mobility 156–157
  - electrostatic drop-on-demand inkjet 429
  - electrostatic forces, *see* electrostatic drop-on-demand inkjet
  - electrostatic repulsive forces 145–146
  - ELISA detection technique 393
  - ellipsometry 372, 390
  - energy conservation equations 22–24
  - equilibrium contact angle 199–200
  - Eulerian-based interface tracking 33
  - evaporating drop radius 216
  - evaporating droplets 252–265
  - extensional behavior 351–356
  - extensional viscosity 8, 96, 160, 343, 352
- f**
- FENE model, *see* finitely extensible nonlinear elastic model (FENE)
  - FENE-CR model 191–193
  - Fick's first law 254
  - final droplet velocity 99–102
  - final printed surface 379–380
  - finite difference method 176
  - finite element analysis 282
  - finite element method 176
  - finite volume method 176
  - finitely extensible nonlinear elastic model (FENE) 129–130, 191–194
  - Flattened-pancake model 214
  - flextensional devices 434
  - Flow3D software program 51, 194–195, 288
  - fluid delivery device 420
  - fluid dynamics 20–25
  - fluid flow governing equations 24–25
  - fluid mechanics 13–53
  - fluid–structure interaction (FSI) 34
  - free-energy model 299
  - free-surface analysis (FSA) 32–35, 37, 41
  - free-surface flow boundary conditions 283–284
  - FSA, *see* free-surface analysis (FSA)
  - FSI, *see* fluid–structure interaction (FSI)
  - function delivery 376–379
  - functional printing 94

**g**

galactomannan heterogeneous polysaccharides 134  
 gases 14  
 gel permeation chromatography (GPC) 122  
 glycol ethers 154  
 GPC, *see* gel permeation chromatography (GPC)  
 graphene-polymer composites 137  
 graphical inkjet printing 94, 368–370, 378, 398  
 gravitational force 161  
 gravitational sedimentation 163

**h**

hard-sphere dispersions 157–159  
 head droplet formation 103–105  
 heat control 64–65  
 hindered settling 162  
 Hoffman-Voinov-Tanner law 291  
 holography 320, 322–325  
 HP Inkjet Web Press 57  
 humectants 153–154

**i**

imbibition 386–387  
 IMI, *see* ink-media interaction (IMI)  
 impact capillary length 214  
 impact effects 424  
 indirect inkjet printing 436–437  
 industrial applications 88–89  
 inelastic scattering 392  
 ink and substrate selection 251–252  
 ink channel behavior  
 ink formulation 340  
 ink recirculation 436  
 ink residue scorching 67–68  
 ink supply system 340  
 inkjet fluids 339–362  
 inkjet print-heads 141  
 inkjet systems 29–34, 36–38, 42–52  
 inkjet technology limitations 421–424  
 ink-media interaction (IMI) 36, 48–51  
 in-line digital holography 321  
 input power characteristics 64  
 interface formation model 285–286  
 interfacial hydrodynamics 199  
 isothermal evaporation 259

**j**

jet directionality 423  
 jetting 159–160  
 jetting fluid constraints 421

jetting process variables 339  
 jetting simulations 169–170, 172–177, 194–195

**k**

Knudsen number 254  
 Krieger-Dougherty equation 157

**l**

LabVIEW 331–334  
 Lagrangian equations 20–21  
 Lagrangian finite-element method 186, 191  
 Lagrangian interface tracking 34  
 Landa process 436  
 lattice Boltzmann simulation 296–307  
 LB, *see* lattice Boltzmann simulation  
 length scales 9–11, 20  
 limiting mode evaporation 258–259  
 line formation dynamics 222  
 line printing model 236–246  
 line printing 219–225  
 linear viscoelasticity 347–350  
 liquid drops on liquid surfaces 385  
 liquid drops on solid surfaces 382–384  
 liquids 14  
 liquid-vapor interface 254–256  
 local humidity 273  
 long drop throw distance 74  
 long wavelength approximation 177–178  
 long-term behavior 380–381

**m**

Marangoni flows 252, 260–263  
 Mark-Houwink-Sakurada equation 123  
 mass conservation equations 21  
 MatLab 335–336  
 maximum spreading diameter 211–213  
 mechanical tests 370, 378, 388–389  
 MEMS techniques, *see*  
 Micro-Electro-Mechanical Systems (MEMS)  
 fabrication techniques  
 mesh resolution 175  
 mesoscopic methods 296  
 metallic inks 404–405  
 Micro-Electro-Mechanical Systems (MEMS)  
 fabrication techniques 419, 431–434  
 microscale ink-medium model 52  
 millimeter-sized water drops 226  
 Mk2 Trimaster device 352–353, 358  
 molar mass distribution 120–121  
 molecular dynamics 296  
 molecular weight determination 120–122  
 molecular weight stability studies 131–134  
 momentum conservation equations 21–22

- moving contact-line droplet simulation 284–286
- Multi Jet Fusion technology 57–58
- multiphase flow and wetting 300–301
- multiphase Shan–Chen LB model 300
- multi-scale and multidisciplinary modeling 31
- n**
- nanochromatography 266–267
- nanindentation 388–389
- nanowire assembly 266
- Navier–Stokes and continuity equations 282
- necking stage dynamics 222–224, 230–234
- net interaction energy curve 147–149
- Newton's law of viscosity 17
- Newtonian fluids 17
- non-graphics applications 440
- non-Newtonian fluids 17, 35–36
- no-slip boundary condition 16, 284–285
- o**
- Ohnesorge number (Oh) 8, 9, 127, 182
- one-dimensional inkjet simulation 177–185
- optical tests 370, 372–376, 378, 390–392
- p**
- paper 367, 380
- parameter space exploration 183–184, 187
- particle character 269, 271–272
- particle migration 268
- particle transport 268
- patents 78
- Péclet number 158
- pharmaceutical development 375
- phase change analysis (PCA) 35
- phase field methods 295
- physical/mechanical tests 370, 378, 388–389
- Piezo Axial Vibrator (PAV) rheometer 349–351
- piezo inkjet (PIJ) print-head 5, 37–38, 57–58, 427–428
- pigmented inks 142–143
- pigments and additives 341
- PIJ print-head, *see* piezo inkjet (PIJ) print-head
- pinch-off and tail breakup 108–110
- PMMA 133
- poly(3,4-ethylenedioxythiophene)polystyrene sulfonate (PEDOT:PSS) 136
- polymer architecture 135
- polymer interactions 149–154
- polymers 117–137
- porous media modeling 51
- postprocessor subprogram 28
- prejetting surface quality 367–373
- preprocessor 26, 28
- pressure and heat generation 66–68
- pressure 19
- printed electronics 371–373, 407–408
- printed image formation 219–220
- print-head designs 340
- print-head performance 356–360
- print-heads 57–89, 419–444
- projectile problem 209–210
- protein printing 380–381
- q**
- quantum dots 406–407
- r**
- Radio Corporation of America (RCA) 77
- Raman scattering 392
- Raoult's law 259–260
- rapid boiling 58
- Rayleigh Plateau instability 93–98, 112–114
- Rayleigh stability theory evaluation 180–183
- Rayleigh's linear stability analysis 328
- RCA facsimile concept 77
- reactive inkjet printing 375–376
- rebound phenomenon 62
- receding contact angle 200
- refill process 42
- reptation 124
- residual oscillations 82–83
- resonant frequency 81
- resting time effect 293–294
- Reynolds number (Re) 8, 127
- Reynolds's lubrication theory 177
- rheology modifiers 153
- rheology 157, 339–346, 356–360
- roof shooter structure 63
- rough surfaces 305–306
- s**
- satellite formation 99
- sedimentation/settling 160–165
- sequestering agents 155
- sessile droplet drying 252, 258–260, 267, 274
- shadowgraphy 186, 314–315
- sharp-interface models 282–288
- shear strain rate 7
- shear thickening behavior 129, 159, 400
- shear thinning behavior 129, 159–160, 400

- shear viscosity behavior 157  
 sheet resistance 390  
 Silverbrook Memjet print-head 439  
 simple jetting model 178–180  
 single solvent evaporation 252–259  
 slender-jet approximation 177  
 solid segregation 272–273  
 solid–vapor interfacial tension 384  
 solutal Marangoni flow 263  
 solver subprogram 28  
 spliced model 189  
 spreading factor 203–204, 206  
 stability regimes 244–246  
 static light scattering 121  
 steady two-dimensional flow  
 284–285  
 step-growth polymerization 118  
 steric stabilization 149–150  
 storage buffers 154  
 strobe illumination 317–319  
 substrate patterning 273  
 super-hydrophobic property 215–216  
 surface characterization 373–393  
 surface chemistry tests 368–385  
 surface forces 19  
 surface tension 6, 18, 208–209,  
 381–382  
 surface wettability effect 206–207,  
 424  
 surfactants 152–153
- t**  
 Tanner’s law 206  
 technological applications 251  
 thermal inkjet (TIJ) print-head 38–42,  
 58–71, 426, 439  
 theoretical model 58–59  
 thermal inkjet (TIJ) printing 31, 38–43,  
 57–71, 425–426, 432  
 thermal Marangoni flows 260–262  
 thermal/bubble-jet process, *see* thermal  
 drop-on-demand inkjet  
 thermoplastics 117  
 thermosets 117  
 three-dimensional (3D) printing 220–222,  
 265, 374–375, 399–404  
 three-dimensional inkjet simulation  
 194–196
- TIJ print-head, *see* thermal inkjet (TIJ)  
 print-head  
 timescales 11  
 tissue engineering 412–414  
 tonejet ink 435  
 Trimaster Mk4 device 355  
 Trouton ratio 8, 343  
 two inkjet-printed drops 230
- u**  
 units 14–15
- v**  
 van der Waals attractive forces 144–145  
 velocity 19  
 viscoelasticity 344–346  
 viscosity 6–8, 16–17, 208–209  
 viscosity modifiers 153  
 viscosity–shear rate profile 128  
 viscosity–temperature profile 16, 128  
 viscous dissipation vs. surface tension 208,  
 213–214  
 Vision Assistant 332  
 volume of fluid (VOF) method 33, 177,  
 286–288
- w**  
 wall correction factor 162  
 Washburn equation 387  
 water evaporation 69–71  
 Weber number (We) 8, 101, 126–127, 178  
 Weissenberg number (Wi) 125, 160  
 Wenzel’s equation 264  
 wide format printing 438  
 work of cohesion 382
- x**  
 Xaar 1001 print head 436
- y**  
 Young’s equation 199, 264  
 Young–Dupré equation 383–384
- z**  
 zero-thickness surface 282  
 zeta potential 156  
 Zimm relaxation time ( $\lambda_z$ ) 126  
 Zimm type model 125–129

# **WILEY END USER LICENSE AGREEMENT**

Go to [www.wiley.com/go/eula](http://www.wiley.com/go/eula) to access Wiley's ebook EULA.